Forward Physics and Scintillating Fibre Trackers at the Large Hadron Collider

Jan de Boer

Niels Bohr Institutet
Det Natur- og Biovidenskabelige Fakultet

KØBENHAVNS UNIVERSITET

LHCb Detector Group

CONSEIL EUROPÉEN POUR LA RECHERCHE NUCLÉAIRE

Supervisor : Jørgen Beck Hansen | Niels Bohr Institute
External Supervisor : Sune Jakobsen | CERN Detector Technologies

May 2020

Submitted as a Master Thesis in Physics
Faculty of Science, University of Copenhagen

I... a universe of atoms,
an atom in the universe.

- *Richard P. Feynman*

Abstract

This thesis reports work related to scintillating fibre trackers. Successively presented are a study on attenuation length measurements of scintillating fibres, the development of a detector control system, a performance study of services, usage of a detector control system during physics data taking and the corresponding analysis of elastic scattered protons.

The Scintillating Fibre (SciFi) tracker is part of the Upgrade I of the LHCb detector that is currently carried out during the second Long Shutdown period of the Large Hadron Collider (LHC). A systematic study was carried out on attenuation lengths measurements of scintillating fibres used for the SciFi tracker. To obtain a percent level precision, needed to determine a possible aging effect, it was shown that a single measurement per fibre does not suffice and multiple measurement are required.

The development of SciFi detector control system has undergone a first iteration from the prototype stage to the assembly and commissioning of final detector components, that is ongoing in the assembly hall at point 8. The controls of low-voltage power supplies have substantially improved by the use of a newly installed OPC-UA server, which to date has maintained a stable connection. The following detector services and front-end components are monitored: Novec cooling, dry gas, vacuum, heating wires, SiPM temperature, SiPM voltage and front-end board temperatures. The monitoring on the first c-frame has been essential for an initial performance study of the services. The obtained results from the analysis have indicated that there is satisfactory control over the SiPM temperature and the cold box environment. Furthermore, it provides a first input to the settings needed for operating the final detector.

In October 2018, data of elastic scattered pp was taken with the Absolute Luminosity For ATLAS (ALFA) detector, a small scintillating fibre tracker. The experiment was conducted at the LHC with $\sqrt{s}$ = 900 GeV and β^* = 100 m collision optics to access the Coulomb-Nuclear-Interference region. Special collimation settings were used to ensure good beam background conditions and has led to a successful data taking campaign. The setup of the optics should enable for measuring the total cross section, σ_{tot}, via the optical theorem and a determination of the ρ parameter, the ratio between the real and imaginary scattering amplitude. The ALFA detector might possibly be sensitive deeply enough into the Coulomb region to enable for a precise measurement of the absolute luminosity.

A first study on the collected data has formed the basis for the analysis framework that ultimately should lead to the extraction of the physics parameters. From a thorough inspection on the layer efficiencies of the detector it can be concluded that the performance of the detector during data taking was satisfactory. No indications of significant aging and radiation damage was observed and the few layers showing low efficiencies were likely to have been affected by non-optimal timing configuration of the electronics. The convoluted detector resolution is found to have a dominant contribution from multiple scattering due to the unusual low energy. Inspection of data plots has revealed a feature in the form of an ellipse orientated perpendicular to the main correlation axis for the x coordinates. As a consequence the current selection criteria of elastic candidates will have to be revisited. A thorough simulation study has shown the dependence of the elastic signal on the beam spot width, divergence, and detector resolution, all in combination with the design optics.

Acknowledgement

A fruitful period of nurturing myself in the field of experimental high energy physics has come to an end by the hand in this work. Not only has it been an exciting dive into the world of particle physics but it also a very interesting encounter with the international culture that came along. I have been privileged to find myself in inspiring atmospheres, both at the Niels Bohr Institute, the ALFA as well as the SciFi community. Therefore, I would like to express my gratitude to the people I encountered in these environments. A special thanks to Lea Halser and Ida Storehaug for the much appreciated corrections and suggestions during the early stage of this work.

I would like to thank my supervisor Jørgen Beck Hansen for being generous with his support in building up the analysis. It has given me a more firm set of coding skills along with abstract approach, I have broadened my knowledge on elastic physics and it has given me a good taste of the numerous effects to be taken account for during analysis. I would like to thank my other supervisor Sune Jakobsen for his support and valuable feedback that helped to form the document. Also, a thanks for offering me the chance to experience the process of building a detector and teaching me practical skills along the way. It has made me even more aware of the great efforts put in place to enable for successful data taking and further established my interest in scintillating fibres.

Preface

The principle scope of this thesis is formed by scintillating fibre trackers in high energy physics. In the work presented, this topic is widely covered from measurements on properties of scintillating fibres to the analysis of data from a scintillating fibre tracker. It elaborates on a number facets one encounters along the way to the realisation of the aforementioned. The outline of the thesis successively deals with the consecutive steps from a physics case to a result. It is intended to be read as a single piece of work, but can alternatively be divided in two distinct parts. The two parts are constituted by the LHCb SciFi tracker and the ATLAS-ALFA detector, both part of experiments conducted at the LHC at CERN. The former is currently build up during the second Long Shutdown period of the LHC, while the latter is operational and has been used during a physics campaign in autumn 2018.

As a technical student at the CERN LHCb Detector Group, the work done on the SciFi Detector Control System is of importance to the successful assembly and operation of the new detector. As a master student at the High Energy Physics group at the Niels Bohr Institute, the work done on the initial setup of the analysis is of relevance in gaining understanding of elastic physics at an extraordinary low energy. The suitable title *'Forward Physics and Scintillating Fibre Trackers at the Large Hadron Collider'* applies to both detectors and intends to emphasize the cohesive character of the presented works.

Contents

List of Abbreviations

ALFA	Absolute Luminosity For ATLAS
ALICE	A Large Ion Collider Experiment
ATLAS	A Toroidal LHC ApparatuS
BCM	Beam Conditions Monitor
BSRT	Beam Synchrotron Radiation Telescope
CMS	Compact Muon Solenoid
CP	Charge Parity
CNI	Coulomb Nuclear Interference
CGC	Color Glass Condensate
CTP	Central-Trigger Processor
CWG	Collimation Working Group
DAQ	Data AcQuisition
DCS	Detector Control System
EW	ElectroWeak
ECS	Experiment Control System
FEE	Front-End Electronics
FMO	Froissaron and Maximal Odderon
FSM	Finite State Machine
G-APD	Avalanche PhotoDiode in Geiger mode
HLT	High Level Trigger
HV	High Voltage
IP	Interaction Point
IR	Insertion Region
L0	Level 0
LED	Light Emitting Diode
LHC	Large Hadron Collider
LHCb	Large Hadron Collider beauty
LINAC	LINear ACcelerator
LS2	Long Shutdown 2
LUCID	LUminosity measurement using Čerenkov Integrating Detector
LV	Low Voltage
MAMPT	MultiAnode PhotoMultiplier Tube
MBTS	Minimum Bias Trigger Scintillators
MD	Main Detector
NOVEC	NOrthern Virginia Electric Cooperative

OD	Overlap Detector
OPC-UA	Object Linking and Embedding for Process Control Unified Architecture
PDFs	Particle Distribution Functions
PDG	Particle Data Group
PMMA	PolyMethylMethAcrylate
PMT	PhotoMultiplier Tube
pp	proton-proton
PS	PolyStyrene (PS)
PS	Proton Synchrotron
PSB	Proton Synchrotron Booster
PT	P-Terphenyl
QCD	Quantum ChromoDynamics
QED	Quantum ElectroDynamics
QFT	Quantum Field Theory
RCM	Remote Controllable Unit
RF	Radio Frequency
RFQ	Radio Frequency Quadrupole
SCADA	Supervisory Control And Data Acquistion
SciFi	Scinitillating Fibre
SiPM	Silicon PhotoMultiplier
SM	Standard Model
SMOG	System for Measuring Overlap with Gas
SPS	Super Proton Synchrotron
TCLA	Target Collimator Long Absorber
TCP	Targer Collimator Primary
TCSG	Target Collimator Secondary Graphite
TCT	Target Collimator Tertiary
TOTEM	TOTal cross section, Elastic scattering and diffraction dissociation Measurement
TBP	TetraPhenyl-Butadiene
UV	UltraViolet

Chapter 1

Introduction

Since ancient times humanity has been wondering about the fundamental structure of the universe. In the past century, tremendous developments in our understanding of fundamental physics paved the way for a new era in which our perceptions of the nature of space, time and mechanics were revolutionized. Decades of effort ultimately led to a detailed picture of fundamental matter. Particle physics has made important contributions to the understanding and development of theoretical models. The Standard Model describes the physical world by elementary particles and their interactions and is the most successful theory to date.

The 2012 discovery of the Higgs boson meant the definite completion of the framework in which three fundamental forces, the electromagnetic, weak and strong force, are described. Even though the Standard Model currently offers the best description of the universe, it does not provide a complete description. In particular, experiments have found the neutrinos to have mass which is in contradiction with the Standard Model prediction and the remaining fourth force, the gravitational force, is not included in the theory. In general, the origin of the neutrino masses, the hierarchy problem, baryon asymmetry, dark matter and dark energy remain open questions in fundamental physics.

The Large Hadron Collider (LHC) at Conseil Européen pour la Recherche Nucléaire (CERN) is the most energetic accelerator in the world. The LHC offers a window to study the processes that took place in the earliest stages of the universe. By recreating these conditions, physicists hope to find the answers to some of the aforementioned questions. Four large experiments take place at different locations along the 27 km circular accelerator: ATLAS, CMS, ALICE and LHCb. The ATLAS and CMS experiments have jointly announced their discovery of the Higgs boson. With the most energetic accelerator at hand the experiments continue to explore the energy frontier. The ongoing studies can be mainly categorised as precision studies of Standard Model processes and searches for new physics beyond the Standard Model. In studies where there is a tension between the prediction and experimentally observed values, the former may be a lead to the latter.

Open questions related the lack of symmetry between matter and anti-matter are partly addressed through the study of CP violation by the LHCb experiment. The initial core of the experimental program of LHCb is formed by precision measurements on CP violation in the c and b quark sector as well as rare decays of B hadrons [1]. The physics is predominantly produced in the forward region, hence the detector holds a special single-arm forward spectrometer design. The program further extends to measurements of rare decays of C hadrons as well as tests of lepton universality. Various crucial measurements are currently statistically limited and to improve the precision of the studies, the luminosity of the experiment will be increased upon completion of the ongoing second Long Shutdown period of the LHC [2]. In order to meet the demands that come with the new conditions, the LHCb detector is currently subject to a major refurbishment, referred to as Upgrade I. The new upstream Scintillation Fibre (SciFi) Tracker forms a major part of this upgrade, which is part of the subject of this thesis.

The ATLAS experiment holds a special set of forward detectors, Absolute Luminosity For ATLAS (ALFA), that are dedicated to study processes in a region where the theory can not provide precise descriptions due to the lack of perturbative methods. Among other things, the ALFA detectors can study elastic scattered protons which appear under very small angles in the forward regions. Hence, the detectors are placed approximately 240 m downstream of the interaction point to be able to measure the scattered protons. Elastic scattering is worthwhile to study since it provides measurements of the total cross section, σ_{tot} and ρ parameter, the ratio between real and imaginary part of the forward scattering amplitude. The total cross section is needed for many analyses and both of these parameters are relevant for the design of a future hadron collider. Recent measurements on these parameters have further established a tension between the results and predictions by theory, underlining shortcomings in current used models [3]. A new elastic physics campaign at a center-of-mass energy of 900 GeV has been carried out that should help to discriminate between newly proposed models.

In High Energy Physics the reconstruction of the trajectories of electrically charged particles, called tracking, is an integral part of event reconstruction. Tracking is an important task in which precise position measurements provide vertex and momentum information. For tracking detectors there are three major technologies: silicon detectors, gaseous detectors and fibre trackers. The measurement closest to the interaction point are usually silicon detectors that aim to measure the primary interaction vertices and secondary vertices from long lived particles. The second class of tracking aims to measure the momentum of charged particles by determining the curvature in a magnetic field. The SciFi tracker belongs to the second class and is composed of scintillating fibres. The ALFA detector is also a fibre tracker made from scintillating fibres, a special type of tracking detector since it does not belong to neither of the above classes. Its precise position measurements are used to reconstruct the four-momentum transfer in the elastic interactions. ALFA and SciFi share their active material, scintillating fibres, and are both forward detectors. The former is likely the smallest type of scintillating fibre tracker covering a sensitive area of only tenths of cm^2, whereas the latter is the largest sized tracker of this technology with a total sensitive area of 340 m^2.

This thesis is divided in four major parts that hold the following titles : Physics, Experimental Setup, Control Monitoring and Operation and is concluded with Data Analysis. The theoretical framework and physics case of elastic physics at a center-of-mass energy of 900 GeV will be introduced in the first part. The second part provides the necessary background information on the Large Hadron Collider, Scintillating Fibres, the SciFi tracker and the ALFA detector. In the third part work on the development of supervision firmware of the SciFi tracker will be presented together with a performance study of the services. The operation of ALFA detector during elastic physics campaign is also presented and provides information on the data taking conditions. The work is concluded with the data analysis of elastic scattered protons at center-of-mass energy of 900 GeV and 100 m optics.

Part I

Physics

Chapter 2

Theory

This chapter provides an introduction to the theory part of the physics that is under study of the elastic physics program at a center-of-mass energy of 900 GeV. It contains a brief introduction of the Standard Model and the relevant forces. This is followed by an explanation of the kinematics involved in proton collisions. Especially, elastic scattering will be clarified along with a theoretical model and expression for the elastic differential cross section. Finally, the physics case for proton-proton elastic scattering at a center-of-mass energy of 900 GeV is presented. Unless otherwise stated, the presented information in this chapter is obtained from [4].

2.1 The Standard Model of Particle Physics

Particle physics studies the nature of the universe through the fundamental constituents of matter and the forces acting between them. Since the development of the theory in the early 1970s, these have been successfully described by the Standard Model (SM). The SM is a theory that contains two types of elementary particles: fermions with half integer spin and bosons with integer spin. The SM consists of 24 types of fermions, which are equally divided into quarks and leptons. Both quarks and leptons are subdivided following a hierarchy of three 'generations'. Each generation consists of a pair of leptons, a pair of quarks and for each particle there is an associated anti-particle. All known matter in the universe is made up out of fermions. The lepton and quarks all have a spin of S = 1/2. The fermions are complemented by gauge bosons responsible for the force carriers of the electromagnetic, weak and strong forces and the Higgs boson, responsible for particles to obtain their masses. The SM is able to describe three fundamental forces. Listed in order of decreasing strength they are: the strong force, the electromagnetic force and the weak force. Characteristic time scales of processes due to the strong force are within 10^{-22} seconds, electromagnetic interactions take place between 10^{-14} and 10^{-20} seconds. Processes due the weak interaction are relatively slow and typically occur within 10^{-8} and 10^{-13} seconds, with way faster and slower exceptions [5].

The interactions of particles due to a particular force acting between them are mediated by the gauge bosons, also called force carriers. All force carriers of the forces contained in the SM have a spin of S = 1. The gluon is the force carrier of the strong force. There are 8 gluons associated to the strong interaction, which are all massless particles. The photon is the force carrier of the electromagnetic force, the W^+, W^- and Z bosons are the force carrier of the weak force. Under gauge symmetry all four force carries should in principle be left massless. Due to the symmetry breaking induced by the Higgs field the W^+, W^- and Z obtain their masses, whereas the photon is left massless. The range of the weak and strong interaction are of very short range, 10^{-18} and

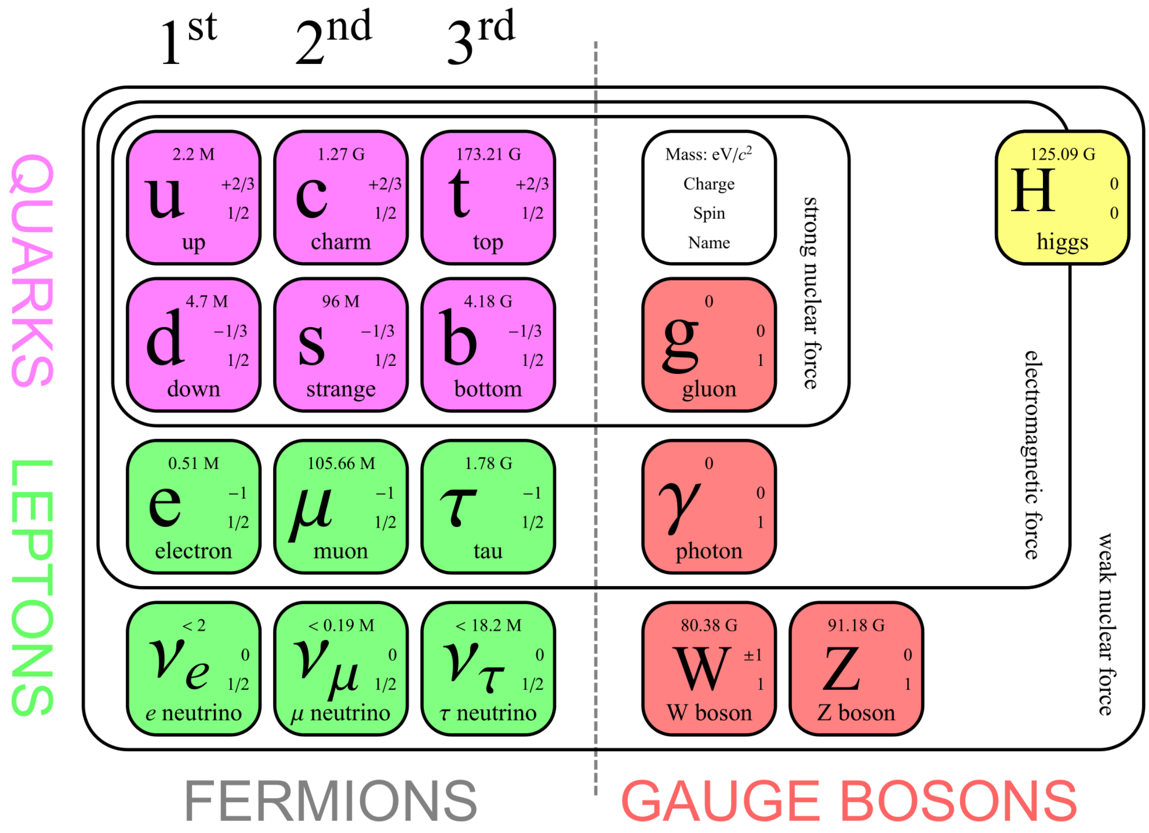

Figure 2.1: The standard model particles, force carriers and the Higgs boson [6].

10^{-15}, respectively. The range of the electromagnetic interaction is in principle of infinite range. The fourth known force in nature, the gravitational force is not yet included in the SM. The postulated force carrier of gravity is the gravition, a massless particle of spin S = 2. The inclusion of gravity into a single theoretical framework containing all forces is subject to many studies.

The electron e^- is probably the most well known particle of the lepton family. The electron neutrino ν_e is an elusive particle associated to the electron, forming a doublet. The lepton family is completed by two other doublets, namely the muon μ^- and its muon neutrino ν_μ and the tau τ^- and its tau neutrino ν_τ. The electron, muon and tau carry a negative charge of -1e, where e is the magnitude of the elementary charge carried by a single proton or electron, the neutrinos are neutrally charged. The electron, muon and tauon interact through the electromagnetic and the weak force, while the neutrinos only interact through the weak force. The properties of a doublet is therefore identical for every generation. The three generations are only distinctive through the masses of the particles, the 1st generation in the hierarchy is the lightest. The electron is the only stable particle. The absolute masses as well as the hierarchy of the neutrinos have yet not been determined. As stated above, for each particle there exists an anti particle, which is almost identical, except it carries the opposite charge of the particle. The positron e^+ is the anti-particle of the electron, the anti particle of the muon, tau and all neutrinos do not have their own name and are referred to with an additional anti- in front of their names.

Similar to the leptons, the quark family is made up out of three generations. Each generation is again represented by means of a doublet. The first and lightest doublet is made up from an up quark (u) and a down quark (d). The quark family is completed by doublets of a charm (c) complemented by a strange (s), and of a top (t) complemented by bottom (b). The up, charm and top carry a charge of +2/3e, the down, strange and bottom carry a charge of -1/3e. The doublets are mutually identical, except for their masses by which they are ordered into the three generations. The hierarchy is identical to that for the leptons. Only quarks of the first generation are stable, quarks found in the second and third generation have (very) short life times. For every quark there is exists anti-quark, which are identical particles of opposite charge. Unlike leptons, quarks carry color charge through which they couple to the strong interaction. Quarks can therefore interact through the electromagnetic force, weak force and the strong force. As a consequence of the nature of the strong force no isolated quark has been ever observed. Composite quarks held together by the strong force are collectively known as hadrons. The proton and neutron are perhaps the most well-known hadrons. They are part of a group called baryons, build up from three quarks. Another group among the hadrons are the mesons, consisting of a quark anti-quark pair. Recently also tetraquarks and pentaquarks have been observed in experiments, consisting of 4 and 5 quarks, respectively [7, 8].

2.2 Coulomb and Nuclear Force

The SM describes the fundamental particles and their interactions through the mathematical framework of Quantum Field Theory (QFT). QFT is concerned with phenomena at small distances up to the size of the atom and at velocities near the speed of light. It therefore combines two pillars of modern physics: quantum mechanics and special relativity [9]. In this formalism the particles are treated as excitations of underlying fundamental fields. For a field to interact via one of the forces it needs to posses the corresponding charge of this particular force. There are three charges incorporated into the SM, namely: charge, flavour, colour. They are the corresponding charges of the electromagnetic force, the weak force and the strong force, respectively. Each force can be described by a theory: the theory of the electromagnetic force and the weak force are usually treated by the unified Electroweak (EW) theory and the theory of the strong force is called Quantum Chromodynamics (QCD). The description of the electromagnetic force is originally developed separately by the theory called Quantum Electrodynamics (QED). The proton-proton interactions studied in this work are all of small momentum transfer. It is in this regime where, under the direct influence of its massive force carriers, the weak interaction is truly weak and can therefore be neglected. QCD and QED are of importance for the interactions studied throughout this work and will be explained a bit more detailed.

The processes studied are under the influence of forces described by QED and QCD, namely the coulumb force and the nuclear force. Already mentioned is that for a particle to undergo an particular interaction it needs to posses the corresponding charge of that field. Beside this, the strength does also depend on a coupling constant between the fields that undergo interaction. The coupling constants are however not true constants, but have dependence on the momentum transfer involved in the interaction between particles. Altering of the coupling constant is an aspect of the underlying formulation of the QFT, referred to as running of the coupling. The behaviour of this running is related to the internal algebra used to construct the theory. A theory should satisfy the gauge principle, the invariance of the laws of physics under local transformations of variables of that field. The transformations form a group satisfying an underlying symmetry. The generators of the group are each associated with a field with a corresponding particle called a gauge boson. The symmetry group of QED is U(1) and has one generator which is the photon. The U(1) group is Abelian and thus the photon does not carry the electrical charge itself. As a consequence there is no self interaction possible between photons, which impacts the running of the coupling constant. Similar to the electric charge of the electromagnetic force, the

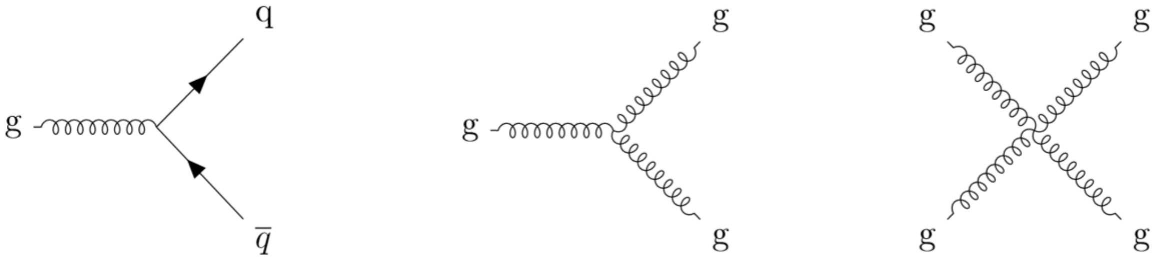

Figure 2.2: Feynam diagrams of the three possible vertices of QCD, g indicating a gluon and $q/\overline{q}$ indicating a quak/anti-quark.

charge associated to the strong force is called color. Color introduces three additional quantum numbers to particles that couple to the strong force, called blue, green and red. The symmetry group of QCD is SU(3) and has 8 gauge fields associated to it that make up the generators of this group. The SU(3) is a non-Abelian group and its generators therefore carry the color charge themselves. Thus, the 8 gluons can interact with each other. As a result of this, QCD has 2 additional vertices which are not present in QED. The three possible QCD vertices are shown in Figure 2.2. Of three vertices only the first type of vertex is possible in QED, given a replacement of the letter g by γ and $q/\overline{q}$ are joined by the $l/\overline{l}$ possibility.

2.2.1 Running of the Coupling Constants

As a consequence of the self interactions that are present in QCD, the behaviour of the running of the coupling constant is different from that of QED. For this one has to look at the effect of charge screening in both theories. In QED, charged particles are surrounded by a cloud of virtual photons and electron/positron pairs that continuously pop in and out of existence. As opposite charges attract each other, an electron is more closely surrounded by virtually positrons that cause the effect of screening of its negative charge. This effect is called vacuum polarisation. As a consequence of this, in QED the effective charge become smaller with increasing distance. The screening effect results in a running coupling constant that becomes large at short distance. Higher interaction transfer thus leads to a stronger coupling constant in QED.

$$\alpha(q^2) = \frac{\alpha(\mu^2)}{1 - \alpha(\mu^2)\frac{1}{3\pi}\ln\frac{q^2}{\mu^2}}. \tag{2.1}$$

Equation (2.1) gives the expression in which one can calculate the fine structure constant α at any given energy transfer q^2 if it is known for a particular momentum transfer μ^2. The fine structure constant α is about 1/137 at q^2 equal to 0 GeV, rising to 1/128 at q^2 equal to 90 GeV, the mass of the Z. Thus, indeed the coupling strength increases, but the q^2 dependence of coupling is rather weak. Charge screening in QCD works similar to the QED, but here the effect of gluons carrying color charge changes the effect. The QCD vacuum consists of virtual quark anti-quark pairs, however in addition it is now also filled with virtual gluon pairs. Since they carry color charge themselves, the effective charges becomes larger at larger distances. This effect is called antiscreening. Higher interaction transfer thus leads to a weaker coupling constant in QCD.

$$\alpha_s(q^2) = \frac{\alpha_s(\mu^2)}{1 + B\alpha_s(\mu^2)\frac{1}{3\pi}\ln\frac{q^2}{\mu^2}}, \quad B = \frac{11N_C - N_f}{12\pi}. \tag{2.2}$$

Equation (2.2) gives the expression for the strong coupling constant at any given momentum transfer q^2, once it is known at a particular momentum transfer μ^2. Here N_C is the number of colors, N_f is the number of quarks and B is therefore a positive number given these are 3 and 6, respectively. The strong coupling constant α_s is about 0.5 at a q^2 equal to the proton mass of about a GeV and decreases to 0.12 at a q^2 equal to the mass of the Z. At short distances the strong coupling constant becomes small. The quarks that are packed together inside hadrons can therefore be regarded as free when probing them with large enough energies. This property of QCD called asymptotic freedom. If we go to large distances, the coupling becomes so strong that it is not possible to isolate a single quark. At a certain distance it is more favourable to create a quark anti-quark pair and the process of hadronization starts. This effect is called color confinement and is the reason that no isolated quark has ever been observed.

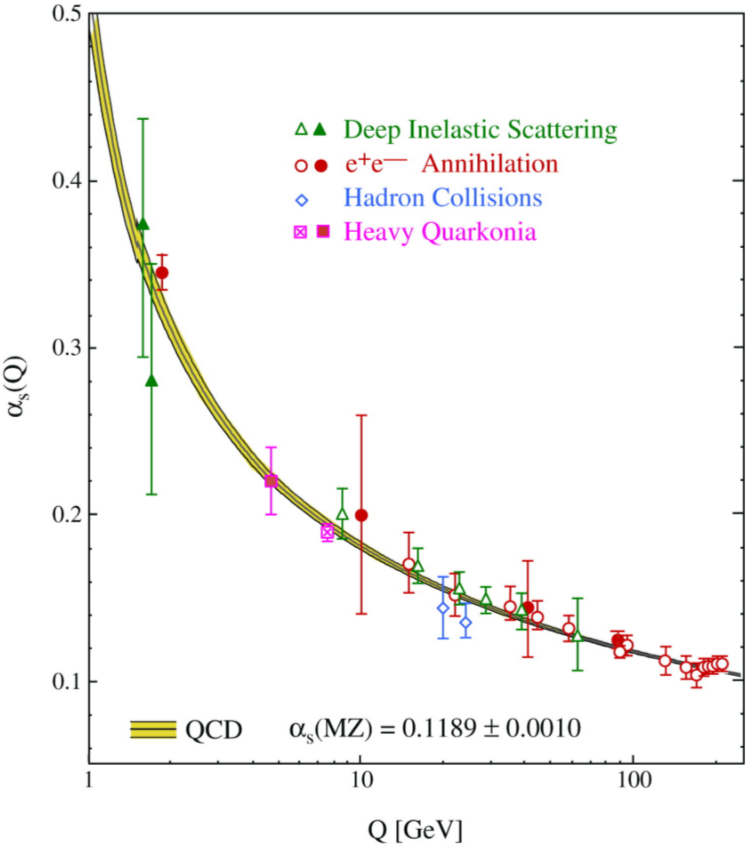

Figure 2.3: The strong coupling constant as a function of the momentum transfer [10].

2.2.2 Proton Collisions

The proton is not an elementary particle and this is of importance when studying proton-proton collisions. When considered at low energy, the proton can mainly be considered as a bound state of two up type quarks and one down type quarks. The color combination is such that it leaves the proton colorless, as a consequence of the color confinement. Probing the proton at higher energies will shift the picture of the proton and will reveal additional sea quarks and sea gluons. Hence to image of the proton continuously changes as a function of the energy at which it is probed. In experiments the dynamical collection of quarks and gluons, called Parton Distribution Functions (PDFs), have been previously studied and are of importance for the understanding of the proton structure. This all is consequence of the nature of the QCD theory, as previously explained the color charge particles are continuously surrounded by virtual quark anti-quark pairs and virtual gluon pairs.

When colliding protons, one collides the valence quarks, sea quarks and sea gluons. At large momentum transfer, the interactions are in fact between two constituents of the proton. However, for small momentum transfer the proton can be considered as a whole. Depending on the energy of the momentum transfer, one can either calculate the interactions with perturbative QCD or not. This depends on the strong coupling constant, when significantly below 1 the processes become calculable since the expansions converge. This makes it possible to calculate interactions at high momentum transfer whereby one can regard the constituents of the proton as quasi free particles. These are the classified as hard interactions, the regime in which processes are calculable with perturbative QCD. For soft interactions the momentum transfer is low and hence perturbative QCD can not be applied. Then there is a special sub class of soft interaction, namely the elastic interaction in which one has (very) small momentum transfer that only leads to a change of momentum. This means the strong coupling constant α_s is largest and hence perturbative QCD is also excluded here. Since QED has a small coupling constant already and it varies little, perturbative QED calculations are applicable for all these processes. Elastic proton scattering is a process dictated by the interplay of QCD and QED, since the exchange of a photon as well a system of gluons can lead to change in momentum.

2.3 Elastic Scattering

Elastic proton-proton (pp) scattering is a process in which only leads to a change of momentum. Since elastic pp scattering involves small momentum transfer, a description of is not calculable with perturbative QCD and instead one has to rely on phenomenological models. With elastic scattering one thus probes the strong force in a regime where the understanding is not sufficient. In this section the kinematics of elastic pp will be explained, the models to describe the elastic differential cross will be introduced and will be concluded with the motivation for elastic scattering at a center-of-mass energy of 900 GeV.

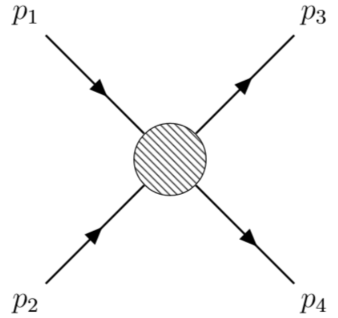

Figure 2.4: A schematic depiction of the elastic scattering process, with the incoming particles denoted with four momentum p_1 and p_2 and the outgoing particles denoted with four momentum p_3 and p_4.

2.3.1 Kinematics

Elastic scattering is defined by the fact that there is only four-momentum transfer between the particles and no quantum numbers are exchanged between the incoming particles. The initial kinetic energy of the incoming particles equals the kinetic energy of the outgoing particles after they have been subjected to an interaction. This is shown by a schematic of the process in Figure 2.4. The center-of-mass energy squared of the system of two colliding particles with four momentum p_1 and p_2 is given by the Mandelstam variable s [9] :

$$s = (p_1 + p_2)^2 = (E_1 + E_2)^2 - (\mathbf{p_1} + \mathbf{p_2})^2. \tag{2.3}$$

Both incoming particles are protons with equal momentum but in opposite direction, therefore this can be written out as follows :

$$\begin{aligned} s &= E_1^2 + E_2^2 + 2E_1E_2 - 2p^2 + 2\mathbf{p_1}\mathbf{p_2} \\ &= 4(m_p^2 + p^2), \end{aligned} \tag{2.4}$$

where p_1 and p_2 are the initial four momentum of the particles, m_p is the mass of the proton. The momentum transfer between particles is given by the Mandelstam variable t :

$$\begin{aligned} t &= (p_1 - p_3)^2 \\ &= (E_1 - E_3) - (\mathbf{p_1} - \mathbf{p_3})^2 \\ &= -2p^2 + 2p^2 \cos\theta, \end{aligned} \tag{2.5}$$

where θ is the scattering angle of the outgoing particles. This angle in the forward direction is very small and hence one can approximate :

$$\begin{aligned} t &\simeq -2p^2 + 2p^2(1 - \frac{\theta^2}{2}) \\ &= -(p\theta)^2. \end{aligned} \tag{2.6}$$

This final relation between the momentum transfer t, the momentum of the proton and the scattering angle is of importance for the design of the detector, since it directly relates the distance to the beam to a smallest reachable t value [11].

2.3.2 Elastic Differential Cross Section

The cross section of a scattering process is the measure of the probability that two particles will undergo an interaction. The differential cross section can be given with respect to momentum transfer t. The protons carry electric charge and color charge and will therefore undergo both interactions described by the Coulomb force as well as the Nuclear force :

$$\frac{d\sigma}{dt} = |F|^2 = |F_C e^{i\alpha\phi(t)} + F_N|^2, \tag{2.7}$$

in which F is the total scattering amplitude that can be split into contributions arising from F_C, the coulomb scattering amplitude and F_N, the nuclear scattering amplitude. Here α is the fine structure constant and $\phi(t)$ is a phase that describes the interference between both components of the scattering amplitude. Both contributions will be explained a bit more detailed in the following parts.

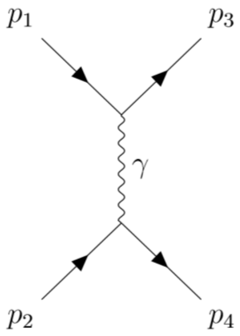

Figure 2.5: Tree level Feynman diagram of the Coulomb part of the elastic scattering amplitude.

Coulomb Scattering Amplitude

The coulomb scattering amplitude accounts for the electromagnetic part of the interactions that elastic scattered protons are subjected to. The fine structure constant is well below 1 for a wide range of momentum transfer and one can therefore apply perturbation theory for the electromagnetic part, described by QED. The dominating Feynman diagram associated to the electromagnetic process is shown in Figure 2.5. In the elastic scattering processes the smallest four-momentum transfers are studied for which the wavelength of the exchanged photon between the protons is long compared to the size of the proton. The photon thus experiences the proton as a whole and the interaction is therefore not between the constituents of the proton but rather it is between the protons. The form factor of the proton is needed for a description of the electric charge distribution. For increasing momentum transfer the wavelength decreases and the photon will become sensitive to a part of the charge held by the proton, hence the scattering amplitude will decrease.

The dipole approximation will be used throughout this analysis, in which the charge distribution of proton is described by an exponential decrease as a function of the distance. The electric form factor is Fourier transformed into momentum space giving the following expression :

$$G(t) = \left(\frac{\Lambda}{\Lambda + |t|}\right)^2, \quad \Lambda = 0.71 \quad \mathrm{GeV}^2. \tag{2.8}$$

This dipole model has been ruled out by data, but many of the alternative models that have been fitted to data lack of physical interpretation. Given a form factor $G(t)$, the expression for the Coulomb term of the elastic scattering amplitude can be written as [4] :

$$F_C = \frac{-2\sqrt{\pi}\alpha G(t)^2}{|t|}. \tag{2.9}$$

Nuclear Scattering Amplitude

The nuclear scattering amplitude accounts for the strong part of the interactions that elastic scattered protons are subjected to. The strong coupling constant is too large in the range of momentum transfer, and perturbative QCD can not be used the calculate the nuclear amplitude.

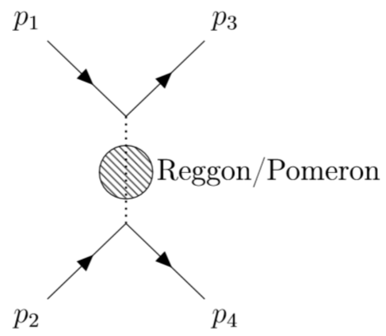

Figure 2.6: Possible interactions exchange multi-bodied objects that may contribute to the Nuclear component of the elastic scattering amplitude.

Furthermore, the corresponding tree level Feynman diagram to that of the photon does not exist in QCD. The gluons carry color charge and can therefore not mediate elastic scattering since it would imply an exchange of quantum numbers. The description of the nuclear component of the scattering amplitude is therefore rather complex and of high interest of ongoing studies to which this analysis might contribute to.

In an elastic scattering no quantum numbers are exchanged and hence the object exchanged on behalf of the nuclear force should be colorless. This would mean a composite particle in which its constituents carry color charges that together form a neutral composition. A description of elastic pp interactions is given by a formulation called Regge theory [12]. Regge solved the non-relativistic scattering equation for a spherically symmetric potential and analytically extended the partial wave amplitudes, expressed as a function of angular momentum, to also obtain their imaginary parts [13]. The singularities of both the real and imaginary parts of the partial wave amplitudes of the solution are function of four-momentum transfer t :

$$l = \alpha(t), \tag{2.10}$$

here l is the angular momentum. These define the Regge trajectories. The real solution are found to correspond to known baryons and mesons, which are colorless particles and hence could function as a mediator of the elastic interaction. Regge trajectories can be expressed using linear expansion as $\alpha(t) = \alpha_0 + \alpha'(t)$ [13]. At low energy the Regge theory was able to describe the cross section at lower center-of-mass energy, but comes short to do so for higher center-of-mass energy. Pomeranchuck proved that the cross sections for hadron anti-hadron and hadron hadron become equal at higher center-of-mass energy, which required the existence of an additional Regge trajectory [13]. This Regge trajectory is called the Pomeron, which dominates at high energies. By including this Pomeron trajectory, the Regge theory is able to describe the behaviour of the scattering cross section with increasing center-of-mass energy. The Pomeron has the quantum numbers of the vacuum and does not correspond to any of the known particles that carry integer spin. In QCD the Pomeron is thought to be compatible with colorless multi-gluon objects called glue balls. A schematic of the possible processes associated to the strong interaction is given by the diagram in Figure 2.6.

The elastic processes involved in the study presented in this work are in the momentum range in which the nuclear amplitude is not required to be derived from Regge theory and a phenomenological model can be used instead. For small t values the following approximation can be used :

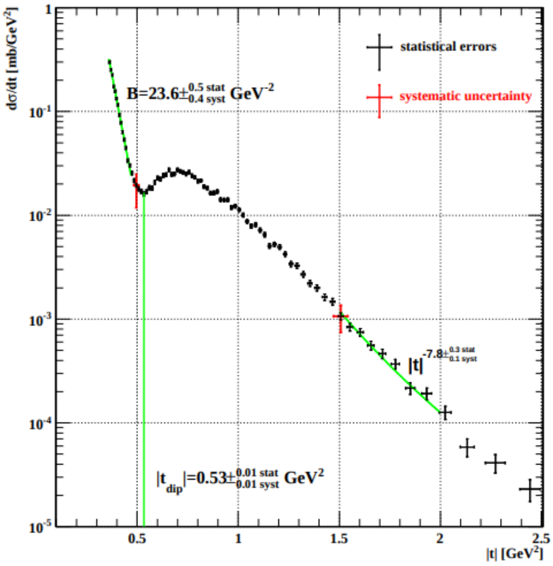

Figure 2.7: The measured elastic differential cross at $\sqrt{s}$ = 7 TeV by the TOTEM collaboration [14]

$$\frac{d\sigma_N}{dt} = \left.\frac{d\sigma_N}{dt}\right|_{t\to 0} e^{-Bt}, \tag{2.11}$$

here the nuclear slope B is a parameter that depends on the center-of-mass energy and should be determined from data. The approximation is valid until $|\,t\,| \approx$ -0.5 GeV^2, the point in the differential elastic cross section where a distinctive dip-shoulder region arises, shown in Figure 2.7. The differential cross section beyond the bump of the slope is better approximated by a power law. The dip-shoulder region is currently under interest by the elastic physics community.

Elastic scattered events can additionally be used to measure the total cross section, σ_{tot}, for pp collisions by exploiting the optical theorem. The optical theorem is based upon the conservation of probability and can be used to relate the σ_{tot} and the imaginary part of the elastic nuclear scattering amplitude :

$$\sigma_{\text{tot}} = 4\sqrt{\pi}\,\text{Im}\,F_N(t\to 0). \tag{2.12}$$

A complete derivation of the optical theorem can be found in the appendix B of reference [13]. Epression (2.12) can be substituted back in to (2.11) to obtain :

$$\begin{aligned} \left.\frac{d\sigma_N}{dt}\right|_{t=0} e^{-Bt} &= |F_N(t=0)|^2 e^{-Bt} \\ &= |\text{Re}\,F_N(t=0) + \text{Im}\,F_N(t=0)|^2 e^{-Bt} \\ &= \left|\left(\frac{\text{Re}\,F_N(t=0)}{\text{Im}\,F_N(t=0)} + i\right)\text{Im}\,F_N(t=0)\right|^2 e^{-Bt} \\ &= \left|(\rho + i)\frac{\sigma_{\text{tot}}}{4\sqrt{\pi}} e^{-Bt/2}\right|^2, \end{aligned} \tag{2.13}$$

with the definition of ρ used for substitution :

$$\rho = \frac{\text{Re}\,F_N(t=0)}{\text{Im}\,F_N(t=0)}. \tag{2.14}$$

A similar substitution to relate the total cross section to the Coulomb part of the scattering amplitude can not be made since it does not contain an imaginary part. The ρ value is connected to the total cross section via dispersion relations and is important to be studied as it affects the behaviour of the total cross section with increasing center-of-mass energy.

Coulumb Nuclear Interference

The Coulomb Nuclear Interference (CNI) describes the interference between contributions from the Coulomb and nuclear amplitude to the total amplitude, expressed by the phase $\phi(t)$, given in (2.15). The CNI term is calculated using only using tree level Feynman diagrams by West and Yennie, which lead to the following expression :

$$\phi(t) = -\gamma - \ln\left(\frac{B|t|}{2}\right), \tag{2.15}$$

here γ is the Euler constant $\simeq 0.577$ and also the nuclear slope B appears. Another model by Cahn using an eikonal approach in which the effect of the form factor of the proton was included :

$$\phi(t) = -\left(\gamma + \ln\left(\frac{B|t|}{2}\right) + \ln\left(1 + \frac{8}{B\Lambda^2}\right)\right) + \frac{4|t|}{\Lambda^2}\ln\left(\frac{\Lambda^2}{4|t|}\right) - \frac{2|t|}{\Lambda}. \tag{2.16}$$

Final Expression

Combining (2.9), (2.11) and (2.15) leads to the full expression of the elastic differential cross section :

$$\begin{aligned} \frac{d\sigma_{\text{el}}}{dt} &= |F_C e^{i\alpha\phi(t)} + F_N|^2 \\ &= \left| \frac{-2\sqrt{\pi}\alpha G(t)^2}{|t|} e^{i\alpha\phi(t)} + (\rho + i)\frac{\sigma_{\text{tot}}}{4\sqrt{\pi}} e^{-Bt/2} \right|^2 \\ &= \frac{4\pi\alpha^2 G(t)^4}{t^2} - \sigma_{\text{tot}} \frac{\alpha G(t)^2}{|t|}(\rho\cos(\alpha\phi(t)) + \sin(\alpha\phi(t)))e^{-Bt/2} + (\rho^2 + 1)\frac{\sigma_{\text{tot}}^2}{16\pi} e^{-Bt}. \end{aligned} \tag{2.17}$$

The first term is attributed to the Coulomb component, the middlest term including the phase is attributed to the interference region and the last term is attributed to the nuclear component. Figure 2.8 shows the elastic differential cross section and separately highlighted in red, green and blue its three components it consists of. Expression (2.17) is used here, in which the dipole approximation for the form factor, the West-Yennie model for the interference phase and a pure nuclear exponential decay are used.

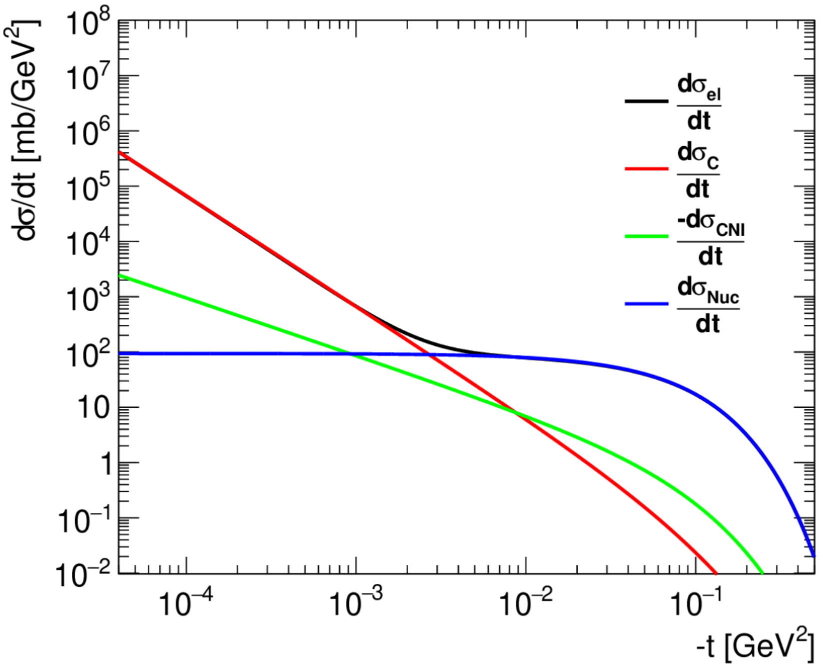

Figure 2.8: Theory plot of the elastic differential cross section with σ_{tot} = 68.0 mb, B = 17.0 GeV^2 and ρ = 0.12

.

From Figure 2.8 it can be seen that the Coulomb part dominates the differential cross section, (2.17), at very small four-momentum transfer squared t, due to its $1/t^2$ dependence. It is under the smallest scattering angles where the Coulomb part dominates the elastic events and where the experiment is sensitive to the delivered luminosity by the LHC machine. The Coulomb term is well understood from QED and can therefore be used to extract the integrated luminosity, L :

$$\frac{d\sigma_{\text{el}}}{dt} = \frac{1}{L}\frac{dN_{\text{el}}}{dt} \approx \frac{1}{L}\frac{dN_C}{dt} = \frac{4\pi\alpha^2 G(t)^4}{t^2}. \tag{2.18}$$

The luminosity is an important experimental quantity that is needed to scale the number of observed events, N, to the cross section of that particular process. The precision on the luminosity is therefore of importance since it directly impacts the precision one can achieve with a certain measurement. Unlike the Coulomb term, the CNI and nuclear terms can not be used to extract the luminosity as they both contain two additional free parameters that need to be fitted from data, namely the σ_{tot} and ρ. The concept of luminosity will be further introduced in Section 3.3.

The increase of the elastic and total cross section are shown in Figure 2.9. The growth of the total pp cross section as a function of the center-of-mass energy is not yet completely understood. The soft scattering processes that contribute to the the total cross section can not be calculated with perturbative QCD and non perturbative methods are yet capable to calculate them from first principles [16]. Thus, the behaviour of the total hadronic cross section at inreasing energy can not directly be predicted by QCD. However, it can be shown through unitarity that the rise of the total cross section with energy is constrained to an upper limit, known as the Froissart-Martin bound [17, 18] :

$$\sigma_{\text{tot}}(s) \leq \ln\left(\frac{s}{s_0}\right)^2. \tag{2.19}$$

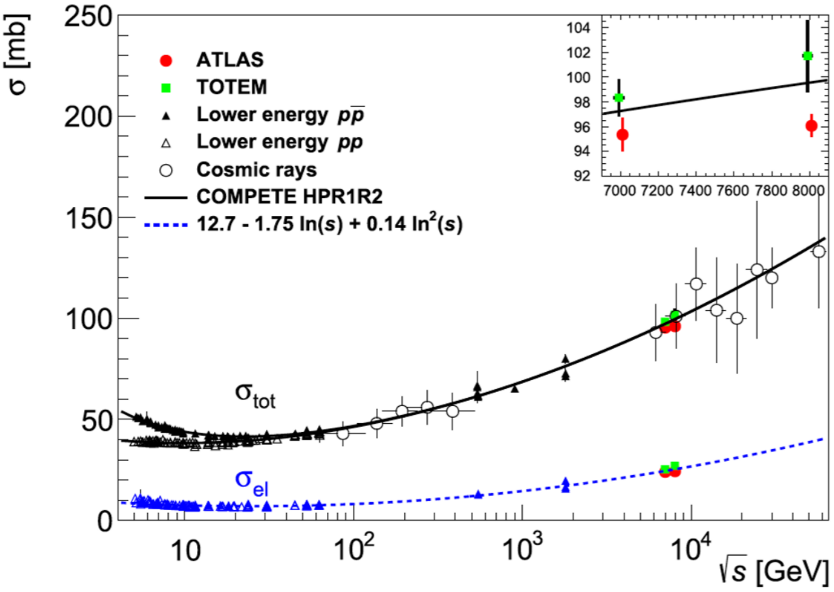

Figure 2.9: Total and elastic cross section as a function of the center-of-mass energy. The fit does not include the ATLAS measurement at $\sqrt{s}$ = 8 TeV [15].

2.3.3 Elastic Models and the Importance of Rho

Theoretical values for the elastic differential cross section, ρ parameter, nuclear slope B and σ_{tot} are predicted by models based on Regge theory. These predicted values will be compared here to the experimental results obtained from the LHC experiments. The models contain a prohibitively large amount of free parameters to be used for fitting purposes in the analysis framework and hence the simplified model given by (2.17) was used in previous elastic analyses by ALFA [19, 15, 4] and [20]. The data used for the analysis presented here is of the smallest reachable t-values, and is aimed to determine the values of σ_{tot} and ρ. The pure nuclear slope region is contained in a second data set, which was also taken during the elastic physics program run at a center-of-mass energy of 900 GeV.

Multiple models and their corresponding predictions for ρ and σ_{tot} are shown in Figure 2.10. All models in here, with the exception of the bottom three in the legend, are calculated by the COMPETE collaboration in 2002 [21]. The remaining three models are, in the order of their appearance in the legend: the best ranked COMPETE model modified by PDG [22], the AGNM model [23] and the FMO model [24]. The FMO model differs from all other models since it is the only model to includes a new exchange of a (quasi) particle called the Odderon. Furthermore, LHC measurements of ρ and σ_{tot} by TOTEM [25, 26, 3] and ALFA [19, 15] are depicted with the black and purple markers, respectively.

The measured value of the ρ parameter at $\sqrt{s}$ = 7 TeV by the TOTEM collaboration has a too large uncertainty and is therefore ambiguous. A deviating value of ρ emerges at $\sqrt{s}$ = 8 TeV, clearly visible in Figure 2.10. The latest values of σ_{tot} and ρ released by the TOTEM collaboration for the center-of-mass energy of $\sqrt{s}$ = 13 TeV are shown on the furthest right in both graphs. Despite the fact that the value of σ_{tot} is in good agreement with the standard best COMPETE prediction, the value of the ρ parameter is in strong disagreement with the COMPETE prediction and confirms the tendency of a decreasing value of ρ [24].

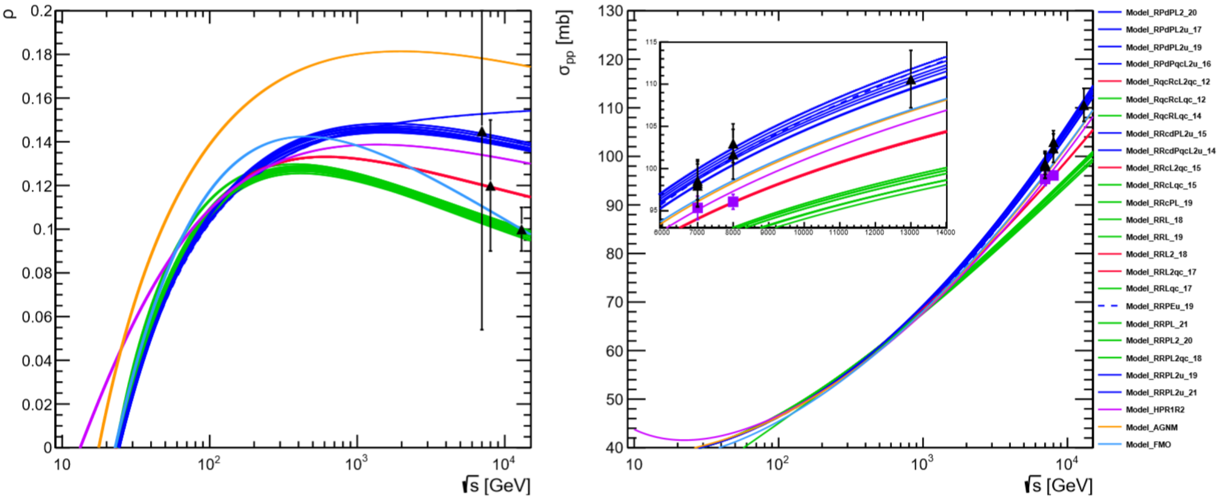

Figure 2.10: This figure shows multiple models and their corresponding predictions for the values of ρ and σ_{tot} [20]. Left: The value of ρ as a function of the center-of-mass energy. Right: The value of σ_{tot} as a function of the center-of-mass energy.

The ρ parameter is related to the total cross section by dispersion relations and the measurement of ρ gives insight in the behaviour of the total cross section with energy evolution. A lower value of ρ might indicate a slow down of the rise of the total cross section with energy. Under the traditional assumptions by the Regge theory, at high enough energy the particle-particle cross section becomes asymptotically equal to the particle-antiparticle cross section, assured by the inclusion of the Pomeron trajectory.

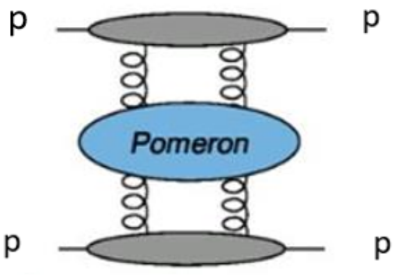

Figure 2.11: Pomeron exchange.

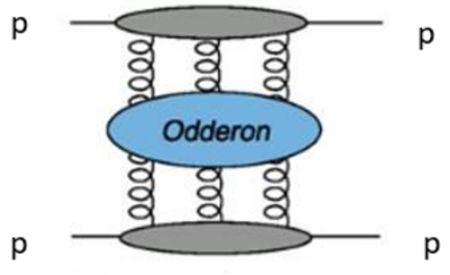

Figure 2.12: Odderon exchange.

Models have traditionally only included an even number of gluons exchanged between protons. The Froissaron and Maximal Odderon (FMO) model is an example of a model including the Odderon [24]. The Odderon is an additional (quasi) particle to the Pomeron, that is exchanged during the interactions between protons. The Odderon has been rediscovered in QCD, but also in approximations such as the Color Glass Condensate (CGC) scheme and in the dipole picute. Where the Pomeron takes account for the exchange of compositions containing an even number of gluons, the Odderon does account for the exchange of odd numbered compositions of gluons.

That there have not been earlier strong indications of the existence of the Odderon comes from differences between particle-particle and particle-antiparticle at high energies. However, at highest energies there are currently no pp and $p\bar{p}$ colliders running at the same energy and furthermore it is only with the LHC that the experiments started to probe the high energy region. The result from TOTEM is therefore of high relevance in the study of this phenomenon. In their paper the authors have refitted all data available for the σ_{tot} and ρ and found that no single COMPETE model is able to describe the latest data. They have found that their model including the maximal Odderon, a particular case of the Odderon, leads to a satisfactory fit value [24]. The phase ρ of the elastic scattering amplitude described by the best COMPETE fit and FMO model are shown in Figure 2.13 for both pp and $p\bar{p}$ interactions.

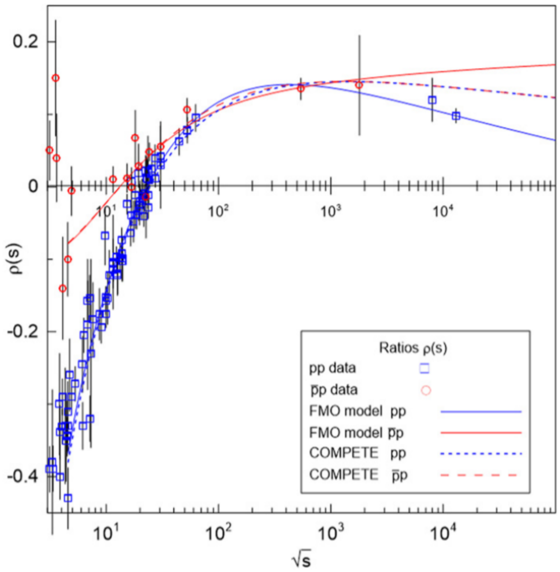

Figure 2.13: The phase ρ of the elastic scattering amplitude, predicted by the FMO model and with the best COMPETE fit for comparison. Only TOTEM data was used for this study [24].

2.4 The 900 GeV Physics Case

The elastic pp scattering physics program in LHC era has provided precise measurements of the ρ parameter and total cross section in a new energy regime. Results from 8 and 13 TeV show strong indications that the high energy physics community is confronted with possible new phenomena. These new possible phenomena related to the value of the ρ parameter have been discussed in the previous section, and are [27] :

1. A slow down of the rise of the total cross section with energy
2. The exchange of a 3 gluon compound in elastic scattering

These two effects, the cross section saturation and the odd gluon exchange could both be present without being mutually exclusive [3]. The first can be calculated via dispersion relations and the second implies new models that incorporate the exchange of a new (quasi) particle. There are several theoretical models and they each provide predictions for the evolution of ρ as a function of the center-of-mass energy. These models all predict the lower ρ value than what was previously anticipated by traditional models of the pre-LHC era. Moreover, the evolution of ρ at lower energies is also modified by these new models. It is in the zone near 900 GeV where a precise measurement of the ρ parameter can contribute strongly to separate between the two scenarios. At 900 GeV, the new models foresee different values for the ρ parameter that do not match the pre-LHC prediction, whereas a slow down of the rise of the total cross section would not modify the value of the ρ parameter compared to the pre-LHC prediction.

Part II

Experimental Setup

Chapter 3

The Large Hadron Collider

Both experiments presented in this work are installed at the LHC, currently the largest and most energetic particle accelerator in the world. The LHC accelerator forms an important part of the experimental setup as provider of particle collisions. Up to this point the accelerator has brought protons in collision at various center-of-mass energies with 13 TeV being the highest accomplished energy. During the second long shutdown period (LS2) the machine and experiments are prepared for operation of pp at the design energy of 14 TeV. Control of the particle beam inside the accelerator is essential for the success of the dedicated elastic physics experiment. In this section the relevant factors for the elastic analysis on the LHC are described. A brief introduction to the accelerator complex and in particular the LHC are given. The collimation has a large impact on the elastic measurements and its schemes are introduced here. Unless otherwise stated, the presented information in this chapter is obtained from [28] and [29].

3.1 The CERN accelerator complex

Located at the border between France and Switzerland, the CERN accelerator complex has gradually evolved since the establishment of the organisation in 1954. Over the course of time, new and more energetic accelerators have been build to always keep exploring the forefront of particle physics. These accelerators have successfully contributed to several breakthroughs in the field. On its way CERN's accelerator complex has developed to more than a facilitator restraint to the experiments conducted at the energy frontier. A complete overview of the accelerator complex as it was during LHC Run 2 (2015-2018) is shown in Figure 3.1.

The injection chain into the LHC starts with the injection of hydrogen gas into a metal cylinder. An electric field ionizes the hydrogen and then the protons are sent into the Radio Frequency Quadrupole (RFQ). The RFQ is the first part of the linear accelerator (LINAC) 2 that bunches, focuses and accelerates the continuous stream of protons by using radio frequency fields only [30]. The bunches are then sent into a linear succession of Radio Frequency (RF) cavities accelerates the protons to 50 MeV. They then enter the first circular and smallest synchrotron of the accelerator chain, the Proton Synchrotron Booster (PSB), increasing the beam energy up to 1.4 GeV. The Proton Synchrotron (PS) accelerates further to 25 GeV and in the Super Proton Synchrotron (SPS) the beam reaches 450 GeV, the injection energy of the LHC. Up to the SPS the protons circulate in one direction only. Injection into the two rings of the LHC is done at two different positions and in opposite direction with respect to each other.

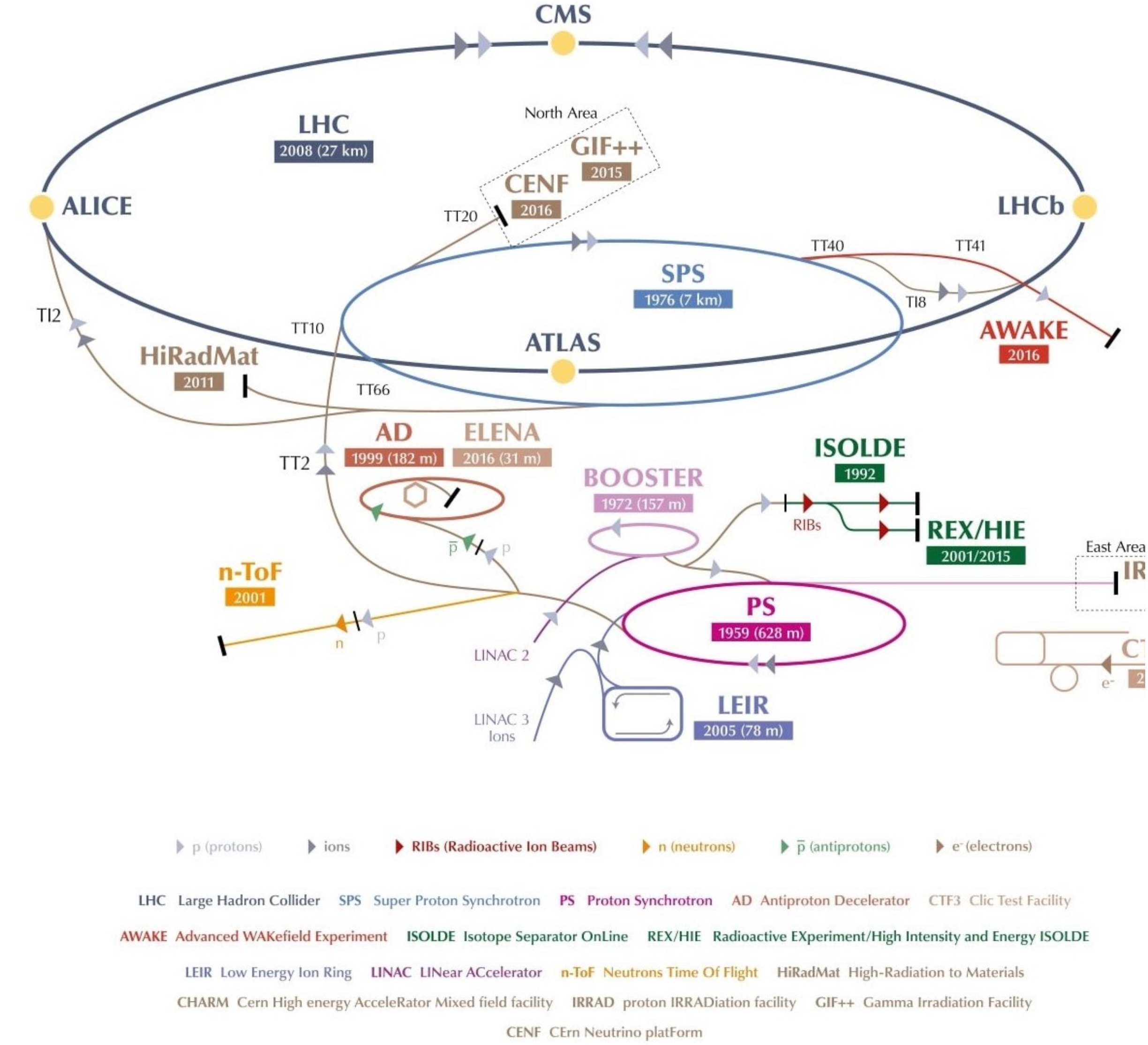

Figure 3.1: The CERN accelerator complex [31].

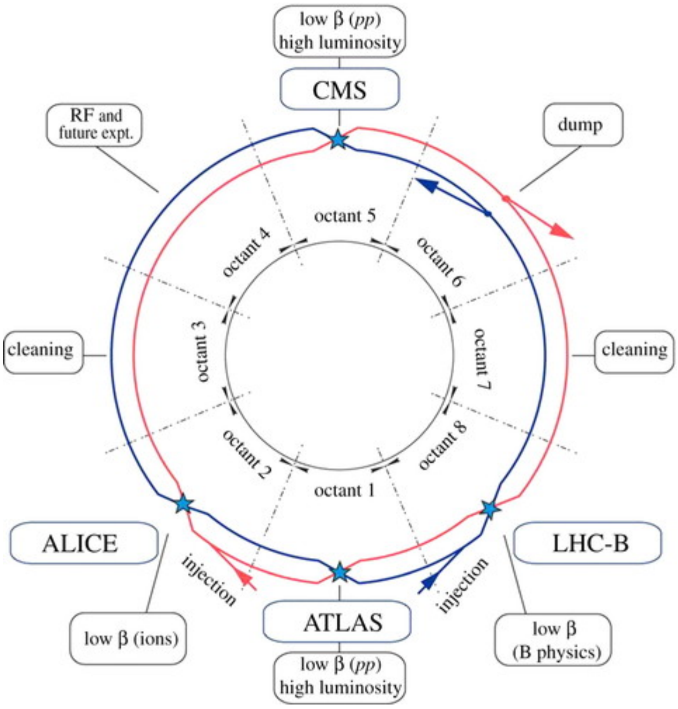

Figure 3.2: Overview of the octants of the LHC [28].

3.2 LHC

The LHC is housed in a circular underground tunnel with a circumference of 27 km that lies between 50 to 175 m beneath the surface. The LHC accelerates and collides the two counter rotating beams, beam 1 clockwise and beam 2 anticlockwise. The 50 mm diameter beam pipes contain an ultra high vacuum of 10^{-10} to 10^{-11} mbar to reduce the likelihood of protons interacting with gas molecules. The ring consists of 8 insertion regions (IR) interleaved with 8 arcs, which together form octants, shown in Figure 3.2. An octant starts at the heart of an arc and continuous until the centre of the next arc, with in the middle one insertion. The insertion consists of one full straight section of approximately 528 m with on each side a dispersion suppressor. In the middle of the insertion is the insertion point (IP), the number following the octant numbering. In 4 of those points the beams are exchanged from the inner to the outer ring or oppositely. These insertions points where beams are brought into collision are also called interaction points (IPs). The interaction points are IP1, IP2, IP5 and IP8. The four IPs are depicted in Figure 3.2 with blue stars and are home to the following experiments: ATLAS, ALICE, CMS and LHCb. At insertions 2 and 8, beams are injected from the SPS into the outer ring. The 16 RF cavities form the accelerator system at insertion 4. Cleaning is done at insertions 3 and 7 using collimation systems. Insertion 6 contains the beam dump system. An arc contains superconducting dipoles, quadrapoles, sextupoles and decapoles.

The accelerator mainly has two purposes: to increase the particles energy and to govern the particles direction. An electric field is used in the RF cavities to accelerate the particles. The dipole magnets are used to bend the beam around the arcs and the higher order magnets are used for focusing and correcting the beams. A particle with carrying a net charge and moving in an electric or magnetic field experiences a Lorentz force. The force is proportional to the particles

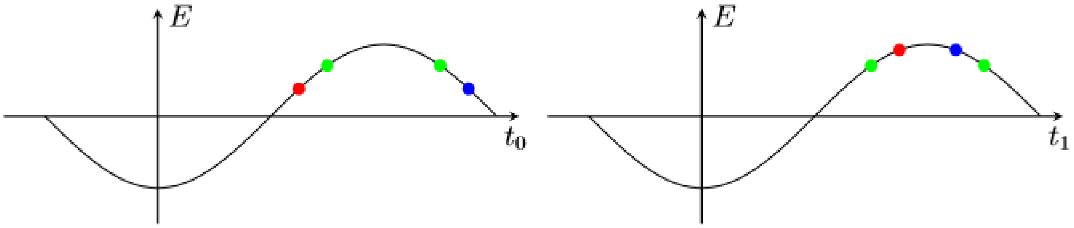

Figure 3.3: The principle behind the RF cavities with the two energy regimes for which the *slip factor* determines how the phase of the electric field should be set [20]. The synchronous particle is depicted by the green dots, the asynchronous low energy particle with the red dots and the asynchronous (ultra) relativistic particle with the blue dots.

charge q, its velocity $\mathbf{v}$ and the electric and magnetic field strengths $\mathbf{E}$ and $\mathbf{B}$:

$$\mathbf{F} = q(\mathbf{E} + \mathbf{v} \times \mathbf{B}). \tag{3.1}$$

The acceleration of the protons is done using an oscillating electric field in the direction of the beam. The cavities of the accelerator system operate at a radio frequency of about 400 MHz. During acceleration the phase of the oscillation is adjusted until the desired energy is reached, which for the special physics run is 450 GeV per proton. This is the energy that is reached by SPS in order to inject the bunches into the LHC. A particle that carries the right energy will always hit the electric field in the same phase. Such a particle is synchronous and receives an equal kick every pass by of the RF system. A synchronous particle is depicted with the green color in Figure 3.3. Since there are many particles contained in the bunches, they will have a certain energy spread and therefore partly hit the electric field in a different phase than the synchronous particle. During the acceleration of a particle there are two energy regimes to distinguish for which the phase needs to be adjusted in order to deal properly with the asynchronous particle. The effect of having too low (high) energy for the two energy regimes leads to an opposite change in the revolution frequency. Initially a momentum increase mainly leads to a velocity increase, hence the revolution frequency increases. When dealing with a (ultra) relativistic particle a momentum increase mainly leads to a circumference increase, hence the revolution frequency decreases [32]. The two cases are depicted in Figure 3.3, the former with the red colored dot and the latter with the blue colored dot. For low energy, a particle carrying too much (low) energy will arrive early (late) and receive a smaller (larger) kick, seen on the left-hand (right-hand) in red. A high energies this is inversed and a particle containing too much (few) energy will arrive too late (early) and receive a smaller (larger) kick, seen on the left-hand (right-hand) in blue. The phase should therefore be adjusted according to the regime, such that the particles will either face the rising or the falling side of the oscillating electric field. In this way balancing around a certain energy takes place and such that the bunch structure remains intact.

The 27 km ring is for the most part filled with 1232 superconductive dipole magnets to bent the beams around the LHC circumference, see Figure 3.4. They are complemented by many thousands of higher order magnets with other functions, including insertion, focusing and correction of the beams. Superfluid helium is used to cool the magnets down to 1.9 K to become superconductive, this allows to them to be operated at a current of 11850 A to produce a field of 8.3 T. The magnet are monitored with the quench protection system since the superconducting state of the material is so critically dependent on the temperature. Heat entering the magnet system can be caused by many origins, including beam related energy release such as synchrotron radiation or beam-gas scattering [34]. Another source that the accelerator equipment should be protected

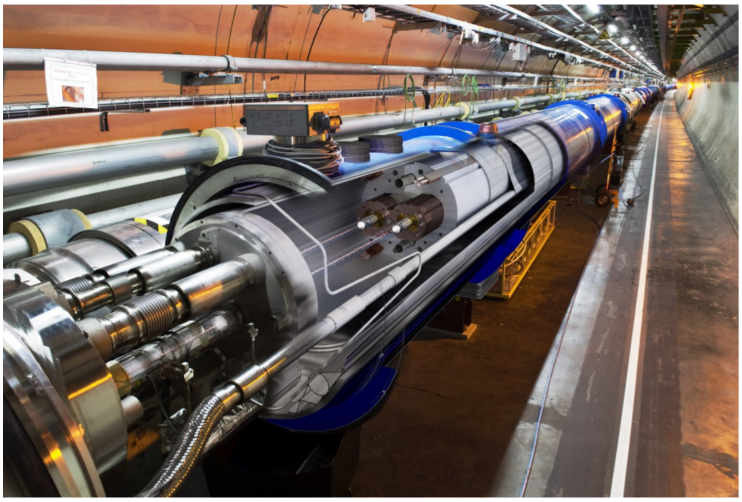

Figure 3.4: Picture of the LHC tunnel with an illustration of a cut out of a superconducting dipole in which the twin aperture inside the cryostat is visible [33].

against is beam halo. These are particles that are too far out from the main trajectory, furthermore they form part of the background in the experiments.

A collimation system at IR3 and IR7 protects against regular and irregular beam losses. Collimation affects the background noise observed in the experiments and managing this is key to the realization of the experiment. Especially for the 900 GeV physics case, prior to the experiment a series of tests were done to optimize the collimation schemes. Because of the importance of the collimation scheme to the total feasibility of the experiment, these will be discussed separately in Section 3.6.

3.3 Luminosity

The presented information in this section is obtained from [35]. In an experiment the beam energy sets the window to which physical processes can be reached and the luminosity is the scaling factor of the production cross section to an event rate. The cross section has the dimensions of area and can in fact be thought of as being an effective cross sectional area. The cross section is the probability that an interaction between two particles will occur. All the fundamental physics is contained in the cross section. Measurement of a cross section at the experiments requires the luminosity to be determined accurately since it is often the dominating source of uncertainty. For a fixed target experiment the luminosity can be decomposed into the number of target particles contained in a surface area perpendicular to the beam (n_{target}) and the rate at which a beam passes through this area, the flux ($n_{\text{beam}}v$) :

$$\mathscr{L} = n_{\text{beam}}v \cdot n_{\text{target}}. \tag{3.2}$$

An example of this is the LHCb experiment that during special physics runs can run as a fixed target experiment by using a SMOG internal gas as target [36]. The flux tells how much the target area is illuminated, together with the number of target particles it sets the luminosity. The luminosity carries the units cm^{-2} s^{-1}. For colliding beams the formula looks slightly different :

$$\mathscr{L} = f n_b \frac{n_1 n_2}{4\pi\sigma_x\sigma_y}. \tag{3.3}$$

This is for a storage ring in which 2 beams continuously cross each other. The beams circulate with a revolution frequency, f, having a number of colliding bunches, n_b, and the number of particles contained in these bunches for beam 1 and 2, n_1 and n_2, respectively. This formula assumes Gaussian beam profiles in the transverse plane and head on collisions. In reality there are additional effects to be taken into account such as: non-Gaussian beam profiles, hourglass effect and the crossing-angle. The luminosity or rather the instantaneous luminosity is part of the design of a particle collider and together with the cross section of a given process it sets the experiment's production rate :

$$R = \mathscr{L} \cdot \sigma. \tag{3.4}$$

Hence, the rate at which events of interest occur is depending on the instantaneous luminosity of the machine. The sizes of the beams σ_x/σ_x are therefore minimized at the interaction point. The sizes of the beam can be controlled through β^* and therefore, for experiments where high luminosity is desired the LHC is set with low β^*. The emittance is inversely proportional to the energy of the beam. Together, the emittance and β set the beam size by relation (3.13). For elastic data taking at 900 GeV the emittance and hence the beam size are rather larger compared to normal runs at the energy frontier. To determine to the total amount of events produced over a certain time period, the integrated luminosity is used. For a particular process, the relation between the total number of occurred events, N, integrated luminosity, L and the cross section, σ, is then given by:

$$N = L \cdot \sigma. \tag{3.5}$$

The integrated luminosity is the instantaneous luminosity integrated over time. It tells the experiments the amount of events that are or can be collected in a given time period. Inversely it is used to determine the production cross section, given the process of interest.

3.4 Beam Dynamics

Unless otherwise stated, the presented information in this section is obtained from [4, 11] and [37]. The storage of particles is characterized by dipole magnets bending the beams along a closed orbit and focusing magnets to keep the particles close together. In order to describe the transverse beam dynamics one needs to know the arrangement of the machine's magnets, including their positions and field strengths along the ring. With a well defined description one can find trajectories of the particles as well as the dimensions of the beam. To describe the transverse motion of a particle we use a co-moving coordinate system (x,y,s). The x-axis pointing towards the center of the LHC, the y-axis pointing vertically upwards and the s-axis moving longitudinally along the ring in counterclockwise direction. The ideal particle perfectly follows the circle, any other particle will oscillate in the tranverse plane by the focusing field, the amplitude of these oscillations will dictate the beam size [37]. The following derivation of the transverse equation of motion holds as a first order linear approximation. The following differential needs to be solved, called the Hill's equation :

$$\frac{du^2(s)}{ds^2} + K(s)u(s) = 0, \quad \text{with boundary condition} \quad K(s+L) = K(s). \tag{3.6}$$

Since the motion in the two planes is uncoupled, the equation holds both in the x and y direction separately, represented by the coordinate u. The quadrapole gradient and the weak focusing effect (only in the x-plane) is parameterized by $K(s)$, L is the circumference of the LHC and hence after one full turn the lattice of magnets will repeat itself. The real part of the solution to

(3.6) can be given by the expression for a pseudo-harmonic oscillator :

$$u(s) = \sqrt{\epsilon\beta(s)}\cos(\Psi(s) - \Psi(0)), \quad \Psi(s) \equiv \int_0^s \frac{ds}{\beta(s)}, \tag{3.7}$$

in which Ψ is the phase of the oscillation, the initial condition given by $\Psi(0)$ and the phase advance by $\Psi(s)$. One recognizes the cosinus term as the oscillating part and its amplitude is given by $\sqrt{\epsilon\beta(s)}$. The number of oscillations per turn is called the tune, Q, and should not be a half integer of integer value to prevent constructing interference to happen caused by magnetic imperfections [32]. The ϵ is the emittance of the beam and the $\beta(s)$ describes the oscillations for particles that are off the design trajectory, called betatron oscillations, under the influence of focusing and defocusing fields along the ring. The local angle of the oscillation with the respect to the longitudinal direction is given by :

$$u'(s) = -\sqrt{\frac{\epsilon}{\beta(s)}}[\sin\Psi(s) - \Psi(0) + \alpha(s)\cos(\Psi(s) - \Psi(0))], \quad \alpha = -\frac{\beta(s)'}{2}. \tag{3.8}$$

This is called the divergence of the beam and it is of importance for elastic scattering as it influences the elastic scattering angle that is measured by ALFA. As depiction of an elastic interaction we can use the following convention for which s = 0 and $\Psi(0)$ = 0 at the interaction point. Additionally the following short hand notations are used : $u(0) = u^*$, $u'(0) = u'^*$, $\beta(0) = \beta^*$, $\alpha(0) = \alpha^*$, $\alpha(s) = \alpha$, $\beta(s) = \beta$, $\Psi(s) = \Psi$ and $M_u(s) = M_u$. Including momentum loss and momentum dispersion together with (3.7) and (3.8), we can rewrite the solution to Hill's equation in the following form :

$$\begin{bmatrix} u(s) \\ u'(s) \\ \Delta p/p \end{bmatrix} = M_u \begin{bmatrix} u^*(s) \\ u'^*(s) \\ \Delta p^*/p \end{bmatrix},$$

$$M_u = \begin{bmatrix} \sqrt{\frac{\beta}{\beta*}}(\cos\psi + \alpha^*\sin\psi) & \sqrt{\beta\beta^*}\sin\psi & D_u \\ \frac{1}{\sqrt{\beta\beta^*}}[(\alpha^s - \alpha)\cos\Psi - (1 + \alpha\alpha^*)\sin\Psi] & \sqrt{\frac{\beta^*}{\beta}}(\cos\Psi - \alpha\sin\Psi) & D_u^* \\ 0 & 0 & 1 \end{bmatrix}. \tag{3.9}$$

For the elastic interaction there is no momentum loss (Δp^* = 0, hence the last entry of the column vanishes. The dispersion only acts on the intrinsic energy smearing of the beam, which is in the order of 10^{-4} rad and can thus be neglected [11]. The third column of the matrix containing the dispersion terms D_u and D_u^* is therefore irrelevant, leading to a simplified depiction of the kinematics :

$$M_u = \begin{bmatrix} \sqrt{\frac{\beta}{\beta*}}(\cos\psi + \alpha^*\sin\psi) & \sqrt{\beta\beta^*}\sin\psi \\ \frac{1}{\sqrt{\beta\beta^*}}[(\alpha^s - \alpha)\cos\Psi - (1 + \alpha\alpha^*)\sin\Psi] & \sqrt{\frac{\beta^*}{\beta}}(\cos\Psi - \alpha\sin\Psi) \end{bmatrix} = \begin{bmatrix} M_{11} & M_{12} \\ M_{21} & M_{22} \end{bmatrix}. \tag{3.10}$$

The parameters in (3.10) can therefore be used with the measured coordinates at ALFA to reconstruct the scattering angle at the interaction point. The set of parameters in this equation are commonly referred to as the optics. The term optics originating from similarity of the the effect of the magnets on the beam and optical lenses controlling light. Thus, given the optics, the measured position at ALFA can be expressed as a linear combination of the transverse position and the transverse angle at the point of collision, u^* and u'^* :

$$u = M_{u,11}u^* + M_{u,12}u'^*.$$

Two protons that make an elastic interaction share the interaction point and the magnitude of the angle, being oppositely oriented, one can subtract the coordinates measured at the right-hand side from the left-hand side of the interaction point to find the scattering angle :

$$u_L - u_R = 2M_{u,12} \cdot u'^{*} \Leftrightarrow u'^{*} = \frac{u_L - u_R}{2\sqrt{\beta\beta^{*}}\sin\psi}. \tag{3.11}$$

Finding the scattering in both planes together with the momentum of the particles allows to reconstruct the t value. Reconstruction methods and their resolution forms are further discussed in Section 9.2. The $\sqrt{\beta\beta^{*}}\sin\psi$ is the effective lever arm, L_{eff}, and is optimized for the vertical direction to enhance the sensitivity to the value of t in this plane. During elastic physics data taking the optics are put such that the phase advance, ψ, between the interaction point and the ALFA detectors equals $\pi/2$ and that the divergence at the interaction point is very small, $\alpha^{*} \approx 0$. This configuration is called *parallel-to-point* optics. With the magnets it is not possible to have simultaneous parallel-to-point optics in both planes, since the beams are approached from above and below at the ALFA stations, resulting in a detector layout for which optimizing to the vertical plane is most advantageous.

3.5 Emittance

Unless otherwise stated, the presented information in this section is obtained from [4, 11] and [37]. Under the influence of focusing and defocusing elements along the storage ring, a particle starts to oscillate around the design trajectory. At every point of the ring, s, it appears with different coordinates in (u, u') space during every turn, mapping out an ellipse over many turns. The many ellipses along the ring are all different. Using (3.7) and (3.8) one can derive the following expression for the integration constant ϵ :

$$\gamma u + 2\alpha u u' + \beta u'^{2} = \epsilon, \tag{3.12}$$

here $\gamma = \frac{1+\alpha^{2}}{\beta}$ is used. Expression (3.12) describes the ellipses and are referred to as Courant-Snyder invariant, since the emittance is a constant with respect to position s. Thus, the integration constant, ϵ, is a characteristic which describes the phase space occupied by a particles trajectory. The physical meaning is found through the area mapped out by the ellipse, given by $\pi\epsilon$. Even though the ellipses look different at each position s at the ring, the area covered in (u, u') phase space and therefore the emittance, remains invariant. Having a look at the extremes, the relative scale of the oscillations is given by β, whereas the absolute scale is set by the emittance :

$$u_{\max} = \sqrt{\epsilon\beta} \quad and \quad u'_{\max} = \sqrt{\epsilon\gamma}. \tag{3.13}$$

From (3.13), it can be seen that for a given emittance β can be either minimized to obtain a small beam spot or maximized to obtain a small divergence.

The emittance is through its relation to the phase space of a particles trajectory considered as a quality factor. A large area in (u, u') space means large amplitudes and angles of transverse motion, which would be considered as low quality. Provided that only conservative forces are acting on the particle, Louiville's theorem states that the area mapped out is constant. The emittance is therefore a property of the beam which can not be changed by external fields, such as the optics of the LHC. However, other non-conservative forces such as interaction between particles in a beam, collisions with beam gas and radiation affects can affect the emittance. Acceleration will decrease the emittance since u' is inversely proportional to the particles momentum. For a beam, an ensemble of particles, the normalized emittance refers to beam size. The transverse particle distribution is measured and the value $\sqrt{\epsilon \cdot \beta(s)}$ defines the area in (u, u') space that contains one sigma, one Gaussian standard deviation, of the beam particles :

$$\epsilon_n = \beta\gamma\epsilon, \quad \textit{with} \quad \beta = \frac{\beta}{c} \quad \textit{and} \quad \gamma = \frac{1}{\sqrt{1-\beta^2}} = \frac{E_{beam}}{m_p}. \tag{3.14}$$

The emittance is measured in the LHC by using wire scans and beam-spot-radiation telescopes and will be explained in Section 3.7. The special physics run at the energy of 450 GeV had a normalised emittance of around 1-2 μm in both transverse planes. The elastic physics program was conducted with β^* of 50/100 m in x/y plane. With *parallel-to-point* optics, $\Psi = \pi/2$ and $\alpha^* \approx 0$, and substituting u' back by θ, we can rewrite (3.11) to :

$$y = \sqrt{\beta\beta^*}\theta^*_y. \tag{3.15}$$

From (3.15) and (3.18) one can notice that the large value of β^* gives access to smaller t values, since it enlarges the y-coordinate at the ALFA detectors. A large value of β^* thus enhances sensitivity to the CNI and Coulomb region of the elastic differential cross section. Assuming now for the moment that the elastic scattering only takes place in the vertical plane, by using (2.6) one finds :

$$-t_{\min} = (p\theta^*_{\min})^2 = \frac{p^2 y^2_{\min}}{\beta\beta^*}. \tag{3.16}$$

The smallest obtainable y-value by the ALFA detectors is given by a multiple, n, of the beam size :

$$y_{\min} = n \cdot \sqrt{\epsilon\beta}. \tag{3.17}$$

For this elastic physics run, n was equal to 3 with a beam size, σ estimated at 1.5 mm. This means that the Roman Pots, introduced in Section 5.2.5, go into the vacuum pipe with approximately 9 mm opening between the upper and lower edge. Expression (3.16) can be written in the following form :

$$-t_{\min} = n^2 \frac{p^2\epsilon}{\beta^*}. \tag{3.18}$$

Using the definition presented in (3.14), the emittance ϵ can replaced by the normalized emittance ϵ_n divided by the Lorentz factor γ (β is approximately 1) to the find the final expression of the smallest reachable -t value :

$$-t_{\min} = n^2 \frac{p^2\epsilon_n}{\beta^*\gamma}. \tag{3.19}$$

The normalized emittance ϵ_n at the beginning of the analyzed ATLAS run was about 1.0 μm, see Section 9.4.2. The γ factor for the 900 GeV campaign is 480. Filling in these numbers, one can estimate the smallest t value:

$$-t_{\min} \approx 3^2 \cdot \frac{450^2 \cdot 1.5 \cdot 10^{-6}}{100 \cdot 480} \approx 3.8 \cdot 10^{-5} \quad \text{GeV}^2. \tag{3.20}$$

For the 900 GeV physics campaign the smallest reachable t-value is approximately around $3.8{\cdot}10^{-5}$ GeV^2. In the experimental setup this value was found to be higher. The reason this is that the active material of the detectors is not directly present at the Roman Pot edge. They are thus placed further out, resulting in higher t-values. From simulation studies prior to the campaign it was known that the acceptance of events by ALFA would become significant from about $\cdot 10^{-4}$ GeV^2. This is still well into the Coulomb region, shown in Figure 2.8. The acceptance of ALFA is discussed in more detail in Section 9.4.1.

3.6 Collimation

The LHC rings each contain a stored beam energy that is potentially highly destructive to the aperture. Especially the superconducting magnets of the LHC can go into transition and loose its superconducting property if only small amounts of the stored energy are released into the magnet. The loss of significant amounts of off-orbit protons must therefore be avoided and suppressed as much as possible. One can not completely prevent the occurrence of beam losses, since primary beam halo will continuously repopulate under various beam dynamics processes. As explained earlier, the particles in the bunches undergo various interactions which leads to a growth of the beam size. Together these processes result in a unavoidable finite lifetime of the beam.

A robust collimation system is required for careful handling of the high beam intensities. Around the LHC, collimators are installed at seven out of eight insertion regions at optimal positions and at various transverse angles, see Figure 3.5 and Table 3.1. The used abbreviations are the following, all starting with a 'T' for target. The collimator primary (TCP), collimator secondary (TCSG), collimator long active absorber (TCLA), collimator tertiary (TCT) and collimator dump quadrupole (TCDQ). They can be oriented to scrape the beam horizontally (H), vertically (V) and skew (S). The material is either carbon (C), carbon fibre composite (CFC), tungsten (W) or cupper (Cu).

There are two main locations, IR3 and IR5, at which a series of collimators are placed called 'warm insertion regions'. The collimation system should, among other things, provide efficient cleaning of beam halo, minimize halo-induced backgrounds in the experiments, scraping of beam tails and diagnostics of halo population. The collimators are the closest elements to the beams and can trigger a beam dump in case of a potential dangerous situation. It consists of two movable jaws that approach each other to constrain the beam halo. They are enclosed in a vacuum tank that can be rotated in the transverse plane to enable effective interception of beam halo in either horizontal (H) , vertical (V) or skew (S) orientation. Most of the LHC collimators contain pairs of 1 meter long jaws which can leave an operational gap as small as 2.1 mm. To reduce the population of halo particles multi-stage cleaning is performed using a setup of primary, secondary and tertiary collimators with additional absorbers. Single-stage collimation would result in too high rates of products, inducing a quench of the superconducting magnets. Beam cleaning is done by primary and secondary collimators made out of a carbon-fibre composite (CFC), additional tungsten (W) absorbers provide downstream protection [38].

For elastic physics the setup of the collimators is crucial to the conditions under which data can be taken, since it affects the level of irreducible beam-induced background. The rate along with the spatial distribution of the background ultimately decides whether the elastic signal can be sufficiently extracted for analysis purposes. Special settings of the collimation system were critical for the feasibility of the unusual conditions of the 900 GeV elastic physics program. An appropriate collimation scheme had to be found to achieve successful data taking, for which the Collimation Working Group (CWG), in close collaboration with the experiments, was responsible. The preparation and final setup of the collimation system is discussed in more detail in Section 8.4 as part of the data taking conditions.

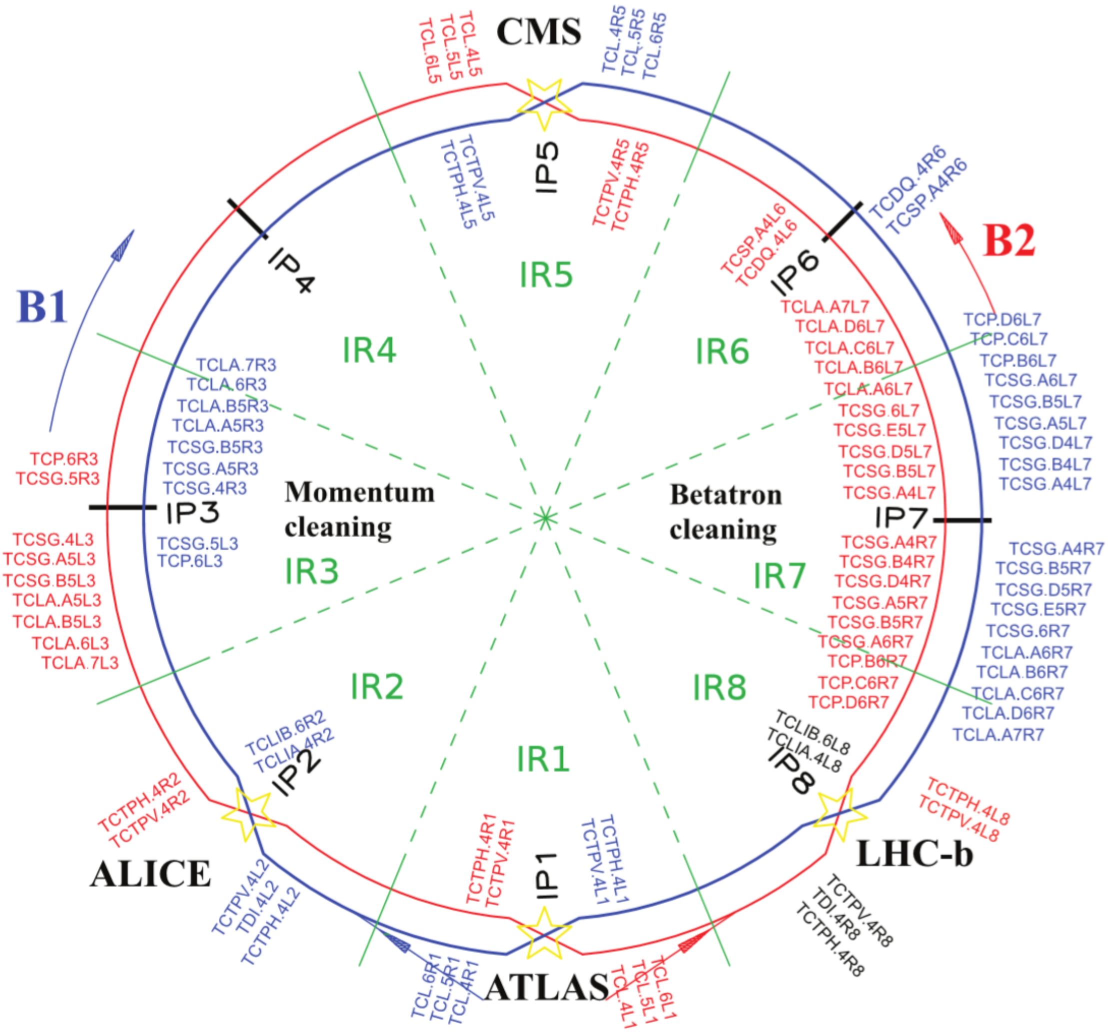

Figure 3.5: Schematic overview of the collimation system around the LHC ring [39].

Functionality	Name	Plane	Number	Material
Primary IR3	TCP	H	1	CFC
Secondary IR3	TCSG	H	4	CFC
Absorbers IR3	TLCA	H/V	4	W
Primary IR7	TCP	H/V/S	3	CFC
Secondary IR7	TCSG	H/V/S	11	CFC
Absorbers IR7	TLCA	H/V	5	W
Tertiary IR1/2/5/8	TCT	H/V	8	W
Physics abs. IR1/5	TCL	H	2	Cu
Dump Protection IR6	TCSG	H	1	CFC
	TCDQ	H	1	C

Table 3.1: List of LHC collimators, per beam pipe. The material is either carbon (C), carbon fibre composite (CFC), tungsten (W) or cupper (Cu). (Injection collimators are not listed) [39]

3.7 Selected LHC Beam Instrumentation

The operation of the accelerator is supported and maintained by various types of instruments of which a part are involved in measuring beam properties. For elastic physics in particular, the measurements of the emittance by the wire scanners and Beam Synchrotron Radiation Telescopes (BSRTs) since they form an important input in the simulation of the elastic signal. These two types of instruments are introduced here and are their measurements are further discussed in Section 9.4.2. Beam loss monitors are used for measuring beam losses that might be of potential danger to the machine. They will be described in the following section since they are also specially used for the positioning of the detectors with respect to the beam. Unless otherwise stated, the presented information in the following sections is obtained from [29, 40] and [41].

3.7.1 Beam Loss Monitors

The beam loss measurement system is part of the LHC machine protection. Its main function is to protect against potential damage caused by energy deposition from lost beam protons, since the repair of a superconducting magnet would mean a down time of weeks [42]. For the LHC, ionization chambers are used that are cylindrical in shape and have a sensitive volume of 1.5 l. The detector is about 50 cm long and has a diameter of 9 cm. The ionization chamber contains parallel aluminum electrode plates and is filled up with N_2 at 100 mbar overpressure. These are contained in yellow insulated tubes and mounted on possible loss locations.

The positioning of the ionization chambers are on the outside of the magnets or near the collimators. Additionaly, they are used for the beam based aligned procedure of the ALFA roman pots, as will be further explained in Section 8.1. The potential damage locations are addressed by particle tracking and particle shower simulations. For the LHC, one such location of losses of off-orbit protons is the transition between a quadrapole and bending magnet. A beam loss monitor near the transition of the quadrapole and bending magnet is shown in Figure 3.6. Limits on timing response of the beam loss measurement system is mainly set by the quench levels of the dipole magnets. The timing resolution of the system on the quadrapole section is 2.5 ms, whereas for the collimation section it is 89 μs, the equivalent of 1 beam revolution.

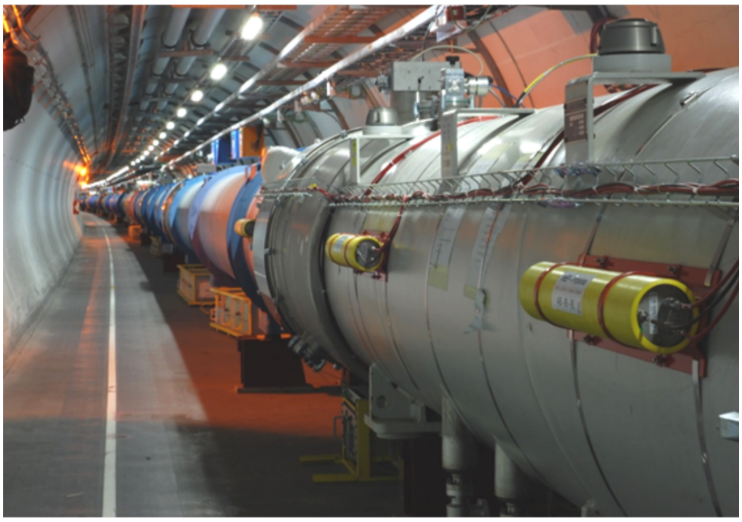

Figure 3.6: Yellow BLMs on a quadrapole magnet [42].

3.7.2 Wire Scanner

The emittance of the beam can not be directly measured and should be determined through the transverse beam size. The two methods of measuring the transverse profile that are of relevance for the elastic signal simulation used in this work will be briefly explained. The wire scanner is used to measure the beam profile at low beam intensity over the whole energy range of the LHC and is used as a calibration apparatus for other beam profile monitors. There are two sets of four wire scanners installed at the LHC, one set at IR4 and one spare set at IR5, at which there is one wire scanner for each beam and plane. The measurements of the wire scanners at IR4 are used in this work as they provide the calibration of the Beam Synchrotron Radiation Telescope (BSRT) located 20 meter upstream of magnet D2.

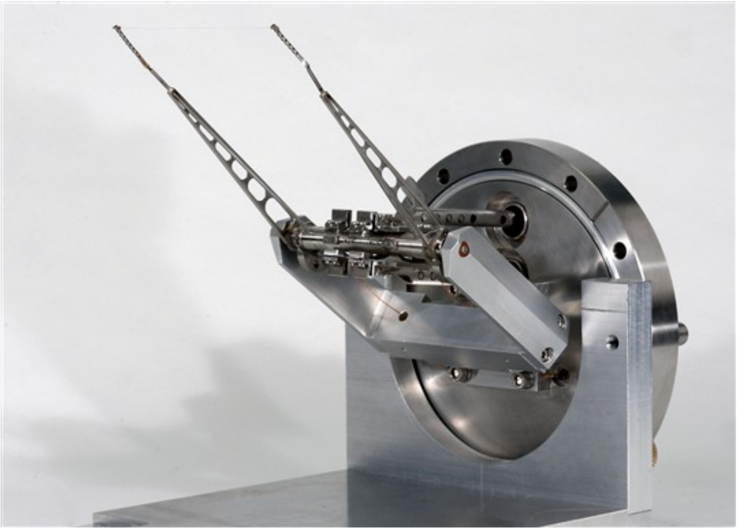

Figure 3.7: Wire scanner used in PS and Booster [43].

The wire scanner consists of carbon wire that is attached at the end of a movable fork. The measurement of the transverse beam profile is done by scanning the beam by a linear movement of the wire through the beam. The speed at which the wire crosses the beam is kept at a constant 1 m/s. The wire scanner makes two scans per measurement, one for the in and one for the out movement of the wire. It gives the transverse profile for each bunch, for which several passages of the bunch are required. The principle of the wire scanner is the measurement of secondary particle particles that are emitted when the wire crosses the beam and are measured by scintillator placed outside the beam pipe. The signal it transported to a PhotoMultiplier Tube (PMT), of which the output current together with the wire position is used to reconstruct the transverse profile.

$$\epsilon = \frac{\sigma^2}{\beta}. \tag{3.21}$$

The obtained profiles are typically Gaussian, the obtained distribution are therefore fitted with a Gauss function. The calculated width of the beam, the beam size σ, can then used to extract the emittance. In dispersion free regions one can infer the emittance through the following relation between the beam size and beta function, as given in (3.21) [44].

3.7.3 Beam Synchrotron Radiation Telescope

On each side of IP4 there is a synchrotron light monitor installed, one for each beam. Synchrotron light is produced by either the D2 dipole magnet or a superconducting undulator, depending on the energy of the beam. At the injection energy of 450 GeV, the dipole does not provide sufficient amounts of visible light and the synchrotron radiation has to be intensified by the superconducting undulator that is installed right before the dipole. An undulator is made up of a periodic magnetic structure that is used to produce quasi-monochromatic synchrotron radiation [45]. The undulator can only be actively used up to a beam energy of 2 TeV, above the wavelength of the synchrotron light does no longer peak in the visible range [40, 46]. In the drift space to the next magnet the light diverges from the beam and with the use of an extraction mirror it is passed trough a vacuum viewport to the optics outside the aperture. Here, 2-dimensional transverse images are taken with a camera. During the ramp up of the energy, the optics can be adjusted to the source of the radiation, undulator or dipole [40].

$$\sigma = \sqrt{\sigma_{\mathrm{bsrt}}^2 - \sigma_{\mathrm{corr}}^2}. \tag{3.22}$$

The BSRTs continuously measure transverse profiles per bunch and need to be calibrated with wire scanners. The 2-dimensional beam images can make beam tilt visible. The BSRT camera measures only actively in the visible range of 400 to 700 nm. Similar to the wire scanners a Guassian fit can be used to extract the transverse beam size in both directions, but due to intrinsic calibration limitations the values need to be corrected with a calibration factor σ_{corr} to be in agreement with the measurement of the wire scanner, see (3.22).

Chapter 4

Scintillating Fibres in High Energy Physics

The scope of this thesis is formed around work related to the commissioning, operation and analysis of two fibre trackers, to be introduced in the next chapters. The active material of these detectors is formed by plastic scintillating fibres. In this chapter the scintillation principle along with properties of scintillation materials are briefly introduced. The scintillation mechanism in plastic scintillators and total internal reflection for scintillating fibres are explained. Attenuation length measurements as part of quality assurance for fibres of the LHCb SciFi detector lead to an systematic error study, the reader is pointed to the extensive report following up on the study. Unless otherwise stated, the presented information in this chapter is obtained from [47].

4.1 Scintillators

In organic scintillating materials a fraction of the energy loss of traversing particles is converted into light. The scintillating phenomenon is also called luminescence and the underlying phenomenon is fluorescence in which absorption of energy in material is followed by a fast re-emission of light, within typical decay times of the range of 1 to 10 ns. The wavelength of the emitted photons is within or near the visible spectrum. The emitted light can be detected using photo sensors that convert the light into an electronic pulse. In general the scintillation principle is widely used for particle detection purposes since it provides a fast response time, it can be operated such that the electronic pulse is proportional the deposited energy and is very inexpensive compared to the covered area. The ideal scintillation material used for trackers should possess, amongst other things, the following characteristics :

- High efficiency for the conversion of energy into detectable light
- Proportionality of the light response to the deposited energy
- Transparency to its own wavelength in order to obtain sufficient light collection at the light sensor
- Short decay time to achieve fast response and thereby high pulse rates

The selection of scintillation material to be used has to be matched to the purpose of the detector as no material simultaneously incorporates all these properties perfectly. The various materials that can be used as scintillators are organic plastics and liquids, inorganic crystals, gaseous scintillators and glasses [48]. Gaseous scintillators are generally noble gases in which individual atoms are excited followed by the emission of light upon relaxation to their ground state. Glass scintillators are generally used for the detection of thermal neutrons due to the large neutron cross section of the constituents lithium and boron. They are very robust and can be used in extreme environmental conditions. For inorganic crystals, the scintillation mechanism depends on the band structure of the crystal. The electrons are promoted from the valence to the conduction band and fall back under the emittance of light. The organic scintillation mechanism will be explained in more detail in the following section.

4.1.1 Organic Scintillation

The majority of organic scintillators are based on aromatic hydrocarbon molecules, these are molecules that contain carbon atoms forming circular structures called benzene rings. The rings are named after the benzene molecule, the simplest aromatic hydrocarbon: a single ring made out of 6 carbon and 6 hydrogen atoms. These are formed through covalent bonds between the respective atoms in which the electrons are not bound to a particular atom by forming molecular σ- and π-orbitals. The π electrons are delocalized and together with the conjugated double bonds of the unsaturated carbon atoms in the benzene rings, they are of importance to the scintillation properties [49]. Opposed to inorganic crystals, the fluorescence in organic scintillators is of molecular origin, the transitions of the electrons take place between energy levels within the molecules. The fluorescence is therefore also independent of the physical state of the matter, in contrast to inorganic crystals which require an orderly structured crystalline lattice.

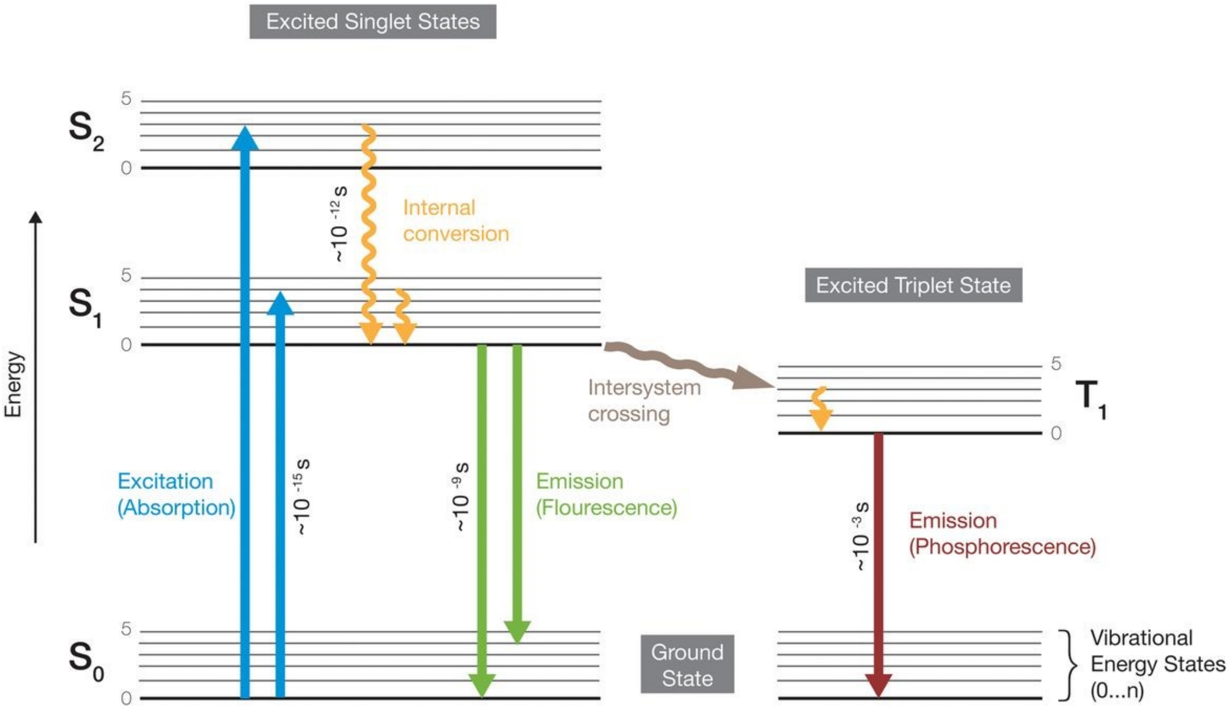

Figure 4.1: Energy levels of an organic molecule with π orbital structure [50].

The energy levels of the π electrons are shown in Figure 4.1. The singlet states, spin 0, are labeled with S_0, S_1 and S_2, additionally a triplet state, spin 1, is labeled with T_1. The energy spacing between the ground state S_0 and first excited state S_1 is about 3 or 4 eV, the spacing between higher excited states is smaller. Each of the energy levels can be further subdivided in finer energy levels corresponding to vibrational states of the molecule. The ground state of the electrons is the S_0 state and upon energy absorption they can be excited to any of the excited states, depicted by the blue arrows pointing upwards. This process occurs upon absorption of kinetic energy of charged particles passing through the material. De-excitation of the higher singlet states to the S_1 state takes place through radiationless decay by giving up energy to their surroundings. This process to loose excess vibrational energy is called relaxation and is of a rather fast timescale in orders of picoseconds [51]. Vibrational relaxation and internal conversion are depicted by the yellow arrows in the figure. As a consequence of energy absorption, the material contains a population of excited S_1 molecules within a negligible amount of time.

From the first exited state S_1 prompt fluorescence occurs under emmission of light in the transition to one of the vibrational modes of the ground state. The process is indicated by the green arrows pointing downwards. The prompt fluorescence intensity can be described by an exponential decay in which the typical life time is in the order of nanoseconds. Additionally, under the influence of the spin-orbit coupling the molecule may undergo intersystem crossing by unpairing the electron spins. This is a non-radiative process and as consequence the molecule is converted into a triplet state. The life time of the T_1 state is much longer, in the order of up to milliseconds, since the return to the ground state is a forbidden decay. This relatively slow process is called phosphorescence and is depicted by the dark red arrows pointing downwards. Some of the T_1 molecules may be thermally excited to the S_1 state again, giving rise to a delayed fluorescence component.

The emission energy of the fluorescence is smaller than the initial excitation energy of π electrons. This can be seen from Figure 4.1, in which the y-axis represents the energy scale of the orbital states. The arrows pointing upwards are larger then the one pointing downwards. This has previously already been explained by the fact the molecules partly get rid of energy through relaxation. The energy of the emitted photons under fluorescence is therefore smaller than the initial energy gap of the ground state to the excited states. In organic scintillators there is only little overlap between the absorption and emission spectra. Hence, the organic scintillator is transparent to its own fluorescence with a wavelength around 300 nm. The difference between the absorption and emission spectra is known as the Stokes shift and an illustration of this is shown in Figure 4.2.

Organic crystals are hard to cut and its response might depend on its orientation. Organic scintillators are therefore commonly dissolved in liquid or plastic materials with concentrations in the order of 1% by weight [52]. In most solvents there is efficient energy transfer between molecules and this is important since most of the absorbed energy is by the solvent. Through intramolecular transfer the energy finds its way to the scintillation molecules that subsequently undergo fluorescence. However, the light yield of organic scintillators remains low compared to other scintillating materials. There is a variety of solvents and organic scintillants, and the use of these binary organic scintillators provide another benefit, namely that the solvent can be loaded with additives. An example of additional components are wavelength shifters that are added in low concentrations of about 0.05% in weight [52]. Wavelength shifters absorb the light from the scintillator and re-emit at longer wavelength. This shift in the emission spectrum can be beneficial to better match the optical sensitivity of the photo sensor and enhance the transparency of the material towards it own radiation. This last point is particularly useful for large detectors volumes, for which liquid and plastic scintillators form attractive materials.

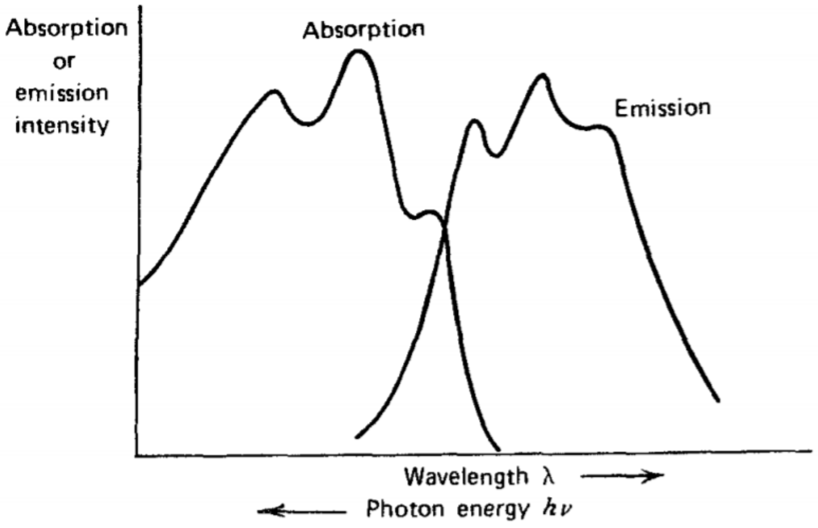

Figure 4.2: Illustration of the Stokes shift for a typical organic scintillator: difference in optical absorption and emission spectra [47].

4.1.2 Plastic Scintillators

Organic scintillators can be dissolved in a solvent which subsequently can be polymerized to produce a solid solution. The styrene monomer is an example of a solvent in which an organic scintillator, called fluor, can be dissolved. After this, the styrene is polymerized to form a solid plastic. Plastic scintillator materials have good rise and decay times of the level of only ns and few ns scales, respectively. Additionally, they are attractive since they can be shaped rather easily in any desired form. Therefore, plastic scintillators are available in a large variety of sizes and shapes. Since the material is relatively inexpensive, plastics are often attractive to use in case large volumes need to be equipped. Degradation is of the material affects the light output and hence the overall efficiency and usability of this type of plastic scintillators. In high energy physics the main cause of degradation is often through exposure to high levels of radiation. The degradation due to irradiation damage depends on a variety of variables such as the dose rate, presence of oxygen and the nature of the radiation. A reduced light yield output can be caused by direct damage of the scintillating component but is typically characterized by enhanced light transmission losses by created absorption centers. The damage might be of temporary nature and the material might show (partly) recovery over time windows that last from hours to days. Plastic scintillators are also available as small diameter fibres, scintillating fibres, which can be used when good spatial resolution of the position of traversing particles is required. Scintillating fibres are the subject of the next section.

4.2 Plastic Scintillating Fibres

Plastic scintillation materials are fabricated as fibres with diameters ranging from as small as tenths of a millimeters to several millimetres. The material is of rather ease use which enables for production of round, square, hexogonal and other cross-sectional fibre shapes. Due to limited energy deposition in small diameter fibres and relatively low scintillation efficiency, the light yield output is moderate. A commonly used core material is made of polystyrene with added dopants functioning as scintillator and wavelength shifter. Additionally, scintillation fibres may contain one or more claddings. Scintillation light originates in the core of the fibre where the scintillator is present. The core is optically denser than the cladding(s) which is required for the total internal reflection at the interfaces, by which the light is guided towards the end of the fibres. Total internal reflection can be understood by exploiting Snell's law, in case of incident light crossing an interface to a medium with lower index of refraction, n. At increasing angle the light will surpass the critical incident angle, resulting in total internal reflection:

$$\sin \Theta_T = \frac{n_{\text{cladding}}}{n_{\text{core}}} \tag{4.1}$$

Only a small part of the light is successfully guided to the end of the fibre. To maximize the light yield, sufficient concentrations of scintillator is usually added. At high enough concentrations the distance between the polystyrene and the scintillator may be sufficiently small to sustain energy transfer through non-radiative dipole-dipole coupling, called Förster transfer [53]. The wavelength shifter enhances the light yield at the end of the fibre by increasing the wavelength of the emitted light towards the more transparent part of the material and therefore the propagated light becomes less prone to absorption along the fibre. However, the intensity of the scintillation light is inevitably attenuated along propagation towards the fibre end. Amongst other things, one can think of several affects such as imperfections at core-cladding interfaces that disrupt total internal reflection, remaining overlap between emission and absorption spectra of the scintillator and fibre material and production of absorption centres created by irradiation. The combined affect of attenuation is an intrinsic property of the fibre and if referred to as the attenuation length, forming the subject of Section 6.2.3. Photo sensors can be placed a both ends of the fibre to have nearly coincidence pulses or only at one end. In the latter case the opposite end of the fibre can be fabricated to create a mirror effect and reflect back and yield as much light output as possible.

4.2.1 Attenuation Measurements and Natural Aging Studies

The production of the 12,000 km of fibre used for the SciFi tracker was done by Kuraray and organised in three phases, namely a pre-series of 500 km, a main series of 10,500 km and 1,000 km spare series. This was delivered over time period of over three years, with batches arriving at CERN weekly or bi-weekly. The batches consist of spools, with each typically 12,5 km of fibre wound up around it. After arrival, samples from all fibres delivered by Kuraray underwent a quality assurance procedure. Part of the quality assurance was to determine the attenuation length and has been reported on by collaborators in [54]. The author has not participated in any of the activities. A detailed introduction on the fibre and its attenuation length properties can be found in Sections 6.2.2 and 6.2.3.

At the end of their lifetime after 10 years of operation, the fibres will reach a foreseen age of up to 14 years since their production date. A small aging rate of a near percent level per year might thus significantly impacts the performance of the detector. Natural aging might appear due to diffusion of small molecules and oxidation of the material, which are temperature and oxygen dependent effects [54]. To gather information on degradation of the fibre attenuation measurements have been carried out and collected since the first deliveries in 2015, batches were re-measured approximately every 3 to 5 months.

In [54], the obtained results from various batches are shown in combined plots for which the aging time is taken with respect to the delivery date. The production date was assumed to be 1-2 months prior to delivery. In general the results show that the behaviour of up to 15 months is unambiguous. Initially, fibres of an initial short attenuation length even tend to improve, which after approximately 15 months also tend to degrade similar to the fibres with an initial long attenuation length. The improvement in attenuation of smaller initial attenuation length is not fully understood. From 15 months onward, the combined result of batches shows a small overall degradation in attenuation length, which to first approximation is taken linear with an aging rate of 1.4% per year.

In order to quantify the attenuation length for the delivered batches and by that verify the quality, the used setup has been adequate. In respect of the presented aging studies one should, however, be cautious with drawing conclusions. Subject to the above, one might think of some remarks regarding the presented data. The shown data points represent a sample in which single measurements of individual fibres are taken together. The fibres belong to different batches produced over a wide time range of up to several years. Even though one aims for homogeneous production conditions, there might be fluctuations in fibre composition. Therefore, one can question whether individual measurements on the fibres originating from various batches can represent a sample of measurements. Furthermore, with retrieved production dates from Kuraray, it was shown that the production dates of the spools in a single batch (shipping) varied stronger than was anticipated. The variation in production dates within the batches was typically 2 till 4 months, with extremes of up to 6 months. Hence, data presented based on a delivery date could be misleading, exact production dates would be more appropriate. Overall, this would lead to significant changes in time labeling and rearrange data points on the graphs. Most importantly, for individual measurements the uncertainty is known with poor accuracy and hence knowledge on this would be beneficial in view of the continuation of the aging study. In view of the relatively small aging effects and better understanding the attenuation length measurements a summer student project was dedicated to repeatability and the investigation of error sizes. The author actively participated and supported the student in his endeavours, the outcome of the error analysis will be briefly presented in the following section.

4.2.2 Error Analysis of Attenuation Measurements

The program on the investigation of attenuation measurements has been carried out by a summer student in close collaboration with the author of this thesis. The workload dedicated to this study takes a relevant share in the efforts that are reported on in this thesis. A full chapter could have been dedicated to the setup and outcome of the various tests that were conducted over the summer of 2019. However, the collaborative work was already extensively described in a report written solely by the summer student, and hence it was decided not to spend time on it since such an extra report would be unnecessary. For the reason that it reflects yet another important aspect of work related to fibre trackers, namely laboratory work on active detection material, it is strongly suggested to reader to have a look at the report [55]. The document describes the full setup, method, conclusions and considerations that were encountered during the study. One of the main conclusions was that multiple measurements of individual fibres are required to be sensitive to the aging effect described in the previous section.

Chapter 5

ATLAS-ALFA Detector

A Toroidal LHC ApparatuS (ATLAS) detector is one of two general purpose detectors at the LHC.The ATLAS detector is built cylindrically around IP1 of the LHC and its barrel is depicted in Figure 5.1. The barrel is composed of many sub-detectors, of which most are illustrated in the figure. and will be briefly introduced below. The ALFA detector is yet another sub-detector of ATLAS. In contrast to the other ATLAS sub-detectors ALFA is not located in the cavern of the ATLAS barrel, but approximately 240 meters away on each side of IP1. The first section provides a brief introduction of the ATLAS detector in which sub-detectors may be pointed out if they are of particular interest for the analysis. The second section provides a more detailed introduction of the ALFA detector and is relevant for the elastic physics data taking campaign and subsequent analysis presented in Chapters 8 and 9, respectively.

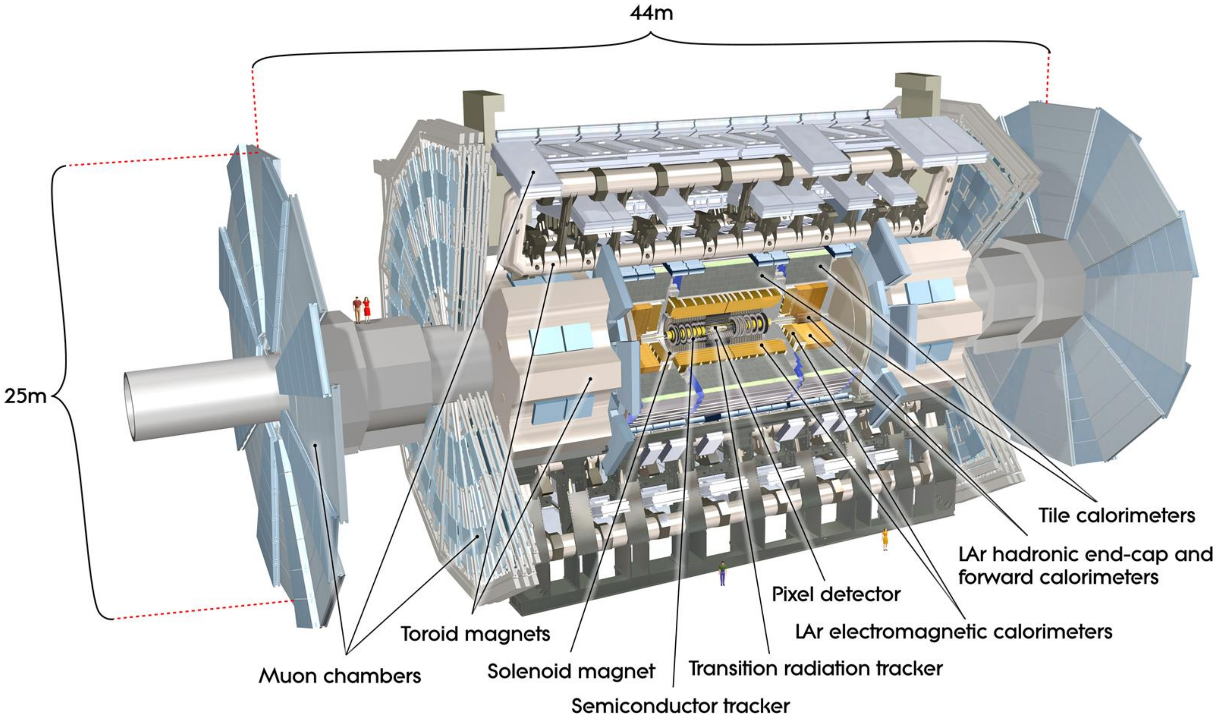

Figure 5.1: An illustration of the ATLAS detector [56].

5.1 ATLAS

The particle collisions take place in the heart of the detector. Following a collision short-lived particles and resonances are created, and undergo subsequent decay. The decay products are moving outward from the innermost part of ATLAS and may traverse the sub-detectors in consecutive order. Unless otherwise stated, the presented material in this section relies on [57].

5.1.1 Sub-detectors

The innermost part of ATLAS is the Inner Detector (ID). The ID consists of the silicon Pixel and silicon microstrip (SCT) trackers and Transition Radiation Tracker (TRT), depicted in Figure 5.2. The TRT straw tubes contain a xenon-based gas mixture. The ID is contained in a solenoidal magnetic field of 2 T. The purpose of the ID is track pattern reconstruction, thereby providing high resolution measurements of momentum and vertices of charged particles. The spatial distribution of the primary vertices, the luminous region, is used to determine the transverse beam spot width. The variation in the exact interaction location is relevant since the IP determines where the events will hit the ALFA detectors. This spread is thus an important input parameter for simulation of the elastic signal in ALFA and is discussed in Section 9.4.2.

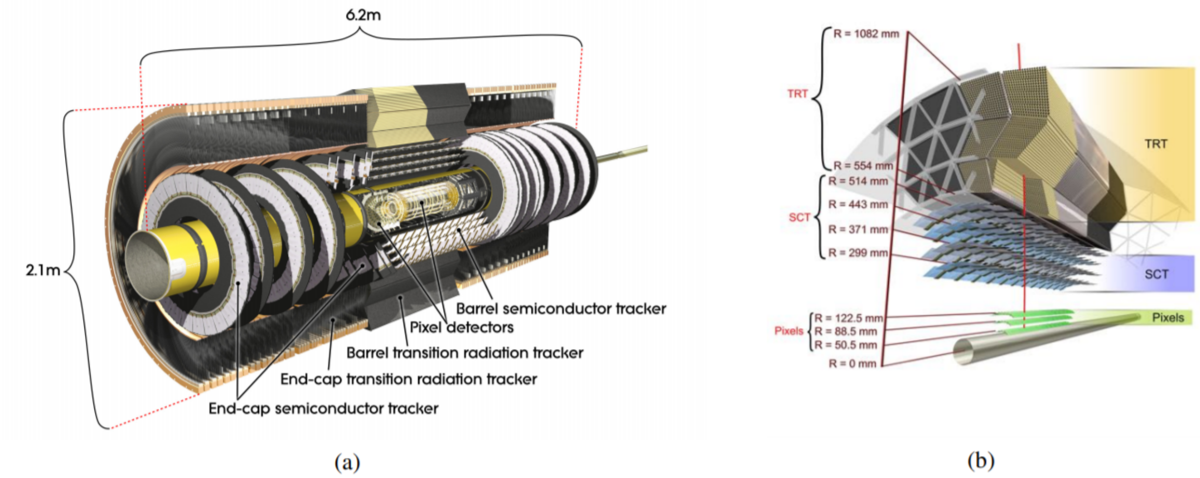

Figure 5.2: An illustration of the Run 1 Inner Detector (during Run 2 it had additional pixel layer) [57]: (a) barrel and end-cap sections; (b) cross-sectional view of the barrel.

The ATLAS calorimetry system consists of an electromagnetic and an hadronic calorimeter that provide energy measurements by fully absorbing particles, illustrated in Figure 5.3. The electromagnetic calorimeter consists of active liquid argon (LAr) layers interleaved with lead absorber plates. The hadronic calorimeter can primarily be divided into two parts: 1) the barrel part using scintillating tiles as active material interleaved with lead, 2) the end-caps and forward parts using LAr as an active material. The absorbing material in the end-cap is solely copper, whereas the forward part is partly built with copper and partly with tungsten plates.

The outermost part is the muon system. The muon spectrometer consists of the superconducting toroid magnets producing a field in the transverse plane. The magnets are complemented by monitored drift tube chambers (MDT) and multi-wire proportional chambers in the form of cathode-strip chambers (CSC) used for precision tracking of the muon.

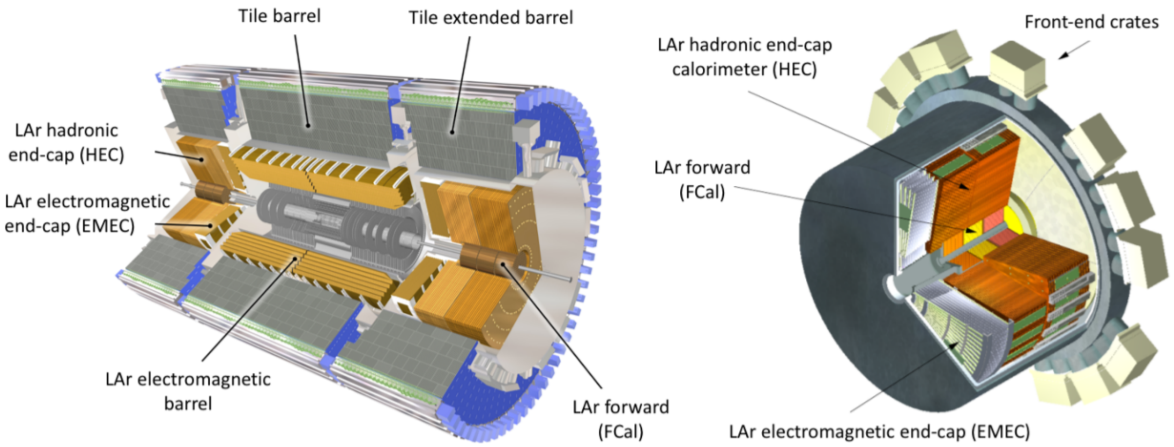

Figure 5.3: An illustration of the calorimetry system (left) and an enlarged view of the end-cap calorimeters (right) [57].

The Minimum Bias Trigger Scintillators (MBTS) are placed on the inside of the electromagnetic end-cap calorimeters. They are of importance for soft QCD physics, and in particular for the elastic physics program. This trigger provides information on inelastic events: single diffractive events in combination with a halo particle might fake an elastic trigger, discussed in Section 9.3.

5.1.2 Trigger System

During normal runs the proton-proton interaction rate far exceeds the capacity of data recording resources. Furthermore, one is only interested in hard scattering processes between partons (quarks and gluons). A trigger system is required to significantly reduce the event rate and thus only select and store events of interest. The ATLAS trigger system can be divided into two parts: the Level-1 (L1) and the High-Level-Trigger (HLT). The Central-Trigger-Processor (CTP) is an integral part of L1 that only selects the events that fulfill combination of a triggers. The L1 trigger is based on reduced granularity of the calorimeters and muon chambers. It is a fully hardware-based trigger that runs at full rate, using custom built electronics. Each individual CTP item consists of logical trigger scheme, together the various CTP items form the trigger menu. If an event meets the trigger logic of an CTP item it continues to next step in the data acquisition. Each item in the trigger menu holds a prescale, n, to reduce the event rate by letting only one out of n events fulfilling the CTP item to pass through to the HLT.

During the normal physics program the L1 trigger reduces the 40 MHz bunch crossing rate to an event rate of less then 100 kHz that is further processed by the HLT. The HLT is a 2-layer software based trigger that refines the selection further. The first layer performs reconstruction in the regions of interest, the second layer has access to the complete information from all sub-detectors at their full granularity. The HLT is an entirely software based trigger using fast algorithms to reconstruct events. After reconstruction it is decided whether an event should be selected. This second layer further reduces the event rate to 1 KHz to be stored for offline analysis [58].

In addition to the calorimeters and muon detectors, the forward detectors are connected to the CTP. The elastic trigger menu items related to the ALFA detector are all of trigger type L1.

5.2 ALFA

The measurement of elastically scattered protons is one method of determining the absolute luminosity for the ATLAS experiment. To accomplish this it is necessary to measure elastically scattered protons that are closest to the beam, i.e. with smallest t-values, as was previously explained in Section 2.3. The Absolute Luminosity For ATLAS (ALFA) detector is designed to approach the beam and measure elastically scattered protons to a few microradians. This section provides a description of the ALFA detector and unless otherwise stated, the presented material in this section is based on [11, 59] and [4].

5.2.1 Detector Design

The ALFA detector system is a set of 8 tracking detectors located on either side of the ATLAS barrel. Elastic interactions between protons occur uniformly in the transverse plane, i.e. equally likely for a given azimuthal angle. The setup of the magnets during an elastic physics program is such that the elastically scattered protons appear in a vertically-shaped hit pattern at ALFA. To reach the smallest possible t-values means that the detector should approach the beam as closely as possible.

These factors require vertical movement of the detector as far as inside the beam pipe while being physically separated from the ultra-high LHC vacuum. The detector is therefore housed inside a vessel called a Roman Pot, to be introduced in Section 5.2.5, is a metal housing that has a thin window to minimize the distance of the detector to the beam and thin walls to minimize the material in front of the detector. The electronics of the detector are all contained outside the Roman Pot. Movement of the Roman Pot is done using high precision roller screws connected to a step motor, which allows for a minimum displacement of 5 μm. The detector is composed of a main detector (MD) to measure the coordinates of protons and two overlap detectors (OD) used for alignment, a frontal view of a detector placed inside the beam pipe is illustrated in Figure 5.5. The main detectors and overlap detectors each have dedicated trigger tiles, shown by the central picture in Figure 5.4.

The detectors are placed on both sides of the ATLAS barrel on the outgoing beam pipes. At each side, there are two stations, the inner station, and the outer station, placed at approximately 237 and 245 meters, respectively. A single station holds two Roman Pots, one that can be inserted into the beam pipe from above and another one that can be inserted from below. The stations are placed in between quadrupoles Q6 and Q7. A complete overview of the ALFA detector system is illustrated in Figure 5.4. The eight detectors are labeled uniquely using a five character string, in the order of their position: B7L1U, B7L1L, A7L1U, A7L1L, A7R1U, A7R1L, B7R1U, and B7R1L. Throughout this thesis this official naming convention will be used, holding the following logical scheme :

- A/B labels whether is an inner/outer detector.
- 7 indicates that it is the 7^{th} element from the IP.
- L/R labels whether it is on the left/right hand side of the IP, denoted by A-side and C-side.
- 1 indicates the location around the LHC, namely IR1.
- U/L labels whether is an upper/lower detector.

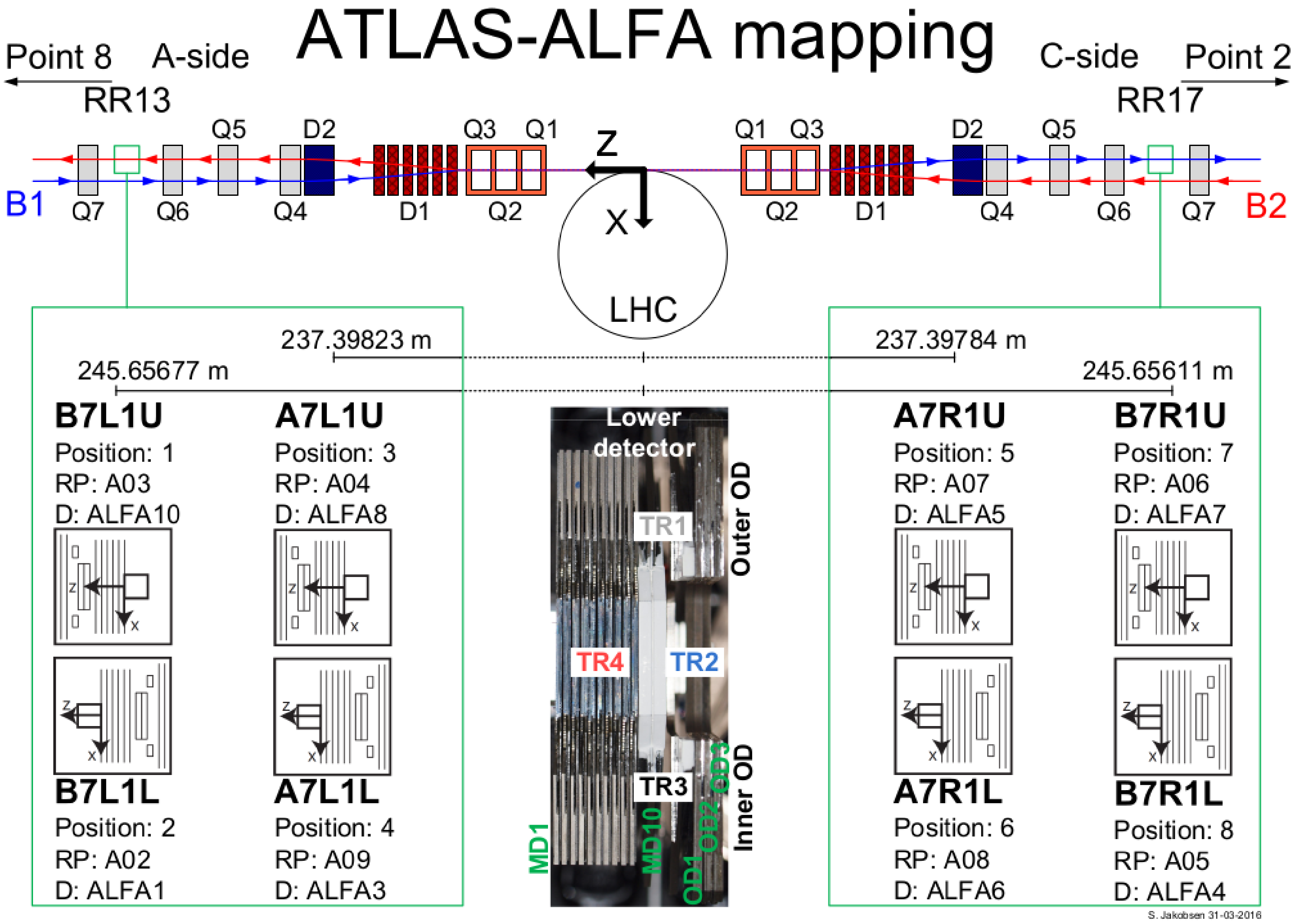

Figure 5.4: Map of the eight ALFA detectors with the naming scheme and their corresponding positions and orientations at the outgoing beams. The quadrupoles are denoted by Q and dipoles are denoted by D. A picture of a top view of the lower detector shows the first and last layer of the main detector labeled in green by MD1 and MD10, its trigger tiles are labeled TR2 and TR4. The inner overlap detector layers are labeled by OD1, OD2 and OD3, its trigger tile by TR3. The trigger tile of the outer overlap detector is labeled by TR1. By S. Jakobsen.

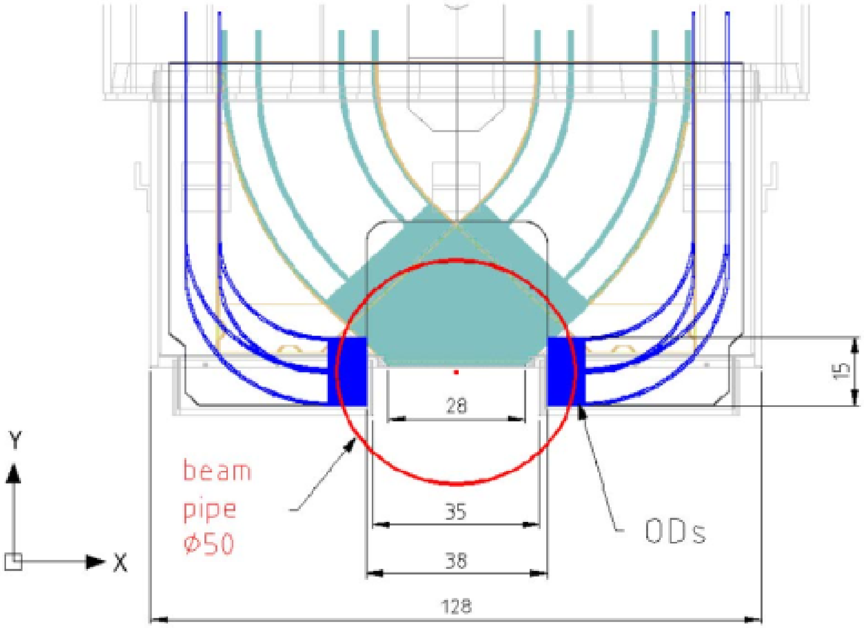

Figure 5.5: Frontal view of the Overlap Detector (purple) positions with respect to the Main Detector (blue), inserted inside the beam pipe (red) with at its center the beam (red dot) [4].

Due to momentum conservation, the experimental signature of an elastic pp interaction is a proton hitting detectors that are diagonally located of the IP compared to the detectors hit by the other proton on the opposite side, illustrated in Figure 5.6. Naturally, one has two configurations in which an elastic interaction can manifest itself, referred to as arms. An elastic event hitting detectors B7L1U, A7L1U, A7R1L, and B7R1L is referred to as an arm 1 event, whilst an elastic event hitting detectors B7L1L, A7L1L, A7R1U, and B7R1U is referred to as an arm 2 event. A set of two upper or lower events is referred to as an armlet. The arms and armlet are shown by the schematic of the ALFA detector in Figure 5.6. As indicated by Figure 5.4, each detector has a corresponding position. Following the increasing position number gives the following order: B7L1U, B7L1L, A7L1U, A7L1L, A7R1U, A7R1L, B7R1U, and B7R1L. For shorthand notation only the position number might be used to indicate a certain detector involved in a particular event. For example, an elastic event hitting detectors 1,3,6, and 8 is an elastic event of type arm 1 consisting of detectors B7L1U, A7L1U, A7R1L and B7R1L.

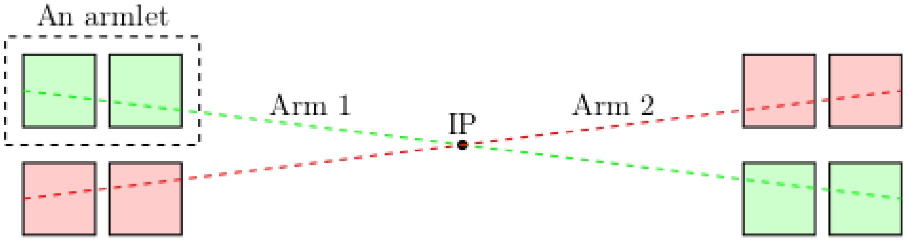

Figure 5.6: Overview of the nomenclature held by the elastic program, in which the dashed green (red) line shows the elastic arm 1 (arm 2). Armlet 1 is indicated by the dashed box around detectors B7L1U and A7L1U. The armlet number following the counterclockwise direction [20].

5.2.2 Squared Scintillating Fibre

The presented material in this section relies on references [11] and [59]. The scintillating fibres used in the ALFA detector are squared single-cladding fibres as illustrated in Figure 5.7. They are produced by Kuraray Co., Ltd (JP). The fibres are of type SCSF-78, S-type with a size of 0.5 x 0.5 mm^2. The emission spectrum of the fibre extends from 415 to above 550 nm, with a peak of the emission light at 450 nm. The main core material is polystyrene surrounded by a PMMA cladding, their properties are listed in Table 5.1. Light is trapped by total internal reflection by the core-cladding interface which for single-cladded fibres shows larger trapping efficiency for squared shaped fibres compared to round shaped fibres: 4.2% against 3.1% [60]. This effect can be attributed to the effect that the reflection angle increases near the corners of the square fibre and are larger compared to the center, which is the equivalent of all the reflections made within a round fibre. The light yield could benefit from a second layer of cladding, but this also implies less cross sectional active material, which is of importance when used stacked structure. The cladding of the square fibre used is made from PMMA and has thickness of 10 μm, 2% of the diameter. Each cladding layer in a round fibre takes account 3% of the fibre diameter. For this reason the squared single-cladded fibres have been chosen to be used for the ALFA detector.

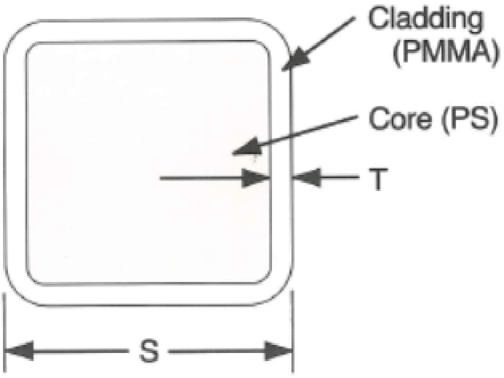

Figure 5.7: Cross-sectional view of a single-cladded squared fibre [60].

	Material	Refractive index	Density $\left[\frac{\text{g}}{\text{cm}^3}\right]$
Core	Polystyrene (PS)	1.59	1.05
Cladding	Polymethylmethacrylate (PMMA)	1.49	1.19

Table 5.1: Main materials for single-cladded squared fibre

The fibres are of S-type, a parameter that describes the axial alignment of the polystyrene in the fibre core. A higher degree of alignment is beneficial for the mechanical properties, however it also reduces the attenuation length. Since the length of the fibres used for the ALFA detector are rather short this is of minor importance. The strength of the fibres are needed in case of the ALFA detector since they are bend, even up to 90° for the overlap detectors.

To avoid optical cross-talk, by which scintillation light propagates from one fibre to a neighbouring, the fibres are coated with a thin aluminum film layer of 100 nm thickness. The quality of the coating at the surface interface is important to light containment and the prevention of cross talk. The end of the fibre are machined to make a mirror finish with aluminum coating, this is beneficial to the overall light yield collected at the other end by the MultiAnode Photo-Multiplier Tube (MAPMT). Radiation hardness of the fibre is of importance for the lifetime of the detector. During radiation studies it was found that obtained losses can be mainly attributed to loss in transparency of the fibre and not by loss of primary scintillation light. The test furthermore showed a full recovery of the fibres within a few weeks after irradiation tests with an accumulated dose below 10 kGy [59].

5.2.3 Main Detector

The MD is used to measure the coordinates of elastically scattered protons. The active part of the detector is formed by scintillating fibres. One ALFA detector consists of ten MDs made out of a titanium plate with a layer fibres on each side of the plate, giving a total of 20 layers of fibres. One MD is shown by the picture in Figure 5.8: a single layer consists of 64 scintillating fibres. Each MD has layers in two orientations: the front side of the titanium plate is a V-plane and the backside a U-plane. The V- and U-plane are put in orthogonal setup giving 2D dimensional tracking. A cut of 45° to the end of the fibre is applied to 40 out the 64 fibres to have the detector edge horizontally and maximize the acceptance. This gives the characteristic diamond shape of the tracking region, more pronounced in Figure 5.5. In this tracking region there is no titanium in between the front and back layers in order to reduce multiple scattering inside the detector. The titanium plates are put such that the consecutive layers of fibres are shifted about one tenth of the fibre width from one plate to another. This creates a staggering that enhances the resolution of reconstructed tracks.

The 24 fibres with a 90° cut have been machined and aluminized at the end to create a mirror finish which increases the light yield at the readout. The 40 fibres cut at 45° have not been finished with an aluminized coating at the end as a dedicated study showed that the reflectivity was almost independent of such mirror finish [59]. The fibres of a single layer are individually connected to a 64-channel MAPMT. Light generated by the passage of proton is converted into an electronic signal by the MAPMTs. The mapping of the fibres is such that neighbouring fibres are not put on neighbouring channels of the MAPMT. This is to reduce the cross-talk between neighbouring channels.

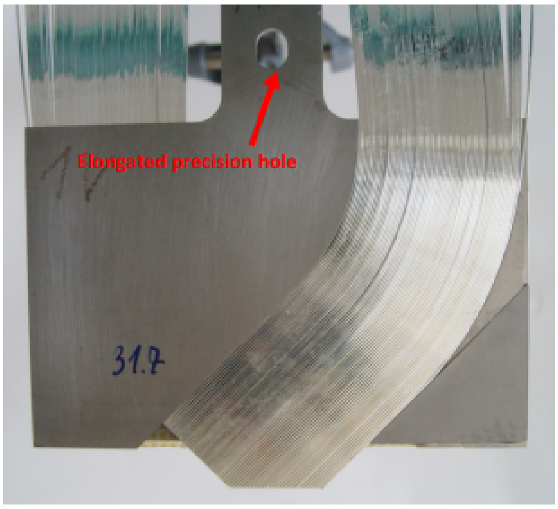

Figure 5.8: ALFA MD: fibres of the V(U)-plane glued on the front(back) of a titanium plate [4].

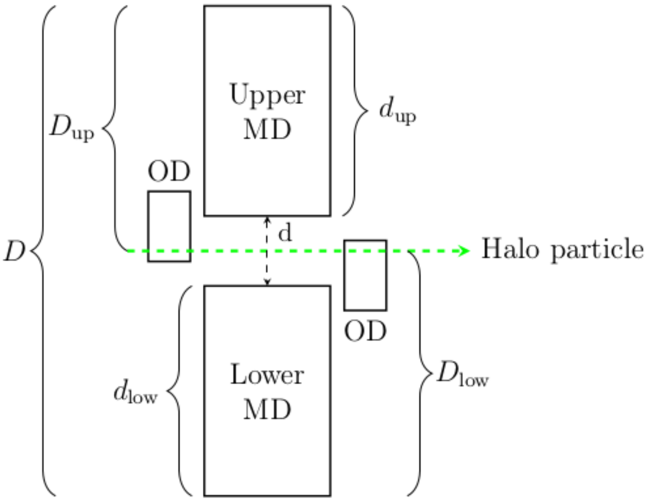

Figure 5.9: Principle of distance determination using Overlap Detectors [20].

5.2.4 Overlap Detector

The OD is used to determine the distance between the detector edges of the MDs in a station. The ODs are placed on both sides of the MD and when the upper and lower detectors approach the beam, these detectors overlap in the longitudinal direction. The active part of the ODs are formed by the same type of scintillating fibres as used for the MDs. The principle of extracting the distance, d, is illustrated in Figure 5.9. During a test beam campaign the relative positions between the ODs and the MD edges have been measured [4]. A halo particle traverses the ODs of the upper and lower detector, giving distances D_{up} and D_{low}. With the measured calibration constants d_{up} and d_{low}, the distance between the detector edges, d, can be determined.

The OD consists of 3 layers made out of titanium plates with 30 fibres on both the right-hand and the left-hand side. The 30 fibres are divided equally, having 15 fibres glued on the front and 15 fibres glued on the back of the titanium plate. The front and back parts do not overlap, but rather they are displaced vertically such that they form a single, continuous active layer when approached frontally. The active part of the fibres are orientated horizontally since the OD only aims to determine the vertical distance between the upper and lower MD. The end of the fibres have a 90° cut with an aluminum coating at the end, giving a mirror finish. The OD fibres are connected to MAPMTs. The 30 fibres of the inner OD and the outer OD of a layer share a MAPMT and cross-talk between ODs is therefore possible. Similar to the MD, no neighbouring fibres share neighbouring channels on the MAMPT. This is in order to minimize the combined effect of optical and MAPMT cross-talk. Similar to the MD, the 3 layers of the OD were intented to be staggered, with 166 μm and 333 μm offset, to increase the track resolution. The actual staggering was not ideal, causing the overlap size to vary between 1 μm and 380 μm. The large deviation from the ideal 166 μm staggering reduces the precision of the distance measurement.

Only halo particles are aimed to be observed by using a small acceptance placed in a region where no elastic events are to be expected. The OD edges are positioned 19 mm from to the beam pipe center, depicted in blue in Figure 5.5. The LHC beam screens are positioned 18 mm outward with respect to the beam pipe center and are located only 4 meters upstream of the inner ALFA stations. This entails that halo particles must have minimum horizontal angle of 1/4000 rad in order to be observed.

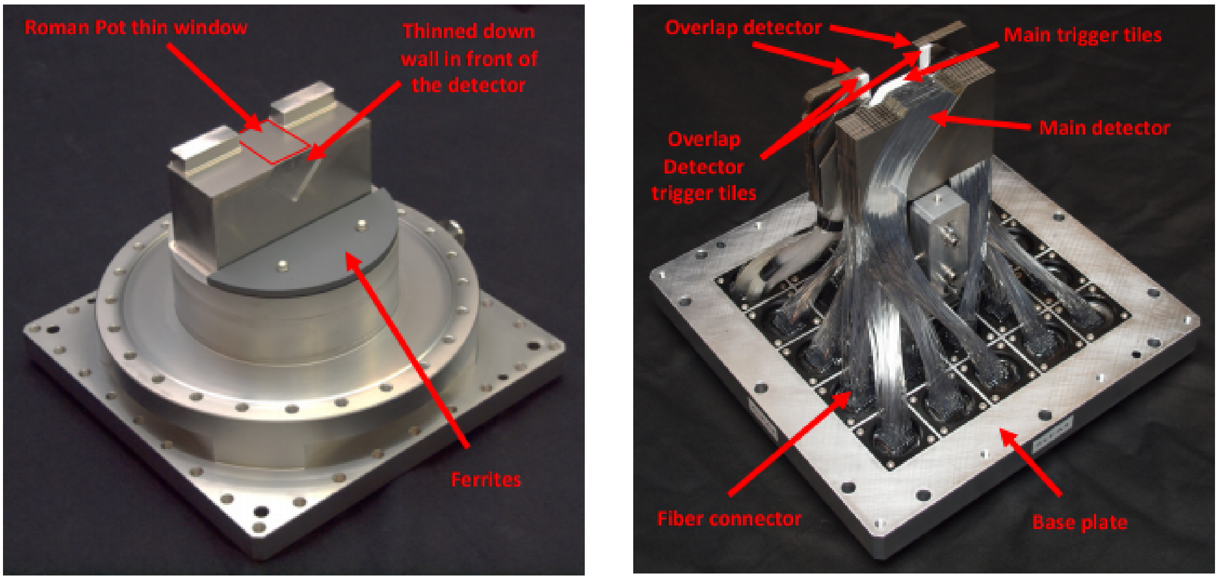

Figure 5.10: Left : An ALFA Roman Pot (A10), the thin window (highlighted) and the thin wall. Right : ALFA4 detector [59]. In front all the aluminized fibres that make up the active part of the detector, in the back left corner the clear fibre used for the triggers, painted in white [59].

5.2.5 Roman Pot

The ALFA detectors need to be separated from the ultra-high LHC vacuum and are therefore put inside vessels called Roman Pots. A Roman Pot houses the active part of the ALFA detector contained in a secondary vacuum that is needed to keep the thin window flat. The fibres end outside the Roman Pot and hence the MAPMTs are placed outside with the benefit that there is no risk of radiofrequency pick up. The positioning of the ALFA edge, i.e. the edge of active part of the MDs, inside the Roman Pot should have a minimal distance to the Roman Pot thin window, to reach lowest vertical distance to the beam and thus the smallest t-values. The thin window, shown in Figure 5.10, only has a thickness of 200 μm. The measured distances between the outside of the Roman Pot thin window edge and the MD edge vary by about 450 μm. The Roman Pot thin wall has a thickness of 500 μm. This ideally would have been as thin as the thin window, to minimize the probability of protons undergoing interactions. Due to a risk of vacuum tightness and the lack of a dedicated study a more safe thickness was chosen [59].

5.2.6 Trigger Detectors

All ALFA trigger signals are directly connected to the ATLAS CTP. Due to the large distance to ATLAS a transmission speed of 91% the speed of light in vacuum is essential for reaching a decision while the data of the event is still in the buffers. The MD and OD are each provided with a dedicated trigger to ensure high trigger efficiency while minimizing the background arising from either noise or non-elastic events. The MD tracking region is fully covered by two diamond-shaped plastic scintillator plates with a thickness of 3 mm, painted white as can be seen in Figure 5.10. The light output is converted into an electrical signal by PhotoMultiplier Tubes (PMTs). A hit coincidence between the two plates releases a trigger signal to the CTP and is used to reduce the noise of the individual PMT channels. The OD region is covered by a single trigger tile of size 15 x 6 mm^2. A single tile suffices since a coincidence is required between an upper and lower ODs in a station for a trigger to be released to the CTP.

Chapter 6

LHCb SciFi Tracker

The Large Hadron Collider beauty (LHCb) detector is a single-arm forward spectrometer located at IR8 of the LHC. Its sub-detectors are not build around the interaction point, but are arranged successively in the forward direction, see Figure 6.1, of which the acronoyms are explained in Section 6.1.2. The angular coverage of detector is 10 to 300 (250) mrad in the bending (not-bending) plane of the dipole magnet. The initial core of the experimental program of LHCb is formed by precision measurements on CP violation in the c and b quark sector as well as rare decays of B hadrons [1]. With the limited coverage, the LHCb detector is able to accept 24% of the produced $b\bar{b}$ pairs, since they are predominantly produced in the forward direction [49]. The sub-detectors of the LHCb detector will be briefly introduced in the next section and also the need for the upgrade will be discussed. The SciFi Tracker will be introduced in more detail in a separate section, since this is relevant for the understanding of the development of SciFi Detector Control System as well the performance analysis of the services, both presented in Chapter 7.

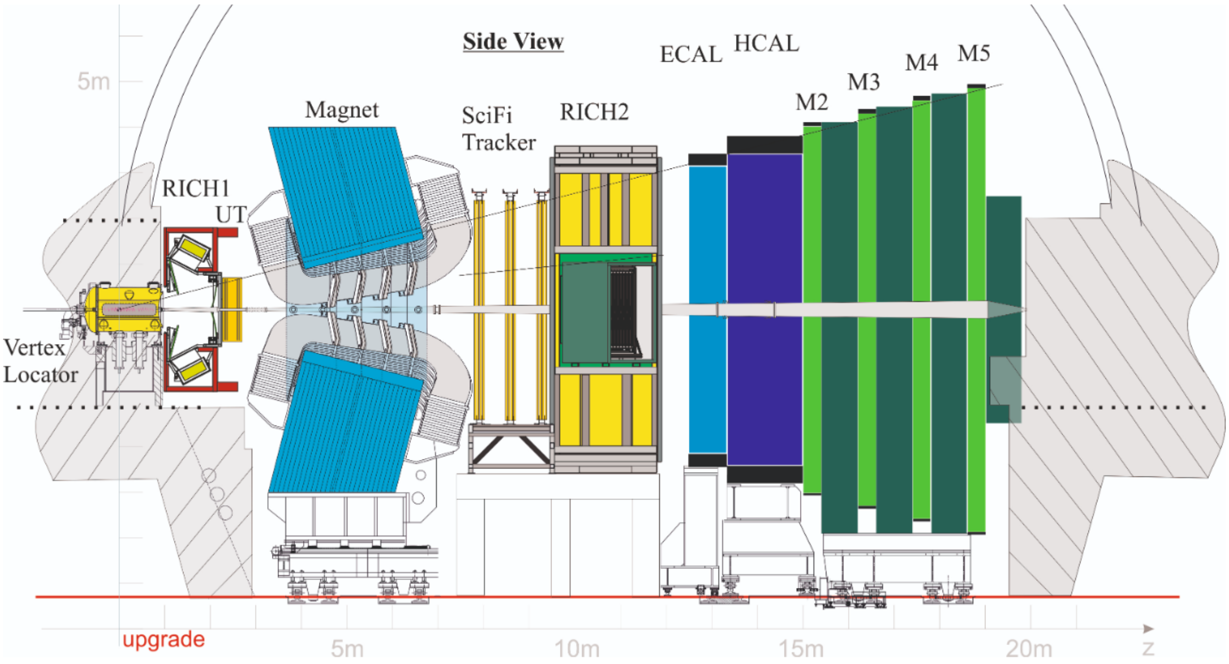

Figure 6.1: A schematic side view of the LHCb detector upon completion of Upgrade I [61].

6.1 LHCb

The collisions of particles take place at IP8, which has been displaced by 11.25 m from the centre of IR8 to free space for detector components. The LHCb detector is oriented in the direction of beam 1 towards IR1. After the collisions, short lived particles and resonances decay and their subsequent products traverse the sub-detectors. In successive order, these sub-detectors as they will be present upon future completion of Upgrade I will briefly introduced throughout the next section. The sub-detectors can be categorized in two groups, namely tracking and particle identification (PID). The tracking system will consist of a warm dipole magnet delivering an integrated field of 4 Tm, 4 tracking station (1 x UT + 3 x SciFi) and the VELO. The PID will consist of 2 RICH detectors, 2 calorimeters and the muon chambers. The presented material is based on information found in [1, 2, 62, 49] and upgrade TDRs [63, 61, 64, 65].

6.1.1 Upgrade I

The LHCb has performed significant successful precision measurements with 3 fb^{-1} of collected data during Run 1. Various crucial measurements are statistically limited and do not reach the experimental precision required for direct comparison to uncertainties given by theoretical predictions [2]. This will only partially improve by the integrated luminosity of 9 fb^{-1} that was reached by the end of Run 2. Significant improvement in the rate of data collection by the experiment is required, which is the main reason for the ongoing major upgrade of the LHCb detector. The upgrade is aimed to collect 50 fb^{-1} by the end of 2028, and enables for a sufficiently large data set to reach comparable precision to theoretical predictions. To reach about ten times the current collection rate of data, the delivered instantaneous luminosity by the LHC will be increased by a factor five to $2{\cdot}10^{33}$ cm^{-2} s^{-1} and upgrading the trigger and readout of the detector will improve the event selection of a factor of two to four, depending on the decay channel. This has implied the need for drastic changes to the infrastructure of the existing detector, currently carried out during the ongoing Long Shutdown 2 period.

The existing trigger system, consisting of a hardware-based trigger Level 0 (L0) and a High Level Trigger (HLT), will be revolutionised to the use of a full software-based HLT only. The new trigger system will improve efficiency and provide maximum flexibility in implementing trigger decisions that even allow for exploiting the detector as a main purpose detector in the forward region. The existing L0 trigger reduces the event rate from the 40 MHz LHC bunch crossing rate down to 1 MHz, this is the equivalent readout rate of the existing frond-end (FE) electronics. The new HLT and readout allow for processing of events at an inelastic event rate of 30 MHz. The HLT generally consists of two parts, the first stage is the full online reconstruction of events at 30 MHz and is followed by the second offline stage, in which particle identification precision and track quality information are added to the selection of events. The second stage reduces the rate further down to 20-100 kHz, the rate at which selected events will be stored.

To deal with the challenges of increased luminosity, higher radiation levels and enhanced data collection rate, sub-detectors need to be upgraded. Higher granularity and radiation hardness is required, particularly for the tracking detectors which are therefore fully replaced. To adapt the readout rate from the existing 1 MHz to the future 40 MHz, existing FE electronics of most sub-detectors will be replaced.

6.1.2 Sub-detectors

The Vertex-Locator (VELO) will be used as a dedicated tracking detector for the precise determination of the primary pp interaction vertices as well as displaced secondary vertices originating from short lived b- and c-hadrons. The VELO will consist of 26 layers of L-shaped silicon pixel modules, with a pixel size of 55 x 55 μm. Each VELO half will be housed in a vessel, similar to Roman Pots, that contain a secondary vacuum and can be horizontally inserted to 5.1 mm of beam center during stable beam conditions.

The Upstream Tracker (UT) will be the next downstream tracker, to be placed in front of the dipole magnet. It will be used to provide precise position measurements for track reconstruction of long lived particles. The UT will consist of 4 stereo layers of silicon strip technology with decreasing size closer to the beam: 99.5 mm x 180 μm, 99.5 mm x 95 μm and 51.5 mm x 95 μm. The acceptance improve as innermost sensors will be placed closer to the beam pipe than its predecessor.

The Scintillating Fibre tracker (SciFi) will be be placed downstream right after the dipole magnet and completes the tracking system. The SciFi tracker is organised over three tracking station with each 4 stereo layers of 2.4 m long scintillating fibres of 250 μm diameter. Each layer consists of 6 layers of fibres, arranged in a way that each successive layer is placed in the grooves of the previous layer, leading to a displacement of half the fibre diameter. The SciFi will be more extensively introduced in Section 6.2.

The two Ring Imaging Cherenkov (RICH) detectors are used used for p, π and K particle identification. The RICH1 detector will be placed between the VELO and UT. The RICH1 will use C_4F_{10} as a radiator of Cherenkov light and covers low momentum range of approximately 1 to 60 GeV/c. The aerogal radiator will be removed due to reduced effectiveness under enhanced luminosity. The RICH2 will be placed downstream, right after the SciFi tracker. The RICH2 uses CF_4 as a radiator and covers the high momentum range up to 100 GeV/c. The readout for both detectors used hybrid photo detectors (HPD) with and will be replaced by Multi-Anode Photo-Multiplier Tubes (MAPMTs).

The calorimeter system is placed in front of muon station M2 and consists of an electromagnetic (ECAL) and hadronic (HCAL) calorimeter. The former is used for energy measurement and identification of e and γ, the latter for measuring the energy of hadrons. Both the ECAL and HCAL are sampling type calorimeters. The ECAL consists of layers of 4 mm thick scintillating tiles interleaved with 2 mm lead absorber plates. The HCAL consists also of layers of 4 mm thick scintillating tiles, but is interleaved by 16 mm thick iron absorber plates. For both systems, the light of the scintillating tiles is absorbed, re-emitted and transported by wavelength-shifting fibres to PMTs.

The muon system will consist of the remaining muon stations M2 to M5 with already existing read-out at 40 MHz, and are placed furthest downstream of the LHCb detector. These are multi wire proportional chambers which use a mixture of Argon, CO_2 and CF_4 as ionization gas. The stations are interleaved with 80 cm thick iron absorber layers that allow only muons of momentum greater than 6 GeV/c to pass the whole detector.

The existing muon station M1, Scintillating Pad Detector (SPD) and the Preshower (PS) will be removed during the upgrade. Previously, they enabled for an adequate L0 trigger decision as well as supporting PID by the calorimetry system.

6.2 SciFi

The tracking stations just located upstream and downstream of the LHCb dipole magnet must provide track reconstruction leading to high precision momentum measurements of charged particles. Additionally, the orientation of the tracks are used as an input to light cone search by the RICH detectors. The increased luminosity would lead to an enhanced occupancy in the innermost regions of the former Outer Tracker (OT) and result in a loss of triggered events. Furthermore, part of the OT modules would need to be replaced. The OT consisted of an inner part based on silicon strip technology and an outer part based on gas straw tubes. For both technologies the read-out electronics would have needed to be replaced to be compatible with reading out at the event rate of 40 MHz. It was therefore decided to replace the complete OT tracker by the Scintillating Fibre Tracker (SciFi). The SciFi Tracker will be introduced in the following sections. Focus will be on the overall requirements of the detector as well the relevant parts related to the development of the Detector Control System (DCS), presented in Chapter 7. Unless otherwise stated, the presented material is based on [66, 61, 67, 49] and [62].

6.2.1 Detector Layout

The SciFi Tracker will consist of 3 tracking stations: T1, T2 and T3. Each Tracking station comprises of 4 four detection layers following a (X,U,V,X) orientation scheme. The letter refers to the angles (0°, +5°, -5°, 0°) of the scintillating fibres with respect to the vertical axes. This is close to parallel to the main component of the magnetic field produced by the dipole magnet, the reason for requiring the best spatial resolution in the bending plane. Each detection layer will leave a hole to enclose the beam pipe and will consist of either 10 (T1/T2) or 12 (T3) modules to satisfy the angular coverage of the detector.

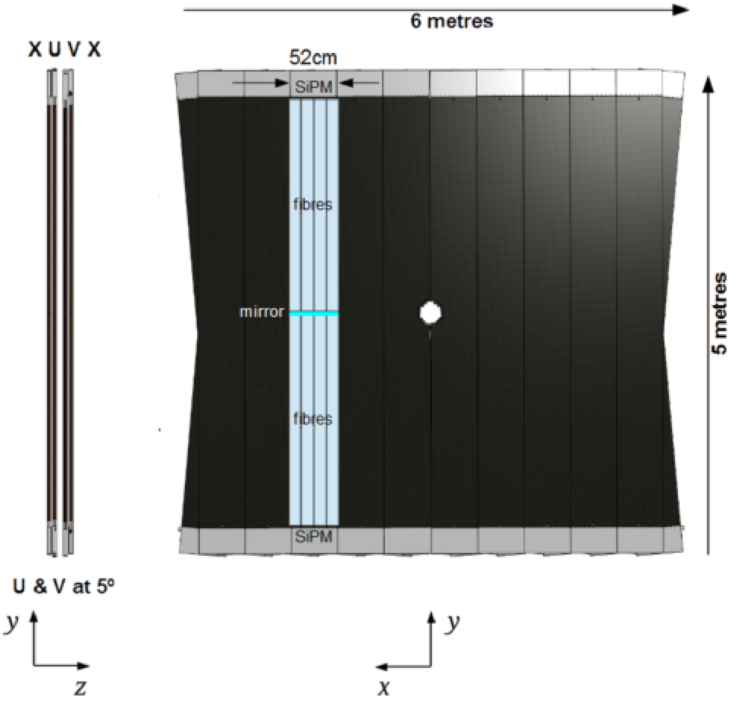

Figure 6.2: A schematic frontal view of a T1/T2 tracking station [68].

6.2.2 Round Scintillating Fibre

The presented material in this section relies on information obtained from references [61, 49]. The scintillating fibres used for the SciFi tracker are double-cladded round fibres as shown by Figures 6.3 and 6.4. Like the square fibres used for the ALFA detector, also these fibres are produced by Kuraray Co., Ltd. (JP). The fibres are of type SCSF-78MJ, with a diameter of 250 μm. The M indicates multi-cladding and the J indicates a process of high purity distillation which results in elongated attenuation length. The emission spectrum extends from 400 to 600 nm and it peaks at 450 nm. The main core material is based on polystyrene, surrounded by two claddings with decreasing index of refraction, see Table 6.1.

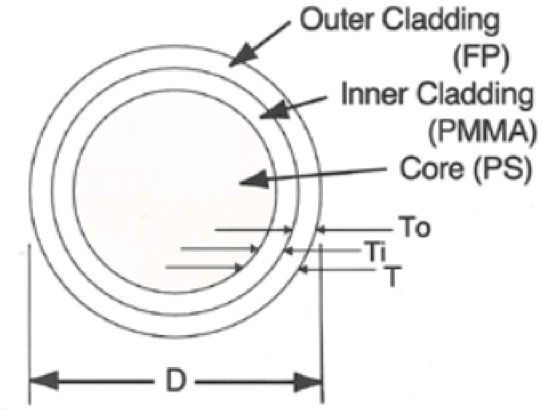

Figure 6.3: Cross-sectional view of a double-cladded round fibre [60].

	Material	Refractive index	Density $\left[\frac{\mathrm{g}}{\mathrm{cm}^3}\right]$
Core	Polystyrene (PS)	1.59	1.05
Inner cladding	Polymethylmethacrylate (PMMA)	1.49	1.19
Outer cladding	Fluorinated polymer	1.42	1.43

Table 6.1: Main materials for single-cladded squared fibre [60]

The total internal reflection benefits from the presence of a second layer of cladding, resulting in a trapping efficiency of 5.4%. This is an significant increase to the efficiency of 3.1% achieved in round single-cladded fibres. Each cladding layer has a thickness of 7.5 μm, 3% of the diameter. The additional light containment of the fibre is of importance for the SciFi tracker. The fibres used are 2.4 m long and therefore light attenuation effects will affect the output at the end of the fibre where it is collected by the SiPM. The fibre has an S-parameter of about 0.4.

The relaxation time as well as the light yield of the base material of the polymer is not sufficient for which a dopant (about 1%) is added to polystyrene. This first dopant is p-terphenyl, an organic fluorescent dye that is matched to the energy levels of the base material, this improves the scintillation mechanism and decays much faster. There is fast transfer (sub ns) of energy to the dye by means of Förster transfer, as was explained previously. The concentrations of p-terphenyl (PT) however affect the attenuation length by self-absorption of the light. For this purpose a second dopant is added to act as a wavelength shifter, for which tetraphenyl-butadiene (TPB) is

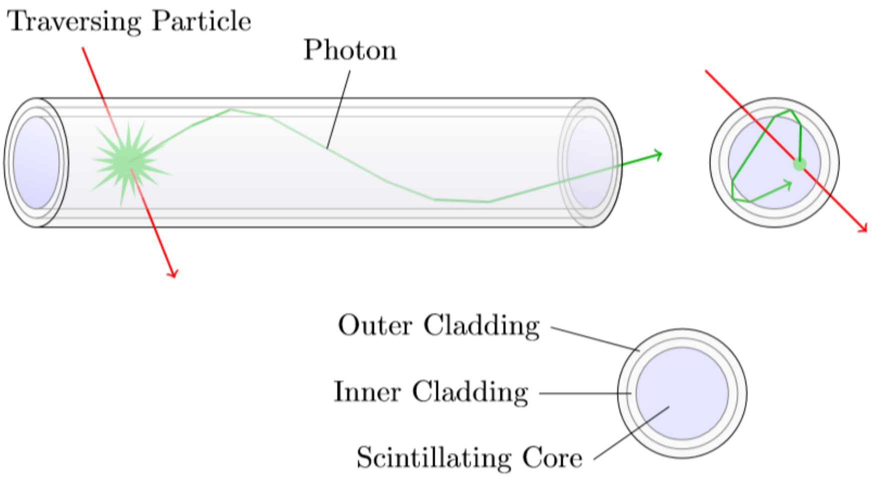

Figure 6.4: Illustration of a round double-cladded fibre used for the SciFi tracker, the creation of scintillation light and multiple reflections made by a photon towards the fibre end [62].

used. The TBP dye absorps the energy from the PT dye, either via radiative or non-radiatve transfer, and re-emits at a longer wavelength. At longer wavelengths the self-absorption is less likely to occur and, additionally, it better matches the sensitivity of the SiPM.

The fibres positioned most closely to the beam pipe are expected to accumulate a ionising radiation dose of about 35 kGy over a foreseen lifetime of 10 years. The expected dose decreases rapidly with distance to the beam pipe. Similar to the fibres used for ALFA, the main reason for reduced light output is transmission loss due to optical changes in the base material. This way the radiation damage causes a decrease in the attenuation length, which is crucial to functioning of a detector with such long fibres. Hence, there have been multiple irradiation tests [49].

6.2.3 Attenuation Length

The scintillation light is produced isotropically in the fibre core of which a fraction is captured by total internal reflection, as discussed in the previous section. The optical way to the fibre end is in most cases not simply straight but follows a helical path, illustrated in Figure 6.4. The light may therefore undergo many reflections at material interfaces which decreases the light intensity along propagation. Also, additional effects such as the previously mentioned re-absorption by used materials and transmission loss by absorption centres due to radiation damage further decrease the collected light output. Attenuation in pure polystyrene is mainly caused by Rayleigh scattering, molecular vibrations and electronic transition, shown in Figure 6.5. The combined effects of attenuation characterizes the attenuation length of a fibre. For a constant attenuation probability along a fibre, the intensity I(x) falls off exponentially over distance x :

$$I(x) = I_0 e^{-x/\Lambda}, \tag{6.1}$$

in which I_0 is the initial intensity at the fluorescence source and Λ is the attenuation length. The appearance of attenuation in reality often deviates from simple exponential behaviour. This can for a large part be attributed to a larger re-absorption fraction of the shorter wavelengths in the emission spectrum compared to the longer wavelengths. The added wavelength shifter causes significant re-absorption of wavelengths shorter than 450 nm, which is also apparent in Figure

6.5. The combined effect of composite attenuation properties is also observed by intensity studies as a function of wavelength, shown in Figure 6.6. The peak of the observed intensity shifts towards longer wavelength for longer distance, as the shorter component is already more attenuated. For small distances, the shorter wavelength component is absorbed resulting in a smaller attenuation length, whereas for large distances the remaining longer wavelength component endures longer since it is characterized by longer attenuation length. The overall light intensity is therefore often better described by a double exponential, taking account for combined attenuation effect over small and large distances [47].

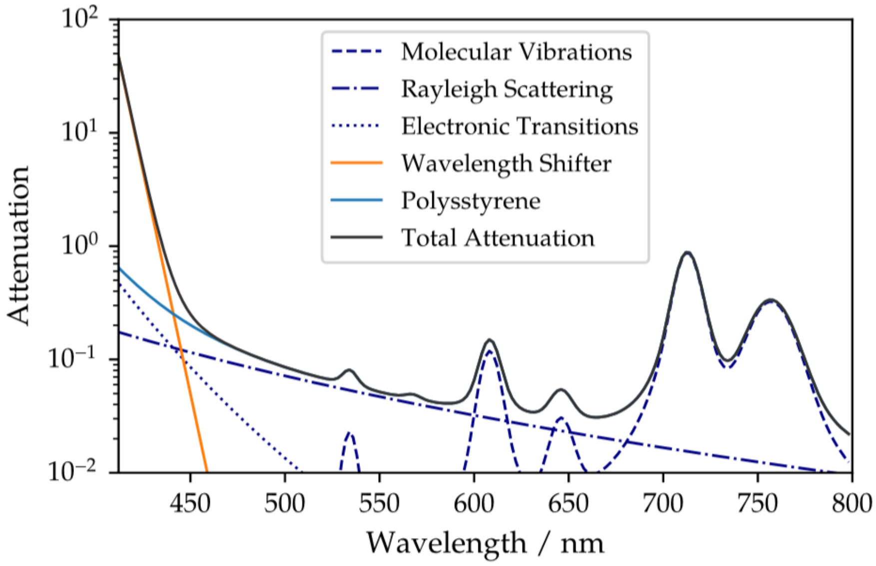

Figure 6.5: Relevant attenuation coefficients for a scintillating fibre.

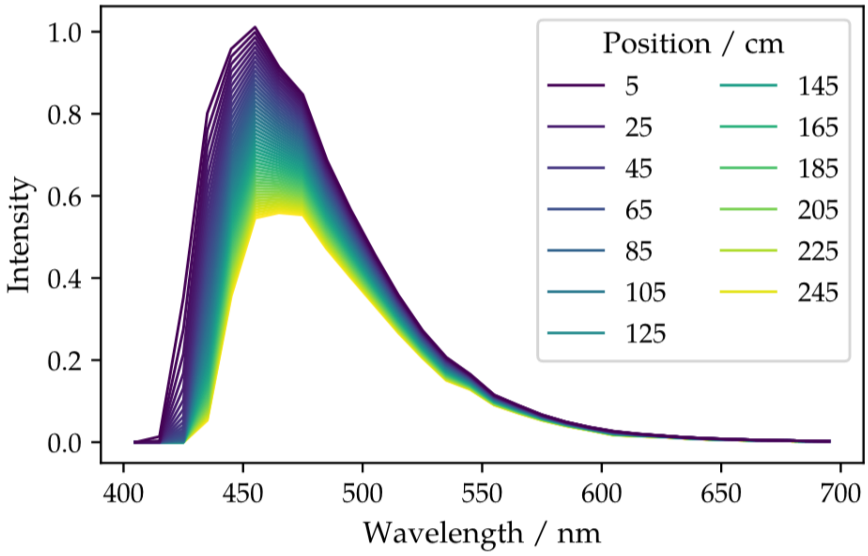

Figure 6.6: Intensity spectrum for a scintillating fibre for different distances to the detector [49]. The distance to the excitation location is varied from 5 to 245 cm in steps of 5 cm.

6.2.4 Detector Module

The module can be considered as the building block of the SciFi Tracker and contains the active material of the detector made out of scintillating fibres. A single module is highlighted in light blue in Figure 6.2 and its support structure is made from plastic and carbon foils. A module consists of two equal parts split in the middle by a mirror, each part is read out at the far end by Silicon Photomultipliers (SiPMs). The 2.4 m long scintillating have a diameter of 250 μm. They are round double-cladded fibres in order to increase the light capture by total internal reflection. The fibre has been chosen by its high light yield and fast decay constant. These are relevant parameters due to the length of the fibres as well as the read-out a the bunch crossing rate of 40 MHz. The mirror at one end of the fibres functions to increase the light yield collected by SiPM. Extensive information on the scintillating fibre and its properties was explained in Section 4.2.

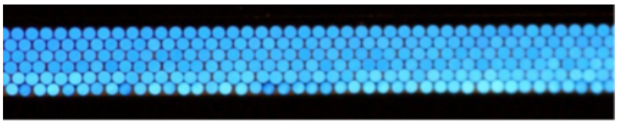

Figure 6.7: Cross sectional view of a fibre mat [69].

A module consists of eight mats with each six layers of fibres to achieve a sufficient amount of light yield output to the SiPMs, see Figure 6.7. A mat has a length of 2.4 m, a width of about 13.0 cm and a thickness of approximately 1.35 mm. To achieve a homogeneous spatial resolution below 100 μm across the full detector, the positioning of the individual fibres has to be exactly parallel. Using a winding machine, the production of the fibre mats has been done with a threaded wheel to guide the first layer of fibres. The remaining layers were guided by the grooves of the previous layer, by which a displaced of half the horizontal position for each successive layer was realised. The mats have been casted and their ends are glued in between two endpieces, these are pieces providing support during milling and serve as a support for both the SiPMs and the mirror. The endpieces have undergone diamond milling by which a smooth surface is created for the SiPM window and mirror to be put against. The transversal diamond cut ensures maximal optical transmission at the fibre ends. The last step in the mat production is glueing an aluminized mylar foil to create the mirror.

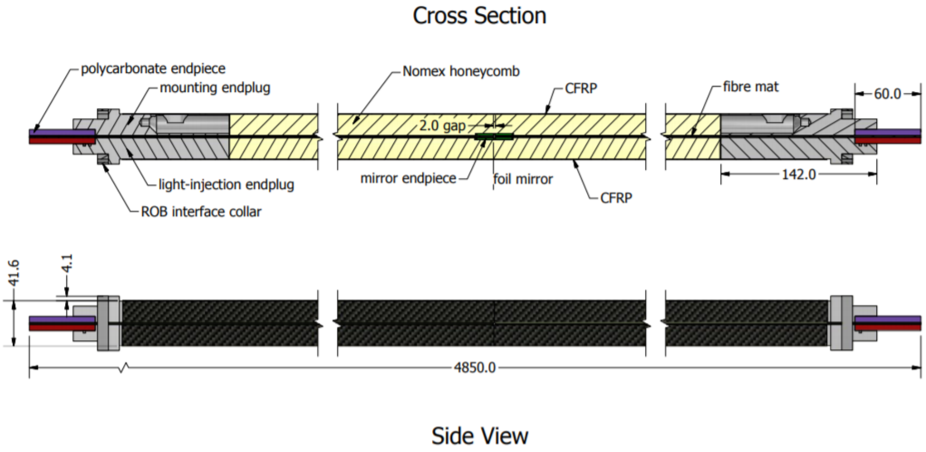

Figure 6.8: Cross sectional view through the centre of a module with fibre mats enclosed by honeycomb structure, carbon fibre skins and mounting endplugs [67].

A module is a rigid structure that can be mounted onto the frames of the SciFi Tracker. A schematic side and cross sectional view of a module is shown in Figure 6.8. The structure assembles 8 mats, which can be clearly seen by the frontal view of the highlighted module in Figure 6.2. Prior to the module assembly the fibre mats have undergone a longitudinal cut to minimize the loss in acceptance at the boundary between mats. The fibre mats are enclosed by endplugs, honeycomb panels and carbon fibre skins from each side. The carbon fibre skins are wider and are used to close the side walls and provide light tightness. The radiation length X/X_0 of a module, i.e. a single detection layer of SciFi, is 1.02% [49]. The module is then ready for installation of the cold box. The readout ends of the fibre mats remain the only part of the mats to stick outside the module and their endpieces are shown in purple and red in Figure 6.8. The endplugs of the modules come in two types, on one side of the module it provides support for the mounting and thereby alignment of a module onto the detector frame and on the other side it contains the light injection system (LIS). The LIS is composed of LED lights that can be used to act as a superficial light source to the fibres in the fibre and can thus be used to check the functioning of the individual SiPM channels. The endplugs are sealed off by a coldbox containing the SiPMs.

6.2.5 Cold Box

On either side of the modules a cold box seals off the readout ends of the fibre mats, the cold box consists of a shell and a top cover, see Figure 6.9. The coldbox shell and top cover structure is made from a glass filled material, which is filled up by a foam for isolation. A cold box serves as the interface between the modules and the readout electronics. The shell is closed by a top cover which houses the cooling of the SiPMs, the SiPMs and the flex-cables. The structures leave little clearance around the parts to minimize the overall heat loss. In Figure 6.10 the inside of the parts are shown, the structure and isolation are left out for clarity. One end of the flex-cable is connected to the SiPM, the other side sticks out at the top of the cold boxes and contains the connectors for the front-end electronics. A detailed cross sectional side view can be seen in Figure 6.11, in which the various parts and their temperatures in the cold box are shown. The SiPMs are glued to a titanium cooling bar, which in turn is aligned in front of the fibres mats using pins mounted at the endpieces. The cold bar is connected with springs from the back and upon insertion of the top cover there is pressure exerted on the SiPMs to the fibre ends. A spontaneous signal can be created in the SiPM by thermal energy and can not be distinguished from a single entering photon. This type of background is independent of the the light falling onto the SiPM and is called dark noise. The dark noise in the SiPM becomes higher with the collected irradiation dose of the detector over its lifetime. This effect can be mitigated by cooling of the SiPM, which is necessary in order to reduce the rate of fake signals. A temperature of -40

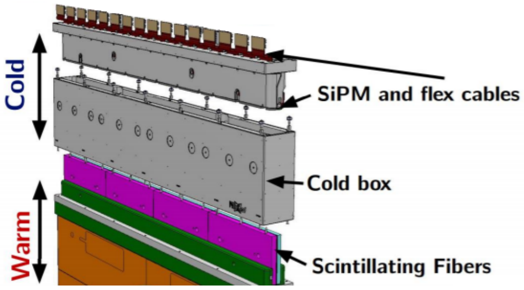

Figure 6.9: Coldbox : shell and top cover.

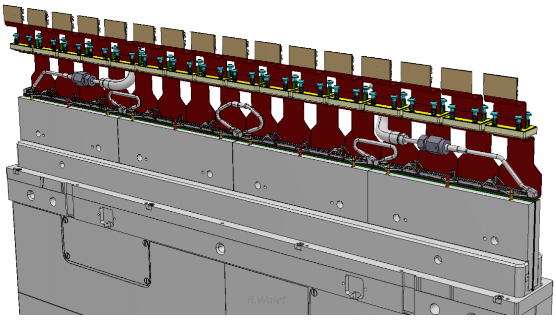

Figure 6.10: Coldbox : inside structure.

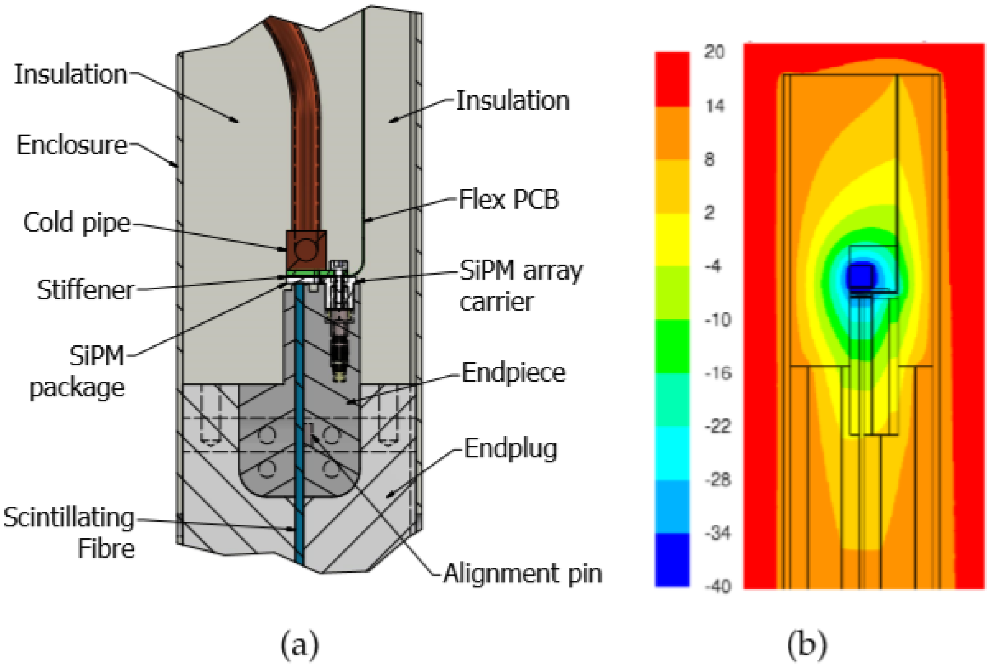

Figure 6.11: Cross sectional side view of the Cold box : (a) elements (b) thermal simulation [61].

°C ensures a sufficient low dark noise level in the SiPM at its full irradiation dose. The cooling bar can however not only be restricted to cooling of the SiPM, but will also lead to drop of temperature in for the surroundings. Therefore, dry air will be circulated through the cold box to prevent from condensation and frost build up.

6.2.6 Clustering

Silicon Photomultipliers (SiPMs) are the photon detection devices used at the module ends to detect photons released in the fibres. The SiPM enables for measurements at single photon level, which is of importance for low light intensities. The emission spectrum of the used scintillating fibre is well matched by the SiPM to have a high photon detection efficiency. The SiPMs consist of an array of Avalanche Photodiodes in Geiger mode (G-APDs), which are semiconductor diodes (pixels) which upon absorption of incident light can generate an electric current by the photoelectric effect. A SiPM channel is made up out of an array of 24x4 pixels and the number of fired pixels is proportional to the number of incident photons. A module is read out by 16 pcb flex-cables which are each connected to 4 SiPM dyes, with each containing 64 channels, giving 256 channels per flex-cable. Per mat there are 1048 channels and a total of 4192 SiPM channels per module. The SciFi tracker will be composed out of 128 modules, resulting a total of 536576 SiPM channels.

With the SiPM channel width of 250 μm, a spatial resolution below 100 μ can be realised using a clustering procedure. The height of the channel is 1.62 mm. In Figure 6.13, a schematic of a particle crossing the fibre mat is shown. A 6-layer mat has been chosen for reasons to have sufficient light yield and resolution while respecting the material budget. The positioning of the individual SiPM channels are marked by dark blue color. A crossing particle traverses multiple fibres and creates an amount of scintillating light that is proportional to the distance of the trajectory to the heart of the fibre. The scintillation light is picked up by individual pixels, typically leading to firing of multiple SiPM channels. Using thresholds (t_1,t_2,t_3) set in electronics, the noise level can be reduced and clusters can be formed. The hit position is calculated by a weighted mean of the channels inside a cluster.

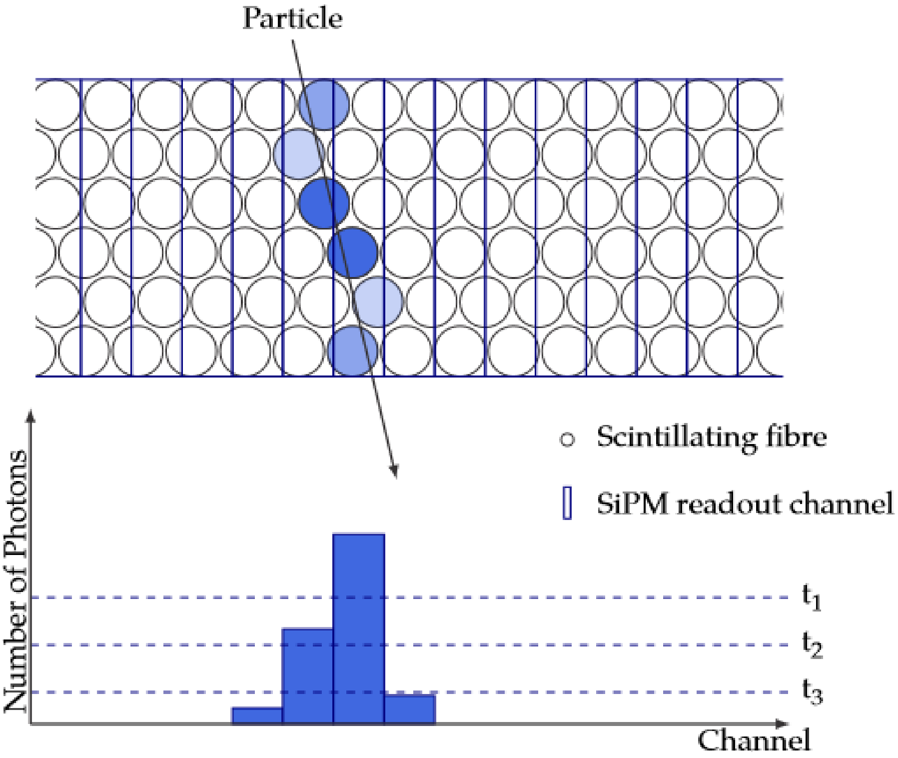

Figure 6.12: The SciFi clustering procedure : A crossing particle generates scintillation light in multiple fibres, resulting in firing of multiple channels. Using three thresholds (t_1,t_2,t_3), the noise level is reduced and clusters can be formed. The hit position is calculated using a weighted mean inside a cluster [49].

6.2.7 Mechanics and Services

The three tracking stations each contain four stereo layers which are divided over four c-shape like mounting frames that can be horizontally moved to enclose the beam pipe either side. These so-called c-frames consist of two detector layers, with 5 (6) modules per layer mounted on the c-frame for tracking station(s) T1/T2 (T3). The SciFi Tracker will be carried by a total of 12 c-frames, enclosing the beam pipe with 6 c-frames on either side. Not only does the rigid structure serve as mounting frame for the modules, it also provides the necessary infrastructure for operation of the detector. These include trays for optical, LV bias and HV bias cabling. Furthermore, it houses services like water cooling of the front-end electronics (FEE), Novec cooling of the SiPMs and a dry gas system to avoid condensation and frost build up at the SiPMs and the insides of cold boxes. Additionally, a heating wire system is placed to act against the appearance of condensation on the outside of cold parts. A schematic of a c-frame together with modules, infrastructure and services is shown in Figure 6.13.

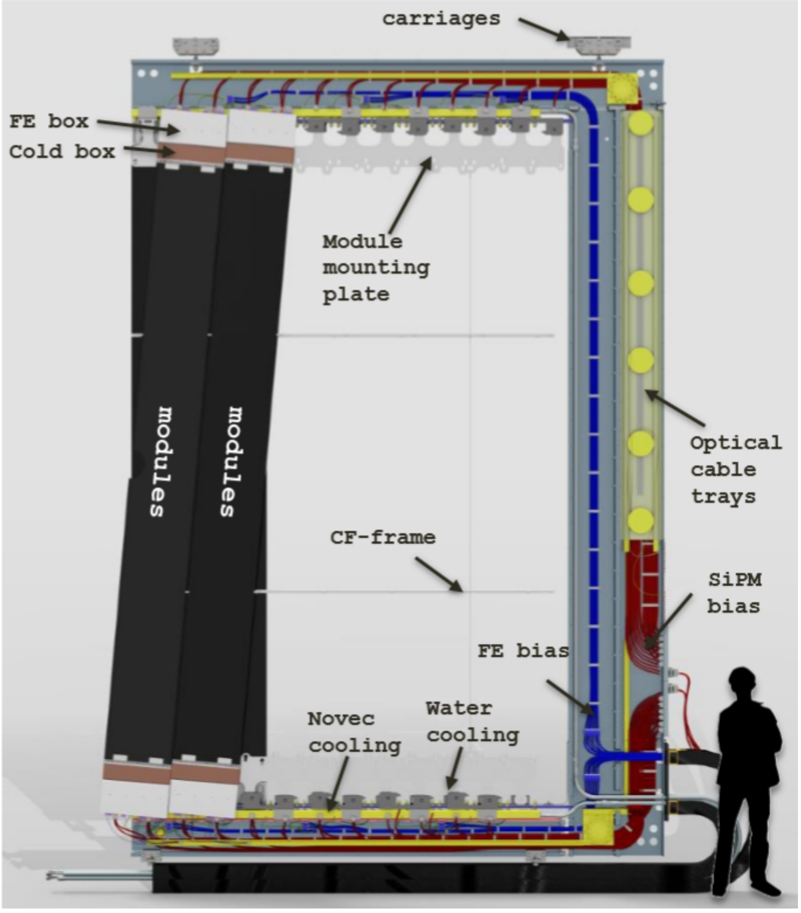

Figure 6.13: The SciFi C-Frame : mechanical structure to carry two layers of modules, front-end electronics and is equipped with all the necessary services for operation of the detectors. The SciFi Tracker will consist of total of 12 frames that provide central enclosure of the beam pipe and total of 12 detector layers [70].

The front-end electronics are contained in a front-end box and will warm up due to heat generation by the electronics. With water cooling the temperature of the electronics can be limited to a maximum of 50 °C. Water cooling is done using a single continuous and straight copper pipe that traverses aluminum cooling blocks, the water flow and temperature is regulated by an external body. During the assembly a chiller regulates water of 20 °C with flow rate of 2.5 l/min per quadrant. The copper pipe connects 5 (6) cooling blocks and is bend in a u-shape at the end by a 180° turn. The inlet and outlet direction of the pipe is separated by a few centimeters from each other. The front-end boxes are placed against the aluminum cooling blocks and need good a thermal coupling for efficient cooling. The cooling infrastructure of the SiPM is more complex and has to ensure a temperature stability of ± 0.5 °C to the SiPMs. This is an important criterion since the temperature of the SiPM directly influences the bias voltage and thereby the gain and pixel cross-talk. The SiPMs are glued to a cooling bar in which the monophase liquid coolant Novec-649 is circulated. The cooling bar is split up in segments to prevent from the build up of mechanical stress due to the large temperature gradient between non-cooling and cooling conditions. A cold box is individually connected to a manifold via an inlet and outlet bellow pair. A c-frame holds two cooling circuits that supply a top and bottom manifold with the coolant. Each manifold holds a total of 12 parallel branches for the cold boxes to connect to.

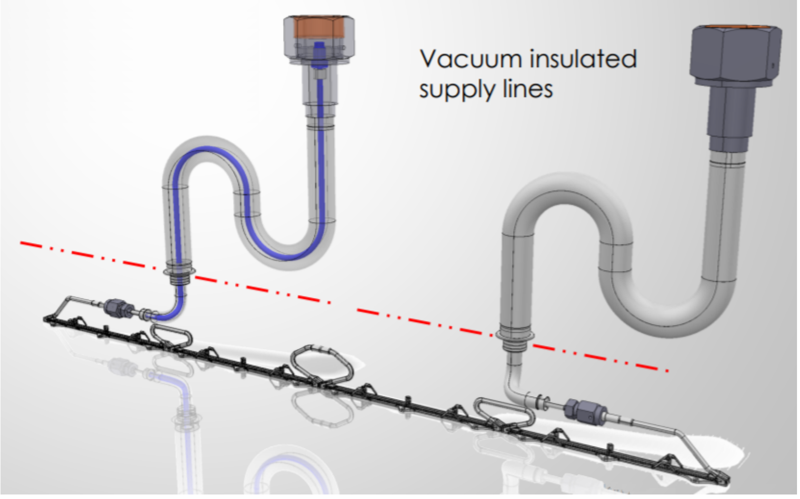

Figure 6.14: Novec cooling : cooling bar and vacuum insulated connectors to the manifold. The red dashed line indicates the interface between the in- and outside of the cold box.

The industrial size cooling plant will be about 70 m away from the detector in the UXA area to allow for interventions during physics data taking. Glass foam insulated transfer lines are used for the supply and return of Novec from the plant to the detector in the UXB area [71, 61]. The transfer lines are split in two at the detector where they are connected to distribution boxes, of which there is one located on each side of the beam pipe. From the distribution box the manifolds on the c-frames are individually connected by a pair of distribution lines, consisting of a feed and return line. These lines need to be flexible and allow for movement of the c-frames to open and close the detector halves. For performance reasons and limited space on the c-frames these distribution lines, manifolds and the connectors to the cold bars are equipped with vacuum isolation. The cooling bar, cooling line and the vacuum insulated flexible connectors (bellows) to the manifold are shown in Figure 6.14. In total there are 48 distribution lines and 24 manifolds that all need to be vacuum isolated. The distribution lines are made from two concentric corrugated stainless steel tubes and are about 20 m long. The Novec coolant will flow through the inner tube and the outer tube will be evacuated to create thermal insulation. The vacuum continues into the vacuum volume of the manifold and further into cold box via the bellows.

The vacuum system has to ensure thermal insulation of the distribution lines, manifolds and connector bellows [71]. To minimize heat losses in the lines it needs to maintain a pressure in the range of about up to a few 10^{-4} mbar. The vacuum system will consist of two independent subsystems, with an identical pumping group on each detector side made of scroll type primary pump together with a pair of turbo pumps, to have one for redundancy. Each pumping group holds a large main vacuum line with the valves and flexible connections to the distribution lines on which also one Pirani pressure gauge is installed to measure the vacuum. One primary pump serves as a back up for the other in case of failure or during maintenance, for this purpose the two main vacuum lines can be connected by opening a valve. A Pirani vacuum sensor is placed between the primary pumps and the valve to the main vacuum line to survey the vacuum at the beginning of the vacuum system. Additionally, a Pirani pressure gauge is installed on each manifold to measure the vacuum at the end of each line. The electronics of the Pirani gauge are placed in a non-radioactive area. Due to the presence of a small magnetic field of up to 10 mT, the turbo pump is required to be placed inside a magnetic shield.

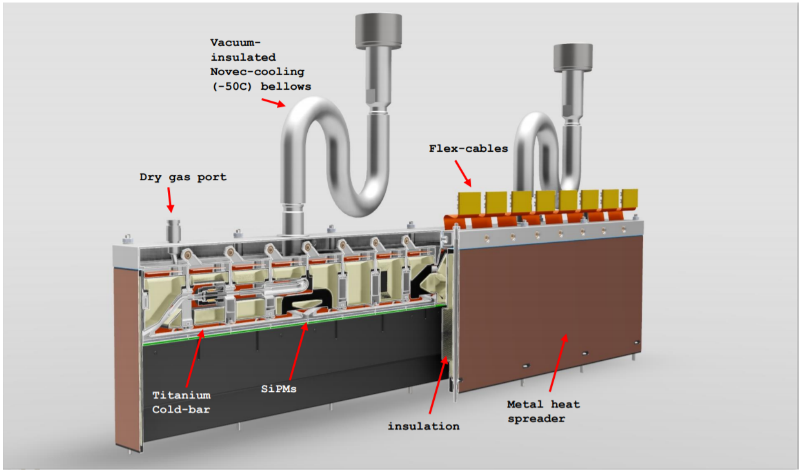

Figure 6.15: Cross sectional view of the cold box: Novec cooling and dry gas flushing [72].

The gas system has to ensure a very low humidity inside the cold box down to a dew point of approximately -50 °C. Dry gas will be constantly circulated through the cold box to avoid condensation and frost build up inside the box. The dry gas port is shown in a cross sectional view of the inside of the cold box in Figure 6.15. The gas system consists of a supply system that is similar to the cooling system divided over the two underground areas UXA and UXB. The system is composed of a gas supply rack with humidity analyzer and pneumatic controls in the UXA area. The supply rack provides two distribution racks with gas, one distribution placed on each detector side. Each distribution rack supplies 6 c-frames with dry gas. At the c-frame the supply pipe is split over the quadrants and then even further with lines to each cold box. At the outlet bellows of the dry gas two flow meters are connected to monitor the flushing rate at all times. The gas outlets will normally be opened to air. External electro-valves can be added to multiplex the gas ouput to a single humidity sensor to assess the dew point inside the cold box. During the commissioning this is analyzed by humidity sensor on an analysis trolley, that later can be used in the cavern for humidity measurement, however this will then be limited during periods in which access to UXB is possible. By default the system will use dried air as gas, but in case of shortage of dry air the system will automatically switch to N_2 supply. This is important in case of power cuts where the immediate lack of gas circulation might be a direct risk to the cooled SiPM environment. The flow regulation for each c-frame is only manually possible for which one needs to access near the detector.

An electrical heating wire system has to prevent from condensation to appear on the outside of the cold box shell, dry gas and novec bellows. For this purpose each module will be equipped with 15.5 m of Kapton insulated heating wire, spread of the named parts. Additionally, PT100 temperature sensors will be installed on the dry gas outlet and on the top of the cold box. Each c-frame contains four quadrants. Each quadrant will be equipped with 10 (12) PT100 temperature sensors and 5 (6) heating wires. The amount depending on the number of modules present for a tracking station T1/T2 (T3). The powering will be provided by using similar infrastructure as is used for the front-end electronics, namely by radiation hard Maraton power supplies.

Part III

Control, Monitoring and Operation

Chapter 7

DCS of the SciFi Tracker

The SciFi Tracker is currently being build up at point 8. Piece by piece a c-frame is assembled by installing modules, front-end boxes together with the necessary services needed for proper control of the SiPM environment. Additional preparations for the final installation of the detector in the cavern are in full progress. Upon completion, the SciFi Tracker will be a complex system consisting of many sub-systems that will have to be controlled. For this purpose a supervisory control and data acquisition (SCADA) system architecture will be used to control, monitor and operate the detector. Adequate and safe operation will be carried out through the tracking detector's Experiment Control System (ECS), that is currently under development by the SciFi online group. The following paragraphs will briefly introduce the relevant sub-systems and their corresponding projects. The author of this work is responsible for the development of two projects in the SciFi infrastructure domain: the Detector Control System (DCS). The projects are the controls of the low-voltage power supplies and the monitoring of services and electronics. Relevance of these projects was exploited by the first ever performance study of integrated services on a full c-frame, which is presented in the final section.

7.1 WinCC OA and the JCOP Framework

Unless otherwise stated, the presented information in this section is obtained from [73] and [74]. WinCC Open Architecture (WinCC OA) is the SCADA system used for the majority of the control systems around the CERN sites. It is used to connect hardware (and software) devices, acquire their produced data and for their supervision, including monitoring and the initialization, configuring and operation. The system consists of a distributed architecture with several autonomous program units, called managers in the WinCC OA nomenclature. An overview of a general WinCC OA application with the basic managers is shown in Figure 7.1.

The architecture contains multiple managers that can be subdivided over several layers as depicted. The event manager (EVM) forms the core of the application and is responsible for all communications. The database manager (DBM) provides the interface to the Oracle database. Device data is structured using datapoints (DP) of a certain datapoint type (DPT). All device information can be grouped together to form a datapoint type, this is a user defined structure in which each datapoint contains particular information related to the device. Defining datapoint types is very useful in case of many devices such that one can create another instance of a datapoint type for every additional device. In this way, all device information can be conveniently grouped in a structure adapted to the desire of the user and uniformly stored for a device type.

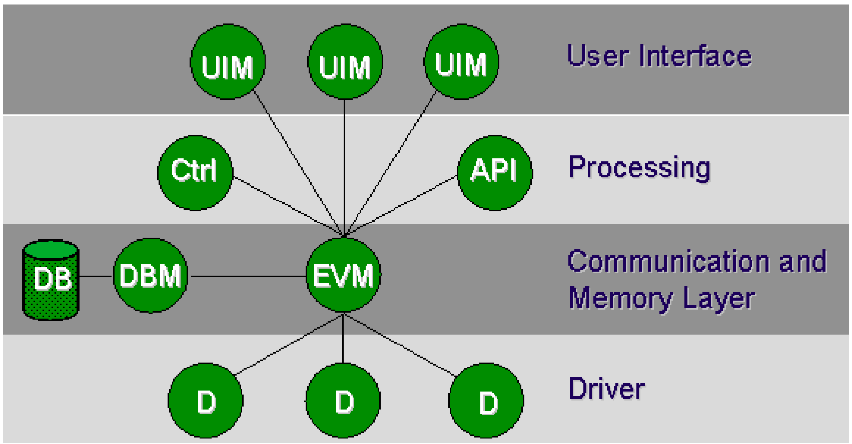

Figure 7.1: Typical architecture of a WinCC OA application [74].

The event manager receives data from the drivers (D) and stores it via the database manager. The driver provides the interface to hard- or software devices to be controlled. In addition there are the user interface manager (UIM), control manager (Ctrl), application programmable interface (API) and other specific manager may be included. The user interface manager is responsible for graphical depiction of the process states, it can retrieve and send device data via the database manager. The manager can request an open connection with the database, meaning it will be informed when new data arrives and trigger an action based upon that, e.g. the update of a sensor value in a panel. The DCS panels of the low voltage and monitoring projects that will be used in the control room by the operators form a good example of graphical user interfaces. The control manager contains the environment for event-driven and run time processes, these are written programs called control scripts that provide a functionality and are run in the background.

A WinCC OA system is an application that holds one event manager, one database manager and can hold any number of the other managers. WinCC OA can be used for very large applications for which one system might not be sufficient. For this purpose a distribution manager can be added to each system to establish connections with other systems. In this way hundreds of systems can be connected via the distribution managers of each system. The SciFi ECS will be such a distributed system, part of the even larger LHCb ECS. The online sub-systems of the SciFi Tracker more or less each hold their own project, i.e. a WinCC OA system.

The WinCC OA software is not an off the shelf control system in itself, rather it supports users with the tools to develop tailor made systems. As the experiments at CERN share similar technical challenges, the Joint COntrols Project (JCOP) of the 4 big LHC experiments was created with the intention to reduce the amount of resources spent on the development of new control systems [73]. WinCC OA was chosen by the joint controls project as the SCADA system to use for the experiments. Since then it has spread and the software is now widely adopted across CERN. In addition, the JCOP Framework has been developed and it consists of a set of standard tools and components that hide much of the WinCC OA complexity underneath. The JCOP Framework is developed and maintained at CERN and is built-in in the WinCC OA environment. The SciFi ECS will be developed on the basis of the JCOP Framework with in addition LHCb specific tools.

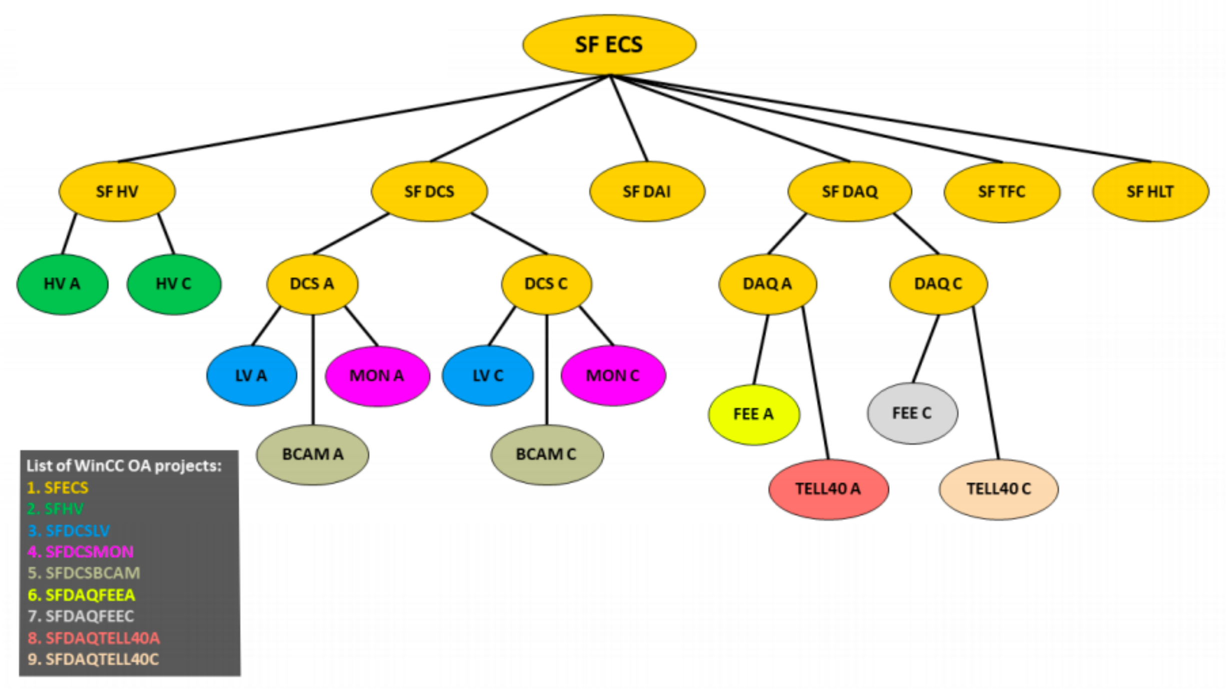

Figure 7.2: Schematic overview of the SciFi Experiment Control System: domains (yellow) with underneath the several WinCC OA projects (colored) [75].

7.2 SciFi ECS

Unless otherwise stated, the information presented in this section is obtained from [76]. The LHCb Experiment Control System (ECS) handles the complete operation of the detector and its interaction with the outside world. The ECS provides an interface to all experimental equipment involved in the different activities of the detector. Example activities may be the start of the data acquisition at the point the LHC machine goes into colliding mode but can also be the intervention in case of high voltages tripping. Among other things, the communication to outside world provides interaction with the LHC machine, CERN safety system and CERN technical services. The SciFi Experiment Control System will have to provide safe and adequate operation of the SciFi Tracker as an embedded piece in LHCb's ECS. The system should provide highly automated functionality to fasten standard procedures and avoid operator mistakes. The detector will mainly be operated as a whole, but sub-detectors can be taken out of the partition to allow for independent operation in a stand-alone manner. This may be during testing, calibration and also for commissioning of the SciFi Tracker.

The SciFi ECS is in charge of operation of the tracker and all its sub-systems. The ECS mainly includes the controls of the high-voltage power supply (SiPM), the low-voltage power supply (electronics and heating wires), the front-end electronics including the data acquisition (front- and back-end). Additionally, the ECS provides monitoring of the electric heating, water cooling of the electronics, the Novec cooling of the SiPMs including the integrated vacuum system, the dry gas system for controlling humidity inside the cold box, and the alignment of the detector. These will be arranged over five domains: DAQ for data acquisition of the front- and back-end, TFC for timing and fast control signals, HLT for the high level trigger, HV for the high voltage and the DCS for the detectors infrastructure. A schematic overview of the SciFi ECS is depicted

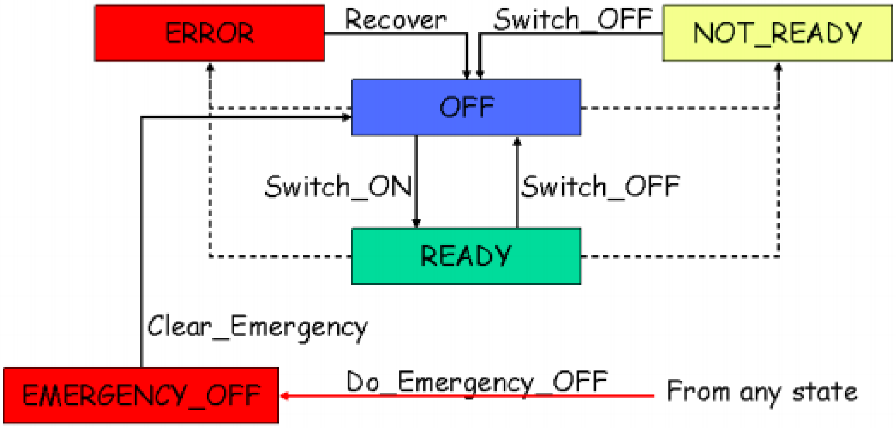

Figure 7.3: The DCS infrastructure FSM [76].

in Figure 7.2. Underneath a domain WinCC OA system(s) are assigned to facilitate the custom made functionality. In principle the hierarchy splits the detector sides (A- and C-side) to allow them to be operated independently. Each color in the overview corresponds to an individual WinCC OA project. For the detector infrastructure there is the detector control system (DCS), a domain that holds three independent projects. The Low Voltage (LV) project accounts for the controls and monitoring of the low-voltage power supplies. The Monitoring (MON) project provides monitoring of the services and the front-end electronics. The Brandeis CCD Angle Monitor (BCAM) system will constantly monitor the surface geometry to detect alignment variations. The first two projects in the DCS domain will be elaborated on the following sections as their development is currently under the responsibility of the author.

The LHCb ECS is a hierarchical supervision architecture that provides the organisation to (partly) control the experiment in a coherent manner. The JCOP framework provides the implementation of this control architecture via the Finite State Machines (FSM) tool. The FSM provides an hierarchical organisation of interconnected control nodes, each node contains of reduced set of lower level children nodes. At higher levels these nodes are all of the type control unit (CU) and at the lowest level these are of device unit (DU) type, connected to the hardware components. Each of the main domains of the SciFi ECS will have its own CU with their own children nodes, the domains have a shared master CU, the SFECS control unit. Each control unit has only one master control unit, i.e. one parent node from which it receives its commands to execute. There are in principle only two types of control flows in this hierarchy. The command initiated by the operator that propagates downwards the tree along the CU's to the lower level DU's to have an action executed and the state change from hardware that propagates upwards the tree until a CU is reached that can take an action upon this state change. The FSM system is such that only one user at a time can take the control over a part of the detector, therefore if a user takes control of a CU at the lower level this is not controllable any longer by a user at higher level until it is released again by the lower level user. This way a full sub-detector can be taken out of the partition of the LHCb ECS to for example conduct stand-alone tests.

Each of the control domains in of the SciFi ECS holds its own specified functions for proper functioning of the detector. The DCS domain will have the FSM functionalities as presented in Figure 7.3. The figure shows state diagram of detector infrastructure domain as presented in the guideline document for the ECS FSM design [76]. The DCS mainly consists of the monitoring of devices and a smaller part with control of low-voltage channels. As shown by the diagram, the DCS FSM contains five states that are defined for the DUs and CUs. Off states the channel is off, which is not meaningful in case of a pressure sensor. The not ready state is used to signal a problem, the ready state means the channel or device is at nominal operation values. The error state can for example be used to indicate a voltage trip or a too high temperature. The emergency off state is raised when a channel is automatically switched off due to an external cause, for example when the electronics temperature surpassed a critical value the low-voltage crates will have to be powered off. The channel can only be switched back to the normal off state upon receiving a clear emergency command. Monitoring of various types of sensors can have their set of defined alarm levels and may depend on the data run type. For the CUs these states reprent the states of all their children, i.e. of they are all off a CU node in the upper level goes to off, when a single child node is not ready this states is propagated up to the master nodes.

7.3 Low-Voltage Controls

The powering of the front-end electronics and electric heating is provided by Maraton power supplies. The Maraton (Magnetism Radiation Tolerant New power supply system) is a radiation hard power supply manufactured by Wiener [77]. It is a water cooled system that provides up to 12 independent low voltage/high current channels with 300W each. The power supply system, shown by Figure 7.5, is mainly composed out of three components: the power box, a primary rectifier and a remote controllable module (RCM). The primary rectifier converts 230V AC to a regulated DC input voltage (385V nominal) for the Maraton. The Maraton uses the 385V DC input for a DC-DC converter to provide up to 12 independent low voltage floating output voltages. The system is capable to measure the voltage on the load via small cross section cables and adjust the voltage dynamically. However, for the SciFi Tracker the dynamic (floating) behaviour of the output voltage will be disabled by jumpers to prevent oscillatory behaviour. The system has adjustable trip level that can be set with the control module. Additionally, for absolute limits on the output voltage, current limit and over-voltage protection, the trip level can only be adjusted at the read of the power supply.

The power boxes need to be installed in the harsh environment near the detector to limit the voltage drop in the cables due to high current. The primary rectifier and Remote Controllable Module (RCM) will be installed a another location in the cavern under normal conditions. The RCM can remotely control the outputs of the channel, i.e. switch the channel on and off, and read the measured sense voltage, output current, channels status. The RCM is connected via a TCP/IP connection to the LHCb network and is accessible via an OPC (Object Linking and Embedding (OLE) for Process Control) protocol driver. The OPC UA server is a WinCC OA manager and forms an abstraction layer between the hardware and the user of the low-voltage project. The OPC server simplifies the communication with the hardware and directly provides a set of available items. This set is mainly composed of the aforementioned items relevant for each of the individual controllable channels on the Maraton power supply. For control via the WinCC OA project, a set of data point elements need their address to be configured to the corresponding OPC items.

SFDCSLV, SciFi Detector Control System Low Voltage, is the name of the project that is currently used for the controls of the low-voltage powering of the front-end electronics. The project owes credit to Karol Poplawski, the author's predecessor who has initiated the DCS low-voltage and monitoring projects, and also Lukas Gruber has to be credited for his supporting role. The current panel used to control and monitor the Maraton is shown in Figure 7.5. The panel has

Figure 7.4: Frontal view of a W-IE-NE-R MAgnetic field and RAdiation TOleraNt (Maraton) power supply, developed for the CERN LHC [77].

been setup up by Karol, but most of the functionalities have been re-designed or further developed by the author. Via this panel the channels can be turned on/off and this status is reflected by the light coloring green (on) and grey (off). Also monitoring of the voltage, current and their trip levels is available. In principle there are two front-end boxes powered by a single channel, which is reflected by the label that is assigned to the data point of the channel. These labels are the aliases of assigned to the data points by the developer and correspond to the module end power by that channel. Failures are indicated on the right side of each channel by a red light and message stating the exact channel failure. The current and voltage are archived to the Oracle data base and a graphical display of the history can accessed by the trending buttons. These show a value over time histogram of the selected data points.

In the course of the assembly and testing work here, a temporary safety system has been developed by the author for projection of the front-end equipment. This is a software-based control script that runs in the back and has an open connection to all the sensor involved for the c-frame under commissioning. This script constantly runs, but the intervention action is made active by enabling it from the panel by the "on" button. Based on critical temperatures reached by a set number of sensors, the system will then automatically switch off the Maraton channels. The FSM and the safety system are under development and will be the final operational systems upon completion of the LHCb Upgrade I.

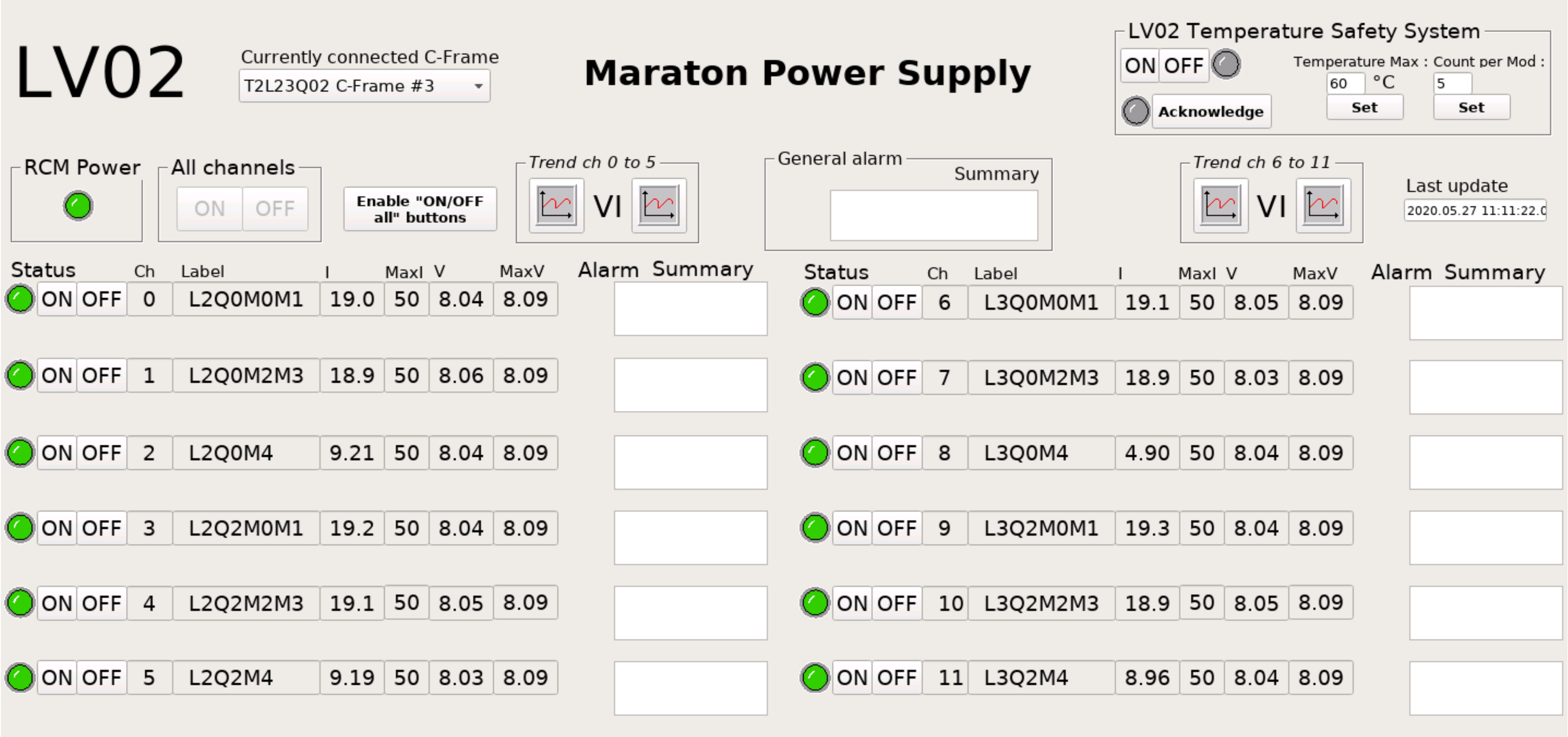

Currently connected C-Frame: T2L23Q02 C-Frame #3

Temperature Max : 60 °C

Count per Mod : 5

Last update: 2020.05.27 11:11:22.0

Status		Ch	Label	I	MaxI	V	MaxV	Alarm Summary
●	ON OFF	0	L2Q0M0M1	19.0	50	8.04	8.09	
●	ON OFF	1	L2Q0M2M3	18.9	50	8.06	8.09	
●	ON OFF	2	L2Q0M4	9.21	50	8.04	8.09	
●	ON OFF	3	L2Q2M0M1	19.2	50	8.04	8.09	
●	ON OFF	4	L2Q2M2M3	19.1	50	8.05	8.09	
●	ON OFF	5	L2Q2M4	9.19	50	8.03	8.09	

Status		Ch	Label	I	MaxI	V	MaxV	Alarm Summary
●	ON OFF	6	L3Q0M0M1	19.1	50	8.05	8.09	
●	ON OFF	7	L3Q0M2M3	18.9	50	8.03	8.09	
●	ON OFF	8	L3Q0M4	4.90	50	8.04	8.09	
●	ON OFF	9	L3Q2M0M1	19.3	50	8.04	8.09	
●	ON OFF	10	L3Q2M2M3	18.9	50	8.05	8.09	
●	ON OFF	11	L3Q2M4	8.96	50	8.04	8.09	

Figure 7.5: Control panel of the Maraton power supply LV02 connected to c-frame 3 during commissioning.

7.4 Monitoring of Services

The monitoring of services and the frond-end electronics will be done via a project called SFDCSMON, SciFi Detector Control System MONitoring, in the DCS domain. Also this project owes large credit to Karol Poplawski and the support from Lukas Gruber. The cooling and vacuum panels are fully developed by Karol. The gas and heating panels owe part credit to Karol, since his quadrant panel with flow meters and the graphical depiction of the c-frame including module numbering has been used to develop these panels. The front-end monitoring, that includes SiPM temperatures, SiPM bias voltage, and board temperature, are completly developed from scratch by the author, with the only exception of the graphical depiction of the c-frames that also re-occur in these panels. The project is in itself fully passive, i.e. there are no controllable devices in this part of the domain. The project in principle monitors the vast majority of infrastructure related to the services as it has been introduced in Section 6.2.7 and can be accessed through a parent panel, shown in Figure A.1 of the appendix. The majority of the panels are put in Appendix A.1 for the readability of this chapter. The project is currently used during the build up of the c-frames in the assembly hall. The monitoring has already been valuable to the detector technologies group as a supervision and feedback tool on the operation of newly installed services. During the commissioning of the frond-end electronics via the DAQ domain the monitoring of the frond-end has been beneficial to get insight in temperature developments on the boards. Furthermore, the services have undergone initial tests to analyse the performance of the integrated infrastructure of a c-frame. This will be presented in the concluding section of this chapter on the development of the SciFi DCS.

7.4.1 Cooling System

The cooling system in the assembly hall is connected to a single c-frame at the time. The baby cooling plant is a temporary system used for cooling during the build up of the c-frames. A c-frame can directly be connected to the cooling plant with a pair of distribution lines. The project is a passive supervision system and collects all the presented information via a PLC connected to the system in the assembly hall. The controls are provided by the engineering cooling and ventilation group (EN-CV). The panel of the temporary used Novec cooling circuit is shown in Figure A.2. The inner structure of the plant is shown on the left with the level of cooling fluid present in the reservoir and on the right the vacuum isolated distribution lines connect to the manifolds on the c-frame. The panel holds a drop down structure in which all c-frames can be selected. During the assembly of the different frames one can select for which c-frame the data has to be stored in the archive. The archive can also be directly visualised using the trending buttons on the panel.

7.4.2 Vacuum System

The vacuum system in the assembly hall directly evacuates the distribution lines at their connections with the cooling plant. Similar to the cooling system this is of temporary use during the assembly period at the surface. The controls are provided by the EN-CV group and the data is collected via a DIP protocol from the CERN technical network. The system consists of two pumps that evacuate the lines and are monitored for the pressure at several points with Pirani and Penning gauges. On the right-hand side of Figure A.3 the same structure as was shown for the Novec cooling system is used as these system go together. Also for the vacuum system the monitored values are archived to the connected c-frame and can be visualised directly on the panels by the trending buttons.

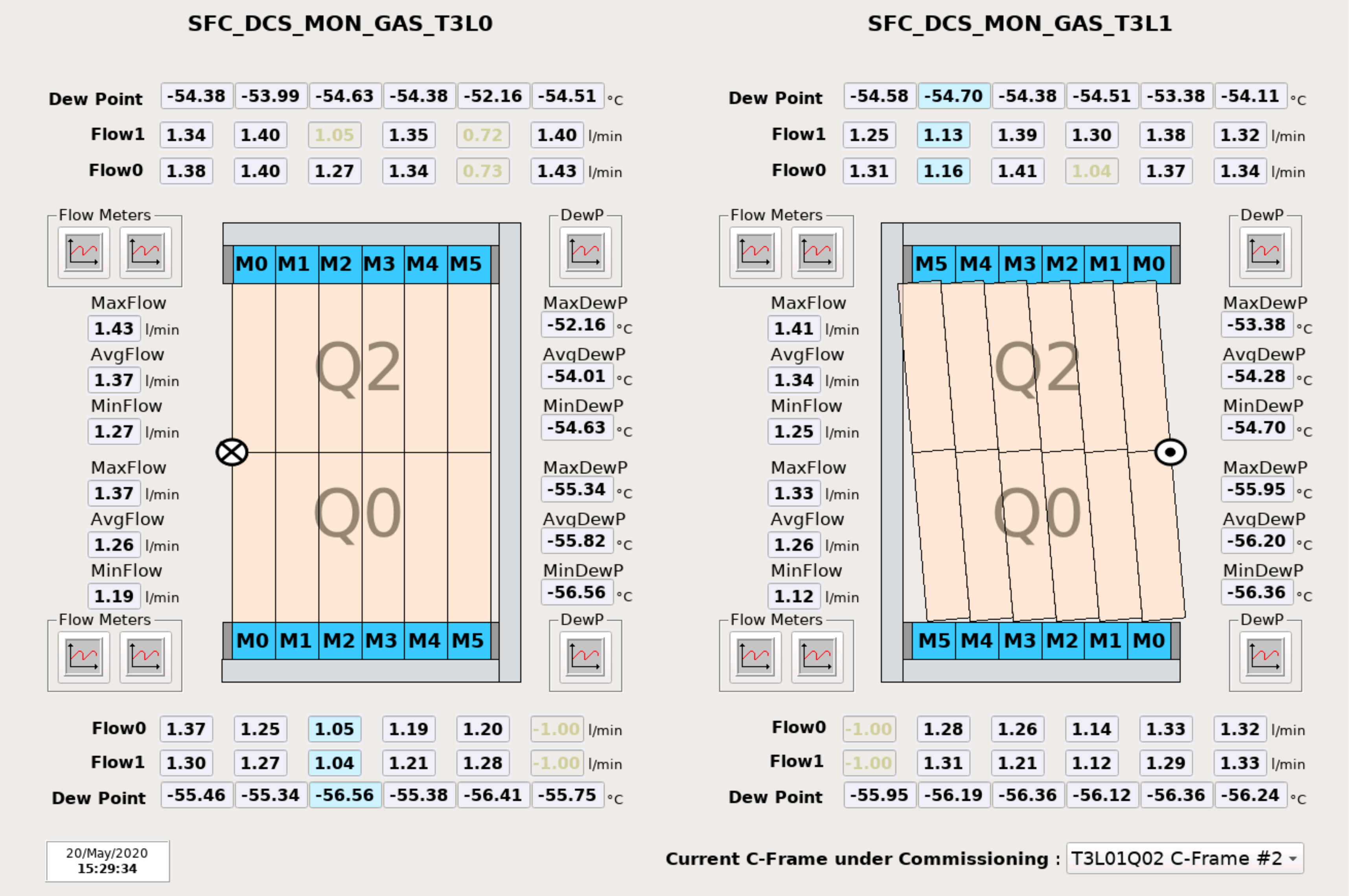

SFC_DCS_MON_GAS_T3L0

Dew Point	-54.38	-53.99	-54.63	-54.38	-52.16	-54.51	°C
Flow1	1.34	1.40	1.05	1.35	0.72	1.40	l/min
Flow0	1.38	1.40	1.27	1.34	0.73	1.43	l/min

MaxFlow 1.43 l/min
AvgFlow 1.37 l/min
MinFlow 1.27 l/min

MaxFlow 1.37 l/min
AvgFlow 1.26 l/min
MinFlow 1.19 l/min

MaxDewP -52.16 °C
AvgDewP -54.01 °C
MinDewP -54.63 °C

MaxDewP -55.34 °C
AvgDewP -55.82 °C
MinDewP -56.56 °C

Flow0	1.37	1.25	1.05	1.19	1.20	-1.00	l/min
Flow1	1.30	1.27	1.04	1.21	1.28	-1.00	l/min
Dew Point	-55.46	-55.34	-56.56	-55.38	-56.41	-55.75	°C

SFC_DCS_MON_GAS_T3L1

Dew Point	-54.58	-54.70	-54.38	-54.51	-53.38	-54.11	°C
Flow1	1.25	1.13	1.39	1.30	1.38	1.32	l/min
Flow0	1.31	1.16	1.41	1.04	1.37	1.34	l/min

MaxFlow 1.41 l/min
AvgFlow 1.34 l/min
MinFlow 1.25 l/min

MaxFlow 1.33 l/min
AvgFlow 1.26 l/min
MinFlow 1.12 l/min

MaxDewP -53.38 °C
AvgDewP -54.28 °C
MinDewP -54.70 °C

MaxDewP -55.95 °C
AvgDewP -56.20 °C
MinDewP -56.36 °C

Flow0	-1.00	1.28	1.26	1.14	1.33	1.32	l/min
Flow1	-1.00	1.31	1.21	1.12	1.29	1.33	l/min
Dew Point	-55.95	-56.19	-56.36	-56.12	-56.36	-56.24	°C

20/May/2020
15:29:34

Current C-Frame under Commissioning : T3L01Q02 C-Frame #2

Figure 7.6: Panel of a c-frame in which gas flow rates and dew points are displayed.

7.4.3 Gas System

The gas system has a temporary supply rack in the assembly hall that in principle provide dried air to the c-frames, but has N_2 as a second gas for backup use. The panel of the supply system is shown in Figure A.4. The flushing rate to the c-frame can be manually controlled in the assembly hall. The data is collected via a DIP protocol from the CERN technical network. The panel used for monitoring of a c-frame is shown in Figure 7.6. This panel serves as the bases for the final system and shows the redundant set of flow meters at the output lines and also the measured dew points for every cold box. A c-frame is composed of two module layers and are graphically depicted in a way as one faces them, i.e. the outer side of a module layer as one stands in front of a side. Per quadrant of the c-frame a control script provides that minimum, maximum and average values. In addition there is trending available for both the flow meters and the dew points, which provides valuable information on the control of humidity in the cold boxes. Higher functionalities of this panel include the blue marking of the cold boxes that currently undergo the humidity measurement, alarms are indicated by flashing squares around the sensor values and broken sensors can be masked after which their color greys out. The flows of cold boxes that undergo a humidity measurement and masked sensors are not taken into account for computation of the minimum, maximum and average values of their respective quadrant.

7.4.4 Electric Heating System

The electric heating system is monitored by 2 PT100 sensors per module end, one on the dry gas outlet connector and one on the top of the cold box shell. Equivalent to the vacuum and gas system, the data is collected via a DIP protocol from the CERN technical network. The panel to monitor these temperatures for a c-frame has a similar outline as the gas panel and is shown in Figure A.6. The sensors are installed to gain feedback on the temperatures on the these parts of the module ends that are the coldest. The electric heating can be used to raise the temperature on the outside when this is required. The minimum, maximum and average values for the two locations are shown per complete c-frame. Also, trending is available to have graphical feedback on temperature developments.

7.4.5 Front-End Monitoring

The front-end boards and SiPMs have their temperatures sensors connected via the Front-End Electronics (FEE) project in the DAQ domain. Additionally, the voltages at the SiPMs and master boards are also measured by the front-end electronics and can thus be monitored from the project. The projects of the several domains for the SciFi tracker form a distributed system and the monitoring project can therefore directly access all the datapoints from the front-end electronics project via a distribution manager. The relevant datapoints for the boards and SiPM are connected to the tables that are used to display the large number of temperature and voltage sensors. The panel displaying all SiPM temperature sensors on c-frame is given in Figure 7.7. The SiPM tables will be taken as an example, the other tables have almost identical functionality and are shown in Figures A.7 and A.9 of the appendix. The SiPM sensors give real time feedback on the Novec cooling. There are 16 SiPM sensors per module or 384 per c-frame. For the monitoring of the board temperatures the table is significantly larger, since it needs to display 66 sensors per module, resulting in 1584 sensors per c-frame. Trending is available by clicking the H0 and H1 push buttons in the Trending column. By clicking the push buttons in the Module column another panel appears, the panel gives a detailed overview of the temperatures on the corresponding read-out box of that module. This panel is shown by Figure A.8 in the appendix, from this panel also trending is available for the cluster boards, pacific boards and SiPMs.

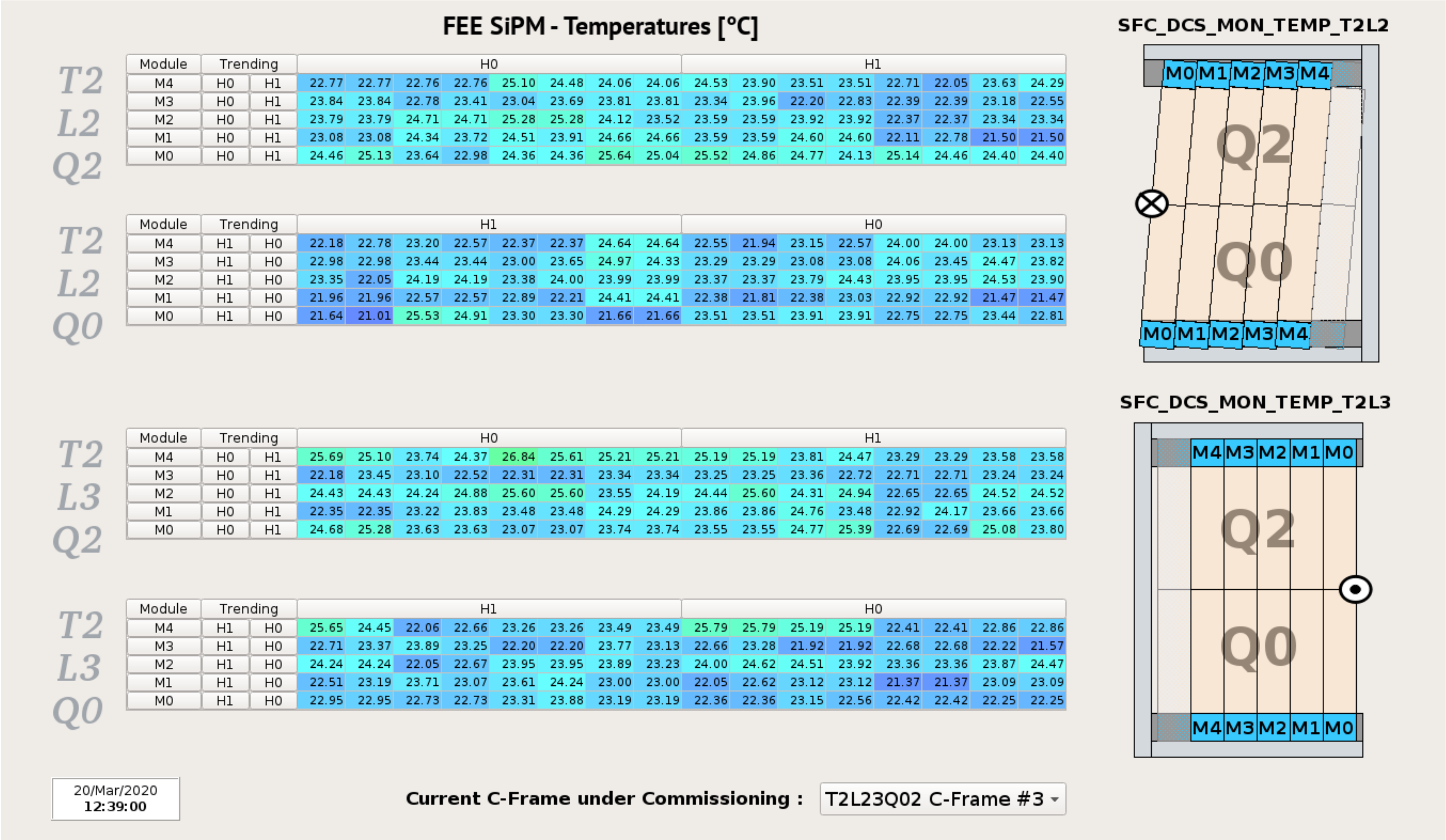

FEE SiPM - Temperatures [°C]

T2 L2 Q2

Module	Trending		H0								H1							
M4	H0	H1	22.77	22.77	22.76	22.76	25.10	24.48	24.06	24.06	24.53	23.90	23.51	23.51	22.71	22.05	23.63	24.29
M3	H0	H1	23.84	23.84	22.78	23.41	23.04	23.69	23.81	23.81	23.34	23.96	22.20	22.83	22.39	22.39	23.18	22.55
M2	H0	H1	23.79	23.79	24.71	24.71	25.28	25.28	24.12	23.52	23.59	23.59	23.92	23.92	22.37	22.37	23.34	23.34
M1	H0	H1	23.08	23.08	24.34	23.72	24.51	23.91	24.66	24.66	23.59	23.59	24.60	24.60	22.11	22.78	21.50	21.50
M0	H0	H1	24.46	25.13	23.64	22.98	24.36	24.36	25.64	25.04	25.52	24.86	24.77	24.13	25.14	24.46	24.40	24.40

T2 L2 Q0

Module	Trending		H1								H0							
M4	H1	H0	22.18	22.78	23.20	22.57	22.37	22.37	24.64	24.64	22.55	21.94	23.15	22.57	24.00	24.00	23.13	23.13
M3	H1	H0	22.98	22.98	23.44	23.44	23.00	23.65	24.97	24.33	23.29	23.29	23.08	23.08	24.06	23.45	24.47	23.82
M2	H1	H0	23.35	22.05	24.19	24.19	23.38	24.00	23.99	23.99	23.37	23.37	23.79	24.43	23.95	23.95	24.53	23.90
M1	H1	H0	21.96	21.96	22.57	22.57	22.89	22.21	24.41	24.41	22.38	21.81	22.38	23.03	22.92	22.92	21.47	21.47
M0	H1	H0	21.64	21.01	25.53	24.91	23.30	23.30	21.66	21.66	23.51	23.51	23.91	23.91	22.75	22.75	23.44	22.81

T2 L3 Q2

Module	Trending		H0								H1							
M4	H0	H1	25.69	25.10	23.74	24.37	26.84	25.61	25.21	25.21	25.19	25.19	23.81	24.47	23.29	23.29	23.58	23.58
M3	H0	H1	22.18	23.45	23.10	22.52	22.31	22.31	23.34	23.34	23.25	23.25	23.36	22.72	22.71	22.71	23.24	23.24
M2	H0	H1	24.43	24.43	24.24	24.88	25.60	25.60	23.55	24.19	24.44	25.60	24.31	24.94	22.65	22.65	24.52	24.52
M1	H0	H1	22.35	22.35	23.22	23.83	23.48	23.48	24.29	24.29	23.86	23.86	24.76	23.48	22.92	24.17	23.66	23.66
M0	H0	H1	24.68	25.28	23.63	23.63	23.07	23.07	23.74	23.74	23.55	23.55	24.77	25.39	22.69	22.69	25.08	23.80

T2 L3 Q0

Module	Trending		H1								H0							
M4	H1	H0	25.65	24.45	22.06	22.66	23.26	23.26	23.49	23.49	25.79	25.79	25.19	25.19	22.41	22.41	22.86	22.86
M3	H1	H0	22.71	23.37	23.89	23.25	22.20	22.20	23.77	23.13	22.66	23.28	21.92	21.92	22.68	22.68	22.22	21.57
M2	H1	H0	24.24	24.24	22.05	22.67	23.95	23.95	23.89	23.23	24.00	24.62	24.51	23.92	23.36	23.36	23.87	24.47
M1	H1	H0	22.51	23.19	23.71	23.07	23.61	24.24	23.00	23.00	22.05	22.62	23.12	23.12	21.37	21.37	23.09	23.09
M0	H1	H0	22.95	22.95	22.73	22.73	23.31	23.88	23.19	23.19	22.36	22.36	23.15	22.56	22.42	22.42	22.25	22.25

20/Mar/2020
12:39:00

Current C-Frame under Commissioning : T2L23Q02 C-Frame #3

Figure 7.7: Tabulated SiPM temperatures for a c-frame, arranged per module.

The panel showing the overview of temperatures in the read-out box is also part of the front-end electronics panel. shown in Figure A.7 in the appendix. Due to the large number of temperature sensors on the front-end electronics panel is tabulated per half read-out box. The tabulated sensors are completely shown by the panel of the overview of read-out box, that is reachable from the push buttons in the Module column. The panels is used during the commissioning of newly installed front-end electronics and also serves as a feedback on the functioning of the water cooling of the electronics. This panel for example lead to the discovery of a bad connection between the cooling plate and a front-end box.

The panel showing the voltages as measured at and by the frond-end electronics are shown in Figure A.9 in the appendix. It shows the high voltage measured by the pacific boards on the SiPMs and the voltage on the master board. The voltages measured by the frond-end can be used as a cross check on the voltage as provide by the CAEN power supplies. No additional functionality is currently available for this panel.

7.5 Performance of Services

A series of performance tests have been carried out during October and November of 2019 to inspect the integrated services of a c-frame for the first time. These performance tests have been collectively referred to under the name of the heating wire test program. The heating wire test program is the name for the performance tests that were done after condensation problems had been solved. More background information on the condensation problems can be found in Appendix A.2.3. It refers to the installation of the heating wire that allowed to cool down to a temperature of -40 °C on the SiPM without condensation forming anywhere. Hence, other than the name might suggest, it is not solely focused on active heating. Yet, there was a special concern that the use of active heating might affect the SiPM temperature. Throughout the heating wire test program three services have mainly been varied, namely:

- the Novec temperature
- the dry gas flow rate
- the supplied heating power per module end

The outcome of these tests are relevant to adequate operation of the SciFi Tracker and form the core purpose of this document. The results are sub-divided over several topics and a separate section is dedicated to each of them. The subsequent subjects are: dew points inside the cold boxes, temperatures of parts prone to condensation, dissipated energy by the cooling system and also SiPM temperatures are discussed. Prior to this, a necessary introduction to the data samples along with the caveats that one should bear in mind is presented.

7.5.1 Data Samples

The data samples were taken during a busy assembly period and due to the strict schedule limited in the number of samples. A more extensive study is prepared to have more complete data set. The measurement program can be divided over numerous sub-sets of data in which the earlier mentioned services have been subject to variation. The plant temperature was adjusted between -50, -30, -10, 0 and 20 °C. The dry gas flow was varied between rates of 0.3, 0.6, and 0.9 l/min. The supplied heating power per module end was changed between 10, 25, and 35 Watts of power. A configuration of settings was typically kept and monitored for time windows of 4 to 10 hours, but exceptionally shorter and longer are included as well. All data taking periods with the corresponding settings are listed in Table 7.1. The data taking can mainly be divided over two separate periods. The first period lasted from the 23rd of October till the 1st of November, during which only two frond-end boxes were installed on modules T3L2Q0M0 and T3L2Q0M1. The second period lasted from the 24th till the 28th of November, during which the remaining 22 frond-end boxes were also installed. During the second period of the program with 24 frond-end boxes available, the readout was limited to a maximum of 12 frond-end-boxes. Hence, it was decided to monitor either the two top quadrants or the two bottom quadrants of the c-frame. Therefore, the data points presented during these measurements are specially referred to with top and bottom in the graphs to follow.

To analyse how the c-frame performed under the various conditions, a total of 518 points were monitored. The values were archived to the Oracle database typically every 120 seconds or with a relative change of the value of the order of 1 to 3 percent. The monitored sensors can be subdivided into the following categories :

- 3 temperature sensors on the Novec cooling plant
- 2 vacuum gauges for the vacuum system, one per manifold
- 1 dew point sensor for ambient conditions in the hall
- 48 flow meters for the dry gas system
- 2 dew point sensors with gas multiplexers for the cold boxes
- 384 SiPM temperature sensors
- 24 temperature sensors on the top of cold boxes
- 24 temperature sensors on the dry gas outlet connectors
- 7 temperature sensors on Novec bellows
- 1 temperature sensor for the ambient conditions in the hall

Pictures of the PT100 temperature sensors placed at the dry gas outlet connector, top of the cold box and novec bellow arcs are shown in the respective Figures 7.10, 7.11 and 7.12. The presented values are the calculated averages of a selected time window during which a certain setting was run. That average is calculated in two steps, first the mean value for each individual sensor is calculated and then the average value of the involved sensors is calculated by averaging their means. The error on the value is represented by the standard deviation among the mean values of the sensors. In case a single sensor is presented, the value and error are represented by its mean and standard deviation.

A picture of a module end is given by Figure 7.8 and is equipped with the following sensors :

- 2 dry gas flow meters
- 1 dew point sensor
- 1 temperature sensor on the dry gas outlet connector
- 1 temperature sensor on the top of the cold box shell

Set	Start Time	Selected Period	T_{NOVEC} (°C)	Dry Flow (l/min)	Heating (W)
1	23 OCT 23:30	24 OCT 04:00-10:00	-50	0.90	35
2	24 OCT 18:30	24 OCT 22:00-06:00	-50	0.60	35
3	25 OCT 11:30	25 OCT 14:00-20:00	-50	0.30	35
4	25 OCT 21:20	26 OCT 00:00-09:00	-50	0.30	25
5	26 OCT 12:00	26 OCT 14:00-11:00	-50	0.60	25
6	27 OCT 13:20	27 OCT 15:00-10:00	-50	0.90	25
7	28 OCT 12:10	28 OCT 14:00-17:00	-50	0.90	10
8	28 OCT 20:00	28 OCT 22:00-09:00	-50	0.60	10
9	29 OCT 11:00	29 OCT 13:00-22:00	-50	0.30	10
10	29 OCT 23:20	30 OCT 01:00-08:00	-30	0.30	10
11	30 OCT 10:20	30 OCT 12:00-16:00	-30	0.30	35
12	30 OCT 18:30	30 OCT 21:00-11:00	-50	0.60	35
13	31 OCT 13:00	31 OCT 14:00-22:00	-10	0.30	10
14	31 OCT 23:10	01 NOV 01:00-10:00	-10	0.30	0
15	01 NOV 11:40	01 NOV 16:30-20:30	0	0.30	10
16	08 NOV 18:20	08 NOV 20:30-13:00	20	0.30	10
17	09 NOV 14:40	09 NOV 15:00-18:30	20	0.30	25
18	24 NOV 14:00	24 NOV 14:30-18:30	-50	0.90	25
19	24 NOV 19:00	24 NOV 20:00-10:00	-50	0.30	25
20	25 NOV 10:40	25 NOV 11:30-13:00	-50	0.15	25
21	25 NOV 19:30	25 NOV 21:00-08:00	-50	0.90	35
22	26 NOV 09:00	26 NOV 10:00-19:00	-50	0.30	35
23	26 NOV 20:20	26 NOV 21:00-10:00	-50	0.60	25
24	27 NOV 19:00	27 NOV 20:00-23:00	-50	0.60	25
25	27 NOV 23:00	28 NOV 00:00-09:00	-50	0.60	35
26	28 NOV 10:00	28 NOV 10:44-11:44	-50	0.60	10

Table 7.1: All data sets taken during the performance campaign of October and November 2019 on c-frame 1. The blank space between setting 15 and 16 marks installation of 22 remaining front-end boxes and the transition from the first to the second data taking period.

- 16 SiPM temperature sensors

It is worth mentioning some important caveats related to the presented material of the test program :

- The measurements of the dew point inside the cold box are done by an external body for which temporarily the cold box has to be flushed. Ideally this flushing is at the same or at a very similar rate to which the dry gas is circulated through the boxes. However, at the time the tests were conducted this was not adjusted accordingly. The dew point measurement was adjusted to take 10 minutes per coldbox, so a full c-frame was measured in about 2 hours. The presented values for the dry gas flow rate are therefore affected by the flushing during the dew point measurement.

- A consequence of the fact that the flushing is not adjusted to the dry gas flow rate is that the dew point measurement itself might be influenced by this difference. The presented values for the dew points might therefore be affected.
- The dry gas is leaving the cold box very cold and strongly cools the dry gas outlet connector, which is the reason for it being the most affected part by condensation problems. The fact that the flushing has not been adjusted to the dry gas flow also means that the temperature measurements on the dry gas outlet connector might be influenced during the flushing and hence these presented temperatures could be affected.
- Shortly before the first test period, module 5 of layer 2 got exchanged and hence the inside of its cold boxes were quite humid at this point. Since dry gas was circulated only for a couple of days before the first test setting, the measured dew point on this module was 5-8 °C higher compared to the average value of the other modules and has thus been excluded in the analysis.
- For temperature measurements on the Novec bellows only 7 sensors were available, which further had to be divided of top and bottom quadrants. They were temporarily placed with tape and the position might vary from one sensor to another, see Figure 7.12. For the first c-frame no bellow stretching was applied on the outer bellow and hence cold spots are still expected to appear. Bellow stretching is a procedure to elongate the outer Novec bellow, such that during cooling the inner and outer bellows do no longer touch each other. The touching led to cold spots at (nearly) touching locations that were shown to be solvable by a stretching procedure [1]. These two facts together with the few temperature sensors used for monitoring might mean that the presented temperature values should perhaps be taken with bigger uncertainty than is shown.
- During the first test period it was noticed that there were sinusoidal temperature fluctuations on the Novec cooling plant. The amplitude of the fluctuations was about 1.5 °C, i.e. 3 °C between the maximum and minimum, see Figure A.10 in the appendix. The period lasted a bit more then three minutes. These temperature fluctuations could simultaneously be observed with the temperature sensors on the SiPMs, hence directly affecting the stability of their environment. Before the second test period the controls of the cooling plant were adjusted which resulted in an amplitude of only 0.1 °C, the accuracy of the temperature sensor.

At this point the motivation of the program has been given, along with a description of the data along with the caveats that one should bear in mind when drawing conclusions from the presented material. The main focus for all parts are temperature effects under the various settings handled by adjustment of the Novec cooling temperature, dry gas flow rate and supplied heat power. The measured dew point in the cold box will be presented first. The next part will be on the parts that were found to be affected by condensation during the earliest Novec cooling tests of the SiPM in July 2019. These are the dry gas outlet connector, the Novec bellows and the cold box shell. The dissipated energy by the cooling plant is given as well as the effectiveness of SiPM cooling. The SiPM temperatures are presented, central to the performance of the services to check if the required -40 °C can be reached and maintained adequately. The Novec cooling temperature is denoted as the Plant T_{out} in the following figures.

---

[1] see e.g. SciFi detector talk during 94th LHCb week: **https://indico.cern.ch/event/859068/**

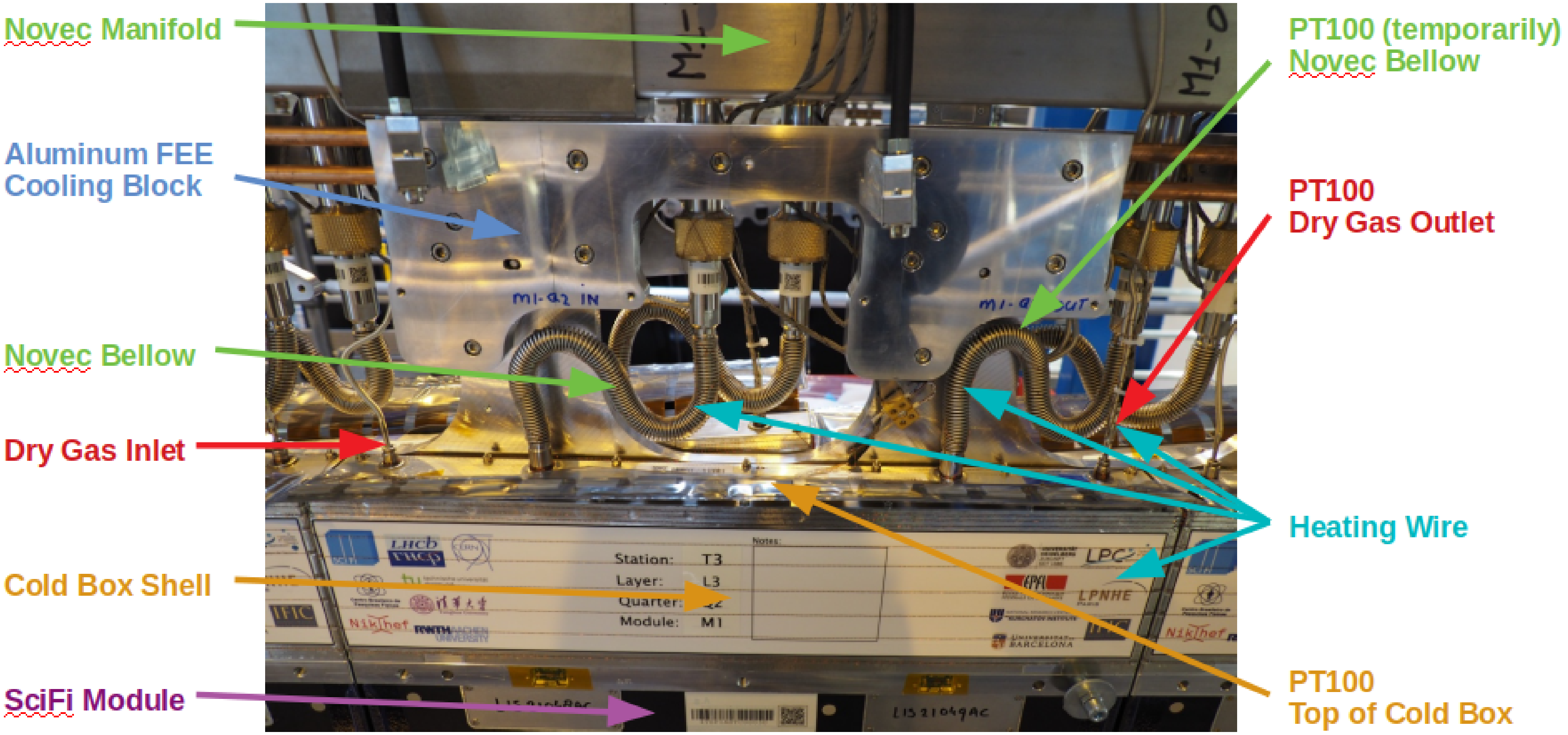

Figure 7.8: Picture of a module end with installed services before read-out box installation.

7.5.2 Dew Points

In Figure 7.9, the average of the measured dew points inside the cold boxes are depicted under various settings, but all taken with a Novec cooling temperature set at -50 °C. The flow rate of the circulating dry gas has been set at roughly the following points: 0.3, 0.6 and 0.9 l/min. The three colors show the supplied heating power per module end by the heating wire system. The obtained measurements depicted in this graph show that with the dry gas flow rate one has a good handle to control the dew point. With the adjustment of the flow rate one is able to manage a dew point that is lower than the Novec cooling temperature with the required safety margin of 5 °C below cooling temperature is in reach. Dry gas had been circulating the boxed for several months at the point of the test program.

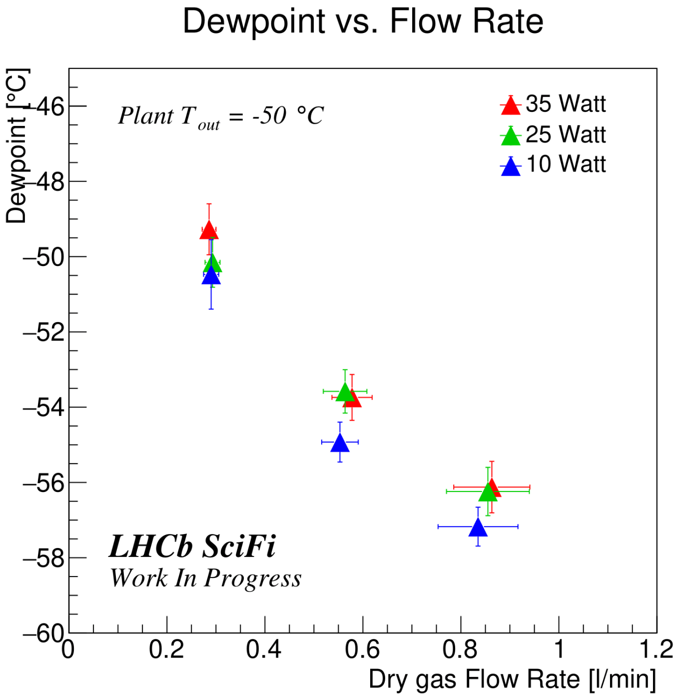

Figure 7.9: The dew point measured as a function of the dry gas flow rate.

7.5.3 Temperature of Condensation Affected Parts

In the following sections the temperatures on the outside parts of modules that were most affected by condensation will be discussed. These critical locations that are strongly cooled are shown by Figures 7.10, 7.11 and 7.12, in which also the heating wires are shown.

7.5.4 Dry Gas Outlet Connector

In Figures 7.13 and 7.14 the average temperature on the dry gas outlet connector is shown for the first data taking period and the first superimposed by the second data taking period, respectively. All data shown is taken with a Novec cooling temperature set at -50 °C. The solid markers represent a setting for which the front-end electronics were not configured and all dry gas outlets are taken into account. A note here has to be put on the fact that during the first period the electronics of the 2 installed read-out boxes were configured at all time, however this

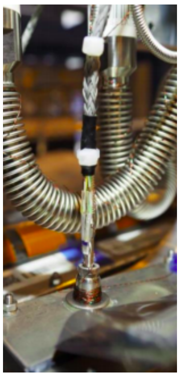

Figure 7.10: PT100 glued onto the dry gas outlet

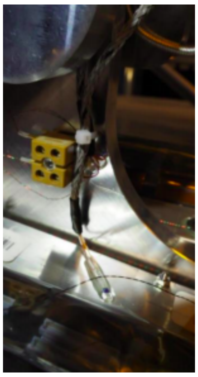

Figure 7.11: PT100 glued on the top of cold box

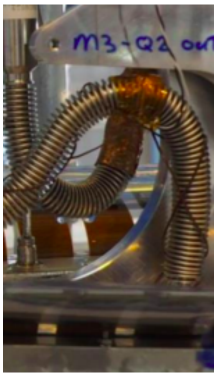

Figure 7.12: PT100 taped onto the arc of Novec bellow

is considered of negligible effect to the full c-frame. The hollow markers represent a setting for which the front-end electronics were partly configured, either only front-end electronics of the top quadrants or of the bottom quadrants were configured simultaneously. Hence, the presented data in this case only takes into account temperature readings from the module ends that had their read-out boxes configured.

The figure shows that with the given range of supplied heating power one is capable of managing the temperature of the dry gas outlets in a range of about 20 °C for a given flow rate. The temperature of dry gas outlet connector is clearly affected by the flow rate of the dry gas. To first approximation a linear fit is used for each heating setting, however a more sophisticated approach might be needed at extended range. It can be envisioned from comparing the data to the linear fit that at lowest flow rates the temperature starts to rise non-linear and at the highest flow rates it starts to flatten. The data from the second period in which all frond-end boxes were

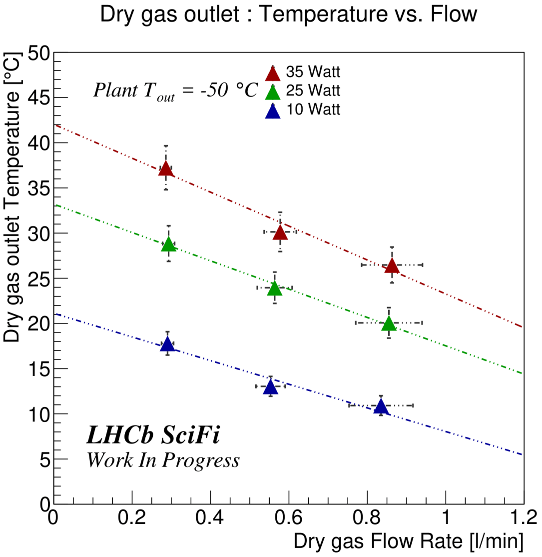

Figure 7.13: The dry gas outlet temperature measured as a function of the dry gas flow rate under three different heating settings.

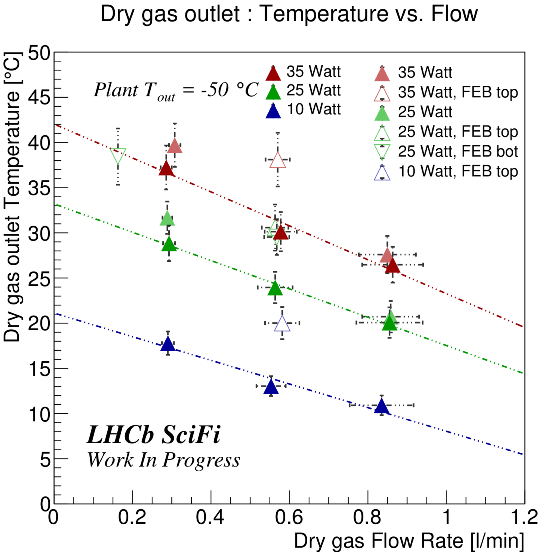

Figure 7.14: The dry gas outlet temperature measured as a function of the dry gas flow rate under three different heating settings.

installed and shows some changes with respect to the first period. Looking to the two additional points at flow rates of 0.3 and 0.9 l/min and a heating power of 35 Watt, there is an increase in temperature visible of about 1-3 °C with respect to the first data taking period. Additionally, in the second data period also settings were run with full quadrants of front-end electronics configured. This is shown by the hollow red marker at a flow rate of about 0.6 l/min. The increase of temperature here is an additional 5-7 °C on top of the non configured setting, which is a rather significant increase. A similar trend is found for the two other heating powers of 25 and 10 Watt. Hence, the conclusion drawn from this is that there is a slight increase of temperature due to the installation of the 22 remaining frond-end boxes and that during periods in which the electronics are actively used, i.e. configured, the temperature rise is a rather significant 5-7 °C.

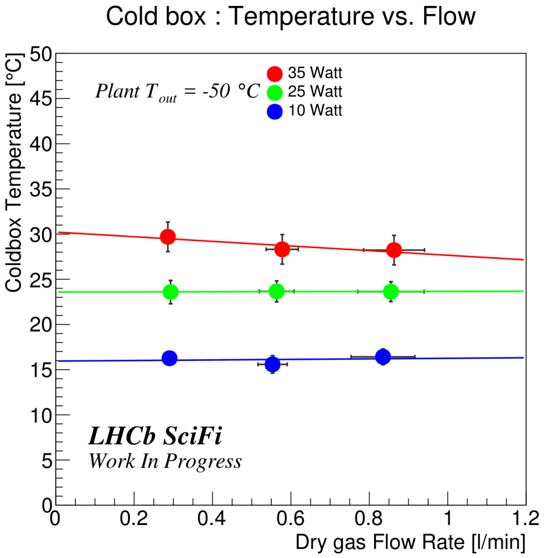

Figure 7.15: The top of the cold box temperature measured as a function of the dry gas flow rate under three different heating settings.

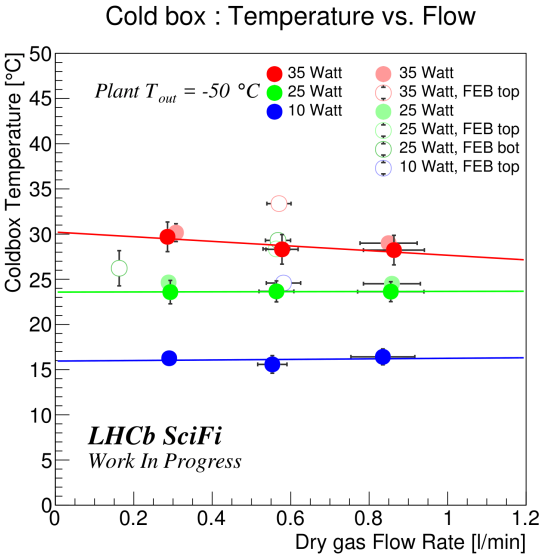

Figure 7.16: The top of the cold box temperature measured as a function of the dry gas flow rate under three different heating settings.

7.5.5 Top of Cold Box

In Figures 7.15 and 7.16 the average temperature on the top of the cold is shown for the first data taking period and the first superimposed by the second data taking period, respectively. All data shown is taken with a Novec cooling temperature set at -50 °C. All the plotted data points correspond the same ones shown in Figures 7.13 and 7.14. Similar to the dry gas outlet figures, the data of the top of the cold box have solid and hollow markers. For the solid markers the front-end electronics were not configured, whereas for the the hollow markers they are, although only partly as explained previously.

The influence of the given range of supplied heating power is apparent, allowing for a temperature range of about 15 °C independent of the flow rate of the dry gas. In fact, for the top the cold box the temperature is relatively flat with respect to the flow rate. Data from the second data period only show a minimal temperature increase of about 1 °C. When the front-end electronics are configured, the increase of temperature is about 2-6 °C with respect to non configured.

The hollow marker at a heating power of 10 Watt might not taken be into full consideration for this estimate as this data set only lasted 10 minutes and was taken shortly after a data taking setting for which the heating power was put to 35 Watt. The cold box mass might therefore not have been fully cooled down.

7.5.6 Novec Bellow

In Figures 7.17 and 7.18 the average temperature on the Novec bellows is shown for the first data taking period and the first superimposed by the second data taking period, respectively. All data shown is taken with a Novec cooling temperature set at -50 °C. All plotted data point corresponds to the same ones shown in Figures 7.13, 7.14, 7.15 and 7.16. And likewise, the same convention for the markers is used as was done for the dry gas outlet and top of the cold box, in which for the solid markers the front-end electronics were not configured and for the hollow markers they were configured, though only partly as explained previously.

The influence of the heating system is apparent for the Novec bellows. For the studied range of heating one can control the temperature to range of about 15 °C. This temperature range is almost independent of the dry gas flow rate. The temperature of the Novec bellows is relatively flat with respect to the flow rate. The data from the second period shows a slight increase of about 0-2 °C compared to the first data taking period. With the front-end electronics configured, there is a rise in the temperature of about 2-8 °C, compared to the first data taking period. Once more, it has to be stressed that the number of temperature sensors on Novec bellows is limited to 7, which gives only 3 or 4 measurements per quadrant for the average on data points where part of the frond-end electronics configured.

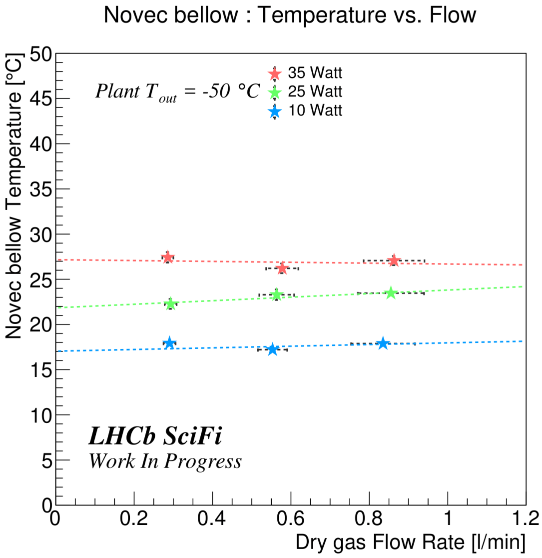

Figure 7.17: The Novec bellow temperature measured as a function of the dry gas flow rate under three different heating settings.

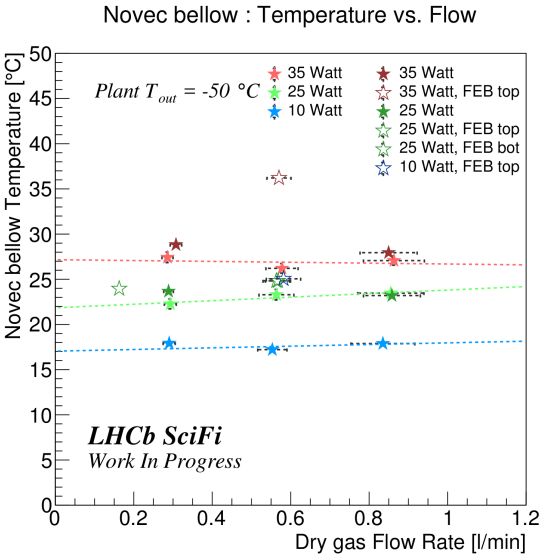

Figure 7.18: The Novec bellow temperature measured as a function of the dry gas flow rate under three different heating settings.

7.5.7 Combined Temperature Plot

A combined plot of the dry gas outlet connector, top of cold box and Novec bellow temperature is shown in Figure 7.19. Only measurements during the first data taking period are shown here, they together form a grid containing 9 points. The superimposure of the 3 monitored locations on a module can be used to deduce a minimum temperature under a particular setting of the dry gas flow and supplied heating power.

The data shown is for the first period in which only 2 out of 24 frond-end boxes where installed and the electronics were configured. As shown by the previous figures for the individual locations is that there is a minor effect due to the installation of the 22 remaining frond-end boxes and a rather significant effect caused by configuring the frond-end electronics. Thus, the current figure functions to give a first estimate for which an offset on the temperature axis should be added for later use. This offset depends on the status of the detector, when the front-end electronics are not configured an offset of about 0-3 °C should be added and when configured 2-8 °C should be added to the given plot. From the plot in Figure 7.19, one is interested to extract the minimum temperature, since this will ultimately determine which part is most prone to condensation. The dew point in the cavern is expected to be up to 12 °C. Already during the first data taking period, one reaches this temperature on all parts for a supplied heating power of 10 Watt. Additional frond-end boxes improve the situation and with all front-end electronics are configured the minimum temperature might be even raised sufficiently enough such that no heating power will be needed during active data taking. However, a suggested safety margin of about 5 °C should take account for uncertainty in actual coldest locations.

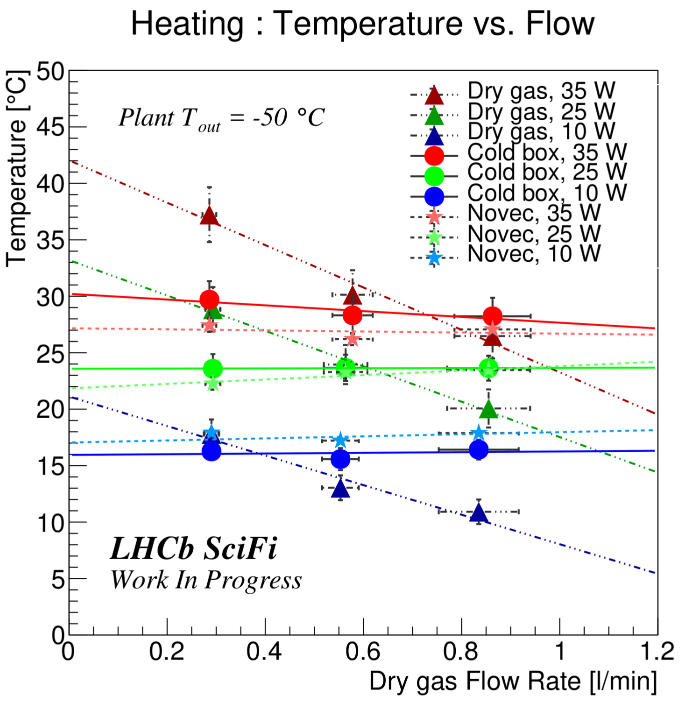

Figure 7.19: Combined plot of temperature measurements on condensation affected parts.

7.5.8 Cooling Plant

The dissipated energy during the cooling process of the SiPMs is measured by comparing the return temperature to the output temperature by the Novec cooling plant. Furthermore, it is also a measure of how well the vacuum isolation shields against convection losses. This is done for several cooling temperatures and under different settings for the supplied heating power and dry gas flow rate, shown in Figure 7.20. All data shown here is obtained during the first data taking period. A similar comparison for the dissipated energy could not be carried out for the second data taking period since the calibration of the sensor was known to be off during this time.

From the graph a minor trend can be noticed for which the dissipated heat increases with a decrease in cooling temperature. This trend can be understood by the fact that the temperature gradient increases when lowering the cooling temperature. It can be noticed from the data points at a cooling temperature of -50 °C that the supplied heat by the heating system has minimal influence on the cooling system. The Novec cooling system thus is separated rather well from the outside environment. The influence of the circulating dry gas is negligible. It should be noted once more that the error bars of about 1.5 °C can be ascribed to the fluctuations of the Novec cooling plant output temperature.

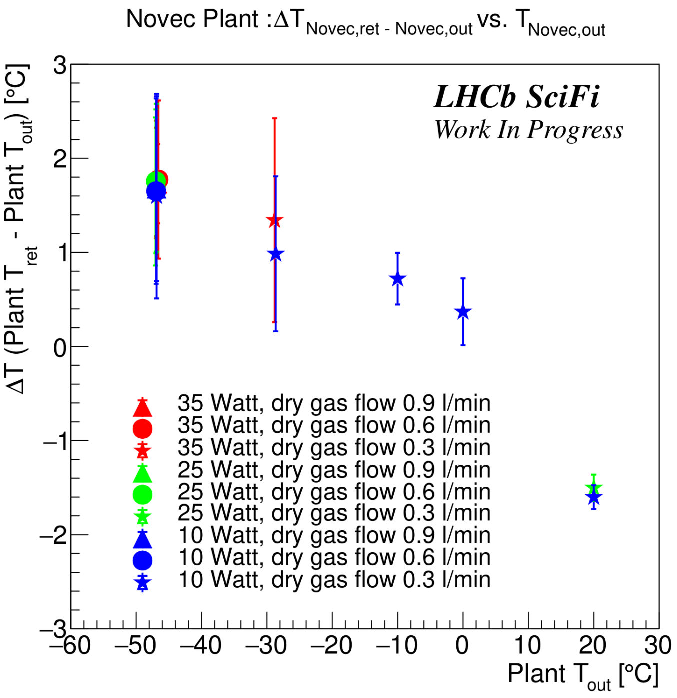

Figure 7.20: Difference between return and output temperature of the Novec cooling plant.

7.5.9 SiPM Temperature vs Plant Set Point

Similar to the study of the dissipated energy of the cooling plant, the offset of the SiPM temperature with respect to the Novec cooling temperature is measured by comparing the average of the SiPM temperature sensors to the plant output temperature. This is of interest to obtain knowledge about the offset compared to Novec cooling plant, and can therefore be used to control the temperature on the SiPMs more accurately. It should be noted that the data shown in Figure 7.21 is all taken with a dry gas flow rate of 0.3 l/min and since it concerns the first data taking period, only two read-out-boxes were installed. Therefore, the data is split in SiPM averages for module T3L2Q0M0 and T3L2Q0M1, denoted as M0 and M1, respectively. Also here it is rather unfortunate that during the second data taking period the calibration of the temperature sensors on the Novec cooling plant was known to be incorrect. A study with a more precise offset from the SiPMs of all frond-end boxes was therefore not feasible.

The graph shows a small trend that with the increase of the temperature gradient the offset of the SiPM temperature to the cooling temperature increases. The influence of the heating power on the SiPM temperature can be noticed, but is no larger than approximately 1 °C. The difference in temperature between the two modules is also visible and will be of interest during data taking with all frond-end boxes installed. This will be elaborated on during the coming pages. In Figure 7.22 the offset of the SiPM temperature to the Novec cooling temperature is shown. All data shown is for a plant output temperature set at -50 °C. The supplied heating temperature is varied as well as the flow rate of the dry gas. As it concerns data from the first data taking period, only measurements from modules M0 and M1 exist as was explained previously.

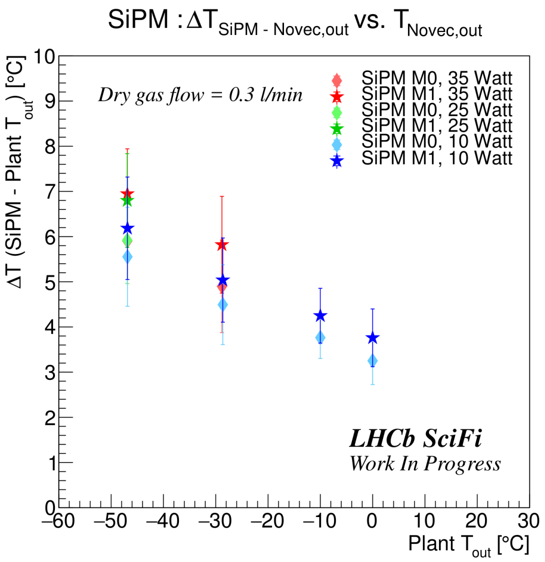

Figure 7.21: Difference between SiPM and plant output temperature.

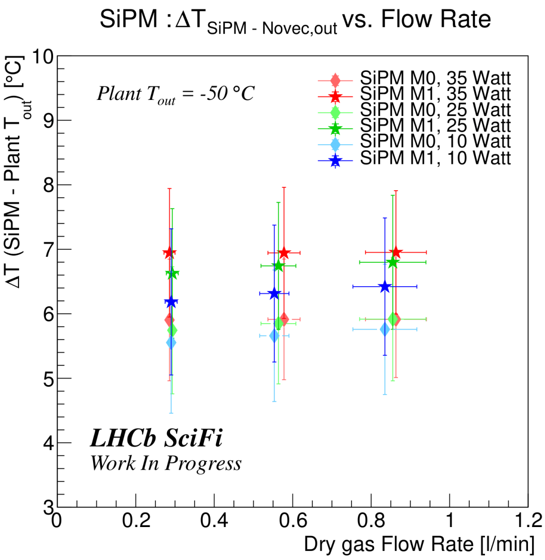

Figure 7.22: Difference between SiPM and plant output temperature.

The flow rate does not have strong influence on the offset of the temperature, which shows almost flat behaviour. From this graph it can also be seen that the temperature spread of module M0 is only about half the spread compared to module M1.

7.5.10 SiPM Temperature

During the second period of data taking all frond-end boxes were installed and due to a limitation only 2 quadrants could be configured at a single instance. Hence it was chosen to configure the front-end electronics for either the top two quadrants or the bottom two quadrants. For all the settings during the second data taking period the Novec cooling temperature remained at -50 °C. Although the flow rate of the dry gas was varied, only data is presented here for which the flow was circulated at an approximate rate of 0.6 l/min.

In Figures 7.23 and 7.24, data is shown for all SiPM temperature sensors present on quadrant T3L2Q0. During this period the control of the Novec cooling plant had been adjusted such that the amplitude of the sinusoidal fluctuations was about 0.1 °C. The temperature spread found on the SiPM temperature is about 0.5 °C, corresponding to the ADC precision. This is significantly smaller than was found before the controls of the plant were adjusted. In Figure 7.23, 96 SiPM temperature sensors are shown that are physically adjacent in neighbouring modules on the quadrant. No clear trend is visible from the first to the last SiPM, the values seem to fluctuate without a clear pattern at first glance. With the guidance of the dashed blue vertical lines to visualise where the module edges are, this changes slightly and the first 2 sensors then seem to be a bit higher then the others. In Figure 7.24, the temperature sensors of the 6 modules are overlayed with each other. Here it becomes clear that a temperature sensor on a particular location on the module is constraint to a fixed range. This pattern is found for all quadrants and one might even able to distinguish the four mats inside a module.

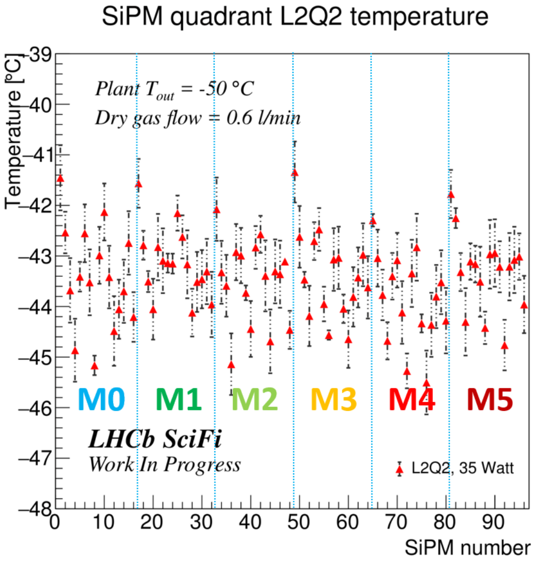

Figure 7.23: Temperature dispersion for the SiPM array of quadrant L2Q2.

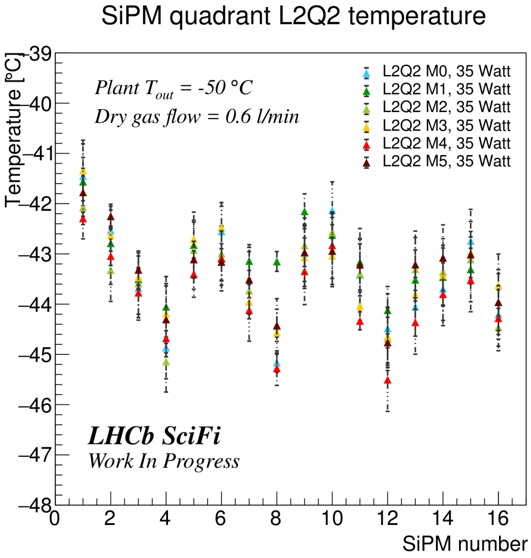

Figure 7.24: Temperature dispersion comparison for modules of quadrant L2Q2.

It was of interest whether the temperature sensors are affected rather strongly by the active heating power system. In Figure 7.25, all SiPM temperature sensors on quadrant T3L2Q2 are shown for the three different heating powers. The effect is similar to what was seen earlier by the averages of the first two modules. For all the individual sensors the response to different heating power is limited to a maximum of about 1 °C when changing from 10 to 35 Watt. Another brief comparison between the top and bottom layers of a quadrant was done to see if there are significant differences in temperature between them. The obtained result is shown in Figure 7.26, from which a clear difference in individual and overall temperature can not be noticed at first glance. Additional figures can be found in Appendix A.2.2.

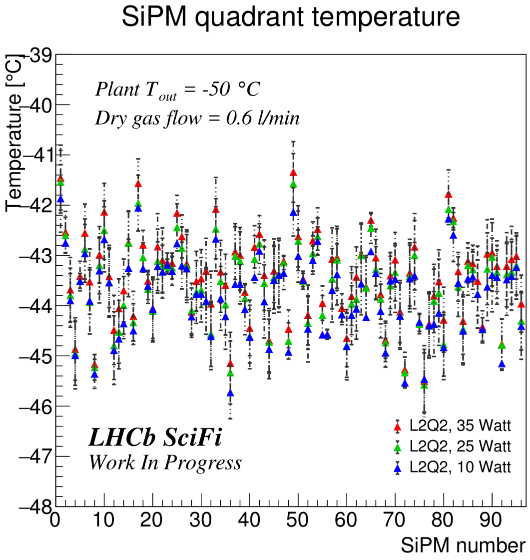

Figure 7.25: Temperature dispersion comparison of heating power for quadrant T3L2Q2.

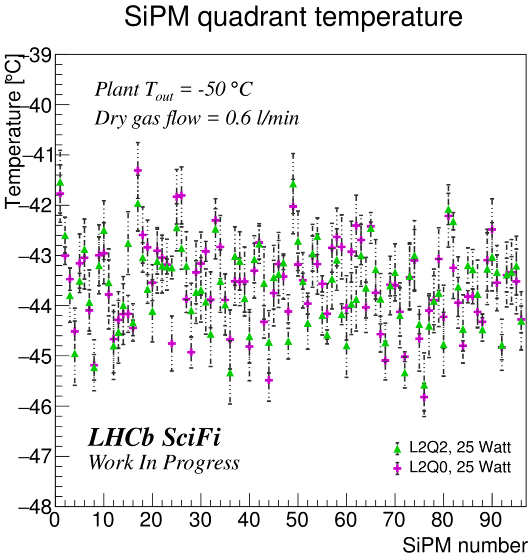

Figure 7.26: Temperature dispersion comparison of top/bottom quadrants of layer T3L2.

7.5.11 Conclusion

This section summarises the first set of performance studies that have been carried out on the first c-frame of the SciFi Tracker. This initial study serves as a stepping stone in the process of gaining understanding on the functioning of the services, which should ultimately lead to competent controls. The results can be categorized according to the presented sections.

With the dry gas flow rate one has a good handle to the control of the dew point inside cold boxes and it meets the requirement of having a 5 °C margin with respect to the cooling temperature. The combined temperature plot of the measured temperatures on the dry gas outlet connector, Novec bellow and cold box gives a good idea of the minimum temperature on the outside parts under various settings. It is shown that with applying power to the heating wires all components reaching adequate temperatures above the expected maximum dew point in the cavern. With the installation of all frond-end boxes, one should take into account that an offset should be added to this plot. This offset depends on the status of the detector, when the front-end electronics are not configured an offset of about 0-3 °C should be added and when configured 2-8 °C should be added to the given plot. A future study could enlighten the details for those effects.

The effectiveness of the cooling plant is given in terms of dissipated energy during the cooling process. The difference in output and return temperature is no more than 2 °C and the supplied heat by the heating wire is of minimal influence to this. The difference, i.e. lost heat during cooling, is proportional to the cooling temperature. Similar, the offset of the SiPM temperature to the cooling temperature has been measured. At a cooling temperature of -50 °C the SiPMs are approximately 6 °C warmer. Also this offset is proportional to the cooling temperature. Hence, with an increasing gradient of the cooling temperature to the ambient temperature the offset is enhances. Thus, this serves to get an idea of how the cooling temperature should be adjusted to reach a certain SiPM temperature.

The SiPM temperatures are found to follow a distinguished module pattern. The 16 SiPM temperature sensors contained per module end are individually constraint to fixed temperature range, this becomes clear when overlaying multiple sensors from different modules. This pattern may likely be a result of the mechanical process by which the SiPMs and their sensors have been glued onto the cooling bars. The influence of the supplied heating by the wires show a temperature difference below 1 °C between 10 and 35 Watts of heating power.

This will study will be continued upon with the coming c-frames that will be assembled.

Chapter 8

Data Taking with the ALFA Detector

The data used for the elastic physics in this thesis was collected during special physics runs in October 2018. The complete 900 GeV elastic physics program lasted from Thursday 11th till Monday 15th. The data taking period was preceded by beam based alignment, the procedure of finding the position of the roman pots relative to the beam. The physics data taking can be separated in two different settings of the optics: the first with a $\beta^* = 100$ m aimed to study elastics physics with t values that lay in the CNI region and the second with $\beta^* = 11$ m for the extension to higher t values. Prior to the second data taking with 11 m optics, again the procedure of beam based alignment was carried out. The campaign was concluded with Van der Meer scans that are used for a precise luminosity determination during the elastic physics program.

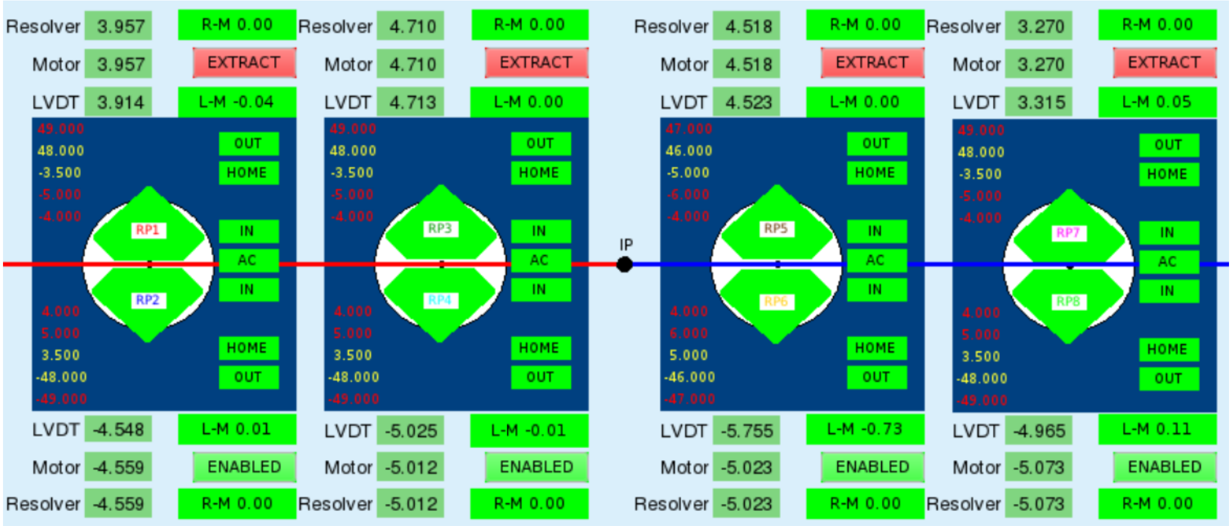
Resolver 3.957 R-M 0.00
Motor 3.957
LVDT 3.914 L-M -0.04
LVDT -4.548 L-M 0.01
Motor -4.559
Resolver -4.559 R-M 0.00

Resolver 4.710 R-M 0.00
Motor 4.710
LVDT 4.713 L-M 0.00
LVDT -5.025 L-M -0.01
Motor -5.012
Resolver -5.012 R-M 0.00

Resolver 4.518 R-M 0.00
Motor 4.518
LVDT 4.523 L-M 0.00
LVDT -5.755 L-M -0.73
Motor -5.023
Resolver -5.023 R-M 0.00

Resolver 3.270 R-M 0.00
Motor 3.270
LVDT 3.315 L-M 0.05
LVDT -4.965 L-M 0.11
Motor -5.073
Resolver -5.073 R-M 0.00

Figure 8.1: ALFA Detector Control System: monitoring of the Roman Pot Control System that shows the detectors in their data taking positions during lumiblock 64 of ATLAS run 363461.

The author has actively participated during the data taking period by means of shifts in the ATLAS control room. The ATLAS experiment also uses the WinCC OA software as their SCADA control system architecture. For data acquisition the ALFA has been brought in a combined partition with the ATLAS TDAQ software. The data acquisition during the 900 GeV campaign was centrally managed for the entire ATLAS detector by dedicated DAQ shifters. The ALFA DCS has been used to by shifters representing the ALFA community throughout the 900 GeV campaign. The DCS allows for monitoring of detector status and the Roman Pot Control System, HV powering of the MAPMTs and trigger PMTs, and powering and configuring of the Mother-Boards (MB) as well as PhotoMultiplier Front-ends (PMFs) and the Triggers. Additionally, with the Online Histogram Presenter (OHP) multiple plots can be used for online monitoring of the activity and status of various processes. Among other things, this includes synchronisation, the MAPMT activity and hit maps of the detectors. The data quality was also monitored through trigger rates and based upon the conditions it was decided when to retract the Roman Pots and scrape the beams from halo particles.

The analysis that is presented in Chapter 9 concerns elastic data taken with β^* = 100 m and hence, only relevant information for this part of the campaign will be treated in more detail. Information about all runs during this part will be presented in this work. However, since the analysis part of this thesis will be restricted to ATLAS run 363461 and presented plots originate from this run. A run is a reference to a data acquisition period within the ATLAS experiment. During the β^* = 100 part of the 900 GeV campaign, the LHC has in total been filled up 12 times resulting in 12 runs.

8.1 Beam Based Alignment

The beam is not necessarily concentrated in the middle of the beam pipe and may vary from fill to fill. Therefore, the position of each Roman Pot needs to be found using an alignment procedure. The positioning of the collimators with respect to the beam around the LHC ring are determined through a procedure called Beam Based Alignment (BBA). During BBA the collimator slightly scrapes the beam. This process has been adopted by the Roman Pots as they can approach the beam very similarly. First, the Roman Pot is put in a position close to the beam, considered as safe. This position is calculated from the nominal emittance and β-function of the beam. The Roman Pot then approaches the beam in steps of 10 μm. Once the Roman Pot starts to scrape the beam, the induced losses will be picked up by a beam loss monitor downstream of the ALFA stations which stops the movement of the Roman Pot. The alignment of the Roman Pot to the beam is then known. The beam loss monitors can react very fast upon induced beam losses and thereby induce a beam dump. During BBA the threshold of the used beam loss monitors is temporarily increased to obtain a bigger margin in order not to dump the beam during the procedure. The actual position of the Roman Pot during data taking is a bit outward from the determined position and depends on the properties of the beam. The positioning is usually 3σ, in which σ is the beam size, which was expected to be about 1.5 mm for this data set. Hence, leaving 9 mm between upper and lower Roman Pots. During BBA the LHC is filled with only a few bunches (3-15) and with a low bunch intensity of about $0.7\text{-}1.2{\cdot}10^{11}$ protons per bunch. The total intensity has to stay below $3{\cdot}10^{11}$, the limit for the LHC to run in beam setup mode [59]. This procedure is repeated for each Roman Pot individually and in total this process takes up to several hours.

8.2 Optics

The LHC beam dynamics at a center-of-mass energy of 900 GeV heavily influence the feasibility of the experiment, as discussed in Sections 3.4 and 3.5. Especially, the settings of the magnets enclosed between the IP and the ALFA stations were optimized to reach very low t values during the β^* = 100 m run. In order to achieve this the β^* was maximised to effectively obtain a large lever arm and the phase advance Φ between the interaction point and the middle in between the stations was $\pi/2$. These combined settings of the magnets are called *parallel-to-point* optics, of which the corresponding design values for the optics are listed in Table 8.1.

The design optics were calculated through simulations with MadX by a collaborator, a software package used in accelerator physics to compute beam dynamics under the influence of the magnetic fields [78]. The effective optics can be calculated by means of a data driven method in which the symmetry of elastic events is used. Preliminary studies have indicated that the effective optics might deviate strongly from the design optics. In this work only the design optics will be used for studying the physics effects, the effective optics remain to be determined.

	$\mathbf{M}_{11}$	$\mathbf{M}_{12}$	$\mathbf{M}_{21}$	$\mathbf{M}_{22}$
B7L1$_x$	-1.69355	4.71859	0.00005	-0.59062
A7L1$_x$	-1.69399	9.59626	0.00005	-0.59062
A7R1$_x$	-1.7658	9.81712	-0.00223	-0.55393
B7R1$_x$	-1.7842	5.24277	-0.00223	-0.55393
B7L1$_y$	-0.02602	165.874	-0.00559	-2.81583
A7L1$_y$	0.02012	189.128	-0.00559	-2.81583
A7R1$_y$	0.02048	186.165	-0.00569	-2.85018
B7R1$_y$	-0.02647	162.629	-0.00569	-2.85018

Table 8.1: Design values for the optics by (3.10)

The M^y_{11} values were very small to realise the *parallel-to-point* optics, leaving M^y_{12} to be decisive in reconstruction of the angle at the interaction point. The M^y_{12} were very large under these optics and enlarge the vertical coordinate of the scattered protons in the detectors. Hence, it was optimized for the acceptance of very low t values and at the same time it should provide a good resolution in this plane. In the horizontal plane these settings did not apply, which can be seen by comparing the elements M^x_{11} and M^x_{12} to the vertical plane. This lead to a poorer resolution in the horizontal angle. The size of the beam, the optics and the geometric limitations ultimately determine the acceptance window of the elastic scattered protons.

8.3 Bunch Structure

During the β^* = 100 m campaign the LHC was filled 12 times, each LHC fill resulted in an individual ATLAS run. In most runs the total beam intensity was roughly in the range of 2-4$\cdot 10^{11}$ protons throughout the entire run. In the majority of the runs the LHC is filled with 6 colliding bunches, additional non-colliding bunches were also present during some runs. Table 8.2 provided an lists the setup of the fill for each run. The non-colliding bunches can potentially be used for background studies. The beam energy together with the optics of the 900 GeV elastic physics program give rise to a relatively large transverse size of the beam at the IP. As a direct result the average pile-up μ is in the order of 10^{-3} and the probability of two or more elastic interactions taking place at a single bunch crossing is thus negligible.

Run	LHC Fill	Crossing	Unpaired B1	Unpaired B2
363452	7280	11, 520, 1019, 1541, 2067, 2555		
363460	7281	11, 520, 1019, 1541, 2067, 2555	2811	2751
363461	7282	11, 520, 1019, 1541, 2067, 2555		
363462	7283	11, 520, 1019, 1541, 2067, 2555	2811	
363469	7284	11, 1019, 1541, 2067, 2555	462	520
363489	7285	11, 520, 1019, 1541, 2067, 2555		
363495	7286	11, 520, 1019, 1541, 2067, 2555	2655, 2855, 3034	2755, 2955
363498	7287	11, 520, 1019, 1541, 2067, 2555		
363499	7288	11, 520, 1019, 1541, 2067, 2555		
363500	7289	11, 520, 1019, 1541, 2067	2655	2755
363506	7290	11, 520, 1019, 1541, 2067, 255		
363510	7291	11, 520, 1019, 1541, 2067, 2555		

Table 8.2: Bunch-Crossing IDs (BCID) and their corresponding setup during each ATLAS run.

8.4 Collimation Schemes

In preparation of the 900 GeV campaign the CWG came up with several setups determined through simulations and were tested during four test runs in 2017 and 2018. During the first of these test runs, several schemes were tested. The expected signal rate during the campaign is about 10 Hz, however the combined rate of signal and background at ALFA was found to be of the order of a few kHz at only a few minutes after scraping the beam. Offline analysis proved that under these conditions the level of background was much too high for properly distinguishing the elastic signal [79].

During the last test campaign held in October 2018, the CWG had prepared new and more advanced collimation schemes. The previous background levels observed by ALFA were now better understood and could be made visual by simulations at the time. Given the fact of improved understanding of the previous dynamics, there was confidence that newly proposed schemes could provide satisfactory conditions for physics data taking. Two of these schemes were found to dramatically improve the beam conditions by which the level of background dropped three orders of magnitude compared to the rates found in earlier test runs. Hence, under these conditions the elastic signal was sufficiently clean from background that green light was given to conduct the proposed 900 GeV elastic physics campaign later that month.

The test runs of early October 2018 had resulted in two collimation schemes, a very tight two-stage scheme and crystal assisted scheme, and were used during the $\beta^* = 100$ m program. This resulted in 9 runs with two-stage collimation setup and 3 runs with crystal-assisted collimation setup. The run numbers that end with a 0, which are run 363460, 363500 and 363510, were all with crystal-assisted collimation setup. During all other runs a two-stage collimation setup was used. The collimation settings have a strong influence on the dynamics of beam halo background and are therefore crucial to the feasibility and success of the elastic physics campaign, as was stressed before. In this section both schemes will be treated in more detail, for which particularly the warm collimation region IR7 is of importance.

8.4.1 Two-Stage Collimation

Two-stage collimation refers to the collimation setup for which two types of collimators were actively used for scraping the beam. These are the primary (TCP) and long absorbed (TCLA) collimators, the former is used for initial scraping of the beam after injection, the latter for re-scraping during throughout a run. During beam injection the Roman Pots were in the retracted 'home' position, likewise all collimators remained at their injection position.

After initial beam stabilisation was realised by the LHC operators, the initial scraping of the beam was carried out by moving the TCP.D6[L/R]7.B[1/2] collimators down to 2.5σ. A schematic depiction of the initial scraping process is shown in Figure 8.2. Following this all the collimators were simultaneously brought to their data taking positions, listed in Table 8.4. The TCP.D6[L/R]7.B[1/2] collimators were then retracted to 3.2/3.0σ. The TCLA.A6[L/R]7.B[1/2] collimators were then moved further in from 2.5σ to 2.0σ. After this, they were moved back to 2.5σ, the data taking position. Finally, the Roman Pots were moved to a 3σ position, at which the ALFA detector took elastic data.

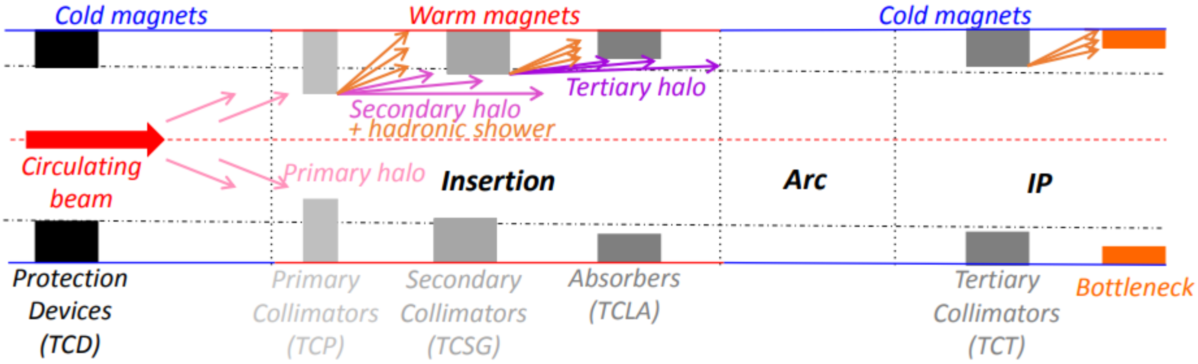

Figure 8.2: Schematic depiction of initial beam scraping after injection [39].

During the operation shifters in the ATLAS control room monitored the rates of various triggers, which will be treated next in Section 8.6. Based on the signal and background levels observed through the monitoring it was decided when the beam should be scraped to clean from halo induced background. Scraping was requested when the observed levels of signal and background roughly balanced each other. Re-scraping of the beam went as follows. First the Roman Pots were retracted to their home positions, following this the TCLA.A6[L/R]7.B[1/2] collimators were moved further in from 2.5σ to 2.0σ. The TCLA.A6[L/R]7.B[1/2] collimators were then retracted back to 2.5σ. Then another data taking period could start by moving back in the Roman Pots to the 3σ position.

8.4.2 Crystal-Assisted Collimation

During the crystal-assisted collimation setup bent crystals located at IR7 were used as primary collimators, shown by the photograph in Figure 8.4. The bent crystals are bent mechanically to create a curve at microscopic angle. Opposed to the conventional collimators, the halo particles scraped by the crystal do not scatter off at random angles but can be steered and channeled directly to absorbers, this is due to the crystalline structure. An additional consequence is that the secondary and tertiary collimators are less of need during this new collimation setup [38]. In Figure 8.3, the scraping process is schematically depicted for the crystal-assisted collimation scheme. For a more detailed discussion, we refer the reader to a presentation held by the LHC collimation working group [80].

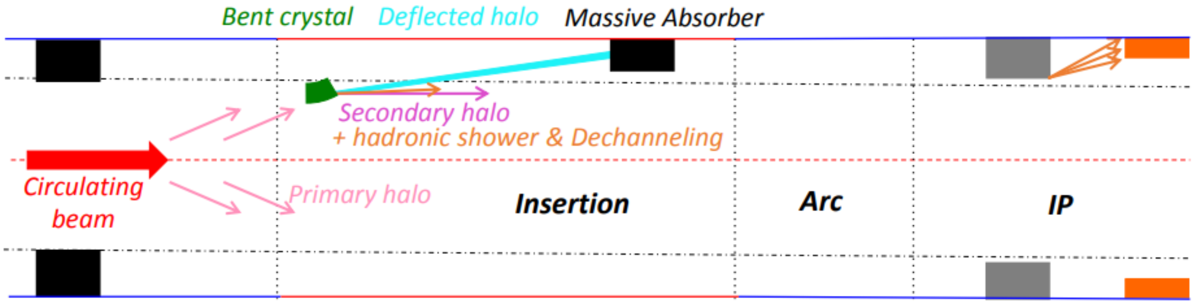

Figure 8.3: Schematic overview of beam scraping in the crystal-assisted collimation scheme [39].

The scraping procedure in the crystal-assisted scheme is identical to that of the two-stage scheme as was described previously. Difference were that after the initial scraping the TCLA.A6[R/L]7.-B[1/2] collimators were retracted further back to 2.7σ and the crystal collimators were moved in to 2.5σ. After stable conditions we reached the Roman Pots were moved to a 3σ position at which the ALFA detector took elastic data. The crystal scheme resulted in very background clean conditions such that no re-scraping of the beam was needed during these runs. Background non-related to colliding bunches can be studied and compared to the two-stage scheme by studying non-colliding bunches that were present during part of the runs, which was carried by ALFA as a matter of feedback to the LHC collimation working group [79].

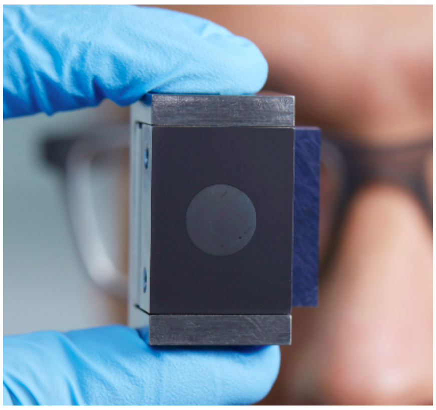

Figure 8.4: The used crystal at IR7 developed by the UA9 collaboration [81].

Collimator	IR	Plane	Two-Stage scheme	Crystal scheme
TCP.6[L/R]3.B[1/2]	3	H	5.3	5.3
All TCSGs @IR3	3	H/S	6.3	6.3
TCLA.A5[L/R]3.B[1/2]	3	V	2.7	2.7
Rest of TCLAs @IR3	3	H	9.0	9.0
TCP.D6[L/R]7.B[1/2]	7	V	3.2/3.0	3.2/3.0
TCP.C6[L/R]7.B[1/2]	7	H	4.0	4.0
TCP.B6[L/R]7.B[1/2]	7	S	5.7	5.7
All TCSGs @IR7	7	H/V/S	5.3	5.3
TCLA.A6[L/R]7.B[1/2]	7	V	2.5	2.7
TCLA.B6[L/R]7.B[1/2]	7	H	8.0	8.0
TCLA.C6[L/R]7.B[1/2]	7	V	2.7	2.7
TCLA.D6[L/R]7.B[1/2]	7	H	10.0	10.0
TCLA.A7[L/R]7.B[1/2]	7	H	8.0	8.0
TCTPH.4[L/R]1.B[1/2]	1	H	13.0	13.0
TCTPH.4[L/R]1.B[1/2]	1	V	2.7	2.7/13.0
TCTPH.4[L/R]2.B[1/2]	2	H	13.0	13.0
TCTPH.4[L/R]2.B[1/2]	2	V	2.7	13.0
TCTPH.4[L/R]5.B[1/2]	5	H	13.0	13.0
TCTPH.4[L/R]5.B[1/2]	5	V	2.7	13.0/2.7
TCTPH.4[L/R]8.B[1/2]	8	H	13.0	13.0
TCTPH.4[L/R]8.B[1/2]	8	V	2.7	13.0
Crystal	7	V	n/a	2.5
Roman Pots	1/5	V	3.0	3.0

Table 8.3: Data taking positions of the collimators in terms of beam width σ for two-stage collimation and crystal-assisted collimation. The table only lists a subset of the collimators that were inserted during the runs, collimators related to injection and beam dump protection are left out. The most relevant elements are highlighted in boldface font, table is adapted from [79].

8.5 Track Reconstruction

A proton traversing the detector will causes several scintillating fibres in the consecutive layers to light up and leave several signals along its trajectory. The signals are combined to reconstruct the position in a certain plane. Using the overlap of the fibres one can reconstruct the track and find the position. The positions of the U- and V-plane are combined and translated into an (x,y) coordinate in the detector coordinate system. These coordinates are given with respect to the precision hole drilled in the titanium plates, depicted in Figure 5.8. In the detector coordinate system the MD edge is located at $y \simeq -135$ mm. In Figure 8.5, part of the U-plane is shown where a proton left a track. The overlap between the 10 layers is shown on the right-hand side. The width of the overlap is a measure of the resolution, which benefits from the increasing number of layers that have fired as well as the staggering between these layers.

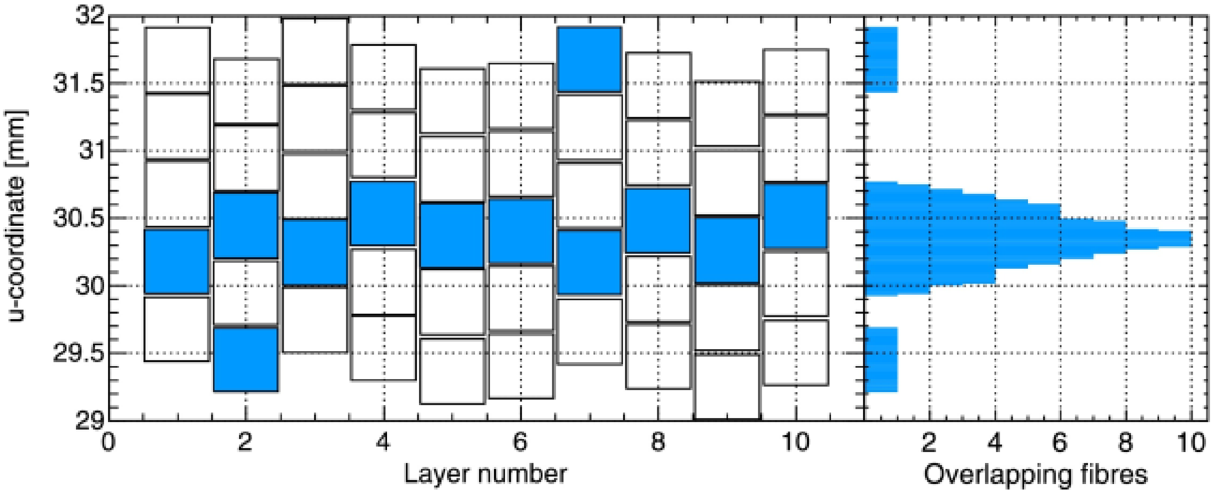

Figure 8.5: Illustration of the track reconstruction principle [19].

8.6 Trigger

8.6.1 Trigger Items

The ALFA trigger menu consists of a list of various logical combinations of ALFA detectors called trigger items. The relevant trigger items for the analysis are listed in Table 8.4. In addition to the trigger logic, each trigger item is paired to two bunch group triggers: BGRP0 and BGRP1. The BGRP0 trigger is used for all possible BCIDs that may be filled, thus excluding the BCIDs of the abort gap. The BGRP1 trigger is used for all paired BCIDs, meaning colliding bunches. The following items of the trigger menu used during the elastic physics program are of interest for the ALFA analysis. The L1_ALFA_ANY is the least tight trigger item, requiring only a single MD trigger release. The L1_ALFA_BGT10 can be randomly triggered on every bunch crossing and is prescaled with a factor 20. For the elastic events the two most important triggers are L1_ALFA_ELAST15 and L1_ALFA_ELAST18, used for elastic events in arm1 and arm2, respectively. They are least strict as they require a coincidence of one detector on the A- and one detector on the C-side of the IP, within a given arm configuration. The L1_ALFA_SYST17 and L1_ALFA_SYST18 triggers are important for background understanding in the upper and lower detectors, respectively. They are triggered on coincidences of only upper or lower detectors, again least strict requiring only one detector on the A- and one detector on the C-side of the IP.

Trigger item	**Trigger logic**	**Prescale**
L1_ALFA_ANY	B7L1U || B7L1L || A7L1U || A7L1L || A7R1U || A7R1L || B7R1U || B7R1L	1
L1_ALFA_ELAST15	(B7L1U || A7L1U) && (A7R1L || B7R1L)	1
L1_ALFA_ELAST18	(B7L1L || A7L1L) && (A7R1U || B7R1U)	1
L1_ALFA_SYST17	(B7L1U || A7L1U) && (A7R1U || B7R1U)	1
L1_ALFA_SYST18	(B7L1L || A7L1L) && (A7R1L || B7R1L)	1

Table 8.4: An overview of the trigger items, their logic and prescales during run 363461 that are used in the analysis. All triggers are paired with coincidence of triggers BGRP0 and BGRP1.

8.6.2 Trigger Conditions

The data collected for the analysis corresponds to LHC fill 7282 on October 12th 2019. During this fill the ATLAS DAQ stored the data in run 363461, which lasted from 04:28 till 08:36. During this period, a variety of event rate types were online monitored, for which histograms were used in which either events were updated per second or per lumiblock (LB), a period of approximately 60 seconds of data taking. These histograms were constantly updated during the run. Throughout the 900 GeV physics campaign they have been closely followed by the ALFA shifters who were present in the ATLAS control room.

In particular, the trigger rates of ELAST15, ELAST18, SYST17 and SYST18 were followed closely with interest. The ELAST are the loosest signal triggers, whereas the SYST are the loosest background triggers, discussed above. With these four triggers, one can have a rough estimate of the data taking conditions throughout a run, as they give an idea of the levels of signal and background. The signal rate should preferably be higher than the background rate. In case the trigger rate of the background approaches the level of the signal rate it becomes increasingly hard to distinguish the actual signal. The background level is mainly due to beam halo which grows during a run, with an increase in halo background the likelihood of fake elastic signals becomes larger. Therefore, the amount of background in the elastic sample enhances as the beam halo grows. For this reason, the beam had to be scraped from halo by collimators if the observed background level became to high.

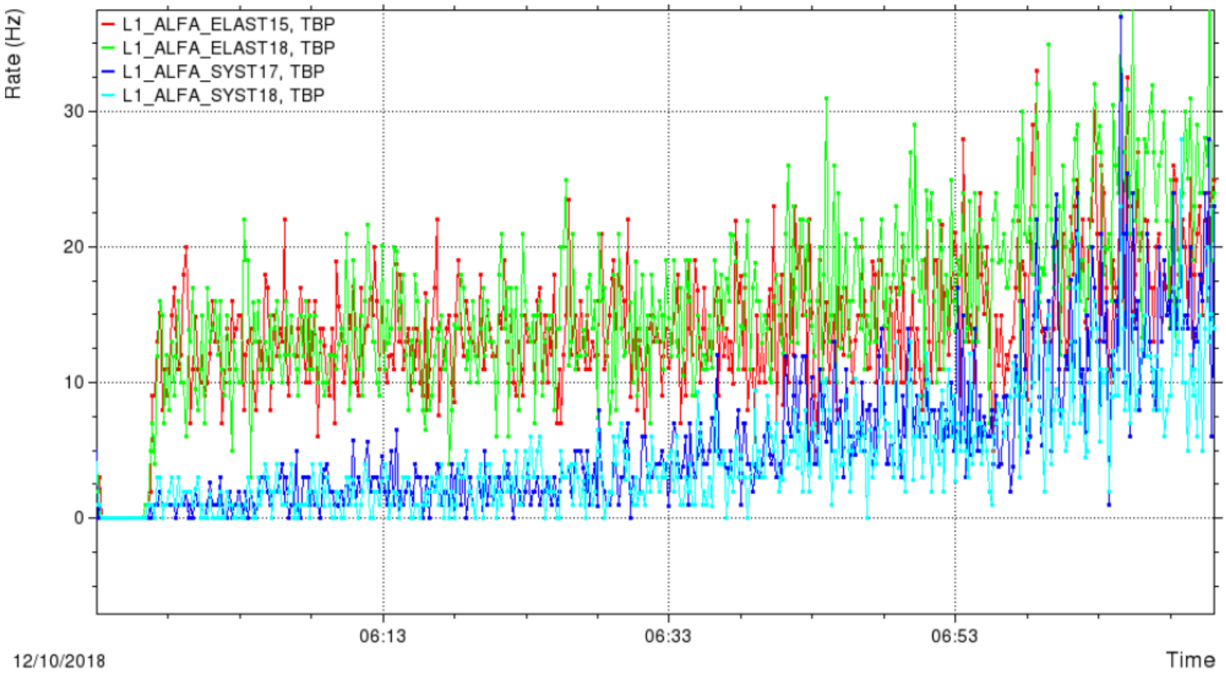

Figure 8.6: Trigger rates during the second data taking period of run 363461, showing the observed levels in the time window corresponding to LB 95-168, just prior to another scraping block.

The elastic trigger rates were typically between 10-20 Hz throughout the run. At the start of run 363461, the signal rate was higher than at the end of the run, were at the beginning of the third data taking period the observed rate was below 10 Hz. Throughout a run the expected signal has to decrease due to a decrease in bunch population. Naturally, protons are consumed by elastic interactions, but also they are lost due other processes during their circulation in the LHC, which in turn may feed the beam halo. Additionally, scraping does not only clean the beam from halo background, but also partly affects the beam itself, resulting in a reduction of bunch population and thus lowering the elastic event rate.

Previously discussed in Section 8.4, the Collimation Working Group had came up with two promising collimation schemes that could sustain promising data taking conditions. For both collimation schemes, the resultant background rate directly upon scraping was between zero and a few Hz. Over time the rates increased until the point was reached that the level of background was considered to have sufficiently closed in on the signal level that it was decided to re-scrape the beam. The request of scraping then conveyed to CERN Control Centre, where the positioning of the Roman Pots as well as the collimators were controlled. The Roman Pots were retracted prior to scraping and inserted after scraping was carried out to not expose the detectors to high shower rates induced by the scraping process. An example of a data taking period with the growth of the relevant trigger rates after scraping shown in Figure 8.6, which is just prior to another scraping period to prepare for a third data taking period. A data taking period is a period between scrapings during which the ALFA detector were inserted and took data. Based on the data taking conditions, out of all data a selection of lumiblocks (LBs) is formed to be used for offline analysis. This is the good lumiblock list and is shown in Table 8.5 for each run. This preliminary list is made by one of the ALFA collaborators and is only based on the raw trigger rates found in each LB during data taking periods. During further selection LBs can be rejected if the trigger deadtime of the ELAST triggers are above 5% and if their duration is below 55 seconds, indicating a deviance from nominal beam parameters. Additional, a comment has to be made on the four runs in which ALFA detector number 6 was not giving data. The amount of

Run	**Selected LBs**	**L [μb^{-1}]**	**Comment**
363452	177-241, 249-308	64	
363460	90-202	80.4	
363461	63-88, 95-168, 178-240	90.2	
363462	53-81, 90-145	32.7	ALFA 6 bad LB 64-End
363469	60-70, 76-118, 126-177, 184-225, 249-275	79.8	ALFA 6 bad LB 1-118, 218-End
363489	76-103, 111-135, 151-236	79	ALFA 6 bad all LBs
363495	62-91, 102-162, 169-229, 237-281	111	ALFA 6 bad LB 1-191
363498	59-84, 93-166, 174-218	105.1	
363499	55-72, 77-137, 145-190	80.6	
363500	26-224	99.4	
363506	50-72, 82-142, 160-196	88.9	
363510	46-210	119.9	

Table 8.5: Preliminary luminosity of the corresponding good LB selection that has been determined offline by looking at trigger rates in each LB, four runs were affected by a disconnected ALFA 6 detector resulting in a drastically reduced number of collected events in arm 1.

events collected by elastic arm 1 is strongly affected during the down time of the detector. The motherboard of detector 6 became irresponsive during run 363462 and could not be recovered for some time. It was attempted several times to recover it by power cycling and came partly back alive during 363469, but was lost 100 LBs later again. This lasted until another power cycling attempt in run 363495 finally was successful: MB6 was recovered and remained up during the rest of the campaign.

8.7 Luminosity

For the special physics runs the luminosity is usually determined by LUCID, BCM or vertex counting. Based on the given good lumiblock list an integrated luminosity for each run can be calculated, listed in Table 8.5. These are preliminary values calculated by the ATLAS luminosity calculator iLumiCalc, for which the run list with good lumiblocks is used as an input. The integrated luminosity during run 363461 is 90.2 $\mu\mathrm{b}^{-1}$. This concerns a preliminary value as the luminosity measurements will still have to be calibrated by an absolute measurement of the luminosity by the Van der Meer scans. The uncertainty of the presented values should therefore be considered large at this stage. The integrated luminosity per run is calculated without taking into considering that detector number 6 has been irresponsive during part of the runs. Therefore, the presented values are the delivered luminosity during the selected LBs, but a correction due to the downtime of detector number 6 will be needed.

8.8 Emittance

The emittance has to be kept as small as possible during the special physics runs. The emittance is measured constantly by the BSRTs throughout the entire run. Additionally, the emittance is measurement by the wirescan at least a single time every run. The wirescan provides a calibration to the BSRTs, as previously explained in Section 3.7. These measurements on the machine side are available through an application called timber, which stores information per LHC fill. The emittance typically grows throughout the run under the influence of various interactions of the particles inside the bunches. The measured emittance during LHC fill 7282, corresponding to run 363461, is used as in input to the Monte Carlo simulation of the elastic signal and will be discussed in Section 9.4.2.

8.9 Beam Spot

During two runs the Inner Detector (ID) was partly taking data, these are runs 363461 and 363500, one ID run per collimation scheme. The ID measures the luminous region by reconstructing vertices from which the position and spread of the interaction point can be determined. The beam spot width and possibly also the position of the beam underwent changes throughout a run. Similar as for the emittance, this is caused by the various interactions that particles inside the bunches may undergo. The information on the beam spot width is used as input for the Monte Carlo simulation of the elastic signal. The measured beam spot by the ID will be discussed in Section 9.4.2.

8.10 Van der Meer scans

The 900 GeV special physics campaign was concluded with Van der Meer scans. The measurement of absolute luminosity by means of beam displacement was introduced by Simon van der Meer at the time of the Intersecting Storage Rings [82]. During a Van der Meer scan, the beams start non colliding and are then simultaneously moved in steps in opposite direction. During the crossing of the beams the interaction rate per step starts to increase and reaches a maximum when the two beams show maximum overlap. From the observed rates during this scanning of the beams one can determine the sizes of the beams.

Using (3.3), one can determine the instantaneous luminosity if one has knowledge of the revolution frequency of the beam, the number of bunches, and the beam size, which is being measured during Van der Meer scans. There are several detectors capable of measuring the instantaneous luminosity over time. These are needed for the normalization factor of measurements of the total cross section. The normalization factor is expressed in terms of proportionality of the total delivered interactions over time, the integrated luminosity. For precise determination of the integrated luminosity, several detectors rely on a calibration by an independent measurement, the absolute luminosity.

In principle when the ALFA detectors are sensitive deep into the Coulombic region, one can directly the determine the absolute luminosity scale, previously explained in Section 2.3.2. This measurement is for which the ALFA detector was originally intended and the acronym originates from. In practise, the sensitivity of the ALFA detectors to this region of elastic physics still has to be proven. Hence, also the measurements of cross sections by ALFA rely on integrated luminosity measured elsewhere, which in turn rely on an absolute calibration of the luminosity by Van der Meers scans. These scans are highly important for a measurement of the total pp cross section, since its systematic uncertainty is often dominated by the knowledge of the absolute scale of the luminosity [83].

Having another look at (3.3), with the revolution frequency, the number of particles circulating the LHC and the transverse beam sizes determined by Van der Meer scans, one has an absolute measurement of the luminosity at a certain time to which other luminosity detectors, for example LUCID or BCM, can be calibrated. Since the Van der Meer scans are only done at a particular time, the calibration must be assumed to be constant for longer periods of time and under various machine conditions [83]. For this a good cross check is provided by the various luminosity measurements through different methods.

Part IV

Data Analysis

Chapter 9

Study of Forward Elastic *pp* Scattering

The final chapter describes the initial work on the analysis of elastic scattered protons with data collected during ATLAS run 363462. The work focuses on data taken with β^* = 100 m optics at a center-of-mass energy of 900 GeV and that is intended to probe the CNI region of the elastic differential cross section. An approximate integrated luminosity of 90^{-1} μb of elastic pp collisions was collected during the data taking campaign, presented in the previous chapter. An elastic collision is an event with two protons of opposite momentum as outcome and without energy transfer to the surroundings. The experiment measures the cross section by counting elastic events as a function of Mandelstam variable t, the four-momentum transfer. The number of events have to undergo a translation into the cross section before physics parameters can be extracted by a performing a fit on the measured elastic differential cross section. This translation incorporates the various experimental effects that have to be accounted for in the experiment :

$$\sigma = \frac{N_c - B}{\epsilon \cdot A \cdot L}, \tag{9.1}$$

in here N_c is the number of candidate events, B the approximated number of background events, ϵ the detector's efficiency, A the detector's acceptance and L the integrated luminosity. The above equation forms the basis of the analysis and of all of these variables will have to be incorporated in the final analysis. Some of the experimental effects have been determined and form the subject of this chapter. The work includes the event selection, reconstruction methods of four-momentum transfer t, background estimation, detector layer efficiency, acceptance of the detector and a the simulation of the elastic signal. Other experimental effects such as the alignment of the detector, evolution of the beams and the detector's resolution will also be discussed. Due to the premature state of the analysis, the presented work is far for complete and a lot of work lies ahead to come to a proper determination of the physics parameters.

The analysis is not a straight set of consecutive steps to be followed in order to get to the final extraction of a result, but forms a rather complex scheme of inter-dependencies between various experimental effects. The used framework heavily relies on an original code used during a previous analysis in [4]. The analysis framework has undergone its first evolution to customize it for the use of the elastic physics campaign at a center-of-mass energy of 900 GeV. The experience from the past is currently used for the development of a more user friendly analysis code. The presented material in this chapter all uniquely belongs to the 900 GeV, 100 m data, but also considerably benefits from obtained knowledge during the previous analyses [4] and [20]. These documents have served as a guideline for the presented work.

9.1 Event Selection

The collected events have all been online selected through the loosest elastic trigger items: ELAST15 and ELAST18 for events occurring in arms 1 and 2, respectively. The offline selection criteria further sort out the events based on track and trigger requirements but also on geometrical and correlation cuts. This section explains the offline selection criteria that are currently used to select elastic candidates in this analysis.

9.1.1 Track and Trigger Requirements

Events are required to have only a single reconstructed track in all four MDs that constitute an arm. Layers do not have a 100% efficiency and directly neighbouring fibres may give a signal, both will affect the width of overlap and thus the resolution. This can be understood from Figure 8.5 that illustrates the reconstruction principle. For this reason as set of criteria are used in the ALFA analysis :

- A track should have a minimum of 5 overlapping layers per plane
- A least 3 of the overlapping layers should have a maximum of 3 fibre hits, referred to as "good layers".
- An event is rejected if it contains an additional 5 overlapping fibres that are not reconstructed into a track, because of failure of the reconstruction algorithm.

The above criteria have to be changed form run to run, depending on the quality of the data. The track reconstruction efficiency and detector resolution are also re-evaluated with each run. The first requirement removes tracks that are due to detector noise, the second requirement reduces the amount of tracks related to cross-talk or shower events. A third requirement is the rejection of events which have in addition to the reconstructed track another 5 additional overlapping layers. This might have indicated that there was another track present for which the reconstruction algorithm has failed to reconstruct it. An example of such an event is depicted in Figure 9.1. From the event display it seems that the A-side of the detector has been simultaneously hit by two particles. In the U-plane the reconstruction algorithm has successfully reconstructed the two tracks, one in blue and the other in green. In the V-plane the reconstruction algorithm has failed to find the second track, although the red fibres indicate its presence. The rejection of such an event as background while it likely contains an elastic event would make the reconstruction efficiency appear better than it actually is [20].

In this stage of the analysis events with multiple tracks are left out. In the case where two protons leave tracks in the U- and V-layer, it is difficult to determine which U-track belongs to which V-track. All four possible track coordinates are then stored and should in principally considered in the analysis.

9.1.2 Geometrical Selection Cuts

Two geometrical selection cuts are applied to the collected events to assure proper data quality. These are the edge and beam screen cut, and are illustrated in Figure 9.2. The geometrical selection cuts are applied in the detector coordinate system and are thus independent of the alignment of the detector with respect to the beam.

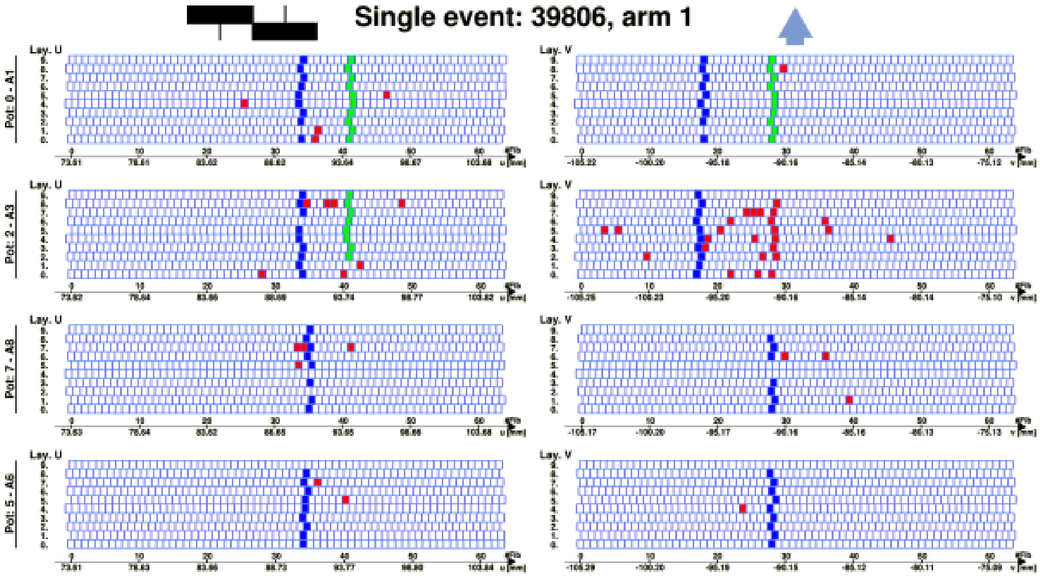

Figure 9.1: Display of an selected arm 1 event that is part of the $\sqrt{s}$ = 8 TeV, β^* = 1 km analysis [4]. The U-plane with all fibres of the MD layers are shown on the left-hand side, all fibres of the V-plane are shown on the right-hand side. The fibres that are filled indicate that they have fired in the event: the blue fibres have been reconstructed into a track, the green fibres have reconstructed into another track and the red fibres have not been related to a track, from [20].

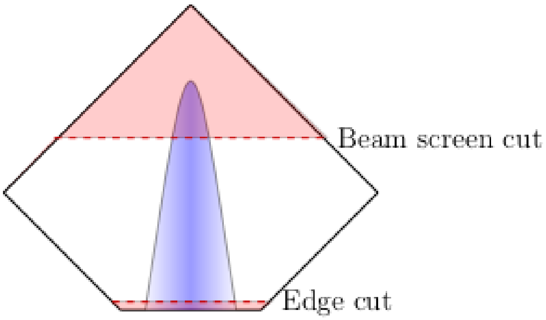

Figure 9.2: A schematic illustration of the hit pattern (blue band) of the ALFA MD during elastic physics runs. The drawn red dashed lines indicate the beam screen cut and the edge cut. The blue band represents the region where elastic scattered protons likely hit the detector, the purple region indicates the events that are rejected by the selection cuts. The edge cut in the illustration is exaggerated for visualisation purposes [20].

Edge Cut

An edge cut has been introduced to ensure the tracking region overlaps with the MD trigger tiles. At the same time this region is most sensitive to the smallest scattering angles and thus t values. Therefore, the edge cut removes part of the events that provide the experiment with the largest sensitivity to L and the ρ parameter. Nevertheless, making this cut is important since it would otherwise lead to trigger efficiency that is position dependent leading to complications during the analysis. The cut also assures that the protons have traversed active material in all

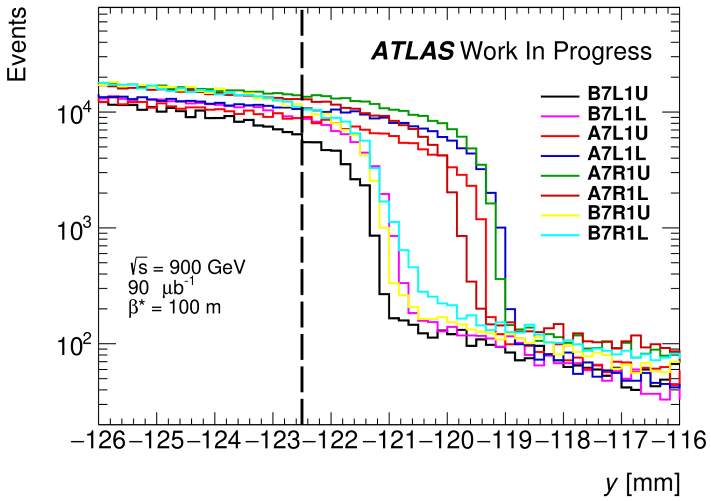

Figure 9.3: Area in the detector coordinate system that shows the significant drop in the y-distributions of collected events due to the presence of the LHC beam screen. A clear difference of 2 mm in the location of the beam screen effect can be observed between the inner and outer detectors. The applied beam screen cut at a value of -122.5 mm is indicated by the dashed black vertical line.

MD layers. Given the amount of background, this cut may have to be optimized for a given data set. Due to the novel collimation schemes the collected events contain a low level of background, hence the least possible edge cut of 90 μm can be applied.

Beam Screen Cut

The location inside the beam pipe naturally puts an upper limit to the detectors acceptance of events. Moreover, elastic particles that leave the IP under an angle will at some point hit the LHC beam screen and undergo multiple scattering and showering. This reduces the quality of the data and therefore the beam screen cut is introduced to remove these effects. The beam screen cut rejects events that are beyond a certain y value. The value is chosen 1 mm before the drop in events due to beam screen becomes apparent. This is illustrated in Figure 9.3 and shows the distributions of all reconstructed tracks that satisfy the first two track requirements for the individual detectors. The drop appears earlier for the outer detectors, since these detector were not as inserted into the beam pipe as the inner detectors. This difference between the inner and outer detectors is about 2 mm. A uniform beam screen cut at a value of -122.5 mm is applied in the event selection. This has been determined by taking 1 mm before the first drop in a detector is visible, in this case case that is B7L1U. Due to the significant differences between the detectors, this ideally should be modified to individual values set for each detector.

9.1.3 Correlation Cuts

The selection of elastic candidates is concluded by a series of correlation cuts on the coordinates of the reconstructed tracks in the four detectors of an arm. The cuts utilize the constraints on the coordinates put by the momentum conservation of elastic events. The cuts are determined by simulation of the elastic signal. From the simulation of the elastic signal it becomes evident that traditional selection cut do longer suffice. The main reason is the presence of an ellipse that is orientated off-axis of the main correlation of the x correlation plots. The elastic signal is simulated using (2.17) with σ_{tot} = 68.0 mb, B = 17.0 GeV^2 and ρ = 0.12. The simulation further requires the following experimental inputs: detector resolution, beam properties, optics and also the alignment of the detector. These inputs are subject of Section 9.4. The following correlations are traditionally used for selection of elastic events:

$$
\begin{gathered}
y^{\text{A}}_{\text{inner}} - y^{\text{C}}_{\text{inner}},\\
y^{\text{A}}_{\text{outer}} - y^{\text{C}}_{\text{outer}},\\
x^{\text{A}}_{\text{inner}} - x^{\text{C}}_{\text{inner}},\\
x^{\text{A}}_{\text{outer}} - x^{\text{C}}_{\text{outer}},\\
x^{\text{A}}_{\text{inner}} - \theta^{\text{A}}_{x},\\
x^{\text{C}}_{\text{inner}} - \theta^{\text{C}}_{x}.
\end{gathered}
$$

The simulation of the elastic signal will be discussed in more detail in Section 9.6. Examples of the elastic signal simulation are depicted in Figures 9.4a and 9.4b. In Figure 9.4a, the local angle, θ_x, is plotted against the x-coordinate of the inner detector. The local angle is measured by dividing the difference in x-coordinates in the inner and outer detector by the 8 meter distance. In Figure 9.4b a correlation plot of the inner detectors in arm 1 is shown. The elastic signal manifests on the diagonal when the y-coordinates are depicted on a 2-dimensional plot. The traditional selection contours are left out. These will have to adjusted to properly incorporate the ellipse at the origin of the x correlation plots. Once these selection are determined by simulation of the elastic signal, they can be used for rejection of background in the candidate example.

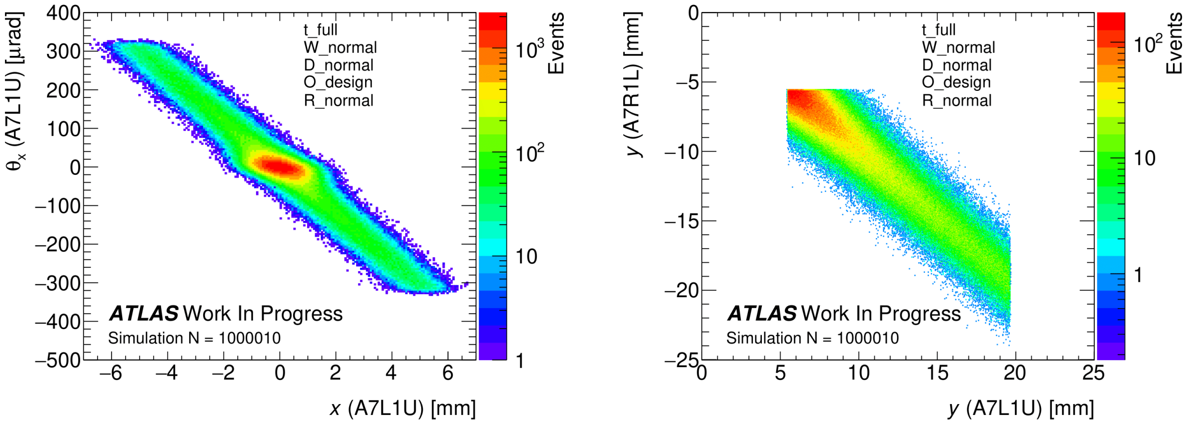

(a) The x_{Inner}-θ_x correlation.

(b) The $y^{\text{A}}_{\text{inner}} - y^{\text{C}}_{\text{inner}}$ correlation.

Figure 9.4: Elastic simulation showing two correlation cuts used for event selection.

9.2 Reconstruction of t

The measured positions and local angle at the ALFA stations can be used to reconstruct the momentum transfer of the candidate event. For this purpose Hill's equation, introduced in Section 3.4, is used to formulate the following relations :

$$u^{\mathrm{A}}_{237} = M^{\mathrm{A}}_{11,237}u^* + M^{\mathrm{A}}_{12,237}(\theta^*_u + D^{\mathrm{A}}_u), \tag{9.2}$$

$$u^{\mathrm{A}}_{245} = M^{\mathrm{A}}_{11,245}u^* + M^{\mathrm{A}}_{12,245}(\theta^*_u + D^{\mathrm{A}}_u), \tag{9.3}$$

$$u^{\mathrm{C}}_{237} = M^{\mathrm{C}}_{11,237}u^* - M^{\mathrm{C}}_{12,237}(\theta^*_u - D^{\mathrm{C}}_u), \tag{9.4}$$

$$u^{\mathrm{C}}_{245} = M^{\mathrm{C}}_{11,245}u^* - M^{\mathrm{C}}_{12,245}(\theta^*_u - D^{\mathrm{C}}_u), \tag{9.5}$$

$$\theta_{\mathrm{A}} = M^{\mathrm{A}}_{21}u^* + M^{\mathrm{A}}_{22}(\theta^*_u + D^{\mathrm{A}}_u), \tag{9.6}$$

$$\theta_{\mathrm{C}} = M^{\mathrm{C}}_{21}u^* - M^{\mathrm{C}}_{22}(\theta^*_u - D^{\mathrm{C}}_u). \tag{9.7}$$

These set of 6 linear equations can be used to solve for the 2 unknowns: the scattering angle and the position of the interaction point. Since there are more equations than unknowns, one can compose various pairs of equations to determine the scattering angle. The divergence is unavoidably present and will limit the reconstruction of the scattering angle. The scattering angles in both transverse planes are used for the reconstruction of t of the elastic interaction. The total momentum transfer t is given by the sum of the momentum transfer in the x- and y-plane :

$$t = t_x + t_y = -(p\theta^*_x)^2 - (p\theta^*_x)^2. \tag{9.8}$$

Three of the reconstruction methods are discussed in the following sections, for which the divergence term is left out of simplicity.

9.2.1 Subtraction

The subtraction method combines the positions measured on the A-side with the one on the C-side. The two pairs are constructed by the combinations of either the inner or outer detectors. The inner pair is formed by (9.2) and (9.4), whilst the outer pair is formed by (9.4) and (9.5). These can be used to solve for the angle θ^*, in which the coordinate from the C-side is subtracted from the A-side:

$$\theta^*_u = \frac{\frac{M^{\mathrm{C}}_{11}}{M^{\mathrm{A}}_{11}}u^{\mathrm{A}} - u^C}{\frac{M^{\mathrm{C}}_{11}}{M^{\mathrm{A}}_{11}}M^{\mathrm{A}}_{12} + M^{\mathrm{C}}_{12}} \approx \frac{u^{\mathrm{A}} - u^C}{M^{\mathrm{A}}_{12} + M^{\mathrm{C}}_{12}}, \tag{9.9}$$

in here the subscripts indicating the inner or outer detector have been omitted. This is similar to (3.11) in Section 3.4, except in this equation the matrix elements M^{A}_{12} and M^{A}_{12} are not taken identical, whereas the matrix elements M^{A}_{11} and M^{A}_{11} are. The validity of this simplification step for the y-plane is supported by the values shown in Table 8.1. However, a note has to be placed on the approximation in the x-plane, since the validity does not hold. In previous elastic campaigns the values of the matrix elements in the x-plane allowed for this simplification. The 900 GeV optics do not allow for this and hence the full formula will be used in the reconstruction. With the reconstructed scattering angles of the inner and outer manner, one can take the simple mean to get the angle of this method :

$$\theta^*_u = \frac{\theta^*_{u,237} + \theta^*_{u,245}}{2}. \tag{9.10}$$

For this to be valid, the matrix elements M_{12} should be of similar size, since the resolution of the reconstruction method is determined by their size. Hence, if they differ substantially in size a simple mean would penalize the better resolution combination. In the y-plane the elements are very large and relatively similar, whereas in the x-plane they differ by a factor 2. A weighted average could suppress the less precise resolution from the outer planes, another option would be to omit the outer detectors.

9.2.2 Local Subtraction

The local subtraction method combines the positions measured within an armlet, thus from one side of the interaction point. For this either (9.2) and (9.3) or (9.4) and (9.5) are used to reconstruct the scattering angle :

$$\theta_u^* = \frac{M_{11,245}u_{237} - M_{11,237}u_{245}}{M_{11,245}M_{12,237} - M_{11,237}M_{12,245}}. \tag{9.11}$$

This equation holds for both detector sides and since the matrix elements are similar for the A- and C-side the angle of both side could be averaged to determine the scattering angle. Since one measures the scattering angle for each of the elastic scattered protons individually, one can calculate the difference between $\theta_u^{*\mathrm{A}}$ and $\theta_u^{*\mathrm{C}}$ to measure the convoluted divergence of the beam :

$$D_{\mathrm{con}} = \sqrt{\frac{\epsilon_u^{\mathrm{Beam1}} + \epsilon_u^{\mathrm{Beam2}}}{\gamma\beta^*}}. \tag{9.12}$$

The convoluted divergence by ALFA can be compared to the measured divergence by the LHC.

9.2.3 Local Angle

The local angle method combines the measured local angle at the ALFA stations on each side to reconstruct the scattering angle. The local scattering angles θ_{A} and θ_{C} are calculated by subtracting the measured positions in the inner and outer station and dividing this by their distance d :

$$\theta = \frac{u_{245} - u_{237}}{d}. \tag{9.13}$$

The angle of the outgoing proton does not change between the inner and outer station since there are no magnets present between quadrupoles Q6 and Q7, where the ALFA detectors are located. Combining (9.6) and (9.7), one can derive the following expression for the reconstruction of the scattering angle :

$$\theta_u^* = \frac{\theta_{\mathrm{A}} - \frac{M_{21}^{\mathrm{A}}}{M_{21}^{\mathrm{C}}}\theta_{\mathrm{C}}}{M_{22}^{\mathrm{A}} + M_{22}^{\mathrm{C}}\frac{M_{21}^{\mathrm{A}}}{M_{21}^{\mathrm{C}}}} \approx \frac{\theta_{\mathrm{A}} - \theta_{\mathrm{C}}}{M_{22}^{\mathrm{A}} + M_{22}^{\mathrm{C}}}. \tag{9.14}$$

9.3 Background Estimation

The elastic candidate sample mainly contains three sources of background: halo particles, single diffractive events (SD) and the double pomeron exchange (DPE). The DPE process leaves two protons in the interaction intact, while in single diffractive events one proton breaks apart and only one proton remains intact. The DPE can give rise to a coincidence on both detector sides, the single diffractive events only hit one detector side is hit and should thus be coincident with an unrelated event at the opposite side. These events usually do not appear as of elastic origin, but incidentally may mimic an elastic event. Such incidents fulfill all the elastic selection criteria and are impossible to distinguish from true elastic events. Consequently, they are inevitably present in the candidate sample. The exact level of background has to be quantified to achieve a correct determination of the physics parameters.

9.3.1 Random Uncorrelated Coincidence Background

Background events due to halo and SD events emerge from halo/halo, halo/SD and SD/SD coincidences on either detector side. Simulation only exist for the SD processes, and due to the low pile up during the elastic physics program the SD/SD contribution can be neglected. The background arising from halo events can only be studied by considering non-colliding bunches that were present in some runs. The level of halo background may be estimated this way, provided that they appear under similar conditions as the colliding bunches to have a valid comparison. Therefore, to cover the background contributions due to halo and SD processes they have been combined into a single background term coined random uncorrelated coincidence (RUC). Since no simulation is available, a data driven method is used to construct the RUC events. These events have to satisfy the following conditions :

- A trigger signal from one of the MDs in an armlet.
- The detectors should have a single reconstructed track.
- The event has to pass the edge and beam screen cut.
- The event is rejected if there is a trigger signal in the diagonal armlet that would constitute an elastic arm.

The events that pass these criteria are combined with events of the diagonal armlet to construct the RUC events. These events are then subjected to the elastic selection criteria. The complete set of RUC events obtained via this procedure are shown in Figure 9.5. The figure contains x_{Inner}-θ_x and $y^{\mathrm{A}}_{\mathrm{Inner}}$-$y^{\mathrm{C}}_{\mathrm{Inner}}$ correlations are shown in Figures 9.5a and 9.5b, respectively. The distribution of the x_{Inner}-θ_x correlation shows a horizontal band that is likely due to beam halo, this was also seen in the two mentioned analysis at 8 and 13 TeV. Beam halo usually does not hit the ALFA station under an angle which is supported by this correlation plot. The black ellipse indicates the traditional selection region of elastic candidates and is rather effective against a substantial amount of background. However, part of the horizontal band remains present in the elastic selection region at small x values, i.e. the region of smallest t values contains relatively the most background events. The rest of the elastic selection region contains approximately 2 orders of magnitude events less on average. The distribution of the $y^{\mathrm{A}}_{\mathrm{Inner}}$-$y^{\mathrm{C}}_{\mathrm{Inner}}$ correlation shows that the selection region is less effective in mitigation of background than the x_{Inner}-θ_x selection region.

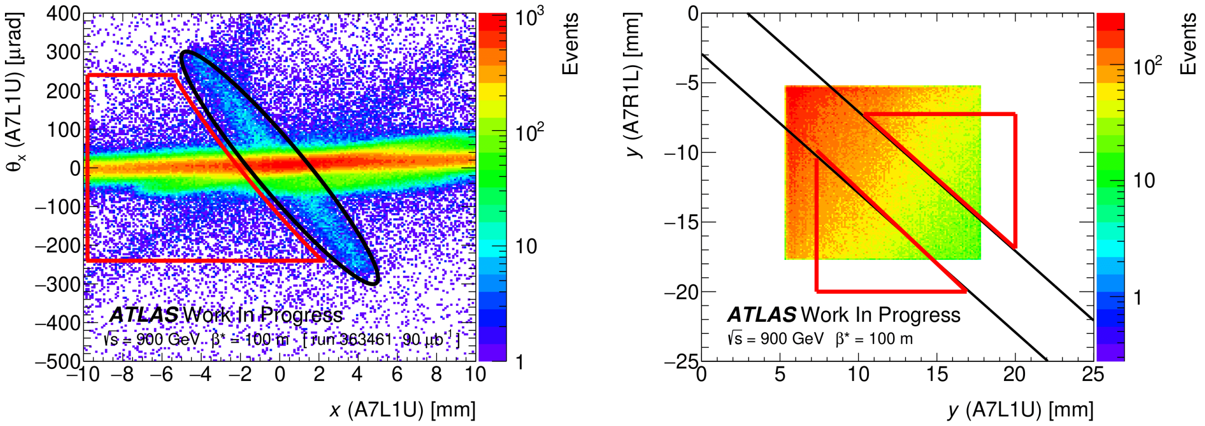

(a) The x_{Inner}-θ_x correlation.

(b) The $y^{\text{A}}_{\text{Inner}}$-$y^{\text{C}}_{\text{Inner}}$ correlation.

Figure 9.5: Two correlation plots containing all constructed RUC events prior to the correlation cuts : the black lines indicate the traditional selection cuts and the red lines indicate the regions used for scaling of the background.

9.3.2 Double Pomeron Exchange

The background contribution from Double Pomeron Exchange (DPE) has not been simulated at this stage. In previous analysis this was simulated using PYTHIA8, generated using the MBR parameterization and pomeron flux [20]. Since the protons have lost momentum, they can not be transported using Hill's equation and will instead be individually tracked from the IP to ALFA using MAD-X [78]. Detector effects are then first applied, before the events are subjected to the elastic selection criteria. Identical to the RUC events, the DPE events can be plotted with the same x_{Inner}-θ_x and $y^{\text{A}}_{\text{Inner}}$-$y^{\text{C}}_{\text{Inner}}$ correlations.

9.3.3 Background Scaling

The RUC and DPE background have to be scaled to the level of background present in the data. For this the scaling region in the two correlations, x_{Inner}-θ_x and $y^{\text{A}}_{\text{Inner}}$-$y^{\text{C}}_{\text{Inner}}$, are used. The scaling region in Figure 9.5a is used for scaling of RUC background. The region does not contain elastic events and in previous analysis the simulation of DPE showed not to contain this type of background either. Therefore, events found in data in this region can only originate from RUC background. The number of events found in data in this region are counted and the RUC sample is then scaled to match this number. The same procedure should be done for the DPE background, but here the region in Figure 9.5b is used for scaling. Unfortunately, due to the lack of the DPE simulation no hard conclusions on the validity of these scaling regions can be made at this stage. However, already from the RUC sample it is clear that there will be RUC events present in its scaling region. This is mainly due to the presence of the SD component in the RUC sample. Since the region does not purely contain DPE events, the scaling might lead to an overestimation of the level of DPE background present in data.

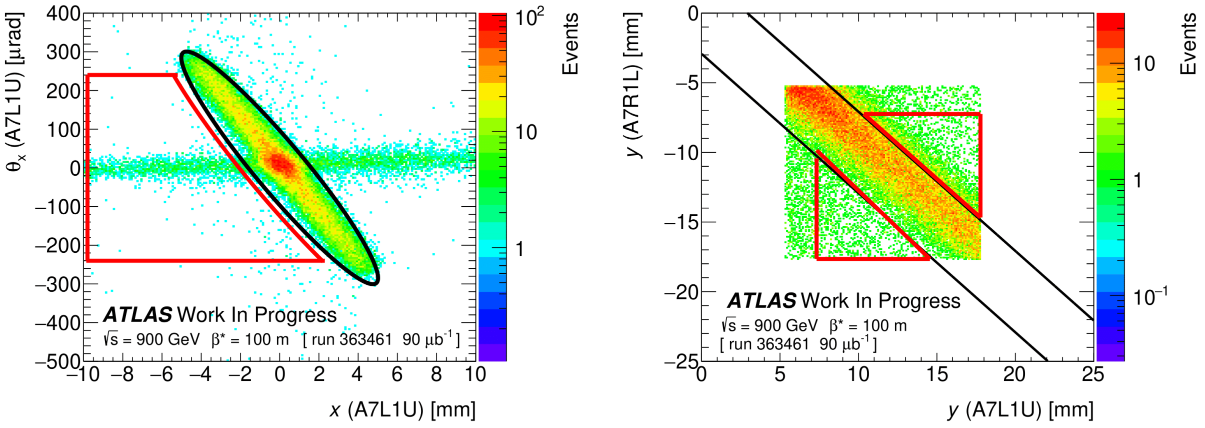

(a) The x_{Inner}-θ_x correlation.

(b) The $y^{\mathrm{A}}_{\mathrm{Inner}}$-$y^{\mathrm{C}}_{\mathrm{Inner}}$ correlation.

Figure 9.6: Two correlation plots containing all elastic candidates in data prior to correlation cuts : the black lines indicate the traditional selection cuts and the red lines indicate the regions used for scaling of the background.

The scaling regions in data are shown in Figure 9.6. The amount of events in the scaling region of Figure 9.6a is sufficient to scale the RUC background. The horizontal band due to beam halo is clearly present in the data. The amount of events in the scaling region in Figure 9.6b are far fewer than what was found in the other region, indicating a low background level of DPE and RUC events combined.

The background scaling may improve by using a time and bunch dependent procedure, since the background changes throughout a run. The halo background start will start to increase immediately after every scraping block due to re-population of beam halo. The interaction rate between protons decreases over time since the beams continuously loose protons. Consequently, the DPE and SD rate will also fall over time and hence their background contribution. This means that over time the composition of the background changes, leading to a constantly changing ratio of the halo and SD in the RUC background throughout a run. The background composition may also vary between the bunches as their emittance and beam spot are not necessarily identical. To take care of the dynamic behaviour of the data taking conditions, the data is split into groups of 10 lumiblocks called superlumiblocks (SLB) with approximately constant background conditions. SLBs should be short enough to catch time dependent effects and long enough to have sufficient statistics for an accurate determination of the background level. The scaling procedure is applied per SLB and the background is then subtracted from the corresponding candidate sample in that SLB. Due to scraping blocks an SLB may not consists of the aimed 10 lumiblocks, since this has significant effects on the background conditions. As a consequence, these SLBs may therefore have a larger statistical uncertainty on the event numbers.

9.3.4 Antigolden Events

The estimated background can be cross checked against the background of the antigolden topology. These are events that were recorded using the L1_ALFA_SYST17 and L1_ALFA_SYST18 triggers, which require one trigger from a detector on either side of the IP. The L1_ALFA_SYST17 is for a pair of two upper detectors and L1_ALFA_SYST18 is for a pair of two lower detectors. A schematic of these type of events is shown in Figure 9.7. These events are not related to elastic scattering since they would violate the conservation of momentum. They can, however, be used as such by inverting one of the y-coordinates on either the A- or C-side. This procedure has been used in the past for background determination. The method assumes a symmetry in background between the upper and lower detectors which does not necessarily hold and for this reason the previously introduced RUC methods was developed [20]. A comparison between the two methods is shown in Figure 9.8. The figure shows fair agreement in number of events collected in the actual antigolden topology and the generated antigolden events by the RUC description. Hence, the RUC methods holds promising description of the background data.

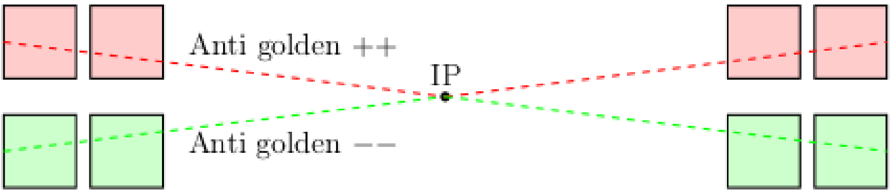

Figure 9.7: The two antigolden arms: ++ refers to upper detectors and – to lower detectors [20].

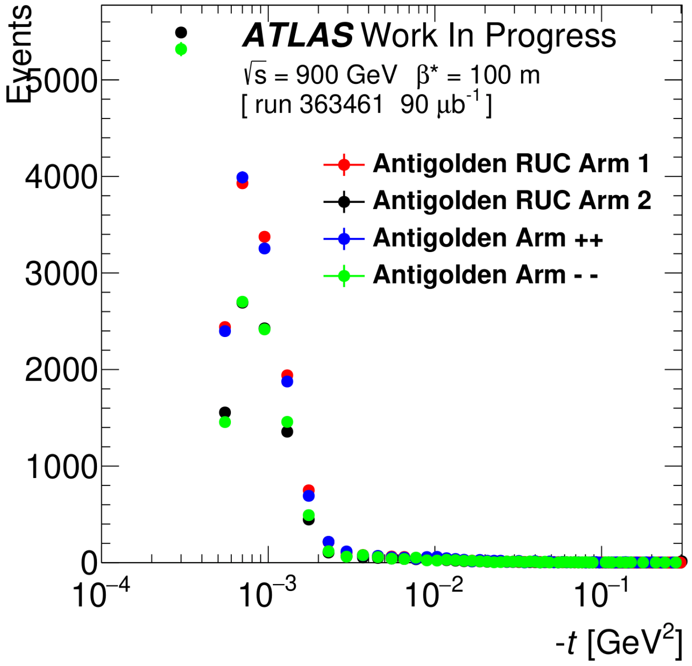

Figure 9.8: Comparison between number of events by RUC antigolden description and the antigolden topology.

9.3.5 Background and Signal Distributions

The number of elastic candidate and estimate background events as a function of the four-momentum transfer -*t* is shown in Figure 9.9. At low -*t*, the estimated level of background in arm 2 is substantially higher compared to the level in arm 1. The number of elastic candidates tends to follow this. In general, the background level is found to only be of about a percent, with an exception found in the two lowest -*t* bins for arm 2 where higher levels are noted.

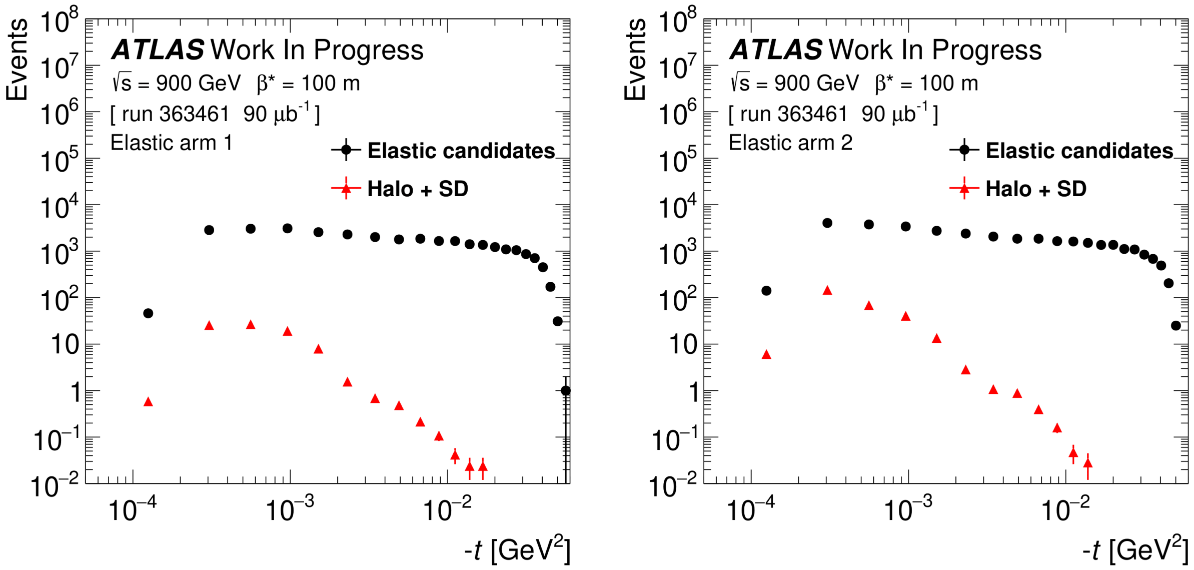

(a) Arm 1.

(b) Arm 2.

Figure 9.9: The number of elastic candidate and estimated background events as a function of the four-momentum transfer -*t*. The DPE background has not yet been simulated and can thus not be included in the background spectrum.

9.4 Experimental Effects

In the previous section the events were selected, the next step is to cover the experimental effects that have to be accounted for. They are of importance for the final step in the analysis, namely the determination of the physics parameters. The beam size grows and therefore also the spread of the interaction points, the beam spot width. The emittance grows throughout a run and affects the scattering angle via the divergence of the beam. The detector's resolution has to be determined and the exact positions of the detectors with respect to the beam, the alignment, has to be determined for accurate reconstruction of the scattering angles.

9.4.1 Acceptance

The acceptance of ALFA is determined by simulation of elastic events and is defined as the ratio between the generated events and events that pass the selection criteria set by the geometrical and correlation cuts. This simulation is also used to determine the correlation cuts as well as the t-resolution. The acceptance of ALFA is shown in Figure 9.10. Figure 9.10a shows the acceptance of events as function of the transverse scattering angles. The transport matrices and correlation cuts are uncorrelated in the x- and y-plane. The transverse scattering angles are, however, correlated through their shared -t value and azimuthal angle ϕ. This can be also be noted from the way that the angles are generated in the simulation :

$$\theta_x^* = \cos\phi\sqrt{-t}/E_{\text{beam}}, \quad \theta_y^* = \sin\phi\sqrt{-t}/E_{\text{beam}}. \tag{9.15}$$

The physics is symmetrical in phi and maps out a circle with radius $\sqrt{-t}/E_{\text{beam}}$. Under the influence of IP and the transport matrices the scattered particles hit the ALFA detectors at different locations. The events have to hit the sensitive area of the detector and are then subjected to the selection cuts. The acceptance in θ^* is shown by the two rectangles that have to two tiny tails towards center of the histogram, which are the smallest reachable -t values. This can also be seen from Figure 9.10b that shows the acceptance as a function of the four-momentum transfer. At $5 \cdot 10^{-5}$ GeV^2 the acceptance starts, though at the minimum level. The reduced level of acceptance only start to rise significantly from 10^{-4} GeV^2 onwards and peaks just below $2 \cdot 10^{-3}$ GeV^2. At the boundaries the acceptance of events fade outs due to the applied selection cuts.

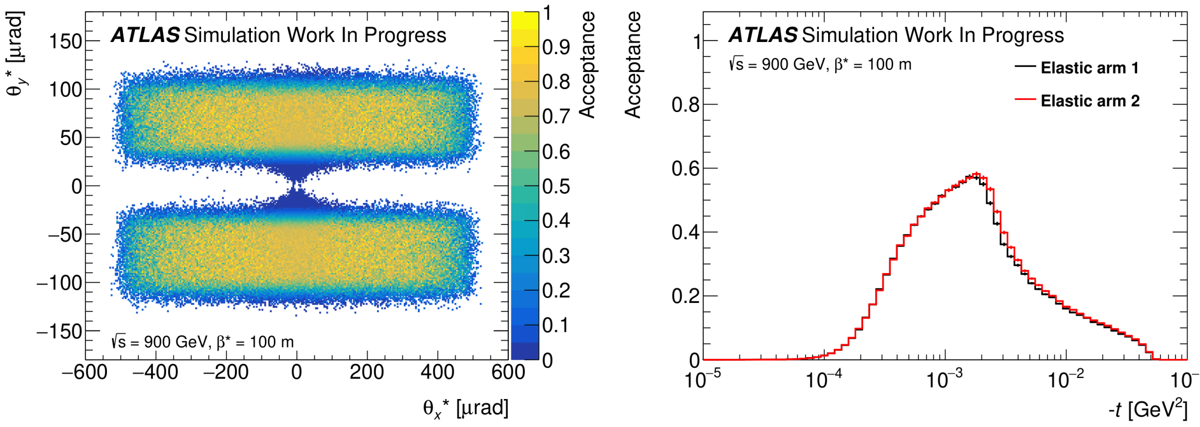

(a) The acceptqance of ALFA as a function of the transverse scattering angles at the IP.

(b) The acceptance of ALFA as a function of the four-momentum transfer -t per elastic arm.

Figure 9.10: The acceptance of ALFA determined using simulation.

9.4.2 Evolution of the Beam

The IP has a certain spread which is called the luminous region. The location of the luminous region as well as the spread define the beam position and beam spot width. The width of the beam is not constant and grows under various non-conservative processes. Also the beam position may even possibly slightly change throughout a run. The IP of an elastic interaction has a direct relation to where the elastic scattered protons ends up in the ALFA detector. This can be seen from (3.9) and, consequently, this effect has to be taken into account for the analysis. The ATLAS beam spot group determines the luminous region by reconstructed vertices by the inner detector. In Figure 9.11, the beam position and width of the transverse planes are shown for run 363461. The inner detector was only turned on partly during two data taking periods, which leave some LBs in data taking periods without measurements of the beam spot. These LBs can be recognised by the white background without markers, the grey regions indicate scraping blocks. The regions that contain measurements can be extrapolated to LBs that lack measurements of the beam spot. This is currently achieved by applying a linear fit to the data points. The information of the beam spot width is directly used as an input parameter for the simulation of

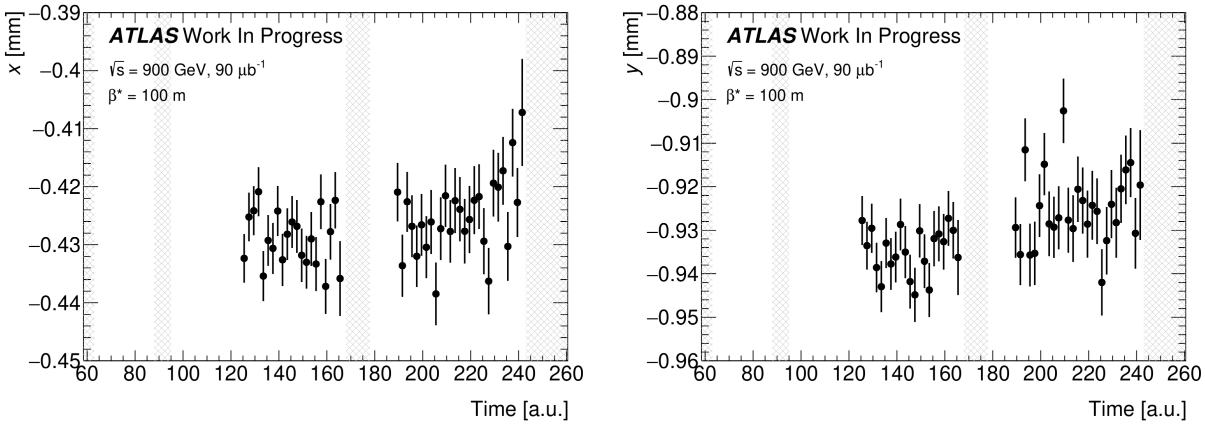

(a) The position of the beam in x.

(b) The position of the beam in y.

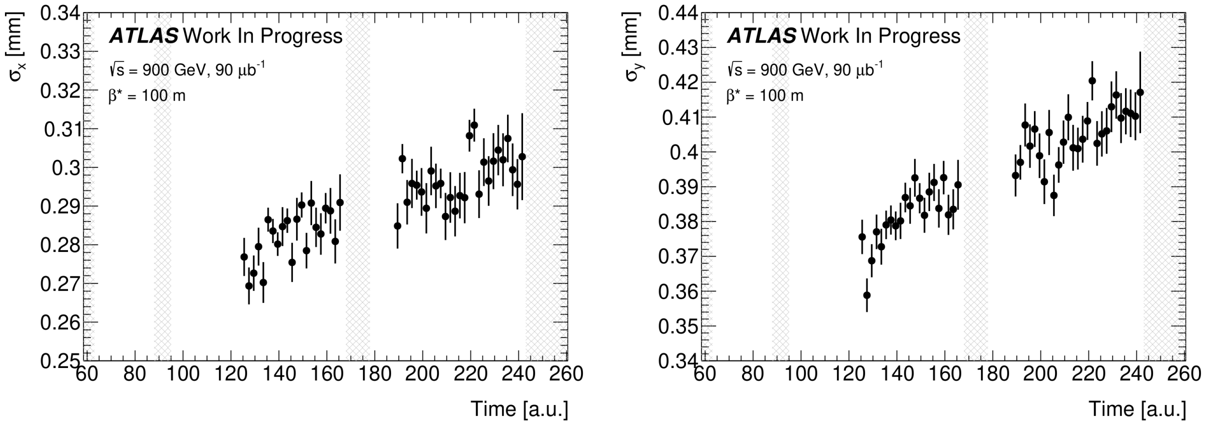

(c) The width of the beam in x.

(d) The width of the beam in y.

Figure 9.11: The position and size of the beam as a function of LB during run 363461, determined by the ATLAS inner detector. The grey bands indicate scraping blocks, the white bands indicate data taking periods. The LBs that do not have markers, the inner detector was turned off.

the elastic signal in ALFA and will be further discussed in the section dedicated to simulation. The beam growth can be directly related to the growth in the emittance of the beam. The emittance is continuously measured by the BSRTs and are normalized using the wire scanners [40]. The evolution of the emittance can be described by an exponential. Using the emittance one can calculate the divergence of the beam, given by (9.16). Knowing the divergence is of importance since it impacts the observed scattering angles at ALFA.

$$D_u = \sqrt{\frac{\epsilon_u}{\gamma\beta_u^*}} \tag{9.16}$$

Measurements of the emittance by the BSRTs and wire scanners are centrally dealt with by the LHC. The information is stored per LHC fill and the database is available through an API called timber. The extracted BSRT data is then fitted with an exponential function for each data taking period. The normalisation of the measurements per fill is found using the measurements from the wire scanners. The resulting normalized emittance of the BSRT data is shown by Figure 9.12.

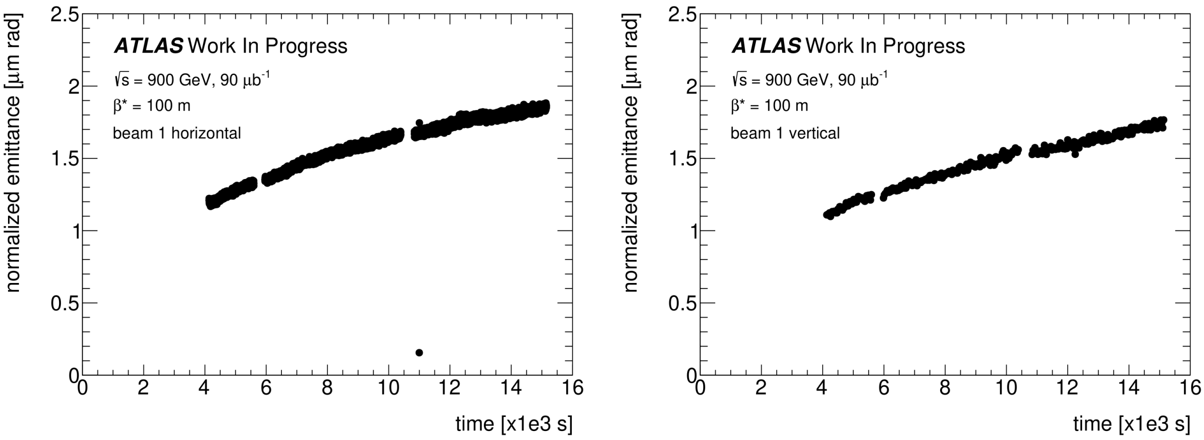

(a) Beam 1 horizontal. **(b)** Beam 1 vertical.

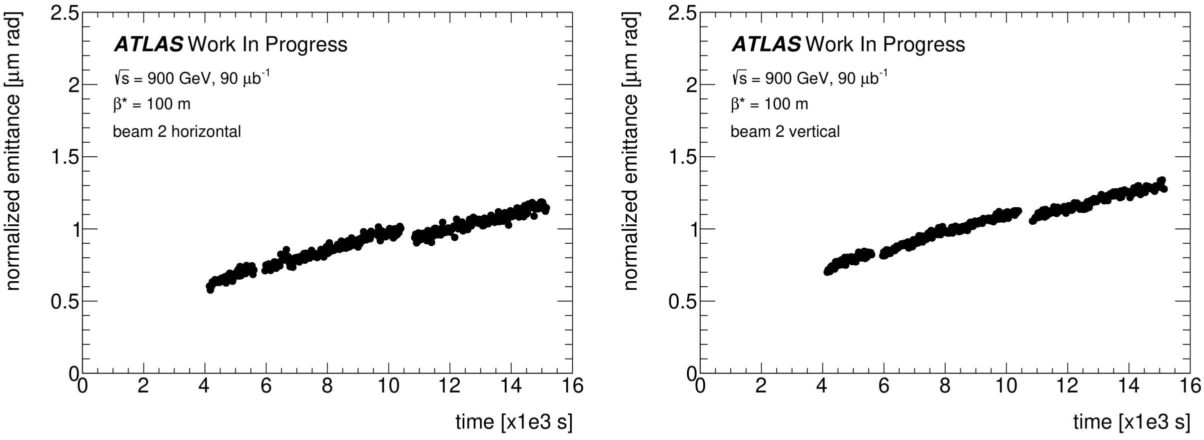

(c) Beam 2 horizontal. **(d)** Beam 2 vertical.

Figure 9.12: Emittance measurements from the BSRT normalized by the wire scanners. The three periods corresponds to the three data taking periods in ATLAS run 363461. The time is with respect to the start of the LHC fill 7282 in which the ATLAS DAQ run 363461 was collected.

9.4.3 Detector Effects

Detector effects have to be determined and taken into account for reconstruction of elastic candidates. A data driven method is used to determine the convoluted resolution of the detector. The convoluted resolution incorporates the combined effect of the intrinsic resolution of the detectors and multiple scattering:

$$\sigma_{\mathrm{conv}}^2 = 2\sigma_{\mathrm{det}}^2 + \sigma_{\mathrm{ms}}^2$$

The measured coordinates in the inner detector are used to predict the coordinates in the outer detector by using the transport matrices. The predicted value is than compared by the measured value in data. The difference in predicted and measured value gives the convoluted resolution of ALFA. It is convoluted since the measured coordinates are already affected by the resolution of the inner the detector. Additionally, by traversing the material of the inner detector multiple scattering will disperse the outgoing angle and thereby the hit position in the outer detector, located 8 meter downstream.

In Figure 9.13, the residuals between the predicted and measured y-coordinates in the outer detector are shown. The distribution has been fitted by Gaussian function to extract the width of 100 μm, the convoluted resolution for the 900 GeV elastic physics campaign. The value of the convoluted resolution is significantly larger compared to previous campaigns at 7, 8 and 13 TeV. Multiple scattering is inversely proportional to the energy and since the energy is about one order of magnitude smaller than the previous campaigns this term becomes more dominant to the convoluted resolution. From test campaigns and simulation the detector resolution is known to be between 25 and 29 μm [59]. With the above relation one can in principle, under the assumption of having an identical detector resolution between two campaigns and the dependence of multiple scattering on energy, determine the individual terms σ_{det} and σ_{ms}.

The 8 TeV has been used to draw a comparison and extract the multiple scattering term, since the detector was in similar condition to 900 GeV. Optimizing lead to a intrinsic detector resolution, σ_{det}, of 28.8 μm under which scaling the multiple scattering term, σ_{ms}, found at 8 TeV by a factor of 8.9 to 900 GeV leads to 100 μm convoluted resolution that is observed in data. At 8 TeV the multiple scattering was only 10 μm, whereas at 900 GeV it is found to be 90 μm and thus dominant for this physics campaign. Hence, the material budget of the detector at this energy might become more relevant to the precision of the measurement. With this scaling method of the multiple scattering the detector resolution is found to be in the expected range. Even though the detection efficiencies might vary between campaigns, one in principle has a handle to determine the actual detector resolution using the scaling method.

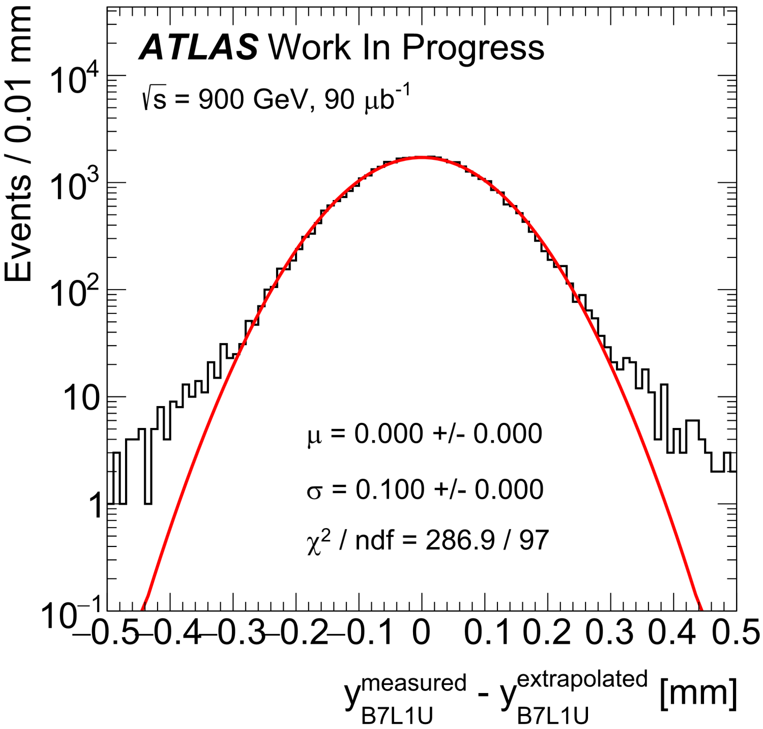

Figure 9.13: The residuals of the predicted and measured y-coordinate in the outer detector B7L1U. The residuals are fitted by a Gaussian function, the results is indicated by the red line and its values are given. A double Gaussian function could be used to account for the tails.

9.4.4 Alignment

The detector alignment directly impacts the reconstructed t-values, since coordinates found in the detector are related to the event at the interaction point, shown by the equations introduced in Section 9.2. For this, the coordinates in the detector have to be translated into the coordinate system with respect to the heart of the beam. This translation depends on the alignment of the detector, i.e. its position with respect to the beam. The alignment determination demands a lot of attention and forms a separate analysis on its own and has dependencies on detector efficiencies that vary with the position were particles hit the detector. At this stage a collaborator has only started with the alignment, but no definite alignment has yet been determined. Therefore, a simple alignment has been determined by the author using the motor values of the Roman Pots extracted from timber together with the positioning of the detectors inside the pots from [59]. This currently lead to the use of the following distances in mm between the detectors:

$$\begin{aligned} d_{12} &= 9.315, \\ d_{34} &= 10.482, \\ d_{56} &= 10.311, \\ d_{78} &= 9.107. \end{aligned}$$

Further analysis is needed to determine the distances precisely, but also to incorporate effects such as transverse tilts of the detector called rotation and offsets both horizontally as well as vertically.

9.5 Detector status and layer efficiency

Not only the background levels, but also the functioning of the detector determines the prospect of analysis. This can be noticed from (9.1), in which the detector's efficiency, ϵ, is embedded. As part of initial data quality checks, the functioning of the detector has been investigated and will presented in this section. These checks are meaningful since they are important indicators of the detectors performance and consequently the feasibility of the analysis. The detector functioning directly influences the track selection cuts and the reconstruction efficiencies. At this stage of the analysis only the basic detector functioning has been studied and will be discussed next.

In Figure 9.14, a 2-dimensional histogram depicts the relative distribution for tracks in elastic triggered events by the number of U- and V-layers. No geometrical and correlation cuts are applied. The tracks are binned according to the layer participation in the selected tracks. Ideally, the majority of events should lie in the top right corner of the histogram, having all individual MD layers involved. Identical histograms are used online during the data taking since they provide feedback on the detector status. In preparation for a physics campaign the timing of signals can be optimized to catch the majority of the signals. Prior to the 900 GeV physics campaign there has not been such a dedicated preparation, leading to less optimal performance of the detector. This can for example be seen for detectors B7L1U (a) and B7R1L (h) in which the peak of the distribution is at 9 U- and V-layers.

Another informative method is to check the individual layer efficiencies. The layer efficiency is computed by the taking the amount of times a layer has participated in an elastic candidate event. This number is normalized by the total number of elastic candidate events in the corresponding elastic arm and are depicted in Figure 9.15. The layer efficiencies are relevant to the tightness of the track requirements in the analysis. In general the layer efficiencies are found to be near 90%, indicating a good level of activity. Detectors B7L1U and B7R1L now have their bad detection layers clearly exposed, which could not directly be seen from Figure 9.14. There are several identified layers with lower efficiencies. All spatial hit distributions for the individual layers in each detector have been looked at. This includes the poor ones, of which some have their spatial efficiencies shown by Figure 9.16. The fibre structure of layers is clear from these plots, but there are no indications of dead layers which would appear white.

There are 160 layers for the eight detector that has been looked at and all have been put in Appendix B.2. The layers with efficiencies significantly below 90% are most interesting and provide some information on the current state of the detector. If fibres were to be dead, they would show up white in these plots, however there weren't any such fibres encountered by check the layers. Therefore aging, radiation and timing seem to be the causes for reduced efficiency. These effects can not be fully disentangled from each other by studying the plots. The first two effects would lead to reduced light transmission, by which the timing of the electronics becomes even more critical to signal extraction. Since these effects are limited to a few of the 160 layers, it is likely mostly due to a timing problem.

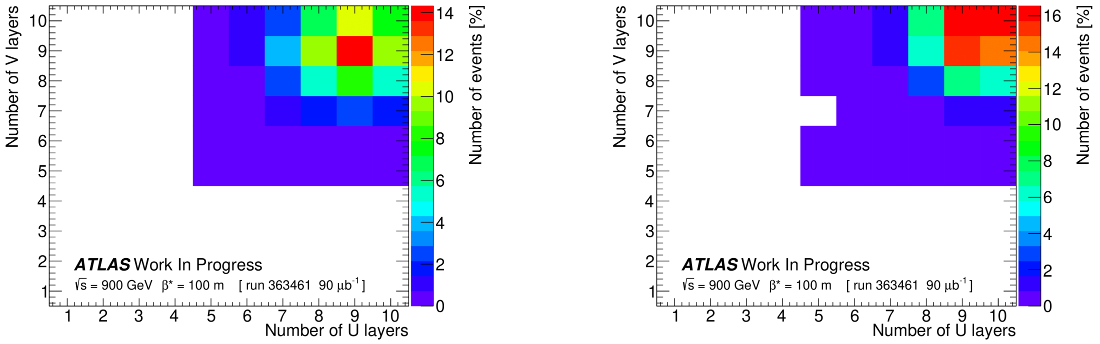

(a) Detector B7L1U. **(b)** Detector B7L1L.

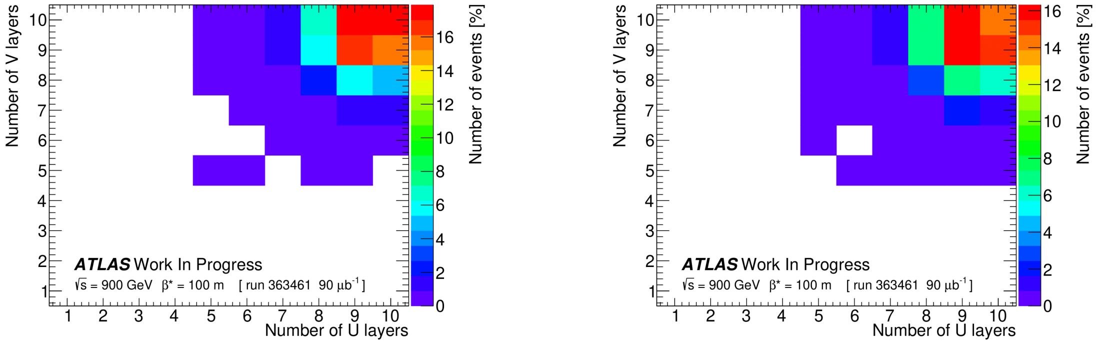

(c) Detector A7L1U. **(d)** Detector A7L1L.

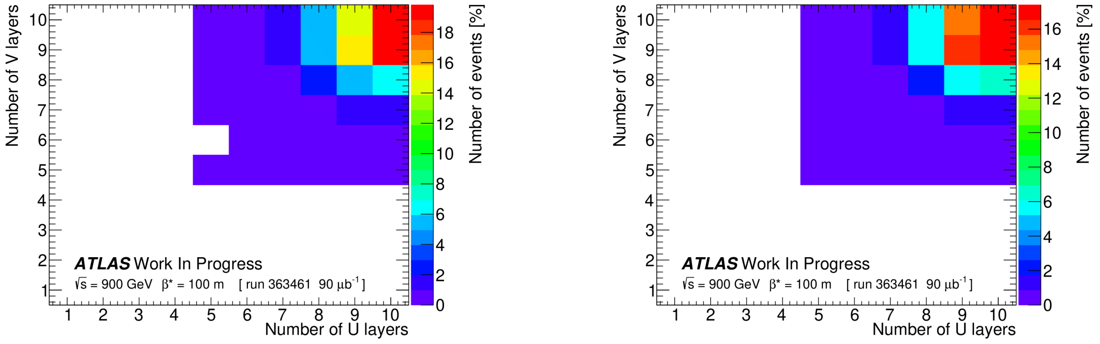

(e) Detector A7R1U. **(f)** Detector A7R1L.

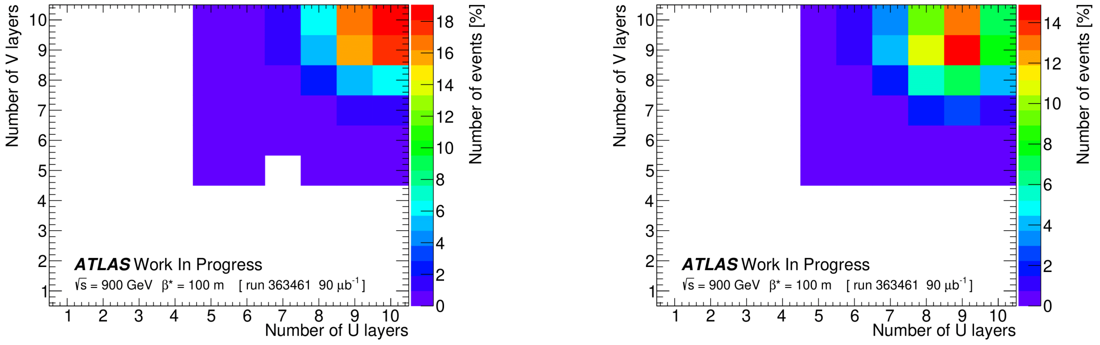

(g) Detector B7R1U. **(h)** Detector B7R1L.

Figure 9.14: Overlapping layers in the U- and V-plane for elastic triggered events.

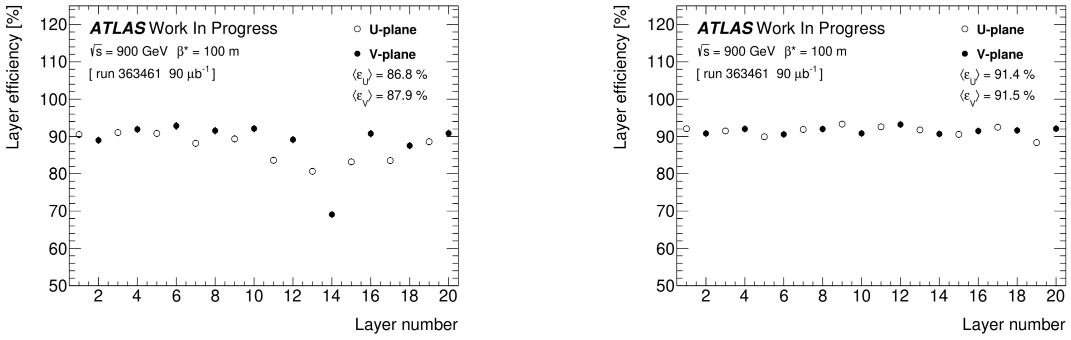

(a) Detector B7L1U.

(b) Detector B7L1L.

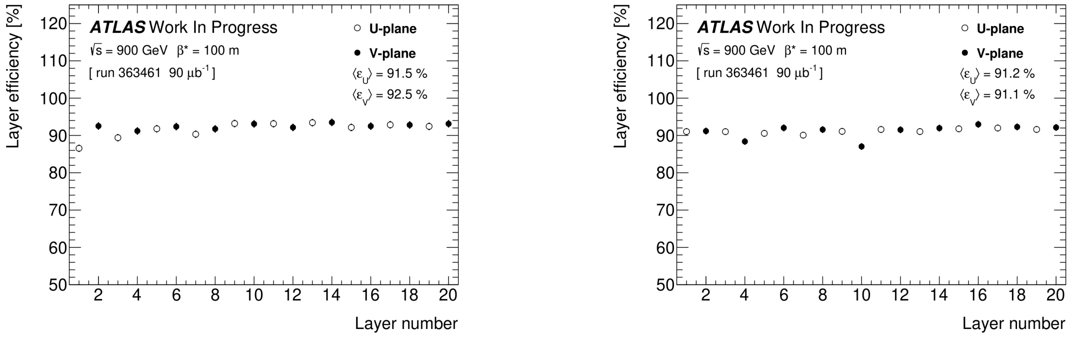

(c) Detector A7L1U.

(d) Detector A7L1L.

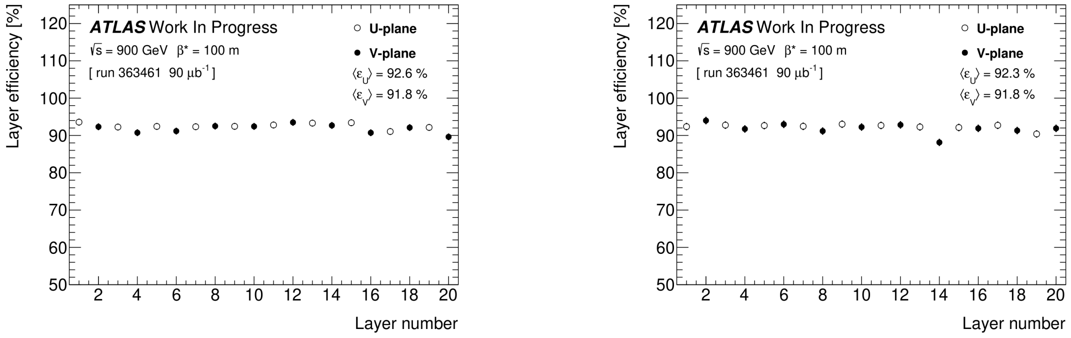

(e) Detector A7R1U.

(f) Detector A7R1L.

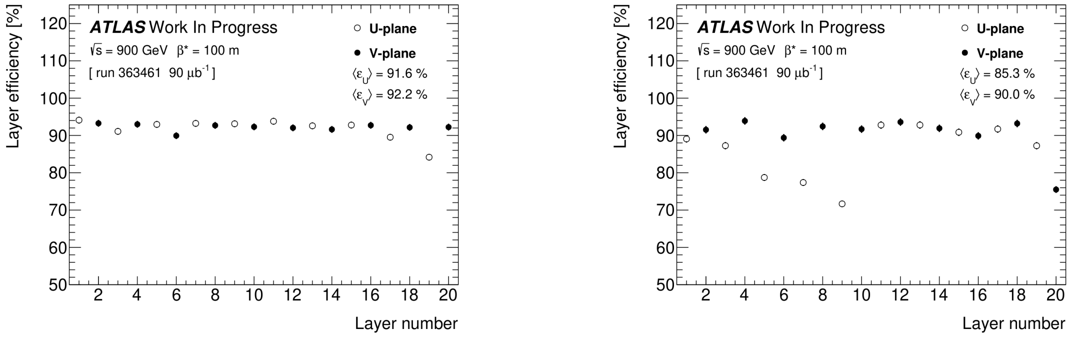

(g) Detector B7R1U.

(h) Detector B7R1L.

Figure 9.15: Layer efficiencies for elastic candidate events.

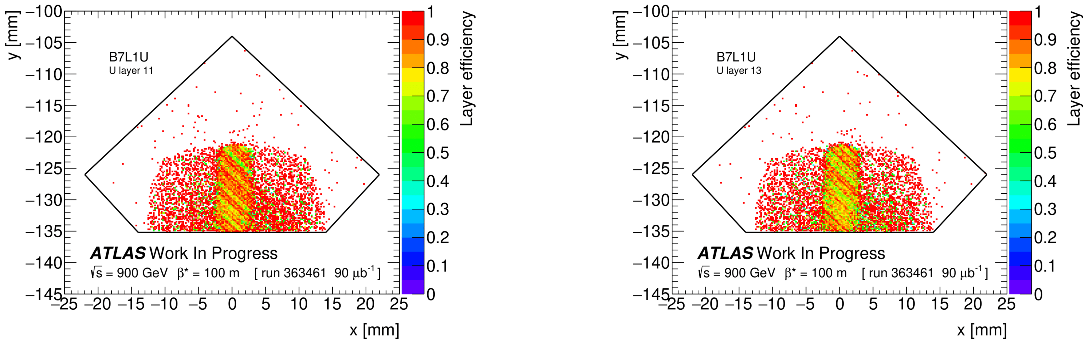

(a) Detector B7L1U U layer 11.

(b) Detector B7L1U U layer 13.

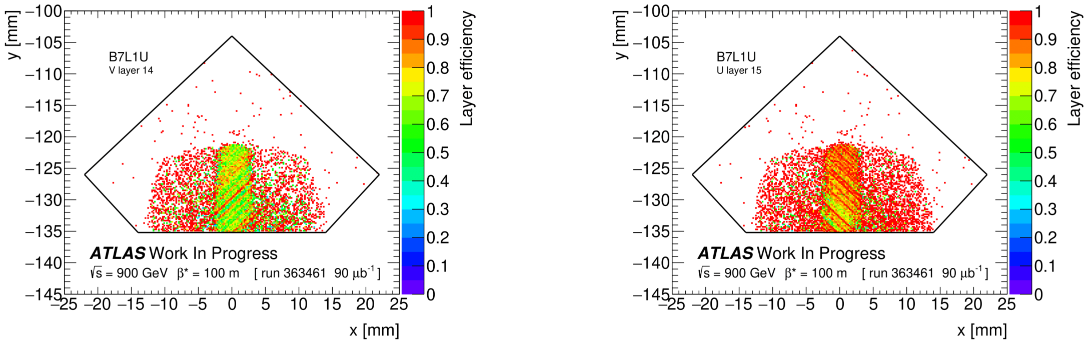

(c) Detector B7L1U V layer 14.

(d) Detector B7L1U U layer 15.

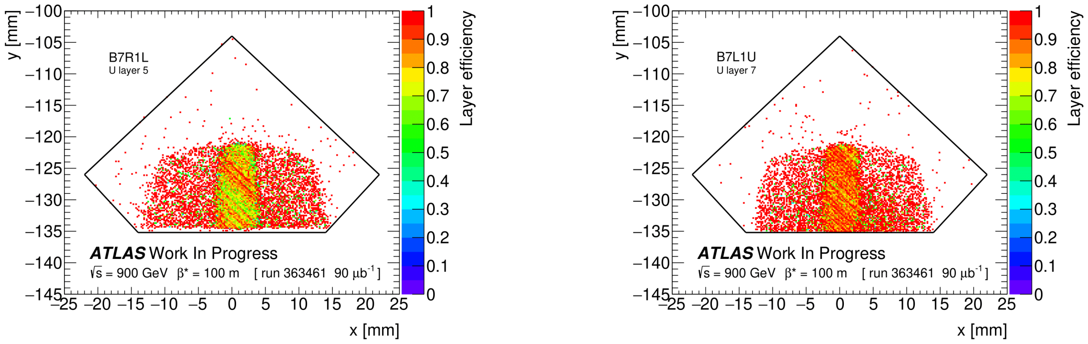

(e) Detector B7R1L U layer 5.

(f) Detector B7R1L U layer 7.

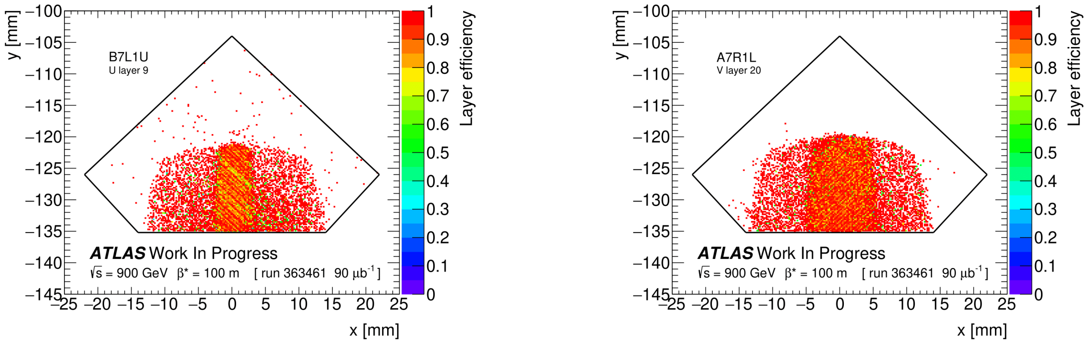

(g) Detector B7R1L U layer 9.

(h) Detector B7R1L V layer 20.

Figure 9.16: Spatial track efficiency for elastic triggered events for poor layers in detectors B7L1U and B7R1L.

9.6 Simulation

The Monte-Carlo simulation of the elastic signal is used to define correlation cuts that are applied in the selection of elastic candidates and ultimately also for fitting of the physics parameters. The simulation depends on a lot of input parameters that need be taken into account from the underlying theory to detector effects. At the current stage of the analysis this simulation can significantly contribute to the understanding of elastic physics at 900 GeV center-of-mass energy at the LHC.

The simulation package incorporates the differential elastic cross section (2.17) as introduced in Section 2.3.2. This model was also used in previous ALFA analysis to serve as fundamental description of the physics. The settings of the magnets as determined by simulation, referred to as $design$ optics, are used for transportation of elastic events from the IP to ALFA. The optics are listed in Table 8.1 of Section 8.2, and the presented matrix elements M_{ij} are used to construct the transport equations (9.2)-(9.7) via Hill's equation. In Section 9.4 the experimental effects have been introduced, including the beam spot width, emittance and convoluted resolution. The beam spot width is used the generate a Gaussian distribution of interaction vertices. The coordinate of the vertex is directly put in the transport matrices. The emittance is used to calculate the divergence of the beam and a Gaussian distribution is used to mimic this effect. Identical to the interaction vertex the divergence of the elastic event is a direct input for the transport matrices. The resolution of the detector is taken into account by using the data driven convoluted resolution for smearing the hit coordinates of the protons in the detectors following a Gaussian distribution.

To briefly summarize: the elastic interaction is generated by randomly picking a t-value according to the underlying theory. The vertex is then generated according to the observed experimental values. The transportation of the elastic scattered protons from the IP in the ATLAS barrel to the ALFA detectors then follows by using the design optics. The resolution of the detector is then applied by smearing the coordinates according the found convoluted resolution. Once events are smeared in the detector they are subjected to the edge and beam screen cut. The events are then stored in histograms to determine and optimize the correlation cuts used in data for the event selection. The resulting correlation plots of a Monte-Carlo sample of 1 million elastic events are shown in Figure 9.17. The dominance of a cross-diagonal shape for the all the x-coordinate plots is a feature not seen before in previous elastic physics campaigns. Variations of the experimental effects were then applied to gain understanding in their influence on the elastic signal in the detector. The acquired results are briefly discussed in the following sections.

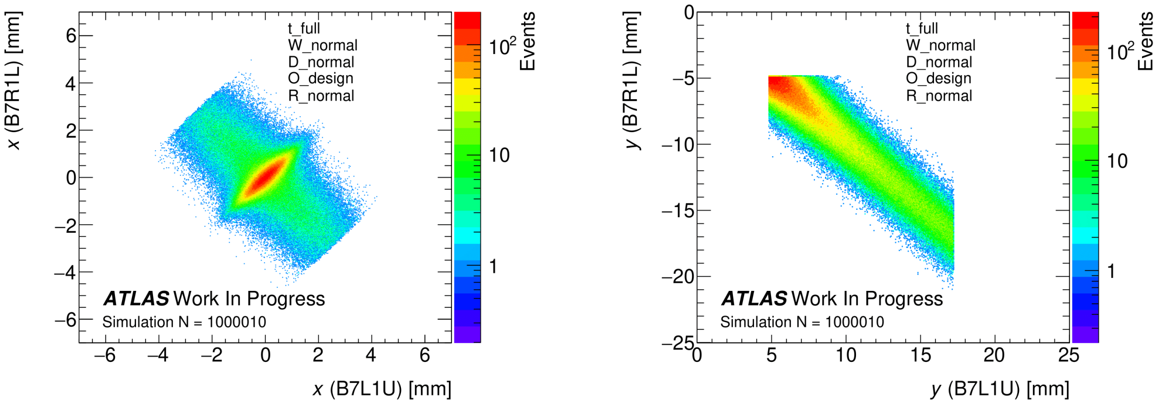

(a) Outer detectors x correlation.

(b) Outer detectors y correlation.

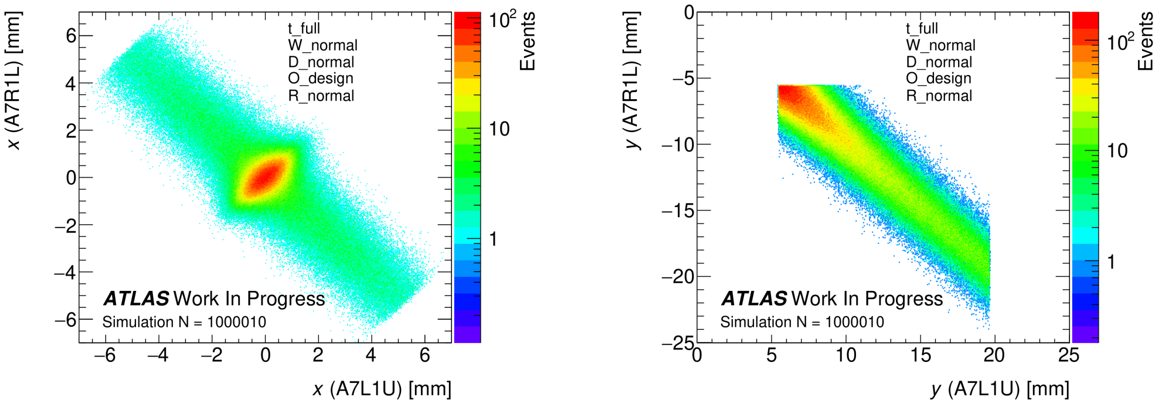

(c) Inner detectors x correlation.

(d) Outer detectors y correlation.

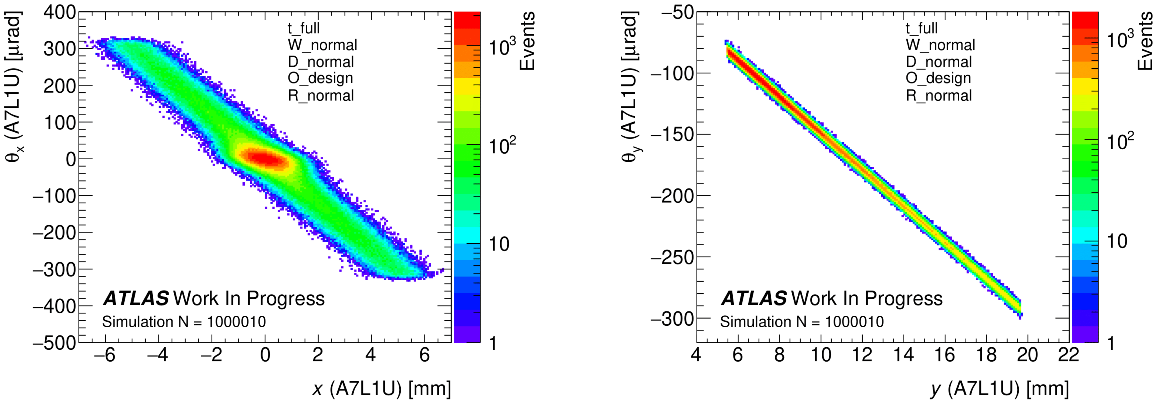

(e) Inner detector x-θ_x correlation.

(f) Inner detector y-θ_y correlation.

Figure 9.17: Correlations for the simulation of the elastic signal in ALFA.

9.6.1 Vertex

The coordinates of the vertex, or IP, are generated according to a Gaussian function that has a width corresponding to the beam spot width: the spread in vertices determined by the ID. The impact of the location of the IP on where the protons hit the detector has been studied by modifying the beam spot width in steps of 0.25 of the observed value. The simulation was repeated for widths of 0, 1/4, 2/4, 3/4, 1, 5/4, 6/4, 7/4 and 8/4 times the observed beam spot width. This was done for both the width in the x- and y-orientation. The results for the x-θ_x and y-θ_y are shown in Figures 9.18 and 9.19, respectively. The beam spot width x clearly determines the behaviour of red ellipse in the heart of the x-θ_x correlation plots of Figure 9.18. The axis of the ellipse rotates from being aligned with the diagonal to horizontal in the plots. In other words, one could state that the events appearing close to the origin of this plot are elongated along x stronger than events further from the origin. The feature of having two correlations in the x-θ_x is new and this study shows that the beam spot width is, in combination with the optics, of direct influence. In addition it is then interesting how well the *parallel-to-point* optics hold under large beam spot width. This can be studied by the y-θ_y correlation plots depicted in Figure 9.19 in which the beam spot width y was varied. The effect of variation in beam spot width is indeed of less influence on the spread in these plots compared to the x-θ_x plots. This is due to the large difference in magnitude of the transport element M_{11} in both planes. The element is minimized in the vertical plane, However, under perfect *parallel-to-point* optics there should be no difference when varying the vertex spread in y. It has to be noted that *parallel-to-point* optics are such to have its focal point in between the inner and outer detectors. Hence, the coordinate is not exactly located of where *parallel-to-point* optics holds. Despite this fact, it is worth noting that the beam spot size in combination with the optics, i.e. close to zero transport element M_{11}, impacts the elastic signal in the detector.

9.6.2 Divergence

The influence of the divergence is of importance to the resolution of the t-reconstruction of elastic events. In Section 9.2 the divergence that are an additional term on the outgoing angle at the interaction point are neglected for simplicity. However, these terms are unavoidably present and hence influence the resolution achieved by the reconstruction methods. The reconstructed angle at the interaction point is not solely due to the elastic interaction. To study influence the divergence on the elastic signal in the detector the value has been studied in three settings: 0, nominal and doubled. The result on the correlation plots are depicted in Figure 9.20. There is a noticeable difference on the local angle, which can be observed by looking at the y-θ_y correlation, in which the red center smear towards the bottom right. From the inner detector y correlation, the effect of divergence becomes more evident, since it affects the interaction oppositely for A- and C-Side. For the equivalent correlations in x, the local angle and coordinates are affected minimally. This is due to the large difference in magnitude of the transport element M_{12} in both planes. The influence of divergence is relatively larger for the smaller t-values compared to larger t-values, and will therefore relatively affect the resolution of smaller t more.

9.6.3 Detector Resolution

In the simulation the influence of the detector's resolution on the elastic signal is minimal. The spread in the plots is on the order of several millimeters and since the convoluted resolution is a tenth of a millimeter the smearing in the detector does not lead significant changes in the correlation plots.

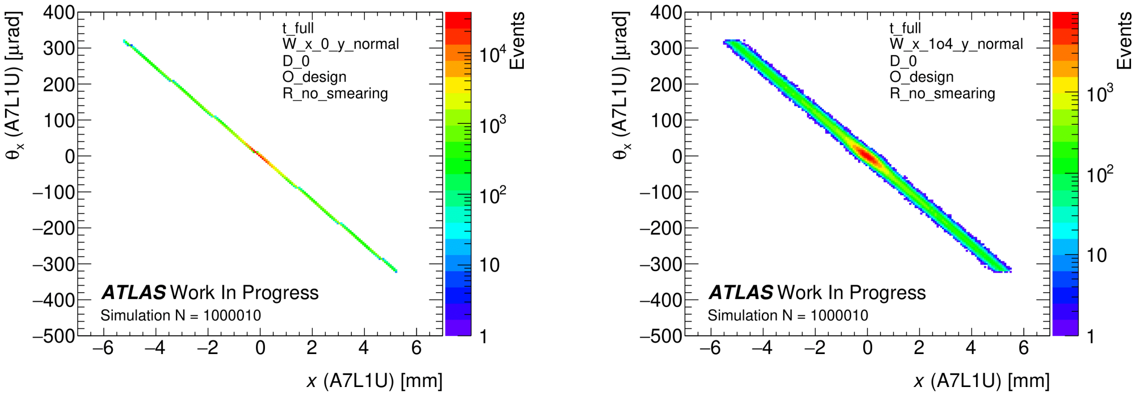

(a) x Beam spot width = $0 \cdot$ nominal width.

(b) x Beam spot width = $1/4 \cdot$ nominal width.

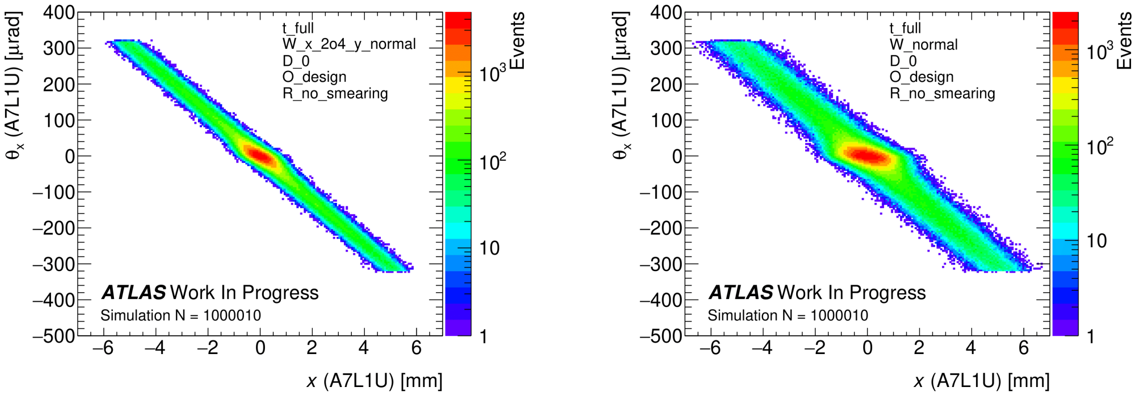

(c) x Beam spot width = $2/4 \cdot$ nominal width.

(d) x Beam spot width = nominal width.

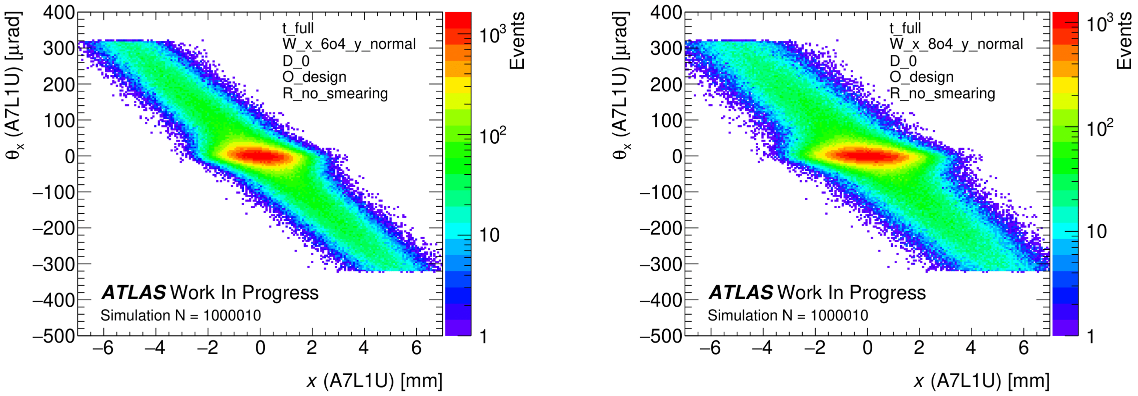

(e) x Beam spot width = $6/4 \cdot$ nominal width.

(f) x Beam spot width = $8/4 \cdot$ nominal width.

Figure 9.18: Inner detector x-θ_x correlation under variation of the beam spot width in x. The effects of divergence and detector resolution are taken out of the simulation in this study.

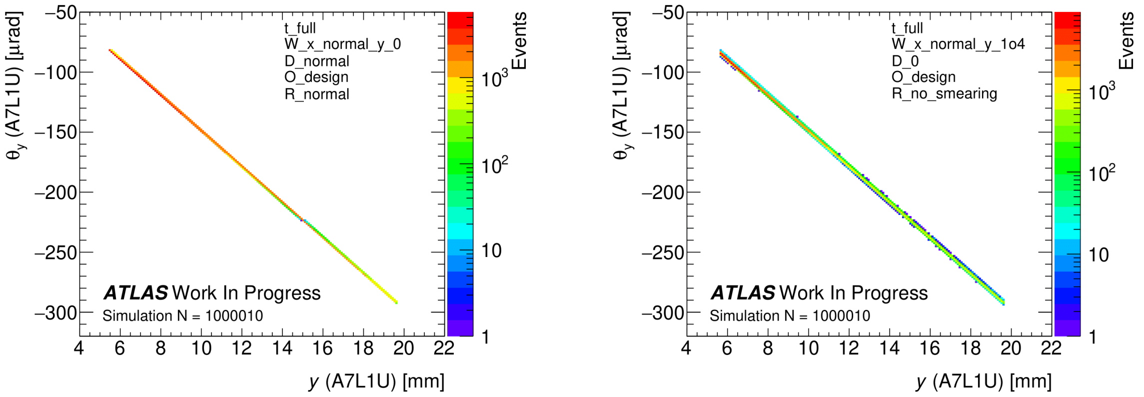

(a) y Beam spot width = $0 \cdot$ nominal width. **(b)** y Beam spot width = $1/4 \cdot$ nominal width.

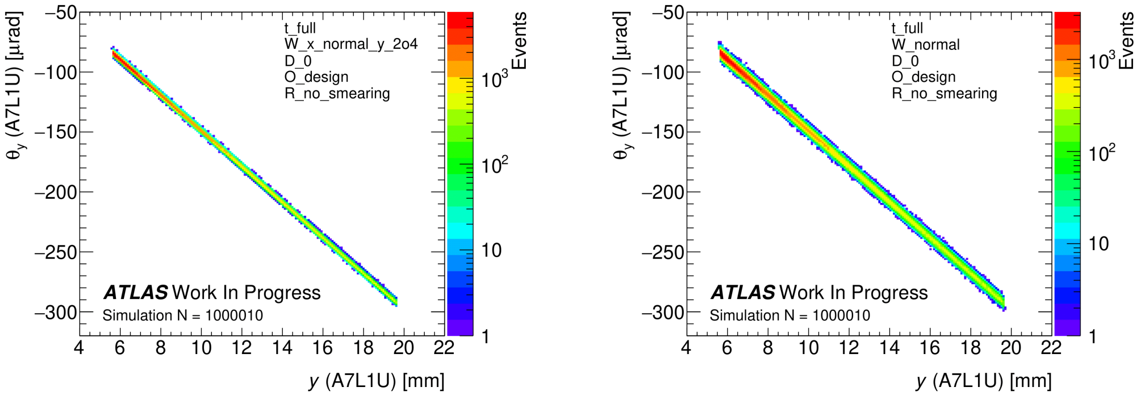

(c) y Beam spot width = $2/4 \cdot$ nominal width. **(d)** y Beam spot width = nominal width.

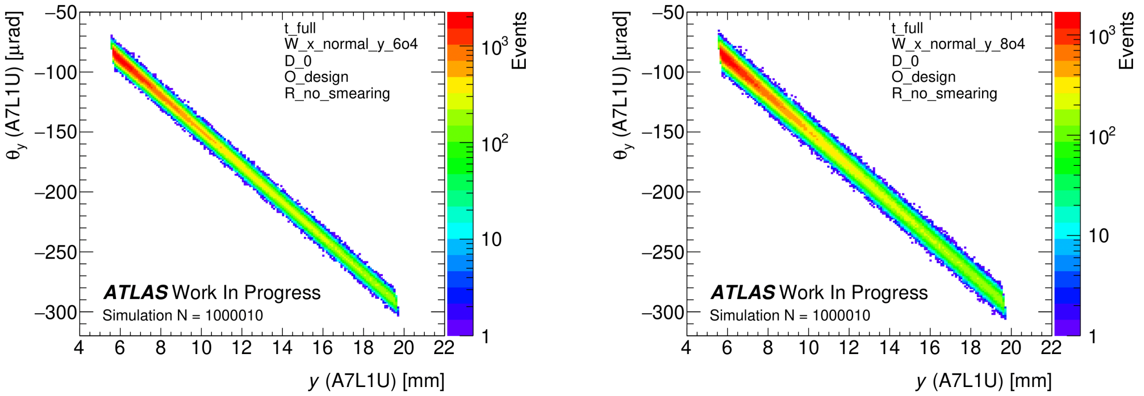

(e) y Beam spot width = $6/4 \cdot$ nominal width. **(f)** y Beam spot width = $8/4 \cdot$ nominal width.

Figure 9.19: Inner detector y-θ_y correlation under variation of the beam spot width in y. The effects of divergence and detector resolution are taken out of the simulation in this study.

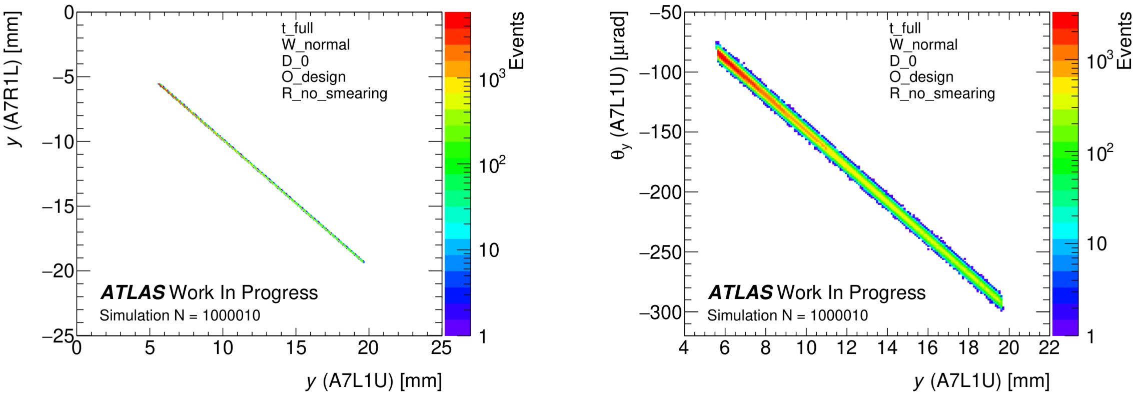

(a) No divergence.

(b) No divergence.

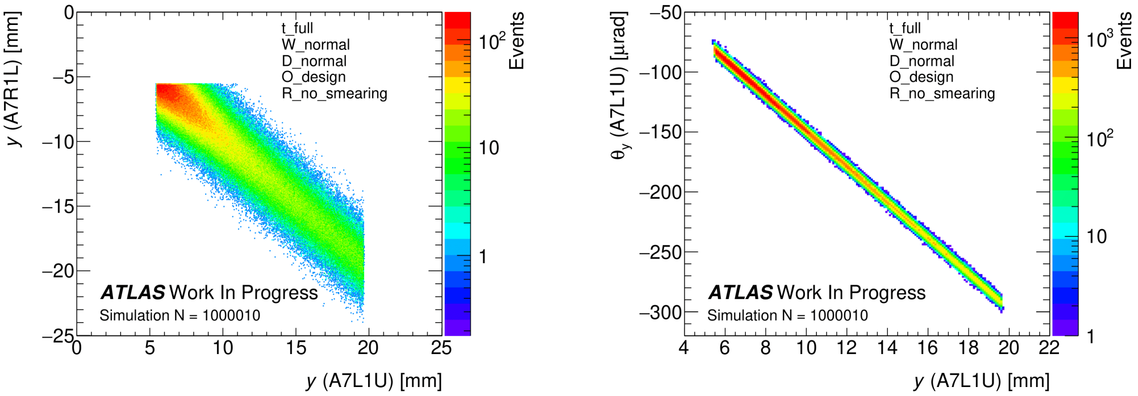

(c) Nominal divergence.

(d) Nominal divergence.

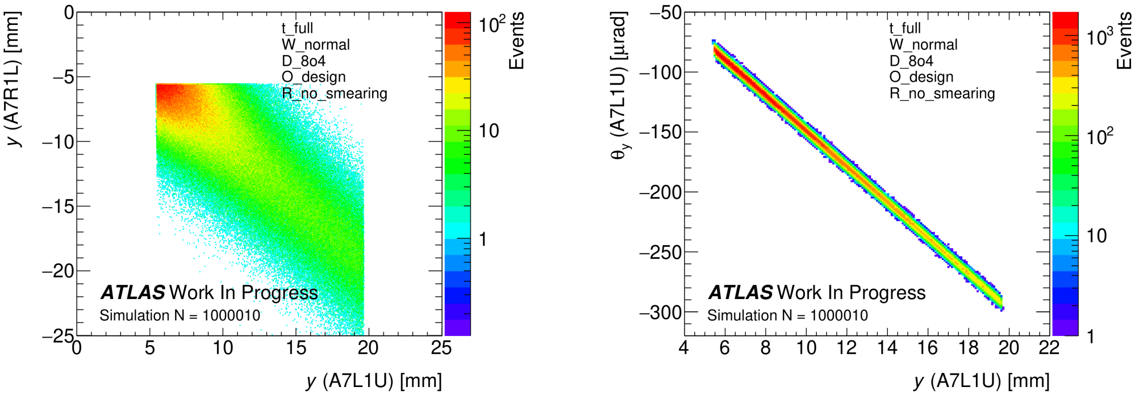

(e) Double the divergence.

(f) Double the divergence.

Figure 9.20: Inner detector y, **(a), (c), (e)**, and y-θ_y, **(b), (d), (f)**, correlations under variation of the divergence. The beam spot width is kept normal and the effect of detector resolution is taken out of the simulation.

9.6.4 *t*-Ranges

To determine where elastic events of different t-values end up in the detector a study is conducted in which the t-range of the detectors acceptance is split in 6 ranges. The 6 ranges are not linearly divided and focus more on the smallest t-values. The used ranges are:

$$\begin{aligned}
1 \cdot 10^{-4} &< t < 3 \cdot 10^{-4}\mathrm{GeV}^2, \\
3 \cdot 10^{-4} &< t < 7 \cdot 10^{-4}\mathrm{GeV}^2, \\
7 \cdot 10^{-4} &< t < 1 \cdot 10^{-3}\mathrm{GeV}^2, \\
1 \cdot 10^{-3} &< t < 3 \cdot 10^{-3}\mathrm{GeV}^2, \\
3 \cdot 10^{-3} &< t < 1 \cdot 10^{-2}\mathrm{GeV}^2, \\
1 \cdot 10^{-2} &< t < 5 \cdot 10^{-2}\mathrm{GeV}^2.
\end{aligned}$$

For each range again 1 million elastic events are created. In Figures 9.21 and 9.22 the resulting x-θ_x and y-θ_y correlation plots are shown, respectively. This correlation is preferred since it both shows the coordinate as well as the local angle the detector. comparing the two figures one can observed a smaller spread of the local angle in the case of x compared to y. It is even such that for y the largest t-values can still overlay events of small t-value. This can be observed by comparing plots (a) and (f) in Figure 9.22. This is something that does not occur in the horizontal orientation, which is due to the large difference in magnitude of the transport element M_{11} in both planes. To study the relative effects that may depend on the t-range and a brief set of variation have also been carried out for the 6 ranges. All these plots are collectively put in Appendix B.3. The reader is strongly encouraged to go through this appendix that includes 6 correlations under 6 variations of the simulation for each t-range.

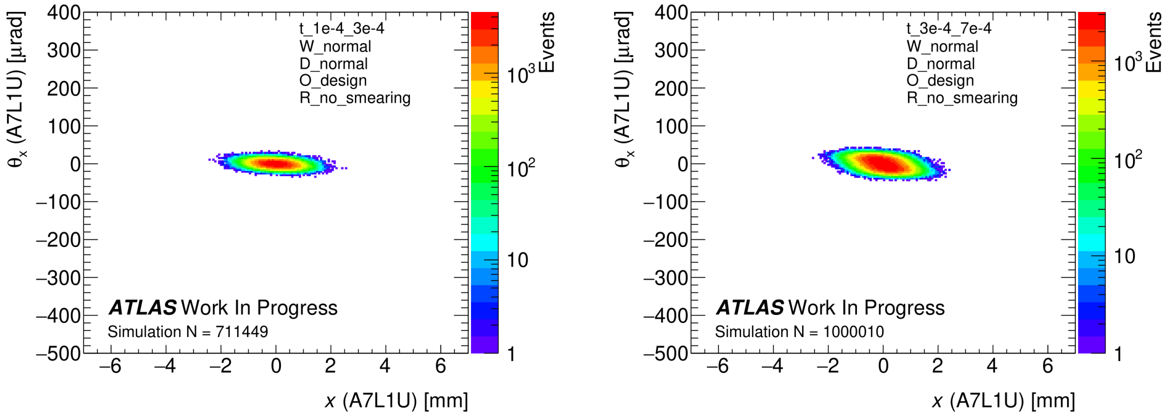

(a) $1{\cdot}10^{-4} < t < 3{\cdot}10^{-4}$ GeV^2. **(b)** $3{\cdot}10^{-4} < t < 7{\cdot}10^{-4}$ GeV^2.

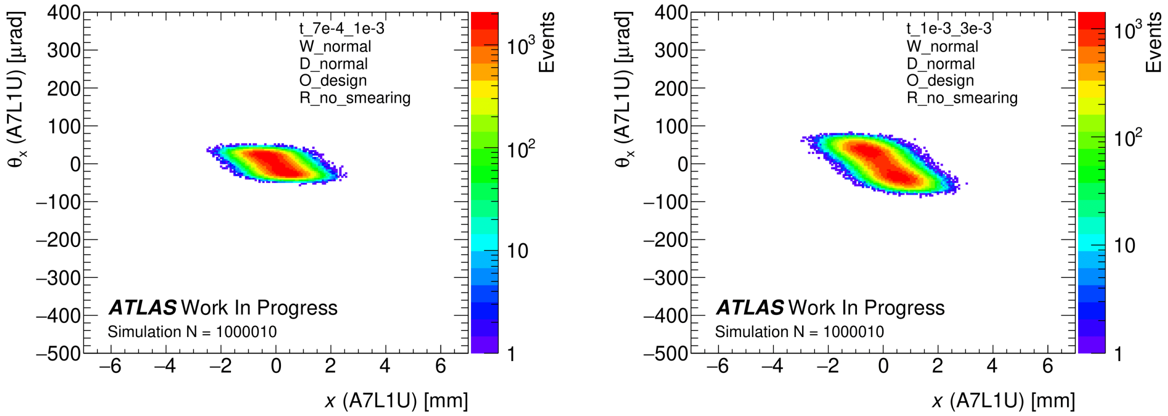

(c) $7{\cdot}10^{-4} < t < 1{\cdot}10^{-3}$ GeV^2. **(d)** $1{\cdot}10^{-3} < t < 3{\cdot}10^{-3}$ GeV^2.

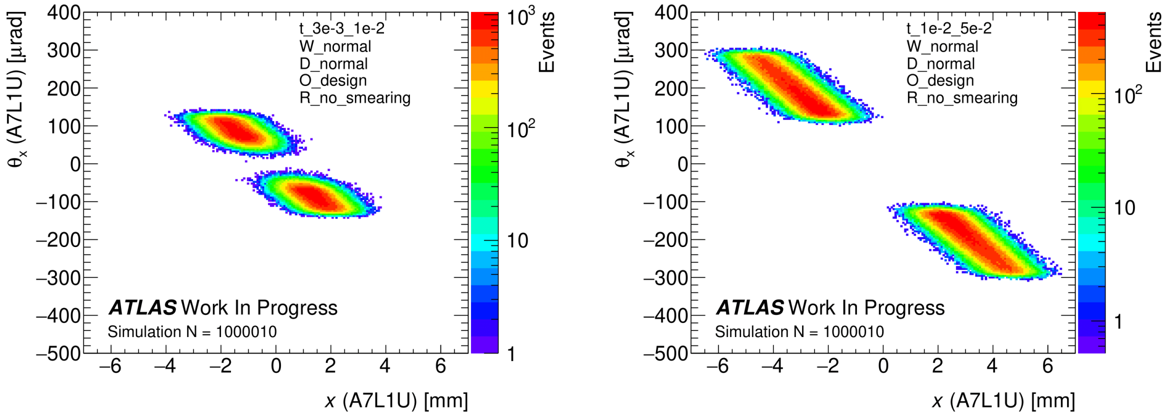

(e) $3{\cdot}10^{-3} < t < 1{\cdot}10^{-2}$ GeV^2. **(f)** $1{\cdot}10^{-2} < t < 5{\cdot}10^{-2}$ GeV^2.

Figure 9.21: Inner detector x-θ_x correlation under variation of the t-range. This is with a nominal beam spot width and divergence, the detector resolution is taken out of the simulation in this study.

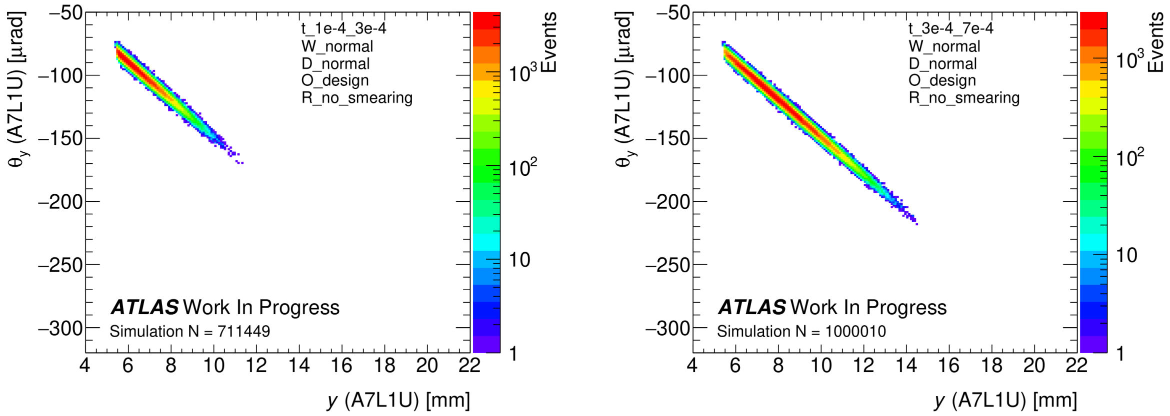

(a) $1{\cdot}10^{-4} < t < 3{\cdot}10^{-4}$ GeV^2.

(b) $3{\cdot}10^{-4} < t < 7{\cdot}10^{-4}$ GeV^2.

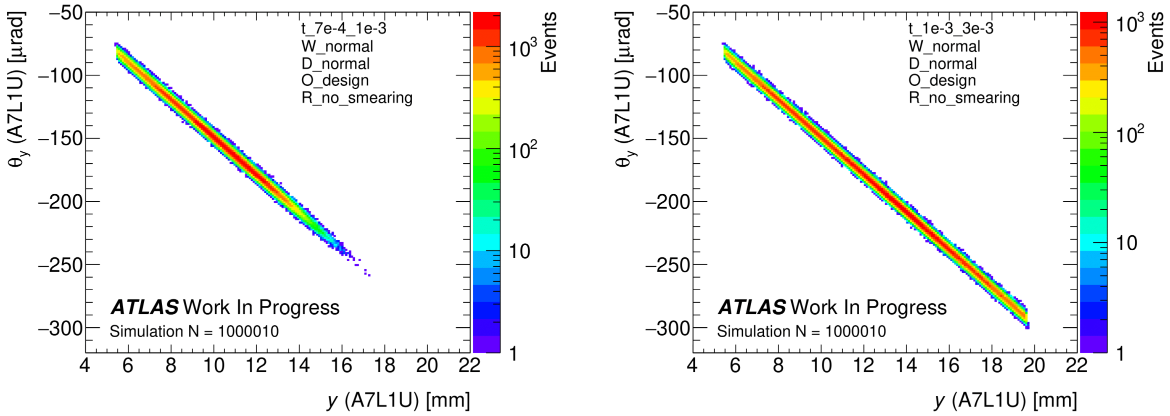

(c) $7{\cdot}10^{-4} < t < 1{\cdot}10^{-3}$ GeV^2.

(d) $1{\cdot}10^{-3} < t < 3{\cdot}10^{-3}$ GeV^2.

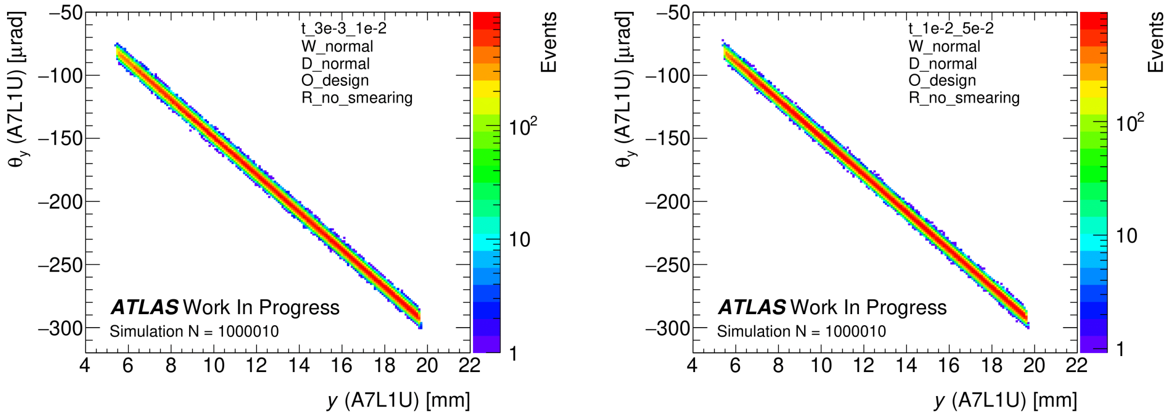

(e) $3{\cdot}10^{-3} < t < 1{\cdot}10^{-2}$ GeV^2.

(f) $1{\cdot}10^{-2} < t < 5{\cdot}10^{-2}$ GeV^2.

Figure 9.22: Inner detector y-θ_y correlation under variation of the t-range. This is with a nominal beam spot width and divergence, the detector resolution is taken out of the simulation in this study.

9.7 Discussion

This chapter is called 'Study of Forward Elastic pp Scattering' and has shown the groundwork of what should result in the analysis of the 900 GeV elastic physics program. A long road remains ahead in preparation of the analysis for a fit to extract the physics parameters. This chapter has contributed to the initial steps and paved the way for further progress. A list on recommended work that the presented material could directly be followed up on is given here:

- In the event selection the beam screen cut currently is set globally but should be adjusted to set it individually per detector. From Figure 9.3 it can be seen that there is a rather significant difference of about 2 mm between the drop in events between inner and outer detectors. Hence the event selection will likely benefit from such a modification.
- The correlation cuts that were used in previous analysis, in particular the ellipse of the x-θ_x correlation does no longer suffice and will have to be replaced by a more optimal shape to better incorporate that off-diagonal ellipse in the inner part of the elastic signal.
- The resolution of the reconstruction methods could be determined using the simulation.
- DPE could be simulated to have a more complete modeling of the background.
- The beam spot width for this run should also be determined using the ALFA detector such that it can be compared with the values from the ATLAS Inner Detector. If this results valid comparison, the ALFA method could used for other runs in which the ATLAS Inner Detector was turned off.
- The normalization of the emittance measurements from the BSRT depends on the presence of wire scans in the data taking periods. A solution should be found for runs in which the lack of wire scans prevents the measurements from the BSRT to be normalized.

Before a final fit can be applied there are several aspects to be accounted for, in addition to the list stated above. Among other things, key features for a precise extraction of the physics parameters include the alignment of the detector, reconstruction efficiency, optics and the integrated luminosity. These are non-trivial tasks that each will demand serious effort from the ALFA collaborators.

9.8 Conclusion

This thesis forms the first study of elastic physics at a center-of-mass energy of 900 GeV with 100 meter optics. A successful data taking campaign in October 2018 led to 12 runs with two different collimation schemes to mitigate background. The schemes are referred to as 'standard 2-stage' and 'crystal supported' collimation and are used during 9 and 3 runs, respectively.

A first look at the data has shown that both schemes resulted in low background levels of the single percent level. The 2-stage collimation has led to background levels of above a percent, whereas the crystal scheme led to just below the percent level. The background shape between the two schemes is slightly different and hence they might need a different approach in the subtraction of the background from the elastic sample.

During all 12 runs the detector showed an overall good performance despite the 4 runs in which ALFA detector 6 was not responding and hence failed to collect data. Therefore, a significant drop in events collected in the corresponding elastic arm resulted in less optimal performance. A look at the collected events showed that the majority of detectors have an average layer efficiency around the expected 90%, with the exception of a few layers in detectors 1 and 6. The status of the detector during the elastic physics program proved to be promising for the analysis that will follow. The additional check on aging and radiation effects currently do not indicate significant deterioration of the detector. The few layers with efficiencies significantly below 90% is likely caused by timing of the electronics.

Two significant experimental effects were observed that indicate dramatic changes to elastic physics encountered by the ALFA community during previous analysis. The first is that the elastic signal in the ALFA detector has a feature in which ellipses is observed in multiple correlation plots. The ellipses have their axis oriented perpendicular to the main axis of events. As a consequence the selection procedure with in particular the x-θ_x cut will have to be revised. A simulation study on the beam spot width has shown that the combination of the IP with the optics can explain the central ellipses observed in the x-correlations. The second is that the convoluted resolution of the ALFA detector system faces significant drop of a factor two compared to previously analysis to a value of 100 μm. Brief calculations have shown that the multiple scattering is dominating over the intrinsic detector resolution at a center-of-mass energy of 900 GeV. The energy is about an order of magnitude lower compared to the previous elastic physics programs and could therefore explain the observed resolution of 100 μm.

This initial study indicated to have an excellent data set in which a well functioning detector has recorded elastic physics with low background levels. New challenges were revealed for the analysis and indicate that the selection cuts and background subtraction will have to be revisited. With a strong physics case and a data set of high quality, the analysis of 900 GeV elastic physics program has a promising perspective and might even include the measurement of the absolute luminosity for ATLAS.

Appendix A

DCS of the SciFi Tracker

A.1 Panels used in DCS Monitoring

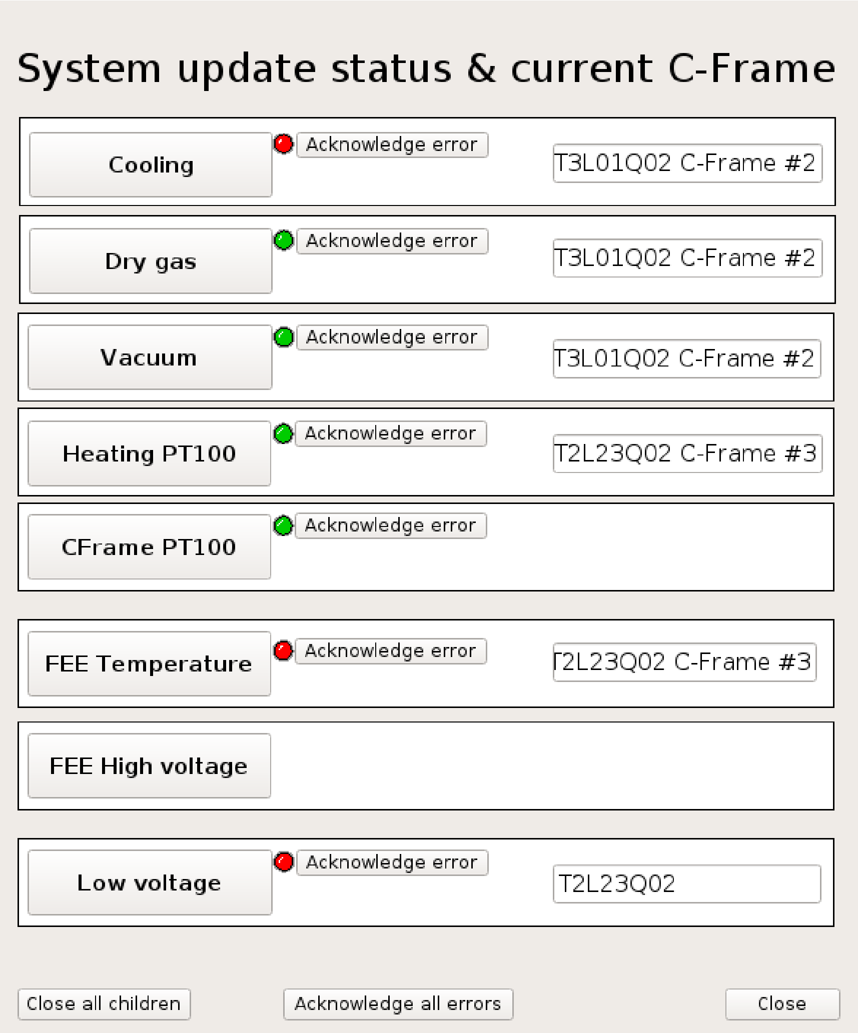

Cooling	🔴 Acknowledge error	T3L01Q02 C-Frame #2
Dry gas	🟢 Acknowledge error	T3L01Q02 C-Frame #2
Vacuum	🟢 Acknowledge error	T3L01Q02 C-Frame #2
Heating PT100	🟢 Acknowledge error	T2L23Q02 C-Frame #3
CFrame PT100	🟢 Acknowledge error	
FEE Temperature	🔴 Acknowledge error	T2L23Q02 C-Frame #3
FEE High voltage		
Low voltage	🔴 Acknowledge error	T2L23Q02

Figure A.1: Parent panel of the monitoring project with all systems.

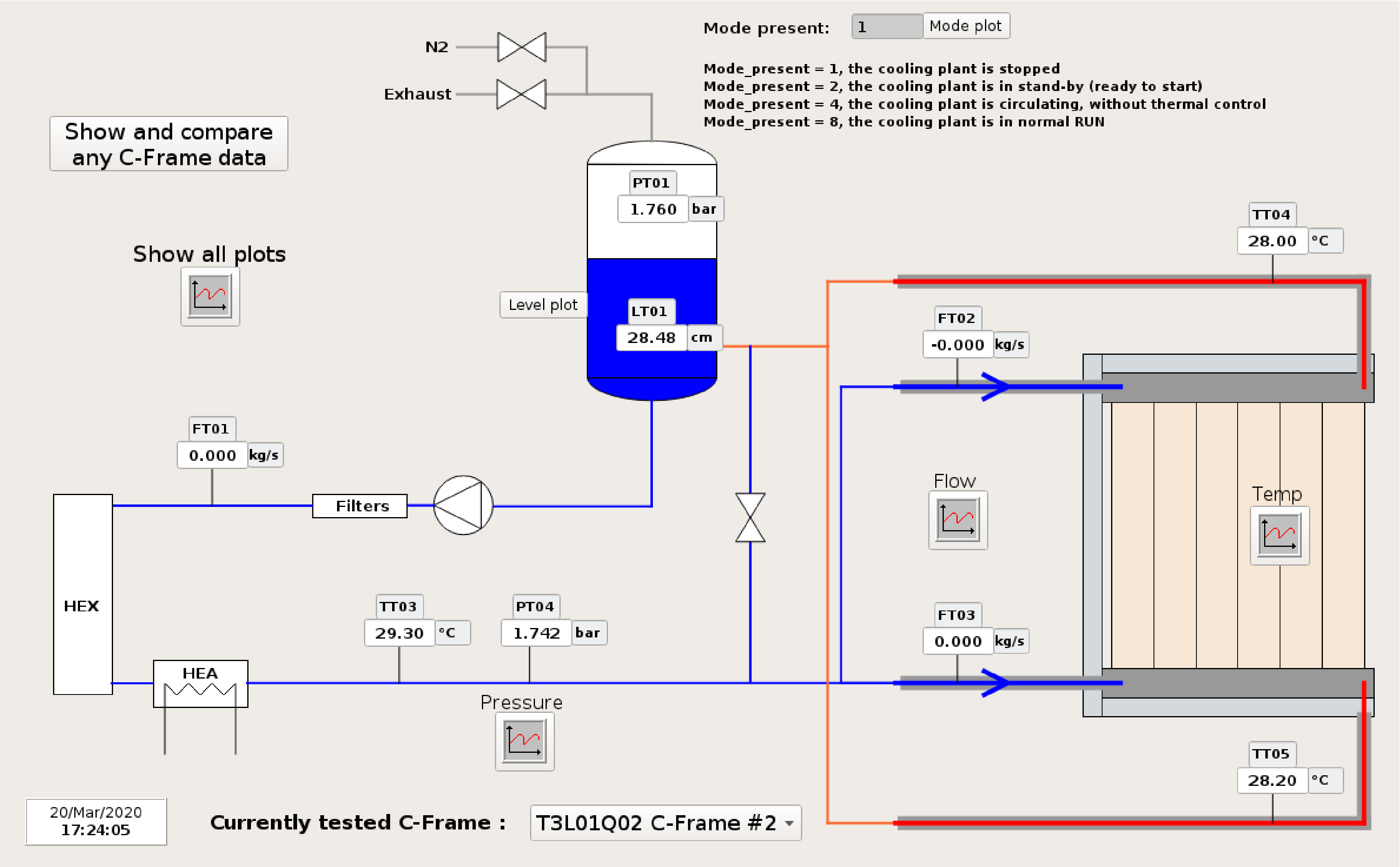

Mode present: 1

Mode_present = 1, the cooling plant is stopped
Mode_present = 2, the cooling plant is in stand-by (ready to start)
Mode_present = 4, the cooling plant is circulating, without thermal control
Mode_present = 8, the cooling plant is in normal RUN

PT01 1.760 bar
LT01 28.48 cm
TT04 28.00 °C
FT02 -0.000 kg/s
FT01 0.000 kg/s
TT03 29.30 °C
PT04 1.742 bar
FT03 0.000 kg/s
TT05 28.20 °C

20/Mar/2020
17:24:05

Currently tested C-Frame : T3L01Q02 C-Frame #2

Figure A.2: Panel of the baby cooling plant attached to a c-frame in the assembly hall.

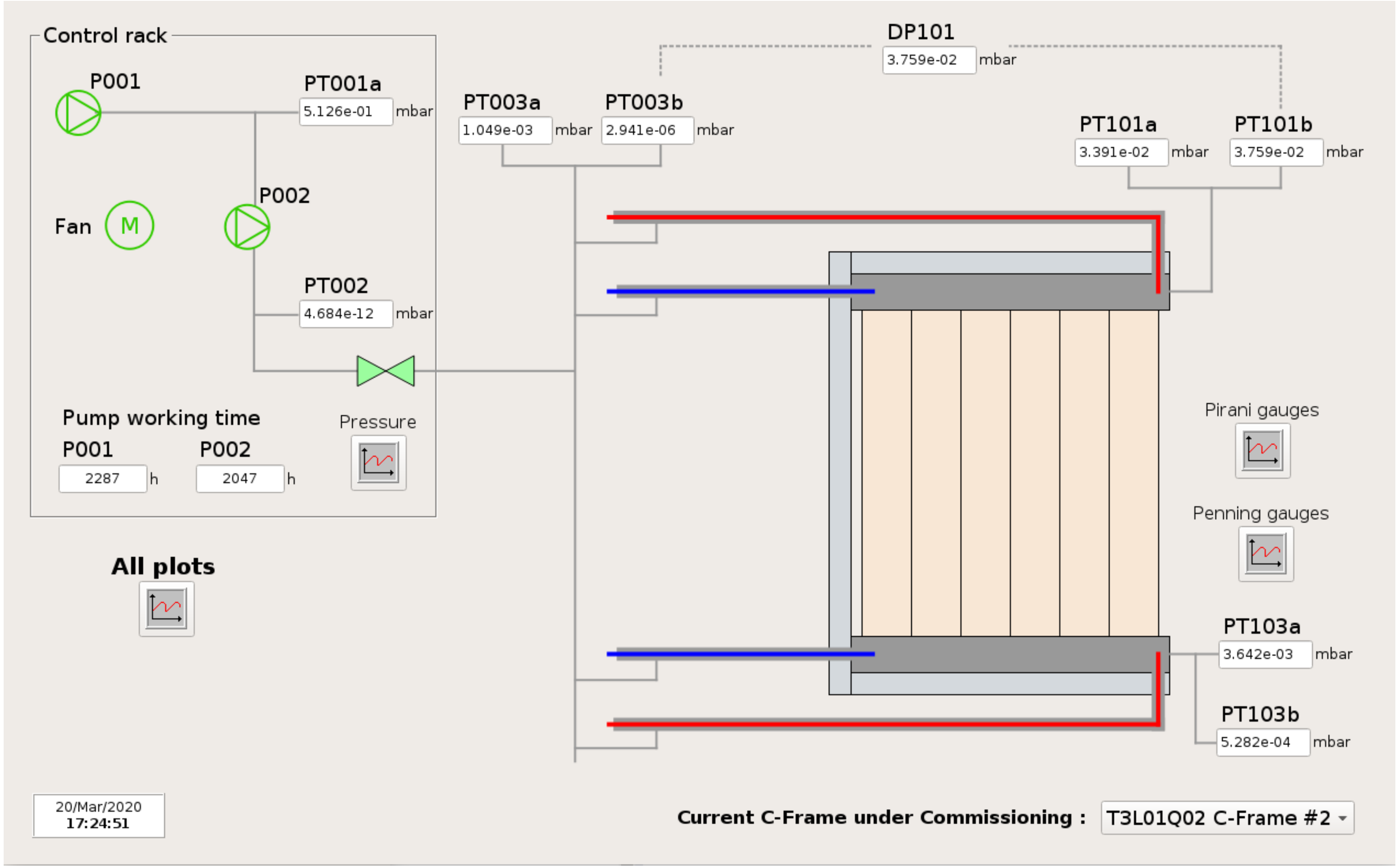

PT001a 5.126e-01 mbar

PT002 4.684e-12 mbar

Pump working time

P001 2287 h

P002 2047 h

DP101 3.759e-02 mbar

PT003a 1.049e-03 mbar

PT003b 2.941e-06 mbar

PT101a 3.391e-02 mbar

PT101b 3.759e-02 mbar

PT103a 3.642e-03 mbar

PT103b 5.282e-04 mbar

20/Mar/2020
17:24:51

Current C-Frame under Commissioning : T3L01Q02 C-Frame #2

Figure A.3: Panel of the vacuum system attached to a c-frame in the assembly hall.

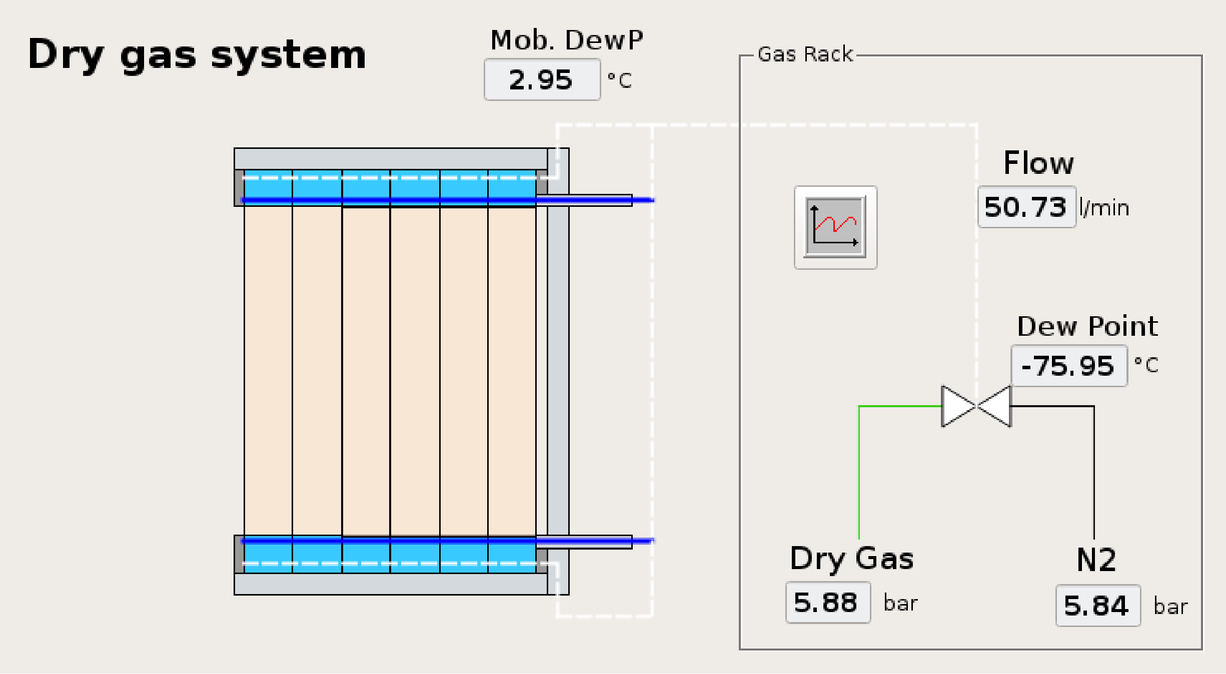

Dry gas system

Mob. DewP 2.95 °C

Gas Rack

Flow 50.73 l/min

Dew Point -75.95 °C

Dry Gas 5.88 bar

N2 5.84 bar

Figure A.4: Panel of the dry gas system and the ambient dew point in the assembly hall..

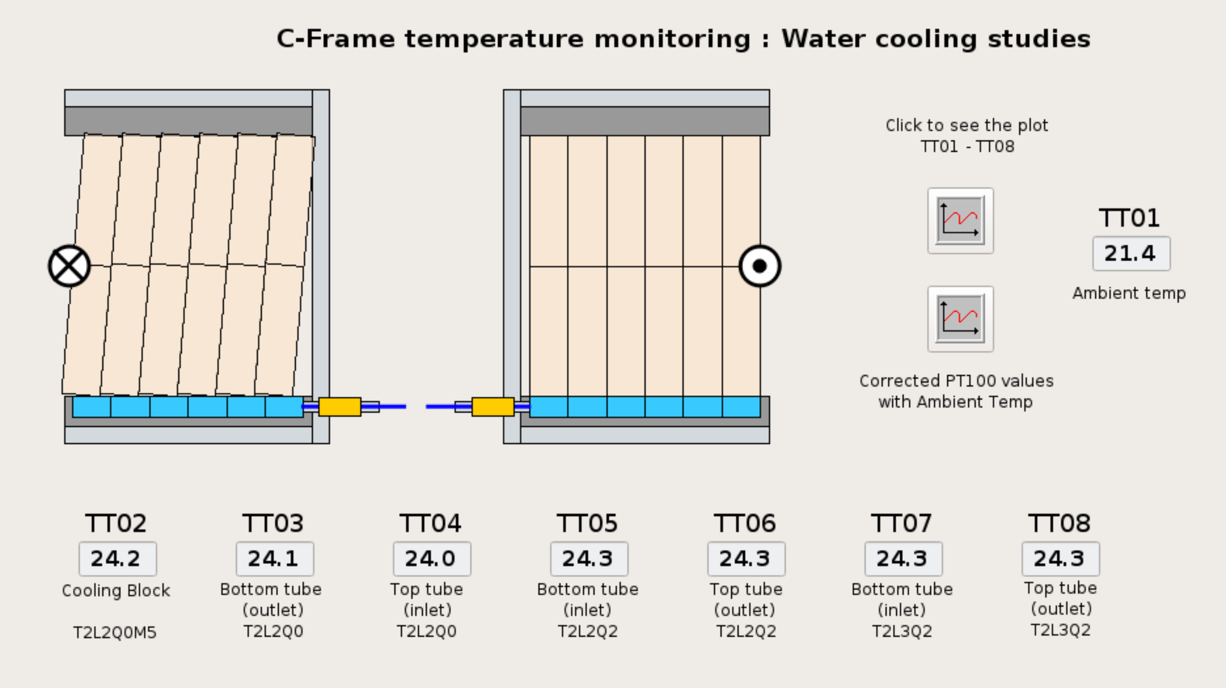

C-Frame temperature monitoring : Water cooling studies

Click to see the plot TT01 - TT08

TT01 21.4 Ambient temp

Corrected PT100 values with Ambient Temp

TT02 24.2 Cooling Block T2L2Q0M5

TT03 24.1 Bottom tube (outlet) T2L2Q0

TT04 24.0 Top tube (inlet) T2L2Q0

TT05 24.3 Bottom tube (inlet) T2L2Q2

TT06 24.3 Top tube (outlet) T2L2Q2

TT07 24.3 Bottom tube (inlet) T2L3Q2

TT08 24.3 Top tube (outlet) T2L3Q2

Figure A.5: Panel of 8 movable PT100 sensors that can be used for temperature studies.

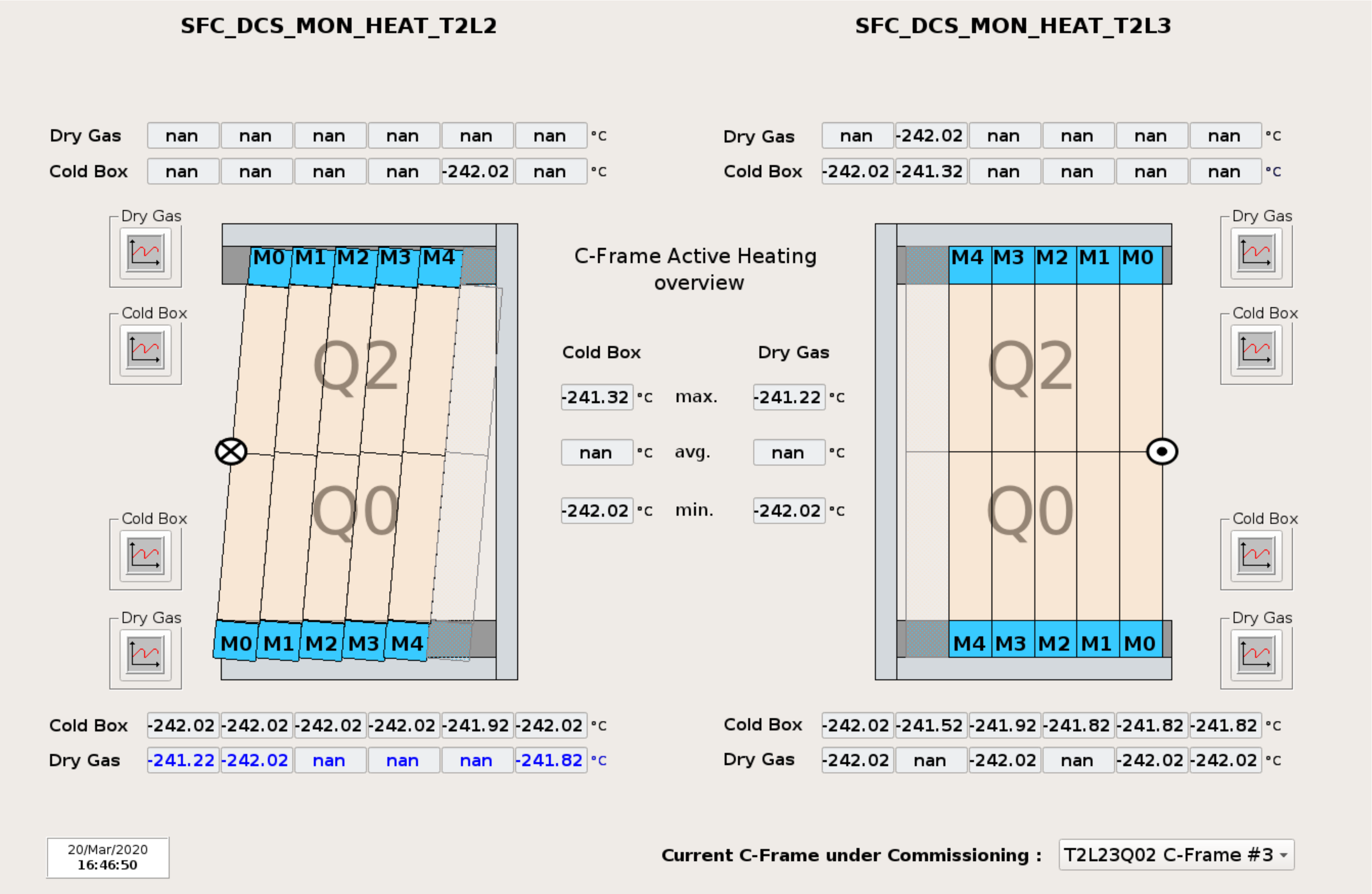

SFC_DCS_MON_HEAT_T2L2

Dry Gas	nan	nan	nan	nan	nan	nan	°C
Cold Box	nan	nan	nan	nan	-242.02	nan	°C

Cold Box	-242.02	-242.02	-242.02	-242.02	-241.92	-242.02	°C
Dry Gas	-241.22	-242.02	nan	nan	nan	-241.82	°C

SFC_DCS_MON_HEAT_T2L3

Dry Gas	nan	-242.02	nan	nan	nan	nan	°C
Cold Box	-242.02	-241.32	nan	nan	nan	nan	°C

Cold Box	-242.02	-241.52	-241.92	-241.82	-241.82	-241.82	°C
Dry Gas	-242.02	nan	-242.02	nan	-242.02	-242.02	°C

C-Frame Active Heating overview

Cold Box			Dry Gas	
-241.32	°C	max.	-241.22	°C
nan	°C	avg.	nan	°C
-242.02	°C	min.	-242.02	°C

20/Mar/2020
16:46:50

Current C-Frame under Commissioning : T2L23Q02 C-Frame #3

Figure A.6: Panel of a c-frame in which temperatures on the top of the cold box shell and dry gas outlet connector are displayed.

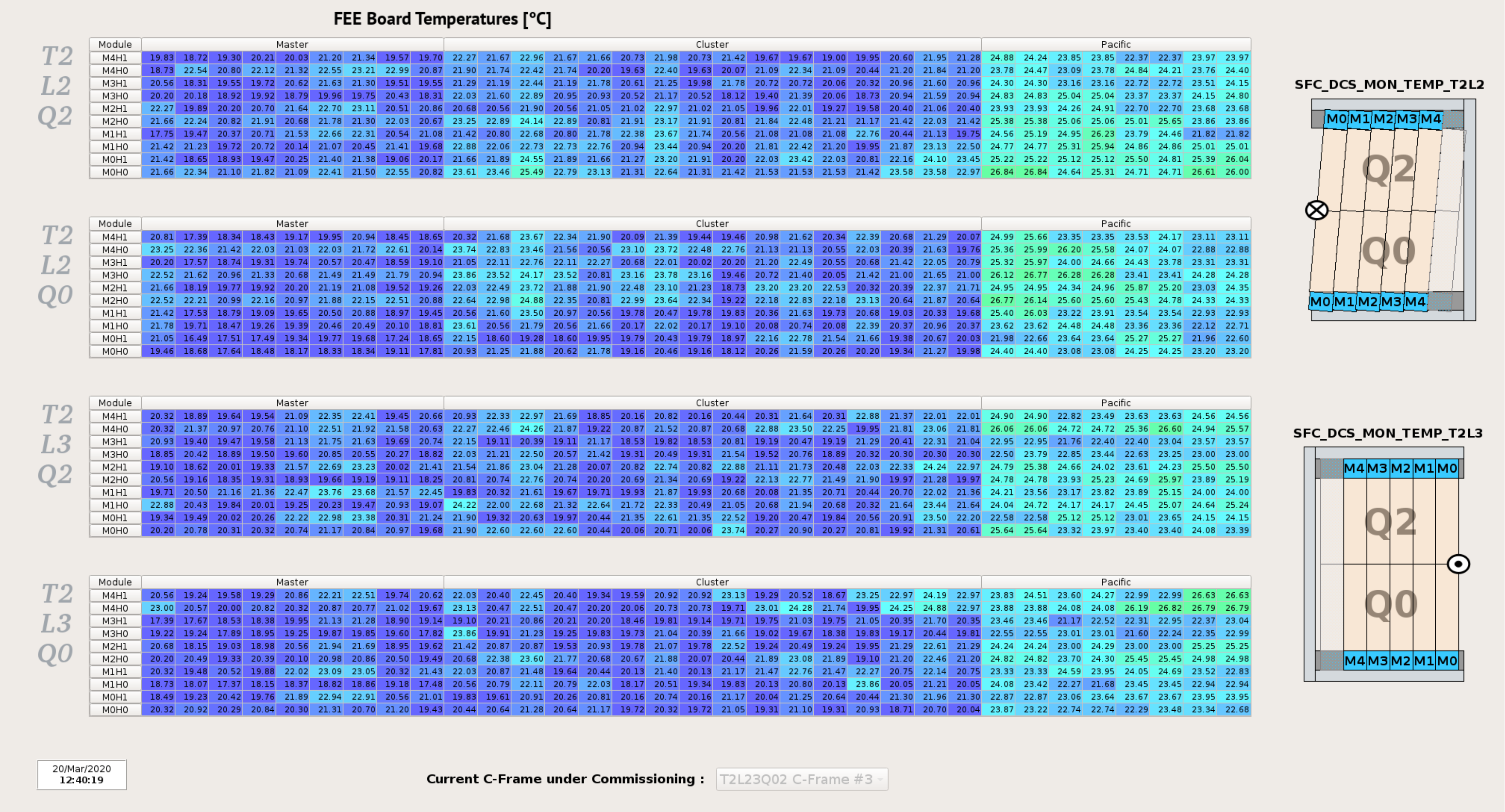

FEE Board Temperatures [°C]

T2 L2 Q2

Module	Master									Cluster																Pacific							
M4H1	19.83	18.72	19.30	20.21	20.03	21.20	21.34	19.57	19.70	22.27	21.67	22.96	21.67	21.66	20.73	21.98	20.73	21.42	19.67	19.67	19.00	19.95	20.60	21.95	21.28	24.88	24.24	23.85	23.85	22.37	22.37	23.97	23.97
M4H0	18.73	22.54	20.80	22.12	21.32	22.55	23.21	22.99	20.87	21.90	21.74	22.42	21.74	20.20	19.63	22.40	19.63	20.07	21.09	22.34	21.09	20.44	21.20	21.84	21.20	23.78	24.47	23.09	23.78	24.84	24.21	23.76	24.40
M3H1	20.56	18.31	19.55	19.72	20.62	21.63	21.30	19.51	19.55	21.29	21.19	22.44	21.19	21.78	20.61	21.25	19.98	21.78	20.72	20.72	20.06	20.32	20.96	21.60	20.96	24.30	24.30	23.16	23.16	22.72	22.72	23.51	24.15
M3H0	20.20	20.18	18.92	19.92	18.79	19.96	19.75	20.43	18.31	22.03	21.60	22.89	20.95	20.93	20.52	21.17	20.52	18.12	19.40	21.39	20.06	18.73	20.94	21.59	20.94	24.83	24.83	25.04	25.04	23.37	23.37	24.15	24.80
M2H1	22.27	19.89	20.20	20.70	21.64	22.70	23.11	20.51	20.86	20.68	20.56	21.90	20.56	21.05	21.02	22.97	21.02	21.05	19.96	22.01	19.27	19.58	20.40	21.06	20.40	23.93	23.93	24.26	24.91	22.70	22.70	23.68	23.68
M2H0	21.66	22.24	20.82	21.91	20.68	21.78	21.30	22.03	20.67	23.25	22.89	24.14	22.89	20.81	21.91	23.17	21.91	20.81	21.84	22.48	21.21	21.17	21.42	22.03	21.42	25.38	25.38	25.06	25.06	25.01	25.65	23.86	23.86
M1H1	17.75	19.47	20.37	20.71	21.53	22.66	22.31	20.54	21.08	21.42	20.80	22.68	20.80	21.78	22.38	23.67	21.74	20.56	21.08	21.08	21.08	22.76	20.44	21.13	19.75	24.56	25.19	24.95	26.23	23.79	24.46	21.82	21.82
M1H0	21.42	21.23	19.72	20.72	20.14	21.07	20.45	21.41	19.68	22.88	22.06	22.73	22.73	22.76	20.94	23.44	20.94	20.20	21.81	22.42	21.20	19.95	21.87	23.13	22.50	24.77	24.77	25.31	25.94	24.86	24.86	25.01	25.01
M0H1	21.42	18.65	18.93	19.47	20.25	21.40	21.38	19.06	20.17	21.66	21.89	24.55	21.89	21.66	21.27	23.20	21.91	20.20	22.03	23.42	22.03	20.81	22.16	24.10	23.45	25.22	25.22	25.12	25.12	25.50	24.81	25.39	26.04
M0H0	21.66	22.34	21.10	21.82	21.09	22.41	21.50	22.55	20.82	23.61	23.46	25.49	22.79	23.13	21.31	22.64	21.31	21.42	21.53	21.53	21.53	21.42	23.58	23.58	22.97	26.84	26.84	24.64	25.31	24.71	24.71	26.61	26.00

T2 L2 Q0

Module	Master									Cluster																Pacific							
M4H1	20.81	17.39	18.34	18.43	19.17	19.95	20.94	18.45	18.65	20.32	21.68	23.67	22.34	21.90	20.09	21.39	19.44	19.46	20.98	21.62	20.34	22.39	20.68	21.29	20.07	24.99	25.66	23.35	23.35	23.53	24.17	23.11	23.11
M4H0	23.25	22.36	21.42	22.03	21.03	22.03	21.72	22.61	20.14	23.74	22.83	23.46	21.56	20.56	23.10	23.72	22.48	22.76	21.13	21.13	20.55	22.03	20.39	21.63	19.76	25.36	25.99	26.20	25.58	24.07	24.07	22.88	22.88
M3H1	20.20	17.57	18.74	19.31	19.74	20.57	20.47	18.59	19.10	21.05	22.11	22.76	22.11	22.27	20.68	22.01	20.02	20.20	21.20	22.49	20.55	20.68	21.42	22.05	20.79	25.32	25.97	24.00	24.66	24.43	23.78	23.31	23.31
M3H0	22.52	21.62	20.96	21.33	20.68	21.49	21.49	21.79	20.94	23.86	23.52	24.17	23.52	20.81	23.16	23.78	23.16	19.46	20.72	21.40	20.05	21.42	21.00	21.65	21.00	26.12	26.77	26.28	26.28	23.41	23.41	24.28	24.28
M2H1	21.66	18.19	19.77	19.92	20.20	21.19	21.08	19.52	19.26	22.03	22.49	23.72	21.88	21.90	22.48	23.10	21.23	18.73	23.20	23.20	22.53	20.32	20.39	22.37	21.71	24.95	24.95	24.34	24.96	25.87	25.20	23.03	24.35
M2H0	22.52	22.21	20.99	22.16	20.97	21.88	22.15	22.51	20.88	22.64	22.98	24.88	22.35	20.81	22.99	23.64	22.34	19.22	22.18	22.83	22.18	23.13	20.64	21.87	20.64	26.77	26.14	25.60	25.60	25.43	24.78	24.33	24.33
M1H1	21.42	17.53	18.79	19.09	19.65	20.50	20.88	18.97	19.45	20.56	21.60	23.50	20.97	20.56	19.78	20.47	19.78	19.83	20.36	21.63	19.73	20.68	19.03	20.33	19.68	25.40	26.03	23.22	23.91	23.54	23.54	22.93	22.93
M1H0	21.78	19.71	18.47	19.26	19.39	20.46	20.49	20.10	18.81	23.61	20.56	21.79	20.56	21.66	20.17	22.02	20.17	19.10	20.08	20.74	20.08	22.39	20.37	20.96	20.37	23.62	23.62	24.48	24.48	23.36	23.36	22.12	22.71
M0H1	21.05	16.49	17.51	17.49	19.34	19.77	19.68	17.24	18.65	22.15	18.60	19.28	18.60	19.95	19.79	20.43	19.79	18.97	22.16	22.78	21.54	21.66	19.38	20.67	20.03	21.98	22.66	23.64	23.64	25.27	25.27	21.96	22.60
M0H0	19.46	18.68	17.64	18.48	18.17	18.33	18.34	19.11	17.81	20.93	21.25	21.88	20.62	21.78	19.16	20.46	19.16	18.12	20.26	21.59	20.26	20.20	19.34	21.27	19.98	24.40	24.40	23.08	23.08	24.25	24.25	23.20	23.20

T2 L3 Q2

Module	Master									Cluster																Pacific							
M4H1	20.32	18.89	19.64	19.54	21.09	22.35	22.41	19.45	20.66	20.93	22.33	22.97	21.69	18.85	20.16	20.82	20.16	20.44	20.31	21.64	20.31	22.88	21.37	22.01	22.01	24.90	24.90	22.82	23.49	23.63	23.63	24.56	24.56
M4H0	20.32	21.37	20.97	20.76	21.10	22.51	21.92	21.58	20.63	22.27	22.46	24.26	21.87	19.22	20.87	21.52	20.87	20.68	22.88	23.50	22.25	19.95	21.81	23.06	21.81	26.06	26.06	24.72	24.72	25.36	26.60	24.94	25.57
M3H1	20.93	19.40	19.47	19.58	21.13	21.75	21.63	19.69	20.74	22.15	19.11	20.39	19.11	21.17	18.53	19.82	18.53	20.81	19.19	20.47	19.19	21.29	20.41	22.31	21.04	22.95	22.95	21.76	22.40	22.40	23.04	23.57	23.57
M3H0	18.85	20.42	18.89	19.50	19.60	20.85	20.55	20.27	18.82	22.03	21.21	22.50	20.57	21.42	19.31	20.49	19.31	21.54	19.52	20.76	18.89	20.32	20.30	20.30	20.30	22.50	23.79	22.85	23.44	22.63	23.25	23.00	23.00
M2H1	19.10	18.62	20.01	19.33	21.57	22.69	23.23	20.02	21.41	21.54	21.86	23.04	21.28	20.07	20.82	22.74	20.82	22.88	21.11	21.73	20.48	22.03	22.33	24.24	22.97	24.79	25.38	24.66	24.02	23.61	24.23	25.50	25.50
M2H0	20.56	19.16	18.35	19.31	18.93	19.66	19.19	19.11	18.25	20.81	20.74	22.76	20.74	20.20	20.69	21.34	20.69	19.22	22.13	22.77	21.49	21.90	19.97	21.28	19.97	24.78	24.78	23.93	25.23	24.69	25.97	23.89	25.19
M1H1	19.71	20.50	21.16	21.36	22.47	23.76	23.68	21.57	22.45	19.83	20.32	21.61	19.67	19.71	19.93	21.87	19.93	20.68	20.08	21.35	20.71	20.44	20.70	22.02	21.36	24.21	23.56	23.17	23.82	23.89	25.15	24.00	24.00
M1H0	22.88	20.43	19.84	20.01	19.25	20.23	19.47	20.93	19.07	24.22	22.00	22.68	21.32	22.64	21.72	22.33	20.49	21.05	20.68	21.94	20.68	20.32	21.64	23.44	21.64	24.04	24.72	24.17	24.17	24.45	25.07	24.64	25.24
M0H1	19.34	19.49	20.02	20.26	22.22	22.98	23.38	20.31	21.24	21.90	19.32	20.63	19.97	20.44	21.35	22.61	21.35	22.52	19.20	20.47	19.84	20.56	20.91	23.50	22.20	22.58	22.58	25.12	25.12	23.01	23.65	24.15	24.15
M0H0	20.20	20.78	20.31	20.32	20.74	21.17	20.84	20.97	19.68	21.90	22.60	22.60	22.60	20.44	20.06	20.71	20.06	23.74	20.27	20.90	20.27	20.81	19.92	21.31	20.61	25.64	25.64	23.32	23.97	23.40	23.40	24.08	23.39

T2 L3 Q0

Module	Master									Cluster																Pacific							
M4H1	20.56	19.24	19.58	19.29	20.86	22.21	22.51	19.74	20.62	22.03	20.40	22.45	20.40	19.34	19.59	20.92	20.92	23.13	19.29	20.52	18.67	23.25	22.97	24.19	22.97	23.83	24.51	23.60	24.27	22.99	22.99	26.63	26.63
M4H0	23.00	20.57	20.00	20.82	20.32	20.87	20.77	21.02	19.67	23.13	20.47	22.51	20.47	20.20	20.06	20.73	20.73	19.71	23.01	24.28	21.74	19.95	24.25	24.88	22.97	23.88	23.88	24.08	24.08	26.19	26.82	26.79	26.79
M3H1	17.39	17.67	18.53	18.38	19.95	21.13	21.28	18.90	19.14	19.10	20.21	20.86	20.21	20.20	18.46	19.81	19.14	19.71	19.75	21.03	19.75	21.05	20.35	21.70	20.35	23.46	23.46	21.17	22.52	22.31	22.95	22.37	23.04
M3H0	19.22	19.24	17.89	18.95	19.25	19.87	19.85	19.60	17.82	23.86	19.91	21.23	19.25	19.83	19.73	21.04	20.39	21.66	19.02	19.67	18.38	19.83	19.17	20.44	19.81	22.55	22.55	23.01	23.01	21.60	22.24	22.35	22.99
M2H1	20.68	18.15	19.03	18.98	20.56	21.94	21.69	18.95	19.62	21.42	20.87	20.87	19.53	20.93	19.78	21.07	19.78	22.52	19.24	20.49	19.24	19.95	21.29	22.61	21.29	24.24	24.24	23.00	24.29	23.00	23.00	25.25	25.25
M2H0	20.20	20.49	19.33	20.39	20.10	20.98	20.86	20.50	19.49	20.68	22.38	23.60	21.77	20.68	20.67	21.88	20.07	20.44	21.89	23.08	21.89	19.10	21.20	22.46	21.20	24.82	24.82	23.70	24.30	25.45	25.45	24.98	24.98
M1H1	20.32	19.48	20.52	19.88	22.02	23.09	23.05	20.32	21.43	22.03	20.87	21.48	19.64	20.44	20.13	21.40	20.13	21.17	21.47	22.76	21.47	22.27	20.75	22.14	20.75	23.33	23.33	24.59	23.95	24.05	24.69	23.52	22.83
M1H0	18.73	18.07	17.37	18.15	18.37	18.82	18.86	19.18	17.48	20.56	20.79	22.11	20.79	22.03	18.17	20.51	19.34	19.83	20.13	20.80	20.13	23.86	20.05	21.21	20.05	24.08	23.42	22.27	21.68	23.45	23.45	22.94	22.94
M0H1	18.49	19.23	20.42	19.76	21.89	22.94	22.91	20.56	21.01	19.83	19.61	20.91	20.26	20.81	20.16	20.74	20.16	21.17	20.04	21.25	20.64	20.44	21.30	21.96	21.30	22.87	22.87	23.06	23.64	23.67	23.67	23.95	23.95
M0H0	20.32	20.92	20.29	20.84	20.30	21.31	20.70	21.20	19.43	20.44	20.64	21.28	20.64	21.17	19.72	20.32	19.72	21.05	19.31	21.10	19.31	20.93	18.71	20.70	20.04	23.87	23.22	22.74	22.74	22.29	23.48	23.34	22.68

20/Mar/2020
12:40:19

Current C-Frame under Commissioning : T2L23Q02 C-Frame #3

Figure A.7: Tabulated front-end board temperatures for a c-frame, arranged per module.

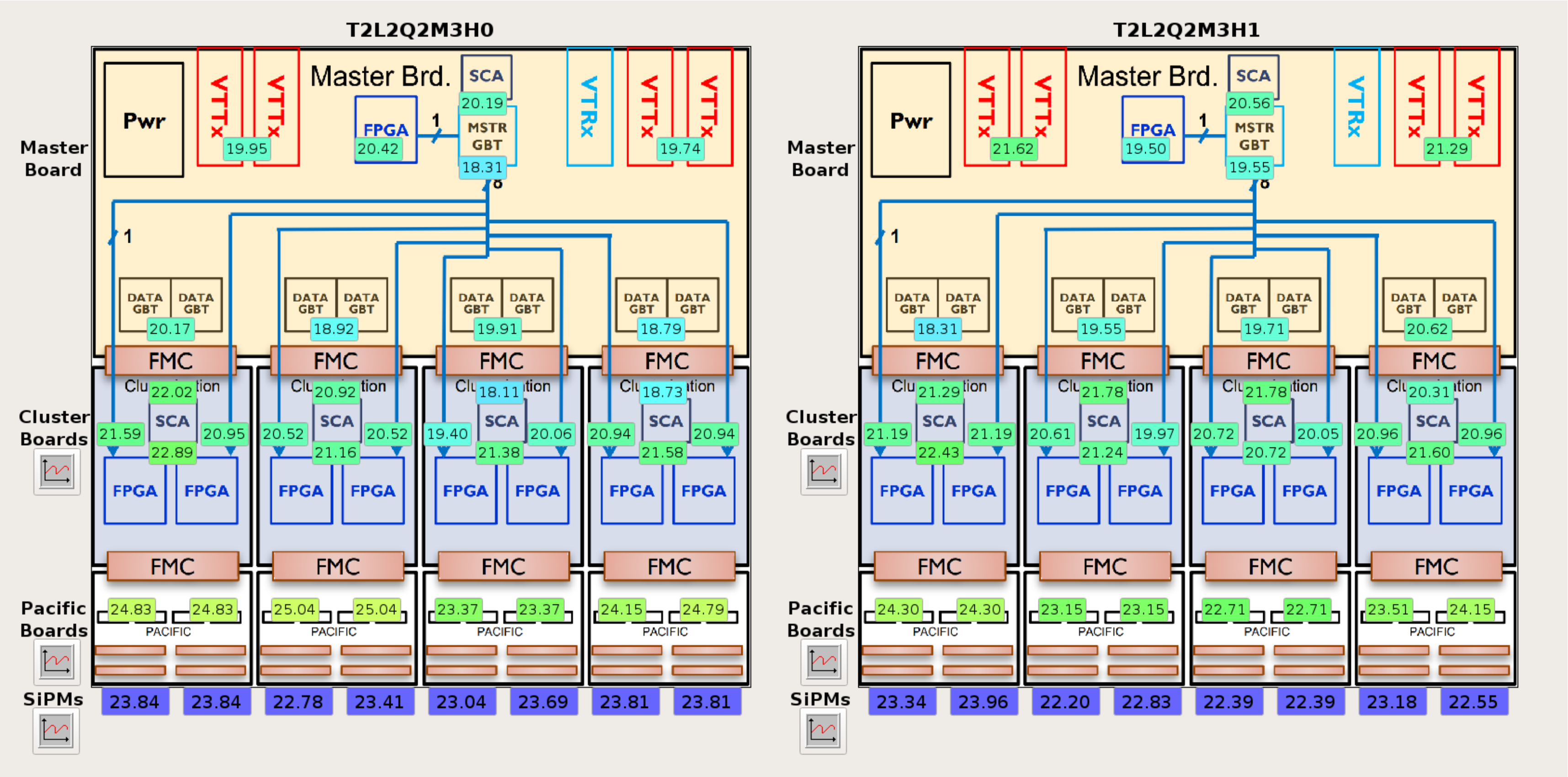

Figure A.8: Overview of the frond-end board temperatures in a read-out box.

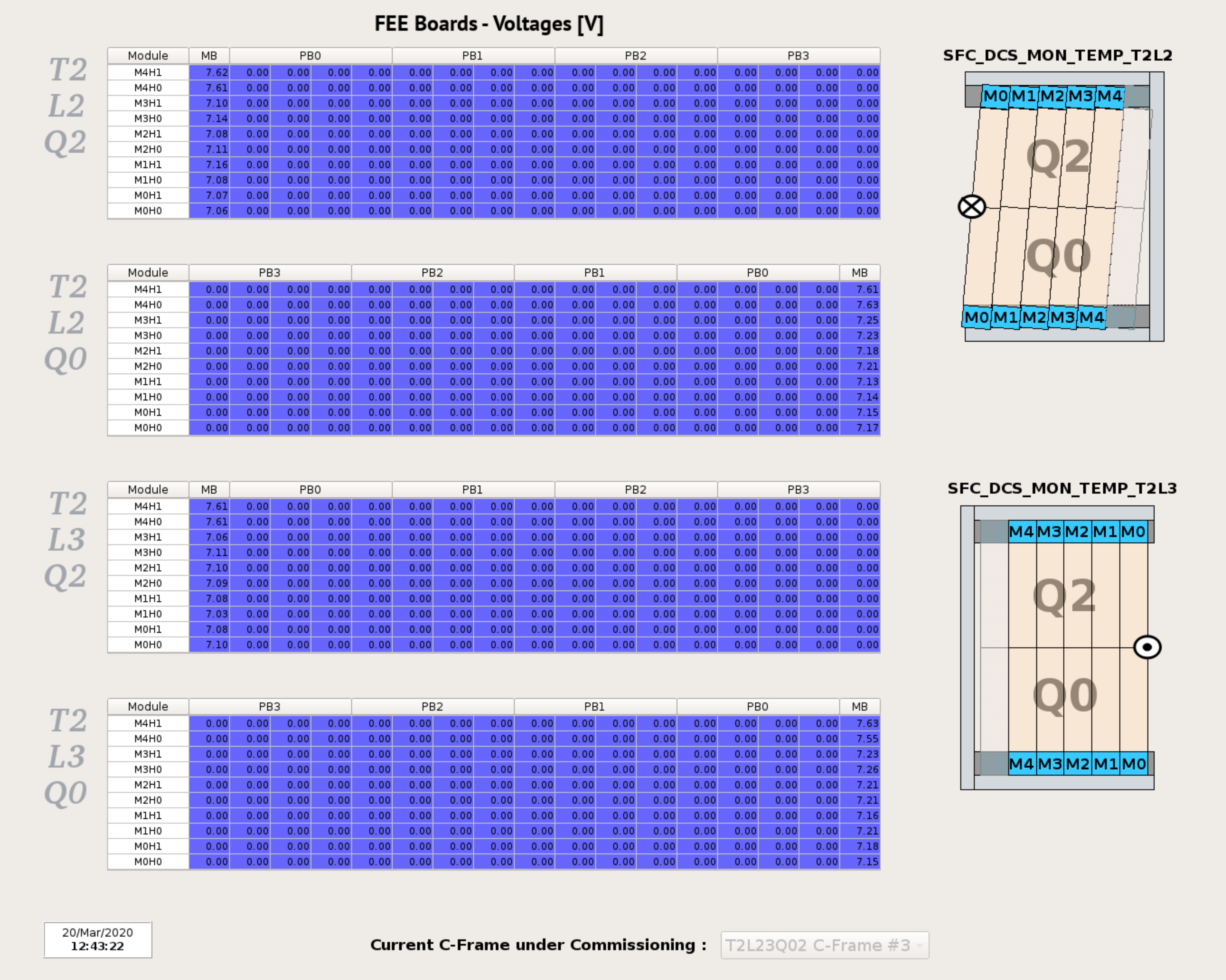

FEE Boards - Voltages [V]

T2
L2
Q2

Module	MB	PB0				PB1				PB2				PB3			
M4H1	7.62	0.00	0.00	0.00	0.00	0.00	0.00	0.00	0.00	0.00	0.00	0.00	0.00	0.00	0.00	0.00	0.00
M4H0	7.61	0.00	0.00	0.00	0.00	0.00	0.00	0.00	0.00	0.00	0.00	0.00	0.00	0.00	0.00	0.00	0.00
M3H1	7.10	0.00	0.00	0.00	0.00	0.00	0.00	0.00	0.00	0.00	0.00	0.00	0.00	0.00	0.00	0.00	0.00
M3H0	7.14	0.00	0.00	0.00	0.00	0.00	0.00	0.00	0.00	0.00	0.00	0.00	0.00	0.00	0.00	0.00	0.00
M2H1	7.08	0.00	0.00	0.00	0.00	0.00	0.00	0.00	0.00	0.00	0.00	0.00	0.00	0.00	0.00	0.00	0.00
M2H0	7.11	0.00	0.00	0.00	0.00	0.00	0.00	0.00	0.00	0.00	0.00	0.00	0.00	0.00	0.00	0.00	0.00
M1H1	7.16	0.00	0.00	0.00	0.00	0.00	0.00	0.00	0.00	0.00	0.00	0.00	0.00	0.00	0.00	0.00	0.00
M1H0	7.08	0.00	0.00	0.00	0.00	0.00	0.00	0.00	0.00	0.00	0.00	0.00	0.00	0.00	0.00	0.00	0.00
M0H1	7.07	0.00	0.00	0.00	0.00	0.00	0.00	0.00	0.00	0.00	0.00	0.00	0.00	0.00	0.00	0.00	0.00
M0H0	7.06	0.00	0.00	0.00	0.00	0.00	0.00	0.00	0.00	0.00	0.00	0.00	0.00	0.00	0.00	0.00	0.00

T2
L2
Q0

Module	PB3				PB2				PB1				PB0				MB
M4H1	0.00	0.00	0.00	0.00	0.00	0.00	0.00	0.00	0.00	0.00	0.00	0.00	0.00	0.00	0.00	0.00	7.61
M4H0	0.00	0.00	0.00	0.00	0.00	0.00	0.00	0.00	0.00	0.00	0.00	0.00	0.00	0.00	0.00	0.00	7.63
M3H1	0.00	0.00	0.00	0.00	0.00	0.00	0.00	0.00	0.00	0.00	0.00	0.00	0.00	0.00	0.00	0.00	7.25
M3H0	0.00	0.00	0.00	0.00	0.00	0.00	0.00	0.00	0.00	0.00	0.00	0.00	0.00	0.00	0.00	0.00	7.23
M2H1	0.00	0.00	0.00	0.00	0.00	0.00	0.00	0.00	0.00	0.00	0.00	0.00	0.00	0.00	0.00	0.00	7.18
M2H0	0.00	0.00	0.00	0.00	0.00	0.00	0.00	0.00	0.00	0.00	0.00	0.00	0.00	0.00	0.00	0.00	7.21
M1H1	0.00	0.00	0.00	0.00	0.00	0.00	0.00	0.00	0.00	0.00	0.00	0.00	0.00	0.00	0.00	0.00	7.13
M1H0	0.00	0.00	0.00	0.00	0.00	0.00	0.00	0.00	0.00	0.00	0.00	0.00	0.00	0.00	0.00	0.00	7.14
M0H1	0.00	0.00	0.00	0.00	0.00	0.00	0.00	0.00	0.00	0.00	0.00	0.00	0.00	0.00	0.00	0.00	7.15
M0H0	0.00	0.00	0.00	0.00	0.00	0.00	0.00	0.00	0.00	0.00	0.00	0.00	0.00	0.00	0.00	0.00	7.17

T2
L3
Q2

Module	MB	PB0				PB1				PB2				PB3			
M4H1	7.61	0.00	0.00	0.00	0.00	0.00	0.00	0.00	0.00	0.00	0.00	0.00	0.00	0.00	0.00	0.00	0.00
M4H0	7.61	0.00	0.00	0.00	0.00	0.00	0.00	0.00	0.00	0.00	0.00	0.00	0.00	0.00	0.00	0.00	0.00
M3H1	7.06	0.00	0.00	0.00	0.00	0.00	0.00	0.00	0.00	0.00	0.00	0.00	0.00	0.00	0.00	0.00	0.00
M3H0	7.11	0.00	0.00	0.00	0.00	0.00	0.00	0.00	0.00	0.00	0.00	0.00	0.00	0.00	0.00	0.00	0.00
M2H1	7.10	0.00	0.00	0.00	0.00	0.00	0.00	0.00	0.00	0.00	0.00	0.00	0.00	0.00	0.00	0.00	0.00
M2H0	7.09	0.00	0.00	0.00	0.00	0.00	0.00	0.00	0.00	0.00	0.00	0.00	0.00	0.00	0.00	0.00	0.00
M1H1	7.08	0.00	0.00	0.00	0.00	0.00	0.00	0.00	0.00	0.00	0.00	0.00	0.00	0.00	0.00	0.00	0.00
M1H0	7.03	0.00	0.00	0.00	0.00	0.00	0.00	0.00	0.00	0.00	0.00	0.00	0.00	0.00	0.00	0.00	0.00
M0H1	7.08	0.00	0.00	0.00	0.00	0.00	0.00	0.00	0.00	0.00	0.00	0.00	0.00	0.00	0.00	0.00	0.00
M0H0	7.10	0.00	0.00	0.00	0.00	0.00	0.00	0.00	0.00	0.00	0.00	0.00	0.00	0.00	0.00	0.00	0.00

T2
L3
Q0

Module	PB3				PB2				PB1				PB0				MB
M4H1	0.00	0.00	0.00	0.00	0.00	0.00	0.00	0.00	0.00	0.00	0.00	0.00	0.00	0.00	0.00	0.00	7.63
M4H0	0.00	0.00	0.00	0.00	0.00	0.00	0.00	0.00	0.00	0.00	0.00	0.00	0.00	0.00	0.00	0.00	7.55
M3H1	0.00	0.00	0.00	0.00	0.00	0.00	0.00	0.00	0.00	0.00	0.00	0.00	0.00	0.00	0.00	0.00	7.23
M3H0	0.00	0.00	0.00	0.00	0.00	0.00	0.00	0.00	0.00	0.00	0.00	0.00	0.00	0.00	0.00	0.00	7.26
M2H1	0.00	0.00	0.00	0.00	0.00	0.00	0.00	0.00	0.00	0.00	0.00	0.00	0.00	0.00	0.00	0.00	7.21
M2H0	0.00	0.00	0.00	0.00	0.00	0.00	0.00	0.00	0.00	0.00	0.00	0.00	0.00	0.00	0.00	0.00	7.21
M1H1	0.00	0.00	0.00	0.00	0.00	0.00	0.00	0.00	0.00	0.00	0.00	0.00	0.00	0.00	0.00	0.00	7.16
M1H0	0.00	0.00	0.00	0.00	0.00	0.00	0.00	0.00	0.00	0.00	0.00	0.00	0.00	0.00	0.00	0.00	7.21
M0H1	0.00	0.00	0.00	0.00	0.00	0.00	0.00	0.00	0.00	0.00	0.00	0.00	0.00	0.00	0.00	0.00	7.18
M0H0	0.00	0.00	0.00	0.00	0.00	0.00	0.00	0.00	0.00	0.00	0.00	0.00	0.00	0.00	0.00	0.00	7.15

20/Mar/2020
12:43:22

Current C-Frame under Commissioning : T2L23Q02 C-Frame #3

Figure A.9: Tabulated frond-end voltages for a c-frame, arranged per module.

A.2 Performance of Services

A.2.1 Cooling Plant Temperature Fluctuations

The figure shows the fluctuations by the cooling plant controls is also sensed at the SiPMs following a small delay[1].

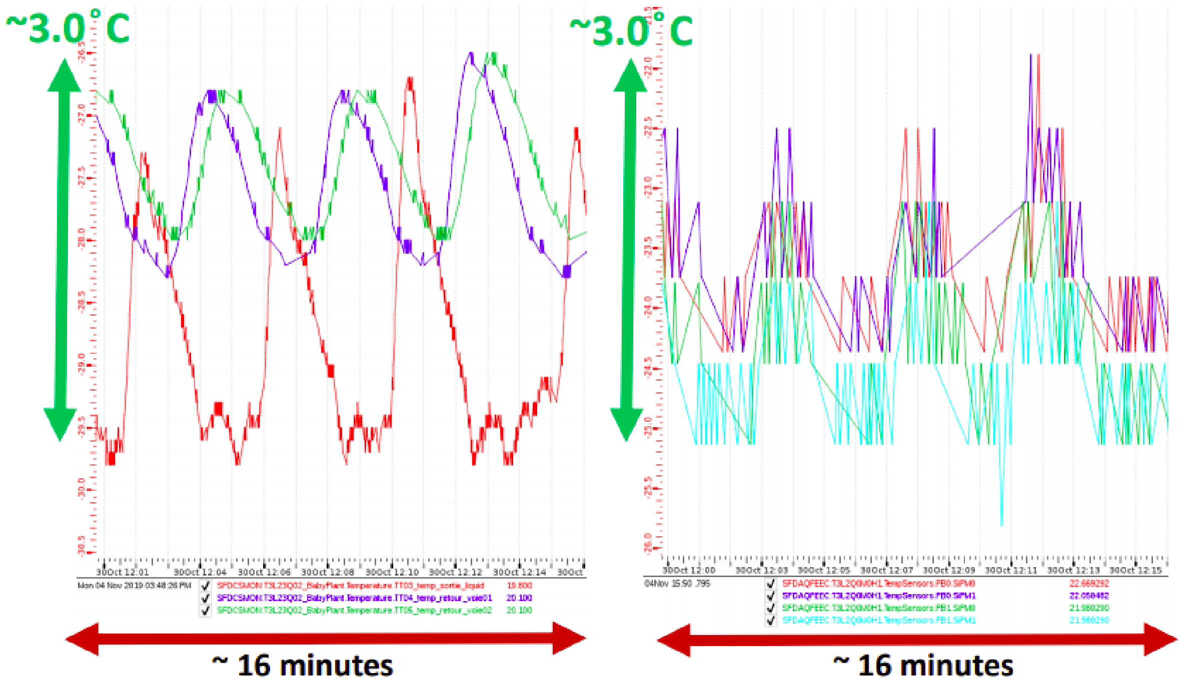

Figure A.10: Left: red the output temperature by the plant and blue/green the return temperature. Right: SiPM temperature that follow the period fluctuation of the cooling plant.

---

[1] https://indico.cern.ch/event/859856/contributions/3620980/attachments/1938817/3213968/SciFi_AssemCoord_JdB_20191105.pdf

A.2.2 Additional Figures on SiPM Temperatures

In Figures A.11 and A.12, the comparison between modules is given for bottom quadrant T3L2Q0. The data for the top and bottom quadrants of layer 3 are shown in Figures A.13 till A.18. These depict the same information as the previous figures for the top quadrantof layer 2, hence the same explanation that was given for layer 2 applies to these figures and can be consulted. The behaviour of layer 2 and layer 3 are very similar and equivalent conclusions can be drawn from all the shown figures for the SiPM quadrant study.

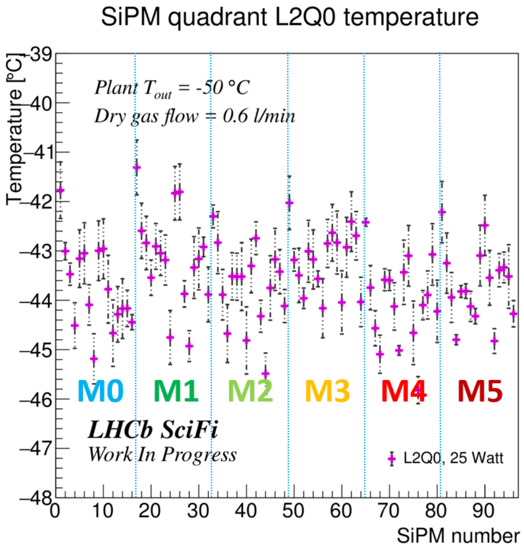

Figure A.11: Temperature dispersion for the SiPM array of quadrant L2Q0.

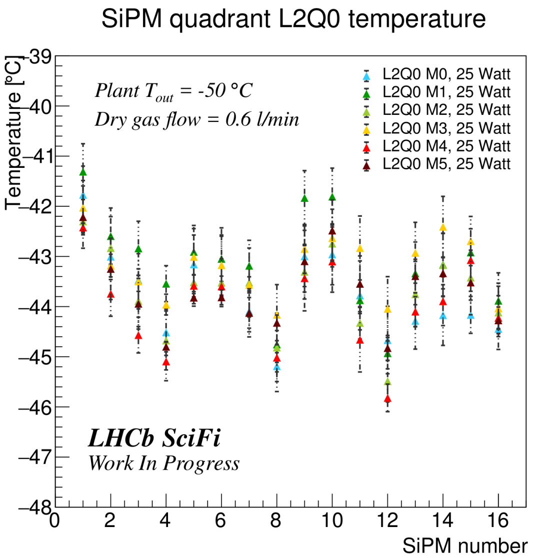

Figure A.12: Temperature dispersion comparison for modules of quadrant L2Q0.

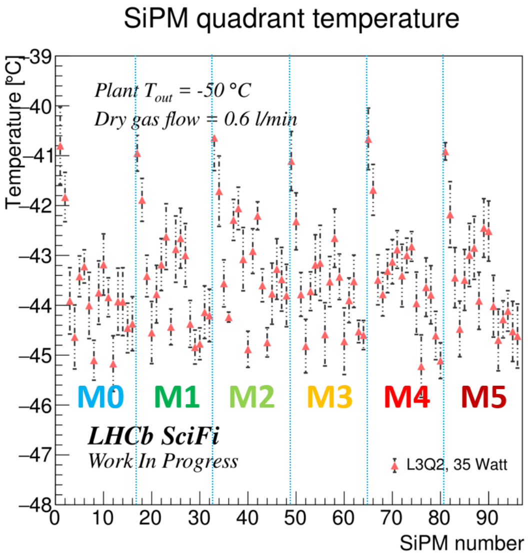

Figure A.13: Temperature dispersion for the SiPM array of quadrant L3Q2.

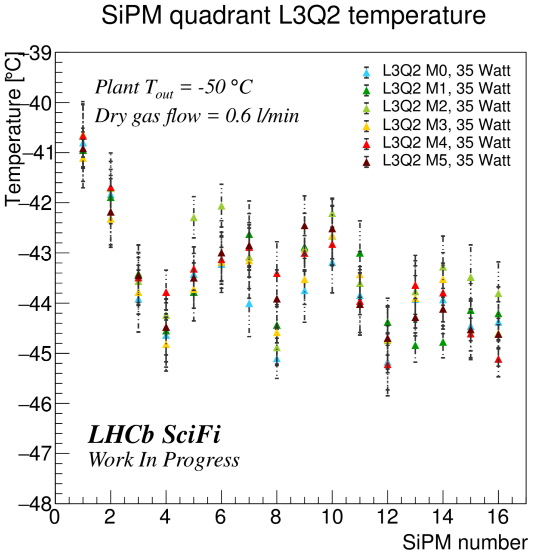

Figure A.14: Temperature dispersion comparison for modules of quadrant L3Q2.

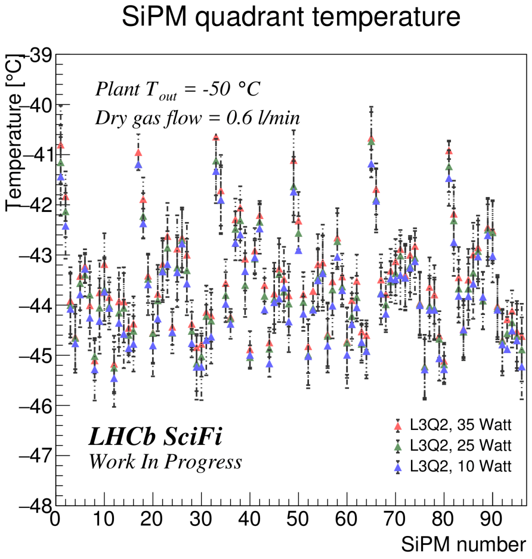

Figure A.15: Temperature dispersion comparison of heating power for quadrant T3L3Q2.

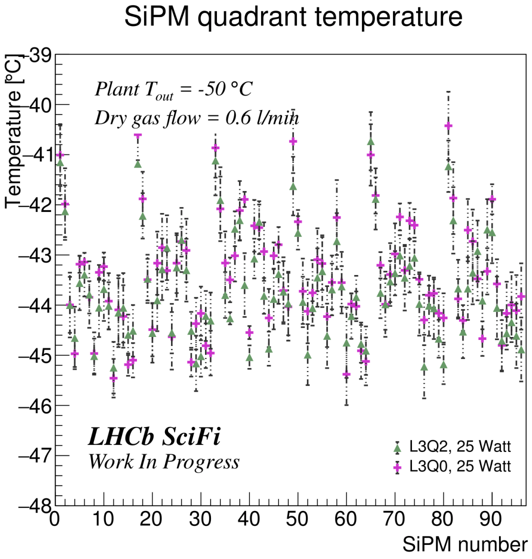

Figure A.16: Temperature dispersion comparison of top/bottom quadrants of layer T3L3.

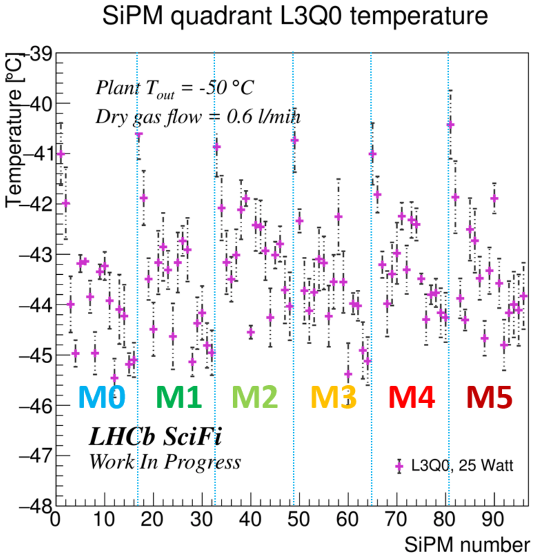

Figure A.17: Temperature dispersion for the SiPM array of quadrant L3Q0.

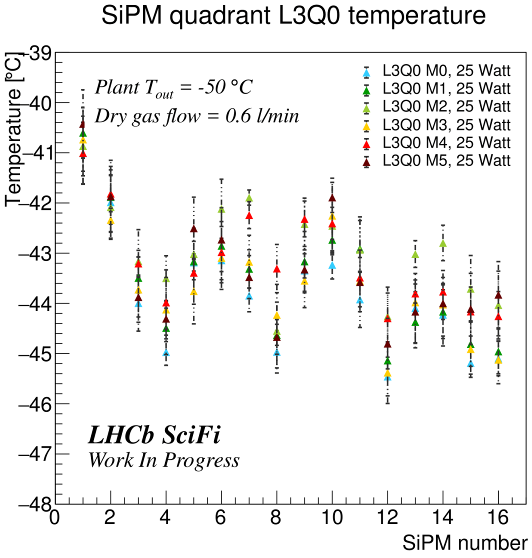

Figure A.18: Temperature dispersion comparison for modules of quadrant L3Q0.

A.2.3 Cooling Tests

A first Novec cooling test was conducted during a period lasting from the 9th till the 11th of July 2019. The dew point in the hall during the test was about +8 °C. The cooling test aims to gradually lower the temperature while monitoring the c-frame. For this test it was aimed to lower the temperature of the SiPMs from around 20 °C to -40 °C by lowering the cooling plant output temperature in steps of 10 degrees. To reach the -40 °C at the SiPMs, the output temperature of the plant should go down to -46 °C. The temperature was lowered five times, when at a plant output temperature of -39 °C serious condensation appeared on the equipment. The condensation heavily affected the dry gas outlets, and also to a less extend the Novec bellows and cold boxes. It was therefore decided to abort the test and heat the system up again to the starting temperature of 20 °C.

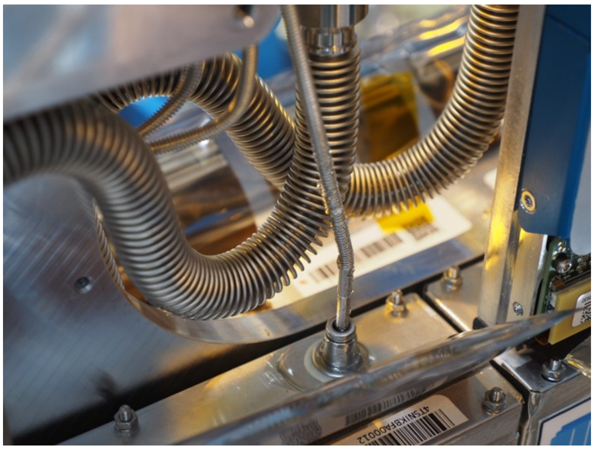

Figure A.19: Condensation forming on dry gas outlet. Photo taken by S. Jakobsen.

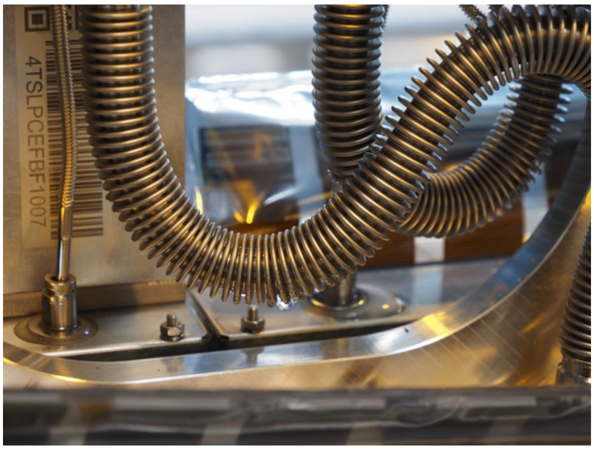

Figure A.20: Condensation forming on Novec bellow. Photo taken by S. Jakobsen.

Investigating the cause of the appearance of condensation led to several suggested ideas. Several movable PT100 temperature sensors were placed on the cold boxes, dry gas bellows and Novec bellows to monitor the temperature on the affected parts. There was no condensation observed on the dry gas bellows when performing a similar test on the prototype, for which plastic dry gas bellows were used. A possible explanation may be that the dew point at the time of the prototype test was lower. Before a second cooling test was performed, several modifications were done to some of the modules to check if this would positively affect the condensation problem. Among other things, the stainless steel dry gas out bellow was replaced with a plastic one, a plastic one covered with aluminium tape, an isolated one and one surrounded by knitted copper connected to water pipes to created a heat sink, which was also done for a Novec bellow.

A the second Novec cooling test was conducted during the 17th and 18th of July 2019. The dew point in the hall during the test was about +11 °C. The cooling plant output temperature was lowered from 20 °C to -46 °C in four steps. The several modifications to both the dry gas outlet as well as the Novec bellow did not result in a clear solution to prevent from condensation to appear. A thermal camera was used this time to inspect the temperatures on the Novec bellows. With the thermal camera, local cold points called ’cold spots’, that appeared on almost all Novec bellows were made visual. These cold spots were mainly observed to be in the bent section of the Novec bellows, which can be seen in two pictures from the thermal camera in Figures A.21 and A.22. The cold spots are depicted by the (dark) purple color in both pictures.

Figure A.22 shows on the left the cold spots on the Novec bellow and on the right the cold dry gas outlet. This supported the idea that the inner bellow does (nearly) touch the outer bellow at these points. During an X-ray campaign on 22nd and 23rd of October, the Novec bellows were X-rayed under various conditions. First, at a cooling temperature of -46 °C, it showed that all inner bellows were touching the outer one. No significant change was observed by reducing the Novec pressure. And again at room temperature, for which only minor difference was found between with and without vacuum. Extra length was added to an outer bellow and this proved to be a promising solution, although not enough length was added at that point. Then it was decided to stretch the outer bellows to obtain extra length. During a second X-ray campaign it was shown that this was an effective method against the cold spots on the Novec bellows. The inner bellow was now placed more centrally, not touching the outer bellow anymore in the curved part. The X-rays showed that the outer bellow should be stretched even a little bit extra to obtain an even more optimal length. It has to noted that no stretching was applied to the Novec bellows of the first c-frame, as it was already assembled at that time.

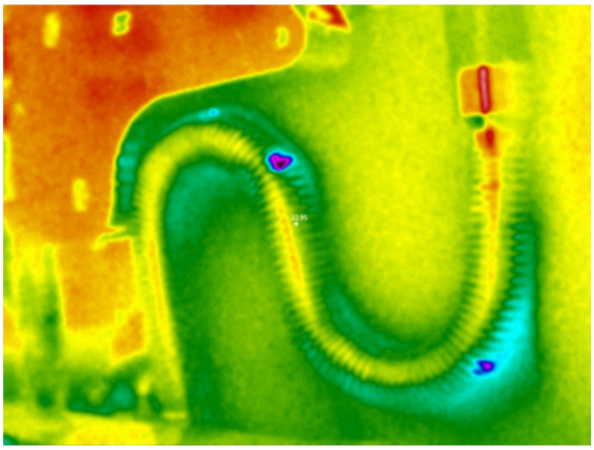

Figure A.21: Thermal picture taken during the second cooling test of C-Frame 1.

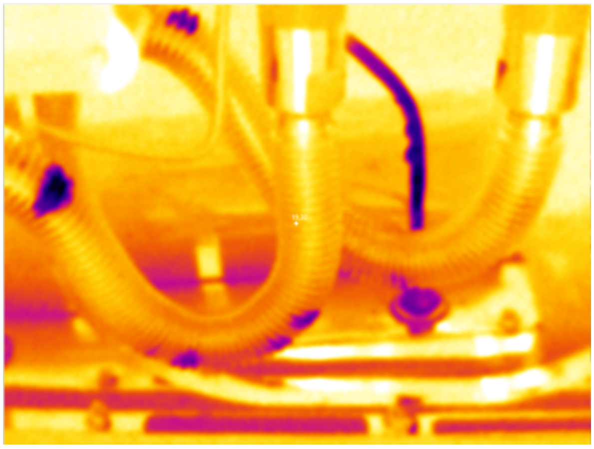

Figure A.22: Thermal picture taken during the second cooling test of c-frame 1.

During the second Novec cooling test the following temperatures on the most affected were measured with the 8 installed PT100 sensors :

- Dry gas outlet connector : 16 °C below air temperature
- Novec bellow : 7 °C below air temperature
- Cold box : 8 °C below air temperature

The implementation of another round of modifications was focused on modification to the Novec bellows, for which the vacuum temporarily needed to be broken. These modifications implied, amongst other things, that the Novec bellow was packed in knitted copper, isolated, packed in aluminum tape and the use of a plastic support to fix the bellow. Knitted copper connected to the mounting plate or water pipes was used on the top of the cold box to create a heat sink. Unfortunately, during the third Novec cooling test, it was observed that also neither of these modifications prevented from condensation to appear on the parts. Additionally, the water cooling temperature was raised from 20 °C to 25 °C, but this did not lead to a significant improvement.

None of the efforts were effective enough to prevent from condensation to emerge. The attempted modifications are all methods to prevent from humid air to condensate on cold parts of the system. This is done through either transferring heat to the most affected parts or prevent from humid air to be directly in contact with the most cold parts. As such they could be considered as passive methods in the prevention from condensation. Since these attempts did not lead to a solution, it was decided to test active heating as a possible solution.

A very brief study with active heating followed with a heating wire that was around at the time. A cold box, two Novec bellows and a dry gas outlet were equipped with heating wire. A total of about 25 W of power was then supplied, such that the each part reached a temperature in the range of 20 °C to 25 °C. All the condensation disappeared and no cold spots could be observed anymore with a thermal camera. Then a Kapton isolated heating wire was selected among several heating wires. The wire is from MWS wire industries Twistite$^{\mathrm{TM}}$, type 2/36 QPN twisted pair of wires with Kapton insulation. The thickness with isolation is 0.065 mm per wire and 0.13 mm for the twisted pair. That it consists of a twisted pair means it has a build-in redundancy: if one wire break still half of the power can be supplied to the parts.

The first test with the Kapton insulated wire involved three module ends, each supplied with 12 meters of wire, this time the length was divided differently for each module end over the coldbox, dry gas bellow outlet and Novec bellow. The first heating test was conducted during the 3rd and 4th of September 2019. The Novec cooling temperature during the test was put to a temperature of -46 °C, to reach -40 °C on the SiPMs. The power supplied per module end was 10 W and was later also briefly raised to 15 W. The test showed that the distribution of the heating wire of the three parts was not perfect yet which lead to overheating of the dry gas outlets, reaching 3 to 18 °C above the air temperature. It further showed that the cold box temperature was within 3 to 4 °C to the air temperature. The fast temperature drop after turning of the heating power means the heat dissipates quickly.

A second test followed for which the module end was wrapped with 14 meters of wire, the distribution of wire over the parts was changed according to the experience from the first wire test. Again, the Novec cooling temperature during the test was put to a temperature of -46 °C, to reach -40 °C on the SiPMs. During the test on the 9th of September 2019, the supplied heating power was adjusted from the initial 15 W to 20 W and later to 25 W. During the period in which the supplied heat was 25 W, all three parts wrapped in wire reached a temperature above room temperature. Then the Novec cooling was stopped to observe what temperatures would be reached without cooling. The maximum temperatures observed were 30 °C for the cold box and 36 °C for the dry gas outlet, temperatures that are not critical to the detector.

Appendix B

Study of Forward Elastic *pp* Scattering

B.1 Spatial detector efficiencies

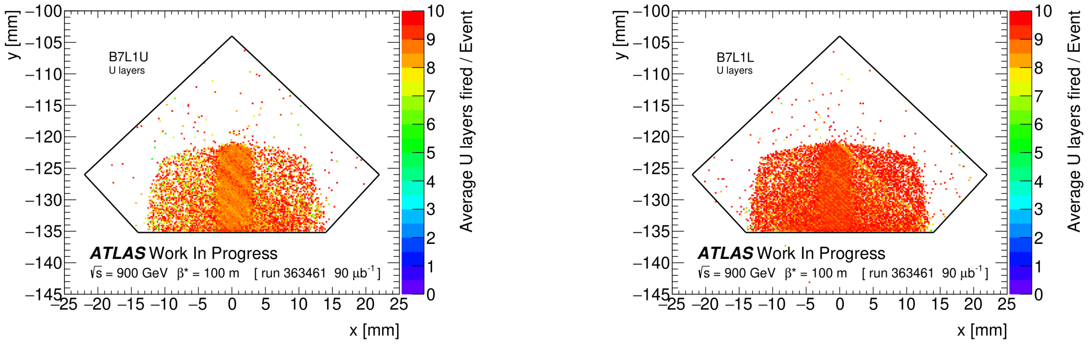

(a) Detector B7L1U.

(b) Detector B7L1L.

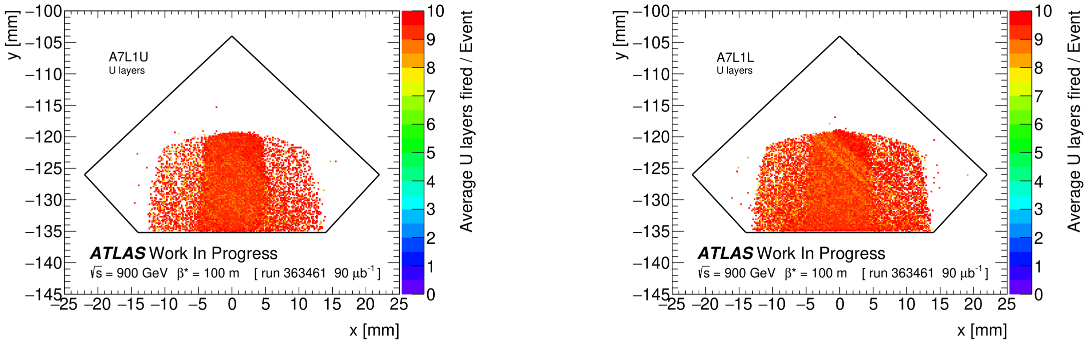

(c) Detector A7L1U.

(d) Detector A7L1L.

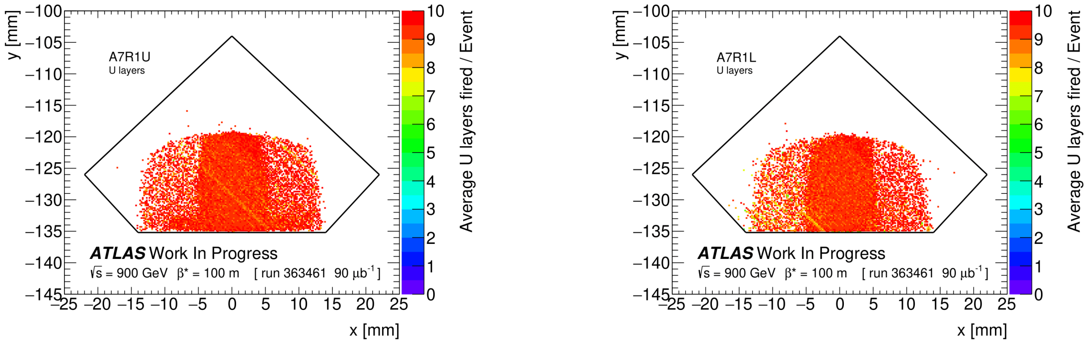

(e) Detector A7R1U.

(f) Detector A7R1L.

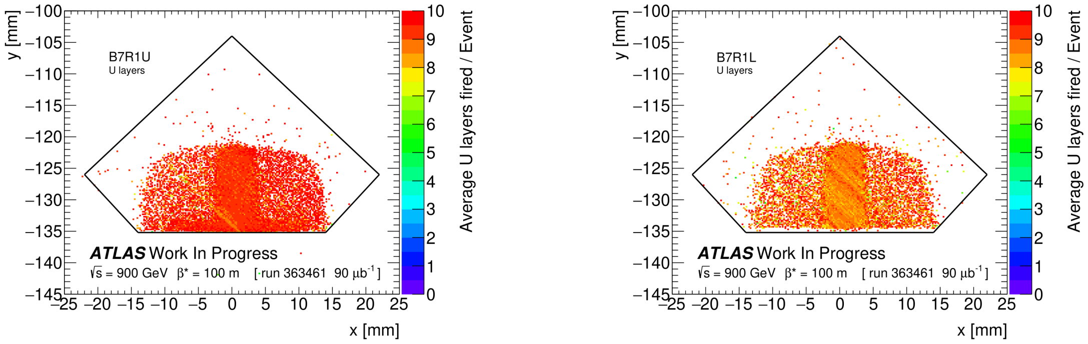

(g) Detector B7R1U.

(h) Detector B7R1L.

Figure B.1: Spatial track efficiency for all U-layers elastic triggered events.

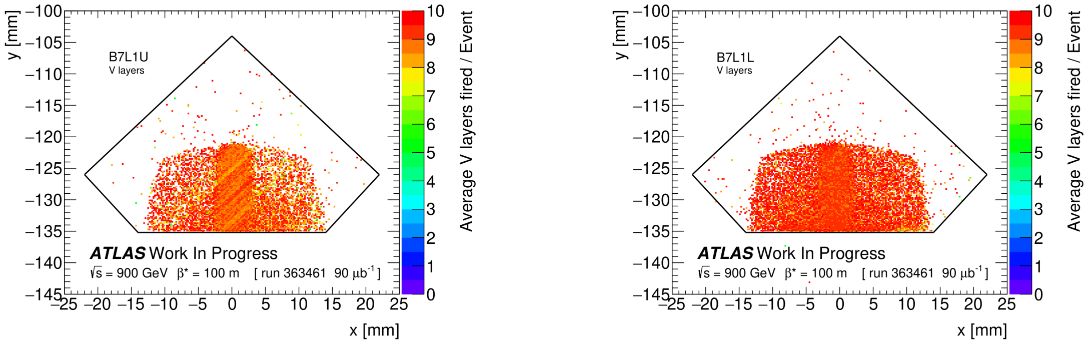

(a) Detector B7L1U.

(b) Detector B7L1L.

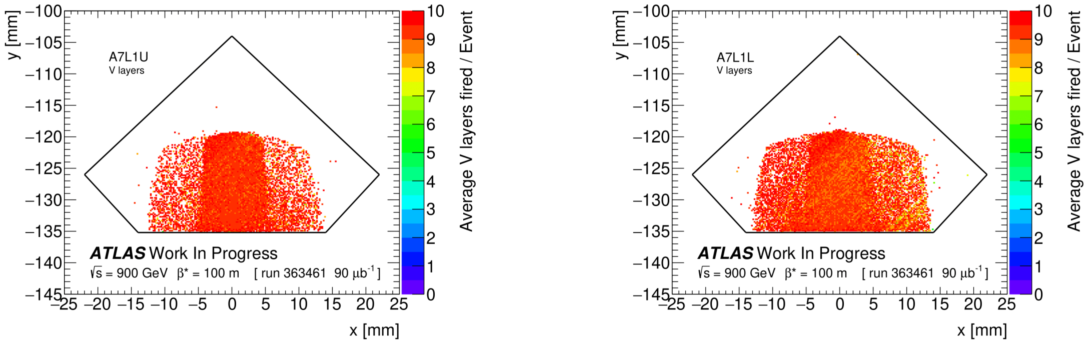

(c) Detector A7L1U.

(d) Detector A7L1L.

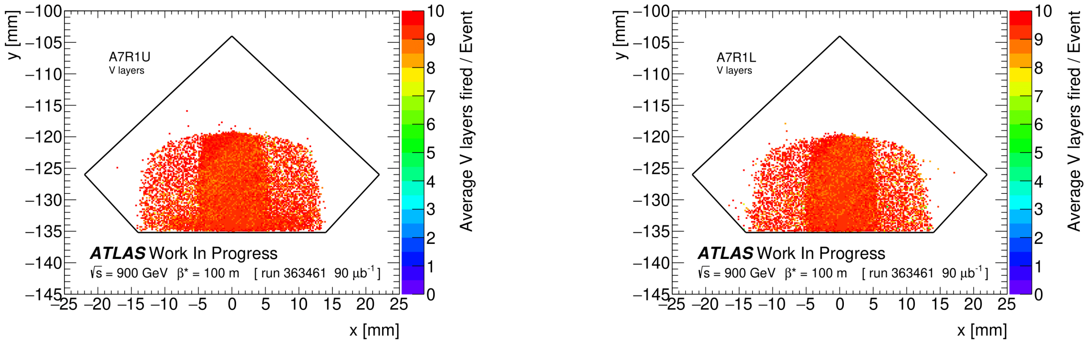

(e) Detector A7R1U.

(f) Detector A7R1L.

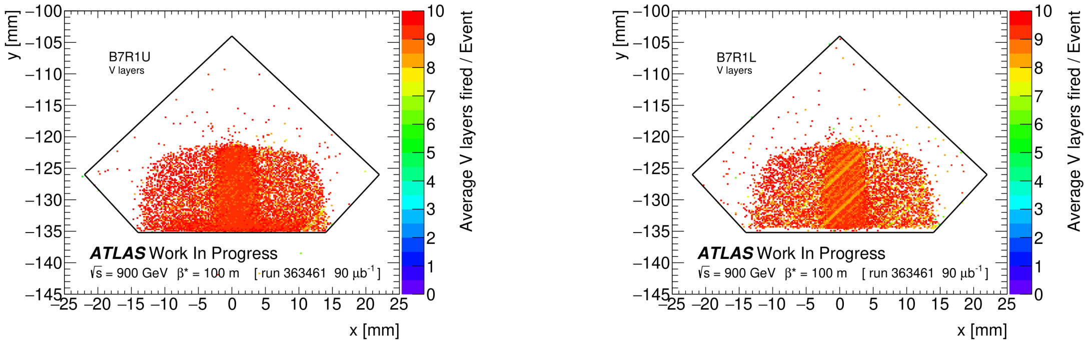

(g) Detector B7R1U.

(h) Detector B7R1L.

Figure B.2: Spatial track efficiency for all V-layers elastic triggered events.

B.2 Spatial layer efficiencies

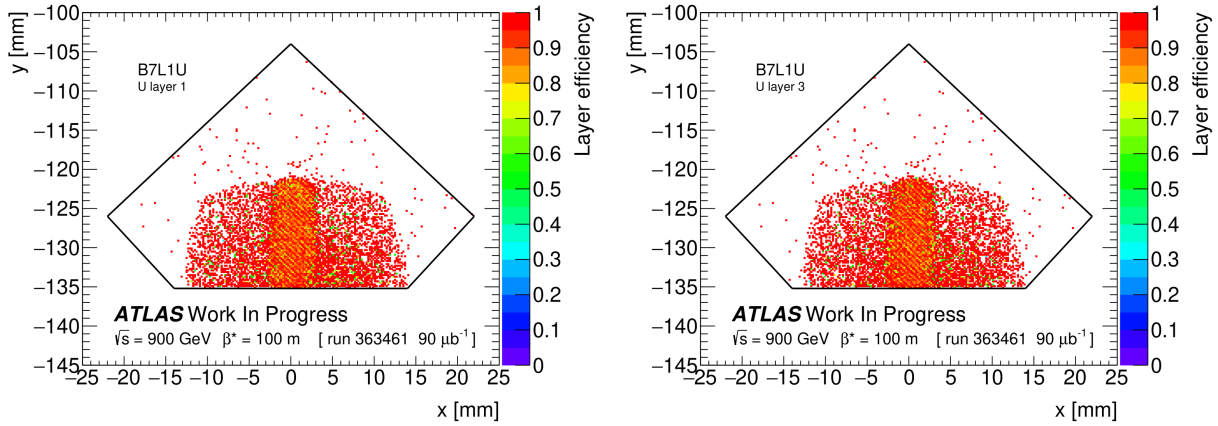

(a) U layer 1.

(b) U layer 3.

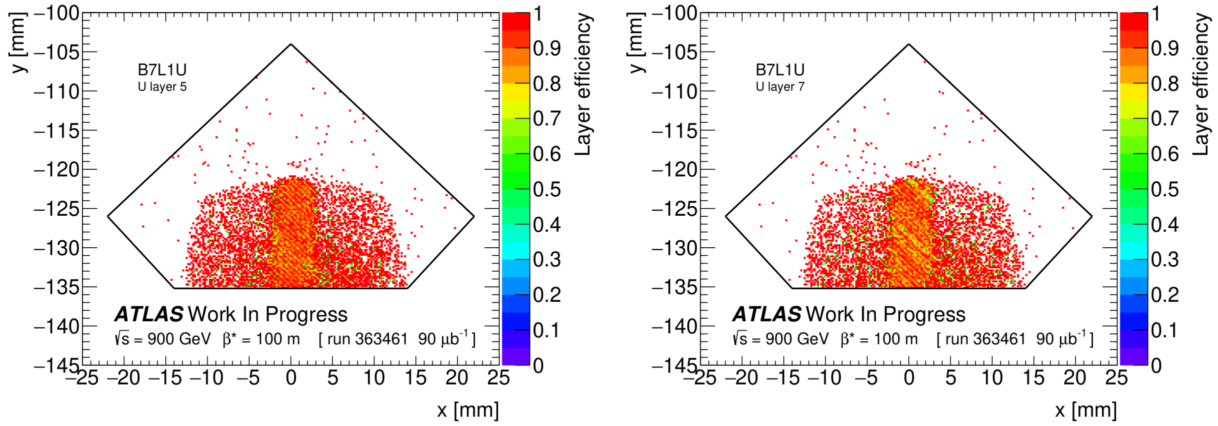

(c) U layer 5.

(d) U layer 7.

Figure B.3: B7L1U: spatial layer efficiency in the U-plane for tracks with elastic triggers.

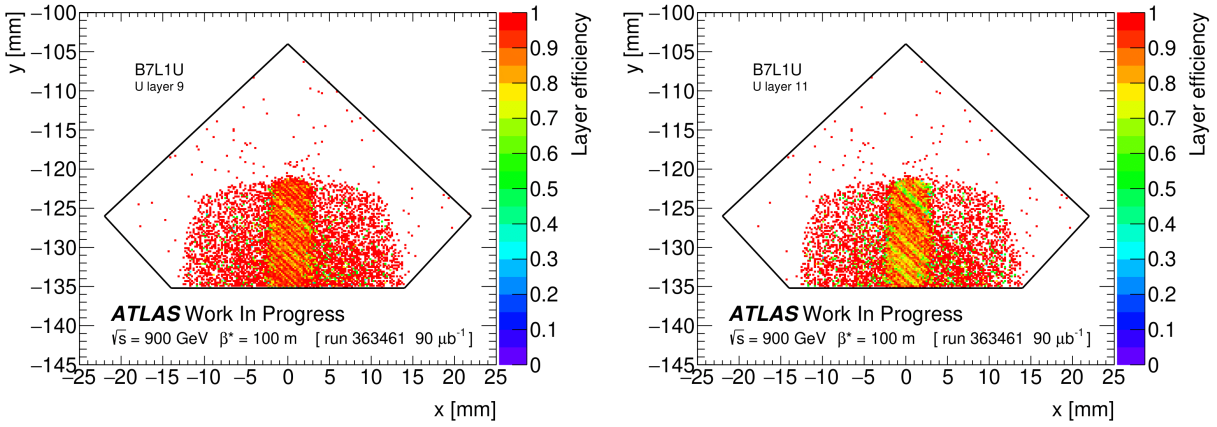

(a) U layer 9.

(b) U layer 11.

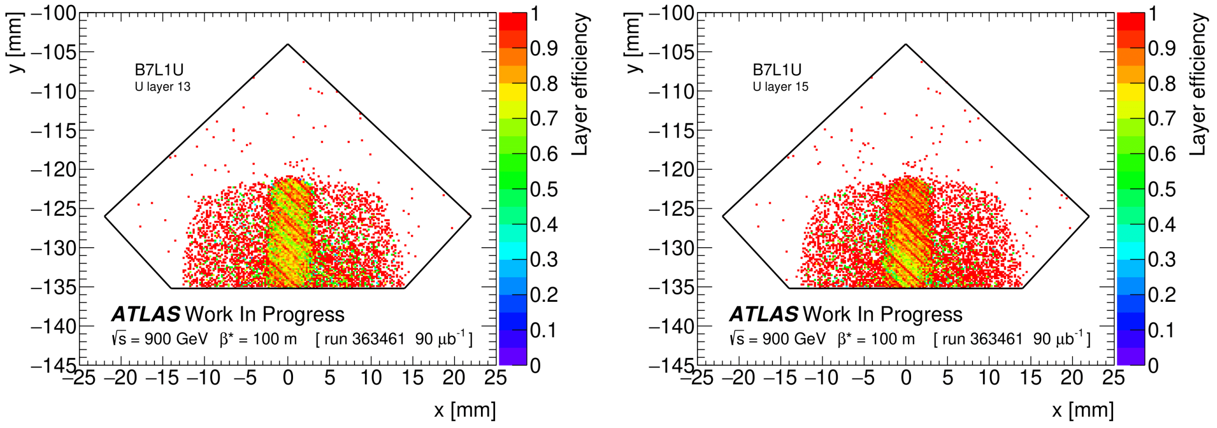

(c) U layer 13.

(d) U layer 15.

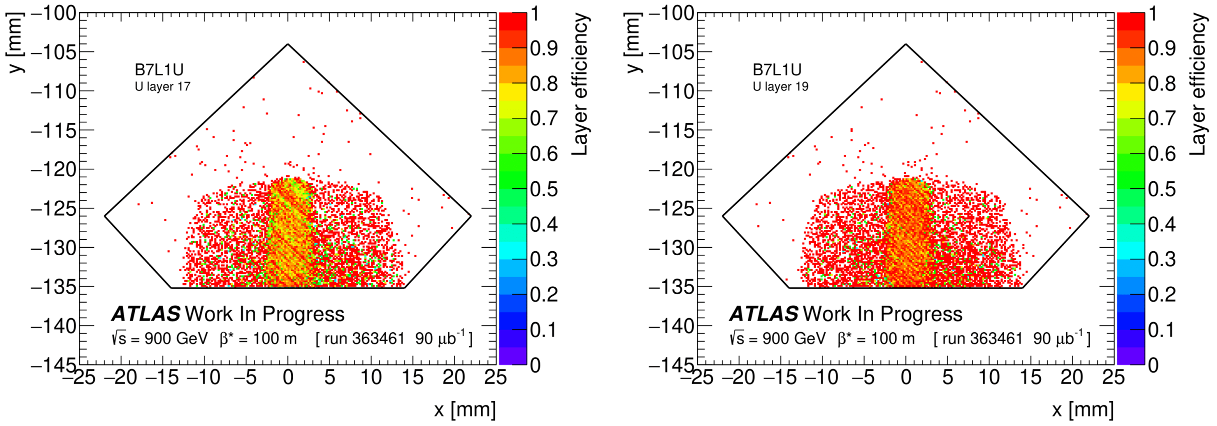

(e) U layer 17.

(f) U layer 19.

Figure B.4: B7L1U: spatial layer efficiency in the U-plane for tracks with elastic triggers.

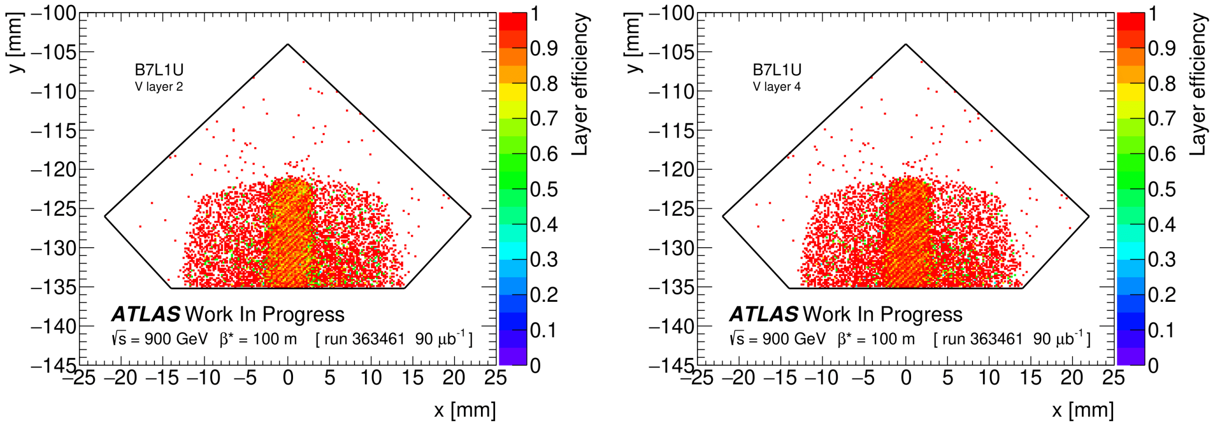

(a) V layer 2.

(b) V layer 4.

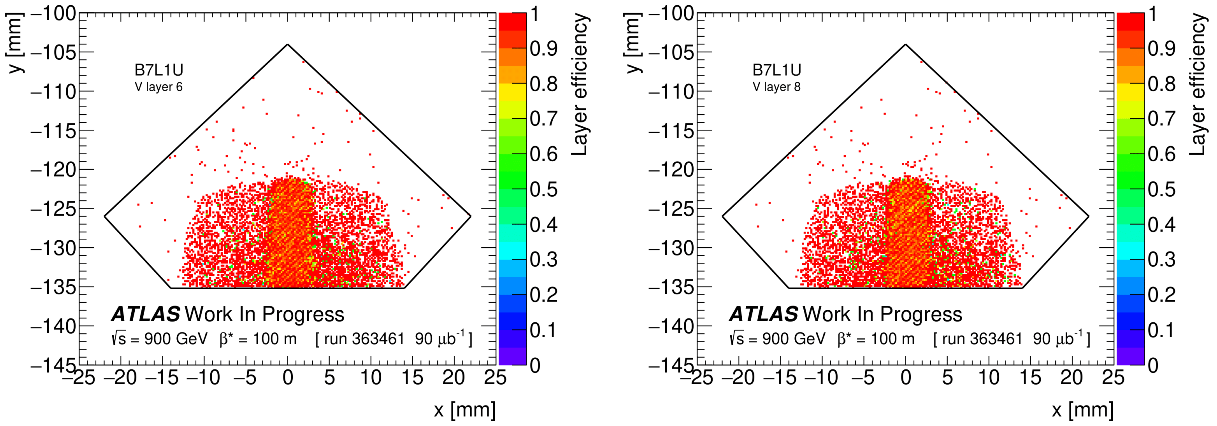

(c) V layer 6.

(d) V layer 8.

Figure B.5: B7L1U: spatial layer efficiency in the V-plane for tracks with elastic triggers.

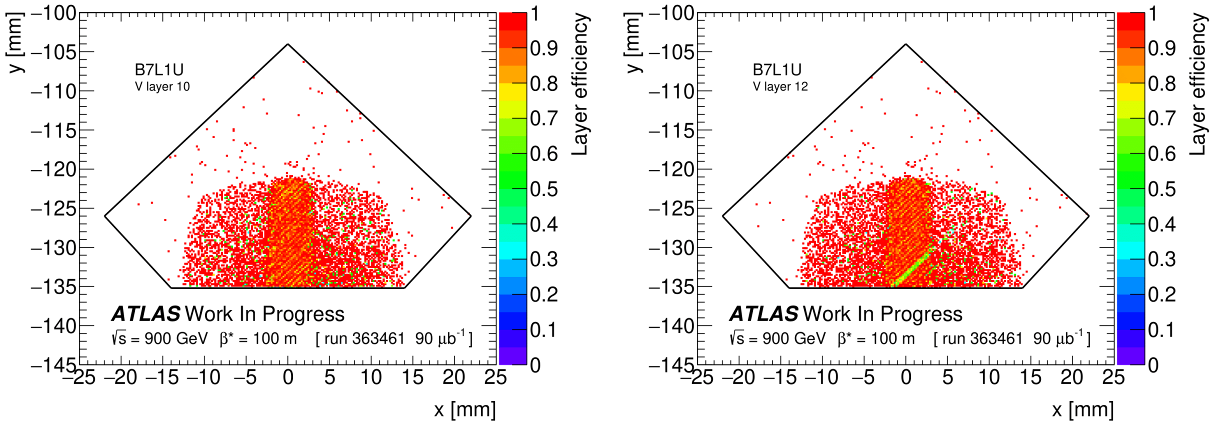

(a) V layer 10.

(b) V layer 12.

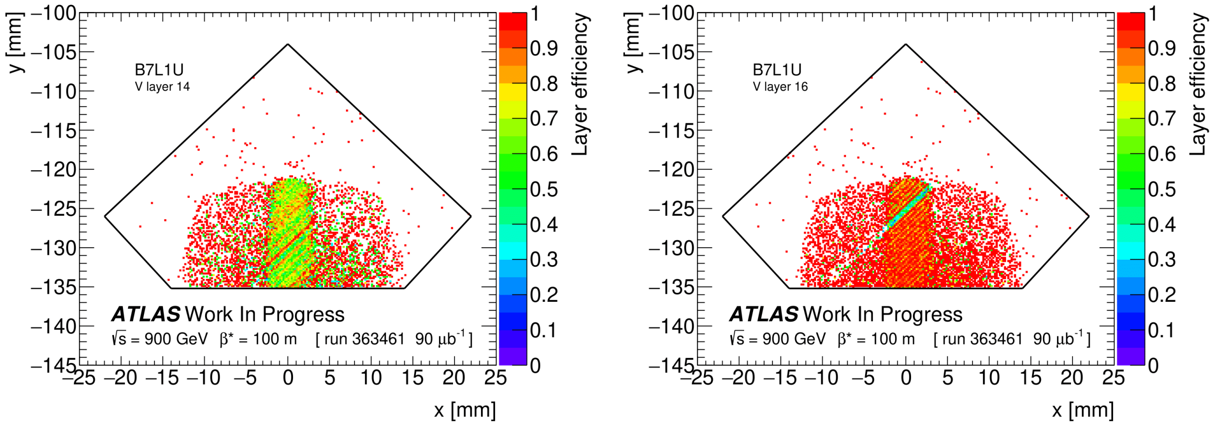

(c) V layer 14.

(d) V layer 16.

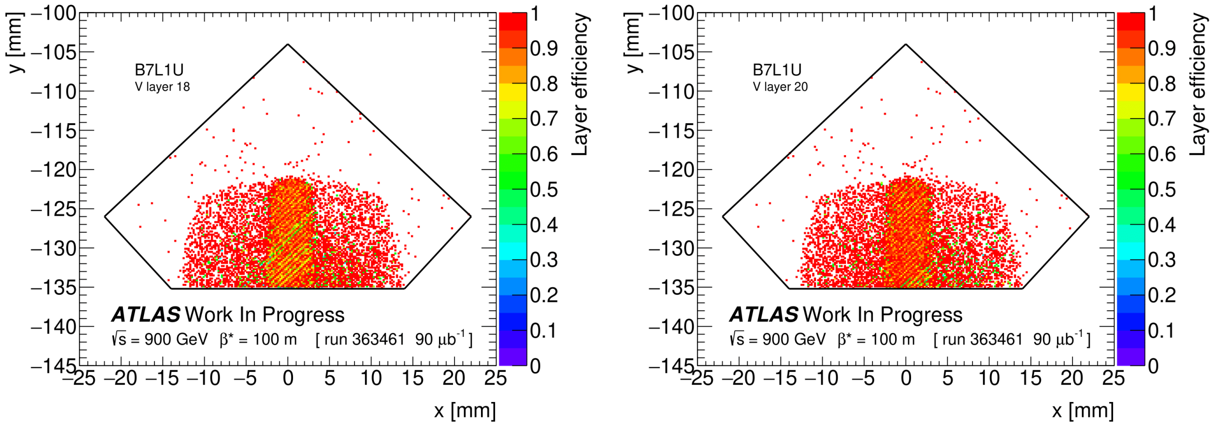

(e) V layer 18.

(f) V layer 20.

Figure B.6: B7L1U: spatial layer efficiency in the V-plane for tracks with elastic triggers.

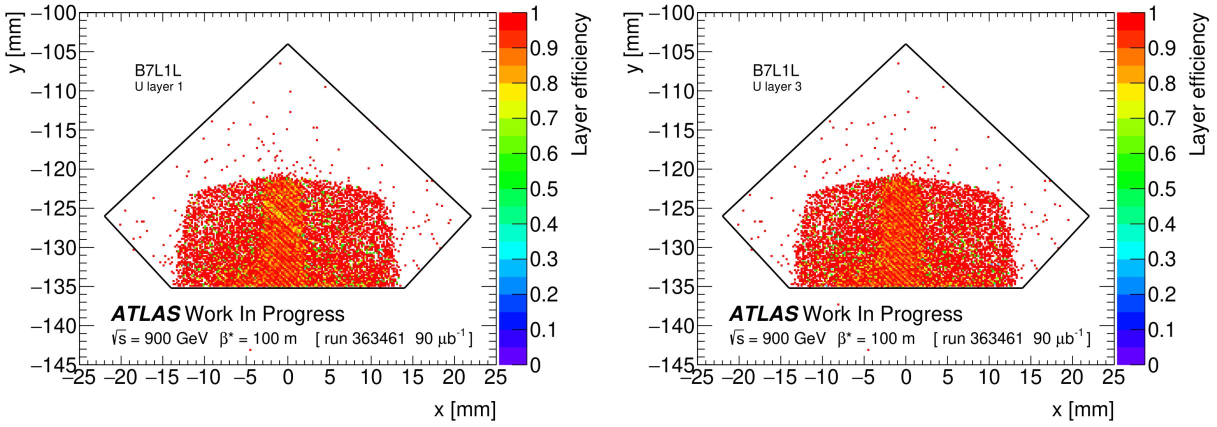

(a) U layer 1.

(b) U layer 3.

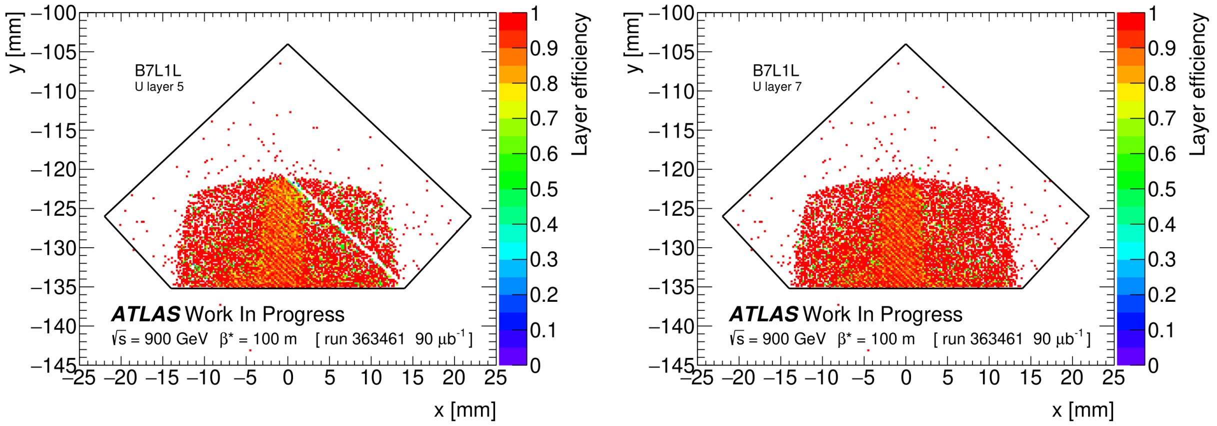

(c) U layer 5.

(d) U layer 7.

Figure B.7: B7L1L: spatial layer efficiency in the U-plane for tracks with elastic triggers.

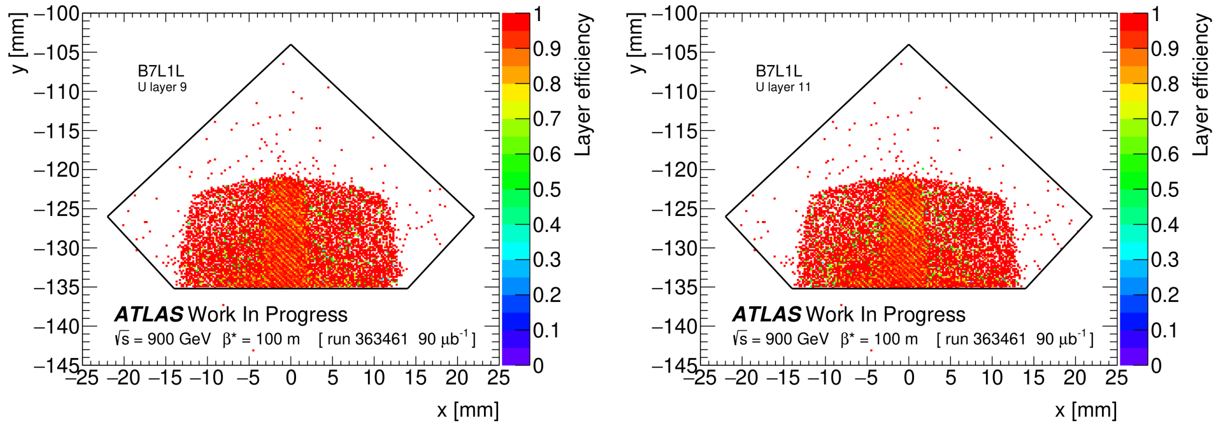

(a) U layer 9.

(b) U layer 11.

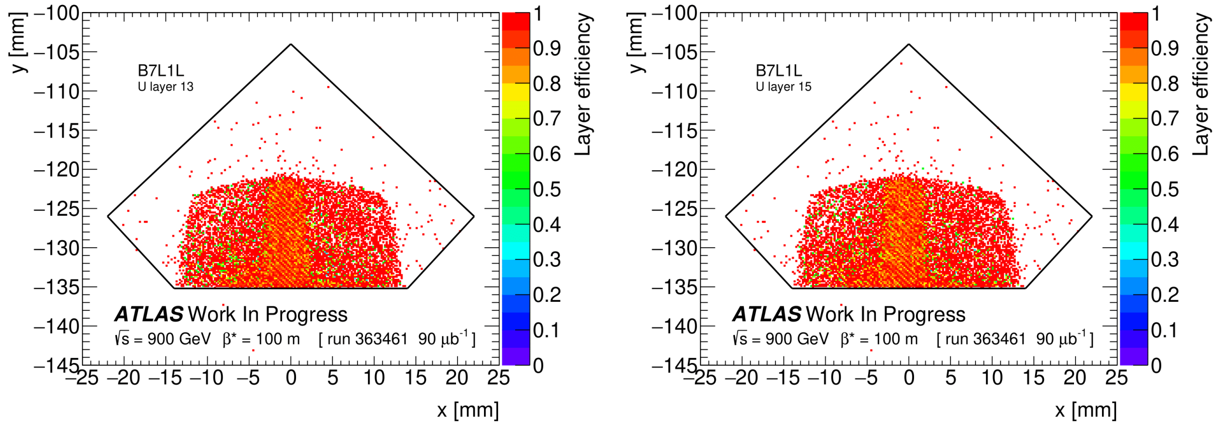

(c) U layer 13.

(d) U layer 15.

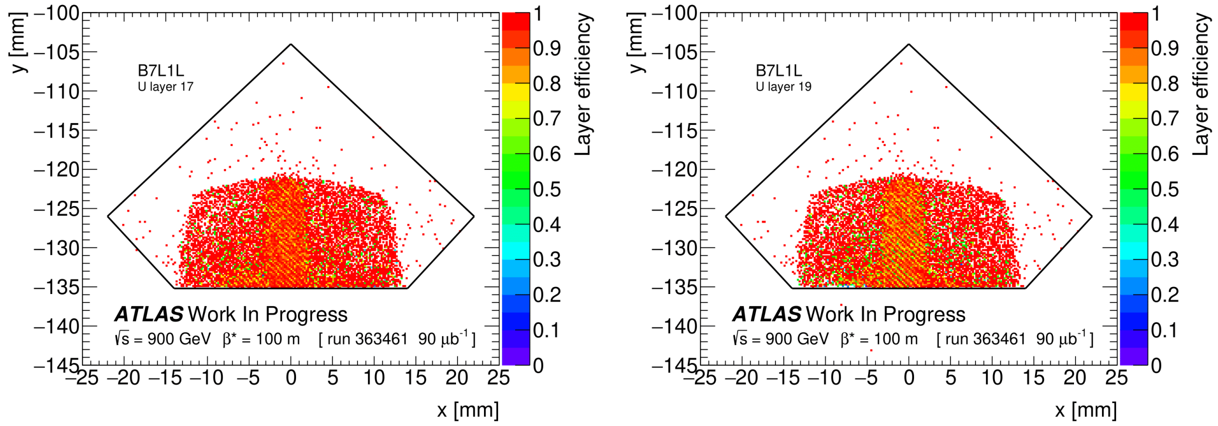

(e) U layer 17.

(f) U layer 19.

Figure B.8: B7L1L: spatial layer efficiency in the U-plane for tracks with elastic triggers.

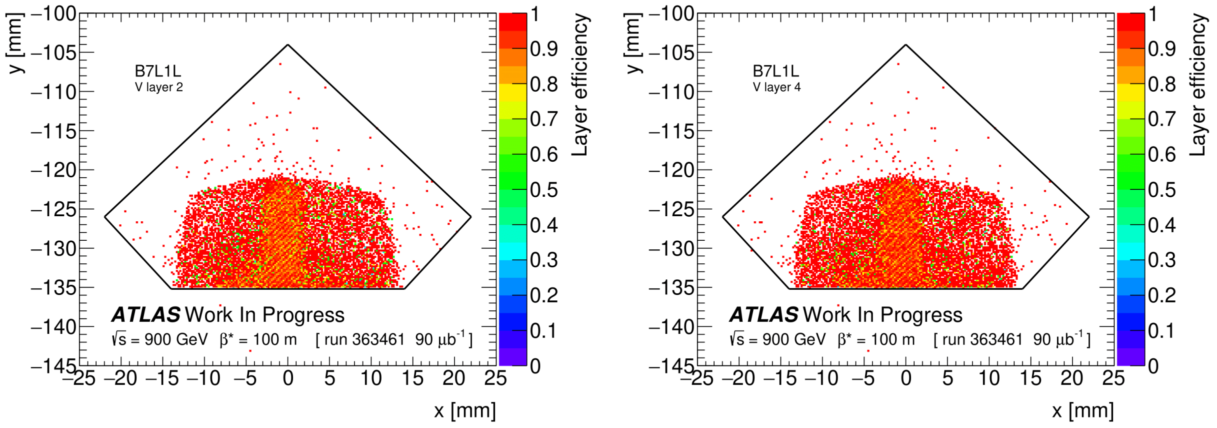

(a) V layer 2.

(b) V layer 4.

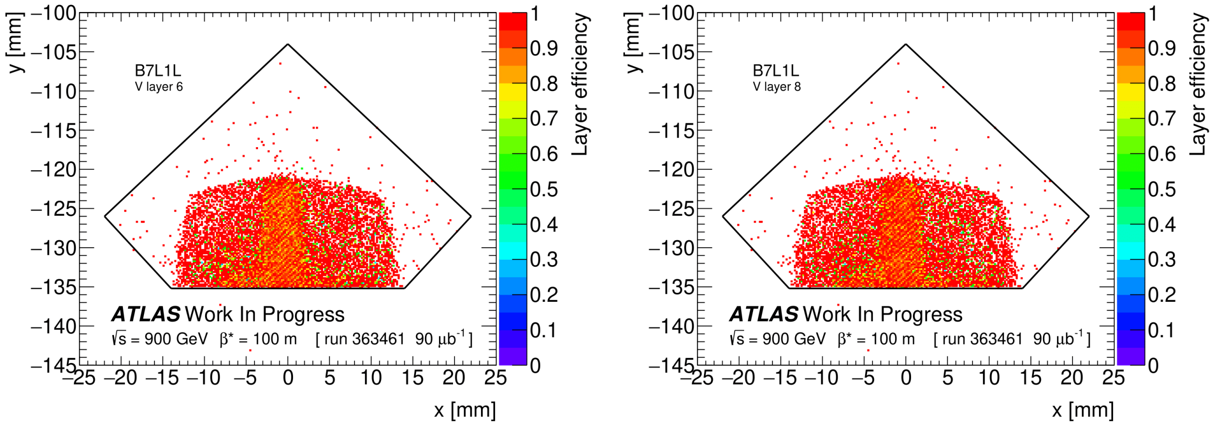

(c) V layer 6.

(d) V layer 8.

Figure B.9: B7L1L: spatial layer efficiency in the V-plane for tracks with elastic triggers.

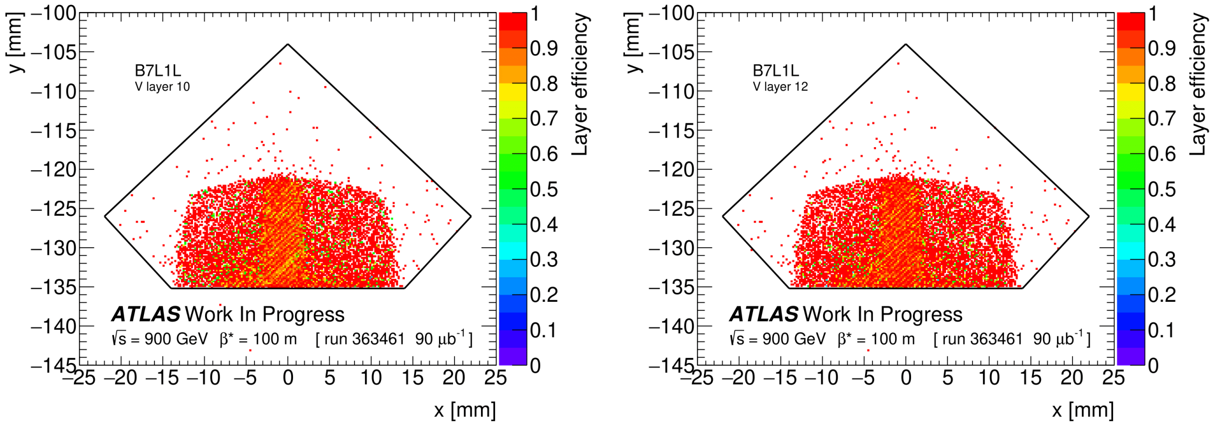

(a) V layer 10.

(b) V layer 12.

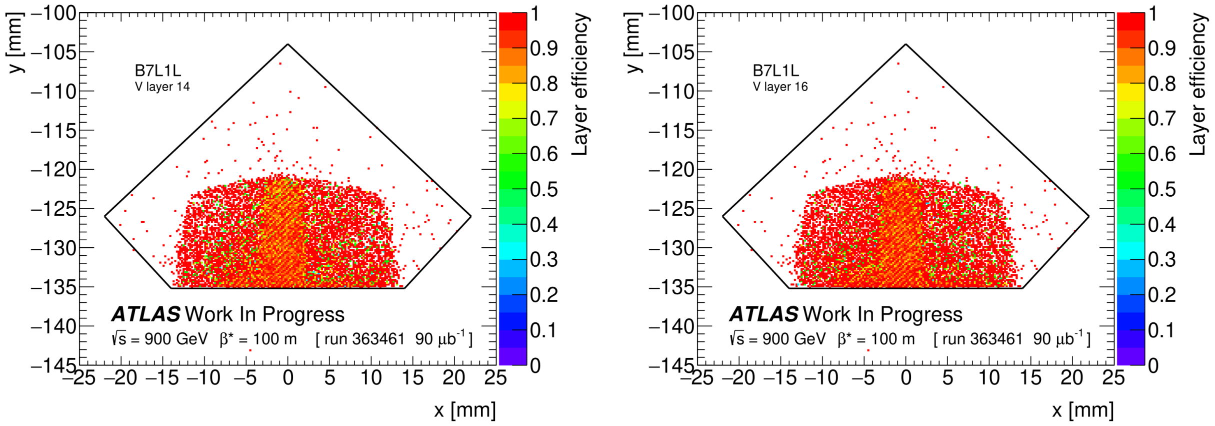

(c) V layer 14.

(d) V layer 16.

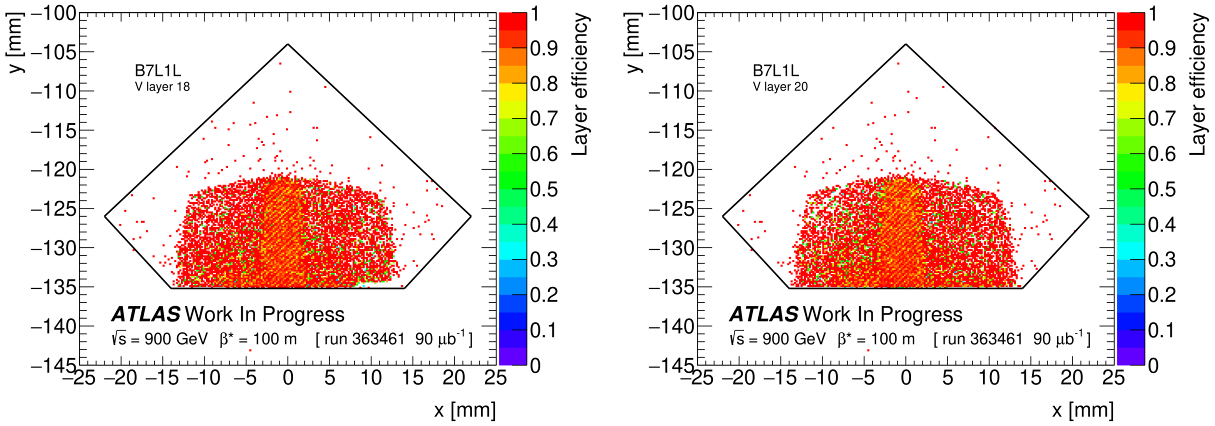

(e) V layer 18.

(f) V layer 20.

Figure B.10: B7L1L: spatial layer efficiency in the V-plane for tracks with elastic triggers.

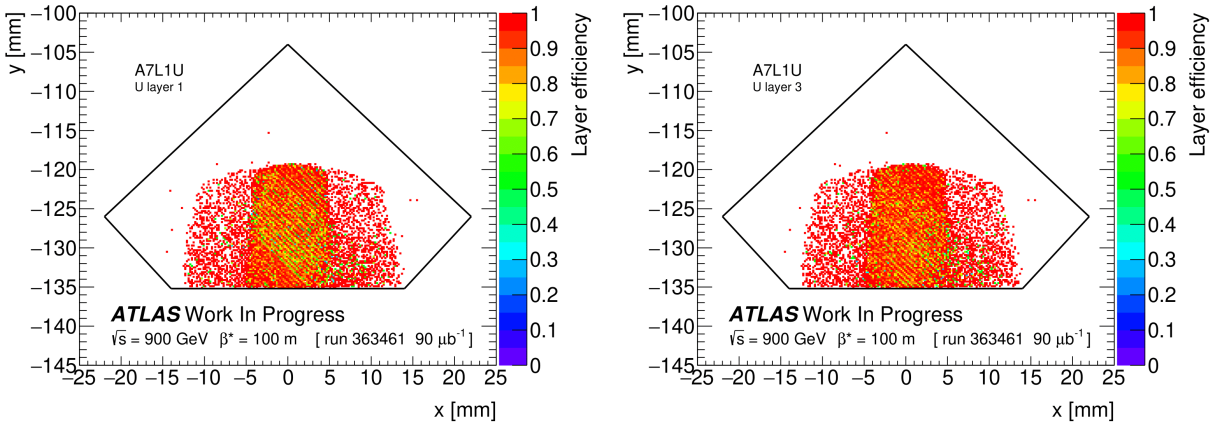

(a) U layer 1.

(b) U layer 3.

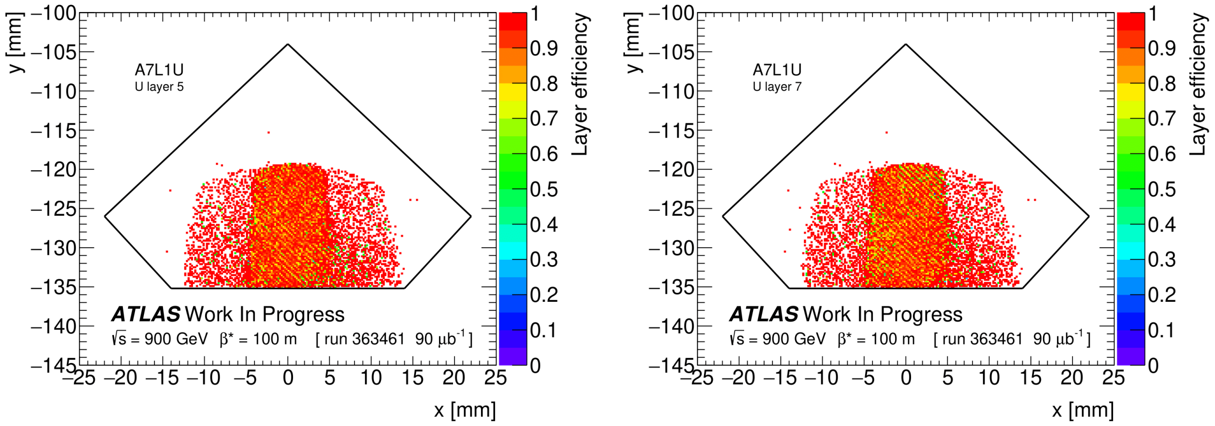

(c) U layer 5.

(d) U layer 7.

Figure B.11: A7L1U: spatial layer efficiency in the U-plane for tracks with elastic triggers.

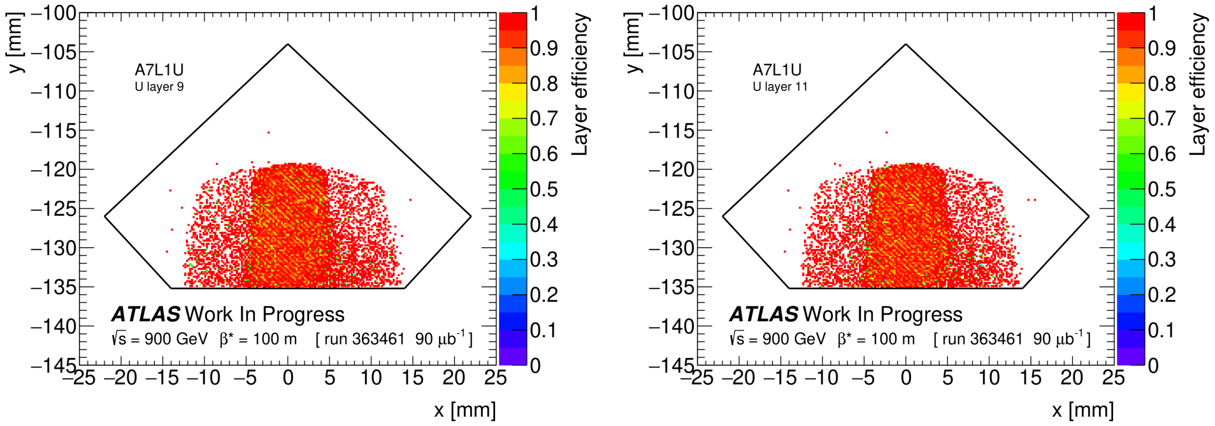

(a) U layer 9. **(b)** U layer 11.

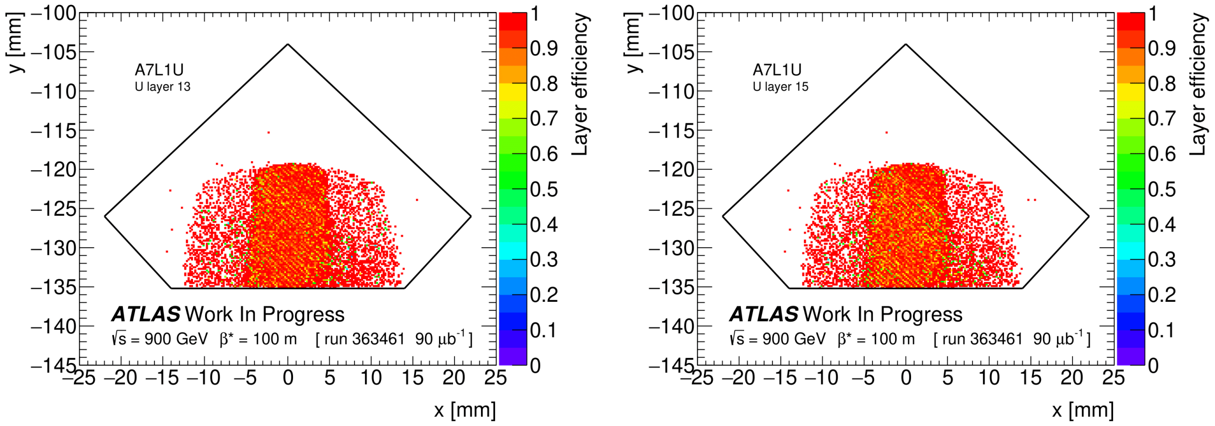

(c) U layer 13. **(d)** U layer 15.

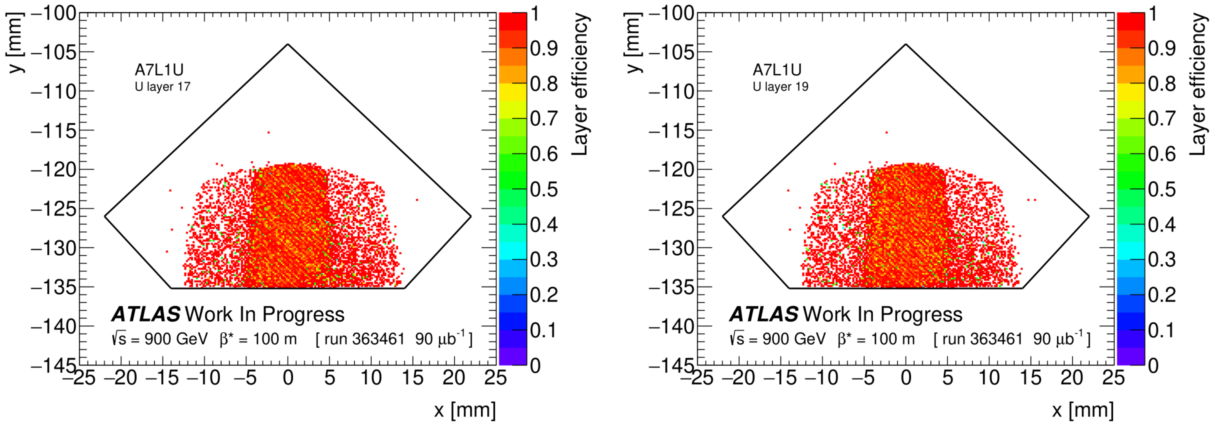

(e) U layer 17. **(f)** U layer 19.

Figure B.12: A7L1U: spatial layer efficiency in the U-plane for tracks with elastic triggers.

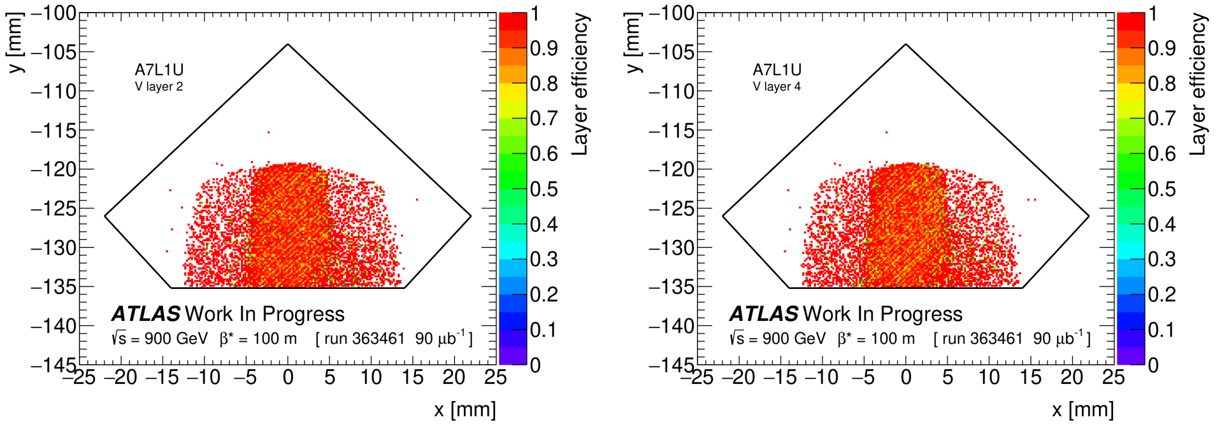

(a) V layer 2.

(b) V layer 4.

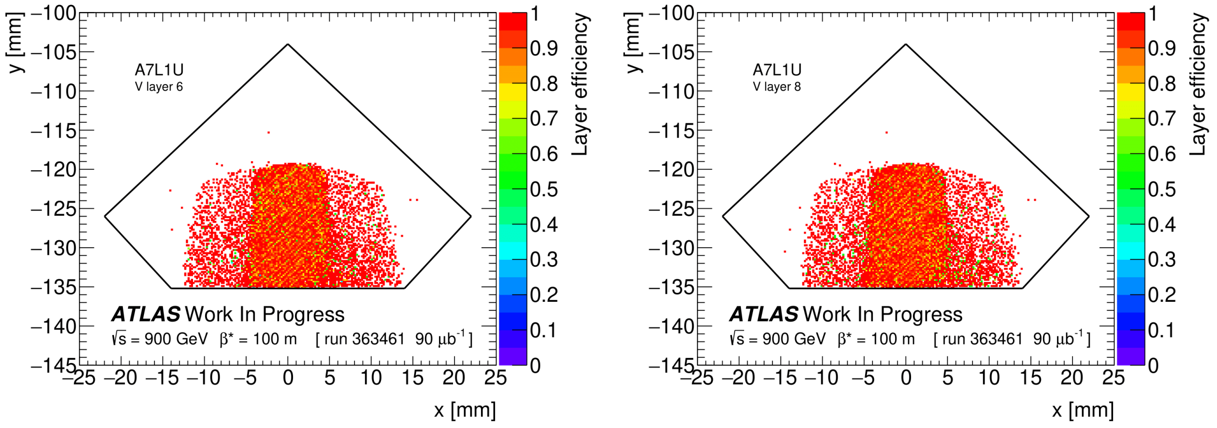

(c) V layer 6.

(d) V layer 8.

Figure B.13: A7L1U: spatial layer efficiency in the V-plane for tracks with elastic triggers.

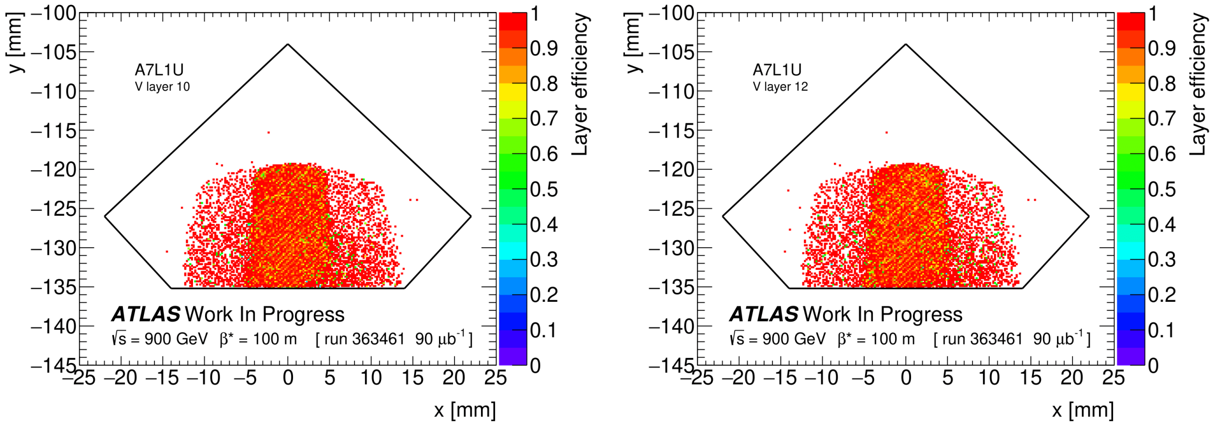

(a) V layer 10.

(b) V layer 12.

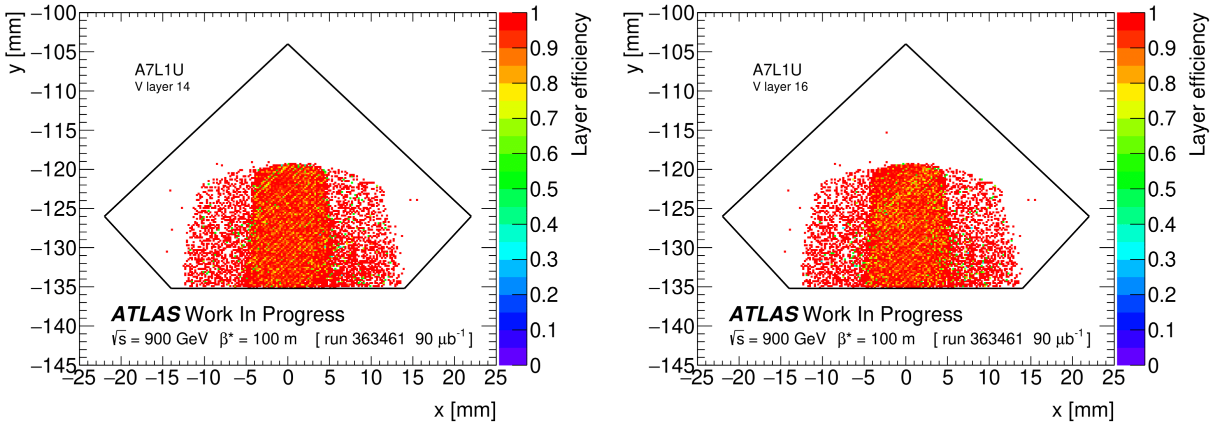

(c) V layer 14.

(d) V layer 16.

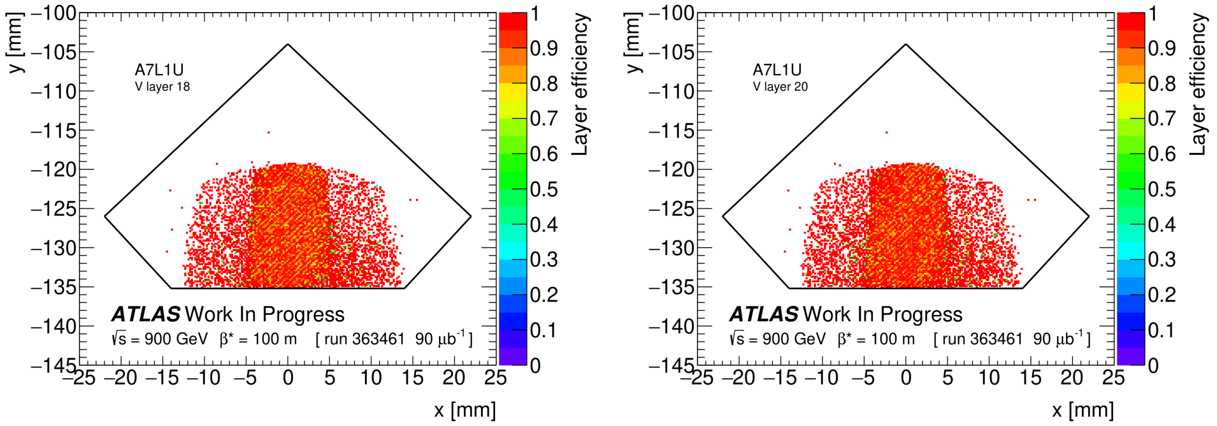

(e) V layer 18.

(f) V layer 20.

Figure B.14: A7L1U: spatial layer efficiency in the V-plane for tracks with elastic triggers.

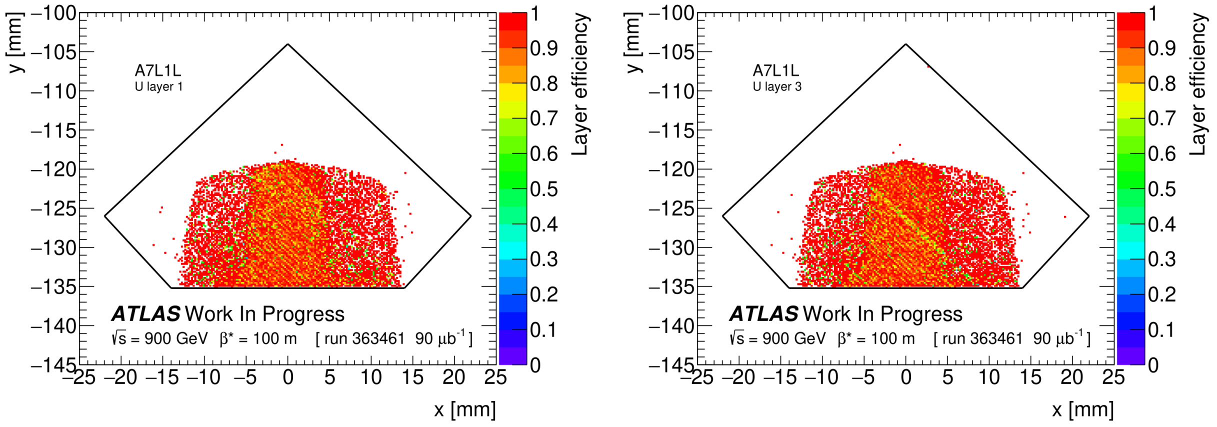

(a) U layer 1.

(b) U layer 3.

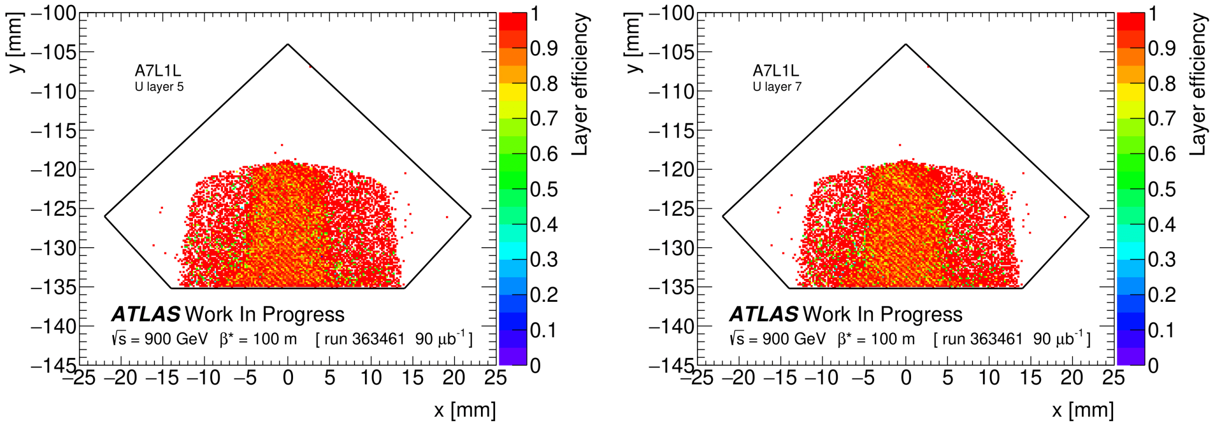

(c) U layer 5.

(d) U layer 7.

Figure B.15: A7L1L: spatial layer efficiency in the U-plane for tracks with elastic triggers.

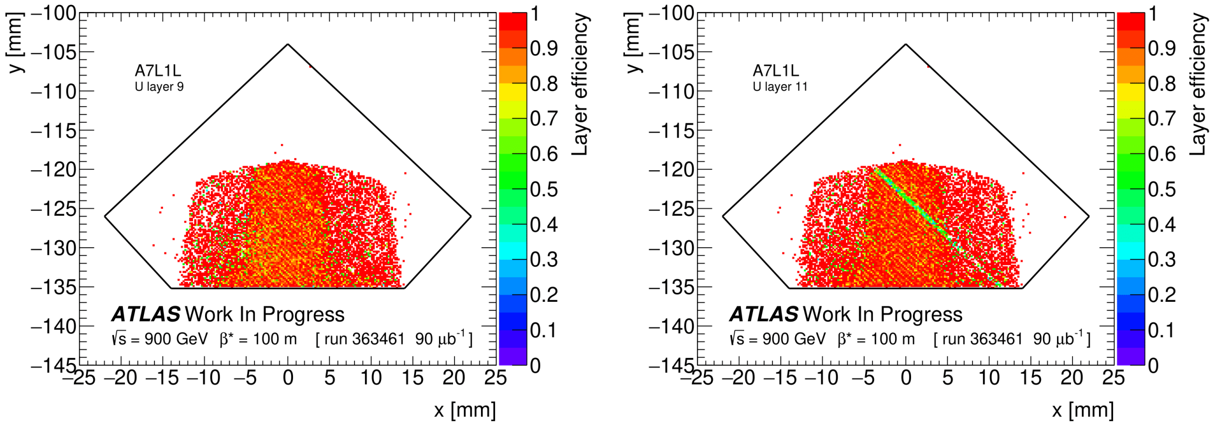

(a) U layer 9.

(b) U layer 11.

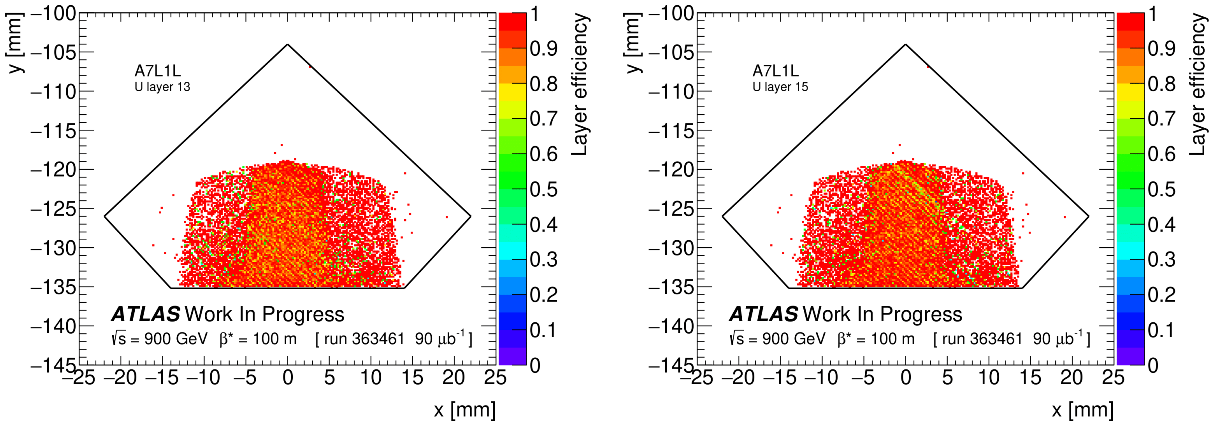

(c) U layer 13.

(d) U layer 15.

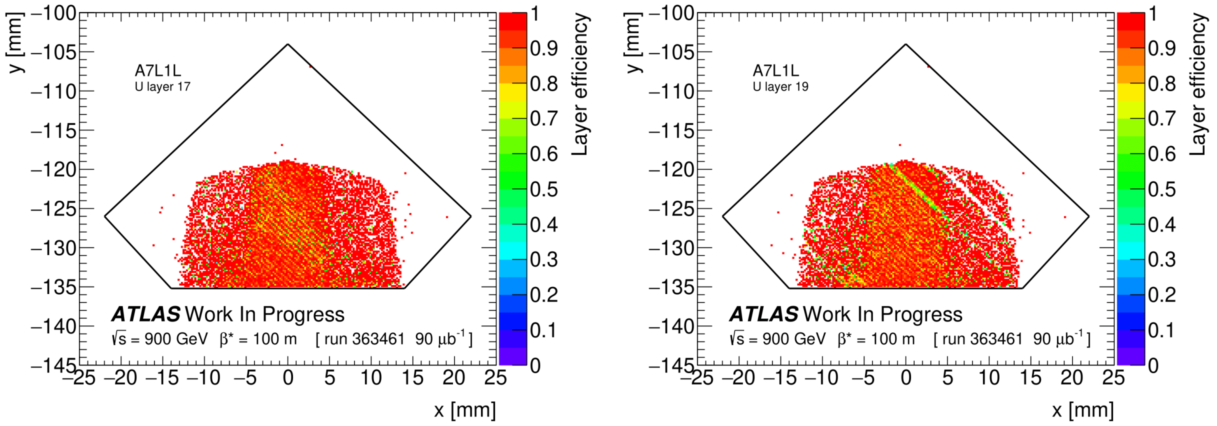

(e) U layer 17.

(f) U layer 19.

Figure B.16: A7L1L: spatial layer efficiency in the U-plane for tracks with elastic triggers.

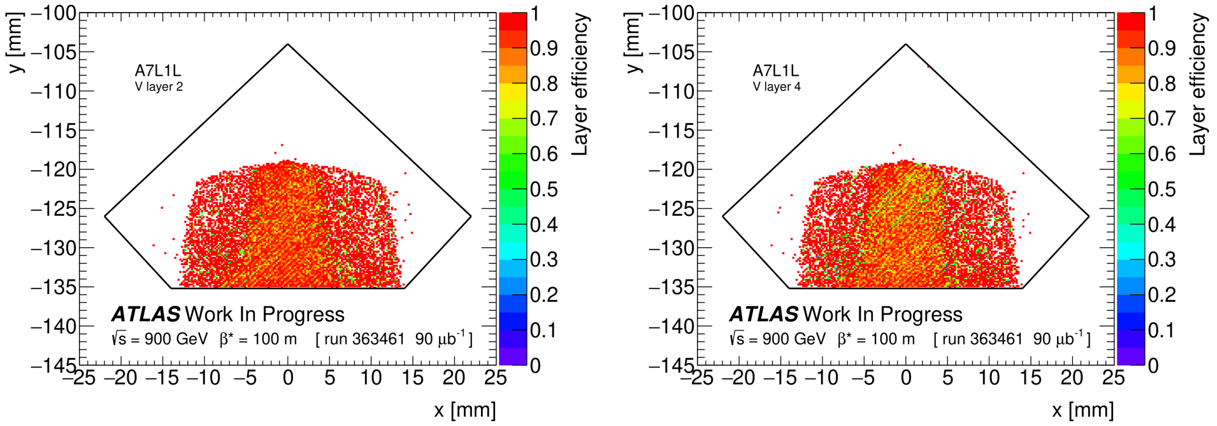

(a) V layer 2.

(b) V layer 4.

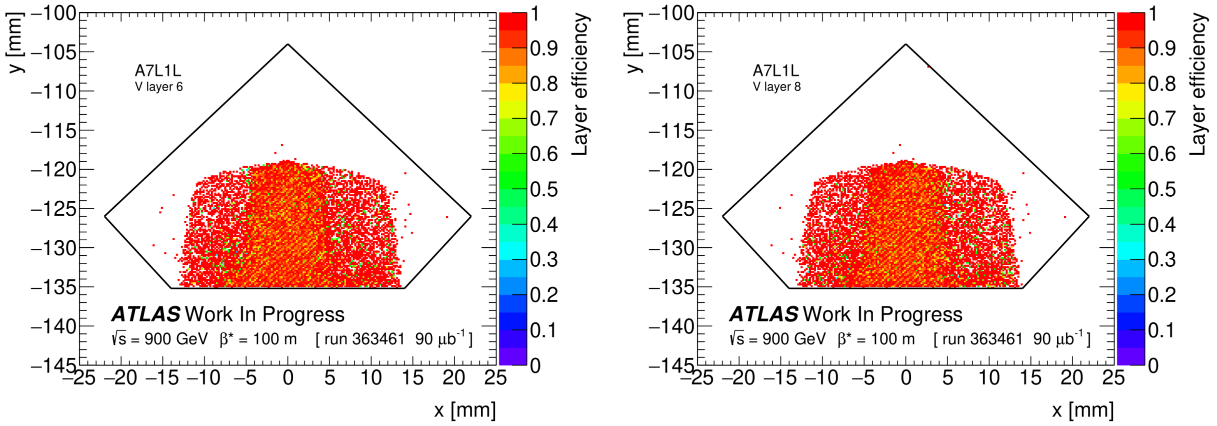

(c) V layer 6.

(d) V layer 8.

Figure B.17: A7L1L: spatial layer efficiency in the V-plane for tracks with elastic triggers.

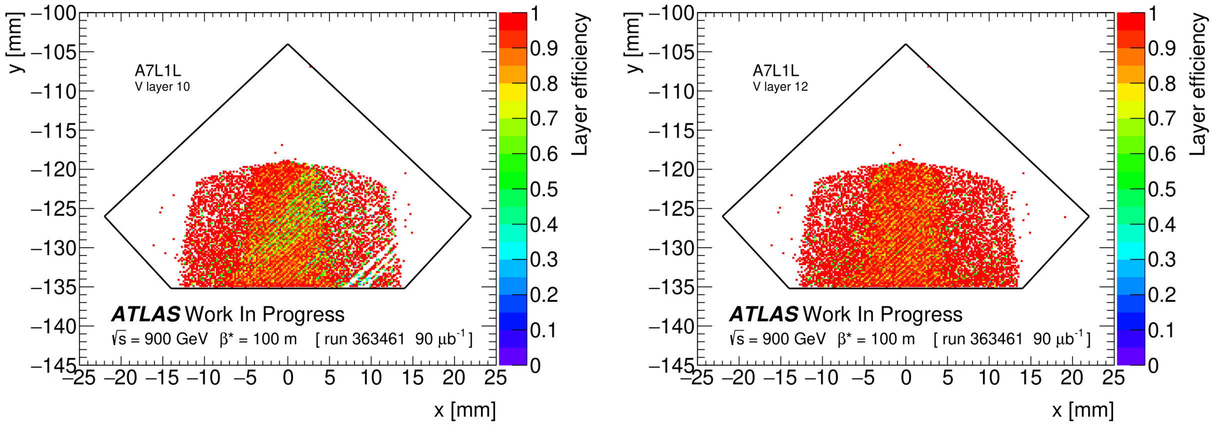

(a) V layer 10.

(b) V layer 12.

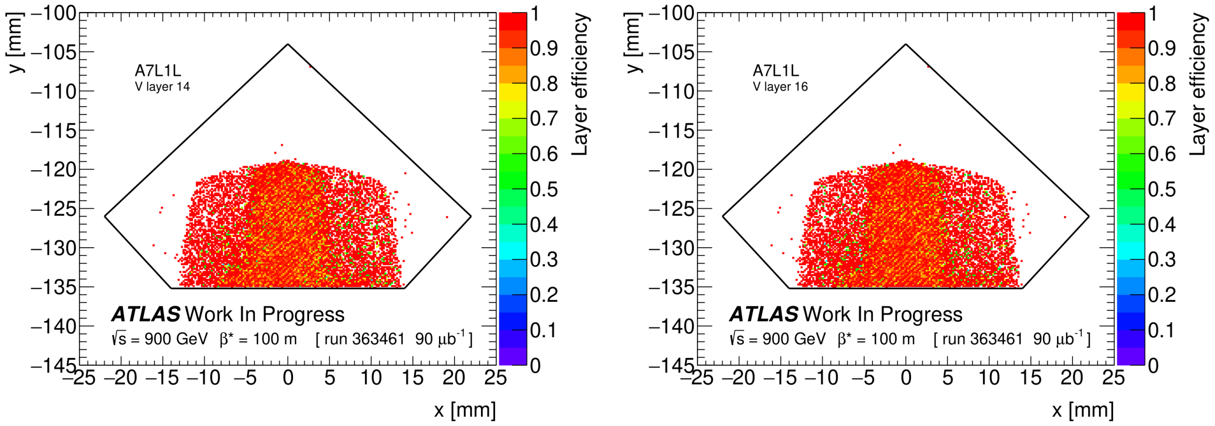

(c) V layer 14.

(d) V layer 16.

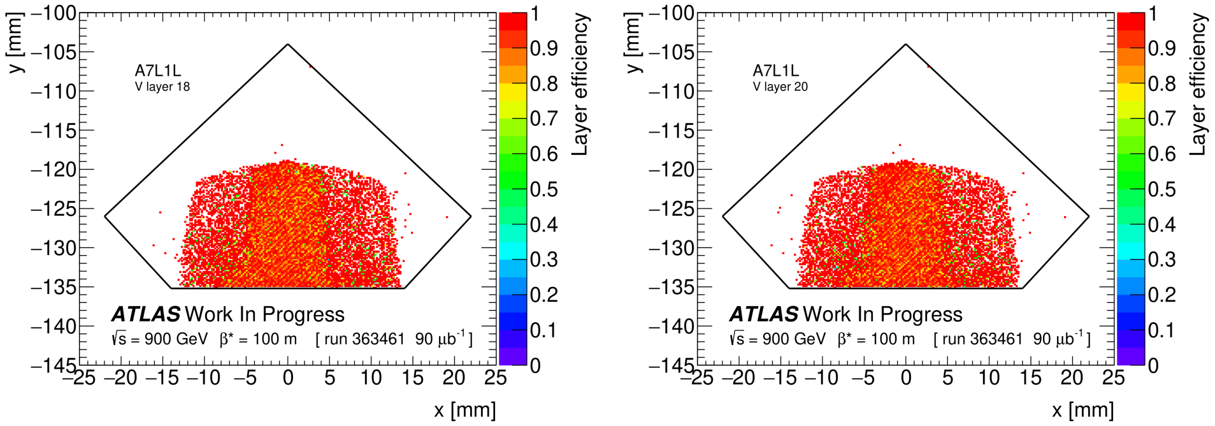

(e) V layer 18.

(f) V layer 20.

Figure B.18: A7L1L: spatial layer efficiency in the V-plane for tracks with elastic triggers.

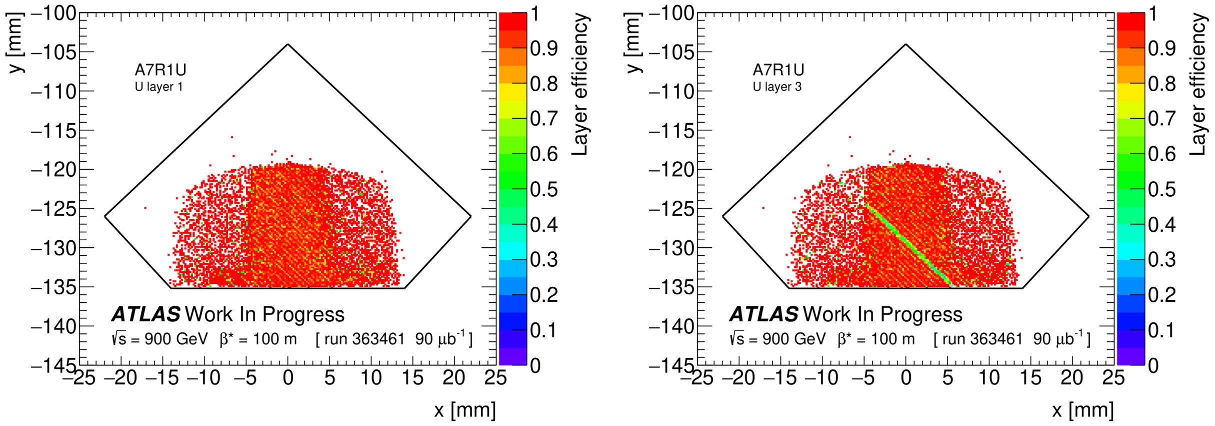

(a) U layer 1.

(b) U layer 3.

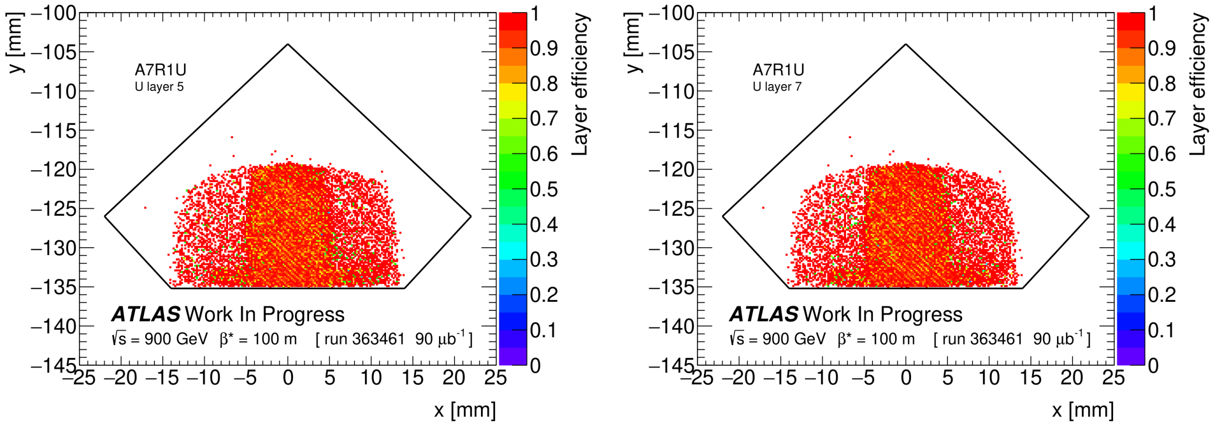

(c) U layer 5.

(d) U layer 7.

Figure B.19: A7R1U: spatial layer efficiency in the U-plane for tracks with elastic triggers.

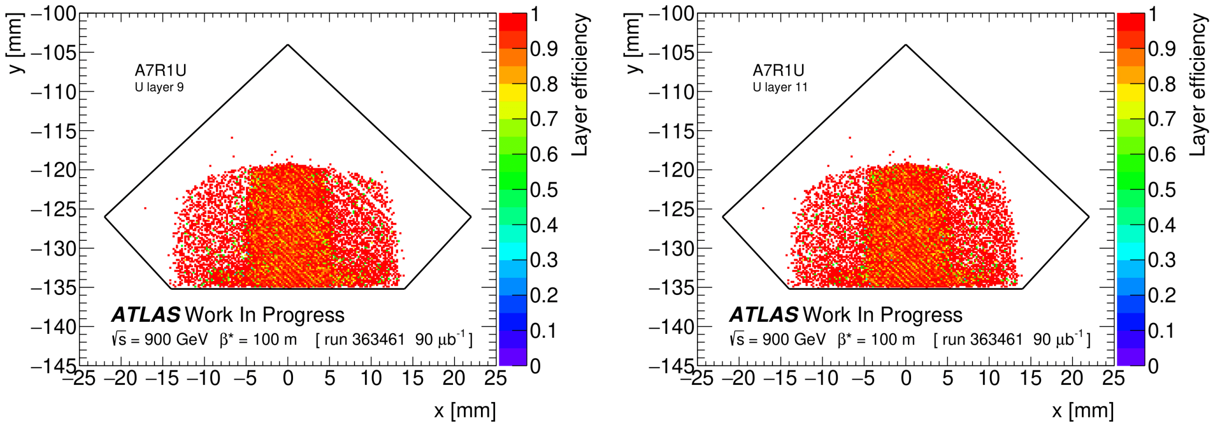

(a) U layer 9. **(b)** U layer 11.

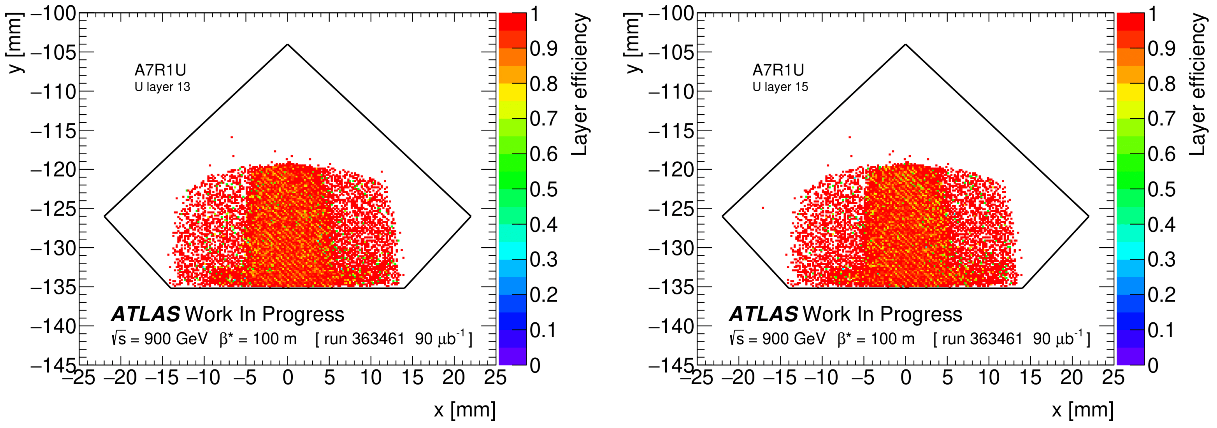

(c) U layer 13. **(d)** U layer 15.

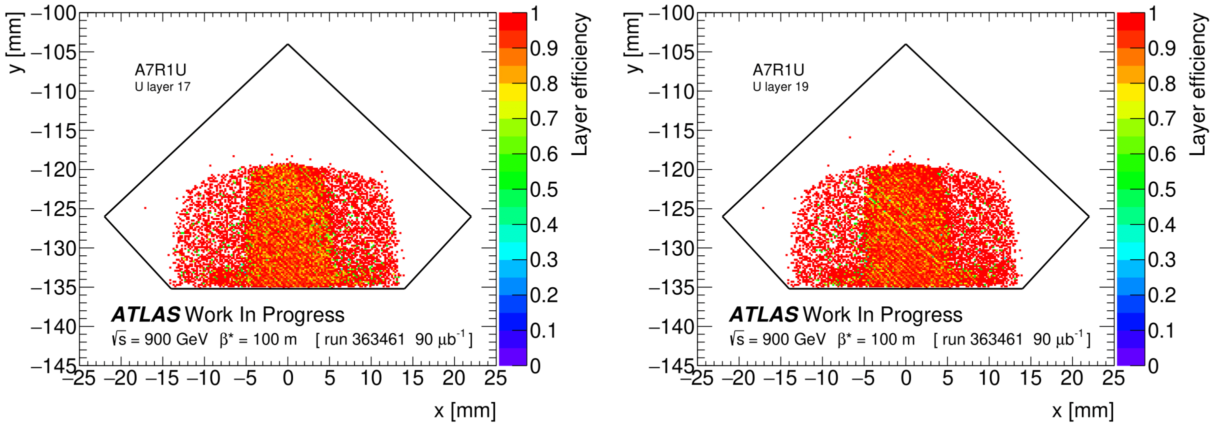

(e) U layer 17. **(f)** U layer 19.

Figure B.20: A7R1U: spatial layer efficiency in the U-plane for tracks with elastic triggers.

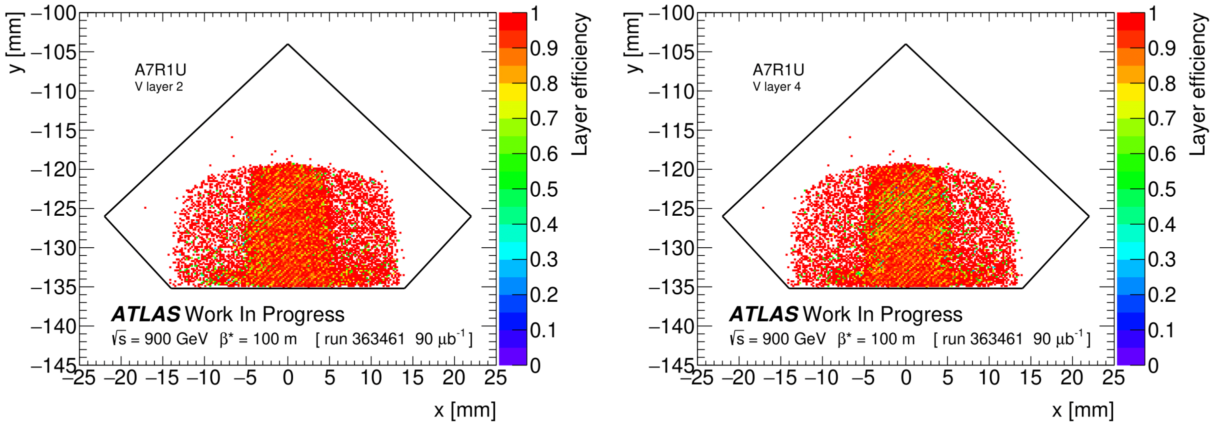

(a) V layer 2. **(b)** V layer 4.

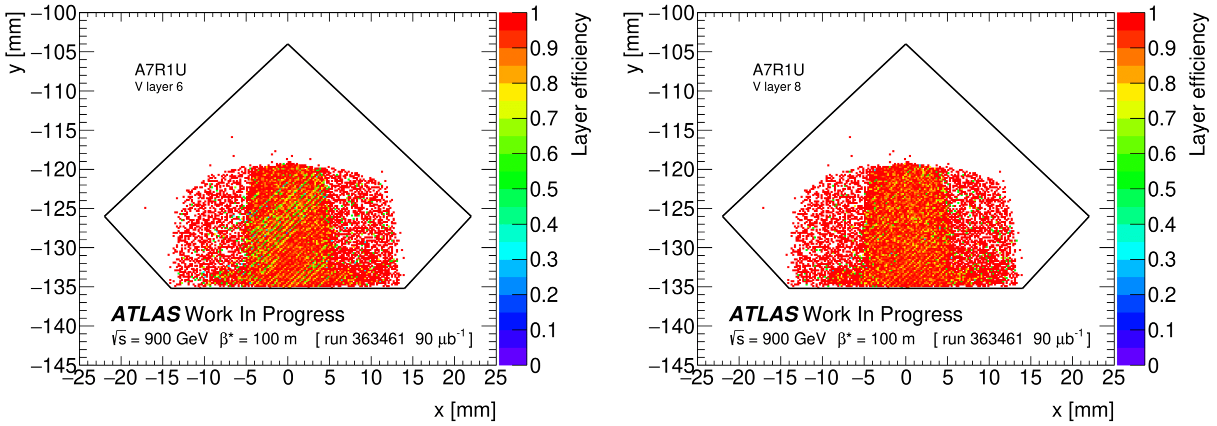

(c) V layer 6. **(d)** V layer 8.

Figure B.21: A7R1U: spatial layer efficiency in the V-plane for tracks with elastic triggers.

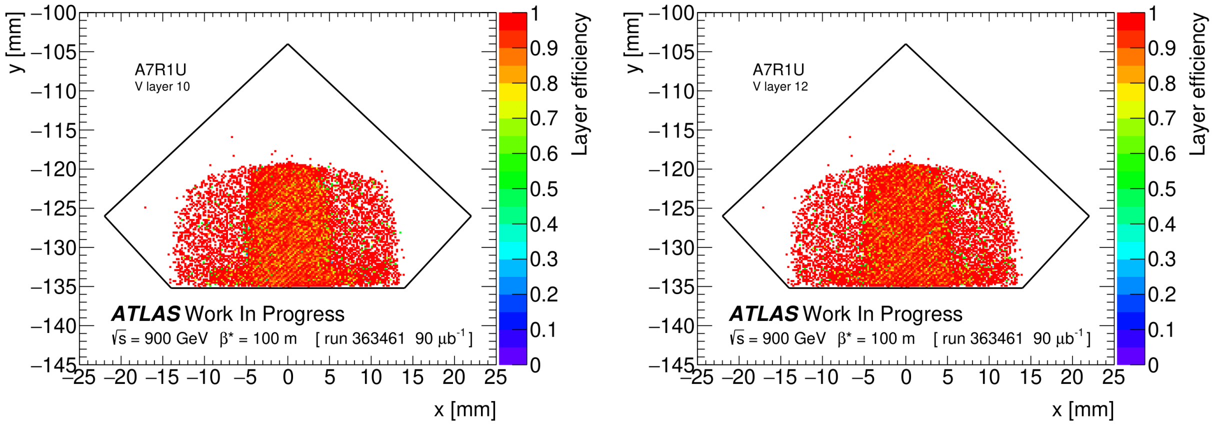

(a) V layer 10.

(b) V layer 12.

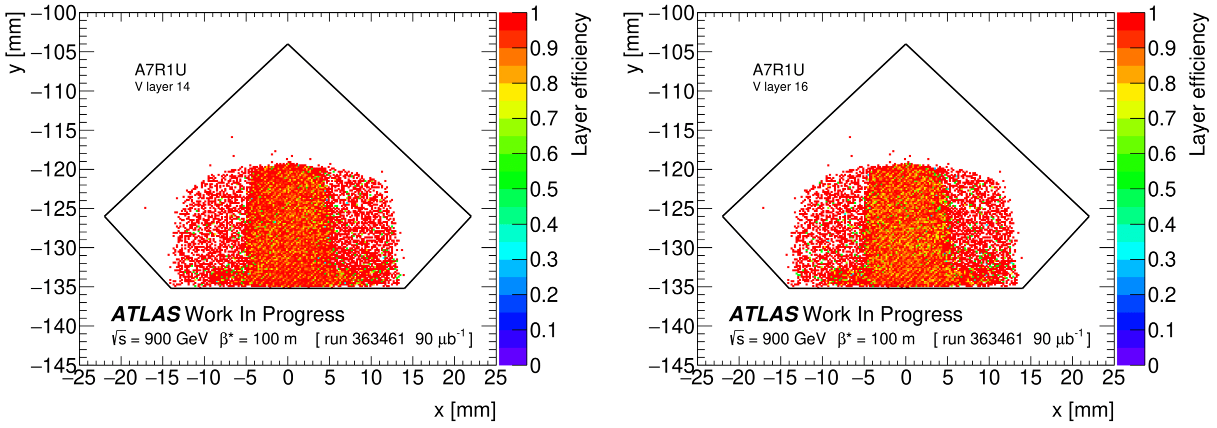

(c) V layer 14.

(d) V layer 16.

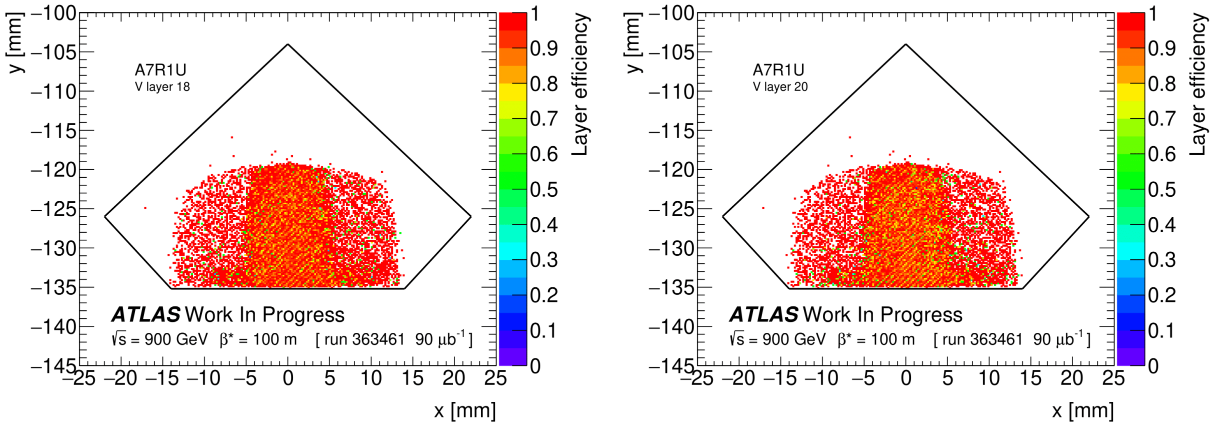

(e) V layer 18.

(f) V layer 20.

Figure B.22: A7R1U: spatial layer efficiency in the V-plane for tracks with elastic triggers.

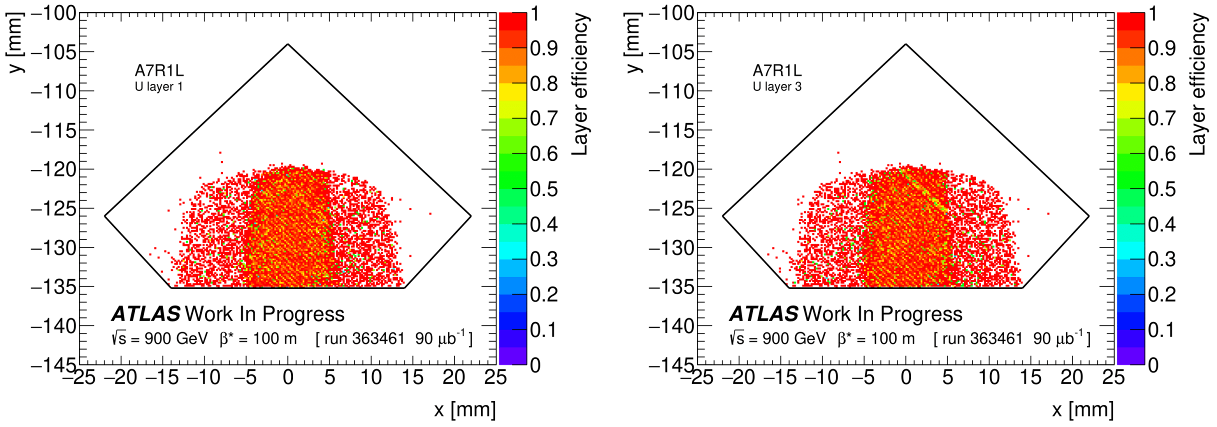

(a) U layer 1.

(b) U layer 3.

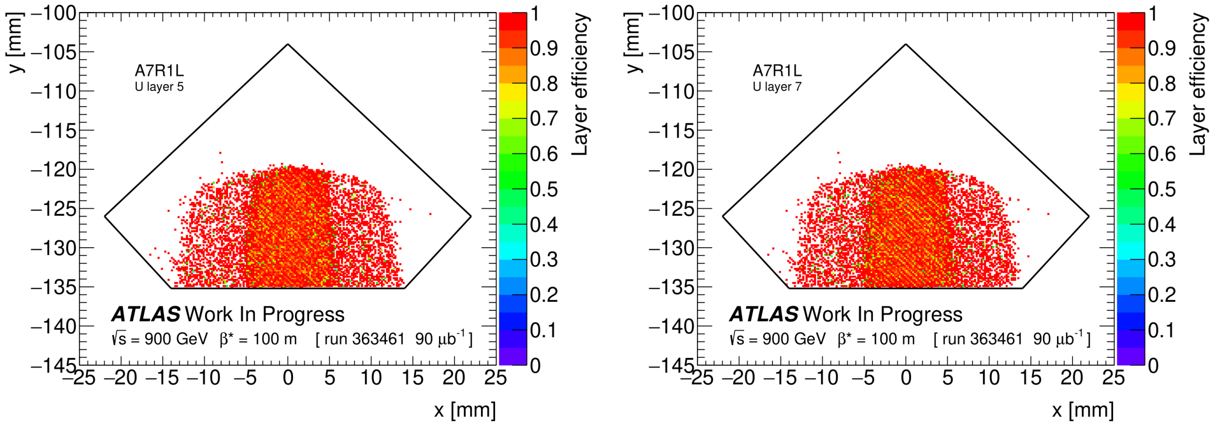

(c) U layer 5.

(d) U layer 7.

Figure B.23: A7R1L: spatial layer efficiency in the U-plane for tracks with elastic triggers.

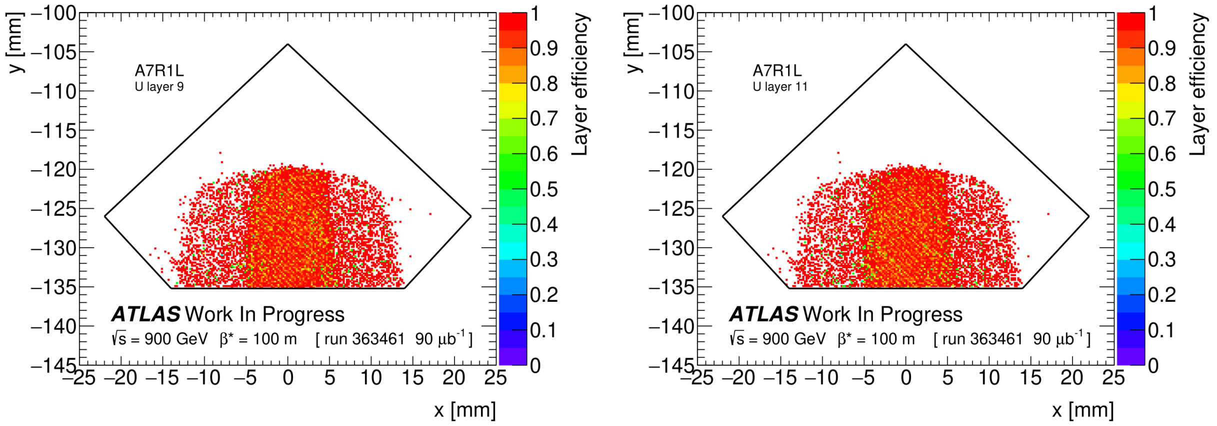

(a) U layer 9. **(b)** U layer 11.

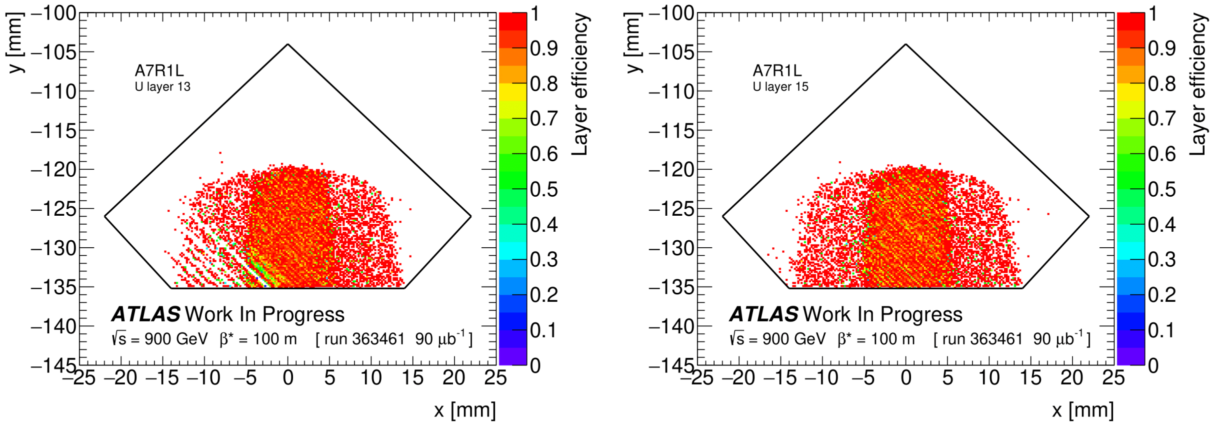

(c) U layer 13. **(d)** U layer 15.

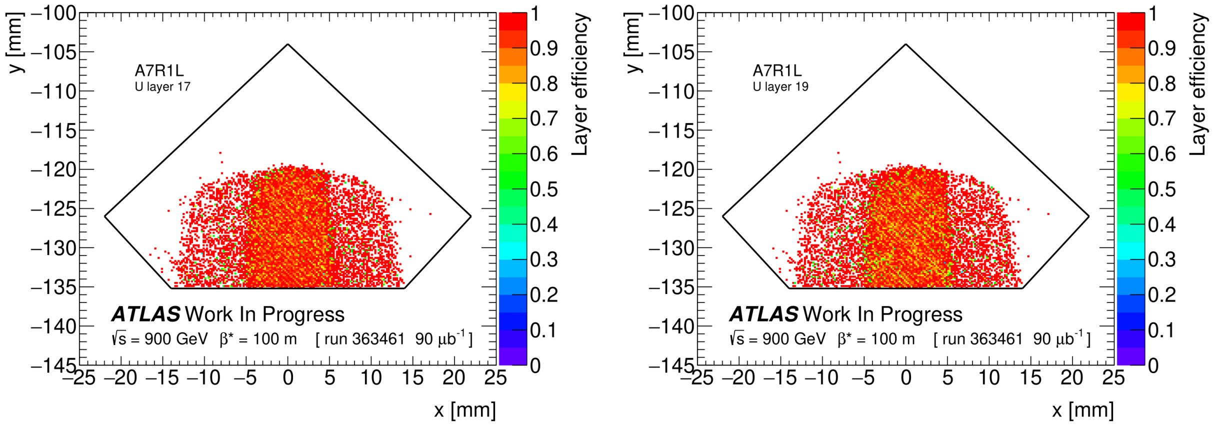

(e) U layer 17. **(f)** U layer 19.

Figure B.24: A7R1L: spatial layer efficiency in the U-plane for tracks with elastic triggers.

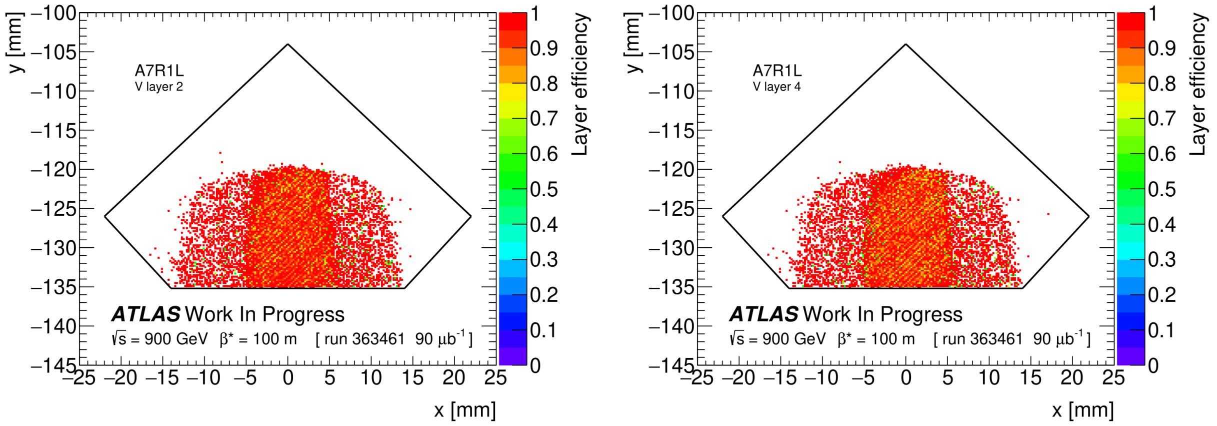

(a) V layer 2.

(b) V layer 4.

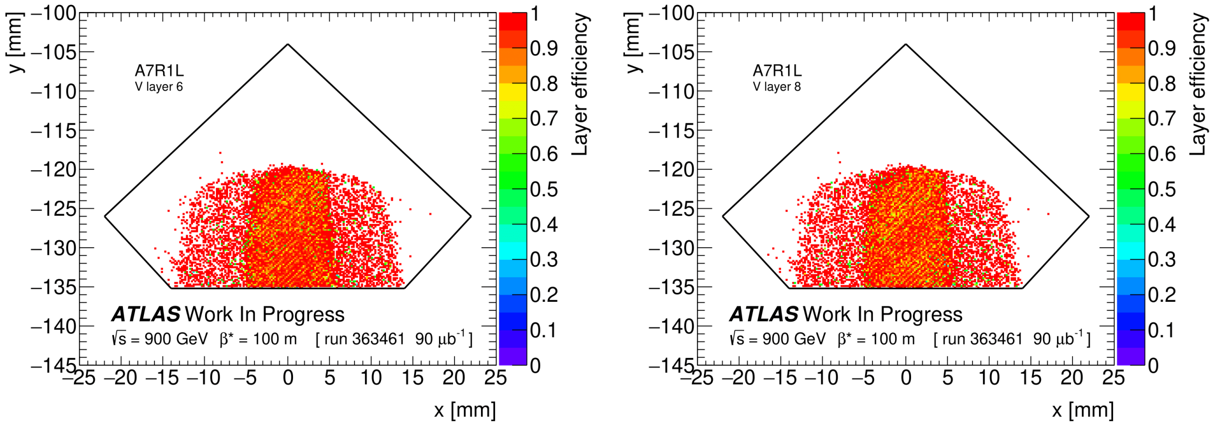

(c) V layer 6.

(d) V layer 8.

Figure B.25: A7R1L: spatial layer efficiency in the V-plane for tracks with elastic triggers.

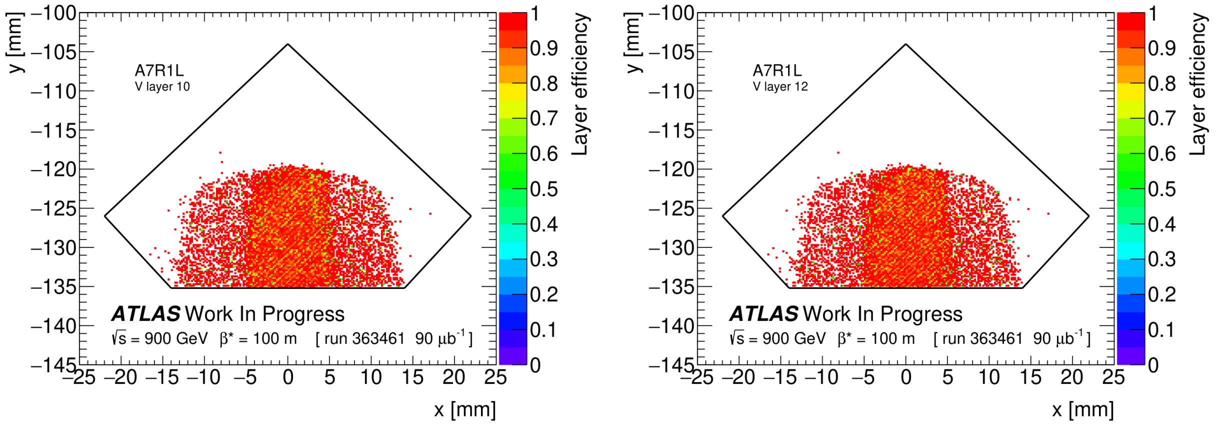

(a) V layer 10.

(b) V layer 12.

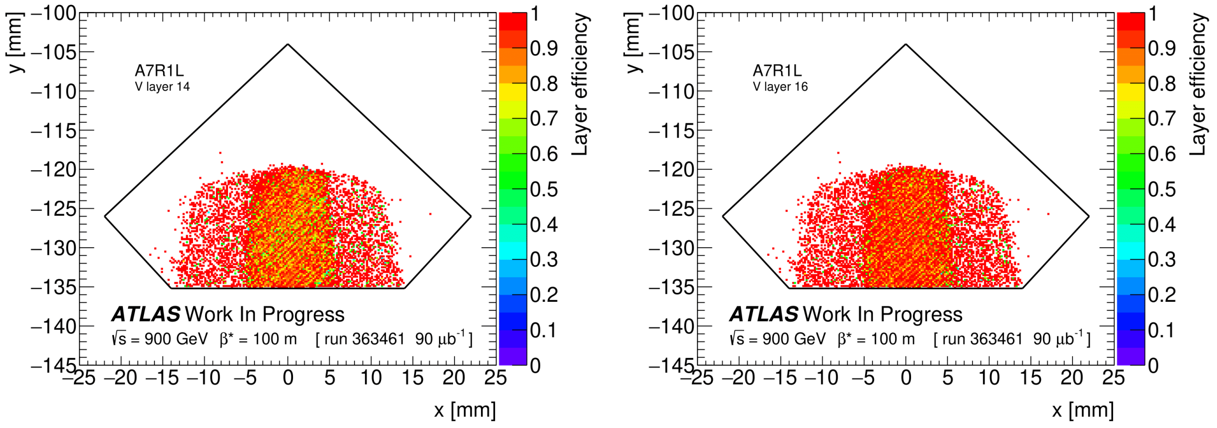

(c) V layer 14.

(d) V layer 16.

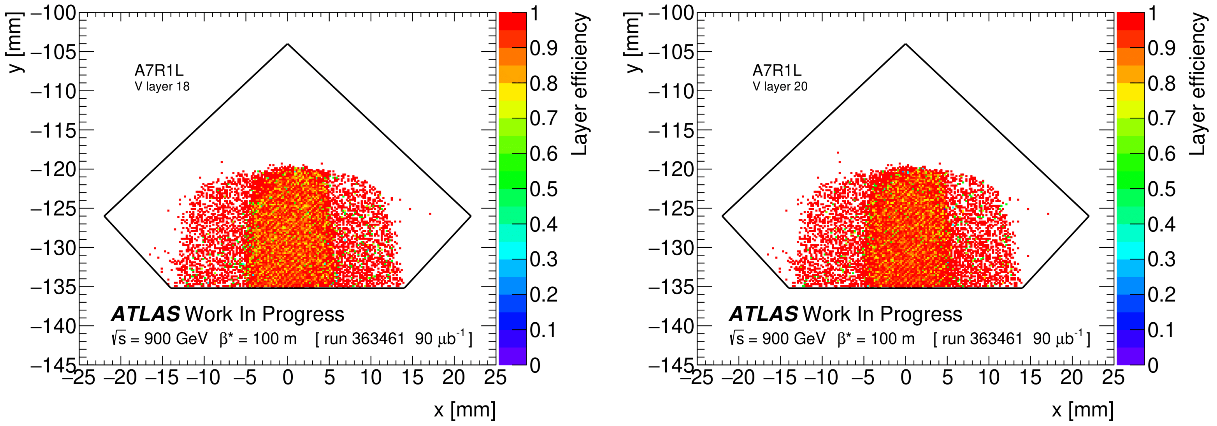

(e) V layer 18.

(f) V layer 20.

Figure B.26: A7R1L: spatial layer efficiency in the V-plane for tracks with elastic triggers.

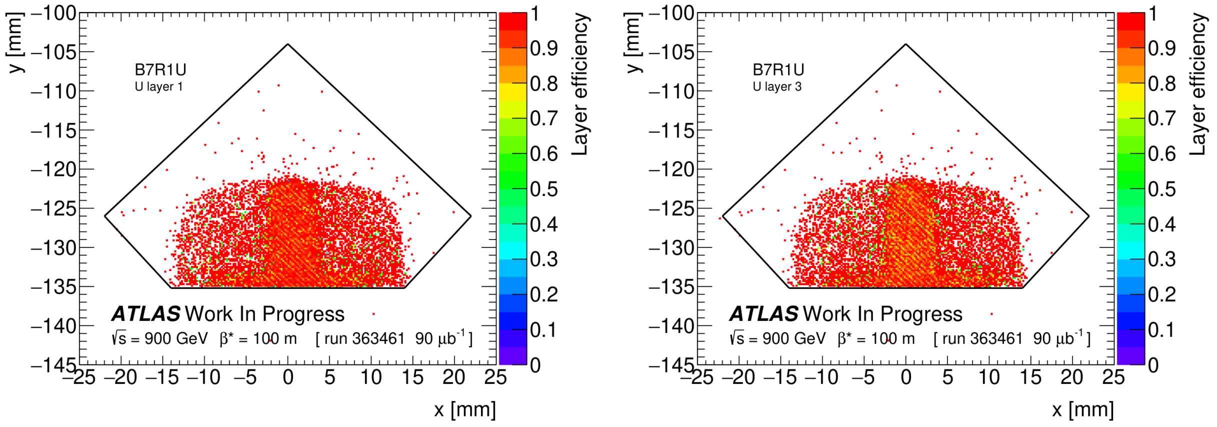

(a) U layer 1.

(b) U layer 3.

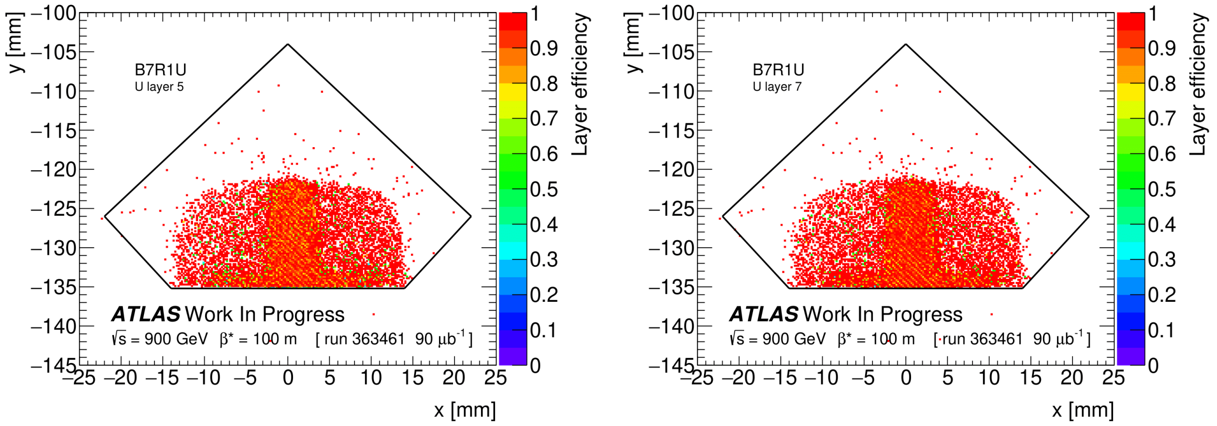

(c) U layer 5.

(d) U layer 7.

Figure B.27: B7L1L: spatial layer efficiency in the U-plane for tracks with elastic triggers.

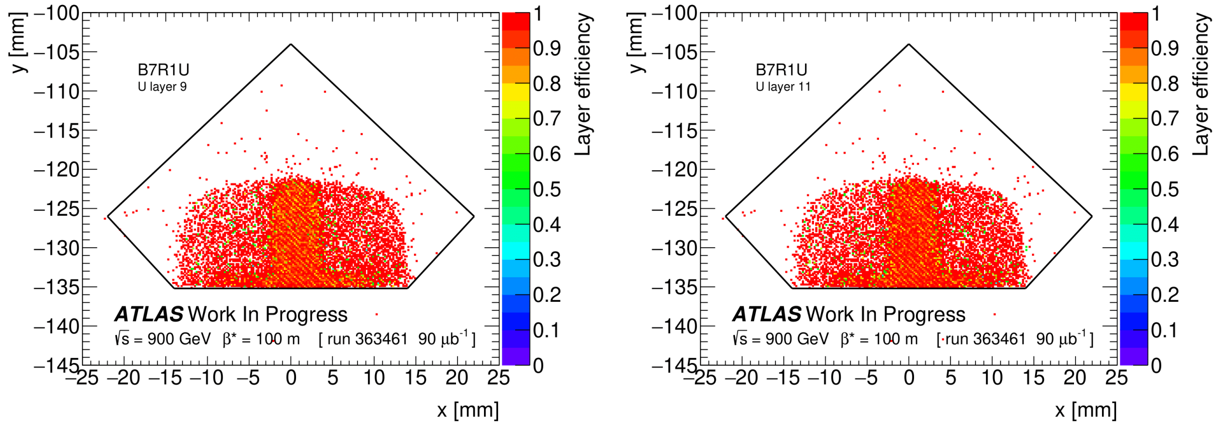

(a) U layer 9.

(b) U layer 11.

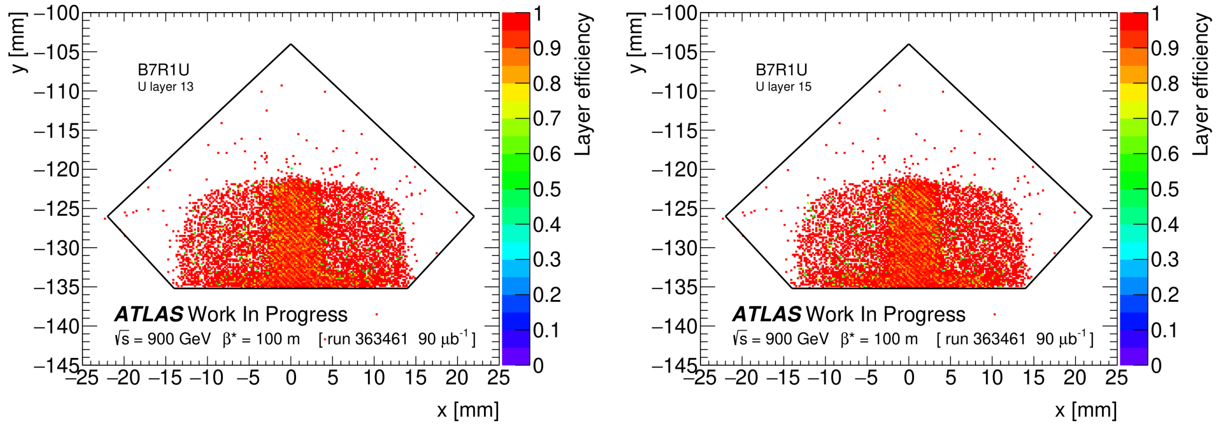

(c) U layer 13.

(d) U layer 15.

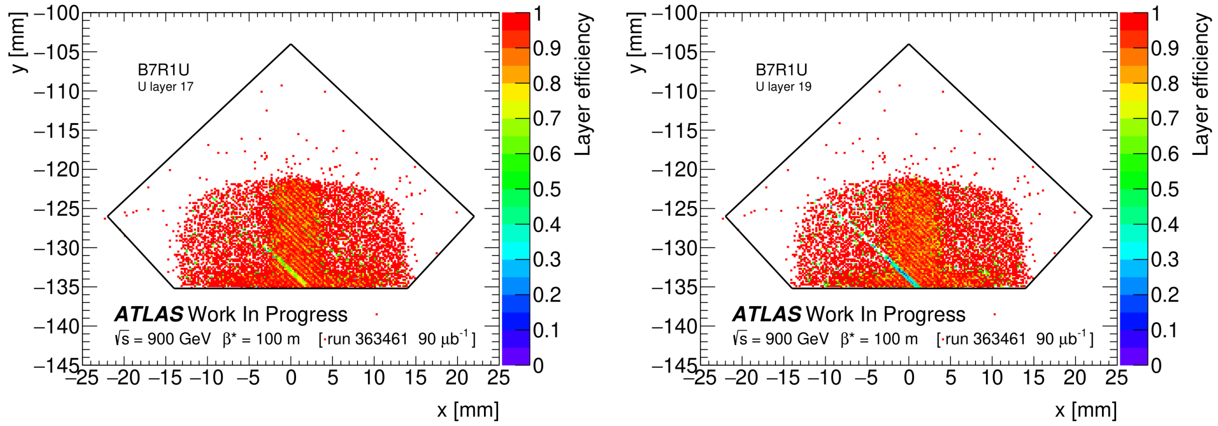

(e) U layer 17.

(f) U layer 19.

Figure B.28: B7L1L: spatial layer efficiency in the U-plane for tracks with elastic triggers.

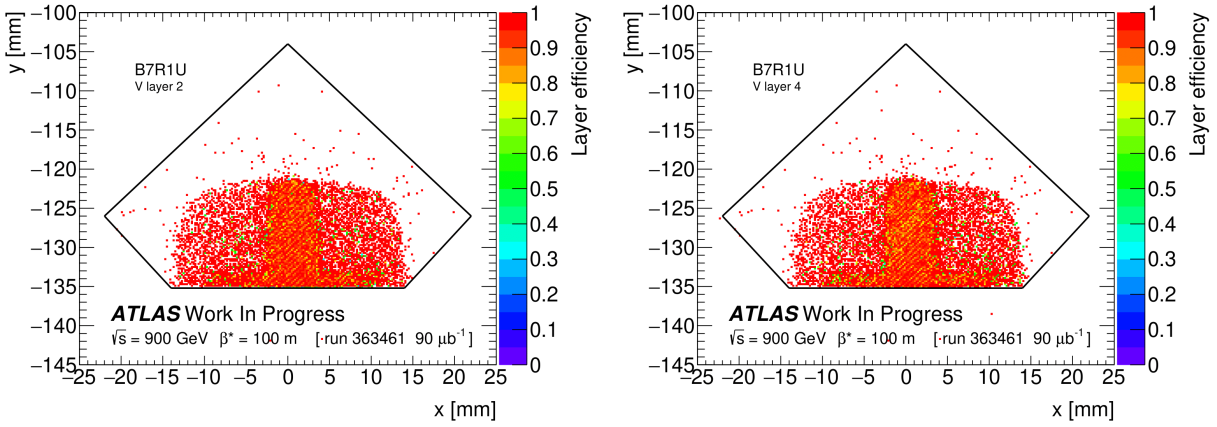

(a) V layer 2. **(b)** V layer 4.

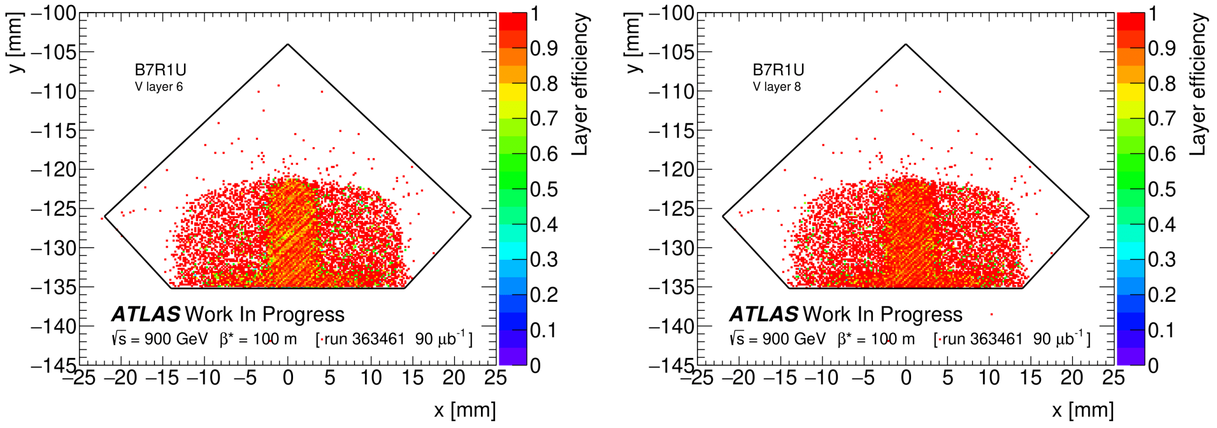

(c) V layer 6. **(d)** V layer 8.

Figure B.29: B7L1L: spatial layer efficiency in the V-plane for tracks with elastic triggers.

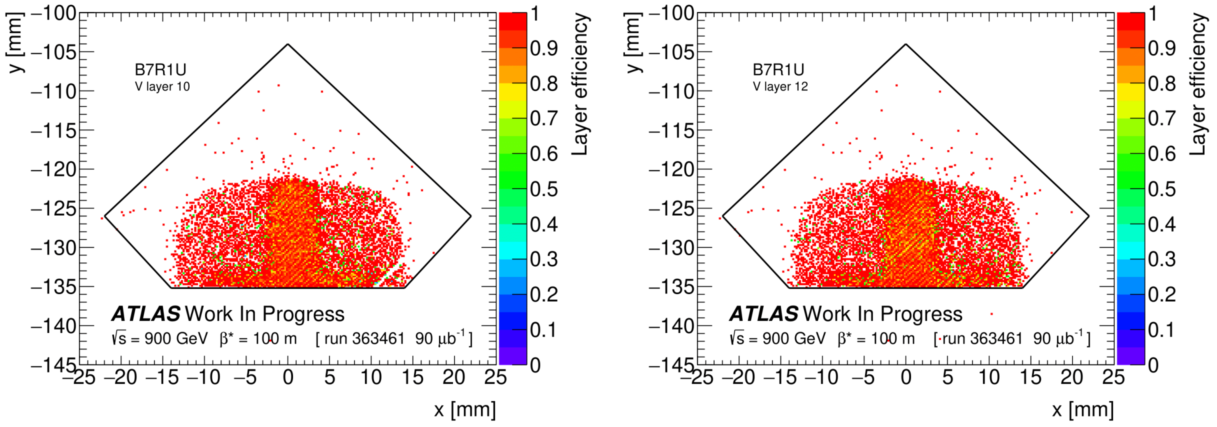

(a) V layer 10.

(b) V layer 12.

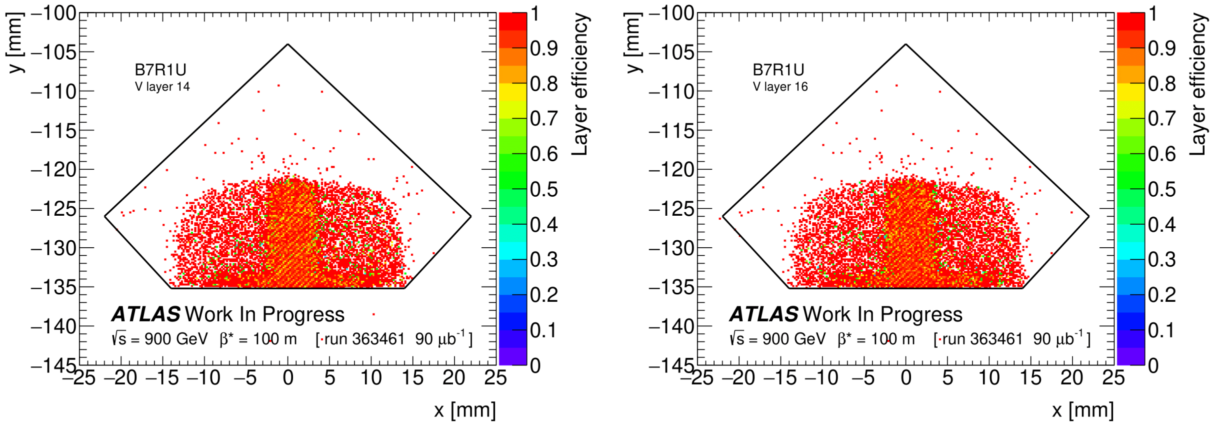

(c) V layer 14.

(d) V layer 16.

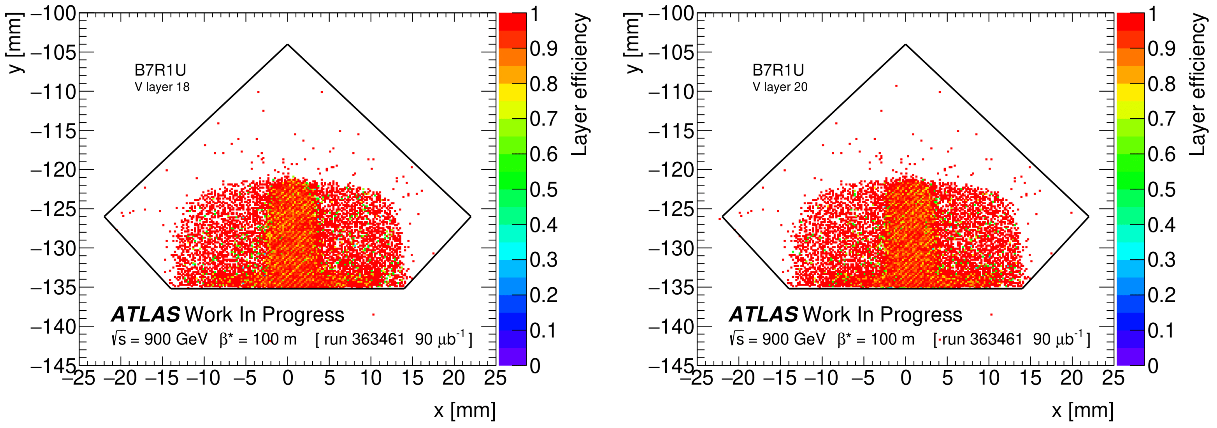

(e) V layer 18.

(f) V layer 20.

Figure B.30: B7L1L: spatial layer efficiency in the V-plane for tracks with elastic triggers.

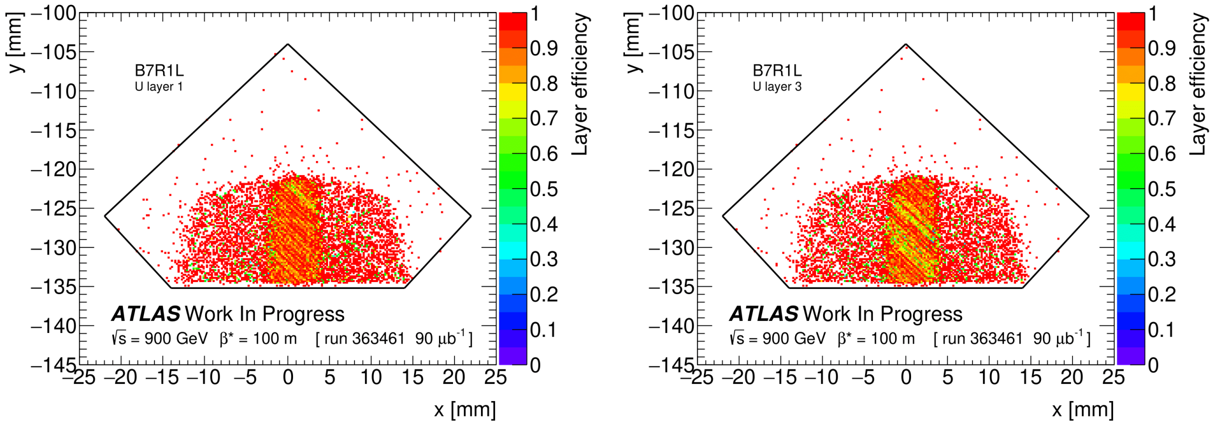

(a) U layer 1.

(b) U layer 3.

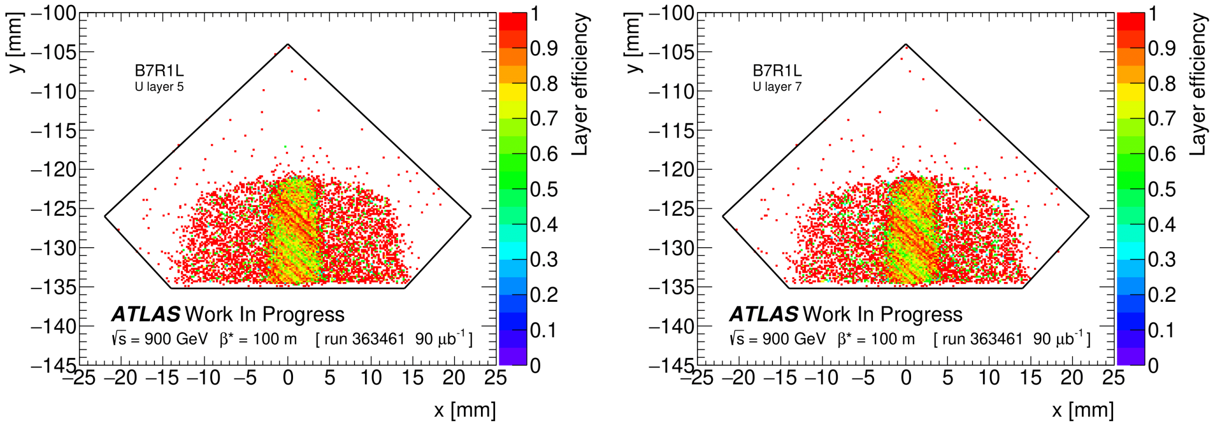

(c) U layer 5.

(d) U layer 7.

Figure B.31: B7R1U: spatial layer efficiency in the U-plane for tracks with elastic triggers.

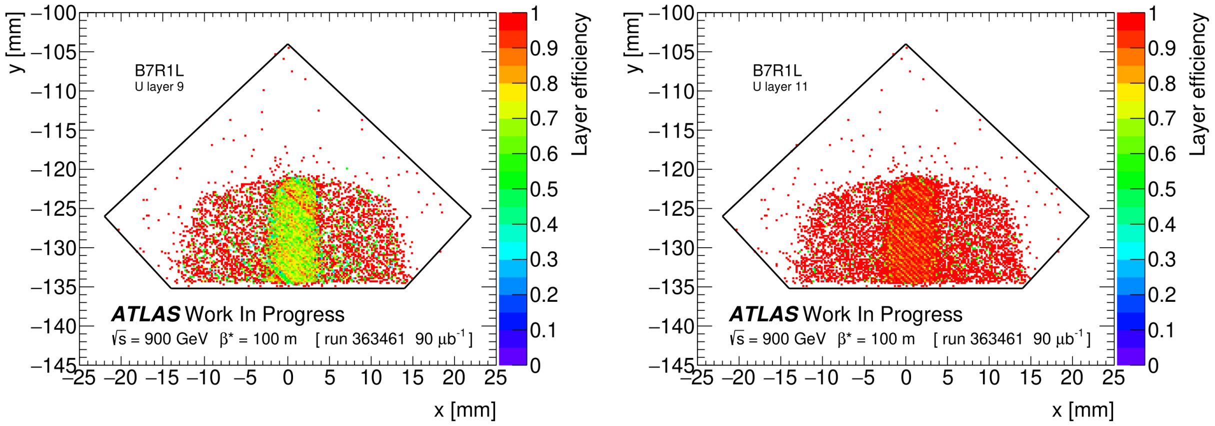

(a) U layer 9.

(b) U layer 11.

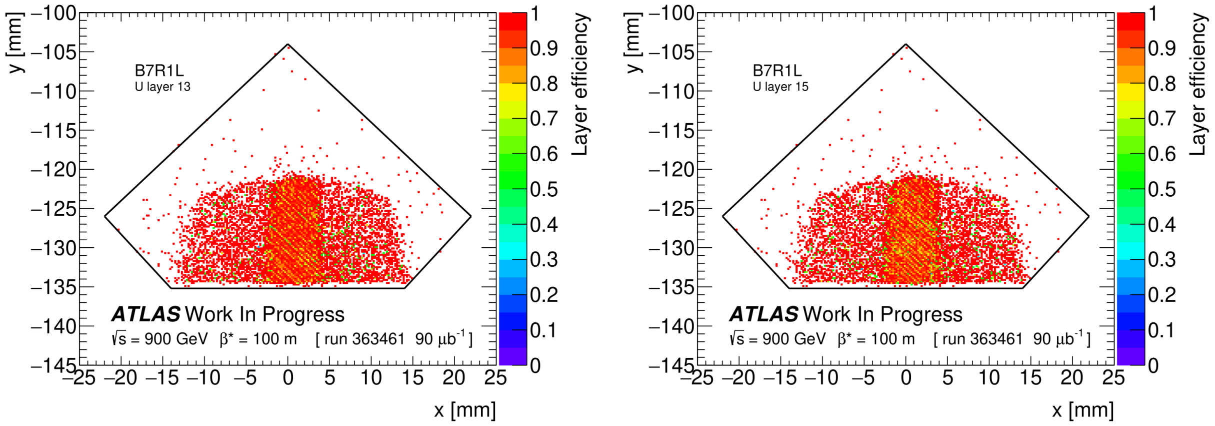

(c) U layer 13.

(d) U layer 15.

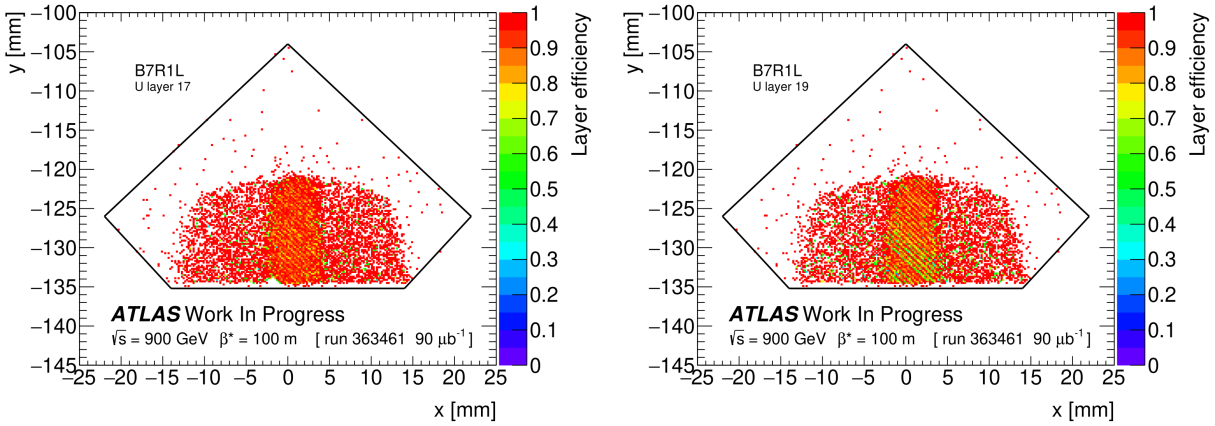

(e) U layer 17.

(f) U layer 19.

Figure B.32: B7R1U: spatial layer efficiency in the U-plane for tracks with elastic triggers.

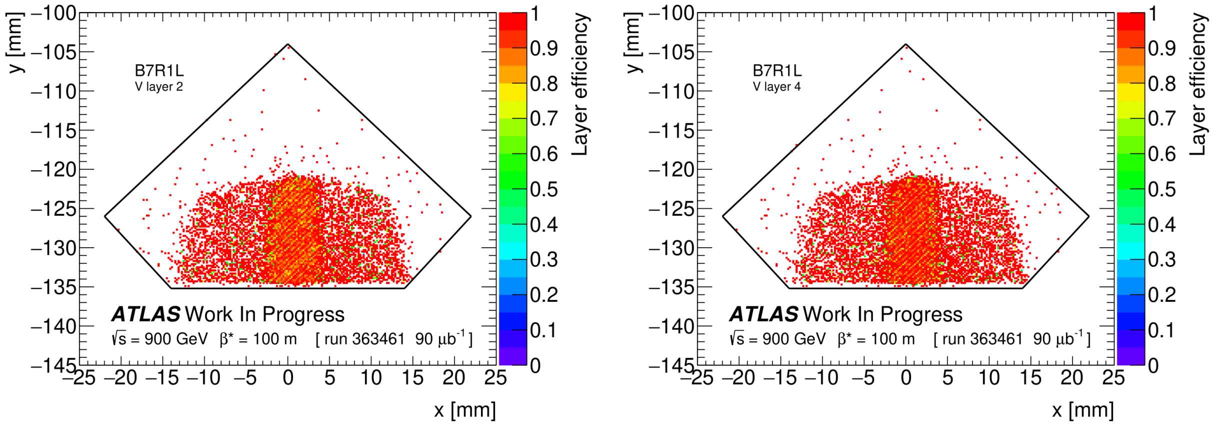

(a) V layer 2.

(b) V layer 4.

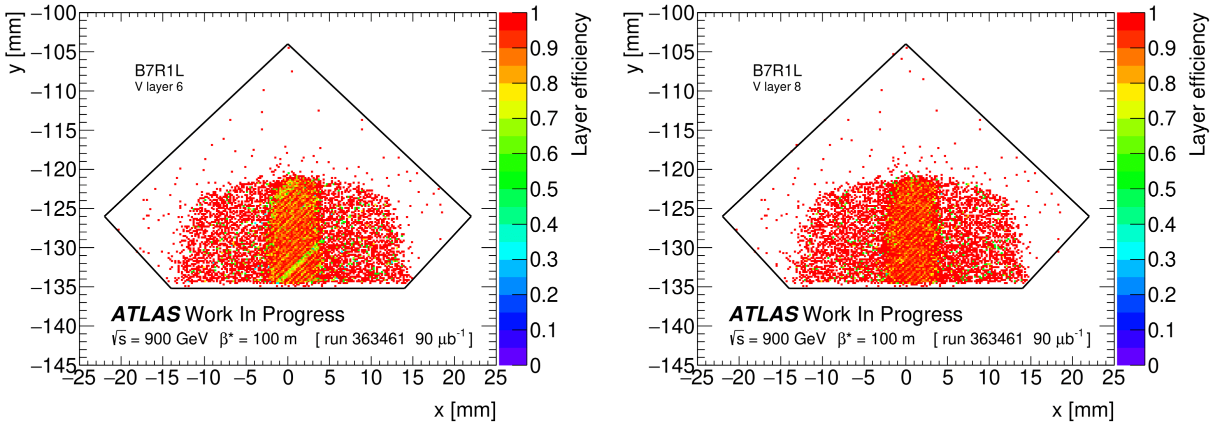

(c) V layer 6.

(d) V layer 8.

Figure B.33: B7R1U: spatial layer efficiency in the V-plane for tracks with elastic triggers.

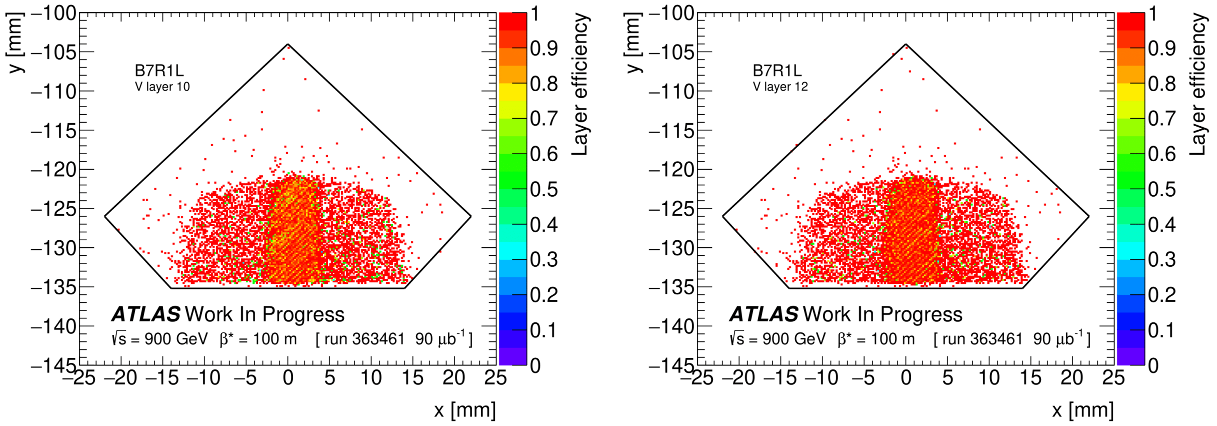

(a) V layer 10.

(b) V layer 12.

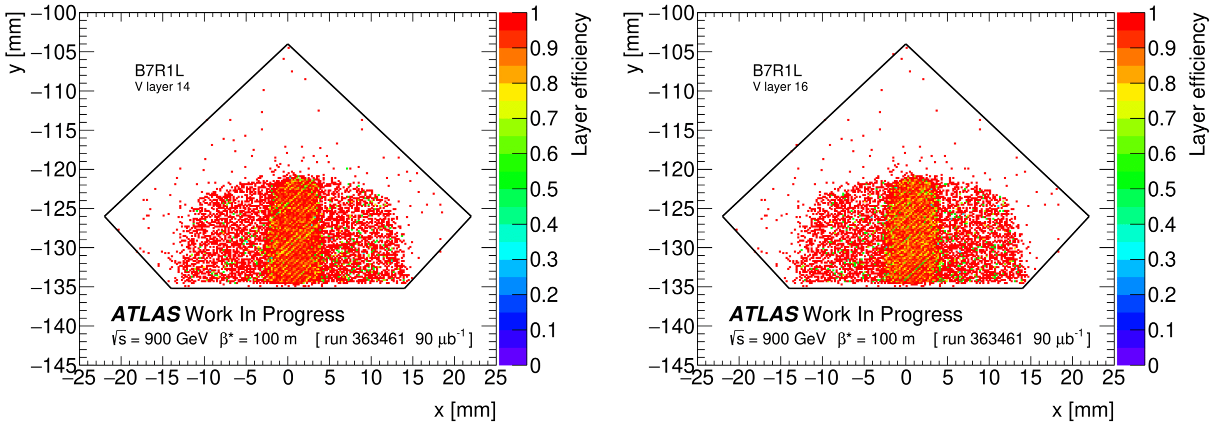

(c) V layer 14.

(d) V layer 16.

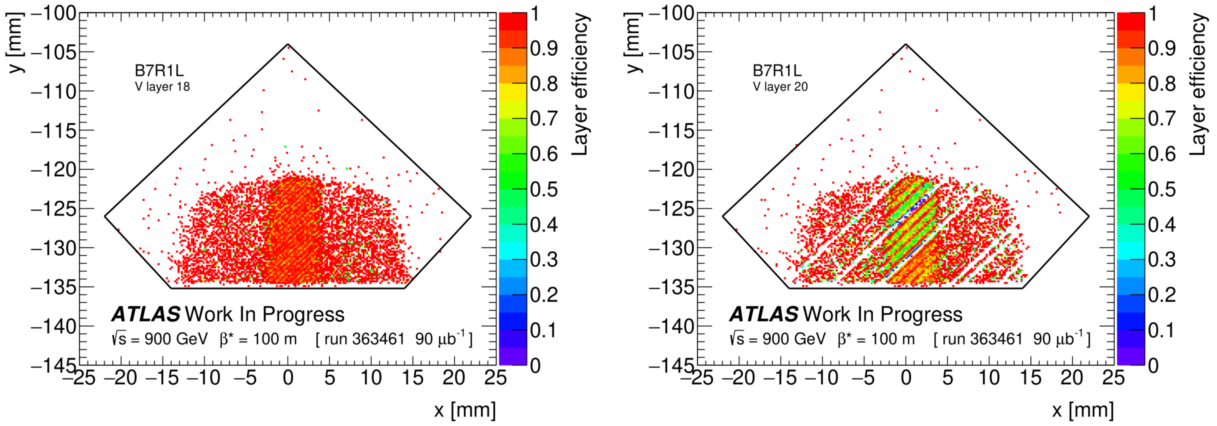

(e) V layer 18.

(f) V layer 20.

Figure B.34: B7R1U: spatial layer efficiency in the V-plane for tracks with elastic triggers.

B.3 Simulation of *t*-ranges

B.3.1 *t*-range 1e-4 till 3e-4 GeV^2

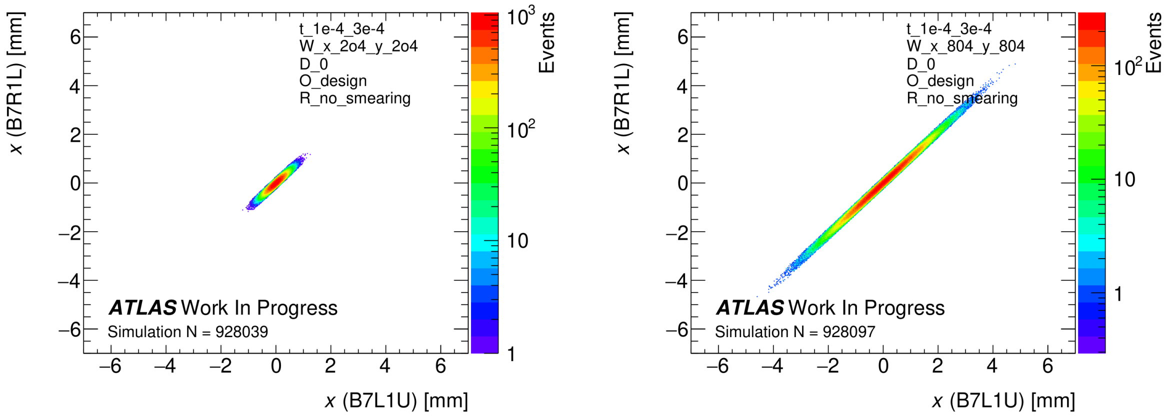

(a) W 2o4 D 0 O design R no smearing.

(b) W 8o4 D 0 O design R no smearing.

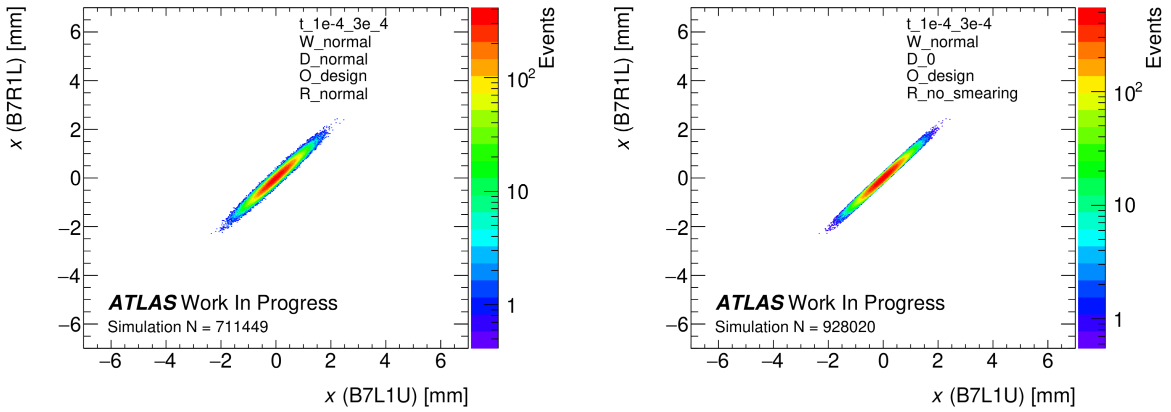

(c) W normal D normal O design R normal.

(d) W normal D 0 O design R no smearing.

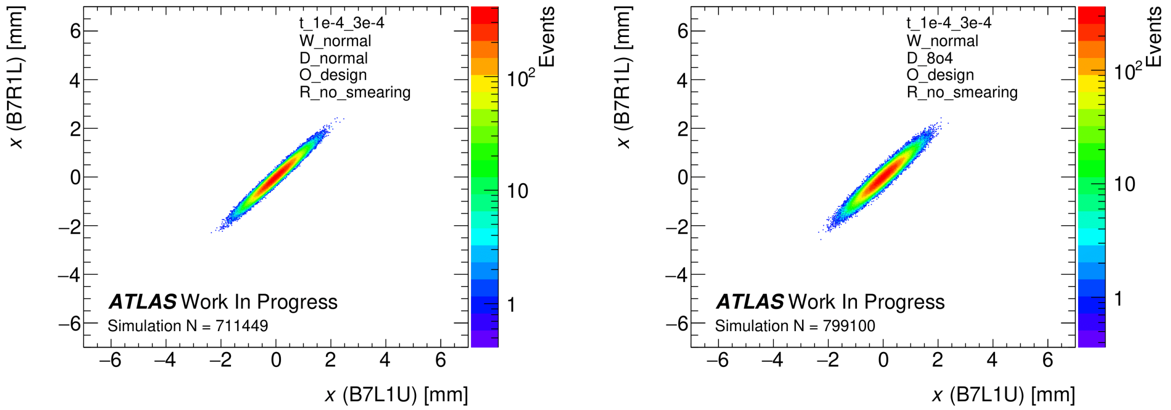

(e) W normal D normal O design R no smearing.

(f) W normal D 8o4 O design R no smearing.

Figure B.35: Outer detectors x correlation for 6 different simulation settings.

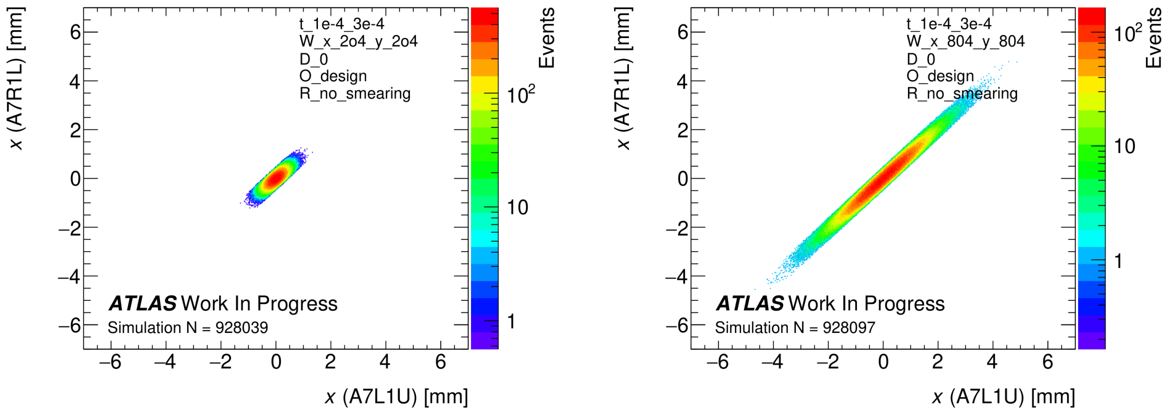

(a) W 2o4 D 0 O design R no smearing.

(b) W 8o4 D 0 O design R no smearing.

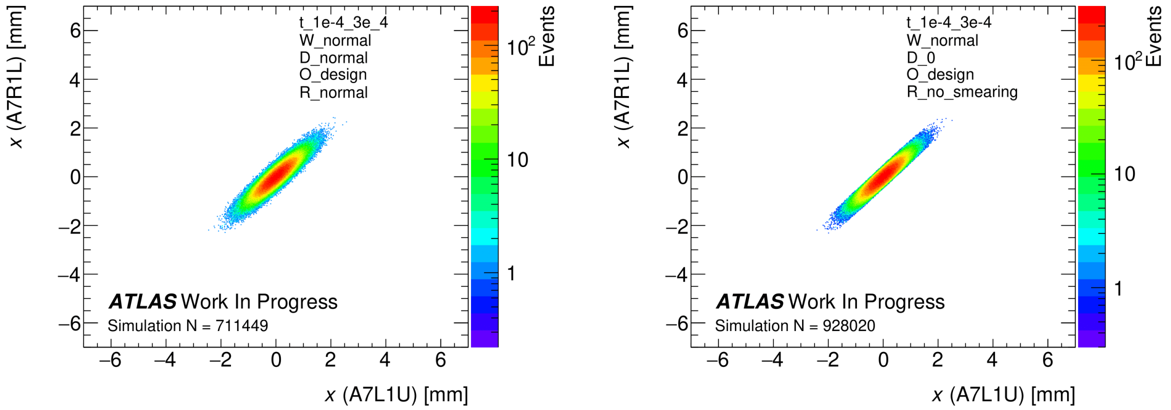

(c) W normal D normal O design R normal.

(d) W normal D 0 O design R no smearing.

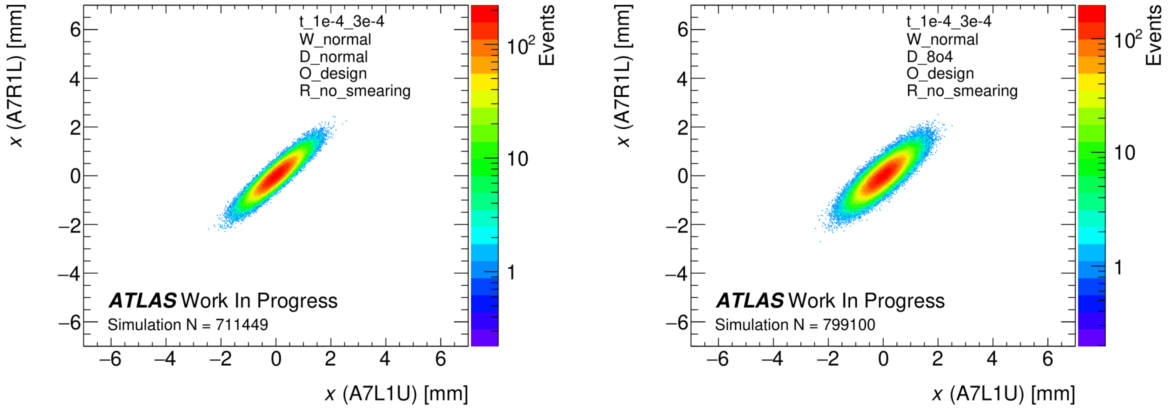

(e) W normal D normal O design R no smearing.

(f) W normal D 8o4 O design R no smearing.

Figure B.36: Inner detectors *x* correlation for 6 different simulation settings.

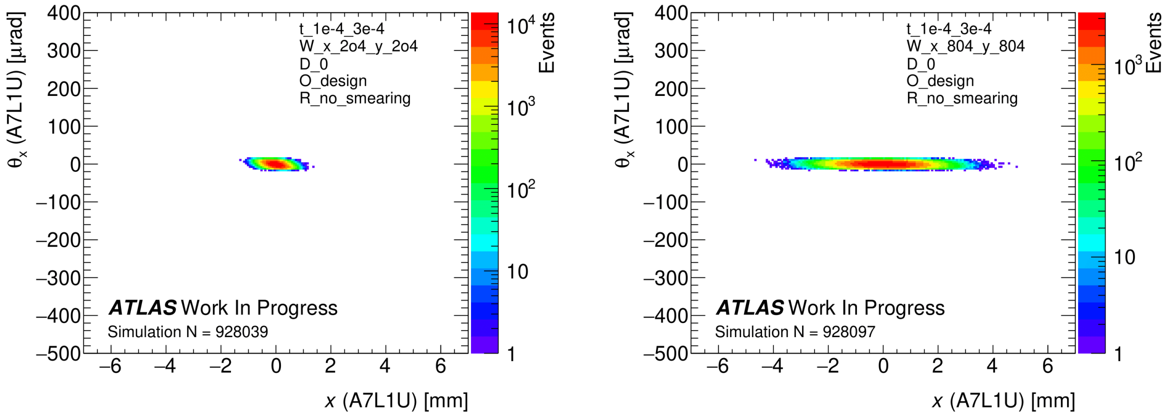

(a) W 2o4 D 0 O design R no smearing.

(b) W 8o4 D 0 O design R no smearing.

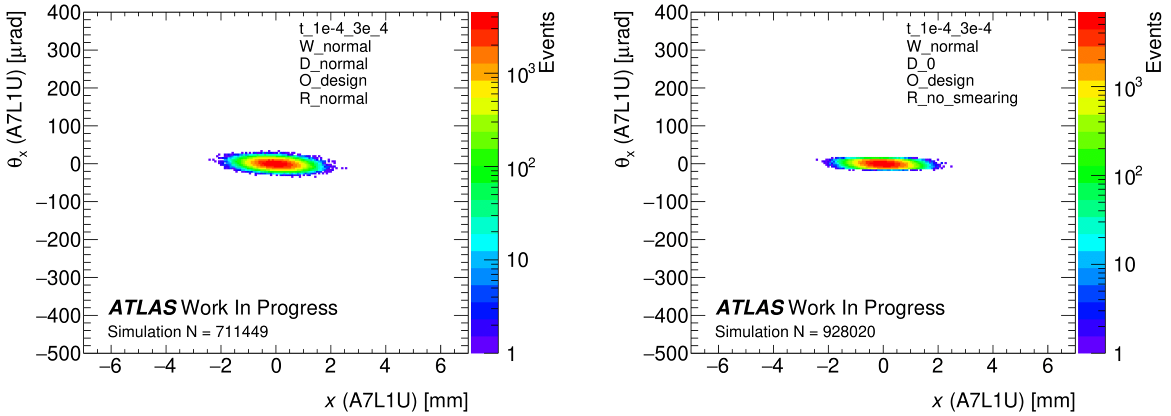

(c) W normal D normal O design R normal.

(d) W normal D 0 O design R no smearing.

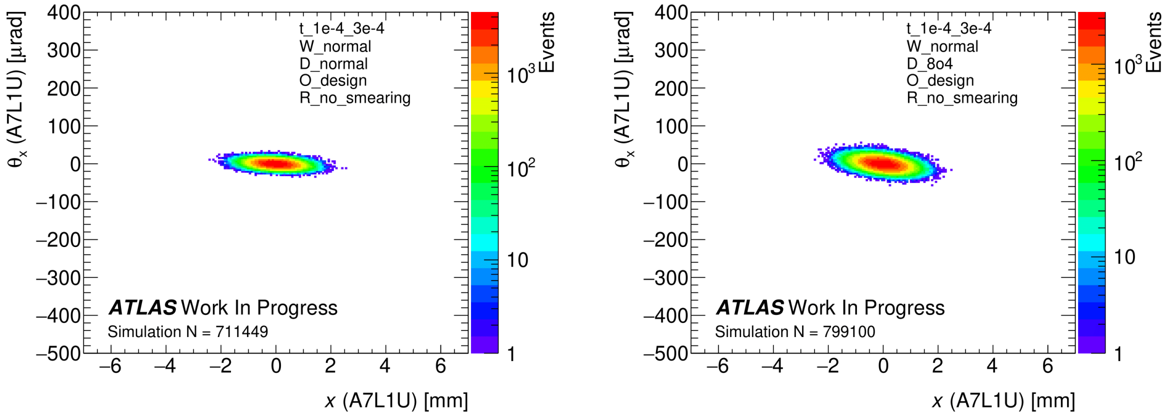

(e) W normal D normal O design R no smearing.

(f) W normal D 8o4 O design R no smearing.

Figure B.37: Inner detector x-θ_x correlation for 6 different simulation settings.

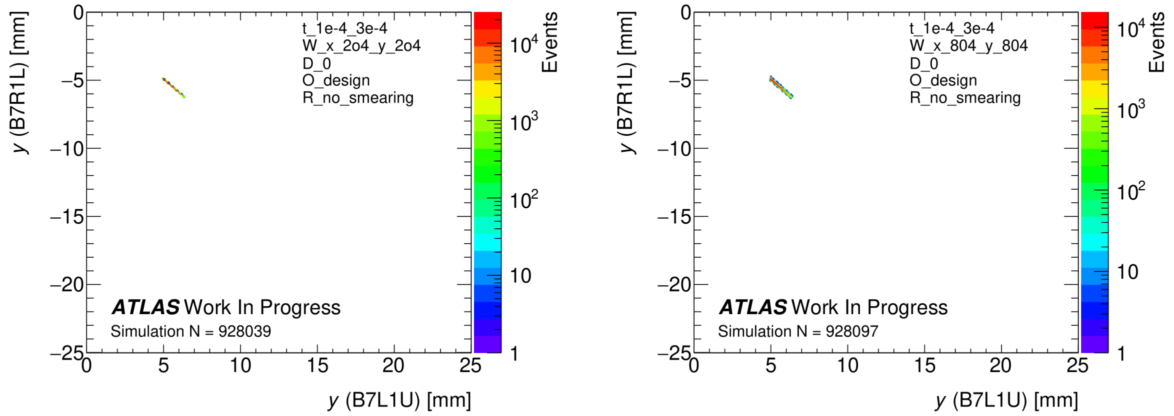

(a) W 2o4 D 0 O design R no smearing.

(b) W 8o4 D 0 O design R no smearing.

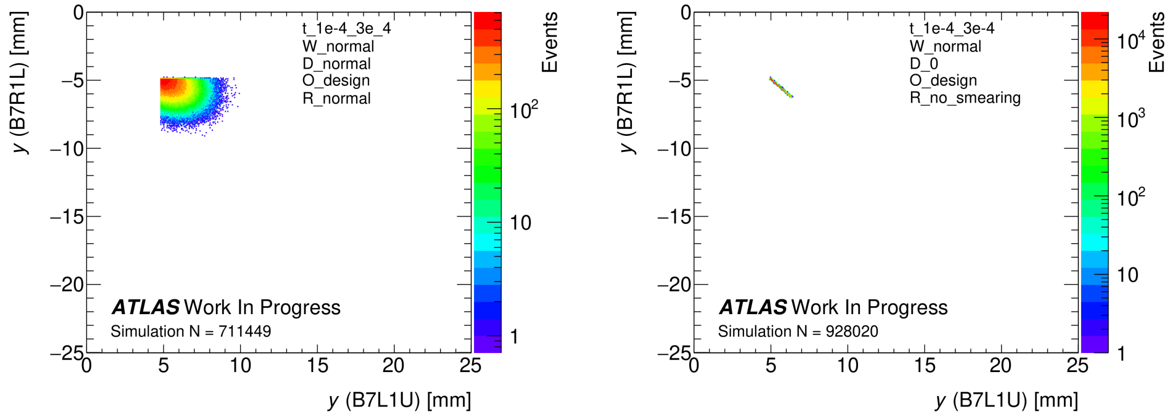

(c) W normal D normal O design R normal.

(d) W normal D 0 O design R no smearing.

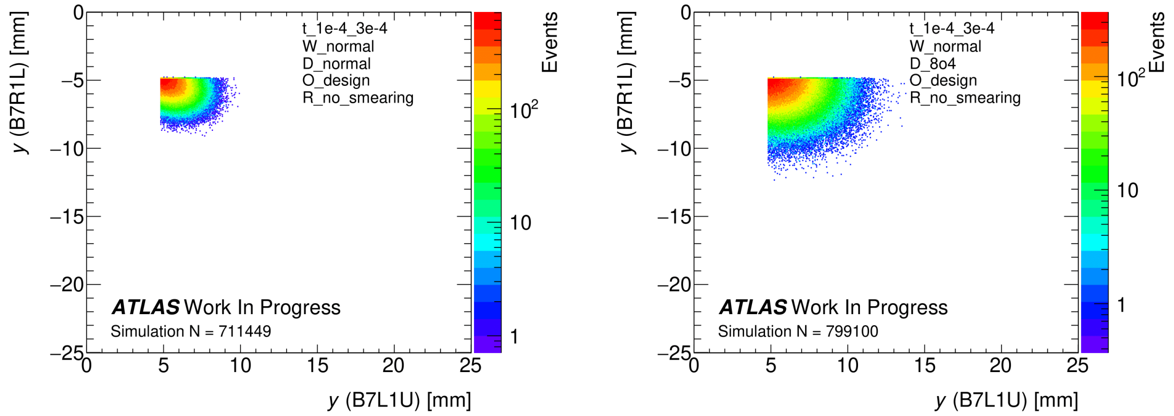

(e) W normal D normal O design R no smearing.

(f) W normal D 8o4 O design R no smearing.

Figure B.38: Outer detectors y correlation for 6 different simulation settings.

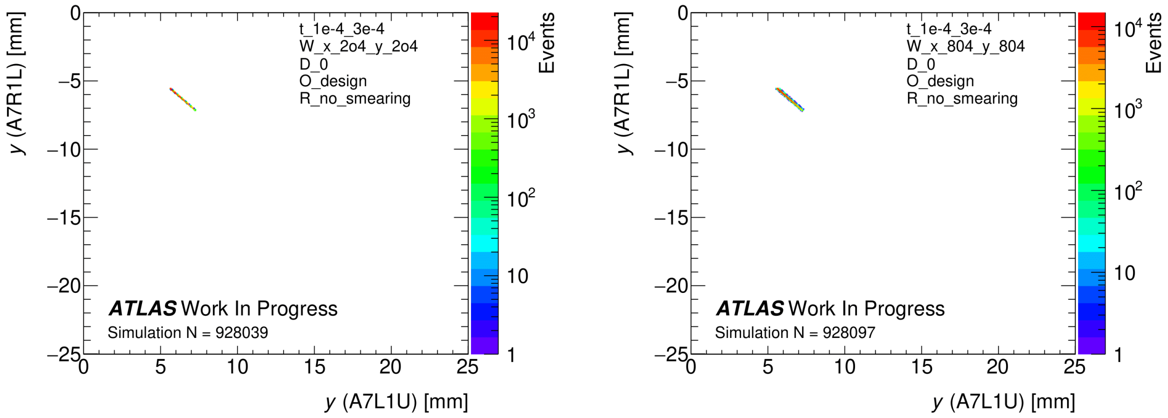

(a) W 2o4 D 0 O design R no smearing.

(b) W 8o4 D 0 O design R no smearing.

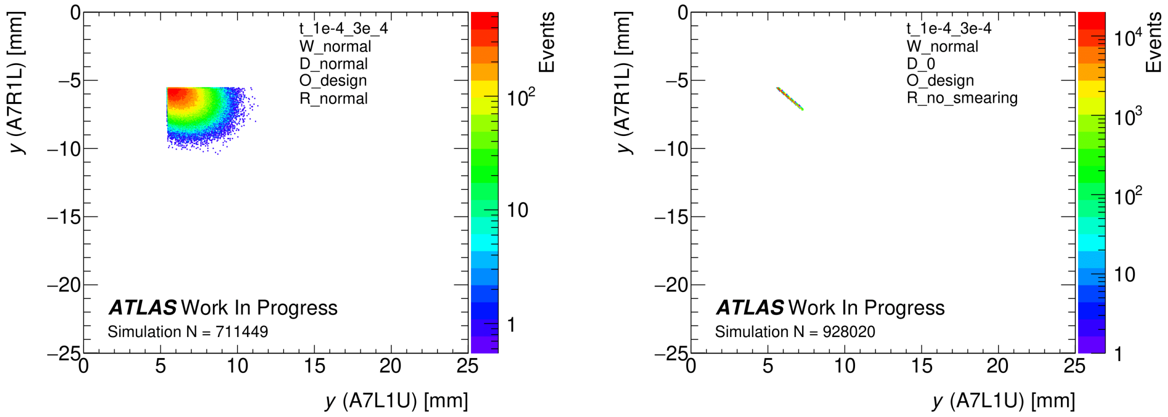

(c) W normal D normal O design R normal.

(d) W normal D 0 O design R no smearing.

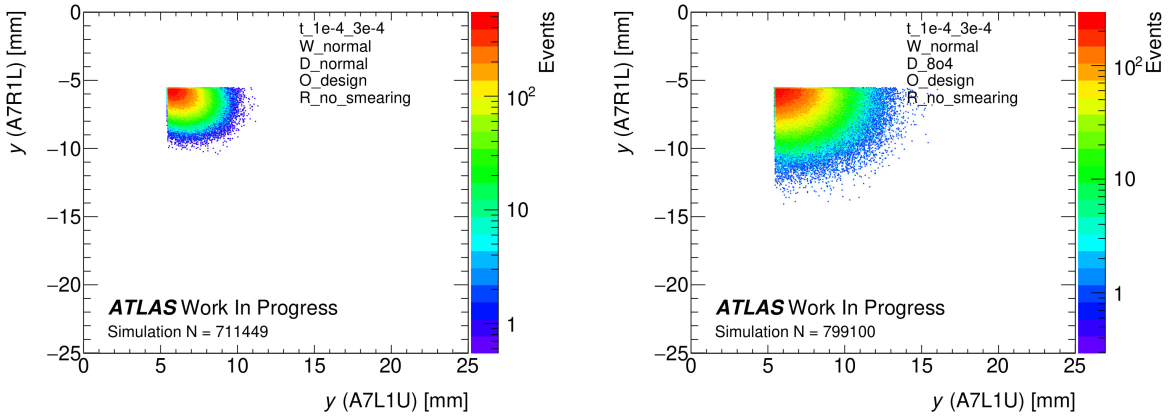

(e) W normal D normal O design R no smearing.

(f) W normal D 8o4 O design R no smearing.

Figure B.39: Inner detectors y correlation for 6 different simulation settings.

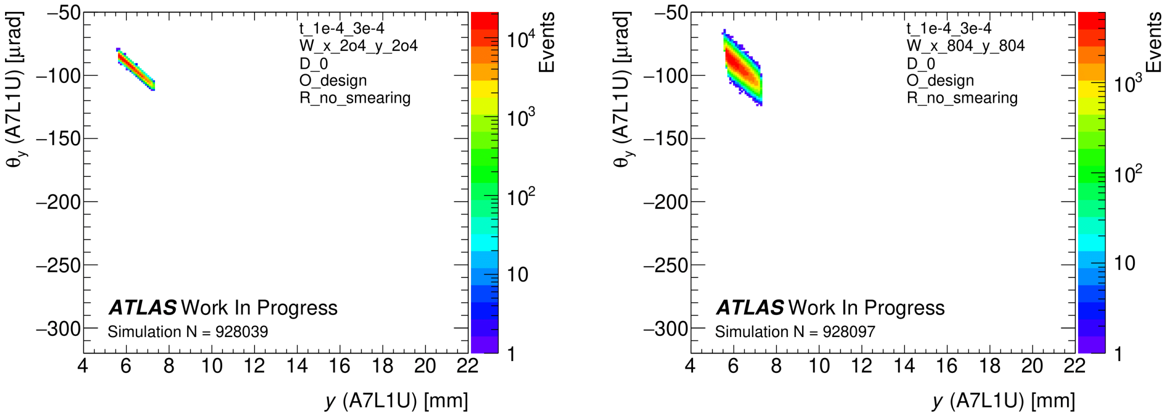

(a) W 2o4 D 0 O design R no smearing. **(b)** W 8o4 D 0 O design R no smearing.

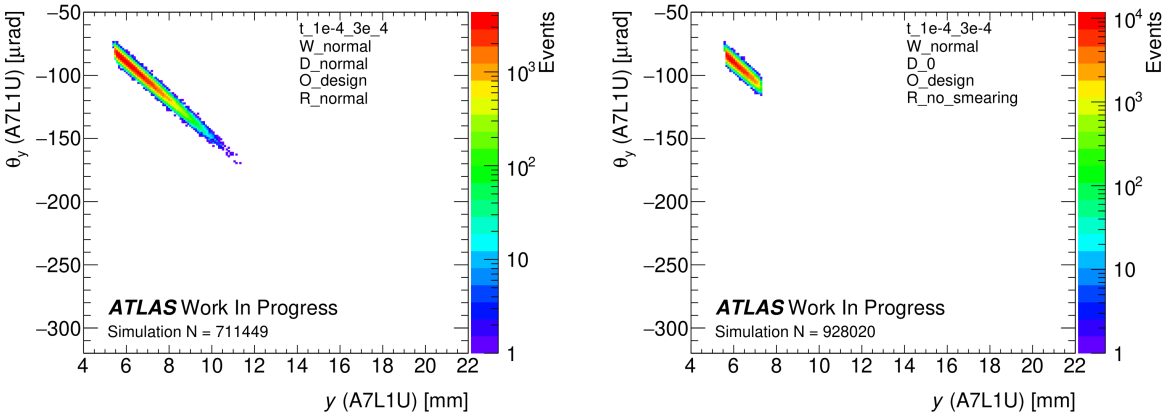

(c) W normal D normal O design R normal. **(d)** W normal D 0 O design R no smearing.

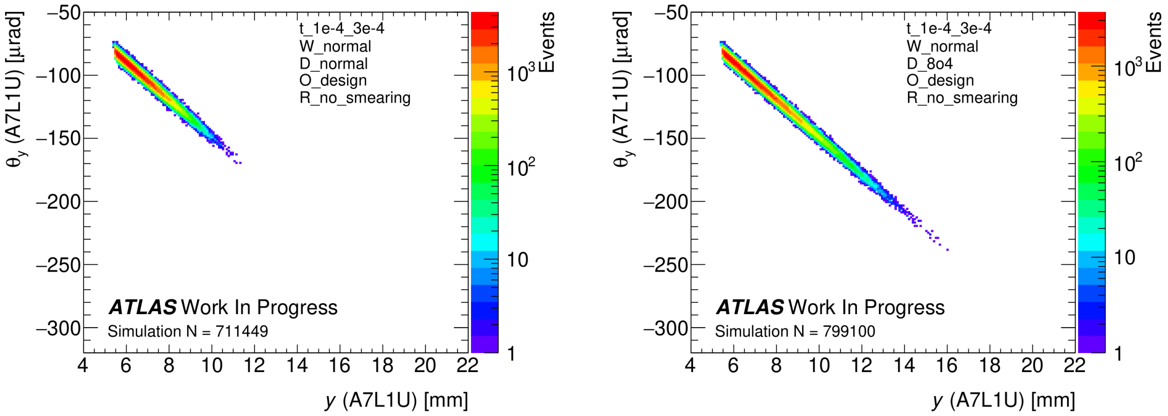

(e) W normal D normal O design R no smearing. **(f)** W normal D 8o4 O design R no smearing.

Figure B.40: Inner detector x-θ_x correlation for 6 different simulation settings.

B.3.2 t-range 3e-4 till 7e-4 GeV^2

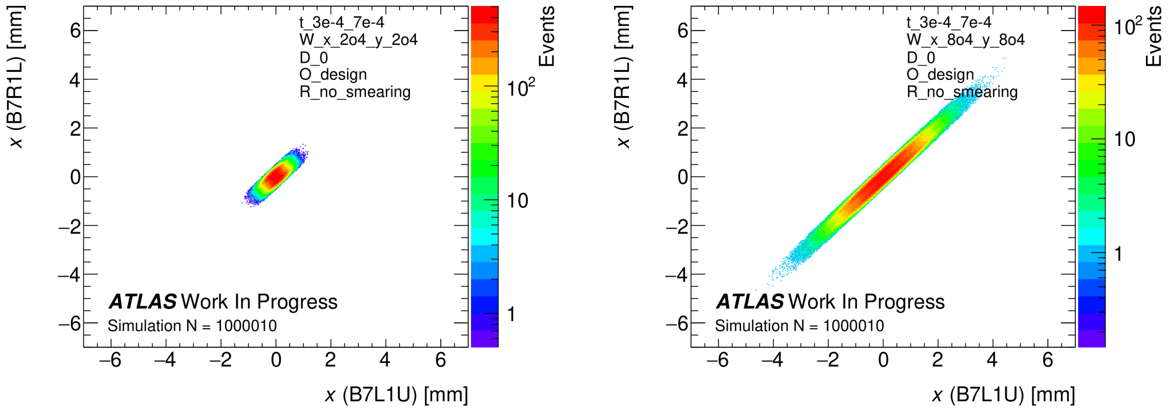

(a) W 2o4 D 0 O design R no smearing.

(b) W 8o4 D 0 O design R no smearing.

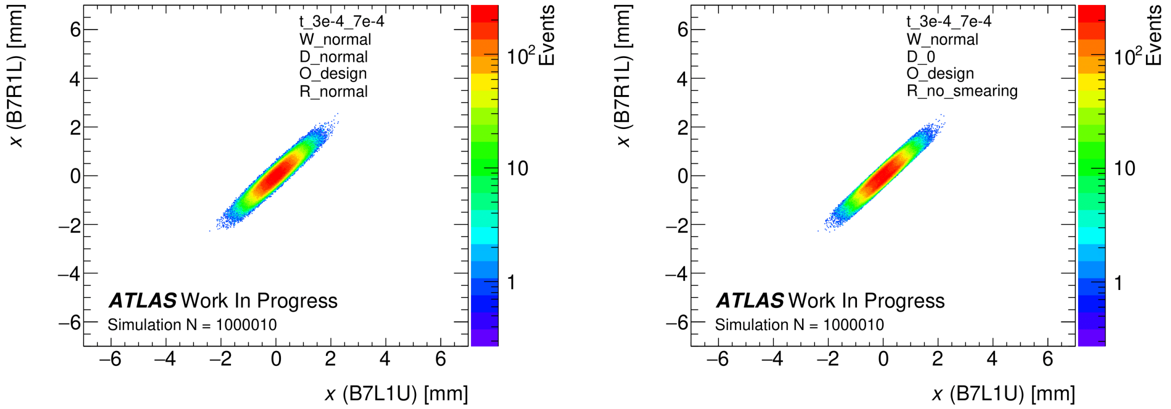

(c) W normal D normal O design R normal.

(d) W normal D 0 O design R no smearing.

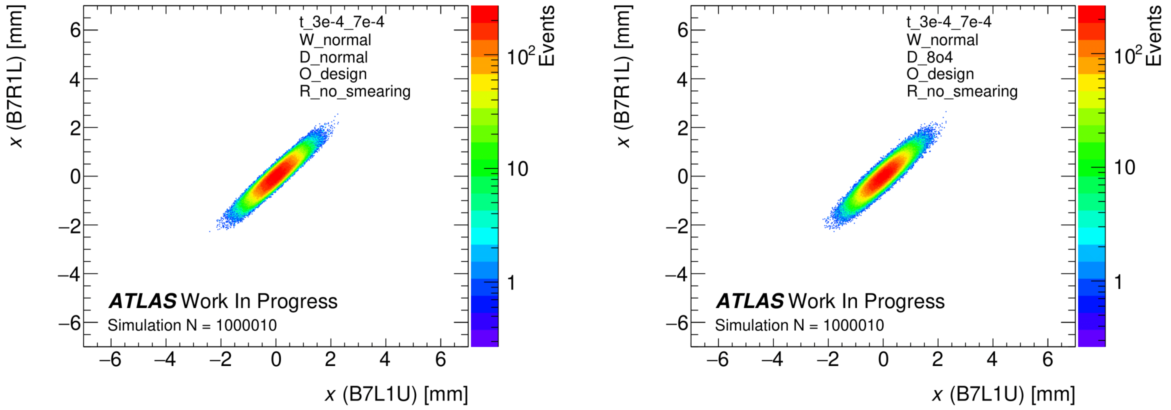

(e) W normal D normal O design R no smearing.

(f) W normal D 8o4 O design R no smearing.

Figure B.41: Outer detectors x correlation for 6 different simulation settings.

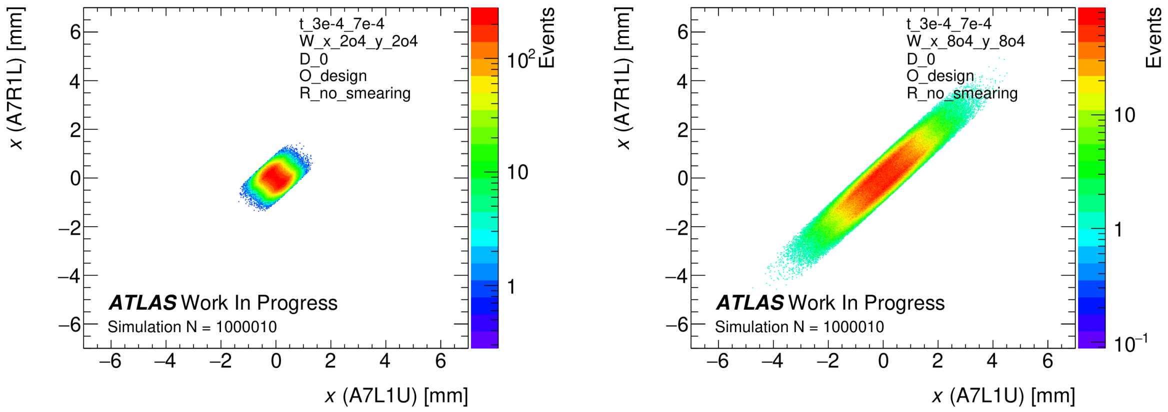

(a) W 2o4 D 0 O design R no smearing. **(b)** W 8o4 D 0 O design R no smearing.

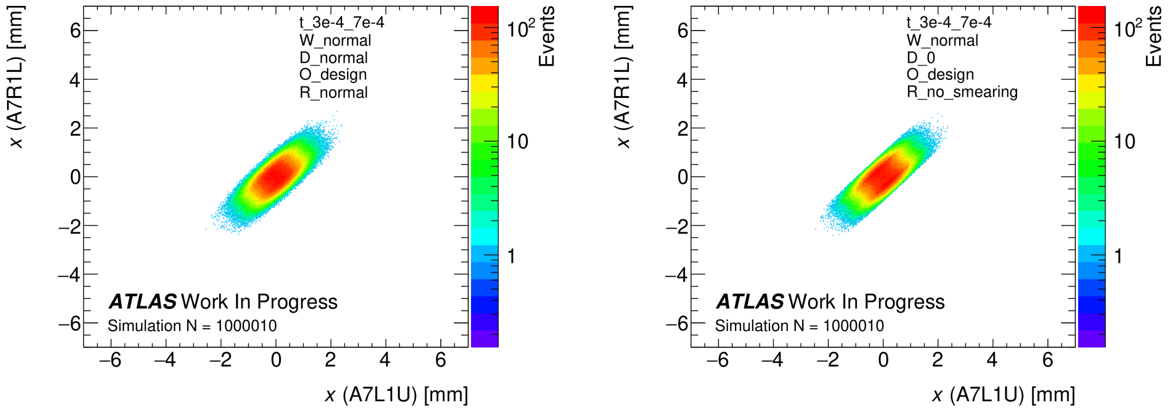

(c) W normal D normal O design R normal. **(d)** W normal D 0 O design R no smearing.

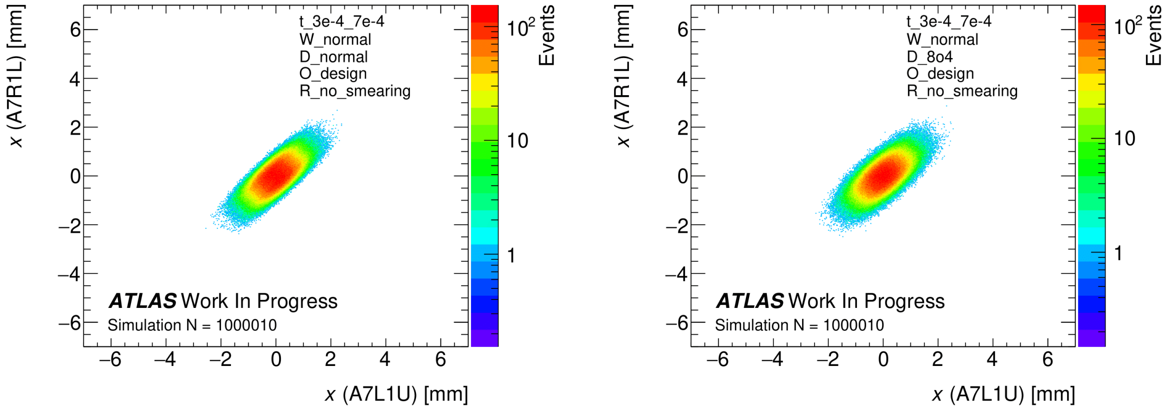

(e) W normal D normal O design R no smearing. **(f)** W normal D 8o4 O design R no smearing.

Figure B.42: Inner detectors x correlation for 6 different simulation settings.

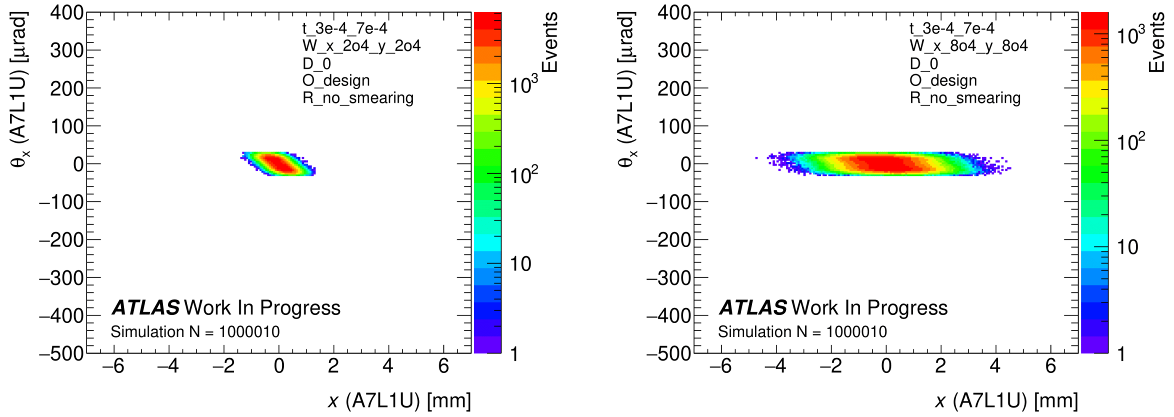

(a) W 2o4 D 0 O design R no smearing.

(b) W 8o4 D 0 O design R no smearing.

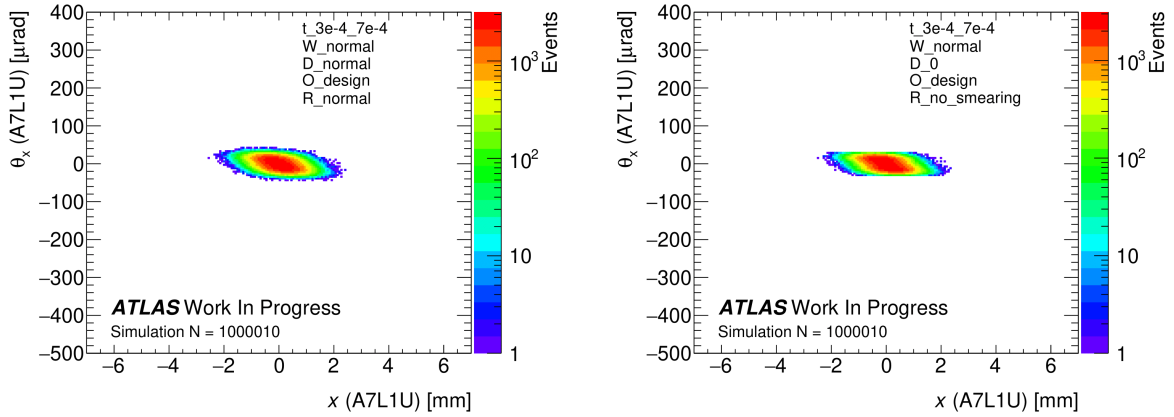

(c) W normal D normal O design R normal.

(d) W normal D 0 O design R no smearing.

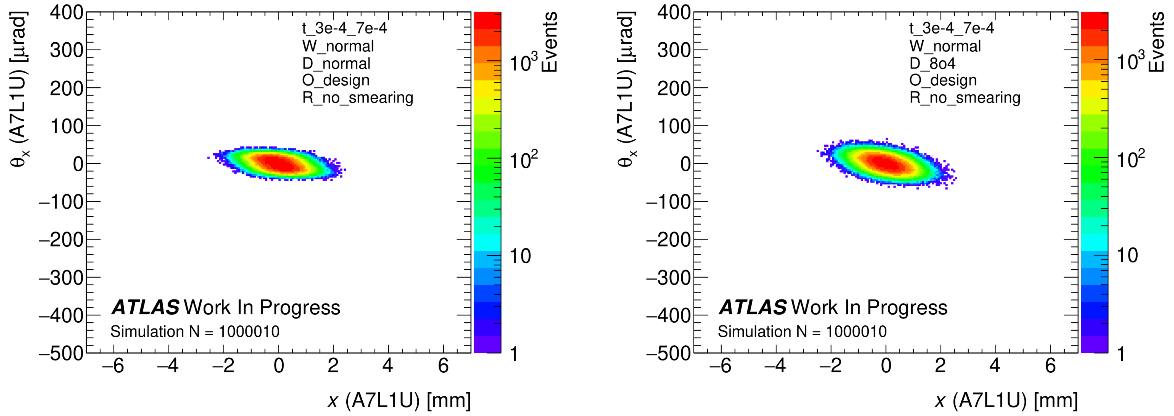

(e) W normal D normal O design R no smearing.

(f) W normal D 8o4 O design R no smearing.

Figure B.43: Inner detector x-θ_x correlation for 6 different simulation settings.

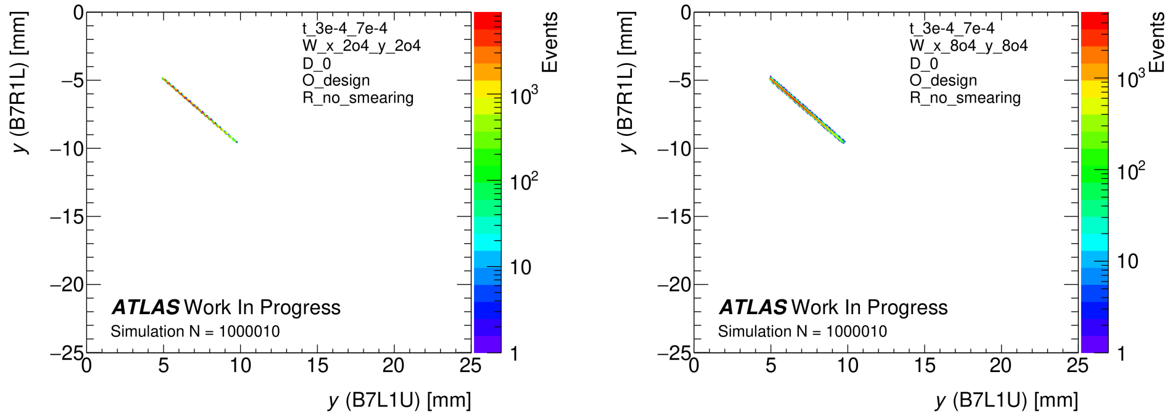

(a) W 2o4 D 0 O design R no smearing. **(b)** W 8o4 D 0 O design R no smearing.

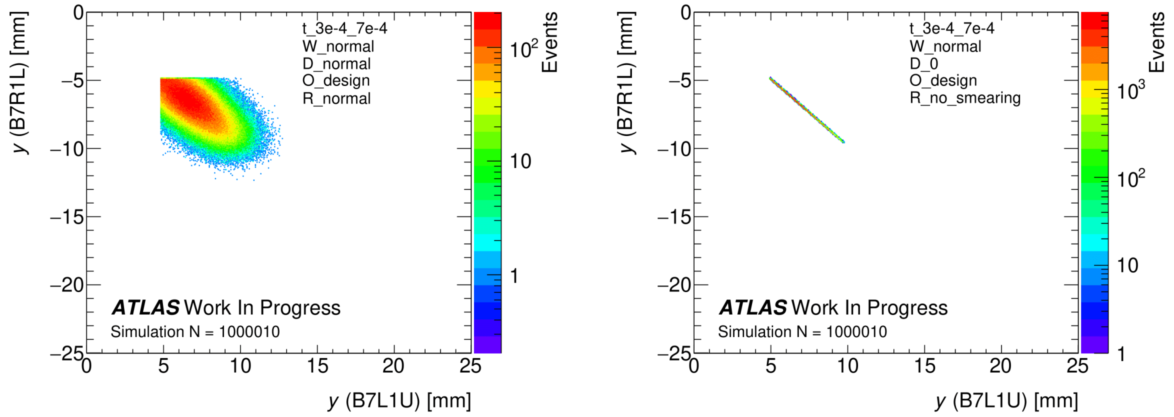

(c) W normal D normal O design R normal. **(d)** W normal D 0 O design R no smearing.

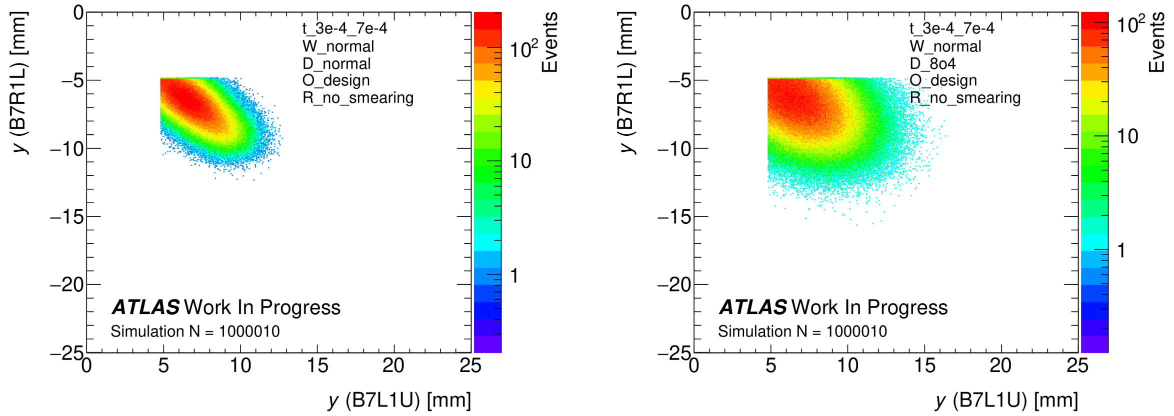

(e) W normal D normal O design R no smearing. **(f)** W normal D 8o4 O design R no smearing.

Figure B.44: Outer detectors y correlation for 6 different simulation settings.

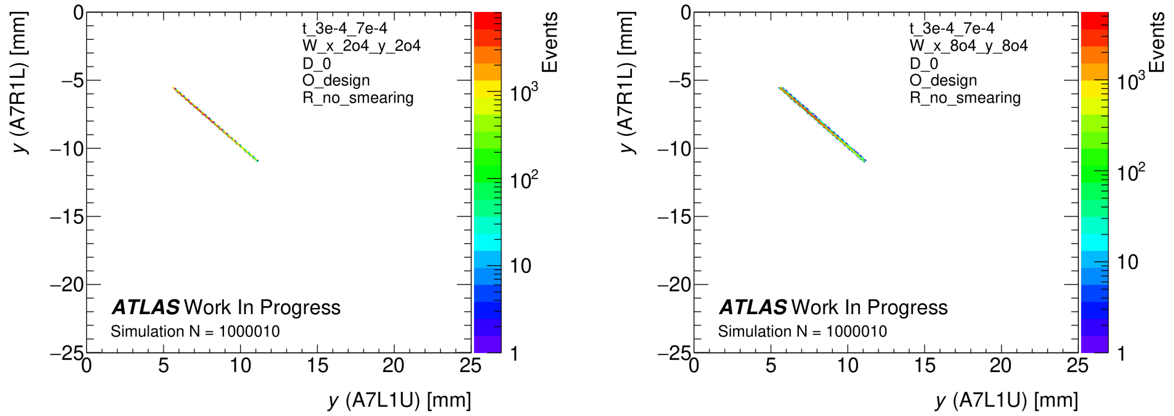

(a) W 2o4 D 0 O design R no smearing.

(b) W 8o4 D 0 O design R no smearing.

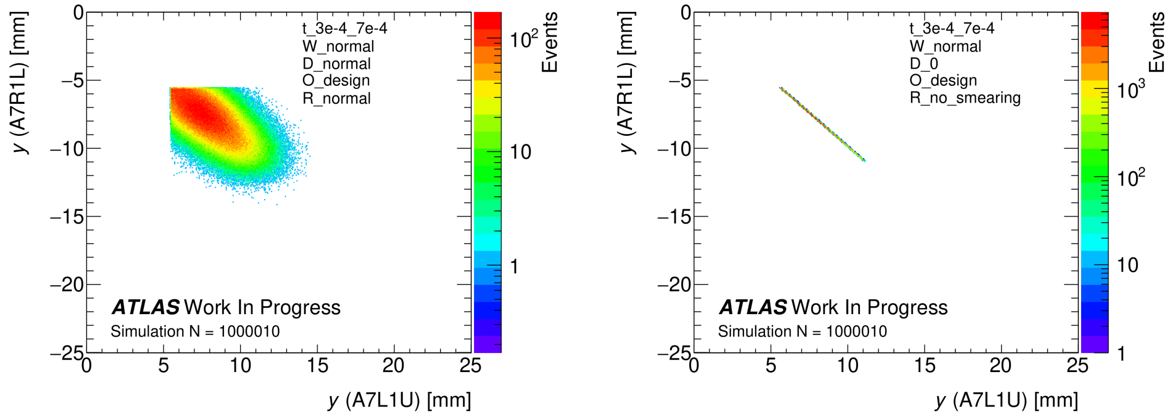

(c) W normal D normal O design R normal.

(d) W normal D 0 O design R no smearing.

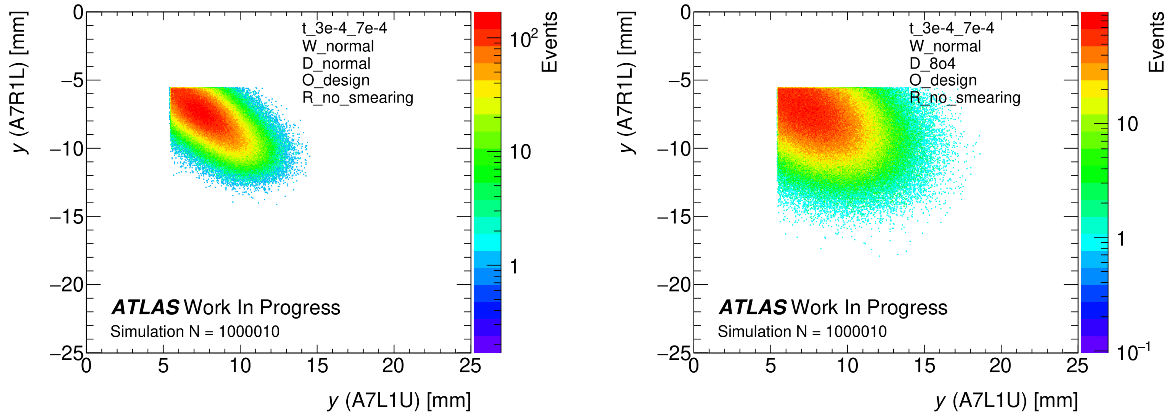

(e) W normal D normal O design R no smearing.

(f) W normal D 8o4 O design R no smearing.

Figure B.45: Inner detectors y correlation for 6 different simulation settings.

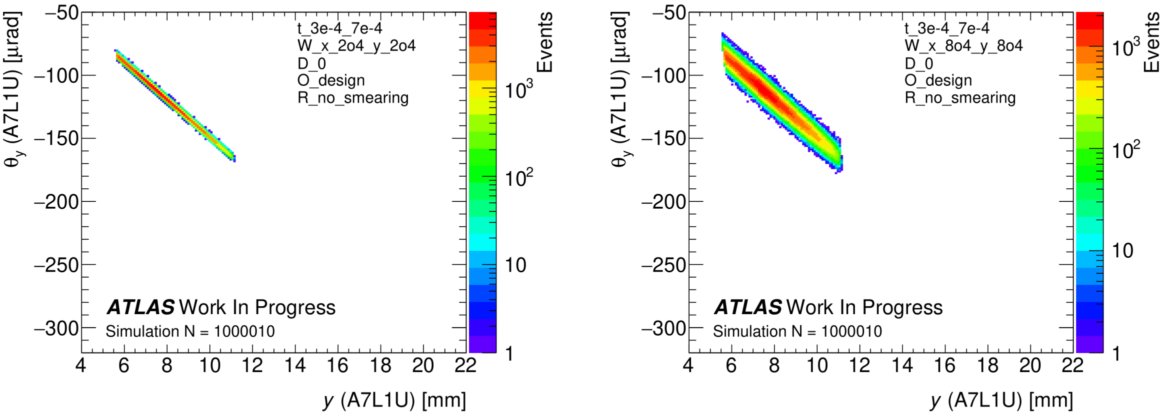

(a) W 2o4 D 0 O design R no smearing.

(b) W 8o4 D 0 O design R no smearing.

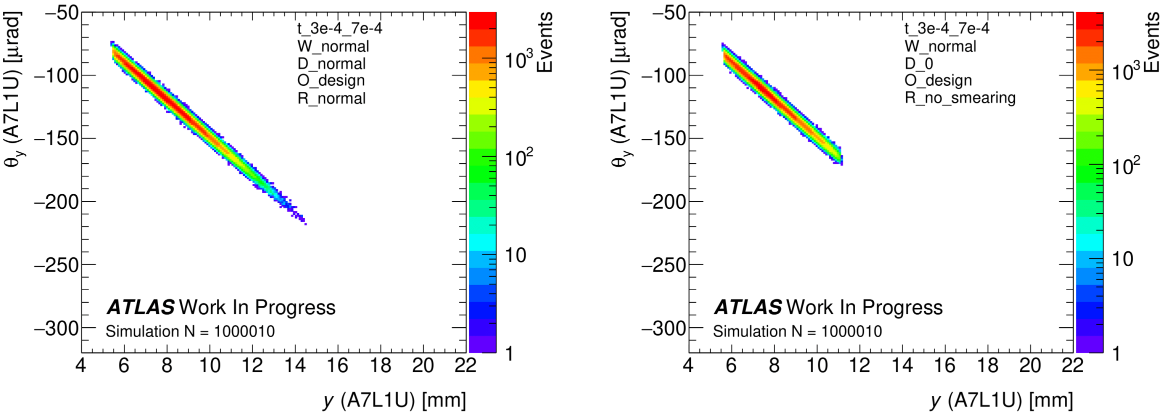

(c) W normal D normal O design R normal.

(d) W normal D 0 O design R no smearing.

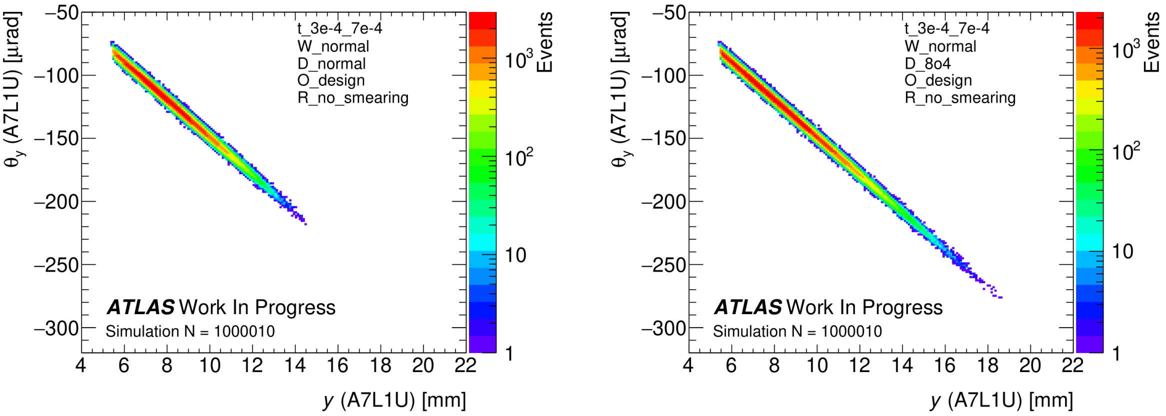

(e) W normal D normal O design R no smearing.

(f) W normal D 8o4 O design R no smearing.

Figure B.46: Inner detector x-θ_x correlation for 6 different simulation settings.

B.3.3 t-range 7e-4 till 1e-3 GeV^2

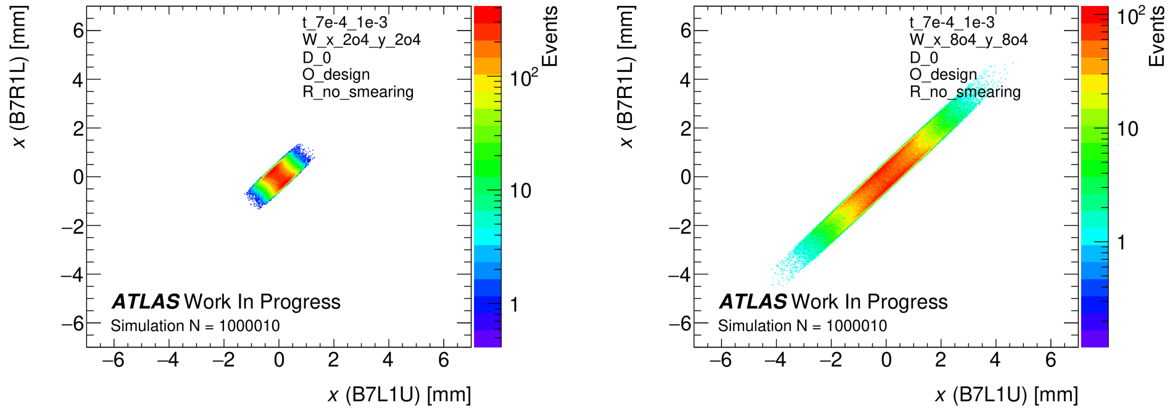

(a) W 2o4 D 0 O design R no smearing. **(b)** W 8o4 D 0 O design R no smearing.

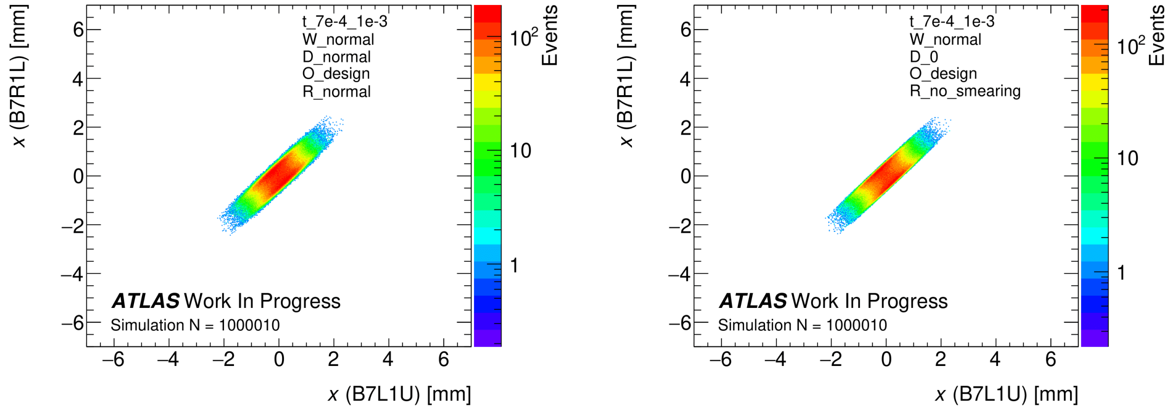

(c) W normal D normal O design R normal. **(d)** W normal D 0 O design R no smearing.

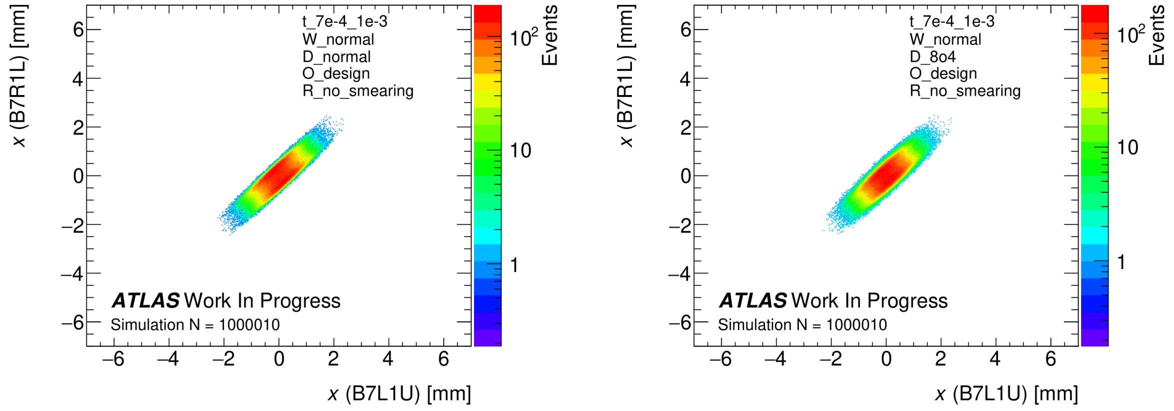

(e) W normal D normal O design R no smearing. **(f)** W normal D 8o4 O design R no smearing.

Figure B.47: Outer detectors x correlation for 6 different simulation settings.

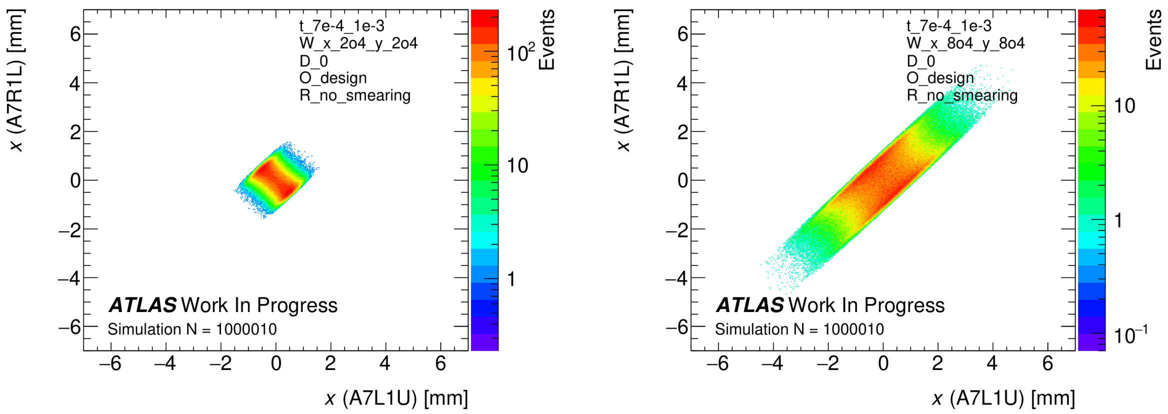

(a) W 2o4 D 0 O design R no smearing.

(b) W 8o4 D 0 O design R no smearing.

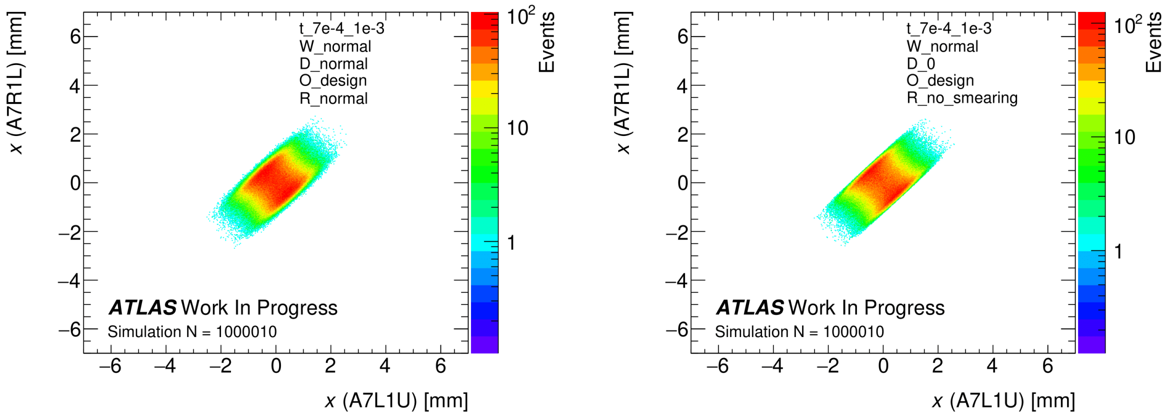

(c) W normal D normal O design R normal.

(d) W normal D 0 O design R no smearing.

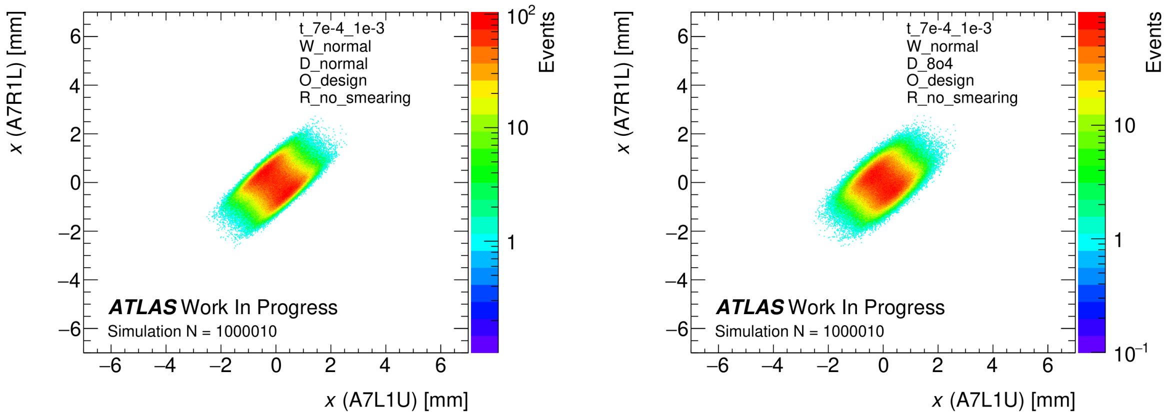

(e) W normal D normal O design R no smearing.

(f) W normal D 8o4 O design R no smearing.

Figure B.48: Inner detectors x correlation for 6 different simulation settings.

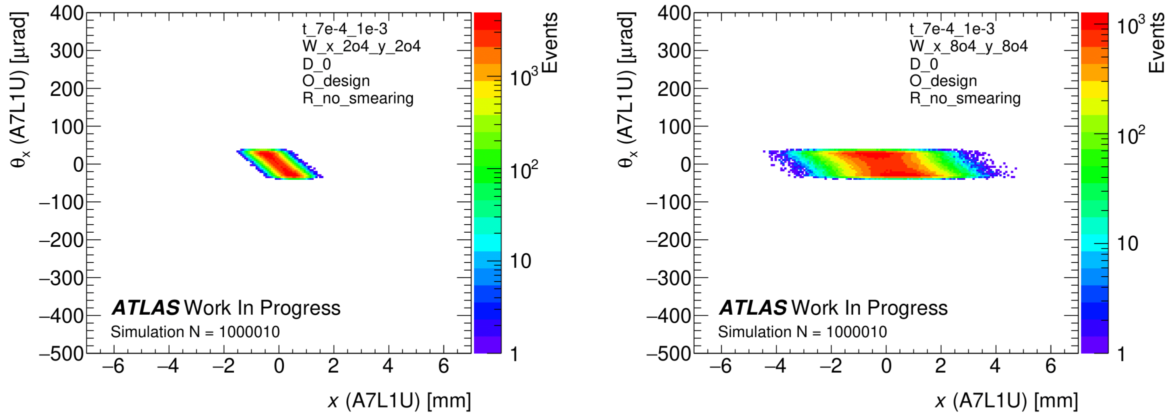

(a) W 2o4 D 0 O design R no smearing. **(b)** W 8o4 D 0 O design R no smearing.

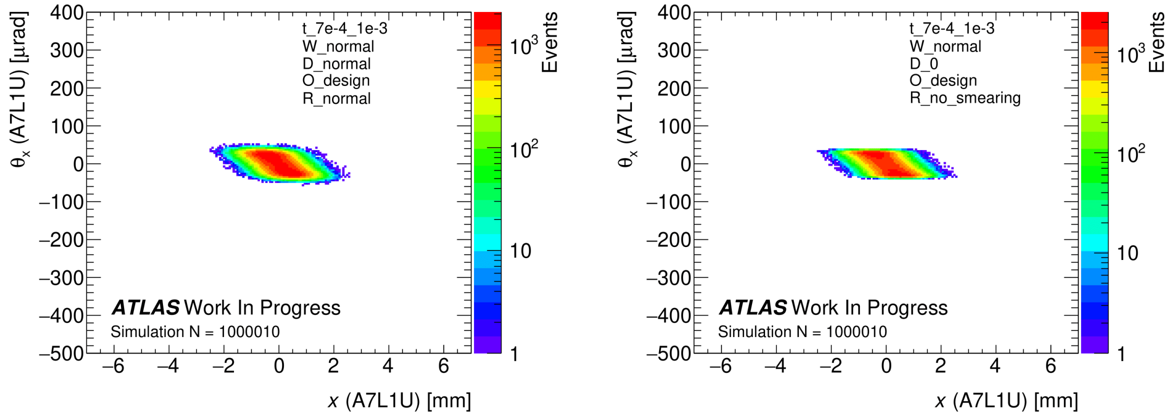

(c) W normal D normal O design R normal. **(d)** W normal D 0 O design R no smearing.

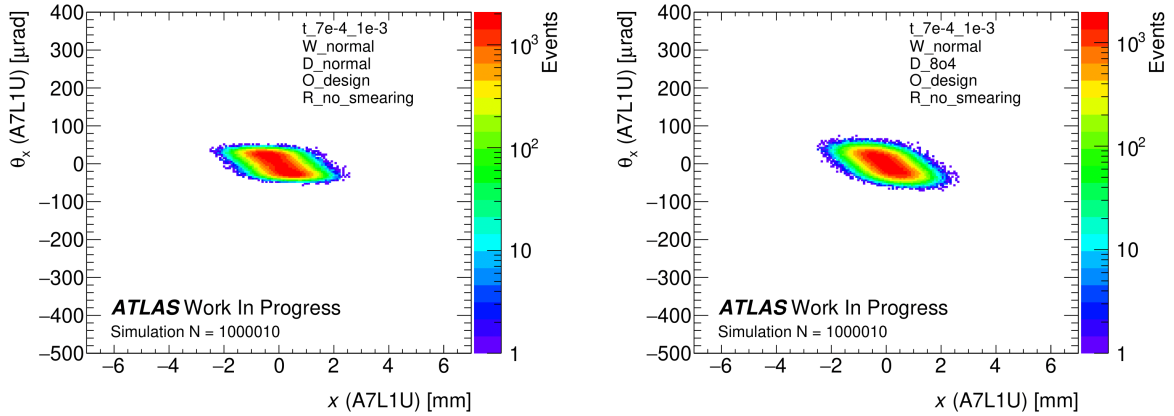

(e) W normal D normal O design R no smearing. **(f)** W normal D 8o4 O design R no smearing.

Figure B.49: Inner detector x-θ_x correlation for 6 different simulation settings.

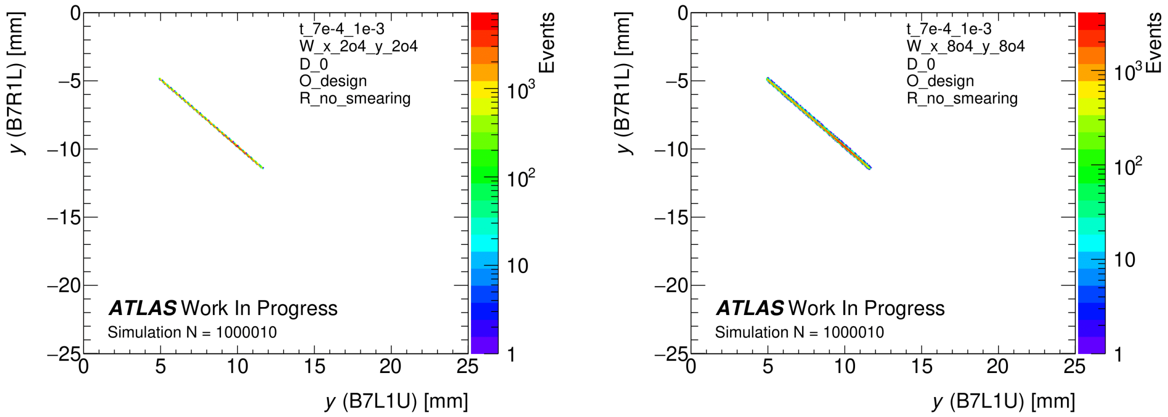

(a) W 2o4 D 0 O design R no smearing. **(b)** W 8o4 D 0 O design R no smearing.

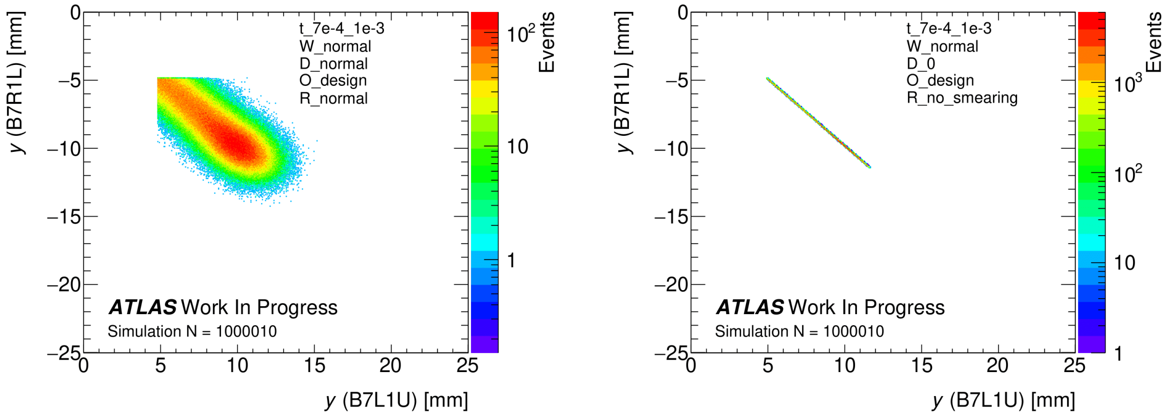

(c) W normal D normal O design R normal. **(d)** W normal D 0 O design R no smearing.

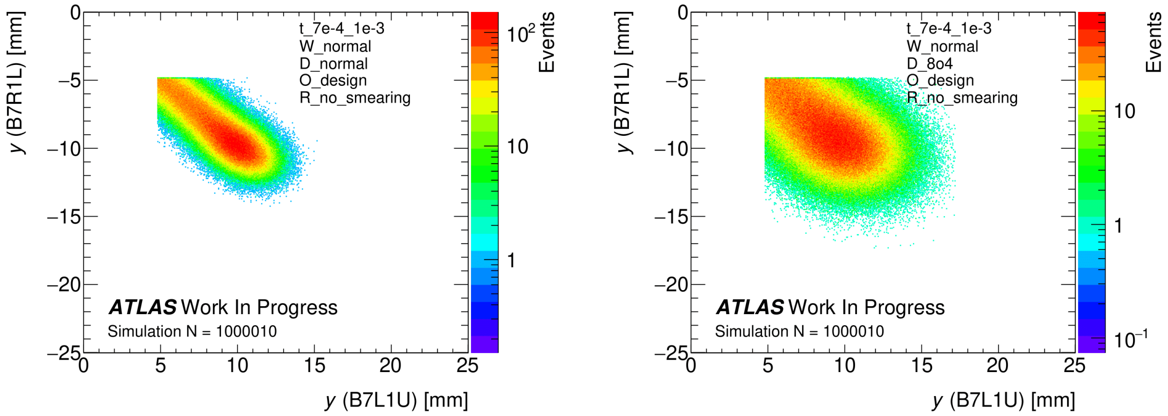

(e) W normal D normal O design R no smearing. **(f)** W normal D 8o4 O design R no smearing.

Figure B.50: Outer detectors y correlation for 6 different simulation settings.

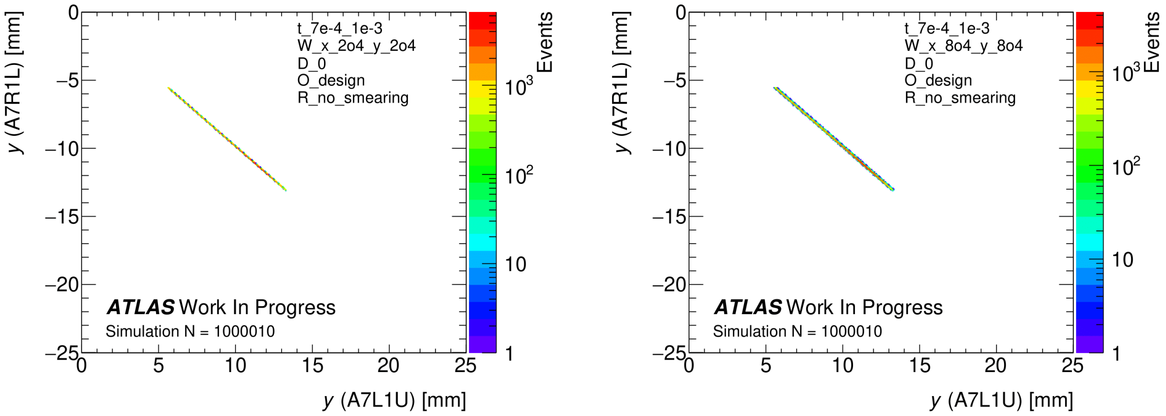

(a) W 2o4 D 0 O design R no smearing.

(b) W 8o4 D 0 O design R no smearing.

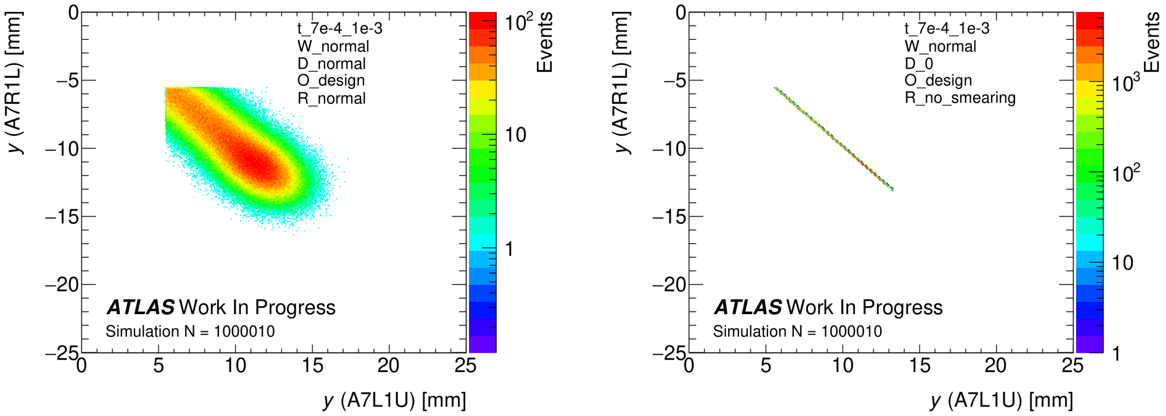

(c) W normal D normal O design R normal.

(d) W normal D 0 O design R no smearing.

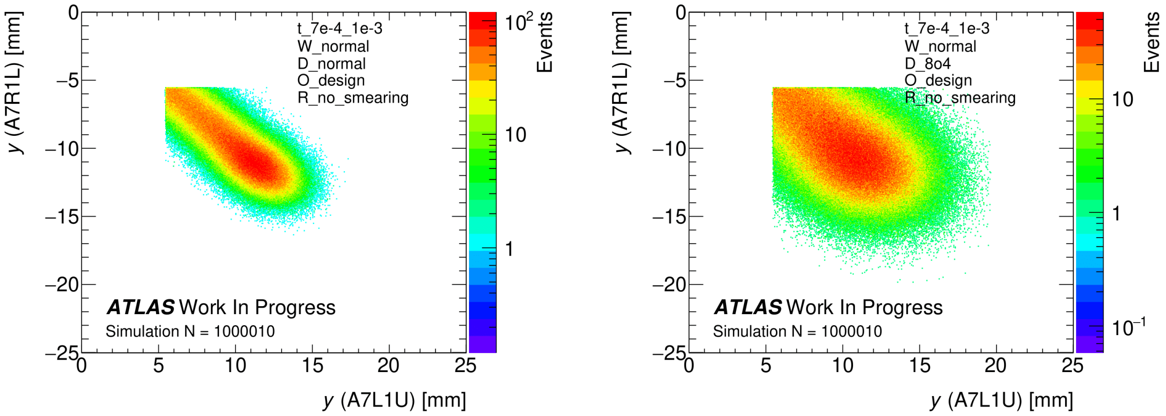

(e) W normal D normal O design R no smearing.

(f) W normal D 8o4 O design R no smearing.

Figure B.51: Inner detectors y correlation for 6 different simulation settings.

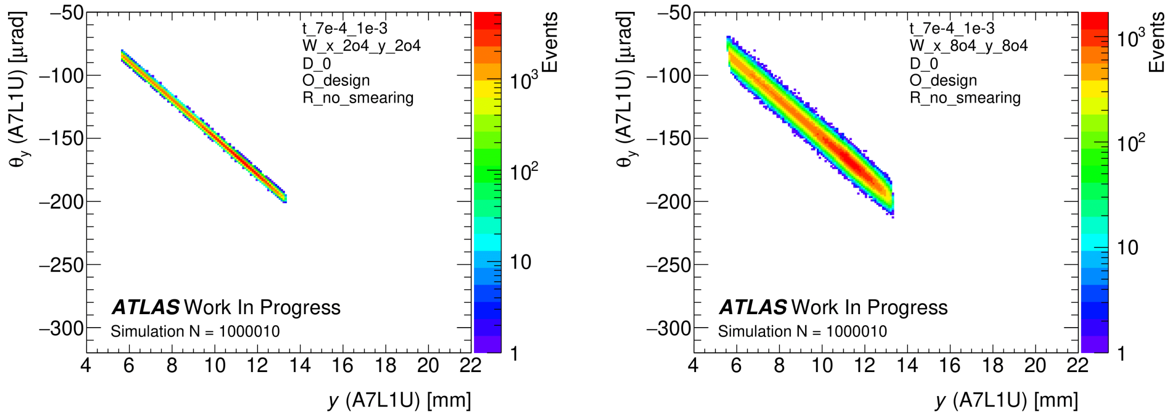

(a) W 2o4 D 0 O design R no smearing.

(b) W 8o4 D 0 O design R no smearing.

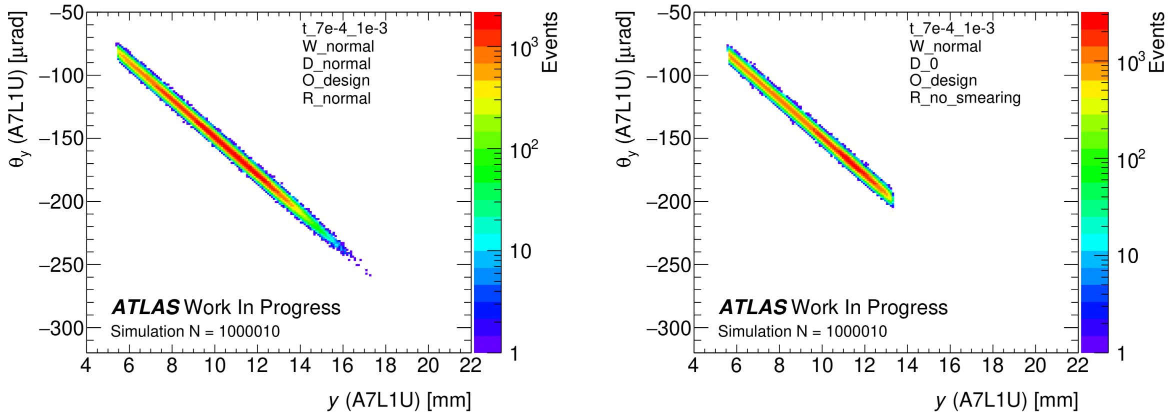

(c) W normal D normal O design R normal.

(d) W normal D 0 O design R no smearing.

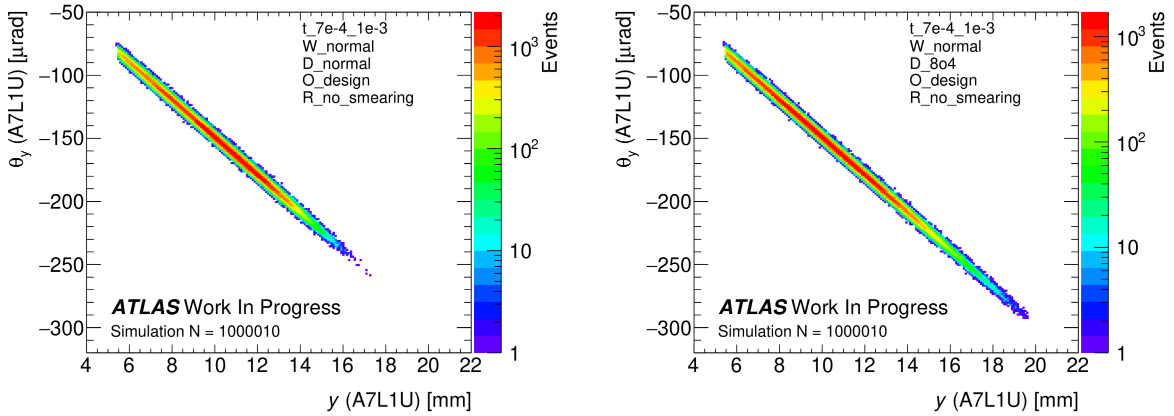

(e) W normal D normal O design R no smearing.

(f) W normal D 8o4 O design R no smearing.

Figure B.52: Inner detector x-θ_x correlation for 6 different simulation settings.

B.3.4 t-range 1e-3 till 3e-3 GeV^2

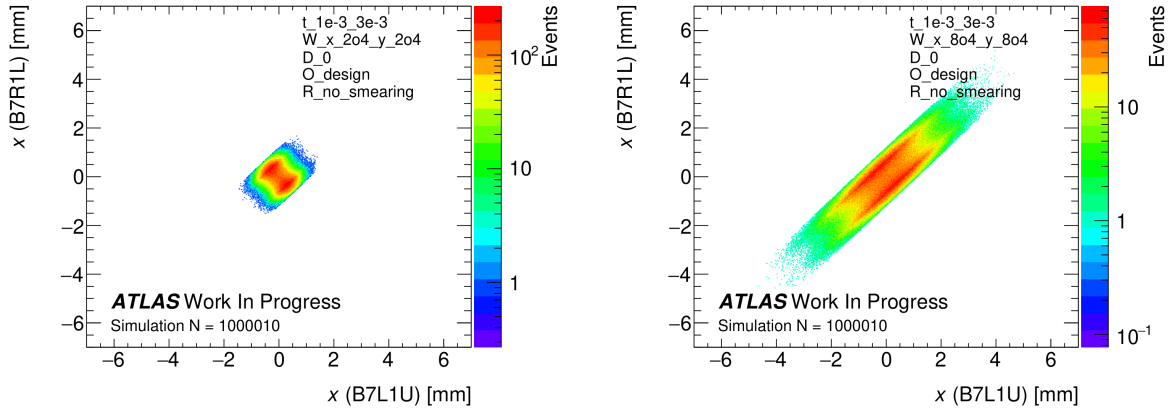

(a) W 2o4 D 0 O design R no smearing.

(b) W 8o4 D 0 O design R no smearing.

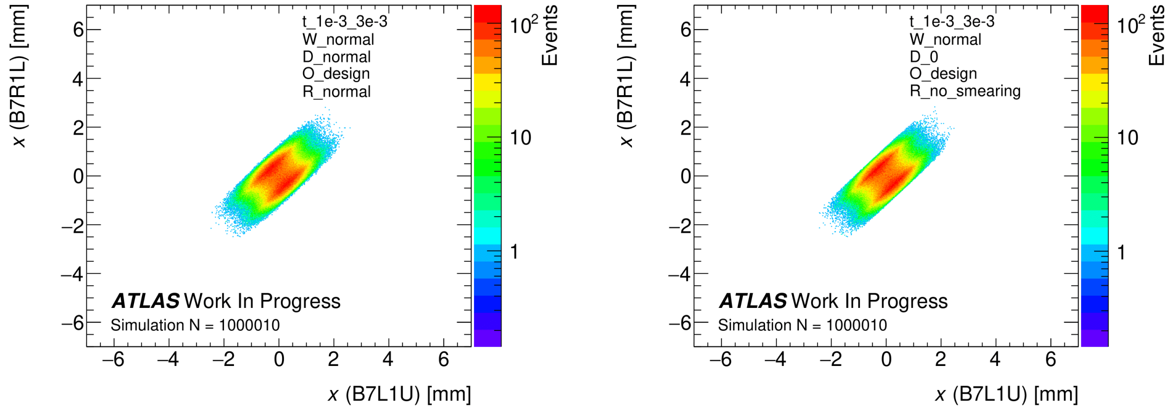

(c) W normal D normal O design R normal.

(d) W normal D 0 O design R no smearing.

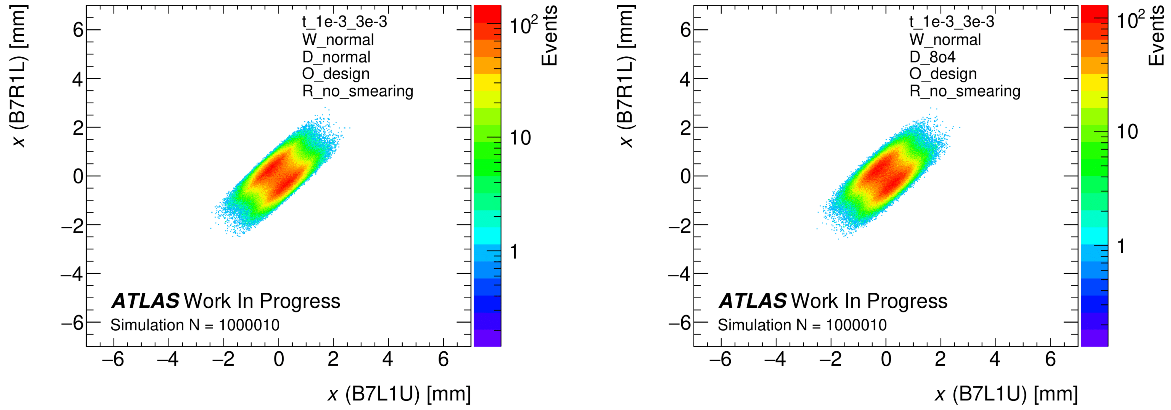

(e) W normal D normal O design R no smearing.

(f) W normal D 8o4 O design R no smearing.

Figure B.53: Outer detectors x correlation for 6 different simulation settings.

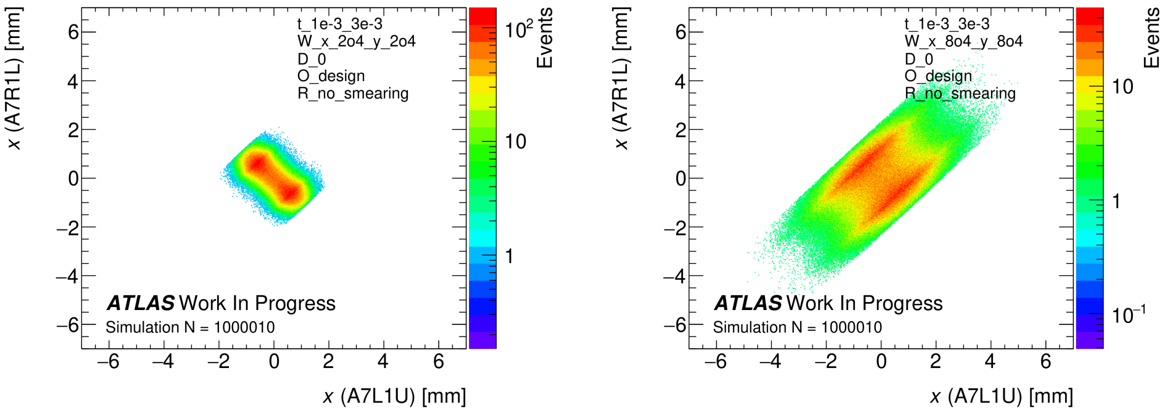

(a) W 2o4 D 0 O design R no smearing.

(b) W 8o4 D 0 O design R no smearing.

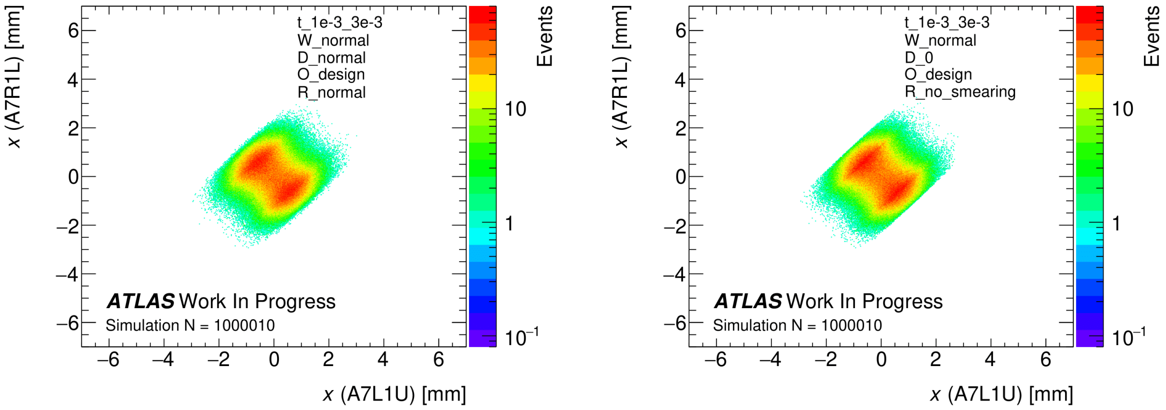

(c) W normal D normal O design R normal.

(d) W normal D 0 O design R no smearing.

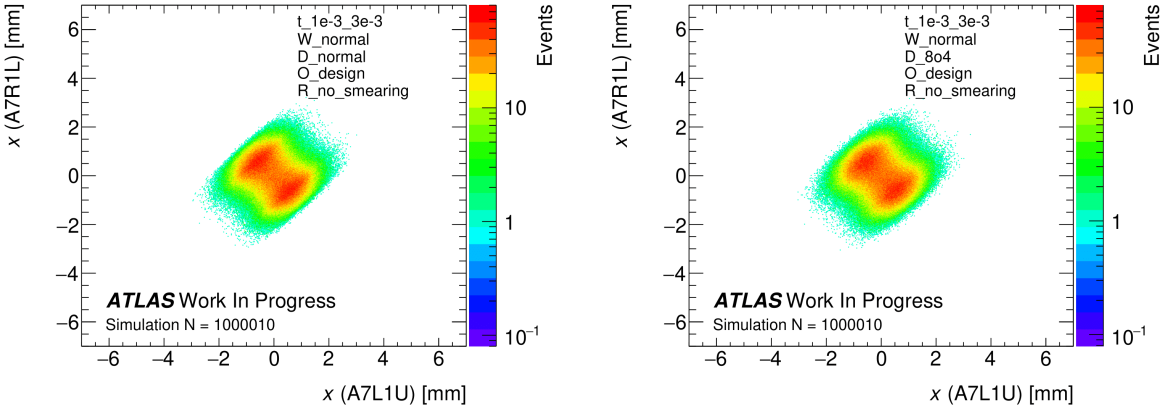

(e) W normal D normal O design R no smearing.

(f) W normal D 8o4 O design R no smearing.

Figure B.54: Inner detectors x correlation for 6 different simulation settings.

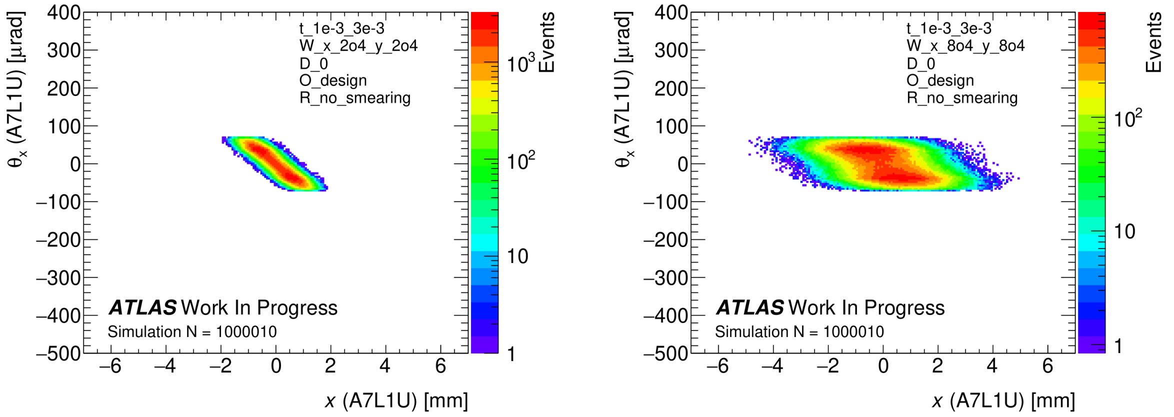

(a) W 2o4 D 0 O design R no smearing.

(b) W 8o4 D 0 O design R no smearing.

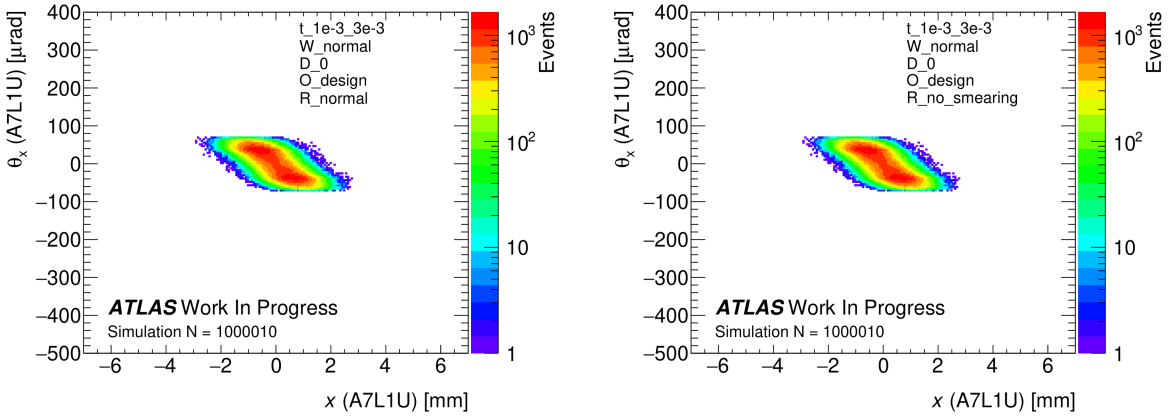

(c) W normal D normal O design R normal.

(d) W normal D 0 O design R no smearing.

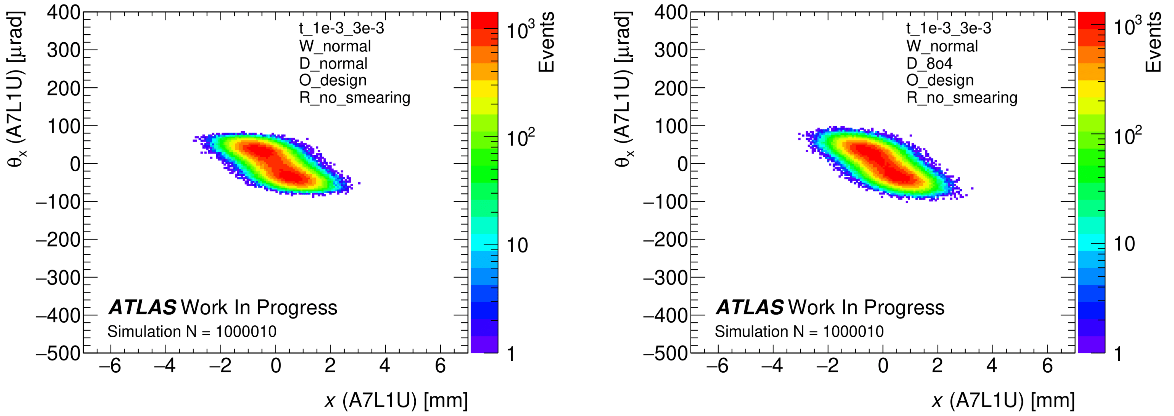

(e) W normal D normal O design R no smearing.

(f) W normal D 8o4 O design R no smearing.

Figure B.55: Inner detector x-θ_x correlation for 6 different simulation settings.

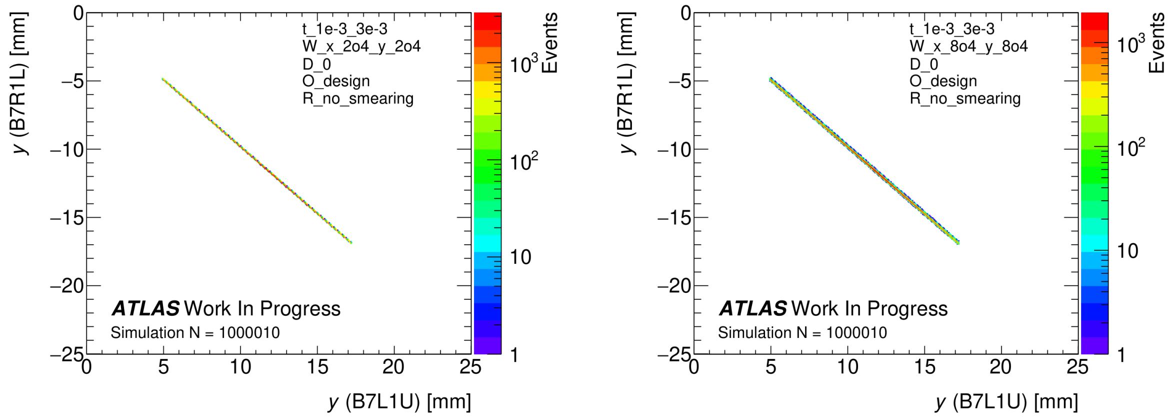

(a) W 2o4 D 0 O design R no smearing.

(b) W 8o4 D 0 O design R no smearing.

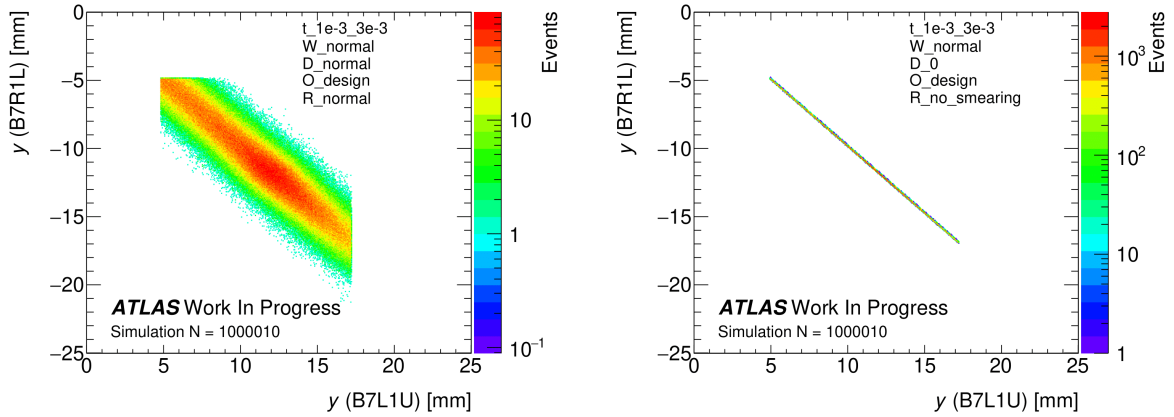

(c) W normal D normal O design R normal.

(d) W normal D 0 O design R no smearing.

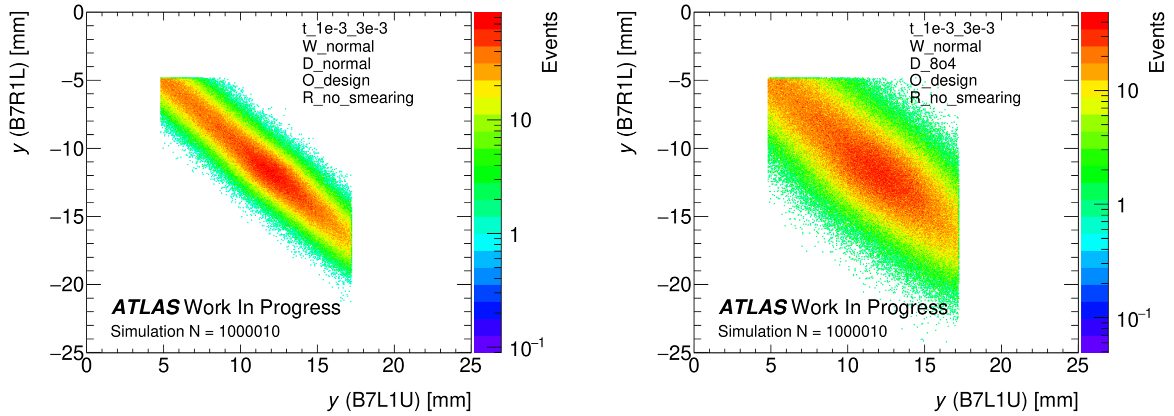

(e) W normal D normal O design R no smearing.

(f) W normal D 8o4 O design R no smearing.

Figure B.56: Outer detectors y correlation for 6 different simulation settings.

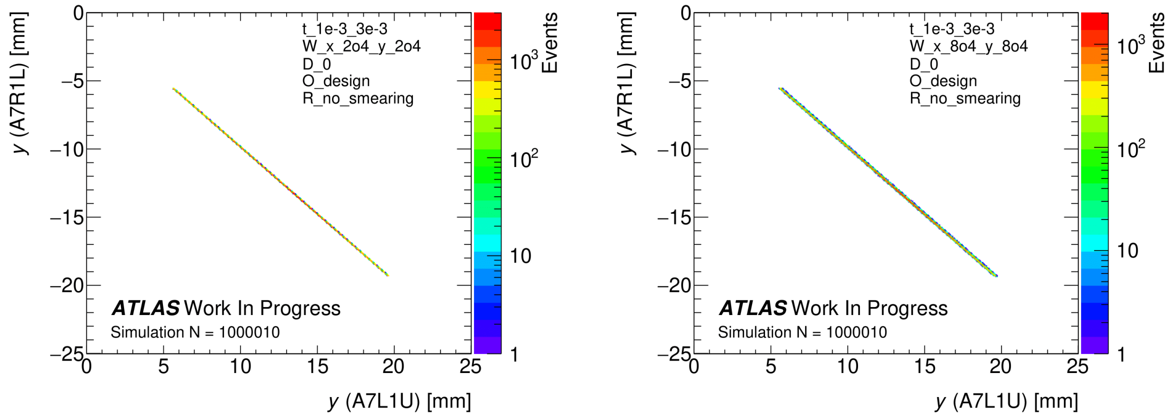

(a) W 2o4 D 0 O design R no smearing.

(b) W 8o4 D 0 O design R no smearing.

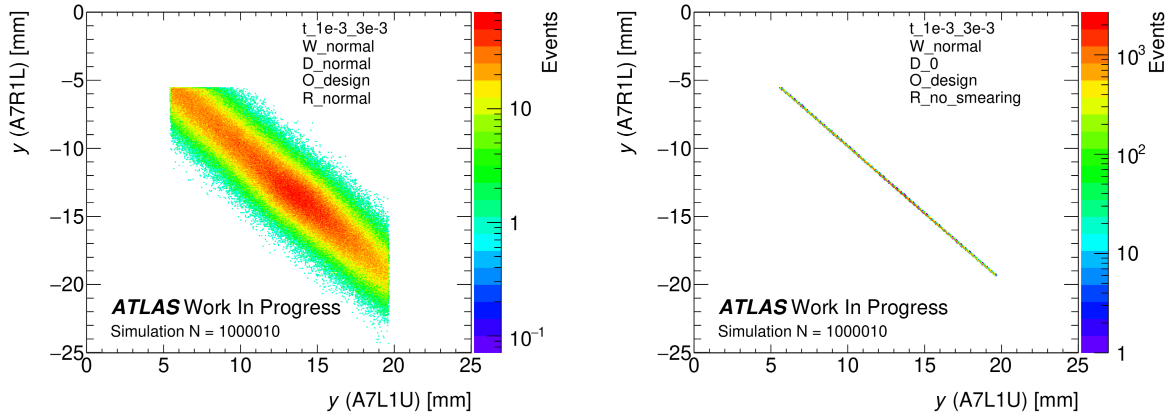

(c) W normal D normal O design R normal.

(d) W normal D 0 O design R no smearing.

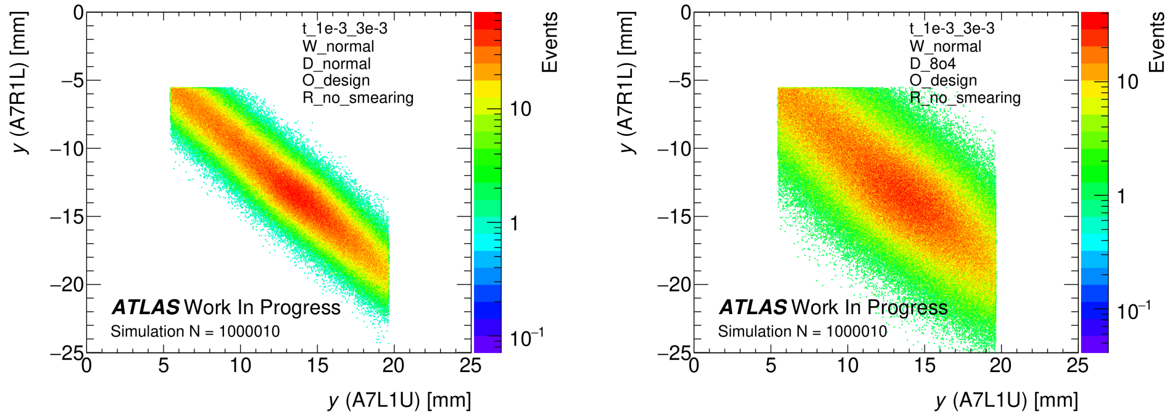

(e) W normal D normal O design R no smearing.

(f) W normal D 8o4 O design R no smearing.

Figure B.57: Inner detectors y correlation for 6 different simulation settings.

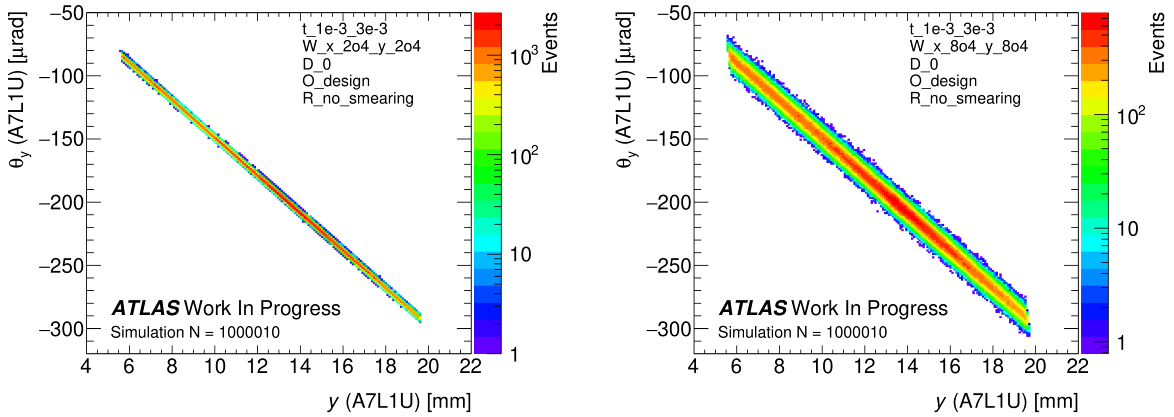

(a) W 2o4 D 0 O design R no smearing.

(b) W 8o4 D 0 O design R no smearing.

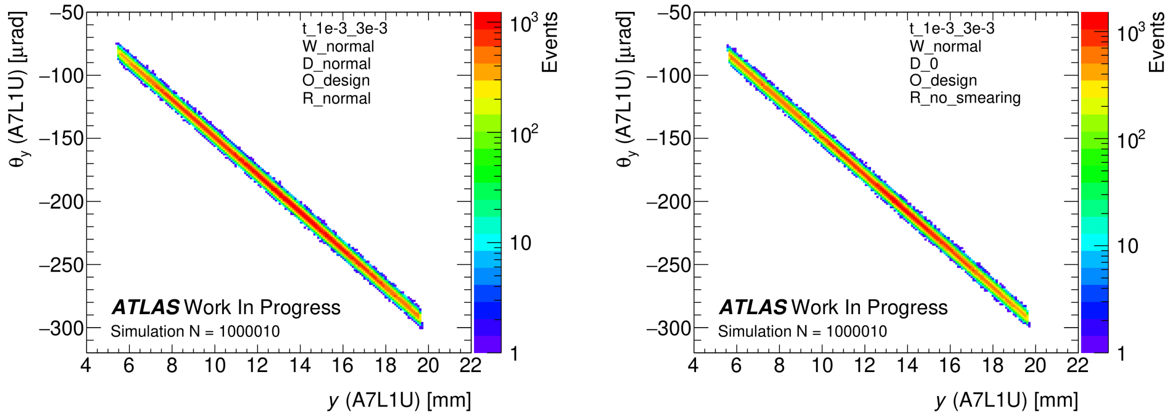

(c) W normal D normal O design R normal.

(d) W normal D 0 O design R no smearing.

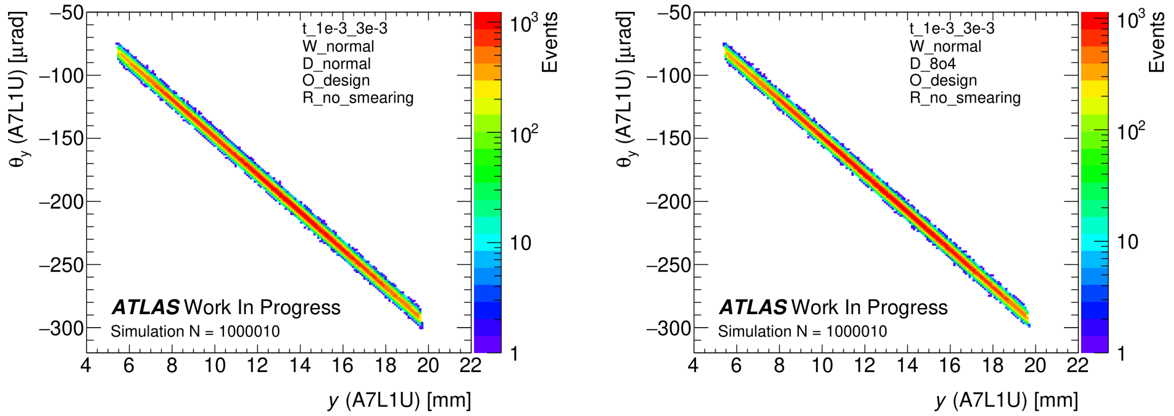

(e) W normal D normal O design R no smearing.

(f) W normal D 8o4 O design R no smearing.

Figure B.58: Inner detector x-θ_x correlation for 6 different simulation settings.

B.3.5 t-range 3e-3 till 1e-2 GeV^2

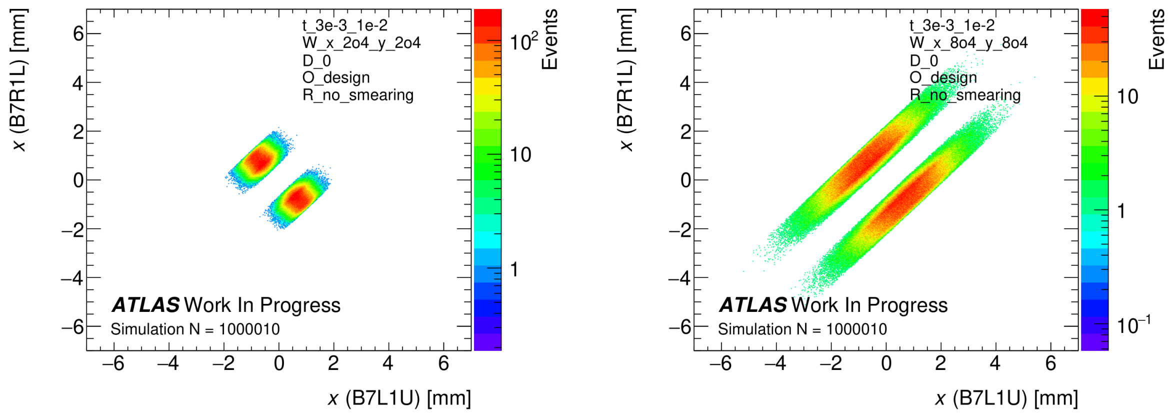

(a) W 2o4 D 0 O design R no smearing.

(b) W 8o4 D 0 O design R no smearing.

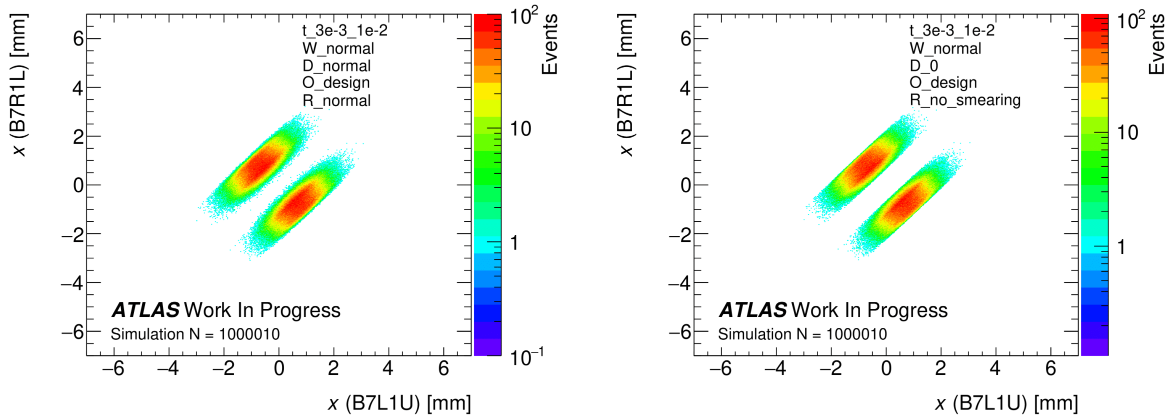

(c) W normal D normal O design R normal.

(d) W normal D 0 O design R no smearing.

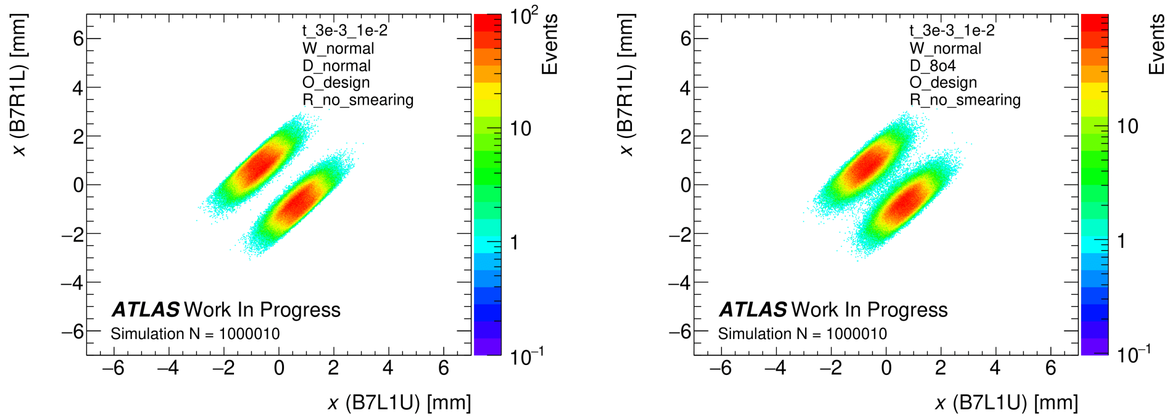

(e) W normal D normal O design R no smearing.

(f) W normal D 8o4 O design R no smearing.

Figure B.59: Outer detectors x correlation for 6 different simulation settings.

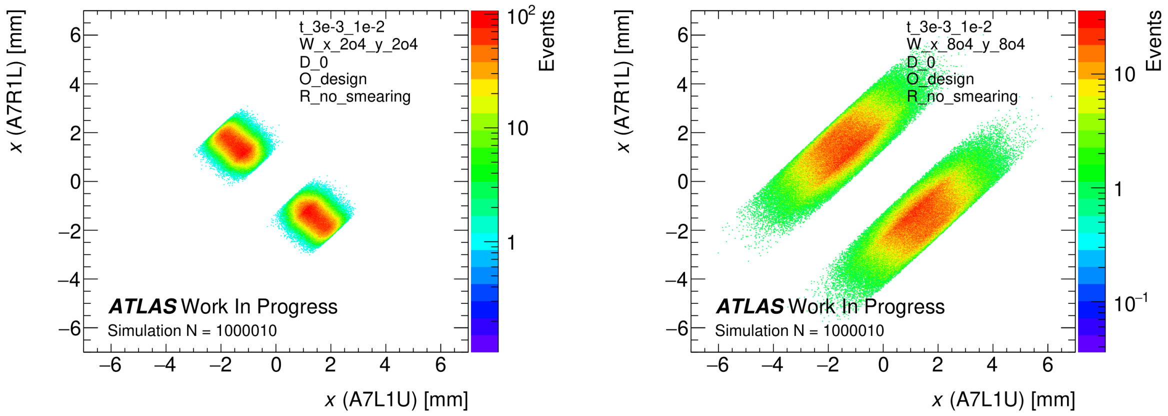

(a) W 2o4 D 0 O design R no smearing.

(b) W 8o4 D 0 O design R no smearing.

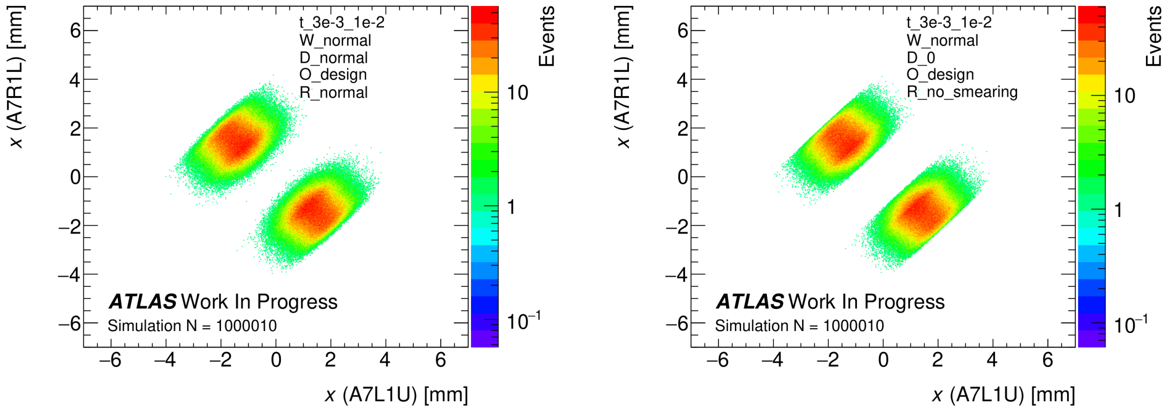

(c) W normal D normal O design R normal.

(d) W normal D 0 O design R no smearing.

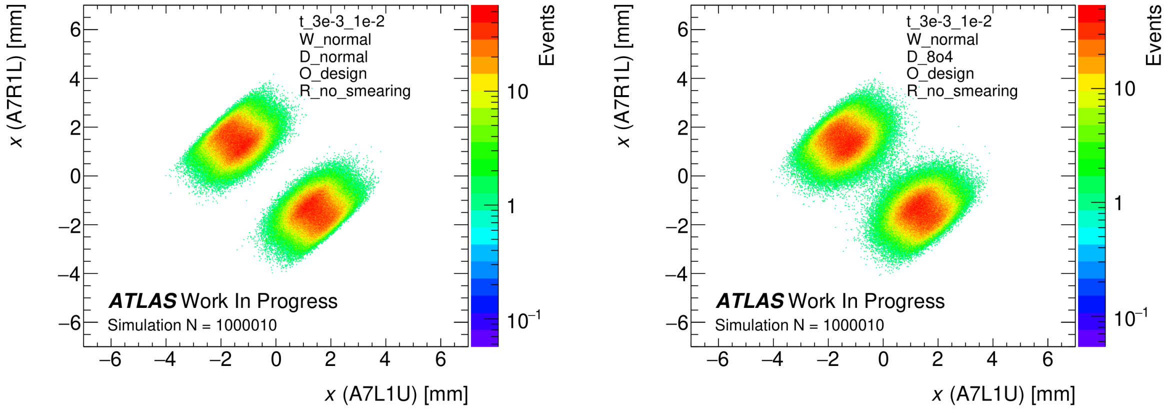

(e) W normal D normal O design R no smearing.

(f) W normal D 8o4 O design R no smearing.

Figure B.60: Inner detectors x correlation for 6 different simulation settings.

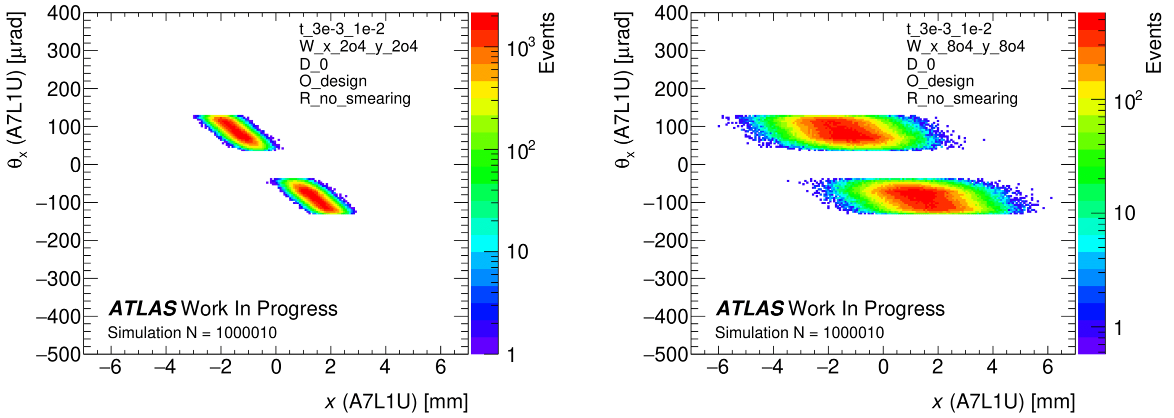

(a) W 2o4 D 0 O design R no smearing.

(b) W 8o4 D 0 O design R no smearing.

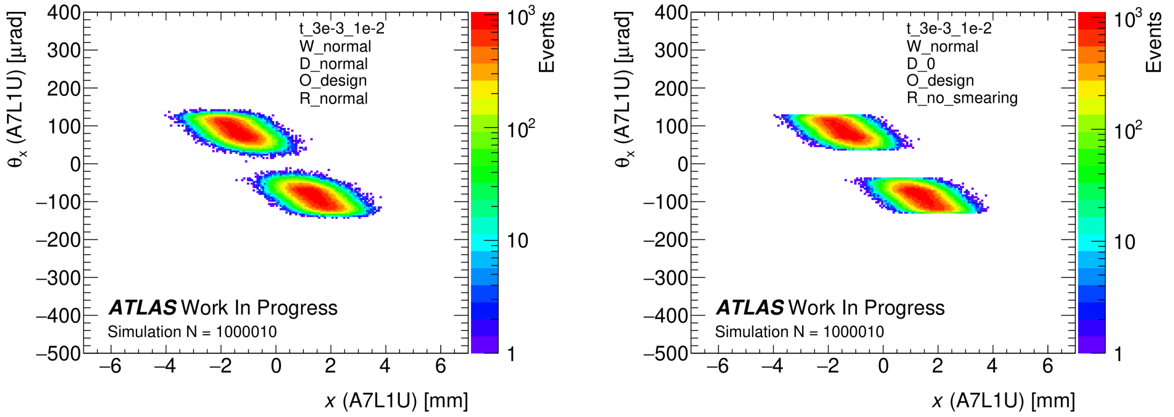

(c) W normal D normal O design R normal.

(d) W normal D 0 O design R no smearing.

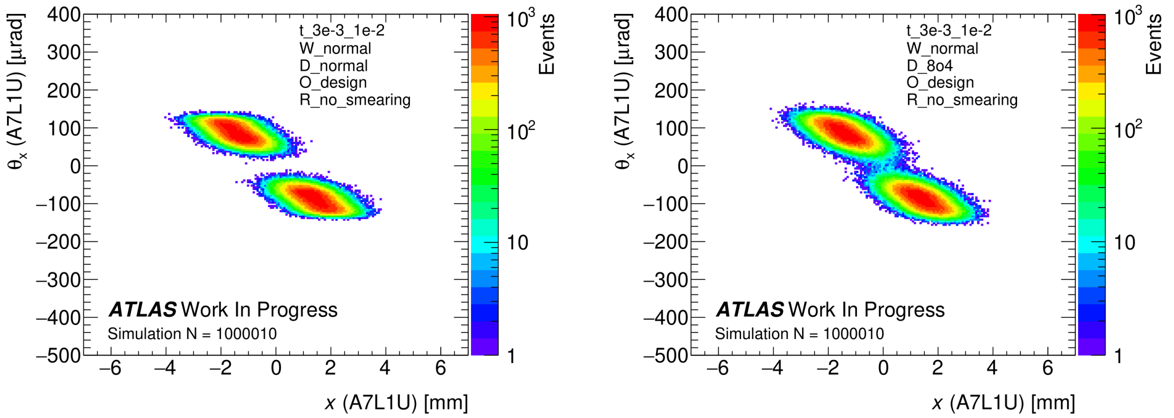

(e) W normal D normal O design R no smearing.

(f) W normal D 8o4 O design R no smearing.

Figure B.61: Inner detector x-θ_x correlation for 6 different simulation settings.

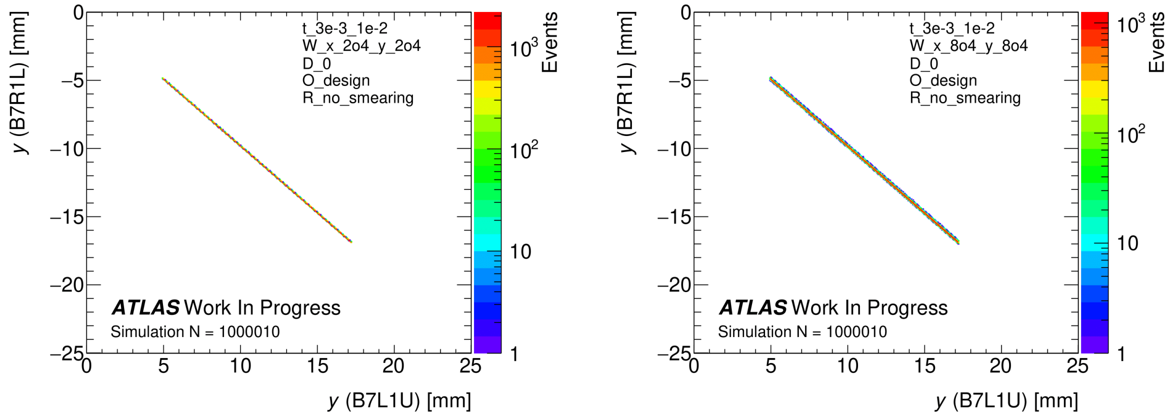

(a) W 2o4 D 0 O design R no smearing. **(b)** W 8o4 D 0 O design R no smearing.

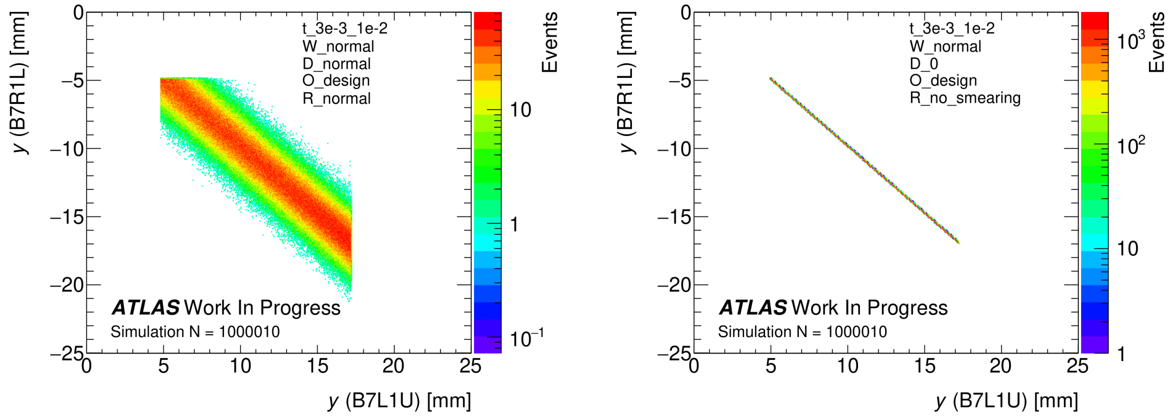

(c) W normal D normal O design R normal. **(d)** W normal D 0 O design R no smearing.

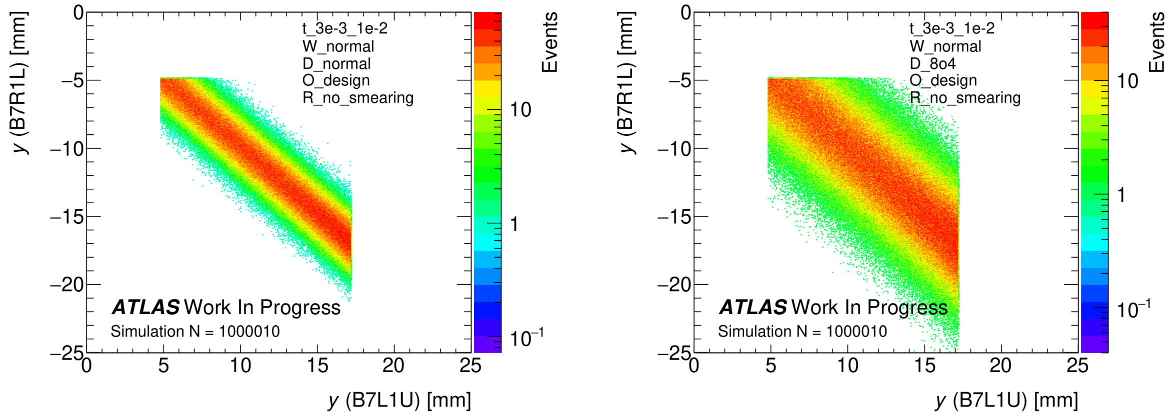

(e) W normal D normal O design R no smearing. **(f)** W normal D 8o4 O design R no smearing.

Figure B.62: Outer detectors y correlation for 6 different simulation settings.

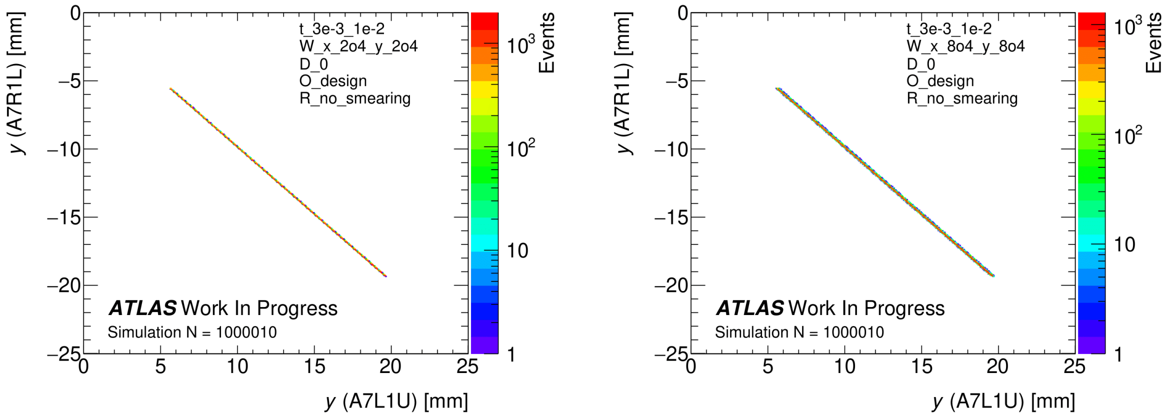

(a) W 2o4 D 0 O design R no smearing.

(b) W 8o4 D 0 O design R no smearing.

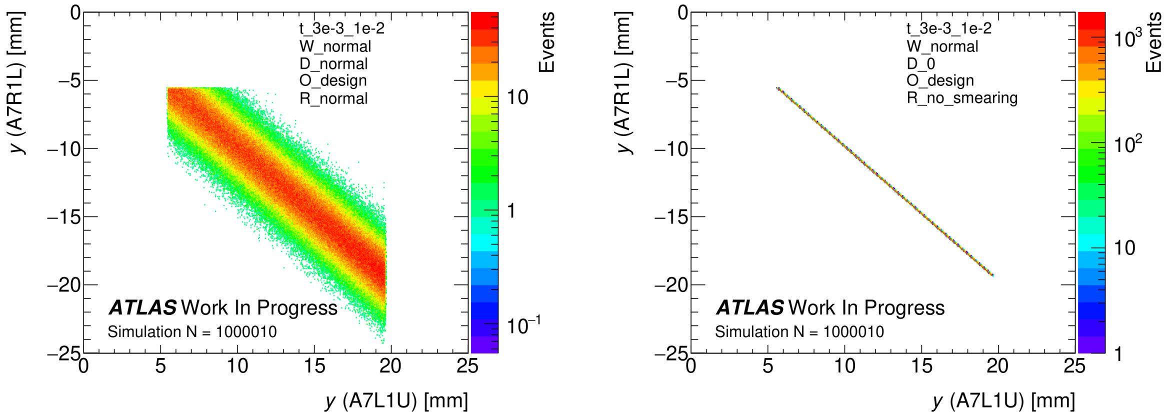

(c) W normal D normal O design R normal.

(d) W normal D 0 O design R no smearing.

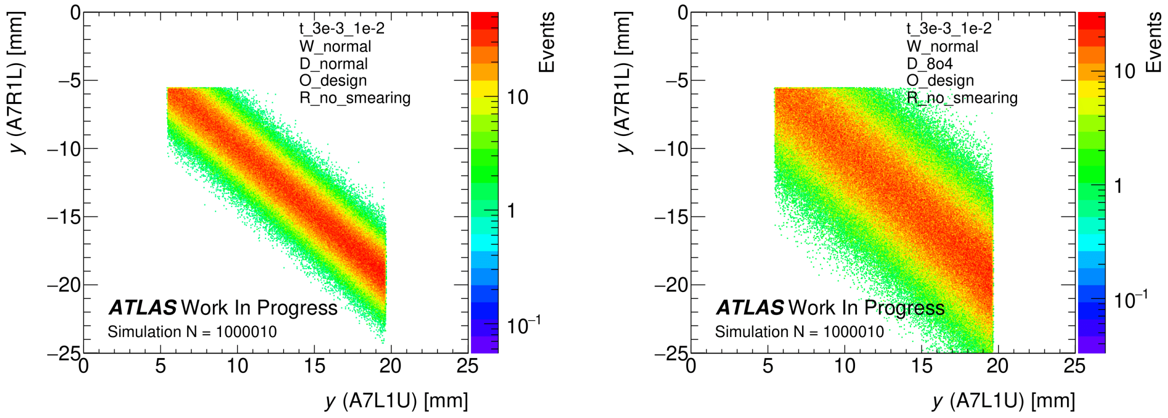

(e) W normal D normal O design R no smearing.

(f) W normal D 8o4 O design R no smearing.

Figure B.63: Inner detectors y correlation for 6 different simulation settings.

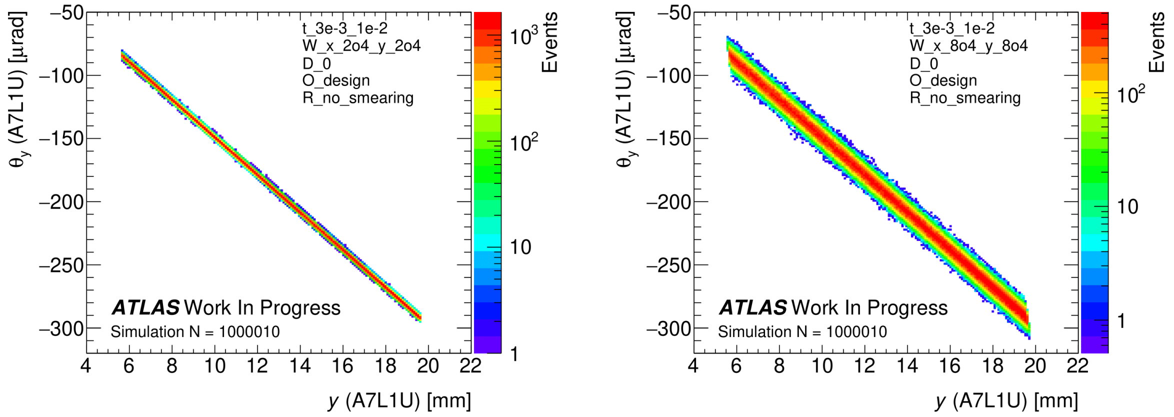

(a) W 2o4 D 0 O design R no smearing.

(b) W 8o4 D 0 O design R no smearing.

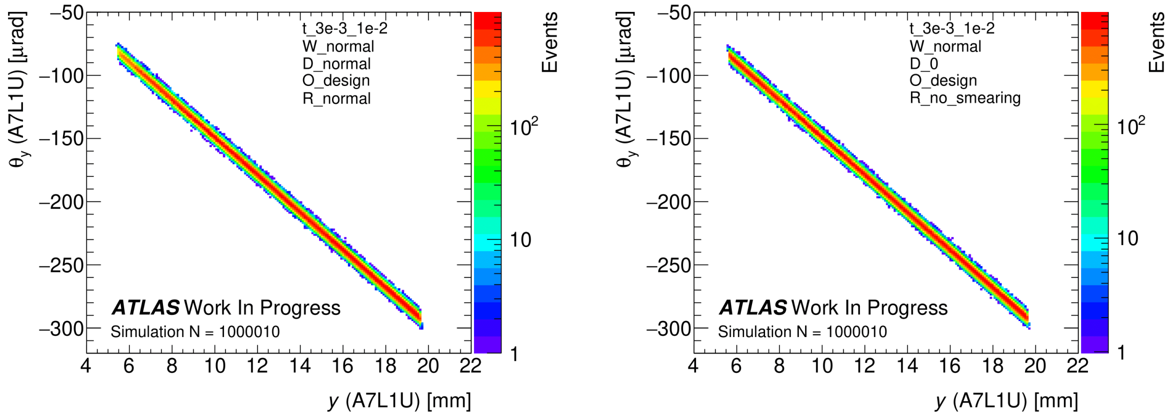

(c) W normal D normal O design R normal.

(d) W normal D 0 O design R no smearing.

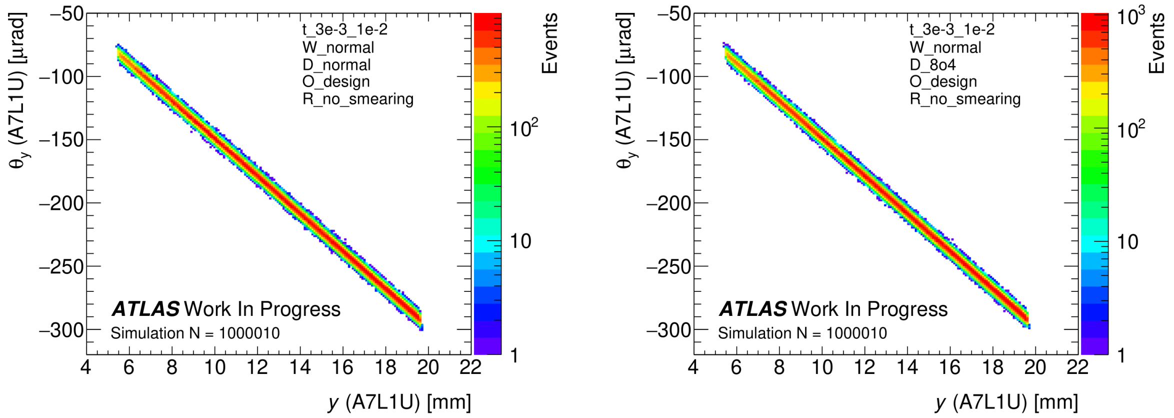

(e) W normal D normal O design R no smearing.

(f) W normal D 8o4 O design R no smearing.

Figure B.64: Inner detector x-θ_x correlation for 6 different simulation settings.

B.3.6 t-range 1e-2 till 5e-2 GeV^2

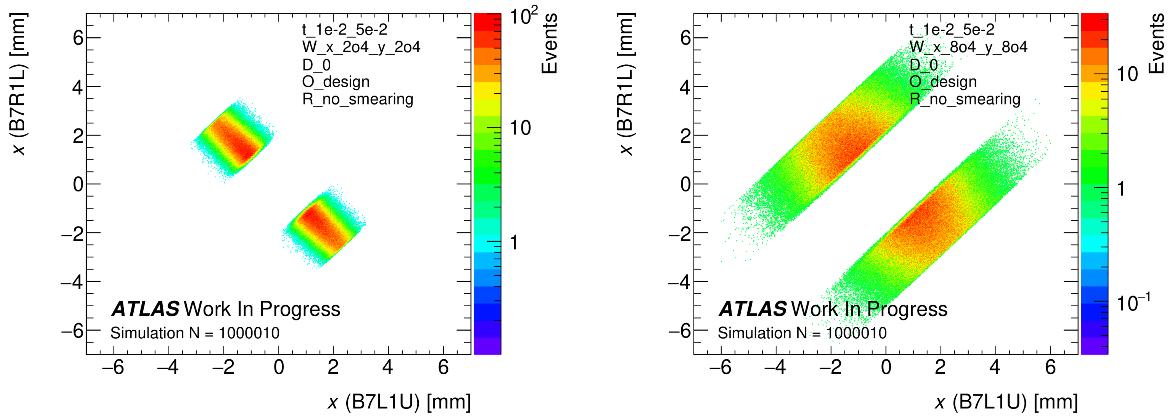

(a) W 2o4 D 0 O design R no smearing. **(b)** W 8o4 D 0 O design R no smearing.

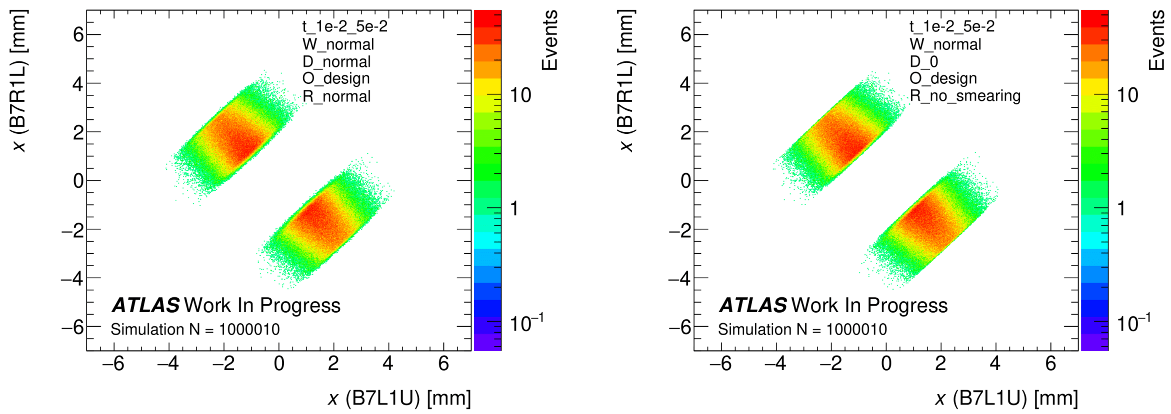

(c) W normal D normal O design R normal. **(d)** W normal D 0 O design R no smearing.

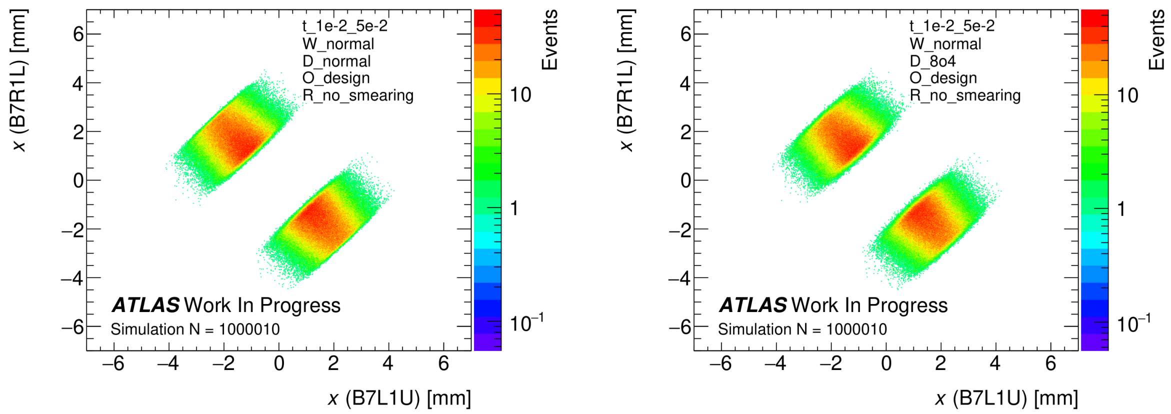

(e) W normal D normal O design R no smearing. **(f)** W normal D 8o4 O design R no smearing.

Figure B.65: Outer detectors x correlation for 6 different simulation settings.

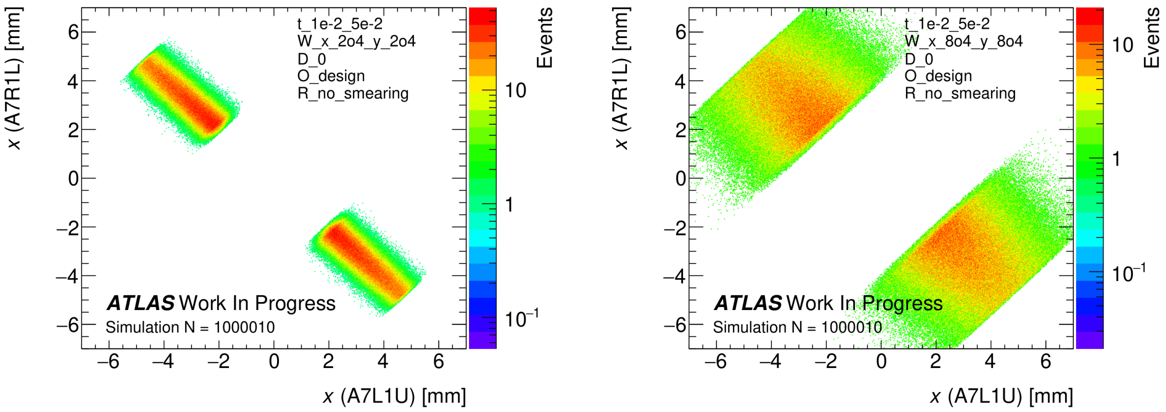

(a) W 2o4 D 0 O design R no smearing.

(b) W 8o4 D 0 O design R no smearing.

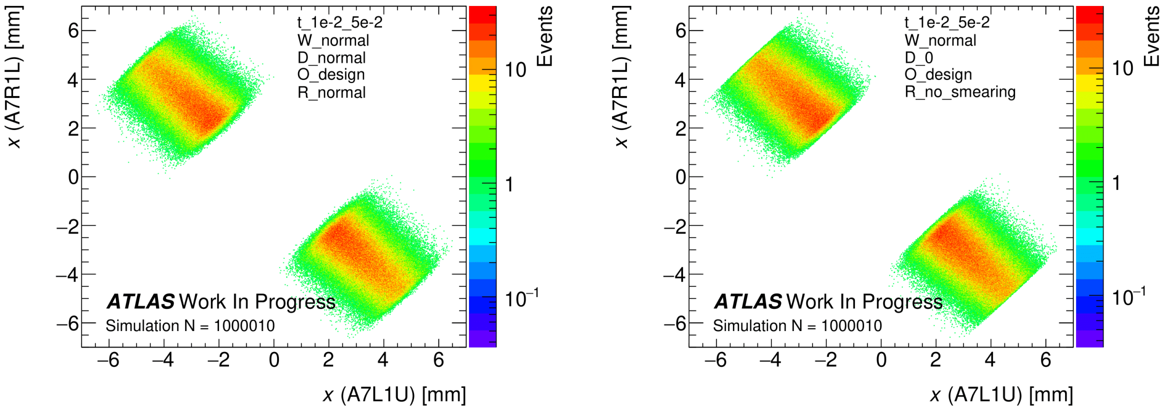

(c) W normal D normal O design R normal.

(d) W normal D 0 O design R no smearing.

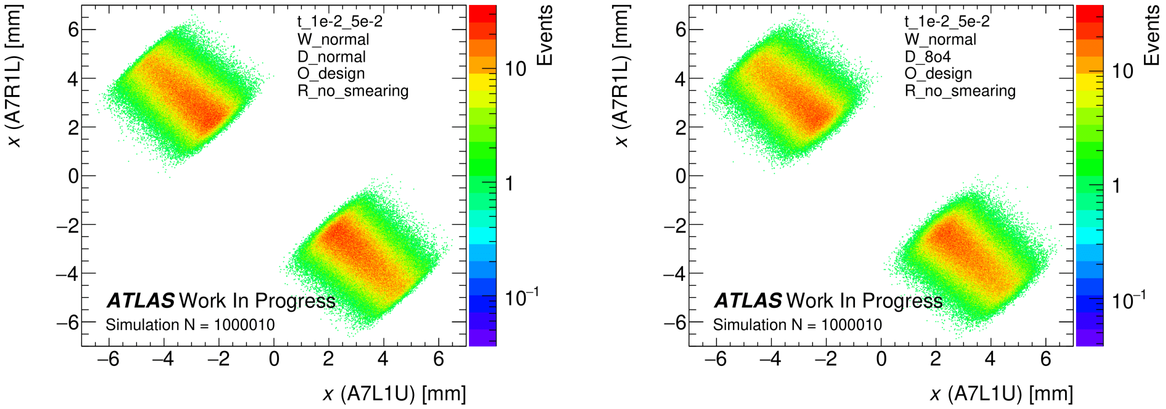

(e) W normal D normal O design R no smearing.

(f) W normal D 8o4 O design R no smearing.

Figure B.66: Inner detectors x correlation for 6 different simulation settings.

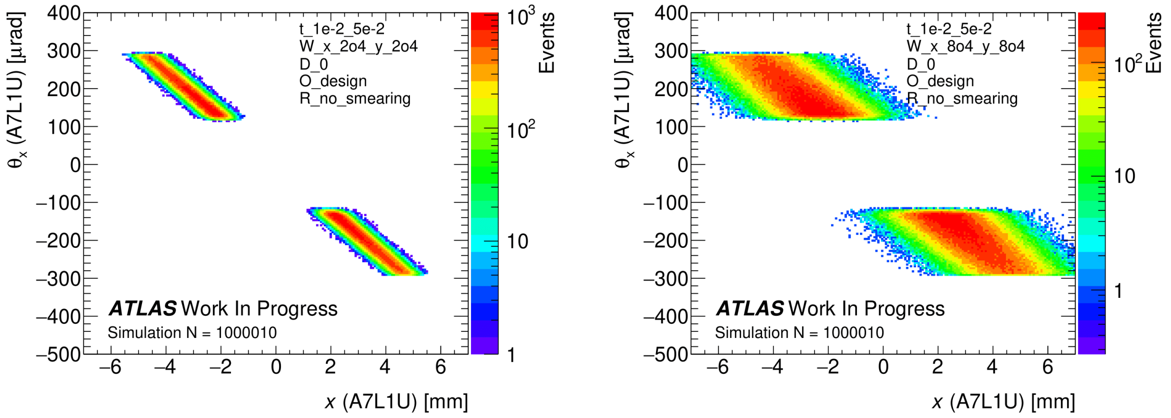

(a) W 2o4 D 0 O design R no smearing.

(b) W 8o4 D 0 O design R no smearing.

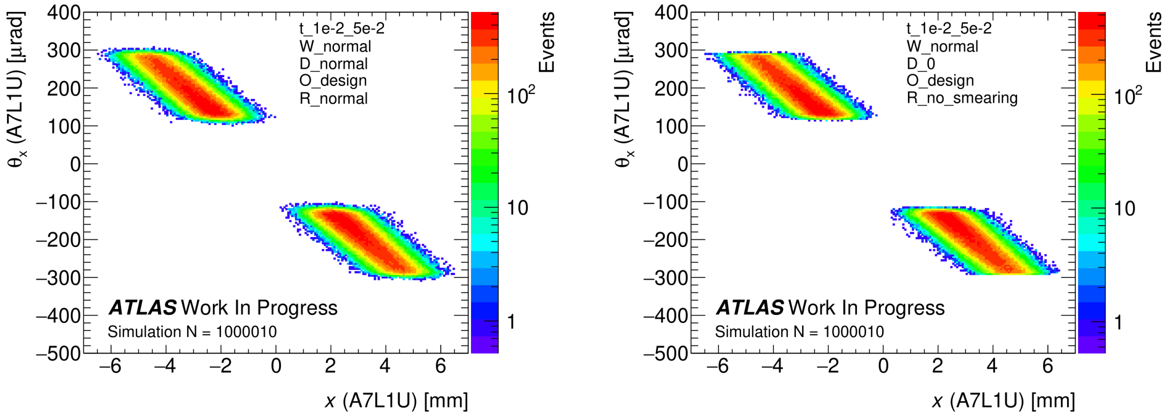

(c) W normal D normal O design R normal.

(d) W normal D 0 O design R no smearing.

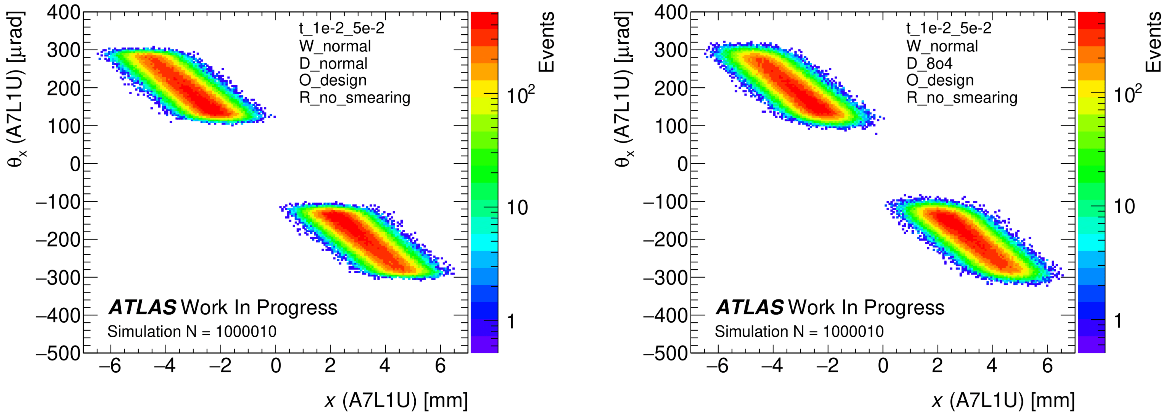

(e) W normal D normal O design R no smearing.

(f) W normal D 8o4 O design R no smearing.

Figure B.67: Inner detector x-θ_x correlation for 6 different simulation settings.

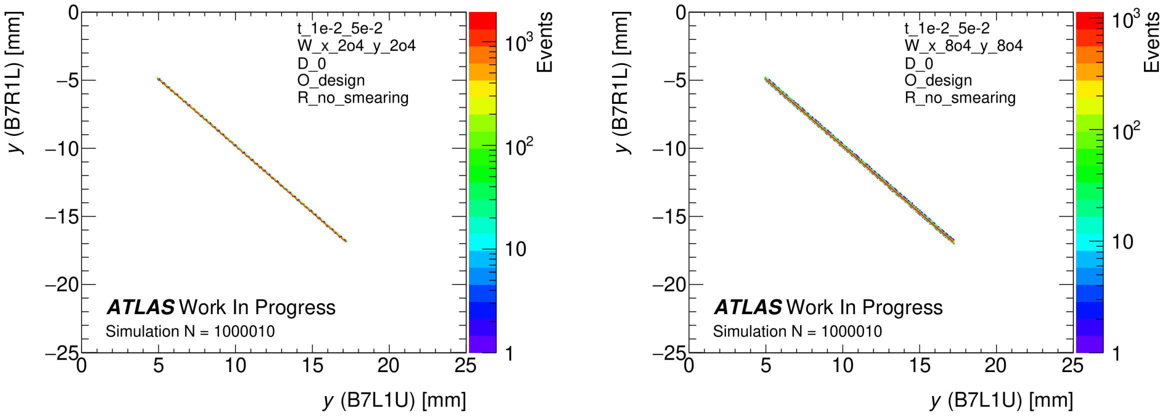

(a) W 2o4 D 0 O design R no smearing.

(b) W 8o4 D 0 O design R no smearing.

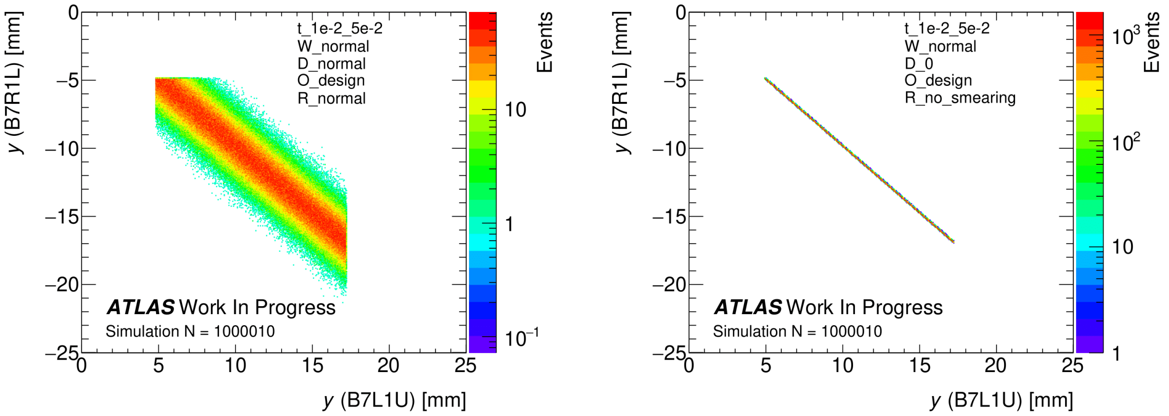

(c) W normal D normal O design R normal.

(d) W normal D 0 O design R no smearing.

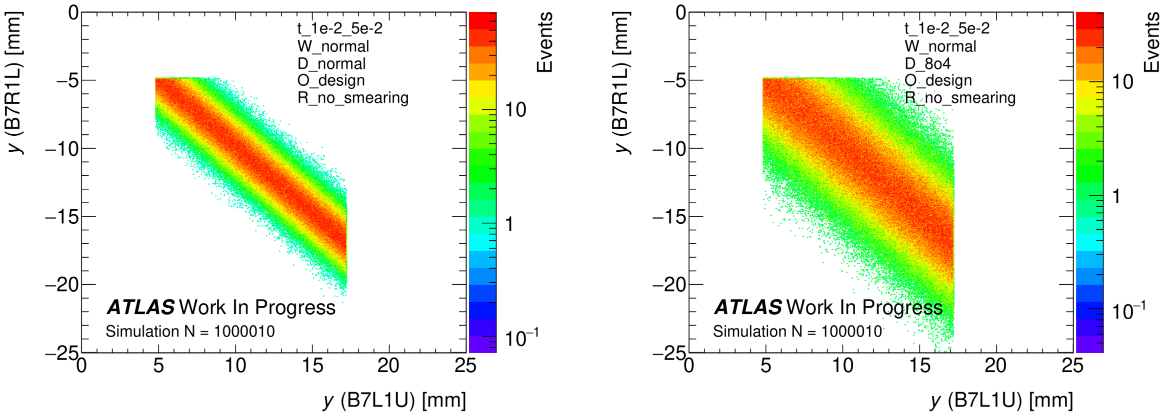

(e) W normal D normal O design R no smearing.

(f) W normal D 8o4 O design R no smearing.

Figure B.68: Outer detectors y correlation for 6 different simulation settings.

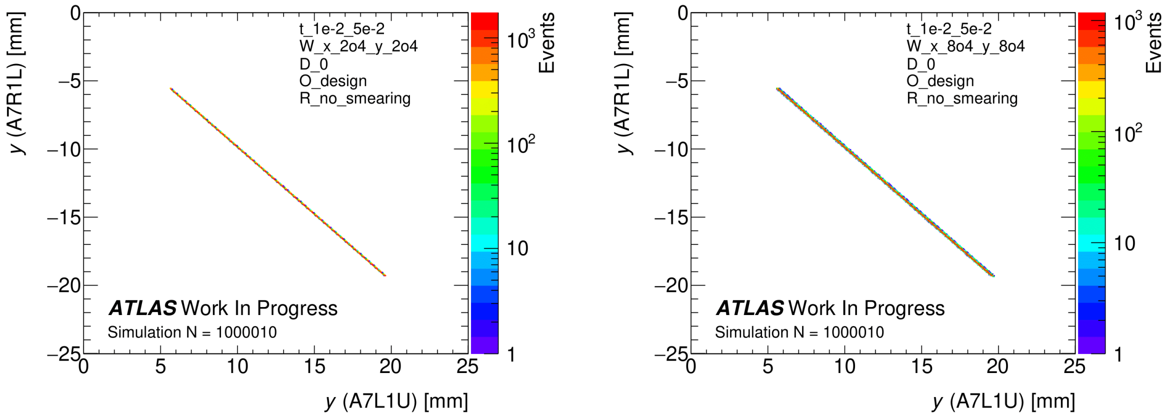

(a) W 2o4 D 0 O design R no smearing.

(b) W 8o4 D 0 O design R no smearing.

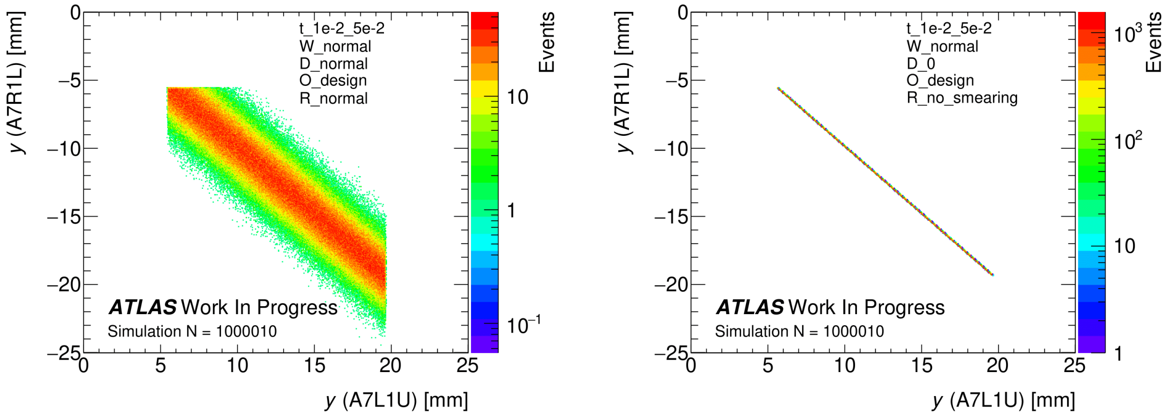

(c) W normal D normal O design R normal.

(d) W normal D 0 O design R no smearing.

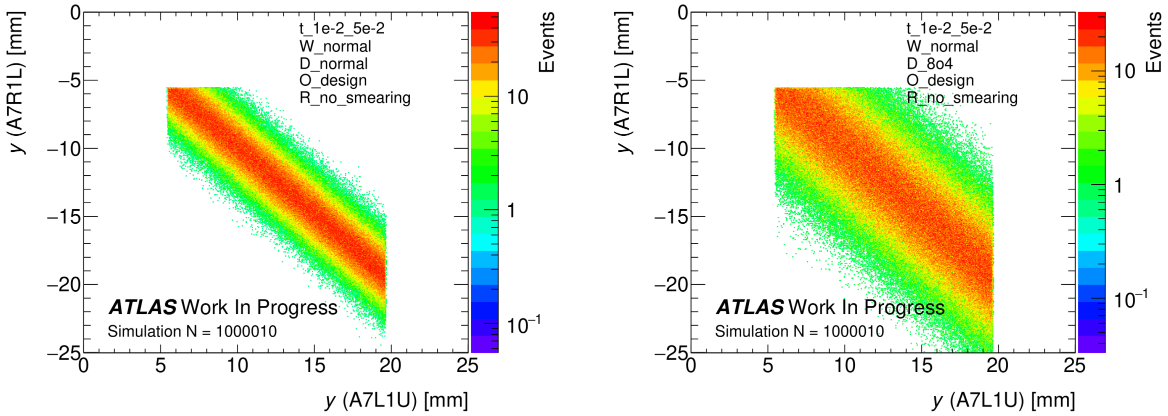

(e) W normal D normal O design R no smearing.

(f) W normal D 8o4 O design R no smearing.

Figure B.69: Inner detectors y correlation for 6 different simulation settings.

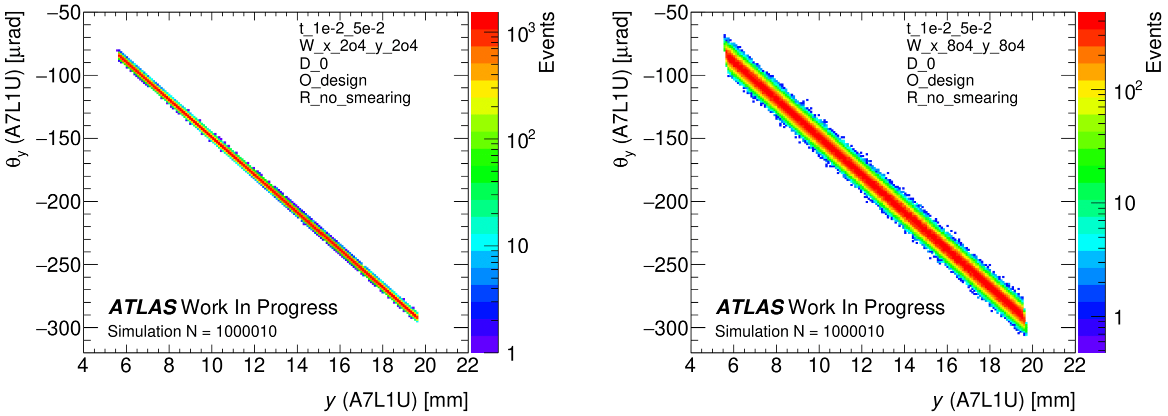

(a) W 2o4 D 0 O design R no smearing.

(b) W 8o4 D 0 O design R no smearing.

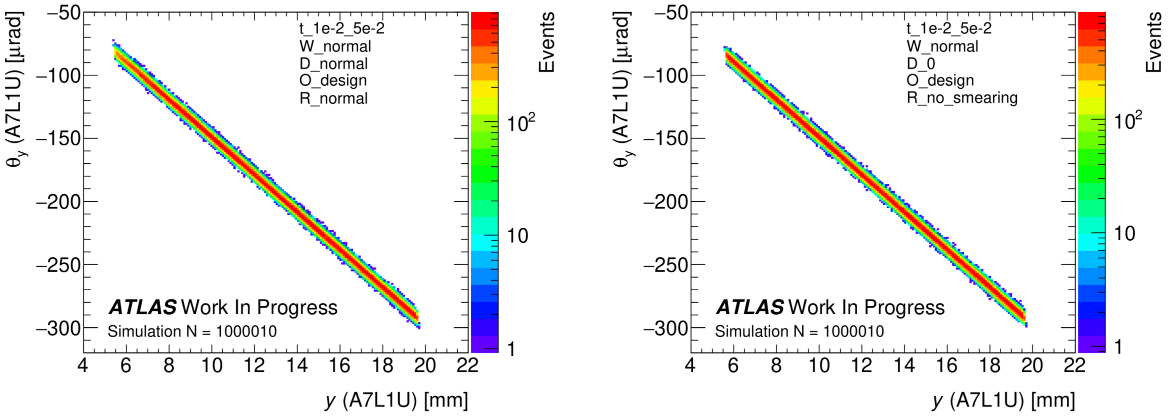

(c) W normal D normal O design R normal.

(d) W normal D 0 O design R no smearing.

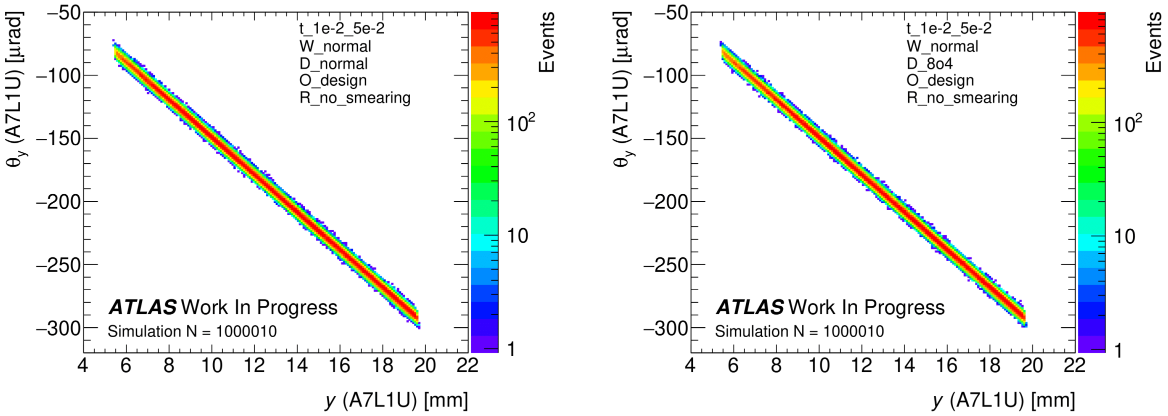

(e) W normal D normal O design R no smearing.

(f) W normal D 8o4 O design R no smearing.

Figure B.70: Inner detector x-θ_x correlation for 6 different simulation settings.

List of References

[1] The LHCb Collaboration, "The LHCb detector at the LHC," *Journal of Instrumentation*, vol. 3, pp. S08005–S08005, aug 2008. URL: **https://doi.org/10.108/1748-0221/3/08/s08005**.

[2] A. Piucci, "The LHCb upgrade," *Journal of Physics: Conference Series*, vol. 878, p. 012012, Jul 2017. URL: **https://doi.org/10.1088/1742-6596/878/1/F012012**.

[3] The TOTEM Collaboration, "First determination of the parameter at s = 13 TeV – probing the existence of a colourless three-gluon bound state," *Phys. Rev. D*, p. 28 p, Dec 2017. Submitted to Phys.Rev., URL: **https://cds.cern.ch/record/2298154**.

[4] S. H. Stark, "Study of forward elastic pp scattering at $\sqrt{s} = 8$ TeV with the ALFA detector," Jan 2017. Presented 24 Feb 2017. URL: **http://cds.cern.ch/record/2283206**.

[5] J. Morrison, *Modern Physics: for Scientists and Engineers*. Elsevier Science, 2009. ISBN: 9780123859112.

[6] Nicola Serra, *Standard Model*, Accessed on 31-12-2019. URL: **http://www.physik.uzh.ch/groups/serra/StandardModel.html**.

[7] The LHCb Collaboration, "Observation of $j/\psi\phi$ structures consistent with exotic states from amplitude analysis of $B^+ \to j/\psi\phi K^+$ decays," *Phys. Rev. Lett.*, vol. 118, p. 022003, Jan 2017. URL: **https://link.aps.org/doi/10.1103/PhysRevLett.118.022003**.

[8] The LHCb Collaboration, "Observation of $j/\psi p$ resonances consistent with pentaquark states in $\Lambda_b^0 \to j/\psi K^- p$ decays," *Phys. Rev. Lett.*, vol. 115, p. 072001, Aug 2015. URL: **https://link.aps.org/doi/10.1103/PhysRevLett.115.072001**.

[9] M. Thomson, *Modern particle physics*. New York: Cambridge University Press, 2013. ISBN: 9781107034266.

[10] S. Bethke, "Experimental tests of asymptotic freedom," *Progress in Particle and Nuclear Physics*, vol. 58, no. 2, pp. 351 – 386, 2007. URL: **http://www.sciencedirect.com/science/article/pii/S0146641006000615**.

[11] P. Jenni, M. Nordberg, M. Nessi, and K. Jon-And, *ATLAS Forward Detectors for Measurement of Elastic Scattering and Luminosity*. Technical Design Report ATLAS, Geneva: CERN, 2008. URL: **http://cds.cern.ch/record/1095847**.

[12] T. Regge, "Introduction to complex orbital momenta," *Nuovo Cim.*, vol. 14, p. 951, 1959. URL: **https://link.springer.com/article/10.1007/BF02728177**.

[13] L. A. Tompkins, "A Measurement of the proton-proton inelastic scattering cross-section at $\sqrt{s}$ =7 TeV with the ATLAS detector at the LHC," 2011. Presented 13 May 2011. URL: **http://cds.cern.ch/record/1367400**.

[14] The TOTEM Collaboration, "Proton-proton elastic scattering at the LHC energy of $\sqrt{s}$ = 7 TeV. Elastic pp Scattering at the LHC at s =7 TeV," *EPL*, vol. 95, p. 41001. 12 p, Oct 2011. Comments: 12pages, 5 figures, CERN preprint, URL: **http://cds.cern.ch/record/1361010**.

[15] The ATLAS Collaboration, "Measurement of the total cross section from elastic scattering in pp collisions at $\sqrt{s}$=8 tev with the atlas detector," *Physics Letters B*, vol. 761, pp. 158 – 178, 2016. URL: **http://www.sciencedirect.com/science/article/pii/S0370269316304403**.

[16] D. Fagundes, M. Menon, and P. Silva, "On the rise of proton-proton cross-sections at high energies," *Journal of Physics G Nuclear and Particle Physics*, vol. 40, 08 2012. URL: **https://iopscience.iop.org/article/10.1088/0954-3899/40/6/065005**.

[17] M. Froissart, "Asymptotic behavior and subtractions in the mandelstam representation," *Phys. Rev.*, vol. 123, pp. 1053–1057, Aug 1961. URL: **https://link.aps.org/doi/10.1103/PhysRev.123.1053**.

[18] A. Martin, "Unitarity and high-energy behavior of scattering amplitudes," *Phys. Rev.*, vol. 129, pp. 1432–1436, Feb 1963. URL: **https://link.aps.org/doi/10.1103/PhysRev.129.1432**.

[19] "Measurement of the total cross section from elastic scattering in pp collisions at $\sqrt{s}$ =7 tev with the atlas detector," *Nuclear Physics B*, vol. 889, pp. 486 – 548, 2014. URL: **http://www.sciencedirect.com/science/article/pii/S0550321314003253**.

[20] P. W. Rasmussen, *Elastic pp Scattering at ALFA with* $\sqrt{s} = 13$ *TeV and* $\beta^* = 2.5$ *km*. Master thesis, University of Copenhagen, Sept 2018.

[21] J. R. Cudell, V. V. Ezhela, P. Gauron, K. Kang, Y. V. Kuyanov, S. B. Lugovsky, B. Nicolescu, and N. P. Tkachenko, "Hadronic scattering amplitudes: Medium-energy constraints on asymptotic behavior," *Phys. Rev. D*, vol. 65, p. 074024, Mar 2002. URL: **https://link.aps.org/doi/10.1103/PhysRevD.65.074024**.

[22] C. P. et al. (Particle Data Group), "Total Hadronic Cross Section.," *Chin. Phys.*, vol. C40, 2017. URL: **http://www-pdg.lbl.gov/2017/reviews/rpp2017-rev-cross-section-plots.pdf**.

[23] E. Martynov and B. Nicolescu, "Unified model for small-t and high-t scattering at high energies: predictions at rhic and lhc," *The European Physical Journal C*, vol. 56, pp. 57–62, Jul 2008. URL: **https://doi.org/10.1140/epjc/s10052-008-0629-z**.

[24] E. Martynov and B. Nicolescu, "Did totem experiment discover the odderon?," *Physics Letters B*, vol. 778, pp. 414 – 418, 2018. URL: **http://www.sciencedirect.com/science/article/pii/S0370269318300625**.

[25] The TOTEM collaboration, "Proton-proton elastic scattering at the LHC energy of $\sqrt{s}$ = 7 tev," *EPL (Europhysics Letters)*, vol. 95, p. 41001, jul 2011. URL: **https://doi.org/10.1209.2F0295-5075.2F95.2F41001**.

[26] The TOTEM Collaboration, "Measurement of elastic pp scattering at $\sqrt{s}$ = 8 tev in the coulomb-nuclear interference region: determination of the ρ-parameter and the total cross-section," *The European Physical Journal C*, vol. 76, p. 661, Nov 2016. URL: **https://doi.org/10.1140/epjc/s10052-016-4399-8**.

[27] P. Grafstrom, "Elastic scattering studies," *ATLAS Standard Model plenary*, 2019. URL: **https://indico.cern.ch/event/801427/contributions/3333393/attachments/1803947/2943279/SM28.2.2019.pdf**.

[28] T. S. Pettersson and P. Lefèvre, "The Large Hadron Collider: conceptual design," Tech. Rep. CERN-AC-95-05-LHC, Oct 1995. URL: **http://cds.cern.ch/record/291782**.

[29] O. S. Brüning, P. Collier, P. Lebrun, S. Myers, R. Ostojic, J. Poole, and P. Proudlock, *LHC Design Report*. CERN Yellow Reports: Monographs, Geneva: CERN, 2004. URL: **https://cds.cern.ch/record/782076**.

[30] M. Weiss, "Radio-frequency quadrupole; 1987 ed.," no. CERN-PS-87-51-LI, 1987. URL: **https://cds.cern.ch/record/371094**.

[31] E. Mobs, "The CERN accelerator complex. Complexe des accélérateurs du CERN," Jul 2016. General Photo, URL: **https://cds.cern.ch/record/2197559**.

[32] P. Hansen, *Particle Detectors and Accelerators - Lecture Notes*. Polyteknisk Kompendie, University of Copenhagen, 2015.

[33] J. Wenninger, "Machine protection and operation for lhc," 08 2016.

[34] A. Siemko, "What happens during and after a quench ?," 2001. URL: **http://cds.cern.ch/record/567209**.

[35] W. Herr and B. Muratori, "Concept of luminosity," 2006. URL: **http://cds.cern.ch/record/941318**.

[36] E. Maurice, "Fixed-target physics at LHCb," in *5th Large Hadron Collider Physics Conference (LHCP 2017) Shanghai, China, May 15-20, 2017*, 2017. URL: **https://arxiv.org/abs/1708.05184**.

[37] B. Holzer, "Transverse Beam Dynamics," *CERN Yellow Rep. School Proc.*, vol. 1, p. 145. 32 p, 2018. URL: **https://cds.cern.ch/record/2674126**.

[38] S. Redaelli, "The collimation system: defense against beam loss," *CERN courier*, 2013.

[39] D. Mirarchi, "Vol. 31 - Crystal Collimation for LHC. Crystal collimation for LHC," Aug 2015. Presented 18 Jun 2015. URL: **https://cds.cern.ch/record/2036210**.

[40] M. Kuhn, "Emittance Preservation at the LHC," Mar 2013. Presented 05 Apr 2013. URL: **https://cds.cern.ch/record/1544573**.

[41] E. B. Holzer, B. Dehning, E. Effinger, J. Emery, G. Ferioli, J. L. González, E. Gschwendtner, G. Guaglio, M. Hodgson, D. Kramer, R. Leitner, L. Ponce, V. Prieto, M. Stockner, and C. Zamantzas, "Beam Loss Monitoring System for the LHC," Tech. Rep. CERN-AB-2006-009, CERN, Geneva, Sep 2005. URL: **https://cds.cern.ch/record/930275**.

[42] B. Dehning, "Beam loss monitors at lhc," *CERN Yellow Reports*, vol. 2, no. 0, p. 303, 2016. URL: **https://e-publishing.cern.ch/index.php/CYR/article/view/238**.

[43] M. Brice, "A fast wire scanner, used to measure the transverse density distribution of beams circulating in an accelerator or storage ring.. Les fils rapides servent à mesurer la distribution de densité transversale des faisceaux circulant dans un accélérateur ou dans un anneau de stockage.." URL: **https://cds.cern.ch/record/43035**, May 2002.

[44] M. Kuhn, "Transverse Emittance Measurement and Preservation at the LHC," 2016. Presented 20 Jun 2016. URL: **https://cds.cern.ch/record/2229712**.

[45] R. Jung, F. Méot, and L. Ponce, *LHC proton beam diagnostics using synchrotron radiation*. CERN Yellow Reports: Monographs, Geneva: CERN, 2004. URL: **https://cds.cern.ch/record/787922**.

[46] R. Maccaferri, S. Bettoni, D. Tommasini, and W. V. Delsolaro, "Manufacture and test of the prototype 5 t superconducting undulator for the lhc synchrotron radiation profile monitor," *IEEE Transactions on Applied Superconductivity*, vol. 16, pp. 1865–1868, June 2006. URL: **https://inspirehep.net/literature/738177**.

[47] G. F. Knoll, *Radiation Detection and Measurement; 3rd ed.* New York, NY: Wiley, 2000. URL: **https://cds.cern.ch/record/441925**.

[48] L. Cerrito, *Radiation and detectors: introduction to the physics of radiation and detection devices*. Graduate texts in physics, Cham: Springer, 2017. URL: **https://cds.cern.ch/record/2244807**.

[49] J. Muller, "The LHCb SciFi Tracker: studies on scintillating fibres and development of quality assurance procedures for the SciFi serial production," Mar 2018. Presented 02 May 2018. URL: **https://cds.cern.ch/record/2316726**.

[50] S. Dunst and P. Tomancak, "Imaging flies by fluorescence microscopy: Principles, technologies, and applications," *Genetics*, vol. 211, no. 1, pp. 15–34, 2019. URL: **https://www.genetics.org/content/211/1/15**.

[51] P. W. Atkins and J. De Paula, *Atkins' physical chemistry; 9th ed.* Oxford: Oxford Univ. Press, 2010. URL: **https://cds.cern.ch/record/1440901**.

[52] C. Joram, G. Haefeli, and B. Leverington, "Scintillating fibre tracking at high luminosity colliders," *Journal of Instrumentation*, vol. 10, pp. C08005–C08005, 08 2015. URL: **https://iopscience.iop.org/article/10.1088/1748-0221/10/08/C08005/pdf**.

[53] T. Förster, "Zwischenmolekulare energiewanderung und fluoreszenz," *Annalen der Physik*, vol. 437, no. 1-2, pp. 55–75, 1948. URL: **https://onlinelibrary.wiley.com/doi/abs/10.1002/andp.19484370105**.

[54] A. Cavalcante, B. Dey, L. Gavardi, L. Gruber, C. Joram, R. Kristic, O. Shinji, and V. Zhukov, "Refining and testing 12,000 km of scintillating plastic fibre for the LHCb SciFi tracker," *Journal of Instrumentation*, vol. 13, pp. P10025–P10025, oct 2018. URL: **https://iopscience.iop.org/article/10.1088/1748-0221/13/10/P10025**.

[55] M. Ozkaynak, "Error Analysis of Attenuation Length Measurements for the LHCb SciFi Quality Assurance Lab," Oct 2019. URL: **http://cds.cern.ch/record/2694149**.

[56] J. Pequenao, "Computer generated image of the whole ATLAS detector." URL: **https://cds.cern.ch/record/1095924**, March 2008.

[57] The ATLAS Collaboration, "The ATLAS experiment at the CERN large hadron collider," *Journal of Instrumentation*, vol. 3, pp. S08003–S08003, aug 2008. URL: **https://doi.org/10.1088/1748-0221/3/08/s08003**.

[58] H. Bertelsen, G. C. Montoya, P.-O. Deviveiros, T. Eifert, G. Galster, J. Glatzer, S. Haas, A. Marzin, M. S. Oliveira, T. Pauly, K. Schmieden, R. Spiwoks, and J. Stelzer, "Operation of the upgraded ATLAS central trigger processor during the LHC run 2," *Journal of Instrumentation*, vol. 11, pp. C02020–C02020, feb 2016. URL: **https://doi.org/10.1088/2F1748-0221/2F11/2F02/2Fc02020**.

[59] S. Jakobsen, "Commissioning of the Absolute Luminosity For ATLAS detector at the LHC," Dec 2013. Presented 31 Jan 2014. URL: **https://cds.cern.ch/record/1637195**.

[60] Kuraray, *Plastic Scintillating Fibers*. URL: **http://kuraraypsf.jp/psf/**.

[61] The LHCb Collaboration, *LHCb Tracker Upgrade Technical Design Report*. No. CERN-LHCC-2014-001. LHCB-TDR-015, Feb 2014. URL: **https://cds.cern.ch/record/1647400**.

[62] M. Deckenhoff, "Scintillating Fibre and Silicon Photomultiplier Studies for the LHCb upgrade," Dec 2015. Presented 23 Feb 2016. URL: **https://cds.cern.ch/record/2140068**.

[63] The LHCb Collaboration, "LHCb VELO Upgrade Technical Design Report," Tech. Rep. CERN-LHCC-2013-021. LHCB-TDR-013, Nov 2013. URL: **https://cds.cern.ch/record/1624070**.

[64] The LHCb Collaboration, "LHCb PID Upgrade Technical Design Report," Tech. Rep. CERN-LHCC-2013-022. LHCB-TDR-014, Nov 2013. URL: **https://cds.cern.ch/record/1624074**.

[65] The LHCb Collaboration, "LHCb Trigger and Online Upgrade Technical Design Report," Tech. Rep. CERN-LHCC-2014-016. LHCB-TDR-016, May 2014. URL: **http://cds.cern.ch/record/1701361**.

[66] The LHCb Collaboration, "Letter of Intent for the LHCb Upgrade," Tech. Rep. CERN-LHCC-2011-001. LHCC-I-018, CERN, Geneva, Mar 2011. URL: **http://cds.cern.ch/record/1333091**.

[67] C. Joram, U. Uwer, B. D. Leverington, T. Kirn, S. Bachmann, R. J. Ekelhof, and J. Müller, "LHCb Scintillating Fibre Tracker Engineering Design Review Report: Fibres, Mats and Modules," Tech. Rep. LHCb-PUB-2015-008. CERN-LHCb-PUB-2015-008, CERN, Geneva, Mar 2015. URL: **https://cds.cern.ch/record/2004811**.

[68] B. D. Leverington, "The LHCb Upgrade Scintillating Fibre Tracker," *PoS*, vol. TIPP2014, p. 113, 2014. URL: **https://inspirehep.net/literature/1360092** doi =.

[69] C. Joram, "Upgrading lhcb with a large scintillating fibre tracker," *Newsletter of the EP department*, 2014.

[70] B. D. Leverington, *C-Frames: Mechanics and Services*, September 2017. SciFi General Meeting.

[71] C. Joram and X. Pons, "A vacuum system for the thermal insulation of the SciFi distribution lines and manifolds," Tech. Rep. LHCb-PUB-2017-022. CERN-LHCb-PUB-2017-022, CERN, Geneva, Dec 2017. URL: **https://cds.cern.ch/record/2295263**.

[72] C. Joram, *Dry gas flushing system for the cold boxes of the LHCb SciFi*, October 2017. SciFi Dry gas flushing system meeting.

[73] P. G. S. S. Oliver Holme, Manuel Gonzalez Berges, *The JCOP Framework*. URL: **https://accelconf.web.cern.ch/ica05/proceedings/pdf/O3_005.pdf**.

[74] C. Gaspar, *WinCC-OA Introduction for Newcomers*. URL: **http://lhcb-online.web.cern.ch/lhcb-online/ecs/pvssintro.htm**.

[75] The SciFi Collaboration, *SciFi Tracker Controls and Monitoring Design of the SciFi ECS*. URL: **https://edms.cern.ch/ui/file/2060160/0.5/SciFi-controls-design-v0.5_docx_cpdf.pdf**.

[76] P.-Y. Duval and L. G. Casdoso, *Guide for ECS FSM design in LHCb sub-detectors*, 28 November 2018. EDMS 655828.

[77] W-IE-NE-R Power Electronics GmbH, *MARATON Power Supply System - Technical manual*, 13 April 2010. URL: **http://file.wiener-d.com/documentation/MARATON/WIENER_MARATON_HighRad_Manual_A0.pdf**.

[78] CERN Accelerator Beam Physics Group, *MAD - Methodical Accelerator Design*, February 2020. URL: **http://madx.web.cern.ch/madx/**.

[79] The ATLAS Collaboration, "Measurement of beam background in special high-β^* runs at $\sqrt{s}$ = 900 GeV using the ATLAS-ALFA detectors." URL: **https://cds.cern.ch/record/2693518**, October 2019.

[80] D. Mirarchi, *Special collimation schemes for reduced background during high-β run*, January 2019. URL: **https://indico.cern.ch/event/775252/contributions/3258425/attachments/1778998/2893392/Collimation_DM.pdf**.

[81] A. E. Phoboo, *Crystal cleaning the LHC beam*, November 2018. URL: **https://home.cern/news/news/accelerators/crystal-cleaning-lhc-beam**.

[82] S. van der Meer, "Calibration of the effective beam height in the ISR," Tech. Rep. CERN-ISR-PO-68-31. ISR-PO-68-31, CERN, Geneva, 1968. URL: **https://cds.cern.ch/record/296752**.

[83] The ATLAS Collaboration, "Improved luminosity determination in pp collisions at sqrt(s) = 7 TeV using the ATLAS detector at the LHC," *Eur. Phys. J.*, vol. C73, no. 8, p. 2518, 2013. URL: **https://link.springer.com/article/10.1140/epjc/s10052-013-2518-3**.